TOPICAL REVIEW • OPEN ACCESS

Production and processing of graphene and related materials

To cite this article: Claudia Backes *et al* 2020 *2D Mater.* **7** 022001

View the article online for updates and enhancements.

Recent citations

- Recent progress and strategies in photodetectors based on 2D inorganic/organic heterostructures
Hongwei Li *et al*

- Properties of Graphene-Related Materials Controlling the Thermal Conductivity of Their Polymer Nanocomposites
Samuele Colonna *et al*

- Approaching the Limit of Electromechanical Performance in Mixed-Phase Nanocomposites
Conor S. Boland

This content was downloaded from IP address 134.130.185.6 on 03/11/2020 at 08:30

2D Materials

OPEN ACCESS

TOPICAL REVIEW

Production and processing of graphene and related materials

RECEIVED
17 May 2018

REVISED
13 March 2019

ACCEPTED FOR PUBLICATION
30 April 2019

PUBLISHED
29 January 2020

Original content from this work may be used under the terms of the Creative Commons Attribution 3.0 licence.

Any further distribution of this work must maintain attribution to the author(s) and the title of the work, journal citation and DOI.

Claudia Backes[1,2], Amr M Abdelkader[3], Concepción Alonso[4], Amandine Andrieux-Ledier[5], Raul Arenal[6,7,72], Jon Azpeitia[8], Nilanthy Balakrishnan[9], Luca Banszerus[10], Julien Barjon[11], Ruben Bartali[12], Sebastiano Bellani[13], Claire Berger[14,15], Reinhard Berger[16], M M Bernal Ortega[17], Carlo Bernard[18], Peter H Beton[9], André Beyer[19], Alberto Bianco[20], Peter Bøggild[65], Francesco Bonaccorso[13,68], Gabriela Borin Barin[21], Cristina Botas[22], Rebeca A Bueno[8], Daniel Carriazo[22,23], Andres Castellanos-Gomez[8], Meganne Christian[24], Artur Ciesielski[25], Tymoteusz Ciuk[26], Matthew T Cole[27], Jonathan Coleman[2], Camilla Coletti[13,28], Luigi Crema[12], Huanyao Cun[18], Daniela Dasler[29], Domenico De Fazio[3], Noel Díez[22], Simon Drieschner[30], Georg S Duesberg[31], Roman Fasel[21,33], Xinliang Feng[16], Alberto Fina[17], Stiven Forti[28], Costas Galiotis[34,35], Giovanni Garberoglio[36], Jorge M García[64], Jose Antonio Garrido[38], Marco Gibertini[39], Armin Gölzhäuser[19], Julio Gómez[40], Thomas Greber[18], Frank Hauke[29], Adrian Hemmi[18], Irene Hernandez-Rodriguez[8], Andreas Hirsch[29], Stephen A Hodge[3], Yves Huttel[8], Peter U Jepsen[65], Ignacio Jimenez[8], Ute Kaiser[66], Tommi Kaplas[32], HoKwon Kim[41], Andras Kis[41], Konstantinos Papagelis[35,42], Kostas Kostarelos[43], Aleksandra Krajewska[26,74], Kangho Lee[31], Changfeng Li[44], Harri Lipsanen[44], Andrea Liscio[70], Martin R Lohe[16], Annick Loiseau[46], Lucia Lombardi[3], Maria Francisca López[8], Oliver Martin[29], Cristina Martín[47], Lidia Martínez[8], Jose Angel Martin-Gago[8], José Ignacio Martínez[8], Nicola Marzari[39], Álvaro Mayoral[7,71], John McManus[2], Manuela Melucci[45], Javier Méndez[8], Cesar Merino[48], Pablo Merino[8,69], Andreas P Meyer[29], Elisa Miniussi[18], Vaidotas Miseikis[28], Neeraj Mishra[28], Vittorio Morandi[24], Carmen Munuera[8], Roberto Muñoz[8], Hugo Nolan[2], Luca Ortolani[24], Anna K Ott[3,73], Irene Palacio[8], Vincenzo Palermo[45,50], John Parthenios[35], Iwona Pasternak[26,51], Amalia Patane[9], Maurizio Prato[23,52,53], Henri Prevost[46], Vladimir Prudkovskiy[14], Nicola Pugno[54,55,56], Teófilo Rojo[22,57], Antonio Rossi[28], Pascal Ruffieux[21], Paolo Samorì[25], Léonard Schué[46], Eki Setijadi[12], Thomas Seyller[58], Giorgio Speranza[12], Christoph Stampfer[10], Ingrid Stenger[11], Wlodek Strupinski[26,51], Yuri Svirko[32], Simone Taioli[36,37], Kenneth B K Teo[59], Matteo Testi[12], Flavia Tomarchio[3], Mauro Tortello[60], Emanuele Treossi[45], Andrey Turchanin[61], Ester Vazquez[47], Elvira Villaro[62], Patrick R Whelan[65], Zhenyuan Xia[45,50], Rositza Yakimova[63], Sheng Yang[16], G Reza Yazdi[63], Chanyoung Yim[31], Duhee Yoon[3], Xianghui Zhang[19], Xiaodong Zhuang[16], Luigi Colombo[67], Andrea C Ferrari[3] and Mar Garcia-Hernandez[8,75]

[1] Physikalisch-Chemisches Institut, University of Heidelberg, Im Neuenheimer Feld 253, 69120 Heidelberg, Germany
[2] School of Physics, Centre for Research on Adaptive Nanostructures and Nanodevices (CRANN) and Advanced Materials and BioEngineering Research (AMBER), Trinity College Dublin, Dublin 2, Ireland
[3] Cambridge Graphene Centre, 9 JJ Thomson Avenue, University of Cambridge, CB3 0FA, United Kingdom
[4] Department Applied Physical Chemistry, Autonomous University of Madrid, 28049 Madrid, Spain
[5] ONERA, Département Physique, Instrumentation, Environnement et Espace—Université Paris Saclay—29 Avenue de la Division Leclerc, 92320 Chatillon, France
[6] ARAID Fundation, Calle Mariano de Luna, 50018 Zaragoza, Spain
[7] Laboratorio de Microscopias Avanzadas (LMA) Instituto de Nanociencia de Aragon (INA), Universidad de Zaragoza, Calle Mariano Esquillor, 50018 Zaragoza, Spain
[8] Materials Science Factory, Instituto de Ciencia de Materiales de Madrid, Consejo Superior de Investigaciones Científicas, C/Sor Juana Ines de la Cruz 3, Madrid, E-28049, Spain
[9] School of Physics and Astronomy, University of Nottingham, University Park, Nottingham, NG7 2RD, United Kingdom
[10] JARA-FIT and 2nd Institute of Physics, RWTH Aachen University, Aachen, Germany
[11] Groupe d'Etude de la Matière Condensée (GEMaC), CNRS—Université Versailles ST Quentin—Université Paris Saclay, 45 Avenue des Etats Unis, Versailles, France
[12] Fondazione Bruno Kessler, via Sommarive 18, 38123 Trento, Italy
[13] Graphene Labs, Istituto Italiano di Tecnologia, Via Morego 30, 16163 Genova, Italy
[14] Institut Néel, CNRS—University Grenoble-Alpes, 25 rue des Martyrs, 38042 Grenoble, France
[15] Georgia Institute of Technology, School of physics, Atlanta, GA, United States of America
[16] Center for Advancing Electronics Dresden (cfaed) and Department of Chemistry and Food Chemistry, Technische Universität Dresden, Mommsenstr. 4, 01062 Dresden, Germany
[17] Dipartimento di Scienza Applicata e Tecnologia, Politecnico di Torino, Alessandria Campus, Viale Teresa Michel 5, 15121 Alessandria, Italy
[18] Physik-Institut, University of Zürich, Winterthurerstrasse 190, CH-8057 Zürich, Switzerland
[19] Physics of Supramolecular Systems, Bielefeld University, Universitätsstr. 25, 33615 Bielefeld, Germany
[20] University of Strasbourg, CNRS, Immunology, Immunopathology and Therapeutic Chemistry, UPR 3572, 67000 Strasbourg, France
[21] Empa, Swiss Federal Laboratories for Materials Science and Technology, Überlandstr. 129, 8600 Dübendorf, Switzerland
[22] CIC EnergiGUNE. Parque Tecnológico de Álava, 01510-Miñano, Álava, Spain
[23] IKERBASQUE, Basque Foundation for Science, 48013-Bilbao, Spain
[24] Institute for Microelectronic and Microsystems (IMM) Section of Bologna - CNR, via Gobetti 101, 40129 Bologna, Italy

© 2020 The Author(s). Published by IOP Publishing Ltd

[25] Université de Strasbourg, CNRS, ISIS, 8 alleé Gaspard Monge, 67000 Strasbourg, France
[26] Instytut Technologii Materiałów Elektronicznych, Wólczyńska 133, 01-919 Warszawa, Poland
[27] Department of Electronic and Electrical Engineering, BA2 7AY, Bath, United Kingdom
[28] Center for Nanotechnology Innovation @NEST, Istituto Italiano di Tecnologia, P.zza S. Silvestro 12, 56127, Pisa, Italy
[29] Chair of Organic Chemistry II and Joint Institute of Advanced Materials and Processes, Nikolaus-Fiebiger-Str. 10, Friedrich-Alexander Universität Erlangen-Nürnberg, 91058 Erlangen, Germany
[30] Walter Schottky Institut Technische Universität München, Am Coulombwall 4, D-85748 Garching, Germany
[31] Institute of Physics, Universität der Bundeswehr München, 85577 Neubiberg, Germany
[32] Institute of Photonics, University of Eastern Finland, Yliopistokatu 7, 80100 Joensuu, Finland
[33] Department of Chemistry and Biochemistry, University of Bern, 3012 Bern, Switzerland
[34] Department of Chemical Engineering, University of Patras, Patras 26504, Greece
[35] Institute of Chemical Engineering Sciences, Foundation for Research and Technology- Hellas (FORTH/ICE-HT), Patras 26504, Greece
[36] European Centre for Theoretical Studies in Nuclear Physics and Related Areas (ECT∗-FBK), 38123, Trento, Italy and Trento Institute for Fundamental Physics and Applications (TIFPA-INFN), 38123 Trento, Italy
[37] Faculty of Mathematics and Physics, Charles University, Praha 8, 180 00 Prague, Czech Republic
[38] Instituto Catalán de Nanotecnologia ICN2, UAB Campus, Bellaterra, (Barcelona) 08193, Spain
[39] Theory and Simulation of Materials (THEOS), and National Centre for Computational Design and Discovery of Novel Materials (MARVEL), École Polytechnique Fédérale de Lausanne, CH-1015 Lausanne, Switzerland
[40] Avanzare Innovacion Tecnologica S.L., Avda Lentiscares 4-6 Navarrete, Spain
[41] EPFL, Electrical Engineering Institute and Institute of Materials Science and Engineering, École Polytechnique Fédérale de Lausanne (EPFL), CH-1015 Lausanne, Switzerland
[42] School of Physics, Department of Solid State Physics, Aristotle University of Thessaloniki, Thessaloniki 54124, Greece
[43] University of Manchester, Manchester, United Kingdom
[44] Department of Electronics and Nanoengineering, Aalto University, Tietotie 3, 02150 Espoo, Finland
[45] Institute of Organic Synthesis and Photoreactivity (ISOF), CNR, via Gobetti 101, 40129, Bologna, Italy
[46] Laboratoire d'Etude des Microstructures (LEM), CNRS–ONERA, Université Paris Saclay, 29 Avenue de la Division Leclerc, 92320 Chatillon, France
[47] Instituto Regional de Investigación Científica Aplicada (IRICA), Universidad de Castilla-la Mancha, Avda Camilo Jose Cela, 13071, Ciudad Real, Spain
[48] ACM Advanced Carbon Materials, Grupo Antolin Ingeniería, SA, Ctra. Madrid—Irún, km. 244.8, E09007 Burgos, Spain
[49] Consorzio Nazionale Interuniversitario per le Telecomunicazioni, Via Moruzzi 1, 56124, Pisa, Italy
[50] Department of Industrial and Materials Science, Chalmers University of Technology, Horsalsvagen 7A, SE-412 96 Gothenburg, Sweden
[51] Faculty of Physics, Warsaw University of Technology, Koszykowa, 75 00-662 Warsaw, Poland
[52] Carbon Bionanotechnology Laboratory, CIC biomaGUNE, Paseo de Miramón 182, 20009 Donostia-San Sebastián, Spain
[53] Dipartimento di Scienze Chimiche e Farmaceutiche, INSTM UdR Trieste, Università degli Studi di Trieste, Via Licio Giorgieri 1, 34127 Trieste, Italy
[54] Laboratory of Bio-Inspired and Graphene Nanomechanics, Department of Civil, Environmental and Mechanical Engineering, University of Trento, Via Mesiano 77, 38123 Trento, Italy
[55] Ket Lab, Edoardo Amaldi Foudation, Via del Politecnico snc, 00133 Rome, Italy
[56] School of Engineering and Materials Science, Queen Mary University of London, Mile End Road, London E1 4NS, United Kingdom
[57] Universidad del País Vasco UPV/EHU, 48080-Bilbao, Spain
[58] Technische Universität Chemnitz, Institut für Physik, Reichenhainer Str. 70, 09126 Chemnitz, Germany
[59] Buckingway Business Park, Anderson Road, Swavesey, Cambridge CB24 4FQ, United Kingdom
[60] Politecnico di Torino, C.so Duca degli Abruzzi 24, 10129 Torino, Italy
[61] Institute of Physical Chemistry, Friedrich Schiller University Jena, Lessingstr. 10, 07743 Jena, Germany
[62] Interquimica, C/Antonio Nebrija, 8- Bajo. CP 26006, Logroño, Spain
[63] University of Linköping, IFM, 58183, Linkoping, Sweden
[64] Instituto de Micro y Nanotecnología, IMN-CNM, CSIC (CEI UAM + CSIC) Isaac Newton, 8, E-28760, Tres Cantos, Madrid, Spain
[65] Center for Nanostructured Graphene (CNG), Technical University of Denmark, Kongens Lyngby, 2800, Denmark
[66] Materialwissenschaftliche Elektronenmikroskopie, Universität Ulm, Albert-Einstein-Allee 11, 89081 Ulm, Germany
[67] Department of Materials Science and Engineering, University of Texas at Dallas, Richardson, TX 75080, United States of America
[68] BeDimensional Spa, Via Albisola 121, 16163 Genova, Italy
[69] Instituto de Física Fundamental, CSIC, Serrano 121, 28006, Madrid, Spain
[70] Institute for Microelectronic and Microsystems (IMM) Section of Roma—CNR, via del fosso del cavaliere 100, 00133 Roma, Italy
[71] Center for High-resolution Electron Microscopy (ChEM), School of Physical Science and Technology, ShanghaiTech University, 393 Middle Huaxia Road, Pudong, Shanghai
[72] Instituto de Ciencia de Materiales de Aragon, CSIC-Univ. Zaragoza, Pedro Cerbuna 12, 50009 Zaragoza, Spain
[73] College of Engineering, Mathematics and Physical Sciences, University of Exeter, Exeter, EX4 4QF, United Kingdom
[74] International Research Centre CENTERA, Institute of High Pressure Physics, Polish Academy of Sciences, Warsaw, 01-142, Poland
[75] Author to whom any correspondence should be addressed.

E-mail: marmar@icmm.csic.es

Keywords: processing of layered materials, inks of layered materials, characterization of layered materials, functionalization of layered materials, synthesis of graphene and related materials, growth of layered materials

Abstract

We present an overview of the main techniques for production and processing of graphene and related materials (GRMs), as well as the key characterization procedures. We adopt a 'hands-on' approach, providing practical details and procedures as derived from literature as well as from the authors' experience, in order to enable the reader to reproduce the results.

Section I is devoted to 'bottom up' approaches, whereby individual constituents are pieced together into more complex structures. We consider graphene nanoribbons (GNRs) produced either by solution processing or by on-surface synthesis in ultra high vacuum (UHV), as well carbon nanomembranes (CNM). Production of a variety of GNRs with tailored band gaps and edge shapes is now possible. CNMs can be tuned in terms of porosity, crystallinity and electronic behaviour.

Section II covers 'top down' techniques. These rely on breaking down of a layered precursor, in the graphene case usually natural crystals like graphite or artificially synthesized materials, such as highly oriented pyrolythic graphite, monolayers or few layers (FL) flakes. The main focus of this section is on various exfoliation techniques in a liquid media, either intercalation or liquid phase exfoliation (LPE). The choice of precursor, exfoliation method, medium as well as the control of parameters such as time or temperature are crucial. A definite choice of parameters and conditions yields a particular material with specific properties that makes it more suitable for a targeted application. We cover protocols for the graphitic precursors to graphene oxide (GO). This is an important material for a range of applications in biomedicine, energy storage, nanocomposites, etc. Hummers' and modified Hummers' methods are used to make GO that subsequently can be reduced to obtain reduced graphene oxide (RGO) with a variety of strategies. GO flakes are also employed to prepare three-dimensional (3d) low density structures, such as sponges, foams, hydro- or aerogels. The assembly of flakes into 3d structures can provide improved mechanical properties. Aerogels with a highly open structure, with interconnected hierarchical pores, can enhance the accessibility to the whole surface area, as relevant for a number of applications, such as energy storage. The main recipes to yield graphite intercalation compounds (GICs) are also discussed. GICs are suitable precursors for covalent functionalization of graphene, but can also be used for the synthesis of uncharged graphene in solution. Degradation of the molecules intercalated in GICs can be triggered by high temperature treatment or microwave irradiation, creating a gas pressure surge in graphite and exfoliation. Electrochemical exfoliation by applying a voltage in an electrolyte to a graphite electrode can be tuned by varying precursors, electrolytes and potential. Graphite electrodes can be either negatively or positively intercalated to obtain GICs that are subsequently exfoliated. We also discuss the materials that can be amenable to exfoliation, by employing a theoretical data-mining approach.

The exfoliation of LMs usually results in a heterogeneous dispersion of flakes with different lateral size and thickness. This is a critical bottleneck for applications, and hinders the full exploitation of GRMs produced by solution processing. The establishment of procedures to control the morphological properties of exfoliated GRMs, which also need to be industrially scalable, is one of the key needs. Section III deals with the processing of flakes. (Ultra)centrifugation techniques have thus far been the most investigated to sort GRMs following ultrasonication, shear mixing, ball milling, microfluidization, and wet-jet milling. It allows sorting by size and thickness. Inks formulated from GRM dispersions can be printed using a number of processes, from inkjet to screen printing. Each technique has specific rheological requirements, as well as geometrical constraints. The solvent choice is critical, not only for the GRM stability, but also in terms of optimizing printing on different substrates, such as glass, Si, plastic, paper, etc, all with different surface energies. Chemical modifications of such substrates is also a key step.

Sections IV–VII are devoted to the growth of GRMs on various substrates and their processing after growth to place them on the surface of choice for specific applications. The substrate for graphene growth is a key determinant of the nature and quality of the resultant film. The lattice mismatch between graphene and substrate influences the resulting crystallinity. Growth on insulators, such as SiO_2, typically results in films with small crystallites, whereas growth on the close-packed surfaces of metals yields highly crystalline films. Section IV outlines the growth of graphene on SiC substrates. This satisfies the requirements for electronic applications, with well-defined graphene-substrate interface, low trapped impurities and no need for transfer. It also allows graphene structures and devices to be measured directly on the growth substrate. The flatness of the substrate results in graphene with minimal strain and ripples on large areas, allowing spectroscopies and surface science to be performed. We also discuss the surface engineering by intercalation of the resulting graphene, its integration with Si-wafers and the production of nanostructures with the desired shape, with no need for patterning.

Section V deals with chemical vapour deposition (CVD) onto various transition metals and on insulators. Growth on Ni results in graphitized polycrystalline films. While the thickness of these films can be optimized by controlling the deposition parameters, such as the type of hydrocarbon

precursor and temperature, it is difficult to attain single layer graphene (SLG) across large areas, owing to the simultaneous nucleation/growth and solution/precipitation mechanisms. The differing characteristics of polycrystalline Ni films facilitate the growth of graphitic layers at different rates, resulting in regions with differing numbers of graphitic layers. High-quality films can be grown on Cu. Cu is available in a variety of shapes and forms, such as foils, bulks, foams, thin films on other materials and powders, making it attractive for industrial production of large area graphene films. The push to use CVD graphene in applications has also triggered a research line for the direct growth on insulators. The quality of the resulting films is lower than possible to date on metals, but enough, in terms of transmittance and resistivity, for many applications as described in section V.

Transfer technologies are the focus of section VI. CVD synthesis of graphene on metals and bottom up molecular approaches require SLG to be transferred to the final target substrates. To have technological impact, the advances in production of high-quality large-area CVD graphene must be commensurate with those on transfer and placement on the final substrates. This is a prerequisite for most applications, such as touch panels, anticorrosion coatings, transparent electrodes and gas sensors etc. New strategies have improved the transferred graphene quality, making CVD graphene a feasible option for CMOS foundries. Methods based on complete etching of the metal substrate in suitable etchants, typically iron chloride, ammonium persulfate, or hydrogen chloride although reliable, are time- and resource-consuming, with damage to graphene and production of metal and etchant residues. Electrochemical delamination in a low-concentration aqueous solution is an alternative. In this case metallic substrates can be reused. Dry transfer is less detrimental for the SLG quality, enabling a deterministic transfer.

There is a large range of layered materials (LMs) beyond graphite. Only few of them have been already exfoliated and fully characterized. Section VII deals with the growth of some of these materials. Amongst them, h-BN, transition metal tri- and di-chalcogenides are of paramount importance. The growth of h-BN is at present considered essential for the development of graphene in (opto) electronic applications, as h-BN is ideal as capping layer or substrate. The interesting optical and electronic properties of TMDs also require the development of scalable methods for their production. Large scale growth using chemical/physical vapour deposition or thermal assisted conversion has been thus far limited to a small set, such as h-BN or some TMDs. Heterostructures could also be directly grown.

Section VIII discusses advances in GRM functionalization. A broad range of organic molecules can be anchored to the sp^2 basal plane by reductive functionalization. Negatively charged graphene can be prepared in liquid phase (e.g. via intercalation chemistry or electrochemically) and can react with electrophiles. This can be achieved both in dispersion or on substrate. The functional groups of GO can be further derivatized. Graphene can also be noncovalently functionalized, in particular with polycyclic aromatic hydrocarbons that assemble on the sp^2 carbon network by π–π stacking. In the liquid phase, this can enhance the colloidal stability of SLG/FLG. Approaches to achieve noncovalent on-substrate functionalization are also discussed, which can chemically dope graphene. Research efforts to derivatize CNMs are also summarized, as well as novel routes to selectively address defect sites. In dispersion, edges are the most dominant defects and can be covalently modified. This enhances colloidal stability without modifying the graphene basal plane. Basal plane point defects can also be modified, passivated and healed in ultra-high vacuum. The decoration of graphene with metal nanoparticles (NPs) has also received considerable attention, as it allows to exploit synergistic effects between NPs and graphene. Decoration can be either achieved chemically or in the gas phase. All LMs, can be functionalized and we summarize emerging approaches to covalently and noncovalently functionalize MoS_2 both in the liquid and on substrate.

Section IX describes some of the most popular characterization techniques, ranging from optical detection to the measurement of the electronic structure. Microscopies play an important role, although macroscopic techniques are also used for the measurement of the properties of these materials and their devices. Raman spectroscopy is paramount for GRMs, while PL is more adequate for non-graphene LMs (see section IX.2). Liquid based methods result in flakes with different thicknesses and dimensions. The qualification of size and thickness can be achieved using imaging techniques, like scanning probe microscopy (SPM) or transmission electron microscopy (TEM) or spectroscopic techniques. Optical microscopy enables the detection of flakes on suitable surfaces as well as the measurement of optical properties. Characterization of exfoliated materials is essential to improve the GRM metrology for applications and quality control. For grown GRMs, SPM can

be used to probe morphological properties, as well as to study growth mechanisms and quality of transfer. More generally, SPM combined with smart measurement protocols in various modes allows one to get obtain information on mechanical properties, surface potential, work functions, electrical properties, or effectiveness of functionalization. Some of the techniques described are suitable for '*in situ*' characterization, and can be hosted within the growth chambers. If the diagnosis is made '*ex situ*', consideration should be given to the preparation of the samples to avoid contamination. Occasionally cleaning methods have to be used prior to measurement.

Contents

I. Bottom-up 9
I.1. Graphene nanoribbons 9
I.2. Graphene and carbon nanomembranes 15
I.3. Heterostructures from CNMs 21
II. Top-down 23
II.1. Precursors 23
II.2. Liquid phase exfoliation 24
II.3. GO and RGO 34
II.4. Chemical intercalation and reductive exfoliation 41
II.5. Electrochemical exfoliation 42
II.6. Sonication-assisted versus chemical versus electrochemical exfoliation 45
II.7. Computational modelling of exfoliation of LMs 46
III. Processing of dispersions 48
III.1. Size selection 48
III.2. Inks formulation 48
III.3. Printing and deposition of inks 52
III.4. Applications 60
IV. Graphene growth on SiC 62
IV.1. Sublimation 62
IV.2. CVD growth on SiC 81
V. CVD, PVD & MBE 84
V.1. Growth on metals 84
V.2. Graphene growth on semiconductors 108
V.3. Graphene growth on insulators 108
V.4. Brief comparison of all methods 119
VI. Graphene transfer, placement and decoupling from substrate 120
VI.1. Wet transfer 120
VI.2. Semi-dry transfer: hot press lamination and UV assisted transfer 128
VI.3. Dry transfer using h-BN 132
VI.4. Graphene/PMMA sandwich structures 132
VII. Growth and transfer of other layered materials 134
VII.1. Hexagonal BN 134
VII.2. Layered semiconductors 140
VII.3. Layered materials heterostructures 156
VIII. Functionalization of GRMs 160
VIII.1. Covalent functionalization of graphene 160
VIII.2. Functionalization of GO 165
VIII.3. Noncovalent functionalization of graphene 167
VIII.4. Defect functionalization of GRM 174
VIII.5. Decoration with nanoparticles 176
VIII.6. Functionalization of other LMs 182
IX. Characterization methods 185
IX.1. Microscopies 185
IX.2. Spectroscopies 210
IX.3. Electrical characterization 226
IX.4. Mechanical characterization 234
Conclusions 241
Acknowledgment 241
References 242

List of acronyms

0d	Zero dimensional
1d	One dimensional
1L	One layer
1LG	1 layer graphene
2D	2D Raman peak of graphene
2d	Two dimensional
2LG	2 layer graphene
3d	Three dimensional
3LG	3 layer graphene
4LG	4 layer graphene
AES	Auger electron spectroscopy
AFM	Atomic force microscopy
AGNR	GNRs with armchair edges
ALD	Atomic layer deposition
APCVD	Atmospheric pressure CVD
APS	Ammonium persulfate
ARGO	Reduced graphene oxide-based aerogels
ARPES	Angle resolved photoemission spectroscopy
BHJ	Bulk hetro junction
Bipy	2,2′-Bipyridine
BL	Buffer layer
BLG	Bilayer graphene
BODIPY	2,6-diiodo-1,3,5,7-tetramethyl-8-phenyl-4,4-difluoroboradiazaindacene
BP	Black phosphorus
BP3	3-(Biphenyl-4-yl)propane-1-thiol
BPT	1,1′-biphenyl-4-thiol
BZ	Brillouin zone
Bz	Benzidine
CA	Cellulose acetate
CCS	Confinement controlled sublimation
c-CVD	Catalytical-chemical vapor deposition
CE	Counter electrode
CES	Constant energy surface
CHP	*N*-cyclohexyl-2-pyrrolidone
CL	Cathode luminiscence
CMC	Critical micelle concentration
CMOS	Complementary metal-oxide semiconductor
CMP	Conjugated microporous polymers
CNF	Carbon nanofibre
CNM	Carbon nanomembrane
CNT	Carbon nanotube
COD	1,5-cyclooctadiene
CPD	Critical point drying
CTAB	Cetyl trimethyl ammonium bromide
CVD	Chemical vapour deposition
D	D Raman peak
DA	Diels-Alder
DAP	Donor–acceptor pairs
db	Dangling bonds
DBT	4-docosyloxy-benzenediazonium tetrafluoroborate
DCM	Dichloromethane
DEA	Dissociative electron attachment
DES	Diethyl sulphide
DFT	Density functional theory
DGM	Density gradient medium
DGU	Density gradient ultracentrifugation
Dh	Decahedral
DI	Deionized water
DIC	Differential interference contrast
DMAc	*N*,*N*′-dimethylacetamide
DME	1,2-dimethoxyethane
DMF	Dimethylformamide
DMSO	Dimethylsulfoxide
DOS	Density of states
DOTA	1,4,7,10-tetraazacyclododecane-1,4,7,10-tetraacetic acid
DSSC	Dye-sensitized solar cell
EA	Elemental analysis
EBSD	Electron back scattering diffraction
EC	Ethyl cellulose
EDA	Ethylene-diamine
EE	Electrochemical exfoliation
EEG	Electrochemically exfoliated graphene
EG	Epitaxial graphene
EVA	Ethylene vinyl acetate
FCC	Face-centered cubic
FESEM	Field emission scanning electron microscope
FET	Field effect transistor
FIB	Focused ion beam
FL	Few layer
FLaT	Functional layer transfer
FLG	Few layer graphene
FoM	Figure of merit
FS	Fermi surface
FTIR	Fourier transform infrared spectroscopy
FWHM	Full width at half maximum
G	G Raman peak
G3DCN	Graphene-based covalent networks
GANF	Grupo Antolin nanofibres
G_{Factor}	Gauge factor
GF	Graphene foam
GIC	Graphite intercalation compound
GnP	Graphene nanoplatelets
GNR	Graphene nanoribbons, nanometer wide graphene strips exhibiting a bandgap
GO	Graphene oxide
GOS	Graphene on silicon
GRM	Graphene and related material
GRMs	Graphene and related materials
HAADF	High angle annular dark field
HATU	O-(7-Azabenzotriazole-1-yl)-*N*,*N*,*N*,*N*′-tetramethyluronium hexafluorophosphate
HBC	Hexabenzocoronene
HBC-Br	2-Bromo-11-(1′-[4′-(S-Acetylthiomethyl)phenyl]acetyl)-5,8,14,17-tetra(3′,7′-dimethyloctyl)-hexa-peri-hexabenzocoronene

HBC-CN	2-Cyano-11-(1′-[4′-(S-Acetylthiomethyl)phenyl]acetyl)-5,8,14,17-tetra(3′,7′-dimethyloctyl)-hexa-peri-hexabenzocoronene
HIM	Helium ion microscope
hMDM	Human monocyte macrophages
HMDS	Hexamethyldisilazane
HOPG	Highly oriented pyrolytic graphite
HPB	*S*,*S*′-(3′,4′,5′,6′-tetraphenyl-[1,1′:2′,1″-terphenyl]-4,4″-diyl) diethanethioate
HPL	Hot-press lamination
HREM	High resolution electron microscopy
HRP	Horseradish peroxidase
HRTEM	High resolution transmission electron microscopy
ICS	Ion cluster source
IFM	Inverted floating method
Ih	Icosahedral
IPA	Isopropyl alcohol
JCNM	Janus carbon nanomembrane
KPM	Kelvin probe microscopy
LCC	Liquid cascade centrifugation
LEED	Low energy electron diffraction
LEEM	Low energy electron microscopy
LIB	Lithium ion battery
LM	Layered material
LMH	Layered material heterostructure
LMs	Layered materials
LPCVD	Low pressure CVD
LPE	Liquid phase exfoliation
LRI	Liquid resin infusion
μ	Carrier mobilities
μ-ARPE	Micro spot ARPES
MALDI-TOF	Matrix-assisted laser desorption/ionization-time of flight
MBE	Molecular beam epitaxy
MC	Mechanically-cleaved
MEG	Multilayer epitaxial graphene
MEP	Minimum energy path
MICS	Multiple ion cluster source
mIPM	Murine intraperitoneal macrophages
ML	Monolayer
MLG	Multilayer graphene
MNP	Metal nanoparticle
MOCVD	Metalorganic chemical vapour deposition
MP	Moire pattern
MS	Mass spectrometry
MSCs	Micro super capacitors
MW	Microwave
M_W	Molecular weight
N	Number of layers
NaCMC	Sodium carboxymethylcellulose
NBE	Near band edge
n-BuLi	*n*-butyllithium
NC	Nitrocellulose
Nc-AFM	Non-contact atomic force microscopy
NDI	Naphthalene diimide
NMP	*N*-methyl-2-pyrrolidone
NMR	Nuclear magnetic resonance
NP	Nanoparticle
NPTH	Naphtalene-2-thiol
ODCB	1,2-dichlorobenzene
OPV	Organic photovoltaics
ORR	Oxygen reduction reaction
Otf	Trifluoromethanesulfonate
OTFT	Organic thin film transistor
P3HT	Poly(3-hexylthiophene)
PAH	Polycyclic aromatic hydrocarbon
PANi	Polyaniline
PCBM	Phenyl-C61-butyric acid methyl ester
PDI	Perylene diimide
PDMS	Polydimethylsiloxane
PE	Polyethylene
PECVD	Plasma enhanced chemical vapour deposition
PEDOT	Poly(3,4 ethylenedioxythiophene)
PET	Polyethylene terephthalate
PhCN	Benzonitrile
PI	Polyimide
PL	Photoluminescence
PMMA	Poly(methyl methacrylate)
PPF	Pyrolyzed photoresist film
PPP	Polu(*p*-phenylene)
PS	Polystyrene
PTCVD	Photo thermal CVD
PTFE	Polytetrafluoroethylene
PVA	Polyvinyl acetate
PVC	Polyvinyl chloride
PVDF	Polyvinylidene difluoride
PVP	Polyvinylpyrrolidone
PVT	Physical vapor transport
QFBLG	Quasi free-standing bilayer graphene
QFSLG	Quasi free-standing single layer graphene
r-(ECR-CVD)	Remote electron cyclotron resonance plasma assisted chemical vapor deposition
RBLM	Radial-breathing-like mode
RCA1, RCA2	Standard sets of wafer cleaning steps which need to be performed before high-temperature processing steps
RE	Reference electrode
RF	Radiofrequency
RF-ID	Radio-frequency identification
RGO	Reduced graphene oxide
RHEED	Reflection high energy electron diffraction
RIE	Reactive ion etching
Rpm	Revolutions per minute
RT	Room temperature
RTM	Resin transfer moulding
RTP	Rapid thermal process
RZC	Rate zonal centrifugation

SAED	Selected area electron diffraction
SAM	Self-assembled monolayer
SARPES	Spin resolved ARPES
SAV	Single atom vacancies
SBS	Sedimentation based separation
SC	Sodium cholate
SDBS	Sodium dodecyl benzene sulfonate
SDC	Sodium deoxycholate
SDS	Sodium dodecyl sulfate
SEC	Size exclusion chromatography
SEM	Scanning electron microscopy
SET	Single electron transfer
SL	Single-layer
SLG	Single layer graphene
Slm	Standard liter per minute
SOI	Silicon on insulator
STEM	Scanning transmission electron microscopy
SThM	Scanning thermal microscopy
STM	Scanning tunnelling microscopy
STS	Scanning tunnelling spectroscopy
SuMBE	Supersonic molecular beam epitaxy
SWCNT	Single wall carbon nanotube
T	Temperature
TAC	Thermally assisted conversion
Tb	Temperature of the bubbler
TCB	1,2,4-trichlorobenzene
TCF	Transparent conducting film
TCNQ	Tetracyanoquinodimethane
TEM	Transmission electron microscopy
TEMPO	2,2,6,6-tetramethyl-1-piperidinyloxy
TGA	Thermogravimetric analysis
THF	Tetrahydrofuran
THz-TDS	THz-time domain spectroscopy
TLG	Trilayer graphene
TMC	Transition metal chalcogenide
TMD	Transition metal dichalcogenide
TOA	Tetraoctylammonium
TPT	[1″,4′,1′,1]-Terphenyl-4-thiol
Tr-ARPES	Time-resolved ARPES
TRT	Thermal release tape
UHV	Ultra high vacuum
ULF	Ultra low frequency
UV	Ultraviolet
UVA	Ultraviolet adhesive
Uv–Vis	Ultraviolet–visible
vdW	van der Waals
VPE	Vapour phase epitaxy
WE	Working electrode
XPS	X-ray photoelectron spectroscopy
Z	Reciprocal of the Ohnesorge number
ZGNR	GNRs with zigzag edges

I. Bottom-up

I.1. Graphene nanoribbons

GNRs are an interesting family of materials combining aspect ratios allowing to bridge the range of (sub-) nanometer dimensions with ultimate structure-properties relationship (GNR width, below 5 nm) and mesoscopic dimensions (GNR length up to 500 nm). This makes GNRs accessible to established top-down contacting strategies and thus allows their device integration. For GNRs with armchair edges (AGNRs), theory predicts the opening of sizable bandgaps as soon as their widths falls below ~2 nm [1–5]. This is due to quantum confinement and edge effects and can qualitatively be understood by slicing the graphene Dirac cone along k-lines in the reciprocal space that are compatible with the hard-wall boundary conditions set by the finite AGNR width. The further these cuts of allowed electronic states are away from the K point of the Brillouin zone of graphene, the larger is their bandgap [6]. AGRNs were predicted to show metallic to semiconducting behavior, depending on their width [2, 7–9]. Generally, AGRNs exhibiting widths smaller than 10 nm behave as semiconductors with non-zero bandgaps that increase as the they become narrower [5, 7–11]. E.g., AGNRs as narrow as 2–3 nm are expected to havea bandgap ~0.7 eV, which is comparable to that of Ge [5]. In contrast, early theoretical studies indicated that zigzag GNRs, ZGNRs, have metallic properties with zero bandgap irrespective of the width, showing strongly localized edge states at the zigzag sites [7], with ferromagnetic coupling along and antiferromagnetic coupling across the edges [12]. Spin-polarized density functional theory DFT calculations have found that AGNRs are always semiconductors and that the ground state of ZGNRs has an antiferromagnetic configuration, where electronic states with opposite spins are highly localized at the two ZGNR edges and are responsible for the opening of a gap [1712, 1713]. Thus, small differences in width and edge configuration lead to large variations in GNR properties [5, 10, 11], making it imperative to control the GNR structure on the atomic level to achieve the desired (opto)electronic and magnetic properties with high accuracy and reproducibility. While this is beyond the level of what can be currently controlled by top-down structuring methods, such as lithographic patterning [13–16] or cutting of CNTs[17–20], advances in bottom-up fabrication have shown that GNRs with specific edge structure and width are accessible [21]. Not only purely A or ZGNRs can be synthesized. Other types in between named chevron- or necklace-type can be designed and prepared as well [1724].

I.1.1. Solution synthesis of GNRs

The concept of solution based bottom-up synthesis relies on the preparation of large polycyclic aromatic hydrocarbons (PAHs), often referred to as nanographenes [22, 23] The reaction is based on the intramolecular oxidative cyclodehydrogenation of corresponding oligophenylene precursors and was extended from defined molecules to polymers, i.e. from PAHs to GNRs [23]. Since then, the synthesis of GNRs through intramolecular cyclodehydrogenation of polyphenylene polymers was achieved, through AA-, AB- and A2B2-type polymerizations as summarized in Refs. [24–27].

The most critical issue in the solution-synthesis is to achieve high ($>600\,000$ g mol^{-1} on average by Diels Alder (DA) polymerization) molecular weight of the precursor polymer. While the width of GNRs is determined by the monomer dimensions, the molecular weight is directly proportional to the number of repeating units, therefore proportional to the length of the resulting GNR after the cyclodehydrogenation -graphitization- step. E.g. DA polymerization provides a molecular weight $>600\,000$, on average corresponding to a length of 600 nm [23].

Figure I.1 provides an overview of the polymerization routes explained in what follows along with the relevant references.

I.1.2. Preparation of polymer precursors by A2B2-polymerization

A2B2-Polymerization requires two monomers with complementary functional groups A and B (see figure I.1). These can be A = Cl, Br, I, Otf (Trifluoromethanesulfonate) in combination with B being a boronic acid or boronic acid ester. In this case, the underlying carbon-carbon bond formation is based on the Suzuki-reaction. In contrast, if A is a diene and B a dienophile, it belongs to the reaction class of a Diels-Alder reaction. The most prominent combination for a Diels-Alder reaction to form PAHs is the combination of a cyclopentadienone and a substituted acetylene [28, 29]. The benefit of this inverse electron demand-Diels-Alder reaction is the tandem cycloaddition and carbon-monoxide-extrusion reaction. Therefore, both reaction classes require different protocols. In all cases, the polymerization follows a step-growth mechanism and is defined by Carother's equation [30]. In this case, the functionalized monomers first react into monomers, dimers, trimer, oligomers and finally high molecular weight polymers. The stoichiometry of both monomers is of fundamental importance to achieve a high degree of polymerization and thus molecular weight. From our experience, a small deviation imbalance in stoichiometry or impurity of at least one monomer of even 2% will not allow high molecular weight polymer formation. To ensure exact stoichiometry, the purity of monomers as well as dryness is a critical issue. A balance used to weight the monomers must require an accuracy of 0.1 mg. In a theoretical example, an impurity of 2% at a degree of polymerization of 98%, will cut molecular weight to half [30].

A Suzuki reaction is a palladium catalyzed reaction. The active catalyst is a Pd(0) species which is oxygen

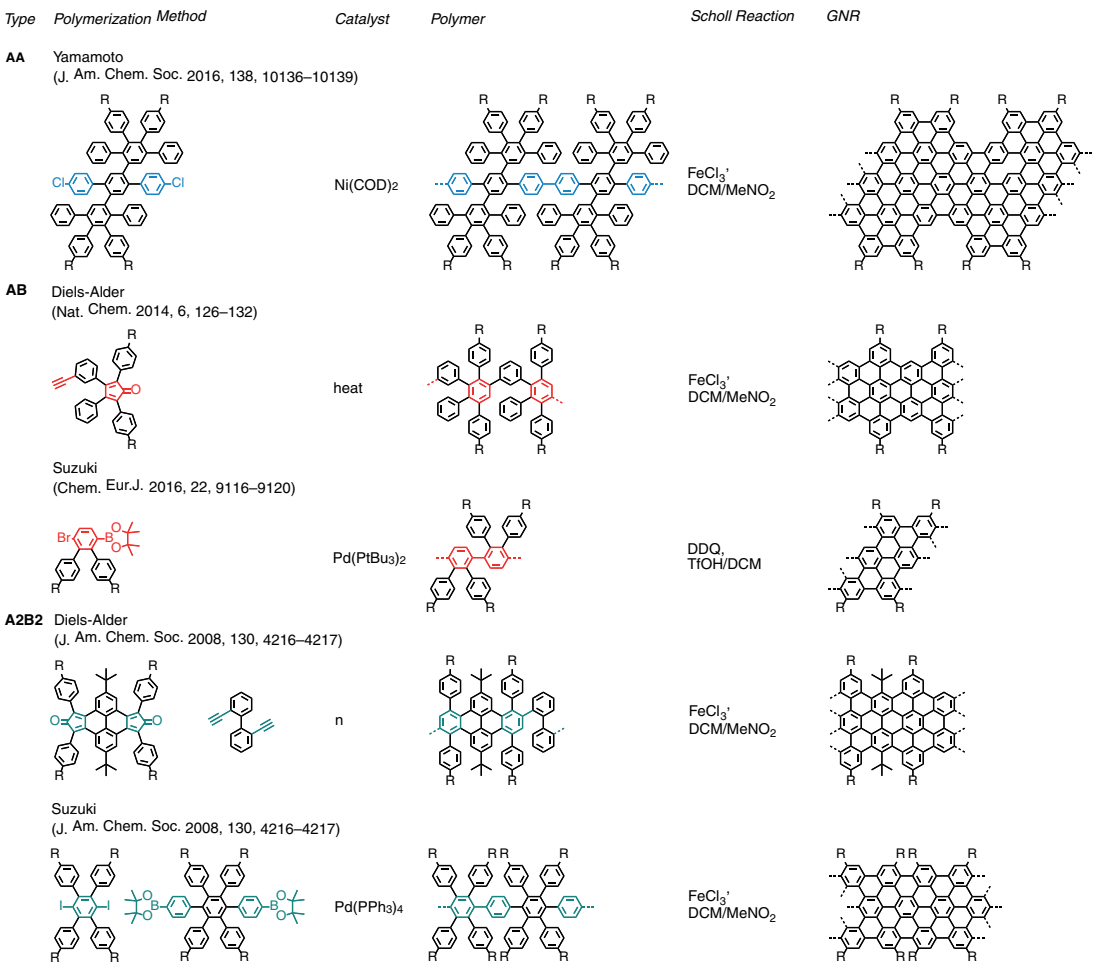


Figure I.1. Overview individual types (AA, AB and A2B2) of polymerization the reactive parts are colored according to the protocol of reactions. References to examples are given on top of the monomer or monomer combination of main polymerization methods employed in solution synthesis of GNRs.

sensitive. This protocol requires the preparation of the reaction under inert condition. To exclude oxygen from the reaction, both monomers and a base (potassium carbonate) are usually evacuated in a Schlenk-type glassware. Afterwards, the solvents (a combination of toluene, ethanol and water, typically 3:1:1), is bubbled with Ar for at least 20 min when a total volume of solvent is in the range of 100–200 ml. It is recommended to apply high (~1200 rpm) stirring during bubbling to ensure a complete saturation of the solvent mixture with Ar. After the reaction apparatus is in contact with the preheated oil bath, the catalyst ($Pd(PPh_3)_4$) is added under Ar. During the reaction, no oxygen should enter the reaction chamber. In addition, it is recommended to cover the reaction chamber with Al foil to protect it from light. To track the reaction, samples can be taken in different intervals of 15 min to several hours, always under Ar protection. These (0.1 ml) can be quenched by adding a drop of water and extracted with an organic solvent such as dichloromethane or chloroform and are required for tracking the molecular weight increase by mass spectrometry [31]. Matrix-assisted laser desorption/ionization-time of flight (MALDI-TOF) [31] using tetracyanoquinodimethane (TCNQ) as matrix is suitable for GNRs.

With prolonged reaction time in the order of hours to days, the molecular weight of the resulting polymer will increase. However, the solubility of the formed polymer will decrease. Before the polymer precipitates out of the solution, the residual terminal functional groups (halogen or boronic acid) must be 'end-capped', to avoid undesired atoms at the terminal positions of the GNR. The 'end-capping' must be performed before precipitation of the polymer to ensure conversion of unreacted functional groups. This is achieved by adding a suitable end-capper, e.g. bromo-benzene followed by adding an excess of phenylboronic acid in the respective solvent. The reaction is continued for several hours (at least one) to ensure the full conversion of the terminal functional groups. Afterwards, the reaction is quenched by the addition of water. After extraction and precipitation into typically methanol, the crude polymer can be characterized by mass spectrometry (MS) and analytical site exclusion chromatography (SEC) using polystrene or Poly(p-phenylene) as internal standard, although the molecular weight values derived from SEC analyses are only rough estimations and the absolute molecular weights may be obtained by laser light scattering experiments [32].

Nevertheless, the SEC data are useful for qualitative comparison of the molecular weights of different polymer samples and a crucial indicator for the resulting GNR's length. At this stage, it is recommended to narrow the broad molecular weight distribution by gel permeation chromatography or centrifugation into fractions of a lower polydispersity index (<1.5). UV–vis absorption spectroscopy can also provide a qualitative analysis of the polymer length since the wavelength of maximum absorption will red-shift with extension of conjugation length.

In contrast to the Suzuki and Yamamoto reaction, the Diels Alder reaction does not require a metal catalyst and can be performed only by the thermal treatment of both monomers [32].This is typically conducted in in either in diphenylether as solvent (reflux, 20–28) or in the pure melt of monomer at $T \sim 260$ °C–270 °C during 5 h. However, the constant solubility of the propagating chain must be ensured similar to the Suzuki polymerization.

I.1.3. Preparation of precursor polymers by AA-type polymerization

AA-type Yamamoto polymerization (see figure I.1) is unrestricted by the stoichiometry problem and is thus easier to handle than A2B2-type polymerization methods [33, 34]. Furthermore, it is a highly efficient even in sterically demanding systems [35, 36] which can improve the molecular weights ($M_W = 52\,000$ g mol^{-1}, $M_n = 44\,000$ g mol^{-1}) of the resulting polyphenylene precursors over the ones obtained by the Suzuki reaction.

The catalytic Ni(0) is not as stable as the Pd(0) derivative. Therefore, for the preparation of the reaction mixture ($Ni(COD)_2$, COD, bipy in THF), precaution in avoiding both oxygen and light must be taken. As a general rule the active catalyst system is deep purple. We observe that it will quickly turn dark in contact with traces of oxygen.

I.1.4. Preparation of precursor polymers by AB-type polymerization

Another effective way to overcome the issues of A2B2-type polymerisations and the labile Ni(0) catalysts is to take advantage of AB-type reactions. AB-polymerizations for the solution synthesis of GNRs are established for Diels-Alder and Suzuki protocols (see figure I.1). Theyovercome the issue of stoichiometry and result in precursor polymers with high molecular weight.

I.1.5. Cyclodehydrogenation of precursor polymer into GNRs

The cyclodehydrogenation of precursor polymers usually follows a similar protocol. The Scholl-reaction, an oxidative cyclodehydrogenation using Iron(III) chloride as both oxidant and Lewis acid is the most used. The handling of the reaction is similar for a broad variety of GNRs (see figure I.1).

In a typical procedure, the precursor polymer is dissolved in unstabilized dichloromethane (DCM), which is saturated with Ar by bubbling for 15 min. It is recommended to apply a continuous DCM saturated Ar stream through the reaction chamber. As a starting point for novel systems, usually six $FeCl_3$ per hydrogen to be removed are recommended as oxidant. The $FeCl_3$ oxidant is added as suspension (~100 mg per ml) in nitromethane.

Samples can be taken in sequential time frames of 15 min to days and analyzed after quenching of methanol. Due to the decreased solubility of the planarized GNR compared to precursor polymers, it is recommended to use MALDI-TOF MS, as well as absorption and Fourier transform infrared spectroscopy (FTIR) for both qualitative and quantitative verification of the degree of cyclodehydrogenation. One of the most dominant side reactions is the formation of chlorinated species. The amount of chlorination can be controlled by the amount of $FeCl_3$ equivalents (6–12), as well as the reaction time, from minutes to days. We conduct the reaction generally at RT.

I.1.6. On-surface synthesis of GRNs

On-surface bottom-up use of specifically designed molecular precursor monomers that carry the full structural information of the final GNR together with leaving groups that can be activated on the surface, so that the target structure is built by establishing covalent bonds between activated sites of adjacent precursor monomers. By this approach, selective growth of a single type of GNR is possible [21], and depends solely on the choice of the precursor monomer and an activation protocol that triggers the surface-assisted reaction steps under optimized conditions. Advances in GNR fabrication and characterization are described in Ref. [37].

I.1.7. Synthesis

The bottom-up synthesis of GNRs on surfaces critically depends on the atomic perfection of the used precursor monomers as well as control over the surface-assisted synthesis steps [21]. In the case of 1d target structures (such as for the case of GNRs) this is even more pronounced, since any defect changes the electronic properties or may act as a growth stopper. It is therefore crucial to start with ultrapure precursor monomer samples so that undesired coupling configurations arising from contaminations are minimized. We find that purity judged from nuclear magnetic resonance (NMR) spectroscopy is not sufficient in order to guarantee the lowest defect density and maximum GNR length, so that precursor monomer samples need to be further purified with up to eight recrystallization steps. Similarly important is the preparation of 'clean' growth substrates: Au(1 1 1) single crystals were used or Au thin films on mica [1725]. The subsequent surface-assisted synthesis steps are schematically depicted in figure I.2.

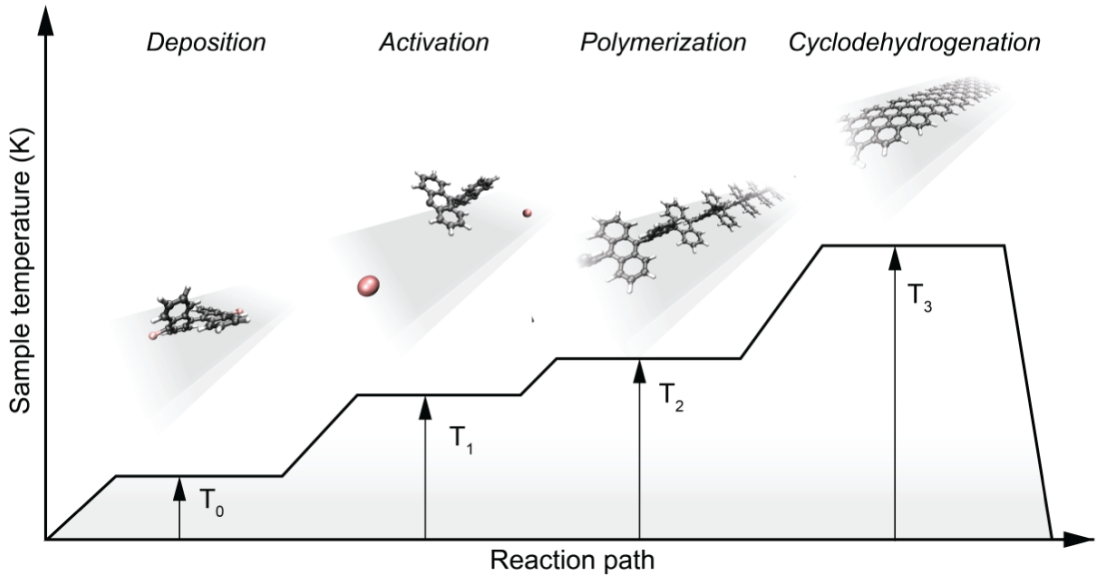


Figure I.2. GNR bottom-up synthesis concept. GNR synthesis is achieved by deposition of halogen-substituted precursor monomers at a substrate temperature T_0, followed by their activation (halogen cleavage) at T_1, polymerization at T_2, and cyclodehydrogenation at T_3.

All steps are accomplished at a pressure below $2 \cdot 10^{-9}$ mbar while heating the sample to a specific T. In the first step, precursor monomers are deposited on a clean substrate held at T_0. Quartz crucibles that are resistively heated up to the T needed are used for maintaining a precursor monomer flux of 0.1 nm per minute at the sample position, as determined with a quartz microbalance. The sample temperature is then raised to T_1 for the halogen cleavage (activation) and to T_2 for the polymerization of the activated precursors. Finally, GNRs are formed by triggering cyclodehydrogenation of the polymers by heating the growth substrate to T_3 [37]. While each of these steps is crucial for GNR synthesis, not all of the intermediate products are easily accessible for structural characterization. E.g. monomer activation at T_1 ideally leads to doubly activated precursor monomers (biradicals) that coexist with the cleaved halogens at the surface. Practically, however, this phase is often not accessible because the activated species frequently undergo polymerization directly at these T [21].

This implies that the activation barrier related to diffusion and covalent bond formation between the biradical species is smaller or equal to the energy barrier for halogen bond cleavage [38]. Deposition, activation, and polymerization steps can be combined into a single step by depositing precursor monomers directly at the polymerization temperature $T_2 = 450$ K. The time for this combined step is the deposition time (1–10 min, depending on target GNR coverage) plus 15 min holding time [37]. This step is followed by the cyclodehydrogenation step, which is triggered by increasing the temperature to $T_3 = 630$ K and holding it for 15 min. It is crucial not to exceed this T in order to avoid further activation of the formed GNRs. For higher $T_3 \approx 660$ K covalent crosslinking of GNRs was found [39], as well as the formation of GNRs of multiple widths related to partial edge dehydrogenation of GNRs, which triggers GNR fusion (cross-dehydrogenative coupling) to form seamless higher-order GNRs [39]. After cyclodehydrogenation, the sample is cooled to RT and either transferred to a connected scanning tunneling microscope for *in situ* characterization (see section IX.1) or directly taken out of the UHV chamber for characterization and/or further processing under ambient conditions.

The above mentioned parameters are valid for the growth of GNRs on Au(1 1 1), for which the highest quality is achieved for all reported GNR types [1726]. GNR synthesis under less stringent conditions was also reported [40]. Using a CVD setup, the synthesis of Chevron GNRs [41] and 9-AGNRs [42] were achieved.

An overview on published GNR structures is given in figure I.3. The most frequently used halogen atom is Br. The two main reasons for using Br is its better synthetic accessibility for most of the precursor monomers (as compared to I) and lower reactivity with the growth substrates (as compared to Cl [43]).

Depending on the choice of the precursor monomer, the selective synthesis of AGNRs with different width and bandgap was achieved [21, 44, 48, 49]. On-surface synthesis of ZGNRs was demonstrated for 6-ZGNRs using a methyl-based monomer design [57]. Chiral GNRs with a controlled sequence of armchair and zigzag segments along the GNR edge were made based on halogen-substitution of bianthryl [58]. GNRs with a controlled width-modulation along the axis, the so-called Chevron GNRs, were synthesized based on dibromo-substituted 1,2,3,4-tetraphenyltriphenylene [21]. This monomer design in particular, is well accessible for substitutional doping [54, 55, 1727]. Since chemical doping is achieved at the level of mon-

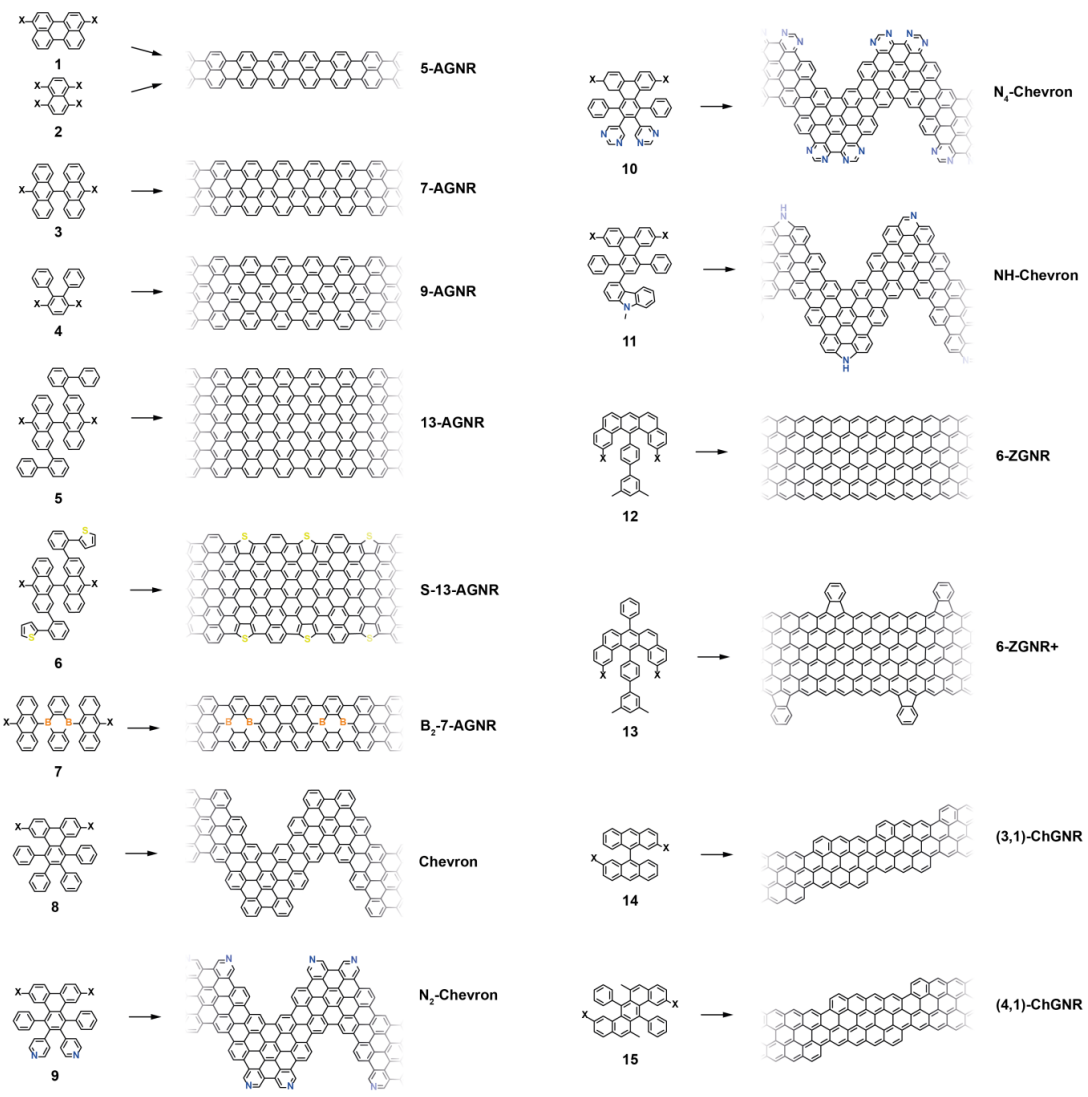


Figure I.3. Overview of bottom-up synthesized GNRs. *X* marks the leaving group, which is typically a halogen atom (X = Br, I, Cl). References are: 5-AGNR [44–47], 7-AGNR: [21], 9-AGNR: [48], 13-AGNR: [49], S-13-AGNR: [50], B_2-7-AGNR: [51, 52], Chevron: [21], N_2-Chevron: [53, 54], N_4-Chevron: [55], NH-Chevron: [56], 6-ZGNR: [57], 6-ZGNR + : [57], (3,1)-ChGNR: [58], (4,1)-ChGNR.

omer synthesis, a fully controlled level of doping and periodic arrangement of the doping sites is reached in the final GNR. Chevron GNRs were fabricated with a number of nitrogen-substitution patterns [54–56]. For 7-AGNRs, substitutional boron-doping was achieved allowing to controllably modify the electronic properties [51, 52]. The combination of different precursors during the polymerization step gives access to different GNR heterostructures with additional opportunities, making specific electronic properties at the interfaces of dissimilar GNR segments available [48, 59–62]. Width-modulated GNRs were prepared, allowing to achieve distinct topological quantum phases [63, 64].

I.1.8. GNR characterization

The main method applied for developing new bottom-up synthesized GNR structures is *in situ* scanning tunneling microscopy (STM, see section IX.1). It allows accessing the growth at the surface-related synthesis steps by interrupting the growth protocol (figure I.2) after a specific step and, subsequently, transferring the substrate to a connected STM chamber. Beside coverage determination, STM was used for the determination of polymer length after the polymerization step as well as for the determination of possible undesired coupling motifs that can occur by either not entirely purified precursor monomer batches or a not fully selective monomer design, which potentially allows for covalent coupling configurations that are not compatible with the envisaged final GNR structure. With the exception of 5-AGNRs, polymerization of the activated precursor monomers yields structures where not all molecular subunits are planar with respect to the substrate surface [21, 48]. The related apparent height imaged by STM is for all monomers above 0.25 nm, higher than the apparent height of the final GNR structure (~0.19 nm). Using this sensitivity, STM allows for a direct access to the onset T of the cyclodehydrogenation step by identifying polymer segments, where lowered

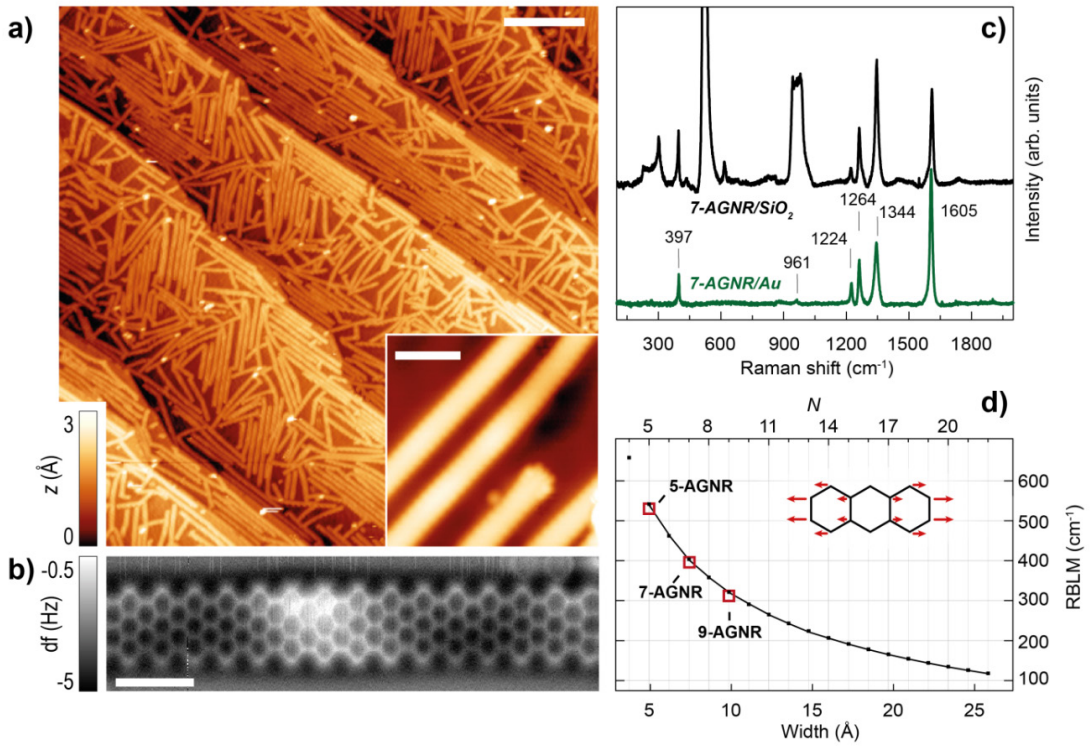


Figure I.4. Characterization of 7-AGNRs on their growth substrate and after substrate transfer. (a) Large-scale STM topography image (bias: −0.5 V; current: 5 pA; T: 4.5 K; scale bar: 30 nm) showing high coverage 7-AGNRs on Au(1 1 1). Inset: small-scale STM image (bias: 0.1 V; current: 30 pA; scale bar: 3 nm). The apparent height of individual 7-AGNRs is 0.19 nm. (b) Constant-height nc-AFM frequency shift image (bias: 2 mV; oscillation amplitude: 0.3 Å; T: 4.5 K; scale bar: 1 nm) taken with a CO-functionalized tip. (c) Raman spectra of 7-AGNR on Au(1 1 1) recorded under ambient conditions after synthesis (green curve) with indicated peak positions of the main modes, and after transfer to Si/SiO_2 (black curve; laser 532 nm, power of 2 mW, three scans of 20 s). (d) RBLM peak position for 5-AGNRs, 7-AGNRs and 9-AGNRs (red markers), together with predicted width-dependent RBLM wavenumbers for AGNRs [65].

apparent height indicates the related planarization of the polymer to the final GNR. For the investigation of individual GNRs, T below ~25 K are needed to suppress their mobility on the surface (figure I.4).

An even higher resolution is achieved by using non-contact atomic force microscopy (nc-AFM) where the tip apex can be decorated with specific molecules or atoms to yield unprecedented insight into the chemical structure of the synthesized carbon nanostructures [66]. Tungsten tips attached to a tuning fork sensor [67] have been used in a low-T STM (ScientaOmicron) functionalized with CO molecules by dosing CO onto the surface and a controlled pick-up procedure [68]. By recording the frequency shift image at constant height (figure I.4(b)), the chemical structure of GNRs can be visualized with a resolution that is going down to individual chemical bonds. The sensitivity is high enough to resolve, e.g. additionally attached hydrogens at ZGNR edges (H_2- instead of H-termination) [57]. With this unique structural sensitivity, nc-AFM is complementary to STM (see section IX.1), which is only indirectly sensitive to the atomic composition by recording an apparent structure defined by the local density of states near the Fermi level. The constant-height imaging mode, however, can only be applied to the flat final GNR structures [48]. Non-planar structures, such as the used precursor monomers and the polymer intermediates, are hardly accessible by nc-AFM due to the related 'constant height' imaging mode [66].

The main *ex situ* characterization tool applied to GNRs is Raman spectroscopy (see section IX.2/Raman) [1714]. Owing to their atomically defined structure, GNRs present well defined Raman peaks (figure I.4(c)). The main peaks are the G and D modes with overtones and the width-dependent radial-breathing-like mode (RBLM) (~396 cm^{-1} for 7-AGNRs) [40]. The D peak is intrinsic for GNRs due to the presence of edges [1715]. For laser energies ranging from 457 to 633 nm, between 1–2 mW power were used (higher power can result in thermal effects at ambient conditions [1725]). For laser energies in the infrared range (785 nm) a max of 10 mW is used [1725]. It is important to select the photon energy of the laser source close to the GNR bandgap to be in resonance [48]. For 7-AGNRs with an optical band gap of 1.9 eV [69], Raman spectra were recorded using a green laser (532 nm, 2.33 eV). For 9-AGNRs with an optical band gap of 1.1 eV [70], Raman spectra were recorded with an infrared laser line (785 nm, 1.55 eV). Exchanging the two laser lines for both examples leads to a loss of resonance conditions and the width-characteristic RBLM mode cannot be resolved anymore [1725].

I.1.9. GNR transfer

The on-surface synthesis of GNRs relies on the catalytic action of the metallic growth substrate, and therefore requires their transfer onto dielectric substrates for further characterization of their electronic or optical properties. Similarly, in order to explore GNRs as active materials in electronic or optoelectronic devices, their transfer to dielectric substrates is required. The potential of GNR-based devices was demonstrated by the realization of GNR-based field effect transistors (FETs) with an on current of 1 μA and on/off ratio of 10^5 [71, 72]. Furthermore, devices using CVD-GNRs as active material were reported with high on/off ratio and high photoresponsivity of 5×10^5 A W^{-1} [41, 42]. Transfer was achieved using a sacrificial PMMA layer deposited onto the as-grown GNRs [72], stripped off after GNR transfer to the target substrate. A transfer method was developed allowing for the transfer of GNRs without PMMA, which avoids possible contamination problems related to PMMA residues [40, 55]. This relies on is delamination of Mica from a Mica/Au/GNR stack in an hydrochloric acid, from which the remaining Au/GNR stack is picked up with the target substrate. In a last step, the Au layer is then dissolved leaving a clean GNR film (without Au or iodine residues) on the target substrate. To do so, the Mica/GNR/Au stack was placed on concentrated (38%) hydrochloric acid (HCl) with the Au/GNR film facing up. After 15–20 min the mica detaches from Au. Once the mica is detached, the acid is removed from the container. In order to prevent sticking of the Au film at the container walls, it is important to not remove the acid completely in one step. After initially removing ¾ of the acid, water is added and the liquid removed in five iterative steps. In the last dilution step, the container is kept full of water for the pickup of the Au film with the target substrate. It is important that the target substrate is free of any impurities.

With the help of tweezers, the target substrate is approached (facing down) and pressed against the floating Au/GNR film until they stick together. The merged Au/GNR/substrate stack is then pulled out of the water. At this stage, the Au film is usually not completely flat on the substrate. In order to increase the contact between Au film and substrate, 1–2 drops of pure ethanol are added and dried under ambient conditions. Once dried, the Au/GNR/substrate stack is further heated on a hot plate (100 °C, 10 min). This two-step process results in a flattening of the Au film on top of the target substrate. The Au film was then removed by adding 1–2 drops of Au etchant (KI/I_2, no dilution) on top of the Au film and waiting until the Au film was completely etched away (around 5 min). Finally, to clean the GNRs/substrate, this was soaked in water (5–10 min), rinsed with 20–30 ml of acetone/ethanol and water and finally dried under N_2 flux [1725].

Using this method, 5-AGNRs, 7-AGNRs, 9-AGNRs and Chevron GNRs were transferred to SiO_2, CaF_2, Al_2O_3, glass slides and TEM grids (lacey carbon supported graphene, TedPella.com). The main characterization tool used to prove that the structure of the GNRs remains intact upon transfer was Raman spectroscopy. An example of Raman spectra taken before and after transfer of 7-AGNRs is in figure I.4(c)). All the characteristic 7-AGNR modes are present in the spectrum taken after transfer. Most importantly, the RBLM at 397 cm^{-1} remains equally intense and does not show significant broadening.

I.2. Graphene and carbon nanomembranes

CNMs with tunable properties can be produced by conversion of aromatic self-assembled monolayers (SAMs), CNMs can be then subsequently converted into GRM and graphene [73–80]. The process is schematically shown in figure I.5(a). First, a SAM is formed on a solid substrate, then the monolayer is converted into a CNM [81] via electron irradiation [82], and finally the CNM is transformed into GRM via annealing in vacuum (pyrolysis) or in an inert atmosphere. By tuning the structure of molecular precursors (figure I.5(b)), parameters of the self-assembly, substrate materials, electron irradiation and annealing conditions, GRM with adjustable crystallinity, thickness, porosity and electronic properties can be produced.

I.2.1. Molecular self-assembly

Molecular self-assembly of aromatic molecules can be performed from solvents [73, 83] or by vapor phase deposition [84, 85]. For the self-assembly on coinage metal substrates such as Cu, Ag or Au, typically thiol functional groups are employed providing a covalent binding of the molecules to the substrate [86]. The solvent-based self-assembly of 1,1′-biphenyl-4-thiol (BPT, (1a), in figure I.5(b)), an aromatic precursor used for the production of SLG [74, 79] on Au substrates, can be conducted by immersing the substrate into a solution of BPT in dimethylformamide (DMF) [85]. Alternatively, a BPT SAM can be prepared by vapor deposition, i.e. exposure of sputter-clean Au substrates to BPT vapor [85]. Both methods allow the formation of BPT SAMs with comparable structural quality, although the solvent-based preparation typically results in a slightly higher (~5%) packing density of the formed SAMs. In case of the self-assembly from solvents the solvent/molecule interactions play an important role [86], and the packing density of the formed SAMs can be tuned by adjusting the solvent polarity and concentration of the precursor molecules [73]. In comparison to solvent-based self-assembly, self-assembly by vapor deposition requires high vacuum equipment, but SAM formation is achieved in a significantly shorter time (~1 h compared to 3 days [74, 84, 85]. For practical reasons, these different aspects have to be considered when designing the experiment. Furthermore, vacuum vapor deposition is preferred over solution deposition in the case of the

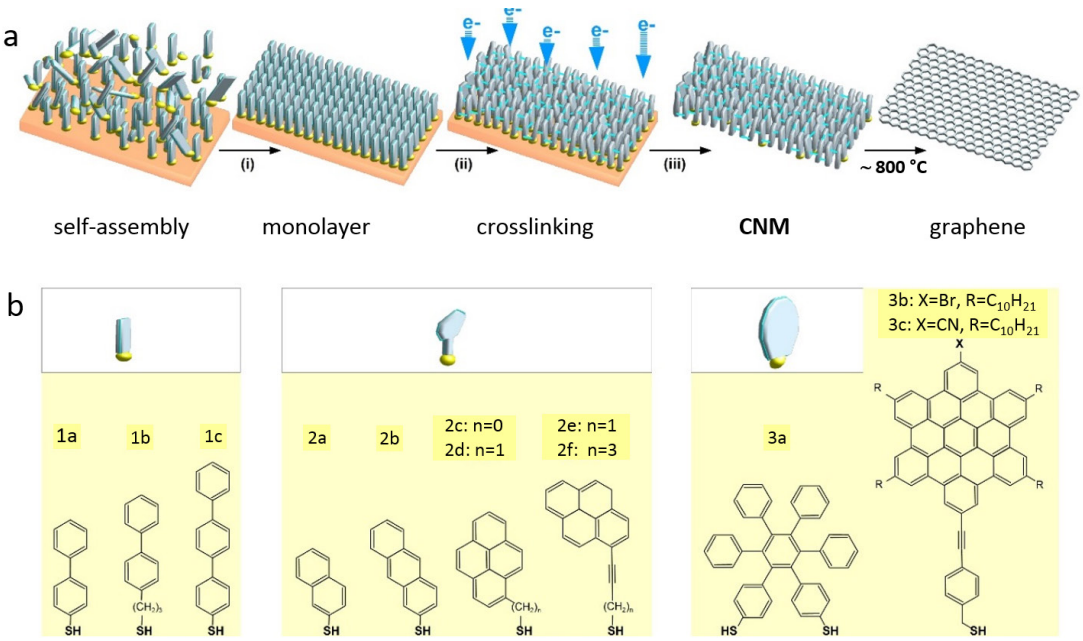


Figure I.5. Formation of CNMs and GRM from aromatic self-assembled monolayers. (a) Schematic illustration of the fabrication route for CNMs and graphene: Self-assembled monolayers are (i) prepared on a substrate then (ii) crosslinked by electron irradiation to form CNMs of monomolecular thickness. The CNMs are (iii) released from the underlying substrate, and further annealing at 900 °C transforms them into graphene. (b) Chemical structures of the different precursor molecules used for synthesis of CNMs and graphene. Figure adapted from Ref. [73], copyright American Chemical Society.

formation of thiol-based SAMs on oxidative metal substrates (e.g. Cu or Ni), as the metal oxidation which hinders the self-assembly is avoided [84, 86].

I.2.2. Electron irradiation induced crosslinking of aromatic SAMs and formation of CNMs

Electron irradiation of aromatic SAMs results in lateral crosslinking of the constituting molecules and formation of CNMs [73, 82, 87]. The mechanisms of this process are discussed in Refs. [82] and [88]. Here, we summarize essential features of this process [89–91]. In aliphatic SAMs, electron irradiation results in significant (up to 80%–90%) molecular decomposition and desorption [92, 93]. In contrast, in aromatic SAMs the same treatment a thin carbon layer is formed. To induce the crosslinking in aromatic SAMs with low-energy electrons (50–100 eV), typically doses of ~50 mC cm^{-2}, corresponding to ~750 electrons per molecule, are used. Because of electron irradiation, C–H cleavage takes place [90], which is the predominant process leading to crosslinking between adjacent aromatic rings. As suggested by UV photoelectron spectroscopy, quantum chemical and molecular dynamics calculations of BPT SAMs on gold, the formation of single- and double-links (C–C bonds) between phenyl rings of the molecules is expected during crosslinking [82]. This is supported by UV–vis spectroscopy of the formed CNMs [76]. Molecular dynamic calculations suggest [91] that a partial dissociation of the aromatic rings can take place and play a role in the formation of a carbon network. Such a mechanism would be in agreement with partial desorption of carbon in purely aromatic SAMs as observed by XPS. The XPS data also show that the irradiation and the subsequent molecular reorganization also affects the S-Au bonds. These structural changes at the molecule/substrate interface are in agreement with the LEED and STM results showing a loss of the long range (>5 nm) order in the SAMs upon electron irradiation [74].

Complete crosslinking of aromatic SAMs can be also achieved via He^+ ion irradiation [94] with exposure dose ~1 mC cm^{-2}, ~60 times smaller than the corresponding electron irradiation dose [82]. Most likely, this effect is due to the energy distribution of secondary electrons that have a maximum at energies below 50 eV, which results in a more efficient dissociative electron attachment (DEA) process. Crosslinking can also be achieved employing UV/EUV [83] and higher energy electrons (few keV) [95].

After electron irradiation of the aromatic SAMs, the CNMs can be separated from the original substrates and transferred using PMMA assisted transfer onto new solid or perforated substrates (e.g. grids, see section VI) [78], where they form large free-standing areas (up to 0.3 mm^2). Figure I.6 shows helium ion microscope (HIM) images of free-standing CNMs from different types of aromatic molecular precursors [73]. These images show unbroken membranes, which demonstrate mechanically stable CNMs. CNMs with large free-standing areas up to ~0.3 mm^2 can be obtained in this way. Since the thickness of CNMs is determined by the size of the precursor molecules and their packing in the SAMs, it can be tailored

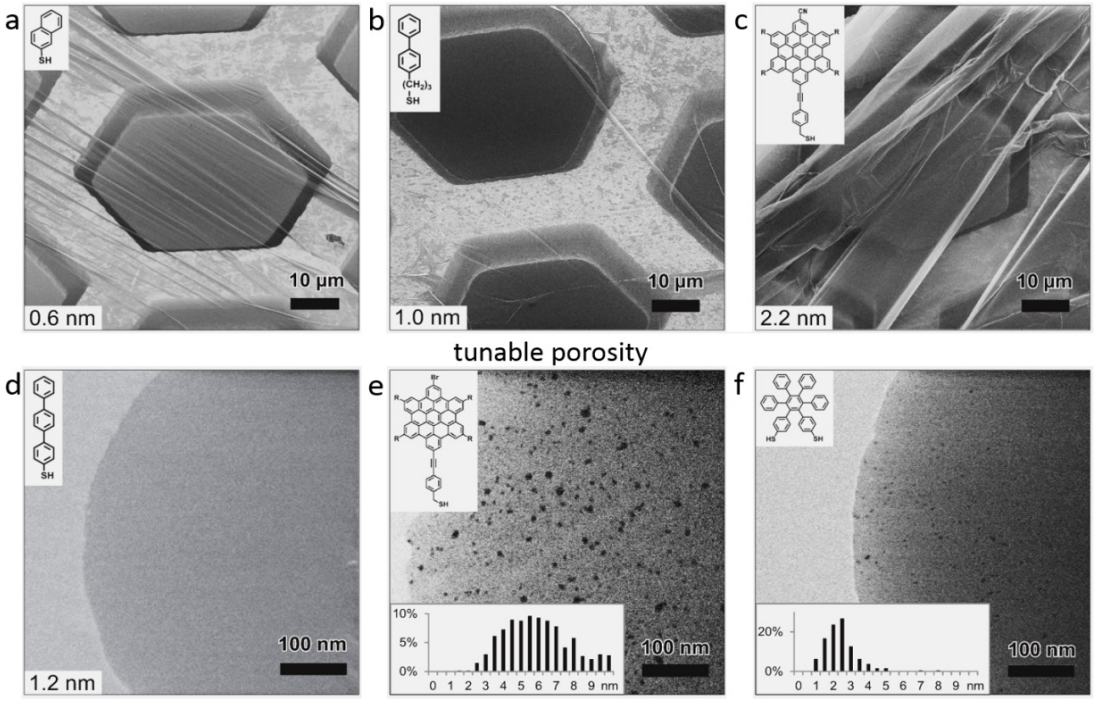


Figure I.6. Helium ion microscope (HIM) images of free-standing CNMs. After crosslinking the nanomembranes aretransferred onto TEM grids and images were taken at different magnifications (see scale bar). CNMs are prepared from: (a) Naphtalene-2-thiol (NPTH, (2a)); (b) 3-(biphenyl-4-yl)propane-1-thiol (BP3, (2b)). (c) 2-Cyano-11-(1′-[4′-(S-Acetylthiomethyl)phenyl] acetyl)-5,8,14,17-tetra(3′,7′-dimethyloctyl)-hexa-peri-hexabenzocoronene (HBC-CN, (3c)); (d) [1″,4′,1′,1]-Terphenyl-4-thiol (TPT, (1c)); (e) 2-Bromo-11-(1′-[4′-(S-Acetylthiomethyl)phenyl]acetyl)-5,8,14,17-tetra(3′,7′-dimethyloctyl)-hexa-peri-hexabenzocoronene (HBC-Br, (3b)); (f) S,S′-(3′,4′,5′,6′-Tetraphenyl-[1,1′:2′,1″-terphenyl]-4,4″-diyl) diethanethioate (HPB, (3a)). The upper left insets show the precursor molecules. The CNMs in (a)–(c) are suspended over Cu grids, CNMs in (d)–(f) over Cu grids with thin holey carbon film. The numbers in the lower left corners in (a)–(d) indicate the CNM thicknesses, as determined from XPS before the transfer. HIM images e and f show CNMs with nanopores, the lower insets show the respective distributions (in%) of pore diameters (in nm). Figure adapted from [73], copyright American Chemical Society.

by varying these parameters enabling nanomembrane engineering. Figures I.6(a)–(c) show examples of CNMs where the thinnest nanomembrane has a thickness ~0.6 nm, while the thickest CNM is ~2.2 nm. Different CNMs have been fabricated and were investigated by HIM [73]. A relation between size and shape of precursor molecules, degree of order in its SAMs and the appearance of the CNM has been established [73]. If the molecule form a densely packed SAM (1(a)–(c), 2(a)–(c) and (e) in figure I.6(b)), the corresponding CNM is homogeneous and free of holes above 1.5 nm diameter. Figure I.6(d) shows a HIM image of such a CNM made from terphenylthiol (1c). Conversely, CNMs made from large molecules, i.e. hexabenzocoronenes (HBC, 3(b) and (c) in figure I.6(b)) or *S*,*S*′-(3′,4′,5′,6′-tetraphenyl-[1,1′:2′,1″-terphenyl]-4,4″-diyl) diethanethioate (HPB, 3a in figure I.6(b)), form less ordered SAMs and exhibit pores, as presented in figures I.6(e) and (f). Here the dark spots are pores with diameters of 2–10 nm. Note that these pores have a narrow size distribution (see histogram insets). In case of the HBC precursor, the mean size of the nanopores is ~6 nm with surface density ~9.1×10^{14} pores m^{-2} The more compact HPB precursor shows a size ~2.4 nm with a surface density `1.3×10^{15} pores m^{-2}. The formation of nanopores in these CNMs can be attributed to the large lateral dimensions of HBC and HPB molecules in comparison to smaller molecular precursors (see figure I.6(b)) and, in the case of HBCs, to the tendency of the disk like molecules to intermolecular stacking, which reduces the ordering in the respective SAMs. The average pore diameter correlates with the SAM thickness and decreases from 6.4 to 3.0 nm when the thickness increases from 1 to 2 nm [73].

I.2.3. Conversion of CNMs into graphene and GRMs via pyrolysis

I.2.3.1. Formation of nanocrystalline graphene/GRMs

CNMs are stable up to to 800 K [83], which enables their conversion into graphene/GRMs via pyrolysis in vacuum or inert atmosphere [73, 78]. The crystallinity of the produced GRM can be tuned by the annealing conditions, i.e. *T* and substrate material. The formation of nanocrystalline sheets by annealing of free-standing CNMs [78] on TEM grids (figure I.7(a)) was reported on Au, on [79] or SiO_2[76, 77]. Although S is initially present in the CNMs both, XPS (of supported sheets) and scanning Auger microscopy (of suspended sheets), indicate that after annealing above 800 K all sheets consist only of carbon [78, 82]. At this *T*, the structural transformation of CNMs sets in, evident from appearance of the characteristic *D*-, *G*- and 2*D* peaks in the Raman spectra [96] [77–79].

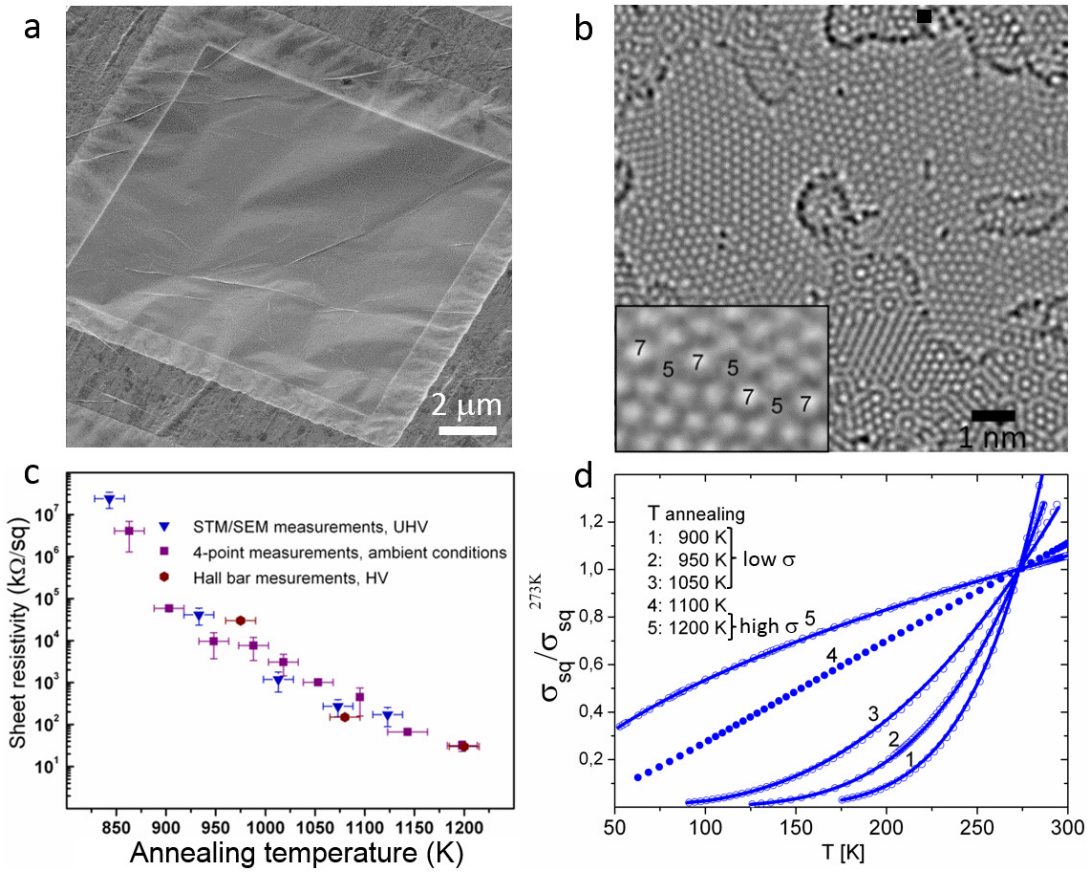


Figure I.7. Conversion of 1,1′-biphenyl-4-thiols (BPT) CNMs into nanocrystalline GRM upon annealing. (a) HIM image of BPT CNM annealed to 1000 K on a AuTEM grid. (b) Atomic structure of a similar sample obtained by aberration-corrected high-resolution TEM (AC-HRTEM, 80 kV). The inset shows a magnified grain boundary where arrangements of carbon atoms into pentagons and heptagons are highlighted. (c) RT sheet resistivity of the samples as a function of annealing T. (d) T dependencies of the normalized sheet conductivity demonstrate the change in electrical transport mechanism, i.e. insulator to metal transition. Figure (b) adapted from [73], figures (c) and (d) adapted from [79], copyright American Chemical Society.

This can also be visualized by HRTEM [73, 79]. As shown in figure I.7(b), after annealing of a BPT CNM (chemical formula (1*a*) in figure I.5(b)), most of the sheet area (~70%) is SLG recognized by the hexagonal arrangement of carbon atoms. Randomly oriented nanocrystalline graphene domains are connected with each other via heptagon-pentagon grain boundaries [97] (see inset to figure I.7(b)); a small fraction (~20%) of the sheet consists of bilayer graphene (BLG) as indicated by the Moiré pattern [98] and some of the area (~10%) shows an amorphous carbon phase [99].

The conversion of CNMs influences the electrical and optical properties [76, 78, 79]. Figure I.7(c) shows the sheet resistivity of BPT CNMs as a function of annealing T. The measurements were conducted at RT by different methods after respective annealing steps on both supported and suspended GRM [78, 79]. The non-annealed CNMs do not show lateral conductivity. Electrical conductivity is first detected after annealing at ~800 K. After annealing a ~1200 K the conductivity increases by six orders of magnitude approaching ~10 kOhm sq^{-1}. To characterize the influence of this transformation on electrical transport, the T dependencies of the electrical conductivity, $\sigma(T)$, and the electric field effect were studied in Hall-bar devices [79]. Samples with lower annealing T (900, 950 and 1050 K), (1–3) in figure I.7(d), have insulating behavior with a positive curvature in T. Their T dependence can be described by $\sigma(T) \propto \exp\left[-\left(\frac{T_0}{T}\right)^{\frac{1}{3}}\right]$, representing the Mott law [79], characteristic of thermally activated variable range hopping in a 2d system with weak Coulomb interactions [79]. For the sample with the highest degree of transformation, (5) in figure I.7(d), $\sigma(T)$ shows a negative curvature with $\sigma(T) \propto T^{1/2}$, i.e. a semi-metallic state. Since the conductivity of nanocrystalline carbon in the insulating regime strongly depends on the density of states, a large ambipolar electric field effect is observed. The electron mobility in the resulting nanocrystalline carbon film~50 cm^2 V^{-1} s^{-1} at RT [79]. The evolution of the transport characteristics upon conversion of CNMs into nanocrystalline carbon is reminiscent of that observed upon the thermal reduction of graphene oxide (GO) into reduced graphene oxide (RGO) [100, 101]. In both cases the final material presents an interconnected network of graphen nanocrystallites. However, in case of the RGO, a residual amount of oxygen

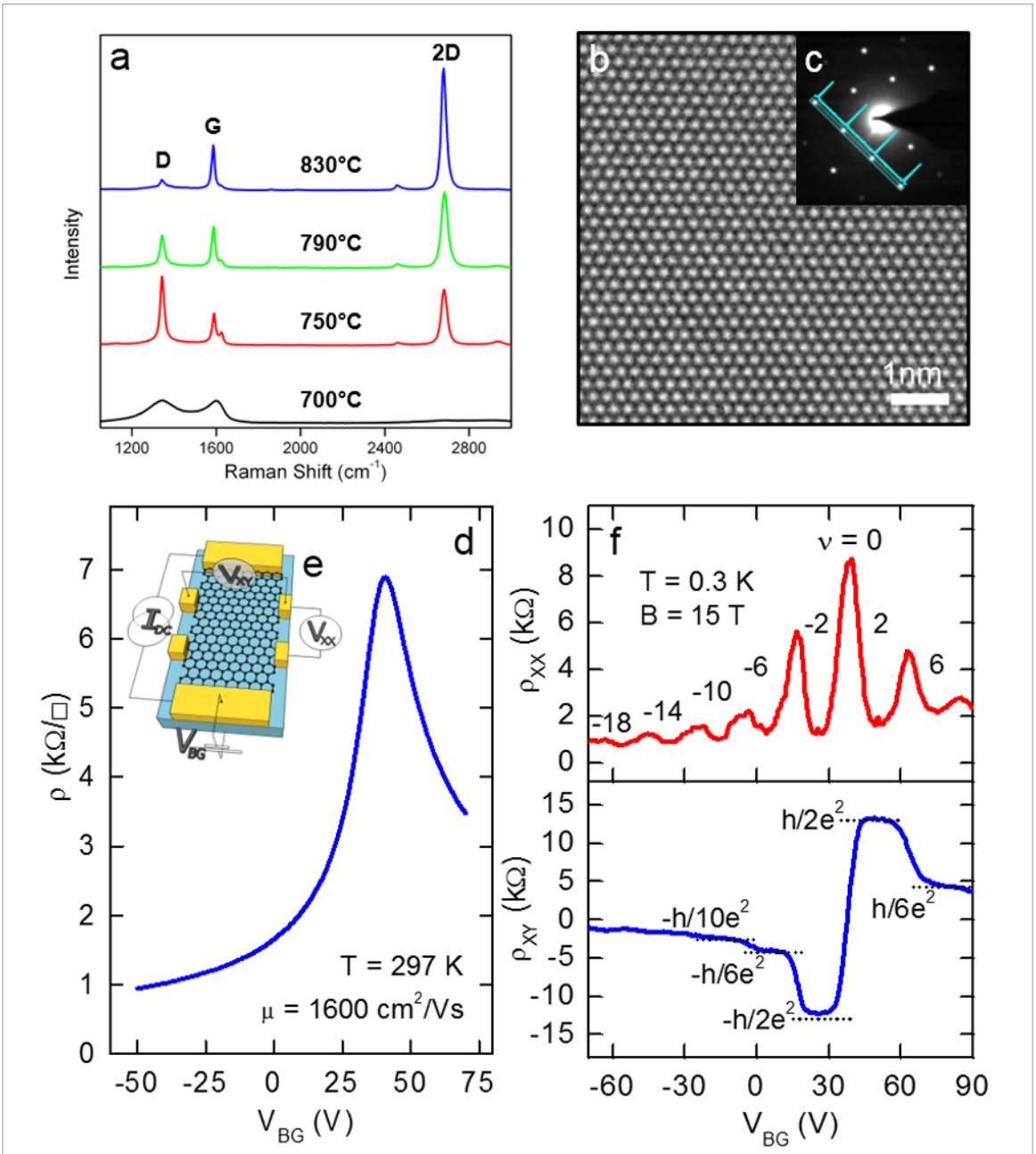


Figure I.8. Conversion of BPT CNMs into graphene on Cu foils. (a) Raman spectra ($\lambda_{exc} = 532$ nm) of the conversion of BPT CNMs as a function of *T*. The sheets after annealing were transferred from Cu onto Si wafers with 300 nm SiO_2. (b) HRTEM micrograph of the sheet resolves the honeycomb lattice of graphene. The single layer nature can be determined from the HRTEM image contrast. It is further verified by the SAEDin (c). (d) RT resistivity in vacuum as a function of back-gate voltage using Hall bar devices schematically depicted in (e). (f) Quantum Hall effect at 0.3 K and 15 T. The upper plot shows Shubnikov–de Haas oscillations with the corresponding filling factors and the lower plot shows the Hall resistance as a function of back gate voltage, i.e. varied charge carrier density. Figure adapted from [74], © Wiley-VCH Verlag GmbH & Co. KGaA.

containing groups is present [102], whereas nanocrystalline GRM sheets obtained by the conversion BPT CNMs consist only of carbon [73, 78, 79].

The thickness of the formed nanocrystalline sheets depends on the structure of precursor molecules, their ability to form SAMs and to be crosslinked into CNMs. Thus, by varying precursors (see figure I.5(b)), the thickness of the formed nanocrystalline sheets can be tuned by a factor ~3 [73]. The resistivity correlates with the thickness of the sheets, with lower resistivity for thicker sheets [73, 76]. An interesting opportunity is opened by using N- or boron-containing precursors, as in this case, GRM sheets doped by these elements can be expected, which are of interest for applications in catalysis [103] or energy storage [104].

I.2.3.2. Formation of polycrystalline graphene

Employing the conversion of CNMs into GRM by performing pyrolysis on catalytically active substrates like copper, graphene layers with high crystallinity and, therefore, high mobility above 2000 cm^2 V^{-1} s^{-1} can be attained [74]. As a model system, the conversion of BPT SAMs is presented (see chemical formula (1*a*) in figure I.5(b)) into graphene on

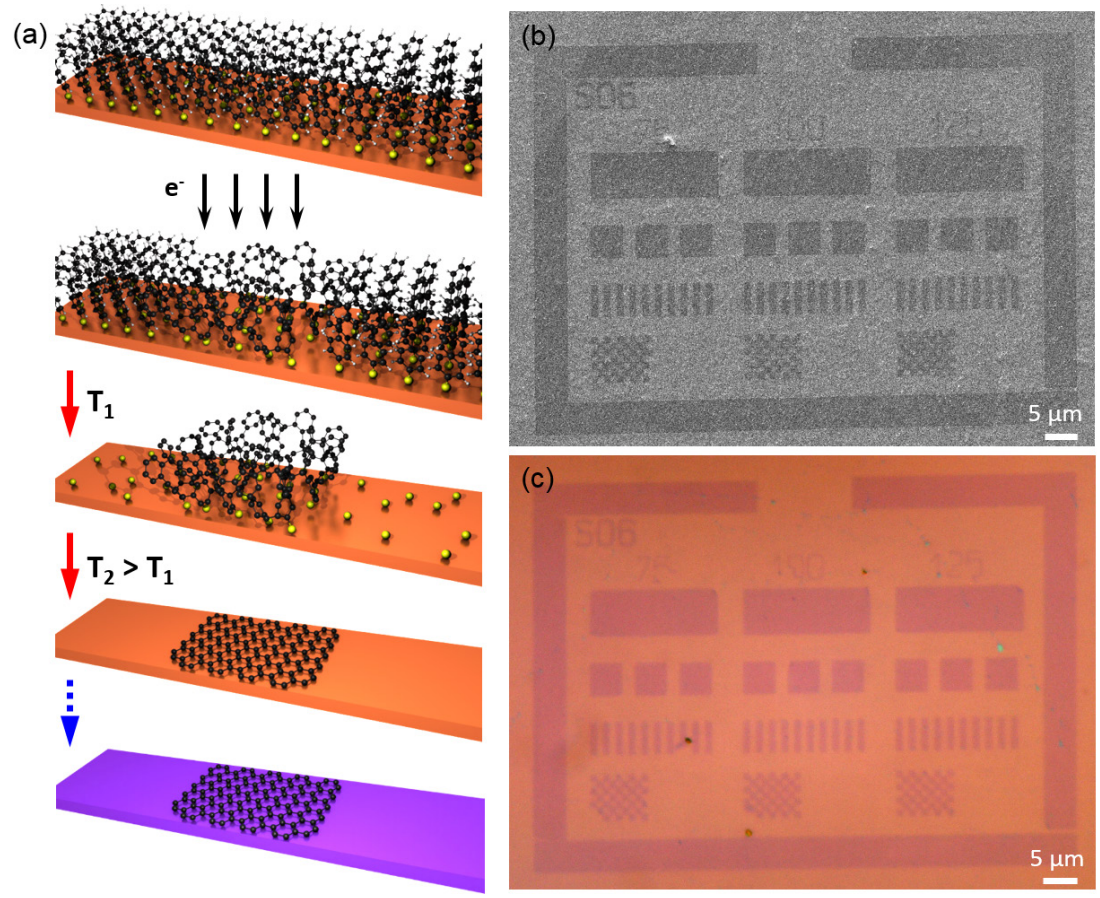


Figure I.9. Direct growth of patterned graphene. (a) Schematic of direct growth of patterned graphene. (b) SEM image of graphene microstructures directly written on top of Cu by irradiating a BPT SAM with a focused electron beam (3 keV, 75 mC cm^{-2} (left)—125 mC cm^{-2} (right)) and subsequent annealing (800 °C). (c) Same structure after transfer to a SiO_2/Si wafer. Figure adapted from [80], © Wiley-VCH Verlag GmbH & Co. KGaA.

copper foils. The Raman spectroscopy data (see figure I.8(a)) show an evolution of the characteristic *D*, *G* and 2*D* Raman peaks as a function of *T* (see section IX.2/Raman for an introduction to the technique). The conversion of a CNM into graphene with *T* is clearly observed. For the highest annealing *T* (830 °C), the same features as known for single-layer graphene prepared by mechanical exfoliation (*G* peak at 1587 cm^{-1} and a narrow Lorentzian 2*D* peak at 2680 cm^{-1} (FWHM = 24 cm^{-1}) [105] are observed after the conversion. The grown sheets were transferred onto grids and onto oxidized highly doped Si-wafers and were characterized by HRTEM and by electric transport [74]. The HRTEM and selected area diffraction (SEAD) data confirm formation of SLG [106], figures I.8(b) and (c). The dark-field TEM imaging shows that the formed sheets consist of graphene single crystals with lateral dimensions up to 1–2 μm [74].

Electric transport properties of the synthesized graphene films were studied by four-point measurements in the Hall bar geometry (see inset in figures I.8(d) and (e)) [74]. Figure I.8(d) presents the observed ambipolar nature as measured in a FET device. The RT charge carrier mobility, μ, extracted from the data at a hole-concentration of 1×10^{12} cm^{-2}, is ~1600 $cm^2\ V^{-1}\ s^{-1}$. μ values at lower charge carrier concentrations are ~2300 $cm^2\ V^{-1}\ s^{-1}$. Further characterization of the transport properties (see section IX.3) at low *T* (*T* = 0.3 K) in a magnetic field of 15 *T* demonstrates that by varying the charge density with the back-gate voltage, Shubnikov–de Haas oscillations and resistivity plateaus of the quantum Hall effect specific for SLG are observed [107]. These results confirm the electronic quality of the grown sheets, l making them attractive for electronic applications.

I.2.3.3. Direct growth of graphenemicropatterns

Since only the electron-beam irradiated areas of SAMs undergo conversion into graphen, both large-area up to 10 cm^2 and more graphene sheets and carbon films of various architectures (e.g. nano-ribbon, dot, anti-dot patterns) can be fabricated from SAMs by employing either defocused electron flood exposures [74, 78] or exposures by focused electron beams [75]. Because only electron-irradiated (crosslinked) regions of aromatic SAMs are converted into grapheneupon annealing, whereas non-irradiated (pristine) SAMs desorb from the surface [83], the suggested approach provides an opportunity to directly grow graphene patterns by area-selective electron irradiation [80], figure I.9(a). Therewith, at least four technological

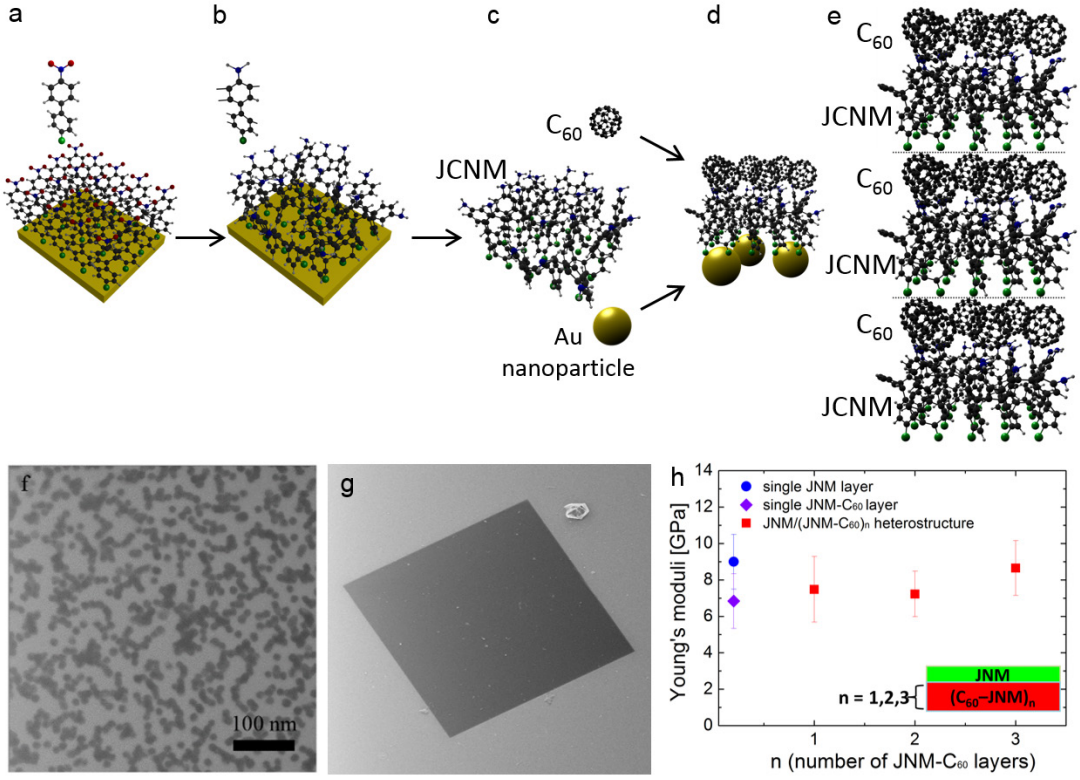


Figure I.10. Hybrid LMH of 0d and 2d carbons. (a)–(e) Schematic representation of the LMH assembly. (a) Formation of a NBPT SAM on Au. (b) Electron irradiation induced crosslinking and reduction of the terminal nitro groups into amino groups. (c) Formation of a free-standing JNM with the terminal N- and S-faces. (d) Functionalization of the N- and S-faces with C_{60} and AuNPs. (e) Assembly of a $(C_{60}$–JNM$)_n$ (here $n = 3$) hybrid heterostructure by mechanical stacking. Color code for atoms: black—C, grey—H, blue—N, green—S, and red—O. (f) HIM images in the scanning transmission ion mode shows the immobilization of 16 nm Au NPs on a JNM which are uniformly distributed with an coverage ~50%. (g) HIM image of an JNM-$(C_{60}$–JNM$)_3$ heterostructure spanning a Si window. (h) Young's moduli of JNM, C_{60}–JNM and JNM-$(C_{60}$–JNM$)_n$ ($n = 1, 2,$ and 3). Figure adapted from [113], with permission of The Royal Society of Chemistry.

steps (spin-coating of photoresist, developing of photoresist, reactive ion etching, stripping of photoresist) employed in the conventional microfabrication of graphene electronic devices are omitted. Figure I.9(b) shows a graphene pattern grown on Cu at 800 °C after a BPT SAM is locally crosslinked by a primary electron beam of 3 keV and doses ranging from 75 mC cm^{-2} to 125 mC cm^{-2}. The transfer of this structure onto a 300 nm SiO_2/Si substrate is presented in figure I.9(c). By comparing the distances between the single structure elements in figure I.9(b) (on Cu) and 9(c) (on SiO_2/Si), the structural integrity is conserved during transfer. Only a few elements show folding defects or missing parts. In this case, the local adhesion to the substrate is too weak to withstand the forces occurring during the removal of the transfer medium in solvent [80]. More advanced transfer techniques, like electrochemical delamination [108] or a clean-lifting transfer [109] may be applied to avoid or minimize the creation of defects (see section VI). The minimum size of the features in the grown pattern correspond to ~1 μm. The lateral resolution is defined in principle by the resolution of electron-beam lithography, ~7 nm for SAMs [110]. Another interesting opportunity is given by the fact that molecular self-assembly can be conducted on non-planar surfaces, thus it is also feasible to apply the developed methodology to create graphene structures on any 3d shape.

I.3. Heterostructures from CNMs

Stacking of 2d sheets including SLG, hBN, or TMDsinto layered materials heterostructures (LMHs) have led to novel materials with a potential for applications and in fundamental research [111, 112]. The integration of other low dimensional materials into these LMHs can extend these borders even further. Here a modular and broadly applicable route is presented to create hybrid LMHs made of individual ~1 nm thick Janus CNMs (JCNM) [113] functionalized with other low-dimensional materials (see figure I.10).

JCNMs are produced via electron irradiation induced crosslinking of 4′-nitro-1,1′-biphenyl-4-thiol SAMs and have different chemical groups on their opposite faces, e.g. amino groups on the top side (N-side) and sulfur species on the lower side (S-side) [114]. They can be independently chemically functionalized with desired building blocks and assembled into hybrid LMHs via stacking, figures I.10(a)–(e). $C_{60}$was covalently bound to the amino groups on the N-side of a JCNM [113]. To demonstrate that in the assembly of hybrid heterostructures also the S-side of

JCNMs can be used, it was functionalized with Au NPs, figure I.10(f). The possibility of bifacial chemical functionalization of JCNMs paves the way to hybrid LMH-swith a variety of other 0d and 1d materials.

In Ref. [113], cm^2-sized heterostructure stacks of hybrids JNCM with coupled C_{60} were fabricated. They were characterized with respect to their structural, chemical and mechanical properties. The characterization by XPS (see section IX.2) shows that the chemical composition and effective thickness of the individual C_{60}/JCNM layers remains unaffected [113]. Individual C_{60}/JCNMs and their heterostructures were further studied by mechanical bulge tests [133] to characterize their mechanical properties. To this end, the sheets were transferred onto a Si substrate with an array of square shaped orifices. Figure I.10(g) shows a HIM image of a homogeneous free-standing hybrid structure of three layers C_{60}/JCNM spanning over an orifice with dimensions of $40 \times 44\ \mu m^2$. The LMH can support its own weight and preserves its mechanical integrity. The Young's moduli of C_{60}/JCNM multilayers were measured by mechanical bulge tests and are presented in figure I.10(h). Within the accuracy of the measurement, the Young's moduli have similar values, demonstrating that the mechanical properties are not degraded upon the assembly of the hybrid.

II. Top-down

II.1. Precursors

A wide variety of GRMs with different characteristics can be obtained through liquid phase techniques [111, 115]. For a given approach, the selection of an appropriate precursor allows to tune the final features and properties of the GRM products in order to optimize their performance for each application. Graphite is the reference starting material to produce graphene, but it presents different characteristics like particle size, crystal size or purity, which have to be considered. E.g., graphite with small crystal size will limit the maximum lateral size of the final graphene flakes. Other precursors, such as nanocarbons (i.e. carbon materials with nanoscale size, such as CNTs) [17, 116, 117] or pre-graphitic carbons (short ranged ordered amorphous carbons) [118, 119] have been also investigated as potential candidates for graphene production, as discussed below.

II.1.1. Graphite

Graphite consists of stacked graphene layers bonded by van der Waals (vdW) forces [120]. Carbon atoms are hexagonally arranged and SLGs are parallel to each other. Graphite has two main allotropic forms, hexagonal [121] (figure II.1(a)) and rhombohedral [122] (figure II.1(b)). In both cases the carbon hybridization is sp^2, the C–C distance in the basal plane is 0.1417 nm, and the distance between the layers is 0.3320 nm. The hexagonal form is the most stable, with layers stacked in an ABAB sequence (unit cell constants: $a = 0.2456$ nm, $c = 0.6708$ nm) [121]. In Rhombohedral graphite the sequence of the layers is ABCABC (unit cell constants: $a = 0.2566$ nm, $c = 0.10062$ nm) [122].

Graphite can be natural or synthetic. The latter can be obtained by subjecting non graphitic carbons as pitches and cokes to high temperatures (1700 °C–2700 °C) in inert atmosphere or vacuum [123–125]. This is the case of graphitizable carbons, i.e. non-graphitic carbons which, upon thermal treatment, convert into graphitic carbon, [126]. The degree of graphitization, the amount of disordered phase converted in their graphitic counterpart, can be further increased by performing thermal treatment under high pressure (100–1000 MPa) [127]. Graphitic materials can also be obtained by CVD of hydrocarbons, such as methane [128] or ethane [129] at $T \sim 1200$ °C or by catalytic (c-CVD) and these synthetic methods are reviewed in section V.

Graphene can be obtained by exfoliation of graphite [130]. The presence of defects in the layers leads to graphene with lower conductivity [120, 131–134]. Graphite with large crystal size allows one to obtain bigger flakes [132]. The crystal boundaries of the starting graphite have an impact on the amount and type of oxygen functional groups introduced in the oxidation reaction resulting in GO [132], influencing also the sonication time required to overcome the vdW interactions [133], as well as the chemical structure of the RGO obtained after thermal [135] or chemical reduction [135]. The microstructure of graphite can be distinguished by polarized light microscopy [120], where the different crystalline domains are defined by the interference colours (figure II.2(a). Figure II.2(b) shows an SEM image of graphite in which these features cannot be observed. The distribution of crystal size also influences the polydispersion in lateral size of the obtained GO/RGO material, limiting the maximum lateral size. The final average size of graphene is usually much smaller than the initial crystal size in graphite, and is mainly dictated by the mechanical process of exfoliation at the meso- and nano-scale [136, 137].

GO/RGO has been prepared from different natural graphites [138]: flaky, (natural graphite of finely powdered crystalline graphite with grain size smaller than 250 μm), lumpy (crystalline graphite with a walnut to a pea size), and amorphous (exhibiting only short range order) [139, 140]. Lower crystallinity of the parent material (lumpy > natural > amorphous) leads to higher defects, smaller GO sheets' size and higher surface areas (figure II.3). Natural graphites can contain silicates and other particles that can contaminate the final GRM, as detected by thermogravimetric (TGA) measurements [141].

Smaller particle size will result in higher content of oxygen functional groups in GO, because of easier diffusion of reagents during oxidation. This influences the final electrical and thermal properties [142, 143]. Graphite with particle sizes >200 μm are adequate for the production of GRM to be used in thermoset composites by infusion [144]. Particle size >600 μm are ideal for conductive thermoset composites [145].

The discrete particle size of graphite, as observed in SEM, is different than the particle size determined by other techniques such as laser diffraction, optical microscopy or granulometry. Laser diffraction or granulometry increase the measured particle size of graphite due to the agglomeration of discrete crystals. SEM can distinguish between different or discrete crystals and allows the measurement of particle size with more accuracy. In the case of optical microscopy, it is more difficult to separate particle sizes.

Expanded graphite is a graphite-derived material formed by a two-step oxidation-reduction process that retains the long-range-ordered layered structure of graphite, yielding a large interlayer distance. It can be used for the preparation of GRM by liquid methods [147]. Typical expanded graphites used for the preparation of graphene flakes have a medium diameter D50, i.e. the value of the particle diameter at 50% in the cumulative distribution of particle size diameters, from 15 to 50 μm.

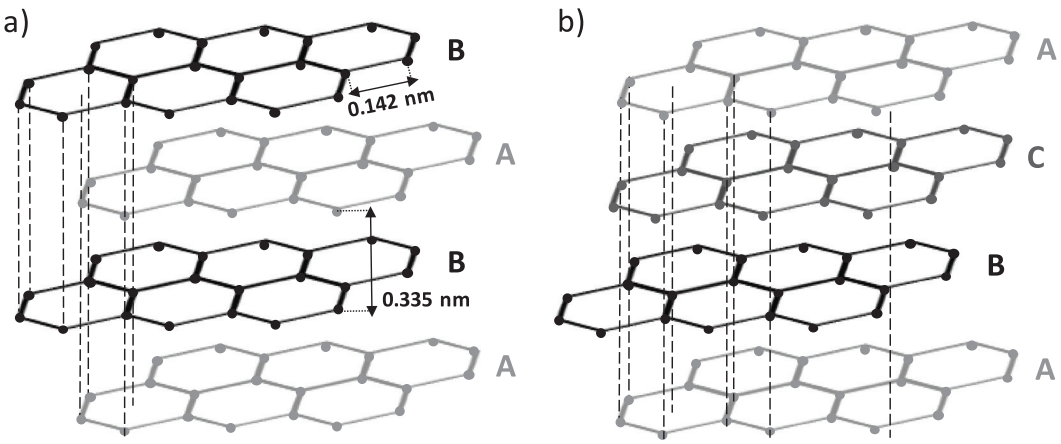


Figure II.1. (a) Hexagonal and (b) rhombohedral structures of graphite.

II.1.2. Non-graphitic carbons

Non-graphitic carbons were also proposed [148, 149] as precursors for the synthesis of GRM by top-down techniques. e.g. petroleum and coal-tar pitches pass through a liquid or liquid-crystalline phase when subjected to heat treatment in inert atmosphere [150]. These materials are graphitizing and develop a graphitic microstructure upon heating to 3000 °C [151]. When these precursors are carbonized at lower temperatures (1000 °C), they become cokes. A coke is a solid carbonaceous material derived from distillation of low-ash, low-sulphur bituminous coal, or derived from oil refinery coke units or other cracking processes [152]. It has a partially organized lamellar structure resulting from the parallel stacking of layers of sp^2-hybridized carbon atoms. Therefore, Refs. [148, 149] suggested that these could be used for the preparation of graphene flakes. Since high T (up to 2500 °C–3000 °C) are required to obtain synthetic graphites, the direct use of cokes as precursors reduces the environmental impact of the whole process. Moreover, the broad range of microstructures and chemical compositions of cokes (as determined by the carbon source and the carbonization conditions) makes them a suitable starting material for the synthesis of graphene or GO with targeted structures and compositions.

Due to the different microstructure and chemical composition of cokes and graphites, the conditions for the synthesis of GRM should also be adjusted. Thus, compared to graphites, cokes require larger amounts of reactants during their oxidation by the Hummers' method. Otherwise, its exfoliation into GO would have a much lower yield [148]. When cokes and graphites were exfoliated in NMP, flakes from coke had a larger number of defects and smaller lateral size (~400 nm) than those from graphite (~1 μm) [148]. Similarly, as the crystallinity of cokes increases, its subsequent exfoliation yields flakes with larger lateral size and in higher yield [149].

II.1.3. Nanocarbons

CNTs or nanofibres (CNFs), have also been explored as alternative precursors to produce graphene sheets and GNRs in liquid media [17, 116, 117]. Twisted ribbon-shaped carbon nanofibers are helical carbon nanofibers comprising 5–6 stacked graphene layers [117, 153–155]. Two approaches have been proposed for the production of graphene flakes and sheets from these [153, 154]. The first is based on a mechano-chemical method, through melamine intercalation during ball milling in different solvents such as isopropanol, THF or DMF. Ref. [153] produced graphene suspensions in low boiling point solvents such as 2-propanol (~83 °C) and THF (66 °C) by a scalable method [153]. Ref. [154] obtained GO/RGO flakes® using the Hummers' method [156] and different reduction techniques [154, 157, 158].

GNRs have been produced from CNTs as the starting material by solution-based oxidative processes [17, 117]. CNTs suspended in concentrated H_2SO_4 were oxidized by adding $KMnO_4$ (500 wt%with respect to CNTs) at $T < 70$ °C [17].The resulting GNRs have straight edges and are dispersible in water and other polar solvents due to the presence of oxygen moieties. Unzipping single-wall carbon nanotubes (SWNTs) [17] gives GNRs, but these are difficult to disentangle. Multi-wall carbon nanotubes (MWNTs) led to less entangled GNRs [17], that can be separated to single layers after sonication. Carbonyls, carboxyls and hydroxyl groups present in the GNRs can be reduced by treatment with aqueous hydrazine ($N_2H_4{\cdot}H_2O$) after dispersing them in aqueous sodium dodecyl sulphate in order to prevent their re-aggregation. CNT unzipping by intercalation of lithium and ammonia and subsequent exfoliation was also reported [116]. However, this procedure yields a mixture of multi-layer GNRs, partially open MWNTs, and flakes, contrary to oxidation with $KMnO_4$, which allows a nearly 100% yield of GNRs with no presence of partially open MWNTs [117].

II.2. Liquid phase exfoliation

Various strategies have been developed to produce colloidally stable GRM dispersions. They can be classified into intercalation-based methods [159–161],

and methods relying on mechanical exfoliation and further stabilisation by suitable solvents/surfactants (LPE) [161–164]. Oxidative intercalation of graphite and subsequent delamination to yield GO are amongst the oldest techniques [156].

LPE is one of the simplest and most versatile strategies to obtain colloidally stable dispersions from a broad range of LMs. Energy in the form of sonication or shear is used to overcome the van der Waals attraction in bulk LM. If this is done in a suitable liquid (solvents with matching solubility parameters, or additives that act as electrostatic and/or steric stabilizers [165]), reaggregation is prevented. The resulting flakes can have low defect densities, and can be further solution-processed by a range of techniques [166]. LPE of MoS_2 and WSe_2 was reported in 1989 [167].

While LPE is a versatile method for producing large quantities of flakes from bulk powders, it has some disadvantages. The flakes are highly polydisperse with a range of sizes and thicknesses (lateral sizes ranging from tens of nanometres to tens of microns, number of layers (N) from 1 to 100 s of layers). The dispersions can also have low monolayer content (YM $<$ 1%). A precise, statistical analysis of size distribution due to exfoliation by ultrasound has been reported, for GO sheets [136]. For application areas where LPE flakes are well suited, such as printed optoelectronic and electrochemical devices, optimized performance is unlikely to arise through direct use of the pristine dispersions. This is especially true for those applications requiring direct bandgap luminescence of transition metal dichalcogenides (TMDs). Thus, size selection must be an integral part of the production process [168].

Many strategies exist for both exfoliation and size selection, depending on the starting material and the desired outcome. A number of review articles on exfoliation in liquid media have been published [115, 161–164, 166, 168–170, 172, 173]. Here, questions such as which medium (e.g. solvent or surfactant) or exfoliation method (e.g. sonication or shear) is more suitable and how to size-select flakes using benchtop centrifuges are addressed.

II.2.1. Choice of medium

II.2.1.1. Solvents and detergents

In a typical LPE experiment, the bulk crystal is immersed into a liquid and subjected to sonication [131, 162, 173–175], shear mixing [176, 177], microfluidization [178], ball milling [179] or similar [180, 181]. Prior to designing an experiment, thought needs to be given to the choice of medium. This can be crucial and will often depend on the starting material in combination with the exfoliation method and the purpose of production. Irrespective of the exfoliation method and/or medium, a purification step of the starting materials (e.g. graphite flakes) is useful, since these may contain impurities that can destabilize the dispersion.

Aqueous surfactant solutions are widely used as stabilizers in LPE [172, 182–184]. Usually, xfoliation, stabilization and size selection is quite robust and reproducible giving access to long-term (weeks-months) stable, dispersions. In order to retain 'pristine-like' optical properties, similar to those of micromechanically cleaved (MC) materials, aqueous surfactant solutions are of advantage. E.g., photoluminescence (PL) of MoS_2 and WS_2 can be observed in single layer (1L)-enriched solutions in sodium cholate (SC) with emission dominated by excitons and at similar spectral positions as MC TMDs [185, 186]. Surfactants such as SC are water soluble and do not require the same level of health precautions as organic solvents [187]. SC is compatible with many processing techniques such as vacuum filtration and spraying. However, printing from aqueous surfactant still remains challenging, as it is difficult to control the rheological properties [166]. In addition, there are two other downsides. First, some materials (such as GaS [188] or black phosphorus [189, 190]), can degrade in the presence of water/oxygen [189, 191] so that aqueous surfactant solutions cannot be used. Second, it is difficult to completely remove the surfactant from the resulting flake surfaces after processing, as it can be trapped between restacked flakes, potentially deteriorating the resulting network properties. A few systematic studies (see [161–164, 166, 168–173, 192]) exist on the impact of the chemical structure of the surfactant or its concentration on the degree of exfoliation, i.e. N or yield of 1L and few layer (FL) flakes as well as their lateral size, with detailed data available for SC or sodium dodecyl benzene sulfonate (SDBS). However, a comprehensive picture is still lacking due to the vast parameter space (materials, surfactants, concentrations, exfoliation techniques, centrifugation procedure). Systematic studies on the effect of less common surfactants, such as polycyclic aromatic hydrocarbons (PAH), have also been reported, correlating the adsorption energy of the single molecule on graphene to the overall exfoliation performance [193, 194]. Flakes produced in aqueous surfactants are smaller, but also thinner than in solvents such as *N*-methyl-2-pyrrolidone (NMP) and *N*-Cyclohexyl-2-pyrrolidone (CHP) [174]. This is most likely related to the higher viscosity of these solvents compared to aqueous surfactant. This can on the one hand hinder intercalation of the solvent between the layers of the crystals during the exfoliation process and in addition lead to a slower sedimentation in the centrifugal field [195] and hence a larger population of larger/thicker nanosheets. Details on differences in sizes/thicknesses and yields of 1L and FLstrongly depend on material, exfoliation conditions and centrifugation conditions making it difficult to quantify these effects.

Solvent stabilisation can be described in the framework of solubility parameters [196]. Solvents or solvent blends can stabilize liquid-exfoliated flakes and prevent them from reaggregating, when solubility parameters, such as surface tension or Hansen parameters, of solvent and solute match [131, 174, 197–200].

Chemically unstable materials, such as black phosphorus (BP), can be protected against degradation through a stabilising solvation shell [190]. In addition, it is easier to tune rheological properties for processing techniques such as inkjet printing [201] and solvent removal is typically easier than for surfactants. However, certain solvents, such as NMP or ODCB, can degrade and polymerize [202, 203], changing the properties of the exfoliated material, while hampering subsequent spectroscopic and microscopic characterization [204]. In such cases, the solvent can also remain on the flakes surfaces. In general, good solvents show a strong, yet noncovalent interaction with the flakes, altering optical properties as, e.g. manifested by PL shifts in TMDs [186]. Another consideration is that many suitable solvents, such as NMP, suffer from high boiling points (>200 °C) and are often toxic [205]. Some solvent blends have been identified as promising (e.g. alcohols and water) [206, 207] to potentially overcome the limitation of the high boiling point solvents.

GRM dispersions in water can also be stabilized by using a wide range of polymers [182, 208–212], such as ethyl cellulose (EC) [209], cellulose acetate (CA) [208], lignin [211], polyvinylpyrrolidone (PVP) [210], and even more complex systems [182, 212]. The use of polymers as stabilizing agents in the LPE process works better than the use of small organic molecules in terms of the concentration of graphene dispersions. Yet, because of the strong polymer/graphene noncovalent interactions, flakes produced by exploiting this approach cannot be completely separated from the polymer/graphene composites [213].

II.2.1.2. Molecule-assisted LPE

Stable dispersions of graphene in water have also been obtained using small polyaromatic dyes as surfactants [194, 214, 215]. Thanks to their aromatic core, these molecules can adsorb strongly on the graphene surface (E_{ADS} ~ 15 Kcal mol^{-1}), forming also ordered layers [193]. They have also a strong (molar absorption coefficient $\varepsilon > 15\,000$ l g^{-1} m^{-1}) and unique absorption and emission spectra in the visible range, which allows to monitor their interaction with graphene in solution and in solid [216, 217]. Many of these molecules are low cost (<100 \$ Kg^{-1}) dyes, widely used in large-scale compounding of polymers, e.g. as industrial additives and colorants dyes [218]. While most of the work has been done with graphene- where a strong interaction of the aromatic core of the dye with the extended π-electron network of the flakes occurs, these molecules can also be used to exfoliate a wide range of LMs, such as BN [219], WS_2 [219] and MoS_2 [219], selenides and tellurides [219].

The use of properly selected small PAH organic molecules or polymers can enhance the exfoliation of graphite, in particular when the molecules/polymers possess a high (E_{ADS} ~ 15 Kcal mol^{-1}) energy of adsorption on the basal plane of graphene. However, these molecules or polymers do not act as graphene dispersants or graphite exfoliators, i.e. they do not trigger the exfoliation. These molecules/polymers mainly act as dispersion stabilizing agent via the non-covalent functionalization, i.e. through the adsorption of their hydrophobic moieties on the graphene surface during the process of exfoliation [165]. Therefore, they can prevent re-aggregation and increase the stability of both aqueous and organic dispersions [165].

Using water as a LPE media is a natural choice because of its non-toxicity and offers potential for the formation of biocompatible graphene-based materials for biomedical applications [220]. Yet, LPE of graphene in water is particularly challenging due to the hydrophobic nature of the sheets. This challenge can be overcome by using surfactants such as SC, which allow exfoliated flakes to remain suspended. Among various molecular stabilizers, PAHs [221, 222], substituted with numerous side groups, are the most studied compounds. Adsorption of PAHs onto the graphene surface occurs through π–π interactions between the planar π-conjugated surfaces. In these noncovalent interactions, both PAHs and flakes surfaces share the π-orbital electrons, ultimately resulting in the reduction of the surface free energy of the dispersion [194]. Various derivatives have been used to stabilize CNTs dispersions [223], and as in the case of NMP, they have been adopted for LPE of graphite [194, 224–226]. Nevertheless, not all stabilizers suitable for CNTs, having a curved surface, would be ideal for dispersing graphene with a flat surface. Because of the improvement of the exfoliation yield (the amount of solubilized material during LPE) and, in particular, increase in the number of SL in LPE in the presence of small PAHs such as pyrenes, NDIs, [227] and PDIs [228], and other PAHs are also expected to be suitable to stabilize graphene produced by LPE.

Regardless of the exfoliation yields (% of SL, concentration) and the stability of graphene in aqueous dispersions, the use of water as an exfoliation medium is not recommended for electronic devices such as FETs. The presence of water at the interface with the dielectric substrate can enhance charge-trapping [229]. Therefore, the use of stabilizers in organic solvents has also been explored [230–235]. For more details on the underlying specific noncovalent interaction, see section VIII.3.

II.2.2. Exfoliation methods

II.2.2.1. General considerations

The purity with respect to contaminations of the commercially available materials is often unpredictable, creating problems for the reproducibility in the exfoliated product. Accordingly, the general recommendation is to perform a two-step exfoliation process [185, 186, 236]. In the first one, the material in the medium of choice is subjected to a short (~20% of the time of the total planned duration) exfoliation. After this initial step, the dispersion should be subjected to centrifugation at

intermediate centrifugal acceleration (~5000 g) after which the supernatant is decanted and discarded and the sediment collected in fresh solvent/surfactant. This can then be followed by a second, longer exfoliation. This approach allows most of the impurities (and very small flakes) to be removed. This is particularly needed when working with ionic surfactants, as the impurities are often ionic and therefore, can destabilize the surfactant dispersion via charge screening effects.

A higher initial concentration of the precursor bulk material will also give a higher concentration of exfoliated flakes, up to when the dispersed concentration saturates. This initial concentration is typically $>30\,g\,l^{-1}$ of precursor concentration [174, 176, 177, 188, 190, 237–240]. Similarly, longer processing times yield higher dispersed concentrations [174, 176, 177, 188, 190, 238–242]. While this can also change the length and thickness distributions in the as-obtained dispersion [241], this effect can be balanced by appropriate size-selection techniques [168].

The choice of the exfoliation method is material dependent. E.g. while graphite is readily exfoliated for various methods [176, 177, 237] (sonication, shear, microfluidization, ball milling), this may not be the case for other materials. In particular for TMDs, the quality of exfoliation (as measured by the concentration/yield of 1L and 2–5 L flakes is better when using tip sonication compared shear mixing [176, 238]. For GaS, bath sonication is most effective [188]. When attempting to exfoliate a new material, it is important to not only consider the stabilizer, but also to test various available exfoliation methods. In particular the role of the crystallite size of the starting material in combination with the exfoliation method has not been investigated systematically.

II.2.2.2. Sonication

Sonication can be performed in tip or bath sonicators. In tip sonication, energy is imparted to the dispersion media directly [243], whereas in the sonic bath, the energy must travel through the tank and dispersion vial before reaching the flakes [243]. Although the scalability of sonication to produce few layer flakes has not been demonstrated (compared with shear exfoliation and ball milling), tip sonication remains useful as lab-scale technique, as the material quantity (hundreds of mg) is generally sufficient to test size-dependent properties in a range of application areas.

For LMs, tip sonication is preferred over bath sonication due to the higher production rates, (i.e. more exfoliated material is produced in shorter times, with concentrations in the range of $\sim 1\,g\,l^{-1}$ in <24 h for initial bulk material concentrations of $30–50\,g\,l^{-1}$) [174, 186, 244]. In this case, various sonic tip configurations are available with different probe sizes and shapes and processors. In typical protocols [185, 186, 245, 246], solid flathead tips are used at sonication amplitudes ~60%–75%. At lower amplitudes, exfoliation can be poorer: the mean N WS_2 increased by ~1 (across eight size-selected dispersions) for sonication at an amplitude of 50% compared to 60% [246]. From experience, higher amplitudes can damage the processor after prolonged (100 s of hours) use. 500 and 750 W do not give noticeable differences [246]. Since the sonic energy falls off exponentially from the probe [243], it is important to match the container to the probe size as recommended by manufacturers. Even though the dispersed concentration of FL flakes increases with sonication time [174, 176, 177, 188, 190, 238–242], 5–7 h of sonication provides a compromise between dispersed concentration and time.

It is crucial to prevent heating of the sample, especially in tip sonication, but also in bath sonication, shear exfoliation, etc. This is not only because heating can deteriorate the properties of the material, but also because dispersed concentrations are lower. While cooling in tip sonication can be achieved by positioning the reaction vessel, i.e. a metal cup in an ice bath, it is far more ideal to install a chiller, as the ice must be replenished every 2 h or so [245]. In addition, keeping the dispersion cool is facilitated by pulsing the sonication through the device controller. For a given combination of sonicator, operating conditions, cooling, sonication time and material, the outcome of tip sonication appears reproducible both in terms of dispersed concentration and size distribution [185].

In general, bath sonication may offer a lower-cost alternative to tip sonication, and additionally, in some cases, such as for GaS [188], this is preferred because tip sonication can damage the exfoliated flakes. The energy input is lower in bath sonication [243], as it is less. Therefore, less material fragmentation is expected. However, longer processing times are required (depending on material) to achieve an equivalent concentration of dispersed material compared to tip sonication. For TMDs, sonication times are longer by a factor ~20 in bath compared to tip sonication. In general, bath sonication is less reproducible than tip sonication, and the outcome varies depending on specific bath used, filling level of the bath, and positioning of the vial within the bath. While more reproducible results can be obtained by rotating the sample in the bath during sonication, this will result in a lower dispersed concentration for an equivalent sonication time compared to placing vials in 'hot spots' (thermolytic centers, where the sonication induced cavitation bubbles of the water in the tank preferentially collapse). Again, it is important to prevent heating of the sample (at least for non graphene LMs) by either installing a cooling system or exchanging the water every 30 min.

II.2.2.3. Shear exfoliation

Alternatively to sonication, one can use shear exfoliation in rotor stator mixers [176] or in blenders with rotating blades [177, 238]. Even a kitchen blender can be used, offering a very low cost alternative to sonication [177]. However, the household kitchen blenders are not designed to

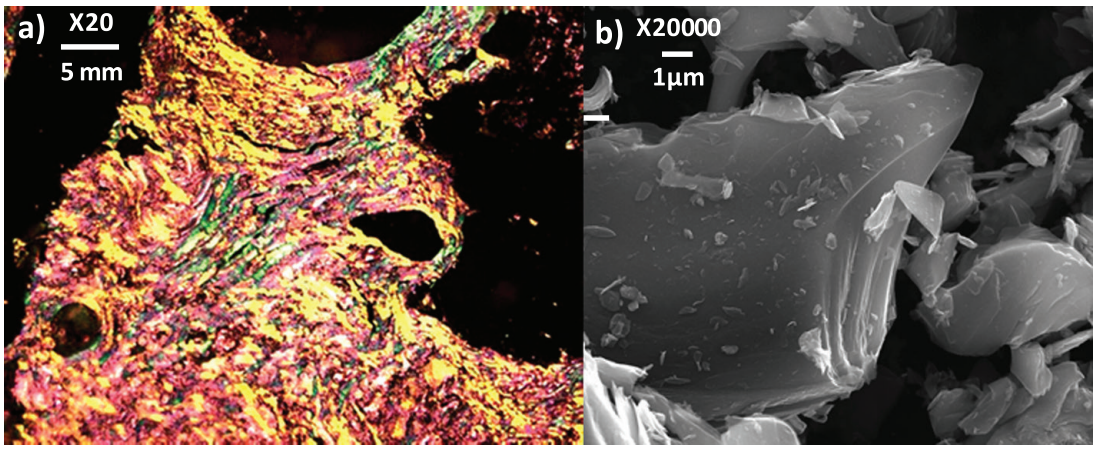


Figure II.2. (a) Optical micrograph acquired with an oil-immersion objective (20×) and an one-wave retarder to generate interference colours and (b) SEM picture of the same graphite.

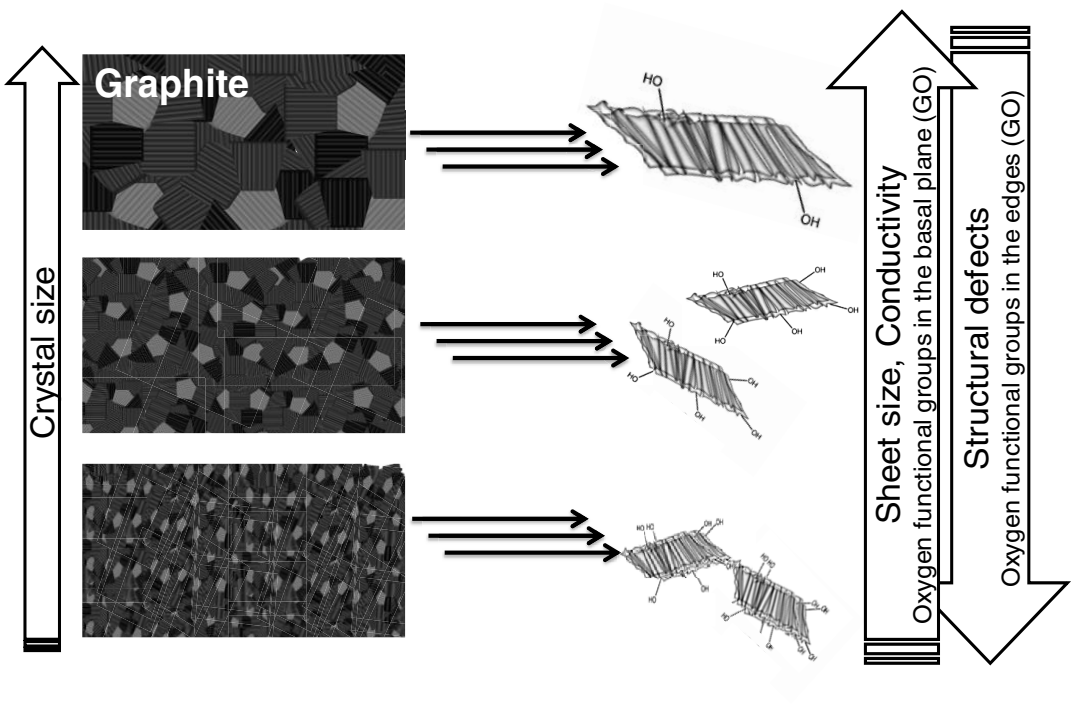


Figure II.3. Schematic model of partially reduced GO and their parent graphites.

operate in organic solvents and can be destroyed when doing so. In addition, continuous operation heats up both sample and mixer, so that the run has to be paused frequently (after 15 min) and mixer and sample cooled in an ice bath. The dispersed concentration of FL flakes is not strongly dependent on the processed volume, so that shear exfoliation is a scalable process with production rates of 0.15 g h^{-1} for graphene and 1.3 mg min^{-1} for MoS_2 [176, 177, 238]. The quality of the material in terms of dispersed concentration and mean N is comparable to sonication in the case of graphene [177].

II.2.2.4. Microfluidization

Microfluidization is a homogenization method that applies high pressure (up to 207 MPa) [247] to a fluid forcing it to pass through a microchannel, figure II.5. The key advantage over other LPE methods is that high shear rates ($\dot{\gamma} > 10^6 s^{-1}$ [248, 249]) can be applied to the whole fluid volume [249], not just locally. Microfluidization was used for the production of polymer nanosuspensions [247], in pharmaceutical applications to produce liposome nanoparticles with diameters smaller than 80 nm to be used in eye drops for drug delivery to the posterior segment tissues of the eye [250], or to produce aspirin nanoemulsions [251], as well as in food applications for oil-in-water nanoemulsions [252]. Microfluidization was also used for the de-agglomeration and dispersion of CNTs [253].

The main step of this process involves placing the graphite/solvent mixture into an inlet reservoir.

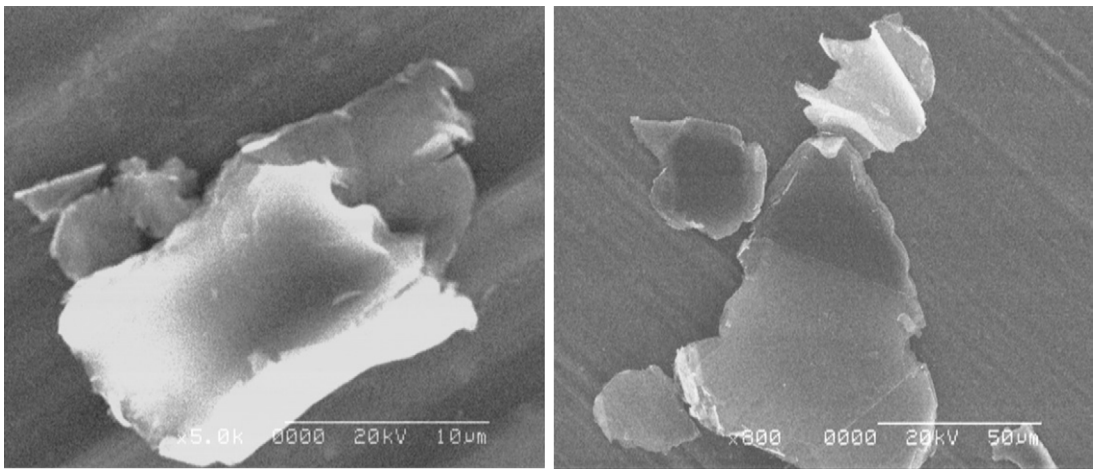


Figure II.4. SEM images graphite 0–200 μm (>0.2 mm; 10% max) and a graphite 0–600 μm. Adapted from [146].

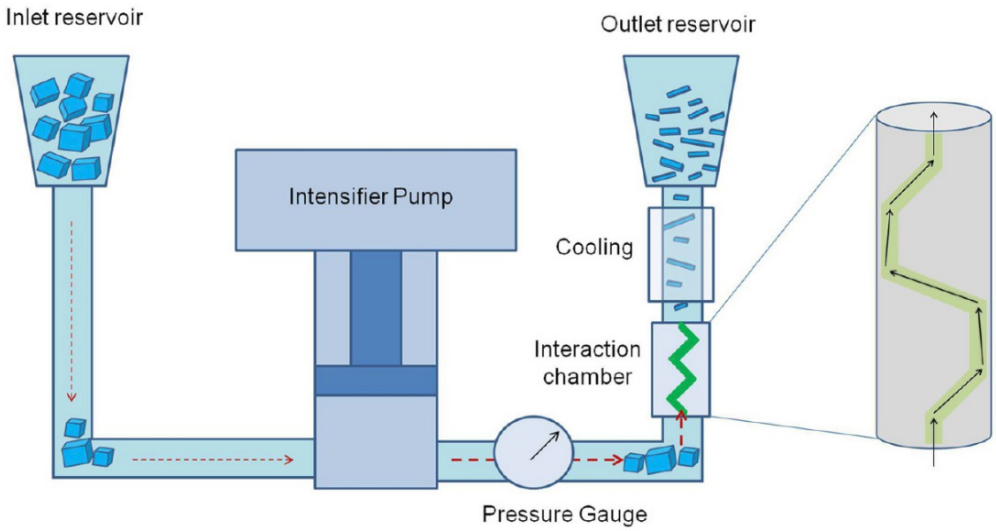


Figure II.5. Schematic of microfluidization process. Graphite flakes in SDC/water are added in the inlet reservoir. An intensifier pump applies high pressure (207 MPa) and forces the suspension to pass through the microchannel of the interaction chamber where intense $\dot{\gamma} \sim 9.2 \times 10^7\ s^{-1}$ is generated. The processed material is cooled down and collected from the outlet reservoir. The process can be cycled several times [178]. Adapted from [178].

An intensification pump, driven by electro-hydraulics, provides two motions, suction and compression, drawing a portion of sample into the processor through a one-way valve, and then pushing this sample fraction past the pressure gauge and through sub-millimetre sized channels within a diamond interaction chamber, where graphite exfoliation takes place [178].

Interaction chambers are typically based on two geometries, *Y*- and *Z* type. The *Z*-type chamber is preferred for graphite exfoliation, since the geometry consists of sharp turns and a narrow rectangular cross-section for optimal shear. The chamber G10Z is ~87 μm in diameter. The motion of the intensification pump creates mixing within these micro channels, generating pressures > 30 000 psi (~2100 bar). The fluid dynamics of the process can be turbulent or laminar as defined by the Reynolds number, dependent on the kinematic viscosity and density of the solvent used [178].

Below are two typical recipes for the production of graphitic flakes without centrifugation (Method 1), or FLGs following centrifugation (Method 2). Due to the dimensions of the interaction chamber, microfluidic processing of large (>100 μm) graphite flakes may block the microfluidic channel. Instead, smaller powder sizes are advisable (typically, the particle diameter corresponding to 90% cumulative (from 0 to 100%) of the undersize particle size distribution (D90), less than 30 μm).

II.2.2.4.1. Method 1: production of multi-layered flakes
This method [178] refers to the production of high yield (100 wt.%), high concentration (up to 100 g l^{-1}) graphene-based inks that are not centrifuged. Graphite powders (natural or synthetic, particle size <30 μm) are mixed at a concentration up to 100 g l^{-1} with SDC at a concentration 9 g l^{-1} in water in typical batch sizes of 250–500 ml. The material is collected in a

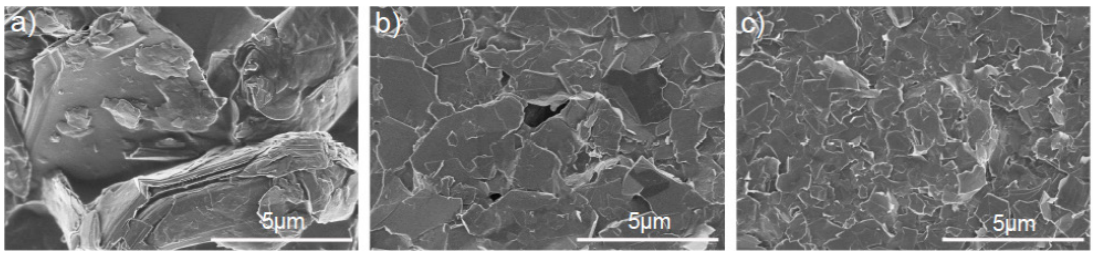


Figure II.6. SEM images taken from coatings comprising (a) starting graphite, (b) after 5 cycles and (c) after 100 cycles. Reproduced from [178].

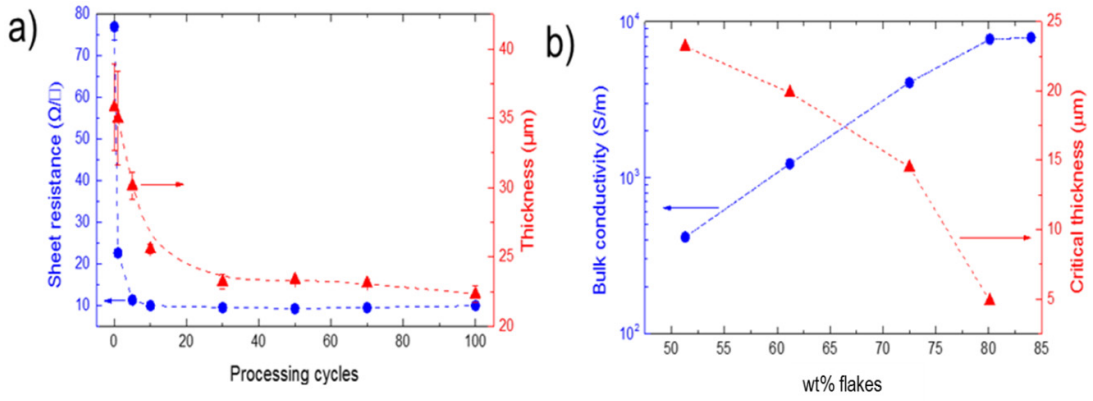


Figure II.7. (a) Rs and film thickness as a function of processing cycles for a formulation with 73 wt% flakes, (b) bulk and critical thickness as a function of loading (70 cycles). All samples are dried for 10 min at 100 °C. Reproduced from [178].

beaker and placed back in to the inlet reservoir to cycle automatically for the desired length of time depending on the number of process cycles, n (where n is typically <70). The final product is collected. Sodium carboxymethylcellulose (NaCMC) (10 g l^{-1}) is added whilst stirring to adjust the viscosity to the required value. NaCMC is slowly added until fully dissolved in order to avoid the formation of clumps. Clumps that are formed should be ground with a spatula and the ink left to stir overnight.

Figure II.6 shows SEM images of the coatings comprising the starting graphite (figure II.6(a)), after 5 (figure II.6(b)) and 100 cycles (figure II.6(c)). Flake size reduction and platelet-like morphology is observed after microfluidic processing.

Since these inks are not further processed by centrifugation, Y_W (yield by weight) is 100 wt.%. 4 wt% of the exfoliated material consists of FLGs (<4 nm thick) that can be isolated using Method 2 below, and 96 wt% are flakes in the 4 to 70 nm thickness range. The stabilized dispersion can be used for blade coating and screen printing. Figure II.7 plots the sheet resistance (Rs) and thickness of blade coated films as a function of process cycles at a flake loading of 80 g l^{-1} (73 wt.%), highlighting that exfoliated materials produce thinner films with lower R_s. The bulk conductivity of films increases with loading with a plateau above 80 wt.%, and the critical thickness at which bulk conductivity is reached is less when loading is higher. After annealing (300 °C–40 min), R_s reaches 2 Ω □$^{-1}$ at 25 μm (conductivity, $\sigma = 2 \times 10^4$ S m^{-1}), suitable for electrodes in devices such as OPVs [254, 255], organic thin-film transistors (OTFTs) [256] or radio-frequency identification (RF-IDs) [257]. The inks can then be deposited on glass and poly(ethylene terephthalate) PET flexible substrates using blade coating and screen printing to demonstrate the viability for these applications (OPVs, OTFTs, RF-IDs). Screen printing is discussed in section III.

II.2.2.4.2. Method 2: production of FLGs

Below we show that FLG can be obtained by adding an additional centrifugation step. Graphite powders (natural or synthetic) with D90 < 30 μm are mixed at a concentration 12 g l^{-1} with SDC at a concentration ~0.5 g l^{-1} in water and microfluidized for n typically <100). Following processing, samples are centrifuged typically at 10 000 rpm (17 000 g) for one hour. Films obtained by vacuum filtration of the FLG ink have R_s ~ 4.5 kΩ □$^{-1}$ at 90 nm thickness, significantly better than the equivalent sonication produced graphene films that have R_s ~ 8.9 kΩ □$^{-1}$ at 160 nm. The effects of processing cycles, pressure, surfactant concentration, centrifugation speed and graphite loading on graphene concentration are shown in figures II.8(a)–(f) AFM indicates that the exfoliated material consists of FLG, with ~18% SLG (figure II.9).

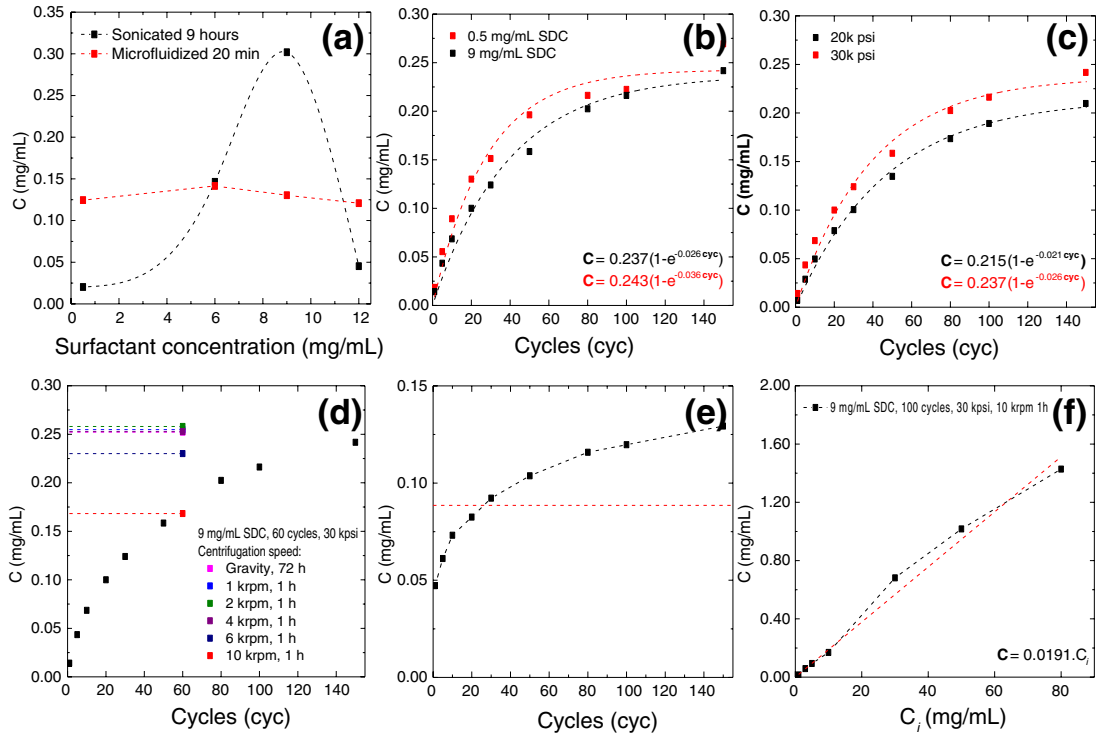


Figure II.8. (a) Effect of SDC concentration at fixed processing cycles (~60 cycles, 20 min, red) compared to sonication processing (9 h, black). (b) Effect of surfactant concentration 0.5 g l^{-1} (red) and 9 g l^{-1} (black) and process cycles. (c) Effect of process pressure 20 k psi (black) 30 k psi (red). (d) Effect of centrifugation parameters; (e) effect of using NaCMC as a stabilizer. Dashed red line represents sonication processing using the same NaCMC loading. (f) Effect of increased graphite loading.

II.2.2.5. Ball milling

Ball milling can produce FLG at low-cost and under environmentally friendly conditions. It does not require solvents, avoiding the use of toxic organics, while increasing efficiency in terms of time and energy.

Two effects take place in ball milling [163]: the shear force, that promotes the synthesis of large-sized flakes, of the order of the starting graphite planes, and the vertical impacts applied by the balls during the rolling actions, which tend to deteriorate the flakes and must then be minimized in order to reduce the number of defects. Ref. [258] reported changes of graphite, during milling processes, through a nanocrystalline phase prior to amorphization. To avoid this and favour the shear force process, the use of solid exfoliating agents is recommended.

Exfoliating agents, including triazine derivatives, can be used to form multipoint interactions with the exfoliated flakes. Amounts around few grams of graphite and exfoliating agents, such as melamine (2,4,6-triamine-1,3,5-triazine), can be used to prepare FLGs, which can subsequently be dispersed in organic solvents, such as DMF or in aqueous media [179]. The lateral size of the resulting flakes can be modulated depending on the ball-milling conditions (atmosphere, revolutions, and time of treatment). Different triazine derivatives were tested, in relation to their ability to exfoliate graphite, not only experimentally but also by computational studies, which evidenced that melamine is a good option to favour exfoliation [259]. Melamine not only has an aromatic nucleus that can interact with the graphene π-system [259], but can also form an extended network on its surface, owing to the presence of hydrogen bonds (figure II.10). Melamine can then be washed away using hot water, leaving high quality graphene suspensions, with very small Raman D peak.

In a typical experiment, 7.5 mg of graphite and 22.5 mg of melamine are ball-milled at 100 rpm for 30 min, under air atmosphere, in a stainless steel grinding jar containing ten stainless steel balls of 1 cm of diameter. The resulting solid mixture is dispersed in 20 ml of solvent, obtaining black suspensions. Filtration can remove melamine from the suspensions, giving rise to FLG dispersions in different solvents. If DMF is used as a solvent, colloidally stable dispersions are obtained with no precipitate observed. If water is used as a solvent, a concentration gradient appears, and some precipitation takes place after stabilization of the dispersion, at room temperature, for 5 days.

When preparing dispersions in water, melamine can also be eliminated by dialysis, which is highly recommended, mainly because this technique allows keeping the flakes always in dispersion [213]. It is advisable to hand-shake the dialysis sack and to apply a pulse of mild (bath sonication for no more than 1 min) if any precipitate appears in the black dispersion during dialysis. Once melamine is removed, the black dispersion is kept in the stabilization container at room temperature for 5 days, in order to obtain a concentration gradient. The liquid fraction with stable sheets in suspension needs to be carefully extracted, avoiding

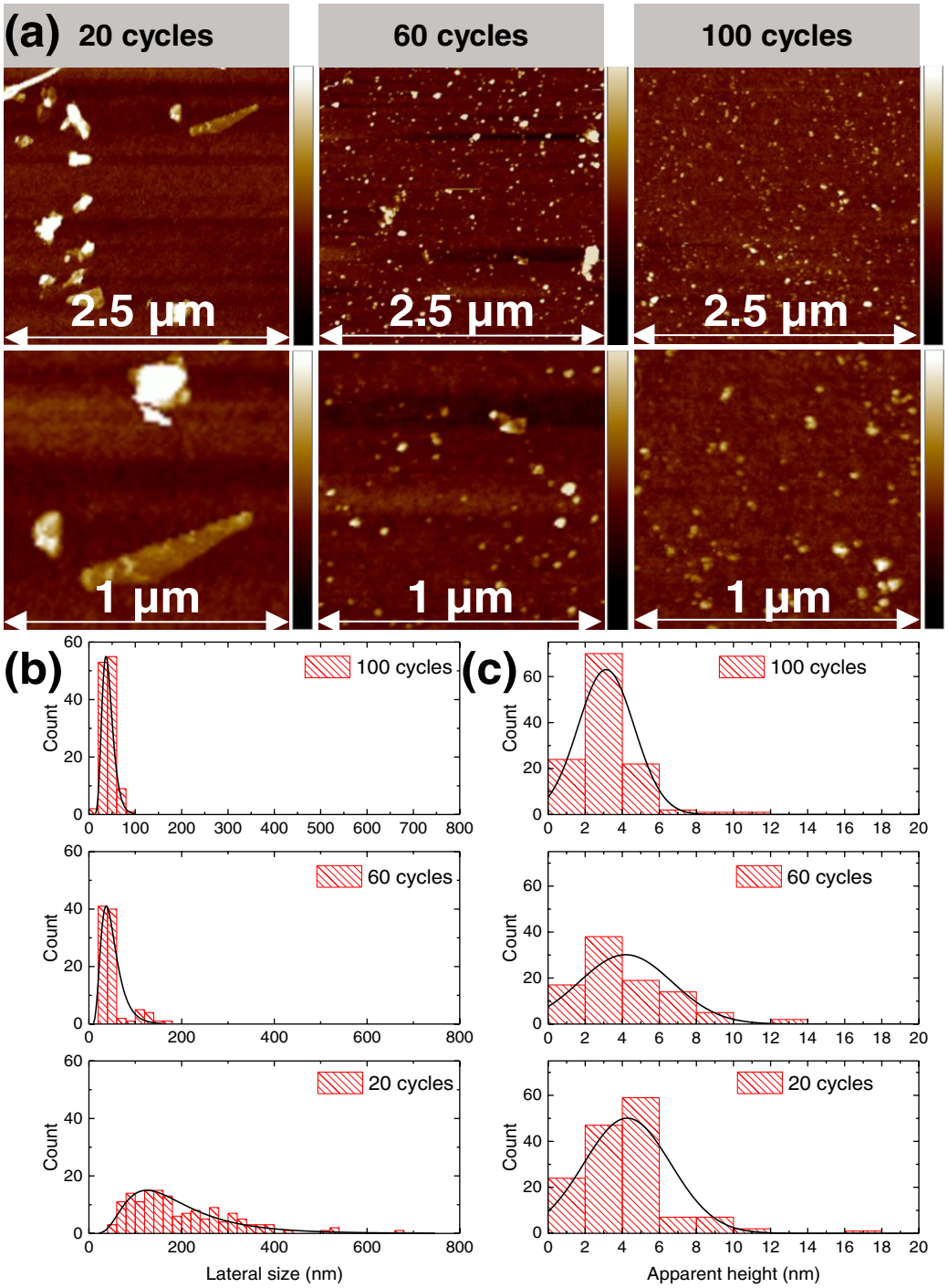


Figure II.9. (a) AFM height scans of flakes microfluidized for 20, 60 and 100 cycles. (b) Histogram showing the lateral size distribution of flakes with increasing process cycles. (c) Histogram showing the AFM height distribution for increasing process cycles.

the meniscus and the precipitate, in which non-exfoliated graphite remains. The obtained aqueous dispersions, with concentration ~0.1 g l^{-1}, are stable at RT for a few weeks. According to elemental analysis, these dispersions contain an amount of melamine lower than 1 ppm, which is considered non toxic [260].

Characterization of the FLG shows a low number of defects, with Raman ~0.2–0.6, confirming that no oxidation occurs during the preparation [179]. In [261], *ab initio* calculations on graphene-melamine-water systems have been performed focusing on how small amounts of melamine molecules tune the adsorption of few water layers on SLG. These reveal that melamine acts as a non-covalent anchor, keeping some water molecules near SLG, providing a quantitative estimation of the non-covalent interactions (dispersion and hydrogen-bonding), which provide the required driving force to stabilize the SLG-water systems.

A further advantage is that the aqueous suspensions can be lyophilized after having been frozen [262]. A very soft and low-density black powder, consisting of FLGs, is produced this way. This solid can be safely

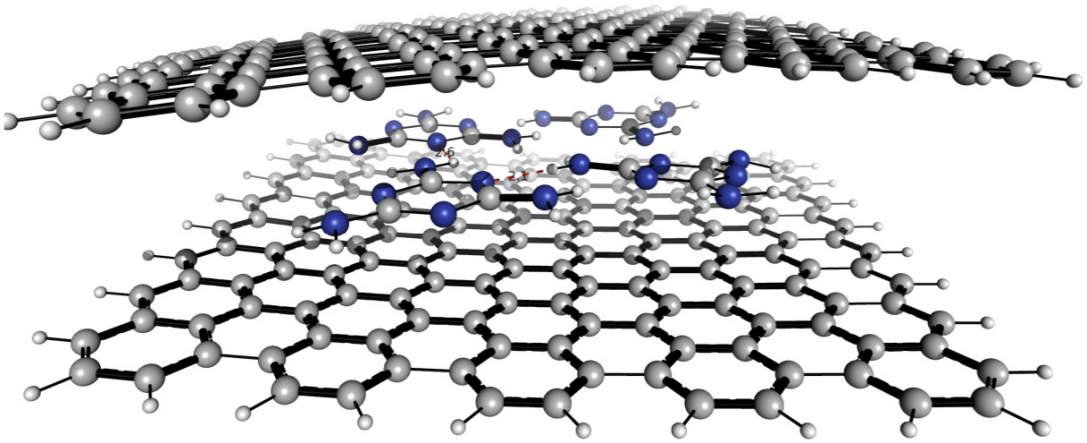


Figure II.10. Supramolecular assembly of melamine between SLG.

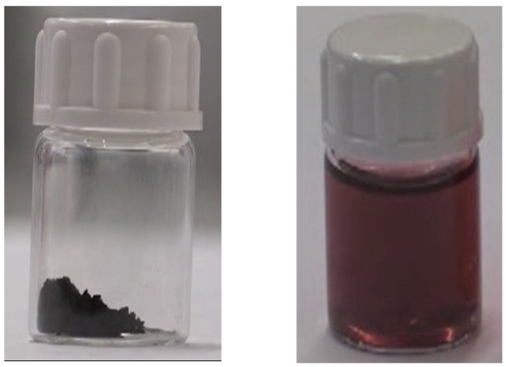


Figure II.11. FLG powder (left) and its dispersion in cell culture medium (right).

stored and shipped, being easily dispersed in water, culture media or other solvents, using mild sonication combined with shaking with no change in its structure (figure II.11). The mass yield of the entire process, starting from graphite, is ~30%.

In [179], powders were characterized with elemental analysis (EA), TGA, XPS, TEM and Raman spectroscopy. EA resulted in average values ~94.3 wt%C, 0.4 wt%H, 0.4 wt%N and 4.9 wt%O [1728]. TGA showed a weight loss [1728], in agreement with EA, confirming the non-oxidative nature of the milling treatment. This feature was also corroborated by XPS [179], as deconvoluted plots confirmed the presence of small amounts of oxygenated groups, from the C 1s and O 1s core level spectra and traces of melamine. XPS spectra (figure II.12) indicate that 15 min ultrasonication does not add a significant number of defects. TEM was used to determine the lateral flake sizes [1729], concluding that FLG have a wide size distribution ~200–2000 nm.

There is an increasing interest in the use of GRMs in biological applications. Dispersions in water and culture media allow the preparation of hydrogels for drug delivery [259], the study of synaptic functions in culture brain cells [263, 264] as well as environmental toxicity studies [262].

The addition of small amounts of solvent during milling was reported to improve exfoliation [153]. Solvent drop grinding was shown to be an effective technique to accelerate mechanochemical reactions [265]. The addition of catalytic amounts of a liquid phase facilitates molecular mobility, inducing reactivity in normally inactive systems. Therefore, wet milling conditions have been probed, and ball milling exfoliation of carbon nanofibers was reported [153]. Melamine was used as the exfoliating agent: 0.5 ml of solvent was added to 30 mg of nanofibres/melamine mixture. The Hansen solubility parameters of each material were studied in order to discriminate SLG from the rest of materials (FLG, poorly exfoliated carbon fibres and melamine) after the milling treatment. This allows one to select a suitable solvent to disperse mainly SLGs [153]. The quality of exfoliation was studied by Raman spectroscopy. Although there is a compromise between exfoliation quality and graphene concentration, these wet conditions follow the same trend established by the Hansen solubility parameters, permitting SLG dispersion [153].

To achieve larger particle sizes (in the range of microns), mechanical exfoliation by ball milling or high-shear mixing can be combined with chemical intercalation. Intercalating Li and ammonium-based ions (such as tetraethylammonium-Et_4N^+- ions) between layers weakens the van der Waal forces [266]. Ball milling supplies shear forces high enough to exfoliate the intercalated compounds. Using ionic liquid (IL) or ammonium based deep eutectic solvents as the milling liquid accelerates the kinetics of the intercalation because it increases the activity of ammonium ions [266]. Deep eutectic solvents are green solvents having the advantages of non-flammability [267], high thermal stability (>150 °C) [267], wide liquid phase range (usually over a range of 200 °C–500 °C) [268], negligible vapour pressure (<10 Pa at RT) [269] and easy recycling [270]. These properties eliminate the safety problems associated with typical organic solvents. An eutectic mixture of urea and choline chloride (2:1) can be produced by stirring the two components

until clear liquid is formed. The liquid can be then charged into the grinding chamber with 2 g graphite, 4 g battery grade Li chips, and yttria stabilized zirconia milling media. The ball milling runs under a flow of N_2 gas inside a glovebox. It is better to pause the grinding process for 30 min every 2 h to allow the system to cool. To recover the exfoliation product, the samples are then washed with DMSO, and centrifuged at 1500 rpm to remove thick flakes. The milling speed should be controlled to below 500 rpm to avoid extensive heating and to minimize defects in the produced flakes.

II.3. GO and RGO

II.3.1. GO

GO has a number of properties that are advantageous for applications. Due to its oxygenated surface, it can undergo complete exfoliation in water [271–275], yielding colloidal suspensions of individual sheets [273, 276, 277], that can be further functionalized, deoxygenated or dispersed in polymeric matrixes to give new multifunctional materials and composites [276]. This, combined with chemical tailoring [216, 217, 278] and biofunctionalization [279–283] makes GO a promising candidate for biomedical applications where water compatibility is crucial, e.g. in tissue engineering, drug delivery, cancer treatment and biosensing [281–289]. Unlike liquid-exfoliated LMs, GO is typically one layer thick [276]. This high surface to volume ratio and the mechanical strength lends itself to using GO as electrode material in energy storage and conversion [290, 291] or as filtration membrane for gas and ion separation [292, 293]. In addition, GO has some unique features. For example, unlike other LMs, it is amphiphilic, due to the non-uniform distribution of the various oxygen functional groups and can self-assemble into a range of nanostructures with different morphology at interfaces [294]. When increasing the concentration in dispersion, GO undergoes a phase transition from colloidal isotropic to nematic liquid crystalline phase, where the GO sheets are oriented in parallel [295]. The liquid crystalline phase leads to an enhanced alignment of GO sheets in those assembled structures, offering improved mechanical and electrical/thermal properties, compared to the random-oriented configuration of GOs which is important for electrochemical applications and opens up possible applications of GO in optical switches and photonic crystals [295].

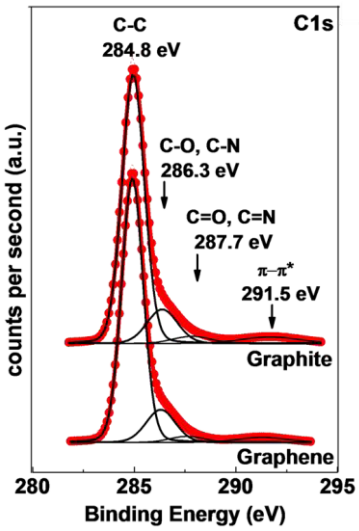
GO can be prepared by oxidation of graphite using highly oxidant reactants such as H_2SO_4, $KMnO_4$, H_2O_2 [156, 157]. The preparation method strongly influences the surface chemistry and related chemo-physical properties, ultimately affecting its functionalities. In 1859, Brodie first reported the synthesis of GO by adding potassium chlorate ($KClO_3$) to a slurry of graphite in fuming nitric acid (HNO_3) in a single portion [296]. In 1898, Staudenmaier improved Brodie's method by replacing ~two thirds of fuming HNO_3 with concentrated H_2SO_4 and by adding $KClO_3$ in multiple portions during the reaction, rather than in a single portion. Such modification had the same oxidation efficiency of reiterative Brodie oxidations (achieving high oxygen contents, up to C:O = 2:1) but in a single synthetic step. However, the Brodie and Staudenmaier method was not widely used because of the potential risk of explosions [297]. In 1958 Hummers and Offeman proposed a safer approach, currently widely adopted and known as Hummer's method [156], consisting of the replacement of $KClO_3$ by $KMnO_4$ and $NaNO_3$ in concentrated H_2SO_4. Ref. [298] reported that excluding $NaNO_3$, increasing $KMnO_4$ and a mixture of H_2SO_4/H_3PO_4 can improve the oxidation process. In these conditions the reaction is not exothermic and no toxic gas is produced.

The method proposed in Refs. [272, 298] allows one to prepare highly soluble (>4 g l^{-1}) water-soluble GO for studying the biological and toxicology effects on living cells [235, 286, 287]. In this way, GO sheets could be prepared with constant surface chemistry, but varying lateral size, spanning from 100 μm down to less than 100 nm [235]. The lateral size of the GO flakes after a typical oxidation can be tuned by sonicating the starting solutions for different times, from 0 to 100 h, in milliQ water (for a systematic study of GO size versus sonication time see Ref. [136]). GO can also be prepared by the Hummer's method directly on SiC wafers from graphene on SiC, with the property that the GO layers remain on the substrate for further surface studies and electronic devices production [299–301].

It is still not clear which are the most relevant factors regulating the interactions between GO and biological molecules, tissue structures and organisms. Numerous studies [235, 286, 287, 302] have shown that GO chemical purity, chemo-physical parameters and morphological properties can play a crucial role on cells viability and functionalities [302].

Taking advantage of the size tunability and high solubility of GO, the effect of the lateral size of GO in different biological systems was investigated for human and murine phagocytic cells [235], human intestinal cells [286], human lung and colon carcinoma cells [303], different enzymes of human [287] or bacterial [304] origin, gelatine membranes and fibres of animal origin [305].

In Ref. [235], three GO solutions, sonicated for 0, 2 and 26 h (with average lateral size ~1.3, 0.27 and 0.13 μm) were mixed with human monocyte macrophages (hMDM) and murine intraperitoneal macrophages (mIPM), revealing that the flake size has significant impact on different cellular parameters (i.e. cells viability, reactive oxygen species (ROS) generation and cellular activation, figure II.13). Ref. [235] reported a strong interaction (>90% internalization) with the cellular membrane, leading to the sliding of flakes under the membrane layer. GO samples could be internalized by both human and murine macrophages in a size-dependent manner. The more the lateral dimensions of GO were reduced, the higher were the cellular



	C1s		N1s	
Graphite	284.93	C-C		
	286.31	C-O		
	287.78	C=O		
	291.48	π–π*		
Graphene	284.93	C-C	399.04	N-H
	286.29	C-O	400.16	N=C
	287.67	C=O		
	291.33	π–π*		

Figure II.12. XPS spectrum of powders produced by ball-milling of graphite.

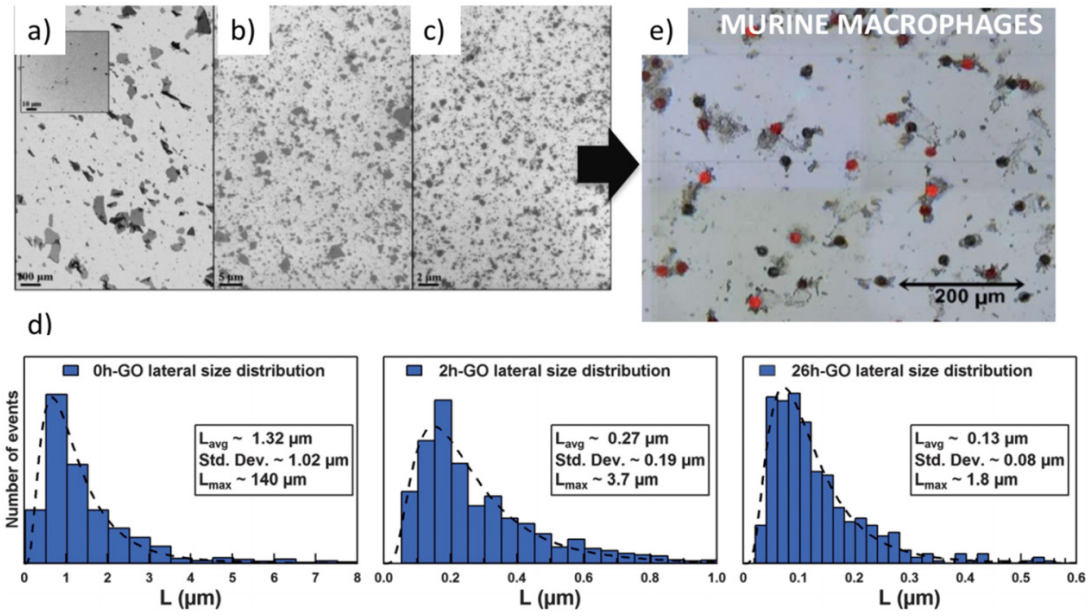


Figure II.13. (a)–(c) SEM image of GO solutions sonicated for different times, then spin coated on 300 nm SiO_2/Si(1 0 0): 0 h-GO (a), 2 h-GO (b), and 26 h-GO (c). (d) Flake size distribution of the 0 h-GO, 2 h-GO and 26 h-GO samples from SEM statistics. (e) Optical map of mIPM cells incubated with GO. Red dots indicate where Raman spectra was taken to detect internalization of GO into the cell. Adapted from [238], with permission of The Royal Society of Chemistry.

internalization and the effects on cellular functionality [235]. Flakes with the smallest lateral dimensions (<300 nm) were better internalized by primary macrophages. A 'mask effect' was observed due to the 2d shape of GO, with a preferential parallel orientation of the GO sheets onto to the cellular surface.

An efficient an green electrochemical oxidation of graphite to GO was reported [306]. Compared to traditional GO synthesis, the process bears the advantage that it is scalable, fast (<30 min opposed to hundreds of hours) and the risk of explosions is minimized. While electrochemical exfoliation has been developed to synthesize GRM with minimal oxidation (see section II.5), it has previously not been used to prepare GO. The electrochemical GO production can be achieved in two sequential steps starting using flexible graphite paper as anode and Pt as a cathode. In the first step (typically 20 min), a stage-I GIC is formed in concentrated H_2SO_4. In the second step, diluted (50 wt%) H_2SO_4 is used as electrolyte and the GIC as anode. Within seconds, the intercalation compound is oxidized and exfoliated. The dispersion produced is then filtered and washed to remove sulfuric acid and then redispersed by bath sonication if desired. Due to the lower acid concentration in the exfoliation step compared to the traditional Hummer's method, the dispersion is less viscous facilitating the filtration and washing step. Importantly, the process can be designed

in such a way that a continuous oxidation and exfoliation is achieved and the degree of oxidation is readily tuneable by the concentration of sulfuric acid. The most critical step is the choice if starting material, as neither graphite powders, not flakes or rods are suitable.

II.3.2. Reduction of GO

There is a growing and active investigation into the preparation and use of RGO due to its good electrical conductivity properties (from 10^{-5} S cm^{-1} to 1000 S cm^{-1}, [307]), and increase in mechanical reinforcement of polymeric matrixes [308]. E.g., 0.2% RGO can improve from 25% to 50% the mechanical properties of epoxy matrix composites[309]. Whereas thermal, chemical and thermochemical reduction of graphene and GO are customizable and versatile methods for preparing different types of RGO, they show several problems that hamper the synthesis of defect–free SLG. Among them, there are difficulties in complete removal of functional groups and the restitution of morphological characteristics of the material prior to the oxidation and sonication processes. RGO is highly polydisperse [307] in the lateral size, from less than 1 μm to more than 100 μm, due to the distribution of crystal size in the starting natural or synthetic graphites, and also due to the scissor effect that breaks the graphenic planes during the oxidation and/or the sonication processes [310]. However, the RGO thickness is controlled by the exfoliation of GO [311] and, depending on the preparation method and conditions, 1L can be obtained [312]. One of the first isolation of graphene was realized by reduction of GO by hydrazine in 1962 [273, 274].

There are several key characteristics of RGO that should be considered and evaluated to obtain optimum performance for a particular application: average lateral size, thickness, *C*/*O* ratio, the quantification of other heteroatoms, and surface area. Lateral sizes >5–10 μm are not suitable for fiber reinforced composites by vacuum assisted liquid resin infusion, LRI, or resin transfer moulding (RTM), due to the difficult filtration of the RGO flakes by the fabrics during the processing [313]. Lateral sizes >30 μm produce low percolation threshold composites, as compared with medium (<20 μm) and small (<5 μm) ones, due to size of overlapped areas and the higher number of contacts between particles [314].

Thickness is also a key factor for the performance of RGO in applications. In photocatalytic applications of RGO-TiO_2 the highest photocatalytic activity was observed with the SLG composites, and it decreased with N; this effect is attributed to higher charge carrier mobility and improved prevention of electron–hole pairs recombination [315]. Better results were obtained by co-exfoliation of graphite and TiO_2 [1716]. In some composites, this effect is also observed [143], however, in most of the applications in composites, SLG is not needed.

The *C*/*O* ratio and the quantification of other heteroatoms are important factors to determine the range of applications suitable for RGO. RGO with high (10%) to medium or low (1%) content of O is not suitable for thermal conductive properties, and a decrease to the oxygen content to lower than 0.5%w and distances between defects >15 nm are needed [141]. Also, the sp^2/sp^3 ratio is relevant for energy applications [309], catalysis [316] and gas absorption [317]. In many applications, such as mechanical reinforcement of polymers, increase dispersion in composites or fire retardancy [318] and for further covalent functionalization, GO with 15%–25% O concentration is needed and ~8%–4% O are recomended.

Surface area is another of the key characteristics. The Brunauer–Emmett–Teller (BET) theory serves as the basis for an important analysis technique for the measurement of the specific surface area of materials. We will refer to those experimental methods as BET specific surface area, SBET, measurements. SBET is related to N and is a key factor enabling a material for energy applications. N can be estimated by dividing the maximum surface area of SLG, 2630 m^2 g^{-1} by the specific surface determined experimentally by BET 2630/SBET, [319]. According to Ref. [320], RGO with SBET ~600–700 m^2 g^{-1} are mostly SLG.

The density of RGOis another key parameter. GRMs with high SBET values produced by thermochemical reduction exhibit low densities, even lower than 4 g l^{-1} [311]. For some applications a compaction of the RGO for further processing is needed [321].

Many strategies exist for the chemical, thermal and thermochemical reduction of GO, which strongly depend on the process and conditions selected for the reduction process, and the final performance required. Toxic hydrazine, sodium borohydride, hydroquinone have been used [322], as well as 'green reducers' such as organic acids [323], alcohols [324] and local high T reduction [300]. Biochemical molecules [325], amino acids [325], natural extracts [325] or metals [326], and several approaches other have been proposed [327].

Hydroiodic acid, often in combination with other acids, has been suggested as potent and versatile reducing agent [328]. GO reduction can be carried out at low T either in solution or for GO films and papers, in the gas phase [328]. GO self-assembled on the air/water interface can also be efficiently reduced by hydroiodic acid [329]. When using hydroiodic acid on GO films, it was found that the strength and ductility of the film was improved [157]. Compared to other methods of thermal reduction, such as reduction with hydrazine or vitamin C, it was found that hydroiodic acid reduces the GO without causing additional damage to the lattice [328].

Based on reproducibility, post-processability and ease up-scaling, alcohols are ideally suited for chemical reduction [324]. GO is first dispersed in the selected alcohol. Concentrations of GO ~5–20 g l^{-1} should be used because, before the reflux of GO in alcohol, ultrasonication (of a batch or in a continuous system) is needed for the exfoliation from graphite oxide to and an increase of viscosity should be avoided. The higher the GO lateral size, the lower GO concentration should to be used, due to the lower stability of the GO in the suspension. The main disadvantage of this process is the high volume of alcohols needed. E.g., to process 100 g of GO, a 20 l vessel is needed. However, alcohols can be recycled by column distillation with recycling yields >95%. Critical parameters are the selection of the alcohol and the time under reflux. By using x-ray diffraction, the reduction can be monitored based in the decrease of the intensity of the (0 0 1) peak of GO and the presence of (0 0 2) peak of RGO [330].

The electrical conductivity of RGO is also dependent on the chemical reduction process [307]. A Longer reflux time in isopropyl alcohol (IPA) produces higher conductivity. However, after 15 h no significant improvements are observed, see figure II.14.

After this reduction step, filtration of RGO at RT is required. This is easy to perform, due to the powdery aspect of the material. This can be air-dried or oven dried at less than 100 °C for 12 h. It is important to control the drying process to prevent contaminations, avoid thermal expansion and decrease density for further processing. High pressure and hydrothermal methods are more complex [331, 332], but efficient reduction of GO can be achieved, obtaining lower O concentration compared with traditional chemical reductors, such as hydrazine [332].

The products obtained from chemical reduction of exfoliated GO [307] have usually poor, <100 S cm^{-1}, electrical properties due to the high O concentration (>10%) and the presence of structural defects [157, 158, 333].

RGO can be prepared by thermochemical methods as an alternative route for reduction of GO [311], where restoring the sp^2 SLG structure is additionally achieved by thermal annealing [276]. Besides O removal by reduction, enhancing the graphitization by repairing the C–C sp^2 π-bond network at defect regions during the reduction process [311] can further improve the electrical properties of exfoliated RGO, for electrical, thermal, and self-sensing applications.

For the preparation of RGO with <1% O, several strategies can be used, such as >1800 °C annealing T, long processing times (>60 min at 1500 °C), reducing atmospheres, such as H_2, alcohols, hydrocarbons, etc. Thermochemical reduction can be done at medium 800 °C or high T (>1200 °C), depending on the final requirements. The choice of the working atmosphere has an impact on the final RGO characteristic, particularly on its O content. Thermal reduction can be done in vacuum [334] or inert atmosphere [311] in a reducing H_2 environment [335] and using carbon donor molecules. Alcohols are very effective in the reduction of GO and the partial restoration of the graphitic structure due to their carbon donor characteristics. Other carbon donor molecules or a combination of hydrocarbons [336] are alternatives for the production RGO with O content <2% O at moderate T < 800 °C.

In thermochemical reduction, the working atmosphere comprises a gas carrier, which in most cases is an inert gas such as N_2 or Ar, and the carbon donor/source molecule or combination of molecules. Ar is preferred as gas carrier over N_2, due to the potential doping of with N RGO during the reduction process. For the restoration atmosphere, it is crucial to control the carbon donor and also the kinetics of the pyrolytic decomposition of the active gas. Carbon molecules result in the decomposition and formation of other non-graphene species and non-desired aromatic molecules [337]. Thus a low concentration, usually <5% is recommended. Significant improvement of the reduction process when compared to the material obtained in H_2 was reported [338].The use of carbon donor atmospheres is the most cost-efficient to obtain highly reduced GO, with O concentration from 0.25% to 1%.

The reduction T determines the kinetics of the thermal decomposition (from 300 to 2000 °C), but a low cost- efficient reduction must be pursued in an industrial enviroment and the time and T of the process should be the lowest possible. Efficient processes at low T have been reported in [339], obtaining graphene for Li batteries at a low T ~ 300 °C in 5 min.

II.3.3. Aerogels based on RGO

Graphene flakes can be used as building blocks for the preparation of 3d low density structures, such as sponges, foams, hydro- or aerogels [340–346]. These materials exhibit a highly open structure, with interconnected hierarchical pores that enhance the accessibility to the whole surface of the material and improve ion diffusion. The assembly of the graphene sheets into macrostructures can also improve the mechanical properties, while retaining other properties associated to individual graphene layers [340, 341]. GO can be used for the preparation of composites with tailored macroporous structure through the assembly of GO sheets with different templates. After template removal, complex GO-based materials with hierarchical porosities can be prepared [347]. The combination of processing at RT and a subsequent treatment at moderate T allows the preparation of highly conductive bare carbonaceous electrodes [348] and composites, which may serve as self–standing electrodes for Li ion batteries [347].

Ice–templating [349] is a useful technique for the preparation of macroporous reduced graphene oxide-based aerogels (ARGO). Ice–templating involves the

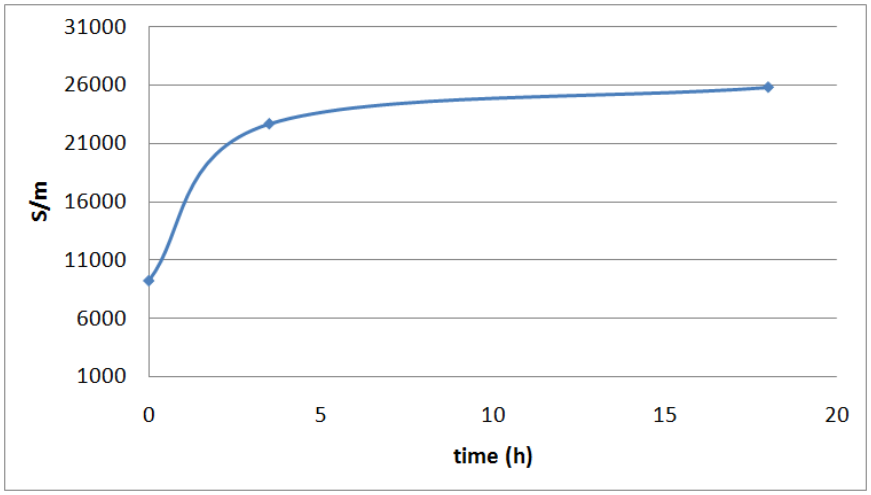


Figure II.14. Conductivity of RGO reduced in IPA reflux versus reduction time.

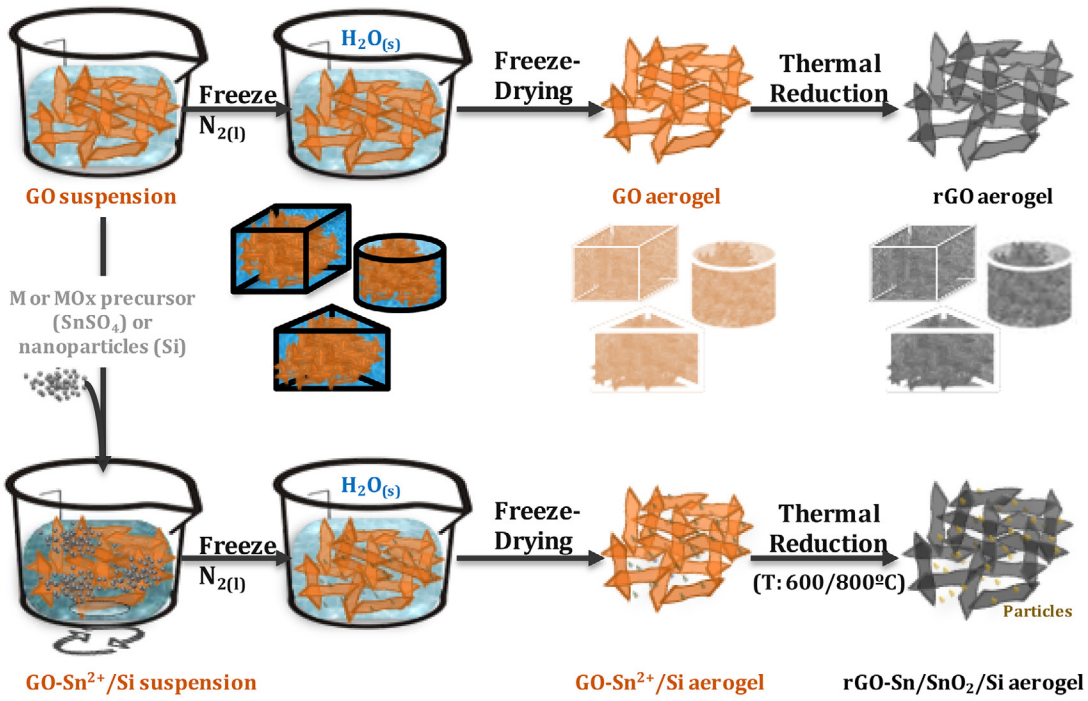


Figure II.15. Schematic representation of the route followed for the preparation of RGO composite aerogels.

freezing of a GO suspension, then subsequently freeze-dried to sublime the ice crystals formed within the structure. This process is useful for the preparation of a variety of a homogeneous nanostructured composites, with application in energy storage, catalysis, sensing or separation [350], it offers a better control on the porosity of the resultant materials. The modification of parameters such as T or immersion rate, impacts the textural properties of the resultant material. Ice-templating also allows gives structures with hierarchical porosity, which can favor the transport and diffusion of molecules to the whole surface of the material, highly desired in adsorption processes for separation and purification purposes and catalytic applications, not only of soluble pollutants in waste waters, but also for immiscible substances in biphasic systems [1730]. In energy storage applications, ARGO was proposed as electrodes for supercapacitors, Li-ion, Na-ion or metal-air batteries [341].

Ice-templated ARGO have been investigated as self-standing electrodes for energy storage devices [351]. These structures can be assembled into the electrochemical cells without the need of binders, which do not contribute to the capacity of the electrode, but can decrease its conductivity and block the access of the electrolyte ions to the surface of the active materials. As anodes for Li ion batteries (LIBs), sp^2 graphene not only improves the electrodes electronic conductivity, thus enhancing the power of the device, but it can also buffer the volume changes undergone by some

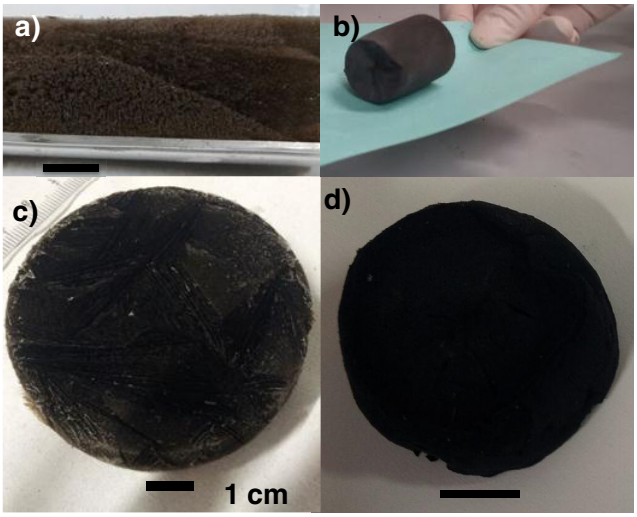


Figure II.16. Photographs of GO aerogels prepared form different suspensions: (a) GO (2 mg ml^{-1}), (b) GO (6 mg ml^{-1}), (c) Sn-GO and (b) RGO composite aerogel, obtained after thermal reduction of GO aerogels at 800 C.

active species used as high energy anodes for LIBs, during alloying with Li [352].

The processing of these materials as self-standing composites provides additional value to the electrodes since they can be directly mounted into flexible portable electronics [353].

II.3.4. Si-RGO and SnO_2-RGO aerogels

ARGO composites can be prepared following the route schematized in figure II.15. First, an homogeneous suspension of GO, alone or in the presence of a certain precursor of the desired particles, is prepared. Second, the suspension is rapidly frozen by its immersion in liquid nitrogen. Then it is freeze-dried to remove the ice-crystals formed upon freezing, leaving the macroporous structured in the GO-based monoliths. Finally, samples are partially reduced by a thermal treatment conducted under inert atmosphere, yielding a macroporous carbonaceous network in which RGO sheets are decorated with crystalline particles.

The microstructure and porosity of the resultant aerogels can be tuned by changing rate and T of freezing. Fast freezing does not allow graphene layers to self-arrange with the ice crystals front, giving rise to materials containing macropores randomly distributed within the structure [354].

Figure II.16 shows photographs of different aerogels obtained by ice templating. In these cases, GO suspensions obtained by the sonication of graphite oxide by the Hummer's method were used [120]. For the synthesis of Sn-based ARGO composites an aqueous suspension was used, but in the case of Si-ARGO, the GO and the SiNPs were initially dispersed in ethanol. Homogeneous GO suspensions in the presence of the precursor are in this way obtained [352, 355]. Then, the suspension is frozen in liquid nitrogen, and subsequently freeze-dried to sublime the ice-crystals, leaving the macroporous structured monoliths. Finally, the samples undergo thermal treatment under inert atmosphere to reduce GO and to form the desired crystalline phase.

For the preparation of the GO suspension in ethanol ~5 g l^{-1}, an aqueous suspension of GO is washed several times with dry ethanol. The suspension is then sonicated and centrifuged to remove aggregates in the sediment. When mixing Si NPs and GO, the use of ethanol is justified, since Si-RGO composites generally need pre-oxidation of the Si NPs or ultrasonication, in order to improve their dispersibility in polar media, to be homogeneously mixed with GO [356, 357]. A highly homogeneous, see figure II.17, and stable dispersion of non-oxidized Si NPs was achieved in this way [355].

Si-GO composites were prepared by mixing Si nanoparticles with the GO suspension in ethanol under inert atmosphere, then, solvent was reduced to 10% to be subsequently frozen and freeze-dried, to be then thermally reduced at 1000 ºC under dynamic Ar/H2 (95:5) atmosphere. The resulting material has large macropores in a highly open porous structure formed by graphitic flakes homogeneously decorated with Si NPs (~50 nm diameter), figure II.17(d).

This procedure also allows the *in situ* deposition of the particles on the surface of the graphene flakes. Sn and SnO_2-ArGO, were prepared by dissolving $SnSO_4$ in the GO suspension and the the pH was increased to 9 using NH_3 solution.Then, the suspension was freeze dried to obtain macroporous $Sn(OH)_4$–GO composites [352].

GO-based aerogels were thermally reduced under a dynamic argon flow to increase their electrical conductivity. Heating the samples under a dynamic argon flow, Sn-ARGO (figure II.17(b)) at 800 °C and SnO_2-ARGO (figure II.17(c)) at 650 °C were obtained [352]. Figure II.17 shows a highly porous material formed by RGO flakes which contain large macroporous randomly distributed along the structure. In both samples, the Sn sub-micrometer particles showed a homogeneous distribution on the graphene sheets and

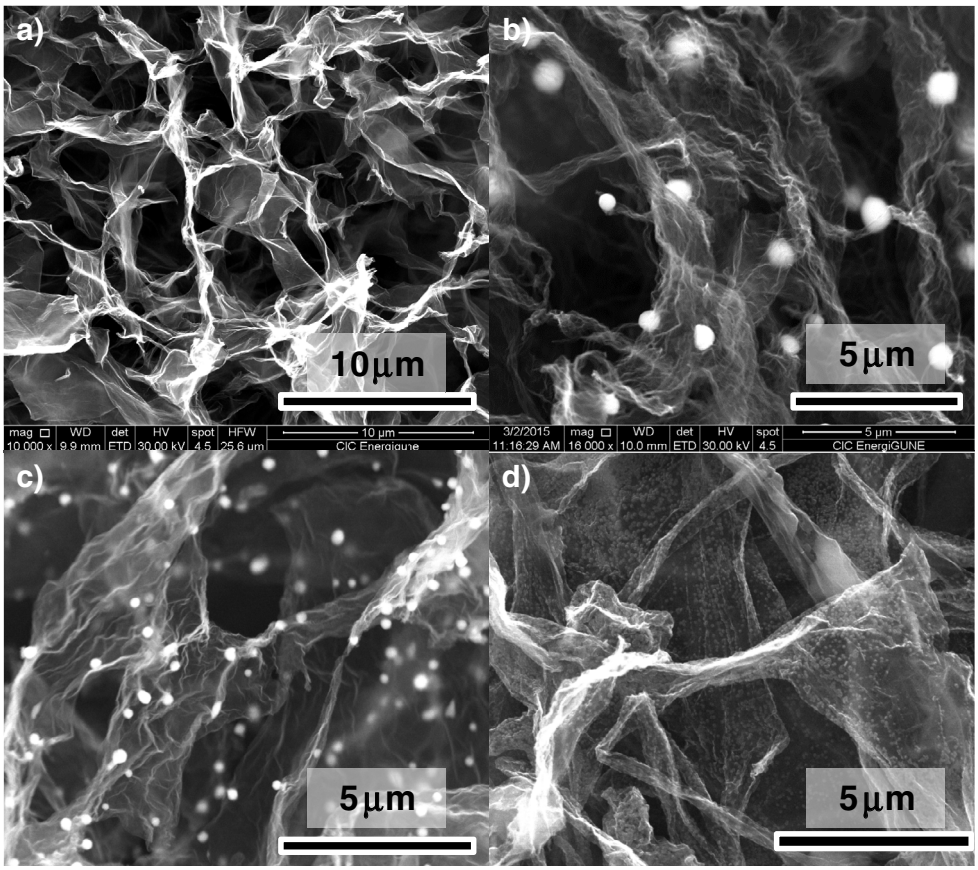


Figure II.17. Representative SEM images of (a) A-RGO, (b) A-Sn-RGO, (c) A-SnO_2-RGO and (d) A-Si-RGO.

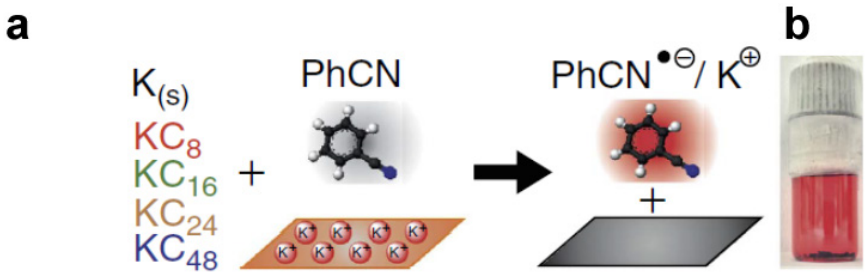


Figure II.18. (a) Reaction scheme for the quantitative electron transfer from various GICs to PhCN leading to dissolved K^+ ions and the red coloured radical anion PhCN.-. (b) Photograph of a sealed vial containing KC_8 in a concentration of 5.0×10^{-1} M in PhCN.-, adapted from [375].

a narrow particle size distribution, higher in the case of the metallic Sn particles (~750 nm diameter) than SnO_2 particles (~250 nm diameter), ascribed to the carbothermal reduction, melting and re-crystallization of Sn particles [358] over 650 °C.

These aerogels have been processed as self-standing electrodes, without any binder nor metallic support, showing promising results as anodes in LIBs[347]. In the case of the SnO_2-ARGO composites, reversible capacity of 1010 mAh $g^{-1}_{electrode}$ was measured at 0.05 A g^{-1} and 470 mAh $g^{-1}_{electrode}$ at 2 A g^{-1}, with reasonable Coulombic efficiencies (>98%) and stability after 150 charge–discharge cycles [355]. Si-ARGO electrodes showed reversible specific capacities ~700 mAh $g^{-1}_{electrode}$ with associated Coulombic efficiencies >99% within 2–0.05 V. These electrodes also showed a good stability during 100 charge–discharge cycles [355]. This indicates that ARGO can accommodate volume changes of Si particles and, at the same time, improve the conductivity of the electrode without additives. Due to their high electronic conductivities and light weight, graphene aerogels are good candidates as support in the preparation of electrodes for next-generation Li batteries such as Metal-air batteries or Li-S batteries [359] or Li ion capacitors [360].

II.3.5. GO membranes

Membranes can be fabricated, e.g. by vacuum filtration, even though other deposition techniques can be used [1731]. GO membranes have gas and ion

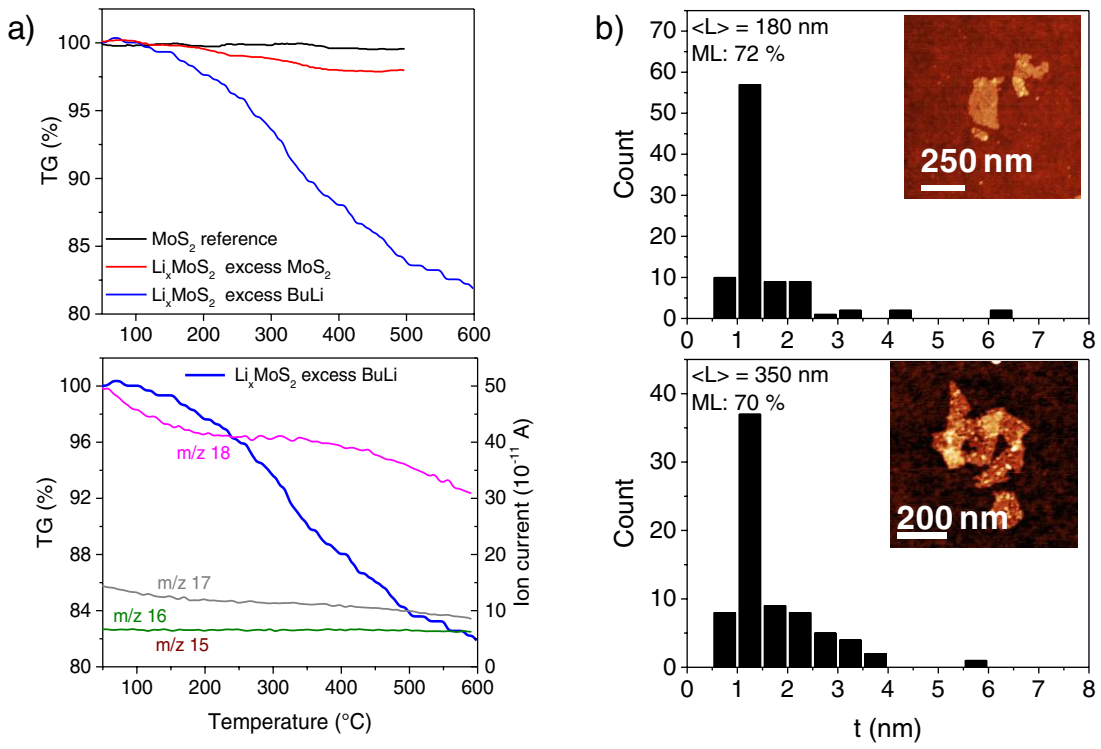


Figure II.19. Characterization of chemically exfoliated MoS_2 with different intercalation conditions. (A) TGA weight loss of MoS_2 and MoS_2 chemically intercalated with excess of BuLi and MoS_2. Bottom: mass profiles for $m/z = 15$–18 which constitute the main weight loss in chemically exfoliated MoS_2 using excess BuLi. (B) AFM thickness histograms of MoS_2 intercalated using excess MoS_2 (top) and BuLi (bottom). Inset: representative images. Adapted from [379], copyright American Chemical Society.

filtration properties [293] making GO an interesting material for water purification and desalination. Ref. [361] reported that GO based membranes are permeable to water, but hold back most other liquid and gases. Research in this area has been expanding with a range of review papers [293, 362–365]. A brief overview will be given here.

GO-based membranes are both selective and highly permeable to water, chemically and physically stable. However, fouling and biocompatibility still need to be addressed [362]. GO/FLG hybrid membranes were reported improved chemical resistance towards chlorine, and enhanced NaCl rejection (up to 85%) [366].

These GO material membranes can be described as an interlayer nanocapillary network, due to the connected interlayer spaces [365]. This network, together with the gaps between edges of non-interlocked neighboring GO sheets, and the cracks or holes of the GO sheet, provide passage for molecules or ions to permeate through the GO membrane in aqueous solutions so that effective separation of different molecules and ions can be achieved depending on the network morphology, degree of GO oxidation, lateral size, stacking in combination with size and chemical nature of molecules and ions. Molecules or ions with smaller hydrated radius, less charge and weaker interaction with GO sheets permeate through the GO membrane more easily than larger ones, driven by the high capillary-like pressure [365, 1731]. The separation performance at high water flux and rejection rates can be tuned by adjusting the GO sheet size, the thickness of the GO membrane, water pH, and the GO membrane structure as summarized in Ref. [365].

The key aspect of these type of membranes is the self-assembly of the flakes into well-ordered macroscopic laminates unlike in GRM-polymer composites, where the flakes are less ordered and less densely packed [363]. The flakes arrangement in the membrane is thus an important parameter influencing separation performance. This not only depends on the characteristics of the flakes themselves (size/thickness, degree of oxidation), but also on the deposition technique [367]. Highly ordered, interlocked GO flakes were obtained by building membranes by spin-coating a GO dispersion in a layer by layer fashion. These interlocked membranes showed better CO_2/nitrogen selectivity than less ordered ones [363, 364]. For a more detailed discussion on transport mechanisms see Refs. [363, 364].

II.4. Chemical intercalation and reductive exfoliation

II.4.1. Graphene from GICs

The intercalation of graphite with sulfuric acid can be exploited for the production of GO. Graphite can also be intercalated by a number of other species to yield GIC [160]. The fabrication of donor-GIC after intercalation with, e.g. alkali metals, has gained increasing importance. Refs. [368–374] reported that such acceptor-GICs are very suitable precursors for covalent functionalization of graphene (see section VIII.1).

In typical covalent functionalization sequences, the negatively charged SLG first act as reductants for electrophiles (for example alkylhalide) [368], which are subsequently attacked by the intermediately generated organic radicals or H-atoms, yielding covalently modified graphene. This wet-chemical functionalization is facilitated by the fact that, due to Coulomb repulsion, the negatively charged graphenide [373] layers within the solid GICs can be dispersed in suitable organic solvents (see Ref [373] for more details).

One fundamental question is if whether all negative charges of the graphenide intermediates can be controlled or even completely removed in such redox reactions [376]. Only complete oxidation is expected to avoid reactions with moisture and O during workup [375], leading to side products with undesired and additional O and H functionalities. More importantly, the controlled removal of all negative charges from the solvent exfoliated graphenide intermediates with a suitable oxidation reagent allows for the bulk production of defect-free graphene. Ref. [375] reported that the treatment of K intercalated graphite with benzonitrile (PhCN) leads to discharging, i.e. taking away of the electrons from charged layers, of the individual graphenide sheets upon the formation of the colored radical anion PhCN.-, figure II.18, which can be used to monitor the accompanying exhaustive and Coulomb force-driven migration of K counterions from GICs into the surrounding benzonitrile phase. The suppression of reactions of dispersed graphenides with moisture and air takes place when no treatment with benzonitrile is provided, resulting in graphene. This represents a mild, scalable, and inexpensive method for wet-chemical graphene production. This reductive graphite exfoliation approach can be extended to water as solvent [377].

II.4.2. Chemical exfoliation of transition metal dichalcogenides

LMs, such as TMDs, can be reductively exfoliated via intercalation compounds [159]. Typically, MoS_2 is intercalated with *n*-Butyllithium (*n*-BuLi) in an inert solvent such as hexane [378]. In contrast to graphite, intercalated MoS_2 does not react with water [378] so that this can be used for subsequent exfoliation.

Water is added to the reaction mixture to destroy excess BuLi. At the same time, gas formation occurs, which acts as driving force to expand MoS_2 and individualize the layers. After further washing and centrifugation-based purification, a colloidally stable MoS_2 dispersion in water can be obtained with negatively charged, predominantly 1L flakes (70%–90%). As a result of the negative charges, a phase transformation from the semiconducting 2H-MoS_2 polytype to the metallic 1T polytype is observed. Such negatively charged MoS_2 can be used as precursor for subsequent covalent functionalisation using electrophiles [379, 380]. Another approach, based on chlorosulfonic acid assisted exfoliation was developed, allowing to keep the original semiconducting properties of 2H-TMD (as MoS_2 and WS_2) [381, 1412, 1413, 1732, 1733].

This intercalation chemistry was explored in the 80s [159], but the interest was not in producing exfoliated flakes in a liquid dispersion. Ref. [379] studied the impact of intercalation conditions on the final product of chemically exfoliated MoS_2. In a typical exfoliation of MoS_2 with *n*-BuLi, the *n*-BuLi is used in ~10-fold excess. These reaction conditions can lead to the introduction of defects, as exemplified by a significant mass loss in TGA under inert conditions (figure II.19(a)). No specific mass fragments can be assigned to this weight loss, suggesting it is not the result of a well-defined surface derivatization [379]. The major mass fragment observed has a mass over charge (*m*/*z*) ~18 and was assigned to -OH groups, figure II.19(a). This disruption of the structure is not observed when MoS_2 is used in excess over *n*-BuLi. The work-up is more tedious, with less material obtained as individualized flakes.After centrifugation, flakes with similar lateral dimensions and thickness distribution are produced (figure II.19(b)) suggesting that there is scope to optimize chemical exfoliation with respect to yield of 1L MoS_2.

II.5. Electrochemical exfoliation

Graphite can be exfoliated to SLG and FLG by applying a bias in ionic aqueous (or organic) electrolytes [137, 382]. Electrochemical exfoliation (EE) requires one graphite electrode and a metallic counter electrode in conductive media, which is not equipment-intensive. The exfoliation completes in minutes to hours, producing gram-scale quantities of flakes with high Yw up to 80%. The graphene quality is tunable: sheet size, *C*/*O* ratio, solubility and electrical conductivity can be modified depending on the types of graphite precursors, electrolytes and operating potentials [383].

The selection of the graphite electrode is an important parameter. Various graphite precursors (including natural graphite and synthetic graphite), in the form of powder, foil, paper, rod, flake and plate, have been studied for electrochemical exfoliation [397, 1734]. From our perspective, graphite foil is considered as an ideal raw material due to the ease of operation, as well as good tolerance to the volume expansion during exfoliation.

II.5.1. Aqueous media

H_2SO_4 can be used to prepare GICs as the ionic diameter of sulfate ion (0.46 nm) is close to the interlayer spacing of graphite (0.33 nm), which is the prerequisite for efficient intercalation. Efficiency here relates to the degree of exfoliation, a higher ratio of MLG is considered more efficient than thicker flakes. In this way efficiency is related to the average thickness of the exfoliated platelets: the lower the thickness, the higher the efficiency. Dilute H_2SO_4 aqueous solutions

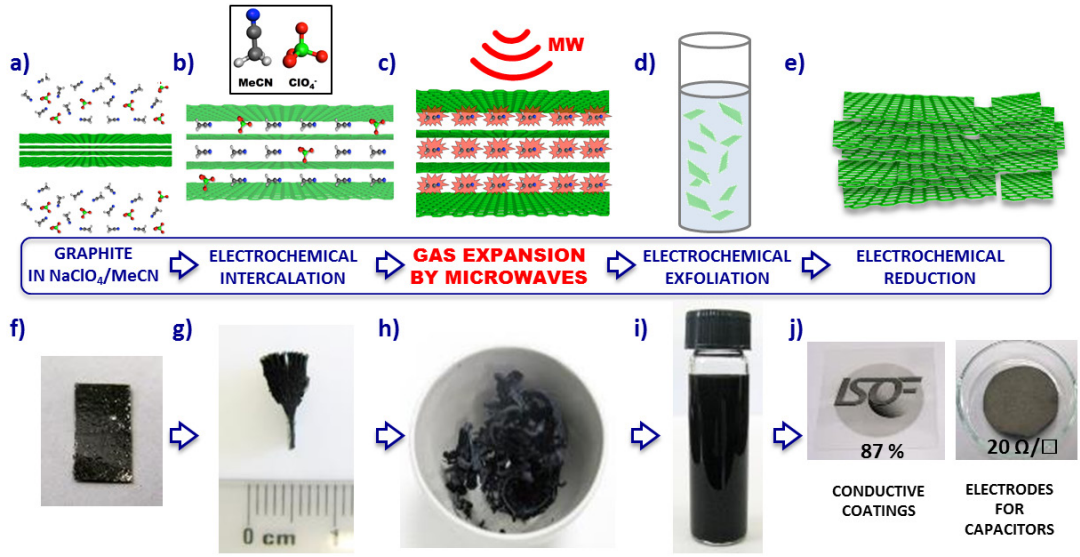


Figure II.20. Illustrations of graphite after intercalation, expansion, electrochemical exfoliation and reduction steps (from left to right).Adapted from [348], © Wiley-VCH Verlag GmbH & Co. KGaA.

were used [384, 385] to encourage graphite exfoliation because it is less corrosive. Ref. [385] immersed a graphite anode together with a counter electrode (Pt foil) into 0.1 M H_2SO_4The exfoliation started when a potential of 10 V was applied. This gave 80% 1-3LG with high exfoliation yield (60%) and high *C*/*O* ratio (12.3). Under electric current, the oxidation effect on graphene is strong, owing to the interplay between proton (H^+) and sulfate ion at low pH. The oxidation effect is defined as the oxygen content in the exfoliated materials, which usually results from the attack of oxygen-containing radicals by water splitting [386]. Water electrolysis generates oxidative radicals (HO· and O·), which contains a collection of sulfate salts (e.g. sodium sulfate, ammonium sulfate, etc) instead of H_2SO_4 [387]. By doing so, Ref. [387] reported >85% of 1-3LG with dimensions up to 40 μm and *C*/*O* ~ 17.2, implying a low level of O functionalization. Another strategy to suppress oxidation is to remove radicals from water splitting [388]. A series of scavengers have been investigated. Ref. [388] reported 2,2,6,6-Tetramethyl-1-piperidinyloxy (TEMPO) to be the most effective, reaching *C*/*O* ~ 25.3, average sizes ~5–10 μm and hole mobility up to 405 $cm^2\ V^{-1}\ s^{-1}$. Electrochemical exfoliation can produce not only graphene but also highly oxidized GO [306]. E.g., a two-step anodic oxidation in concentrated (98 wt%) and diluted (50 wt%) H sulfuric acid enables the synthesis of GO with *C*/*O* < 2 and high yield (95%) of 1L similar to those achieved by traditional Hummer's methods.

There are still several challenges: (1) the exfoliation only occurs at a single electrode (anode or cathode), limiting the production rate; (2) insufficient intercalation results in polydisperse flakes (with varying N), which requires additional separate procedures; (3) flakes trend to restack in solution, due to strong in-plane interaction when the stabilizers are absent, which needs careful selection of suitable electrolytes.

II.5.2. Non-aqueous media and molten salts

Another strategy to minimize O content is to use cathodic intercalation and O-free electrolytes [389]. The intercalation of small cations with graphite from organic solvents is the principle of many energy storage devices [389–393]. Graphene can be prepared by electrochemical intercalation of Li^+ within the graphite interlayer space, followed by dissociation of the resultant intercalating compound using prolonged sonication. Ref. [394] tried to reduce the sonication time by intercalating graphite with Li, followed by a second intercalation of large tetra-*n*-butylammonium ions. In both cases, the strong decomposition reaction of the solvent cations hindered the formation of LiC_6 and/or ammonia GICs. Therefore, another sonication step was need to completely detach the graphene flakes.

Graphite can be fully exfoliated via an electrochemical process in organic solvents without the need of sonication or an inert atmosphere, by using DMSO saturated with Li and small alkylammonium ions (triethylammonium, Et_3NH^+) [395]. An electrochemical program is used to apply a controlled cathodic potential on the graphite electrode, enabling the formation of exfoliated powder [266]. In a three-electrode system, a chronoamperometric step of −1.7 V on Ag/AgCl is applied for 5 min, followed by linear sweep voltammetry at a rate of 10 mV s^{-1}. The potential is then kept at −5 V for 5 min, to allow intercalation of the electrolyte cations, finally it is swept linearly back to the open-circuit potential to decompose the resultant complex compound. During the first chronoamperometric and the second linear sweep voltammetry steps, solvated carbanion complexes are formed according to reactions II.1-5. The second chronoamperometric step at −5 V is important to complete the intercalation process. This intercalated compound could decompose cathodically if the potential is held at negative values according to reaction (6) or on the oxidation

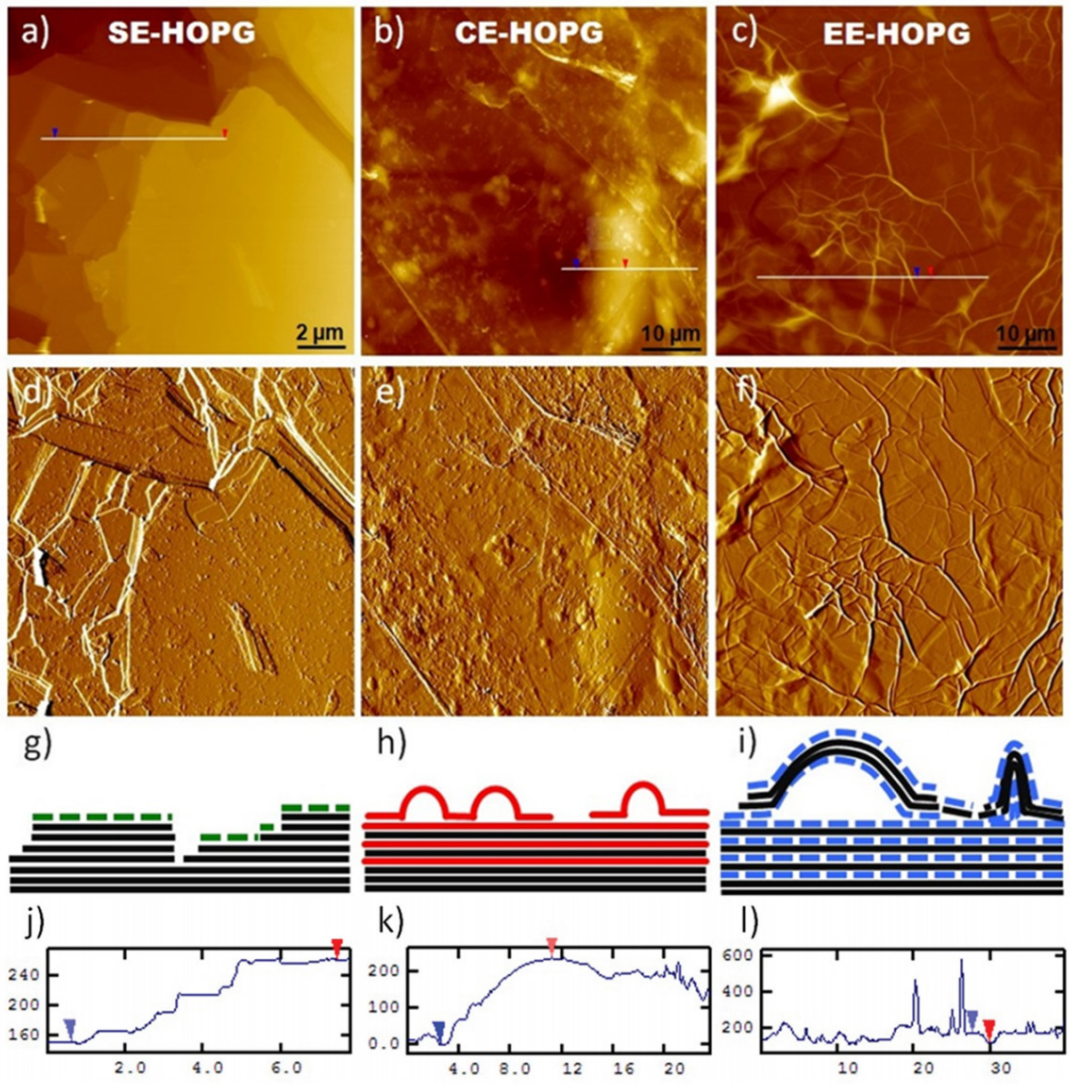


Figure II.21. AFM images of HOPG basal surface after treatment by (a) sonication-assisted, (b) chemical exfoliation, (c) electrochemical exfoliation. *Z*-range: (a) 400 nm, (b) 600 nm, (c) 1 μm. (d)–(f) gradient-filtered version of each image. (g)–(j) Schematic representation of the structure of the HOPG substrate after exfoliation procedures. (j)–(l) Height profiles taken along the lines shown in (a)–(c). From [137], © Wiley-VCH Verlag GmbH & Co. KGaA.

cycle according to 7. In both cases, dissociation of the intercalated compound is associated with Et_3N gas formation, more likely taking place between the graphene layers, which applies more stress on SLGs and separate them further apart.

$$2Et_3NH^+ + 2e^- = H_2 + 2Et_3N \quad \text{(II.1)}$$

$$n Et_3N + e^- + C = (Et_3N)_n C^- \quad \text{(II.2)}$$

$$Li^+ + e^- = Li \quad \text{(II.3)}$$

$$m Li + e^- + C = Li_m C^- \quad \text{(II.4)}$$

$$n Et_3N + m Li + e^- + C = Li_m (Et_3N)_n C \quad \text{(II.5)}$$

$$Li_m (Et_3N)_n C^- + e^- + 2Et_3NH^+ = C + m Li + (n+2)\, Et_3N + H_2 \quad \text{(II.6)}$$

$$Li_m (Et_3N)_n C^- = C + m Li + n Et_3N + e^-. \quad \text{(II.7)}$$

The intercalation from RT electrolytes is a slow process (diffusion coefficient $<1.2 \times 10^{-10}$ cm^2 s^{-1}) [396] and limited to few μm from the edge of the graphite grain [397]. Attempts to increase chemical activities of Li ions or other cations by using pure ILs or deep eutectic solvents did not overcome the kinetic barriers [398]. Hence, it is important to repeat the exfoliation process for more than one cycle to obtain a yield >70% the big flakes [389]. Another alternative is to use molten salts at T > 500 °C as the electrolyte. [399–401] developed for the exfoliation of graphite based on Li intercalation from molten LiCl electrolyte containing water. In a typical experiment, anhydrous LiCl powder, which serves as anode, is charged in a graphite crucible. The cathode is graphite. The cell is heated to ~800 °C, above the melting point of LiCl, and a stream of water is bubbled into the molten bath. Electrolysis is achieved by applying a constant direct current between cathode and anode. After allowing

the cell to cool down to RT (Ar gas flow), graphene powder can be recovered from the solidified salt by washing with hot distilled water and vacuum filtering. Finally, the black powder is heated at 1300 °C under inert gas atmosphere containing hydrogen. The process demonstrates commercial viability and a molten salt volume ~10 L can produce ~4.5 kg flakes in a day [400, 402].

II.5.3. Combination of electrochemical and microwave expansion

Microwave (MW) irradiation is currently employed in many fields of organic synthesis to shorten reaction times, to enhance both reaction yields and product purity, to provide eco-sustainable synthetic methodologies, by replacing or reducing the use of polluting reagents [217]. Graphite can interact with the oscillating electrical field of MW radiation, giving high T gradients and increased reaction rates (e.g. for fast functionalization of GO) [217] as compared to conventional, procedures such as conventional chemical functionalization at RT in solution. Therefore, the T attainable using MW (>80 °C) can be applied to exfoliate graphite [217].

Electrochemistry can be used for a fast (<30 min) and massive (>70%w/w intercalated molecules/graphite) intercalation of suitable molecules, such as perchlorate ions, into graphite [217]. Degradation of these molecules in GICs is then triggered by MW irradiation, creating a gas pressure surge in graphite and yielding exfoliation [217].

Charged perchlorate ions could act as 'Trojan horses', to favour the intercalation of uncharged acetonitrile molecules [348]. These work as nanoscopic foaming agents, and decompose with MW irradiation to generate a pressure surge within graphite, resulting in exfoliation. The process yields soluble, monoatomic (52% SLG), large (72% of the sheets extending beyond 1 μm) GRM sheets characterized and then tested as transparent electrodes [348] and capacitors [348]. These electrodes can also be functionalized with nanoporous layers of inorganic oxides, after the pre-intercalation of electrolyte species (e.g., $FeCl_3$–nitromethane electrolytes), to obtain, e.g. composite electrodes for LIB [1735].

Electrochemical treatment can be performed starting from HOPG as a working electrode and a Pt wire as a reference electrode. Ions such as sulfates and perchlorates can be efficiently intercalated into graphite, whereas intercalating uncharged molecules is more difficult [131], and can usually be achieved only by several hours sonication, with a lower yield (few%) of both exfoliated material and 1L. The exfoliation process works only if the surface energy of the intercalated organic liquid is similar to that of graphene [131]. The process is limited to high-boiling solvents ($T > 100$ °C), such as NMP or DMF. To overcome this challenge, Ref. [348] used perchlorate ions to promote the intercalation of an organic, uncharged molecule (acetonitrile), which was present in high excess, as a solvent. Graphite was intercalated and partially expanded by electrochemical insertion of ClO_4- in acetonitrile by applying a + 5V for 0.5 h. In this way, negatively charged ClO_4- ions intercalated through grain boundaries or defect sites and favoured the penetration of the smaller, uncharged acetonitrile molecules. The fundamental role of ClO_4- was demonstrated in a comparison experiment by using acetonitrile alone, for which no intercalation was observed [348]. The amount of molecules intercalated into graphite was high (70% w/w), as estimated from TGA of the intercalated graphite electrode [348].

After electrochemical intercalation, MW irradiation expanded the graphite interlayers through decomposition and gas evolution of acetonitrile to yield a foam-like, multilayered powder [348]. The expansion was fast (~10 s) and yielded an increase in volume of the initial graphite ~600% [348]. The role of acetonitrile in the expansion was demonstrated in a comparison experiment, in which no expansion was observed for graphite treated only in aqueous solutions of $HClO_4$ or $NaClO_4$ without acetonitrile [348]. Figure II.20 shows a schematic of the process, and photographs of the material at the different processing stages.

II.6. Sonication-assisted versus chemical versus electrochemical exfoliation

Graphite can be exfoliated by different chemical methods in the liquid phase. One of the simplest approaches is ultrasonic treatment in organic solvents (see II.2). Some dipolar aprotic solvents (e.g. DMF, NMP) or surfactants in aqueous solutions are effective to stabilize graphene in solution without re-aggregation [131].

A more effective, but disruptive, approach to solubilize graphene is covalent modification, in particular by the formation of GO (see Section II.3). In presence of strong oxidants, the aromatic carbon network is oxidized with the creation of hydroxyl, carboxyl and epoxy moieties. The hydrophilic nature of these moieties on GO facilitates solution processing of concentrated 1L on different substrates substrates (>60% 1L[277]). The GO flakes can be then reduced to give electrically conductive RGO. However, numerous defects on GO are not fully restored after reduction and the electronic properties of RGO are poorer compared to pristine graphene.

Another more controllable, slightly less disruptive approach to exfoliate graphite takes advantage of electrochemistry (see Section II.4). By adjusting the applied potential in suitable electrolytes, graphite electrodes can be either negatively or positively intercalated to obtain GICs, and then exfoliated by solvent decomposition directly during electrochemical treatment or by further thermal treatment.

The most common LPE methods are compared: sonication in solvent, chemical oxidation, and electro-

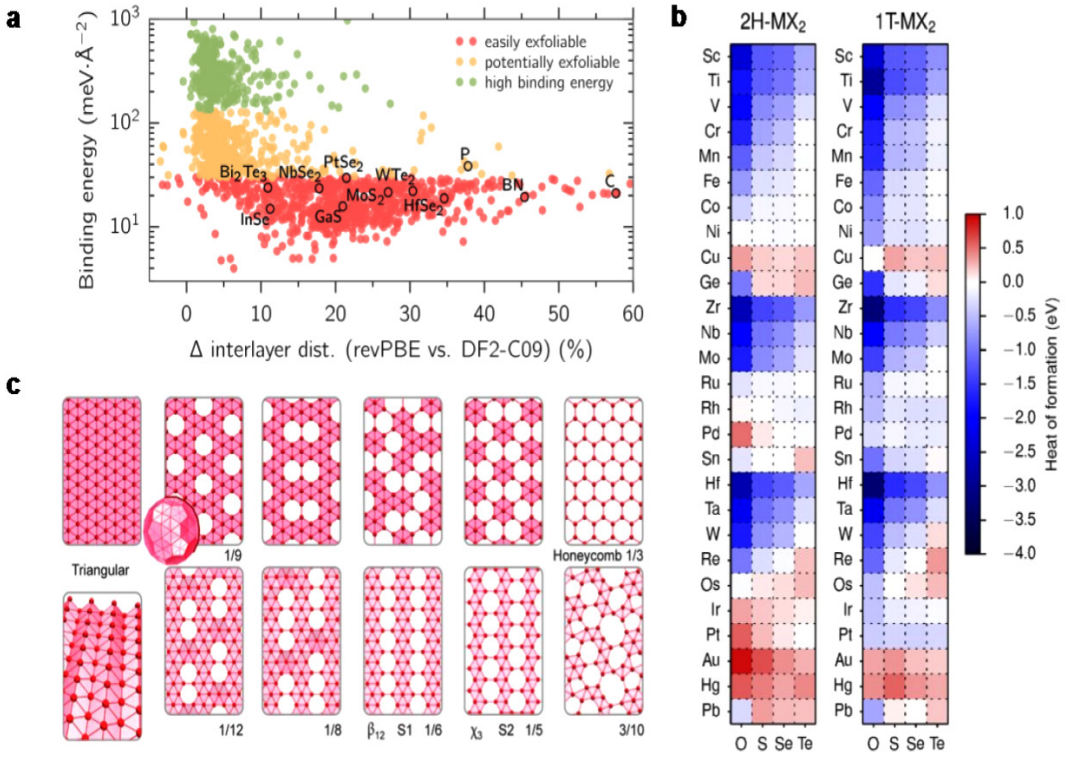


Figure II.22. (a) Binding energy versus relative difference in interlayer distance predicted by vdW (DF2-C09) or non-vdW (revPBE) functionals. Materials classified as easily exfoliable, potentially exfoliable, or with high binding energy are colored differently. Well-known LMs are highlighted in the plot. Adapted from [407], © Springer Nature. (b) Calculated heat of formation for 216 1L-TMDs in the 2H and 1T phases. Oxides have the highest stability, followed by sulfides, selenides, and tellurides, in that order. The stability decreases as the metal ion goes through the transition-metal series. Adapted from [412], copyright American Chemical Society. (c) Examples of patterns predicted for free-standing 1L B polymorphs, from close-packed triangular, honeycomb. The numbers at the bottom right of each model mark the hole density, S1 and S2 are the observed phases. Adapted from [423], © Springer Nature.

chemical oxidation. By using a graphite crystal as starting material, it was possible to study the structure of both the exfoliated and the non-exfoliated fractions on the nanometric and mesoscopic scale [137].

Figure II.21 shows AFM images of graphite basal surfaces that are left behind after different exfoliation processes. Exfoliation by sonication in DMF proceeds layer-by-layer. Only the upper part of the HOPG is interested, and the process is slow, requiring several hours to alter the substrate roughness [137]. CE is the most damaging treatment for HOPG, destroying significantly the crystalline layer through deformation and intercalation.The obtained sheets are mostly 1L soluble, tending to re-stack in a uniform LM. EEproceeds by mechanical expansion due to gas formation. Whole areas of the substrate rise up due to gas formation, tearing apart the superficial layers and removing large amounts of material. EE works on a larger scale, oxidizing the upper HOPG layers, with more cracking and swelling on the macroscopic scale. Damage to HOPG is proportional to the applied bias, with disruption of crystalline stacking. Exfoliation is fast and more efficient than in solvent, yielding 1-2L GO $>$ 50%, with tunable oxidation.

The differences between the three methods highlight the trade-off between speed and efficiency of exfoliation on one side, and preservation of material quality on the other.

II.7. Computational modelling of exfoliation of LMs

The rush towards innovative applications has stimulated the synthesis and exfoliation of novel LMs. Graphene, BN, TMDs, and BP are nothing but the tip of the iceberg of a rapidly increasing LM family. To keep up with this experimental thrust, it is of uttermost importance to expand the portfolio of potential LMs. In this respect, first-principles simulations offer unprecedented opportunities to predict and design novel LMs [403, 404] providing new directions for experimental explorations. To achieve this computational synthesis of novel LMs, two main strategies have been put forward, that mirror the bottom-up or top-down techniques of experiments.

Top-down approaches consist in systematically exploring databases of known experimental compounds, looking for LMs that can be exfoliated into 1L. This requires first to recognize if a parent bulk 3d crystal structure results from the stacking of chemically disconnected components. Geometrical algorithms based on the comparison between interatomic distances and van der Waals or covalent radii can be adopted to assess the chemical connectivity between units. The dimensionality of each unit can then be estimated, leading in particular to the identification of 1L. Ref. [405]data-mined subset of structures with low packing ratio from the Inorganic Crystal Structure Database (ICSD) and

identified 92 LMs, nearly half of which had never been discussed before. More recently, this portfolio has been significantly enriched by Refs. [406, 407], who not only extended the investigation to other databases (including the Materials Project database and the Crystallographic Open Database), but also validated their results against accurate van-der-Waals density-functional-theory calculations of the binding energy. This led to the discovery of 681 [406] and 1825 [407] exfoliable LMs that will provide a rich portfolio of candidates to explore for optimal electronic, optical, catalytic, topological, and magnetic properties. E.g. instance, a new magnetic LM, Fe_3GeTe_2, has been already found [408] among these new exfoliable structures [406], but many more promising candidates await discovery. This approach has been adopted not only to collate these extensive databases [1737–1740] but also as a one-shot effort to find novel LMs from bulk layered compounds; e.g. for arsenene and antimonene [409] or 1L Hittorf's phosphorus [410].

Novel LMs materials have also been 'synthesized' computationally through bottom-up approaches, starting directly with some chemical intuition. In this regard, a first possibility is to consider structural prototypes of known LMs and create hypothetical new structures by substituting elements with chemically similar species [403]. This led, e.g. to the theoretical prediction of germanene and silicene [411] by looking for stable Ge- and Si-based analogues of graphene. A list of 171 TMDs and oxides with favorable formation energies has been obtained by decorating the so-called H and *T* structural phases with 27 different transition metals [412, 413]. Ref. [414] extended this approach to other classes of materials including halides, semimetal monochalcogenides and atomically thin 1Ls, identifying 146 hypothetical LMs for which the electronic and magnetic properties have been computed [1736]. Another promising way to theoretically synthesize new LMs bottom up relies on global optimization techniques. Starting from a given set of elements, the ground-state structure is obtained by searching for the most stable atomic configuration and (possibly) stoichiometry using either evolutionary [415–417] or particle swarm optimization [418, 419] algorithms. These methods have been adopted for instance to predict 1L materials with no bulk layered counterpart, like SiS [420] novel phases of InP [417] and several 2d allotropes of boron [416, 421], known as borophenes. In the latter case, statistical methods based on cluster expansion have been put forward and predicted the structure of borophene on metallic substrates in agreement with experiments [422]. Figure II.22 provides a classification of LMs as easily exfoliable, potentially exfoliable, or with high binding energy.

III. Processing of dispersions

III.1. Size selection

III.1.1. Sedimentation-based separation

The exfoliation of LMs usually results in a heterogeneous dispersion of flakes having different morphology, i.e. lateral size and thickness [166]. There are many methods for the selection and processing of flakes [115, 131, 183–185, 424, 425] by means of ultrasonication [115, 131, 174, 183–185, 204, 424–427], shear mixing [176, 177, 238, 428–430], ball milling [179, 431–436], microfluidization [178], and wet-jet milling [437–440]. Centrifugation based size selection methods can be classified into sedimentation based-separation (SBS) and density gradient ultracentrifugation (DGU) [195]. Materials subjected to SBS are sorted on the basis of different sedimentation rates in response to a centrifugal force. Owing to its ease in handling, SBS is the most commonly applied size selection technique for GRMs. Typically, small and thin flakes are separated from larger, thicker counterparts. However, achievable size distributions are still rather broad except for the smallest and thinnest flakes. To tackle this, a number of variations to traditional single step SBS have been developed, such as band sedimentation [185] and liquid cascade centrifugation [186]. Different to SBS, DGU exploits the movement of the dispersed object to the point in the centrifuge tube where the buoyant density of the material matches that of the surrounding liquid. The addition of density gradient media to the mixture is typically required to adjust the density of the liquid to the higher density material [168]. As such, DGU has the potential to separate flakes by thickness, but is more challenging to perform than SBS. In the following sections we will discuss these different strategies, highlighting pros and cons.

III.1.2. Single step sedimentation

The SBS process is widely used to separate materials of different nature and morphology ranging from metallic nanoparticles (MNPs) [441], CNTs [442–445], to GRM flakes [115, 131, 174, 177, 183–185, 204, 238, 424–428, 430]. A theoretical description of the sedimentation process can be found in Ref. [195]. In brief, three forces act on the objects during the centrifugation, which determine their sedimentation rate (see figure III.1(left)): (I) the centrifugal force $F_c = m_{2D}\omega^2 r$, which is proportional to the mass of flake itself (mGRM), to the square of the angular velocity (ω), and to the distance from the rotational axes (r), (II) the buoyant force $F_b = -mS\ 2r$, which is linked with the Archimedes' principle, being proportional to the mass of the displaced solvent (mS) times the centrifugal acceleration, and (III) the frictional force $F_f = -fv$, i.e. the force acting on the GRM flakes moving with a sedimentation velocity (ν) in the solvent. F_f is proportional to the friction coefficient (f) between solvent and the GRM flake. f depends on both physical parameters of the dispersed flakes, i.e. lateral size and thickness, and physico-chemical properties of the solvent they are dispersed in, i.e. the viscosity (η). Both parameters have a strong influence on the value of f.

Overall, the sedimentation of GRM flakes depends on their mass and frictional coefficient, which is shape dependent [115, 166, 424]. In first approximation, thick and large GRM flakes, having larger mass with respect to small and thin flakes, sediment faster with respect to the latter, since these have smaller mass. This allows to separate GRM flakes with different morphology [166, 424], see figure III.1. However, it is challenging to isolate large and thin flakes. The definition of large/thick and small/thin depends on the material that is used in combination with the centrifugal acceleration and the medium. This will be detailed further down below for a few examples.

Thus, taking into account the dependence of the physical dimensions of the flakes on the centrifugal acceleration (expressed as relative centrifugal field, RCF, in units of the earth's gravitational field, g), it is possible to exploit SBS to prepare GRM flakes of different morphology. In a typical experiment, a dispersion is centrifuged at a fixed g-for a given time. Supernatant and sediment are then separated. The sediment contains larger and thicker flakes than the supernatant. By changing the centrifugal acceleration and centrifugation time, the flake sizes can be adjusted. E.g. the flakes in the supernatant will be smaller after centrifugation at higher accelerations or longer times. Any centrifuge (benchtop or ultracentrifuge) with either fixed angle rotor or swinging bucket rotors can be used.

Even though it is not required that the centrifugation is run for several hours until an equilibrium is reached, i.e. all flakes that will sediment at a given centrifugal acceleration have reached the bottom of the vial, it is recommended not to use centrifugation times shorter than 30 min. When centrifugation times are short, a steeper size/thickness gradient is formed in the vial. As a result, the size and thickness distributions in supernatant and sediment will depend on how the sample is decanted, leading to poor reproducibility. Centrifugation times ~1–3 h are recommended and lead to reproducible results. This also depends on the rotor and vial size, hence the distance the flakes need to travel to reach the bottom [246]. Often sediments are then discarded and supernatants collected for analysis and/or further processing. However this makes it a wasteful process.

With SBS, it has been possible to prepare samples having lateral sizes ranging from few nm to a few μm, both for FLG [131, 176, 184, 424–427, 446, 447] and other LMs [174, 185, 244, 425, 448, 449]. In terms of thickness, dispersions with SLG content up to ~60% were demonstrated in an SDC based aqueous dispersion [446], while ~33% SLG was reported for dispersion in NMP [447]. Such 1L-rich dispersions from SBS also contain predominantly laterally very small

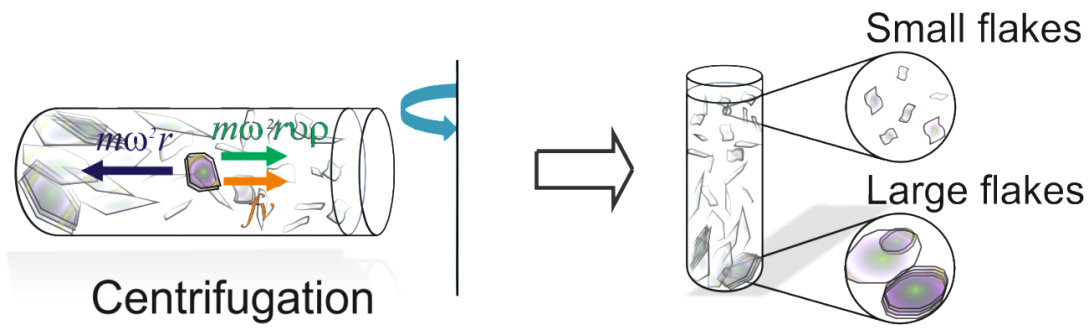


Figure III.1. Sorting of GRM flakes by ultracentrifugation. The SBS approach allows separating thin and small lateral sized flakes (supernatant) from thicker and larger ones, which precipitate at the bottom of the ultracentrifuge tube as pellet. The final flake Dimensions (lateral size, final flake N) depend on the centrifugal acceleration, material and medium.

(<50 nm) flakes [446, 447]. Apart from the difference in percentage of SLG, the flakes processed in water-surfactant dispersions are, on average, also smaller (~200 nm) [184, 427, 446] with respect to NMP (~1 μm) [131, 447]. This difference is related to the difference in the viscosity of the solvents. When comparing the most widely used solvents (NMP and water where, with the addition of surfactant, the viscosity decreases) the viscosity of NMP (1.7 mPa s) [450] is significantly higher than water (~1 mPa s) [451]. A higher solvent viscosity increases the frictional force [195], reducing the sedimentation velocity [195]. Therefore, when using similar centrifugation conditions (centrifugation time and centrifugal acceleration), the flakes retained in the supernatant will be larger/thicker in higher viscosity solvents.

SBS also suffers from the further disadvantage that all flakes(also small < 50 nm) remain in the supernatant when operating at the low centrifugal acceleration (<1000 g) used to isolate large (μm) flakes. Hence, dispersions containing larger flakes on average are significantly more polydisperse and show broad size (20-few μm) and thickness (1–20 layers) distributions. This can be partially overcome by a band sedimentation approach, where the dispersion is placed on top of a solvent race layer (without flakes) prior to centrifugation [185]. E.g. a dispersion containing flakes in an aqueous surfactant can be onto a race layer of deuterated water containing the same surfactant [185]. During centrifugation, the flakes spread throughout the vial according to their sedimentation rate, related to their size. The centrifugation is stopped before the dispersion constituents reach the bottom of the vial, allowing for a collection of various fractions in one run. Smaller/thinner flakes remain closer to the top and are thus efficiently isolated from larger/thicker ones, closer to the bottom. This was demonstrated for MoS_2 [185]. In this case, centrifugation at 1500 g for 10 min yielded various fractions ranging from mean lateral sizes of 350 nm and arithmetic mean N~15 in fractions close to the bottom, to 40 nm and 2L in fractions extracted from the top of the vial. Compared to traditional homogeneous SBS, the distribution histograms were narrower, i.e. the standard distribution was reduced by ~2 [185].

Even though this approach can be advantageous when various fractions with narrower thickness distributions than SBS are required, it suffers from a few disadvantages. First, the material quantity that can be processed in a single step is lower because it is beneficial to keep the sample layer thin, so that most of the volume in the cuvette is taken up by the race layer. Second, the final size-selected sample is diluted during the process, making high concentrations inaccessible. Third, a swinging-bucket rotor is required, as a fixed-angle rotor will not lead to such a defined movement of flakes through the race layer. Therefore, liquid cascade centrifugation (LC) has been suggested as versatile alternative to the above mentioned single step SBS.

III.1.3. Liquid cascade centrifugation

LCC is versatile and can be carried out using benchtop centrifuges [186]. This is a multi-step procedure, whereby various cascades can be designed according to the desired outcome. To demonstrate this process, a general cascade is portrayed in figure III.2. It involves multiple centrifugation steps, each with a higher centrifugal acceleration [186]. After each step the sediment is retained and the supernatant is then used in the proceeding stage. As a result, each sediment contains flakes in a given size range, 'trapped' between two centrifugation stages with different speeds. Similar to band sedimentation, small/thin flakes are removed from dispersions with predominantly larger/thicker flakes. As with traditional SBS, the lateral dimensions and N obtained depend on the design of the cascade (centrifugal accelerations), starting material and solvent. A few examples of lateral sizes and thicknesses are summarised in table III.1.

Critical to LCC, the resulting sediment can be redispersed by mild agitation (shaking, or <5 min bath sonication) in the respective medium, enabling one to reach any desired flake concentration, as well as modification of the concentration of additives (such as polymers or surfactants). Virtually no material is wasted in LCC, resulting in the collection of larger masses of size-selected flakes from a single

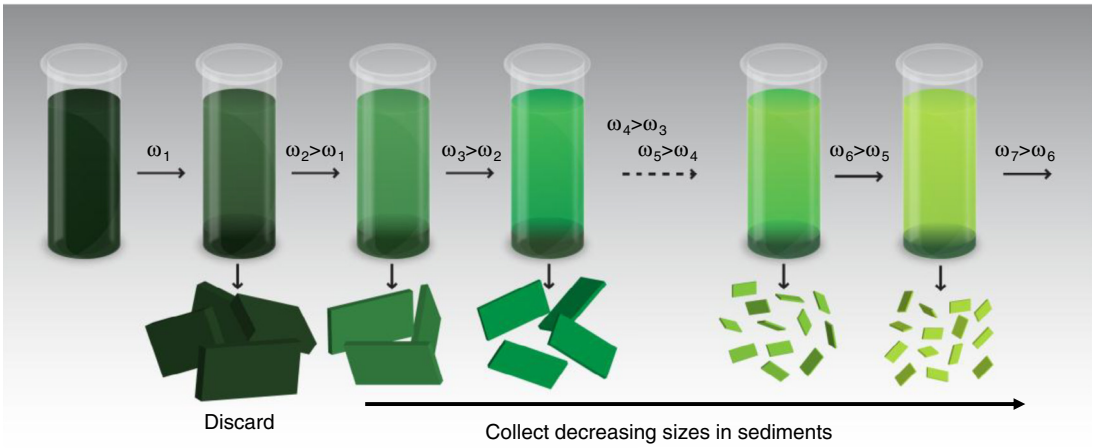


Figure III.2. Schematic representation of liquid cascade centrifugation. Adapted from [186], copyright American Chemical Society.

Table III.1. Overview of mean lateral sizes using LCC. For each material, the 'large/thick' and 'small/thin' fractions are defined by the midpoint of the centrifugation boundaries (given as central g). Data includes centrifugation in solvents (NMP, IPA) and aqueous SC solution.

	FLG SC [236]		FLG NMP [176]		WS_2 SC [245]		MoS_2 SC [245]		BP NMP [190]		GaS IPA [188]	
Central g	550	21 000	80	1800	0.33	7500	0.33	9900	690	17 500	170	850
(nm)	360	90	1000	160	170	35	270	55	615	150	450	100
	8.1	3.3	Not determined		7.5	2.1	7.4	2.4	Not determined		29.5	11

dispersion compared to homogeneous SBS, where the sediments are discarded. The procedure was thus found to be ideal to study size effects in applications [452]. It was applied to WS_2 and MoS_2 [186, 245, 452, 453] as $Ni(OH)_2$ [240], GaS [188], BP [190] and FLG [176, 236] in solvents [176, 188, 190] as well as aqueous surfactant [177, 186, 236, 240, 452] or polymer systems [453]. Due to its versatility and the large accessible quantities, other reports adopted the procedure [454, 455]. Typical mean lateral sizes and N are given in table III.1 for a range of materials.

From this table it is clear, that the outcome of the size selection depends on the centrifugal accelerations, the density of the material and medium. A deeper understanding and systematic analysis will enable the prediction of the outcome of the size selection. In any case, to achieve efficient size selection, it is critical to remove the supernatant from the sediment as completely as possible. This also means that for this procedure to work, the centrifugation time has to be long enough to allow the majority of the flakes to sediment to the bottom of the vial. This does not require centrifugation to equilibrium (unlike DGU). One can obtain a good separation of supernatant and pellet-like sediment after 2 h of centrifugation, when the filling height of the dispersion in the vial is <10 cm. Centrifugation times should be extended if greater filling heights are used [246].

The chosen size-selection cascade can be modified readily to suit a desired outcome. While this specific procedure yields flakes sizes and thicknesses over a broad size range in the different fractions, if only specific sizes are targeted, some centrifugation steps can be skipped. E.g. if medium-sized flakes are desired, the sample can be centrifuged at only two different centrifugal accelerations and the sediment redispersed. In first approximation, flake size selection occurs by mass in such a standard cascade, still making it difficult to select large (μm), thin (1–3 L) flakes like in homogeneous SBS. However, a design of secondary cascades [186] involving a combination of long (14 h), low-speed centrifugations (~1/5 of the lower *g*-boundary of the initial trapping) to remove thicker material and short (60 min), high-speed centrifugations (above the higher *g*-boundary of the initial trapping) to remove very small (10–20 nm) flakes has shown potential to overcome this limitation yielding a ~75% 1L (mean N ~1.3) with an average lateral size ~40 nm in the case of WS_2 [186].

III.1.3.1. Density gradient centrifugation

The key disadvantage of the SBS process, not allowing one to isolate a high percentage ($>10\%$) of 1L flakes of reasonable lateral size (>100 nm), can be overcome with the exploitation of DGU. This enables control on *N*, when flakes are subjected to ultracentrifugation in a preformed DGM.

Two approaches can be exploited for the separation of GRM flakes: isopycnic [456] and rate zonal separation [456]. Isopycnic separation allows spatial separation inside the cuvette of GRM flakes depending only on their buoyant density. This is defined as the density of the medium at the corresponding isopycnic

point and is measured in g cm^{-3}. GRM flakes, during isopycnic separation, move along the cuvette, until they reach the corresponding isopycnic point, i.e. the point where their buoyant density matches that of the surrounding DGM [457]. Hence, in principle, flakes should be sorted according to N. However, it is nonetheless difficult to obtain dispersions of exclusively large (micron-sized) 1L-GRMs. This is likely related to the fact that micron-sized SLG is a minority fraction in LPE samples. Hence, even if all SLG flakes are isolated from the dispersion, the average lateral size will still be in the range of hundreds nm.

For isopycnic separation, the choice of DGM is fundamental. Salts (e.g. sodium chloride, cesium chloride, and lithium chloride), sucrose, and iodixanol are the most widely used DGMs [458, 459]. The use of salts has some issues. First, they induce aggregation on the hydrophobic solutes [460, 461] which may negatively affect the sorting process. Second, density gradients produced with salts are less stable with respect to those using sucrose and iodixanol, due to their lower viscosity [462]. Sucrose suffers the opposite problem: it has high viscosity, which further increases exponentially at high concentrations [463]. Iodixanol seems to be better suited, due to density tuneability, with respect to sucrose, and higher viscosity compared to salts.

The effectiveness of the isopycnic separation is also strongly determined by the type of density profile of the DGM and its variation. During centrifugation the density profile redistributes as the DGM responds to the centrifugal force, resulting in a steeper gradient over time [464]. The density profile of the DGM can be: linear, nonlinear, or step [465, 466]. Linear gradients are used when the materials to be sorted have small (<0.05 g cm^{-3}) buoyant density differences. For this reason, linear gradients can sort surfactant-micelle encapsulated CNTs with very small buoyant density difference, such as (6,5) (1.06 g cm^{-3}) and (7,5) (1.08 g cm^{-3}) dispersed in SC [467–469]. In nonlinear gradients, the DGM density changes nonlinearly along the cuvette and the density gradient is established during the ultracentrifugation process [465]. Nonlinear gradients are particularly suited to sediment particles over the entire length of the cuvette [465]. By exploiting nonlinear gradients, a variety of depth-density profiles can be produced according to the density variation. This allows the trapping of particles of different densities along the cuvette's length. Step gradients, formed by stacking layers of different density, are usually employed when the materials to be separated have larger difference in density (>0.1 g cm^{-3}) [470]. The sharp variation in density at the interface of two different layers stops materials with a density smaller than the denser layer, letting the larger density ones pass through [470].

For separating GRM flakes, the problem is that these materials have high densities, with no intrinsically different density with N (e.g. MoS_2, $\rho = 5.06$ g cm^{-3}, WS_2, $\rho = 7.5$ g cm^{-3}, WSe_2, $\rho = 9.32$ g cm^{-3}), except for the surfactant shell, making this an important aspect of DGU. This fact makes the sorting of inorganic GRM flakes challenging in common DGM, such as iodixanol, with $\rho = 1.32$ g cm^{-1} [115, 469]. Therefore, in order to separate flakes by *N*, it is important to ensure that they have uniform surfactant/polymer coverage [183, 446]. This requirement is crucial, because the surfactant/polymer layer also contributes to the buoyant density of the entire system, thus resulting in slight variations of the buoyant densities of 1L- and FL- flakes, which can lead to isopycnic separation. This results in a spatial separation inside the cuvette, overcoming the limitations of conventional ultracentrifugation in a density constant medium.

A successful GRM flakes sorting by isopycnic separation mainly depends on the following: (1) a large as possible amount of 1L-and FL- flakes in the starting dispersions. Differences in buoyant density can be correlated to specific thickness (1L, 2L, 3L) only if individualized GRM flakes are encapsulated by the surfactant micelles or polymer molecules. This also implies the folding and wrinkling of the flakes will be problematic. (2) Uniform flakes coverage. This is ruled by the adsorption of surfactant or polymer molecules, and their aggregation, which can lead to clusters formation (i.e. aggregates of several molecules around the flakes basal plane). The effectiveness of the isopycnic separation is demonstrated by the yield of SLG to date, ~80% [183] with SC as surfactant or N separation of GO [471].

Isopycnic separation was also used to sort inorganic LMs [168]. One of the main issues is their high density. Thus, surfactant molecules, such as SC [469] cannot reduce their buoyant density sufficiently to match the density of the gradient. By using Pluronic F68, a greater hydration shell than SC is formed. This procedure allows to reduce the buoyant density of the encapsulated LMs [472, 473]. Pluronic F68 allows to reduce the buoyant density of BN [473] as well as TMDs such as WS_2, WSe_2, MoS_2, and $MoSe_2$ [472], within the limit of the DGM allowing for isopycnic N separation.

Another approach to sort inorganic LMs via isopycnic separation relies on the mixing of two DGMs [474]. The addition of cesium chloride to iodixanol, determines an increase of the maximum buoyant density supported by the DGM (i.e. 1.56 g cm^{-3}) to the point where even high-density rhenium disulfide can be sorted layer-by-layer [474]. The addition of salts as DGM is not compatible with dispersions based on ionic surfactants, as these will crash due to charge screening.

Isopycnic DGU-based separation allows one to sort GRM flakes by thickness and lateral size, rather than mass, unlike SBS. However, DGU separation, although widely used in biology [195] and successfully applied to GRMs [168], has the drawback of being a process involving multiple iterations and, as such, it is time-consuming. Another issue for the further processing

Table III.2. Specifications to consider for different printing methods.

Printing method	Viscosity [Pa s]	Layer thickness [μm]	Feature size [μm]	Registration [μm]	Throughput [$m^2\ s^{-1}$]
Gravure printing	0.05–0.2 [477]	0.8–8 [477] <0.1 [478–480]	75 [481]	>10 [481]	60 [481] 3–30 [482]
Flexography printing	0.05–0.5 [477]	0.8–2.5 [477]	80 [481]	<200 [481]	10 [481] 3–30 [482]
Offset printing	30–100 [477] 5–50 [483]	0.5–2 [477]	10–50 [481]	>10 [481]	5–30 [481] 3–30 [482]
Screen printing	0.5–50 [477]	3–15 [477] 0.015 [484] 30–100 [481]	20–100 [481]	>25 [481]	2–3 [481]

of the sorted flakes, i.e. ink formulation, is linked with the presence of the DGM in the dispersion, that may be problematic for processing and/or its removal.

Another methodology to sort GRMs in a centrifugal field is rate zonal separation (RZS) [457, 475]. In RZS, the ultracentrifugation is stopped during the transient centrifugal regime, i.e. before the materials under ultracentrifugation reach their isopycnic points [475]. RZS exploits differences in the sedimentation coefficient of particles under ultracentrifugation. Therefore, particles with different sedimentation coefficients will move along the cuvette at different sedimentation velocities [457, 475], determining their spatial separation [441, 475]. RZS was used to separate GO flakes with different lateral size [476], exploiting the fact that the larger is the flake lateral size, the larger is the sedimentation coefficient. RZS was also used for the lateral size selection of BP flakes [425]. Similar to DGU, a downside of RZS is that usually an ultracentrifuge is used (rather than a benchtop centrifuge) and that a DGM is added to slow down the sedimentation and lead to a more gradual distribution along the cuvette, which has to be removed prior to further processing. This contrasts to band sedimentation [185] as discussed above.

III.2. Inks formulation

The production of GRM flakes in dispersion following exfoliation and sorting finds a direct use for applications, such as in polymer composites. In many other cases, the as-prepared dispersion cannot be used directly. For applications requiring coating and printing, the dispersion needs a formulation process to obtain an ink. The composition of functional inks is linked with the target deposition/printing process [166], see table III.2. There are deposition/coating approaches where the ink formulation is not stringent, depending on the nature of the solvent used for exfoliation and sorting, the deposition can be carried out directly with the as-prepared dispersion. This is the case for vacuum filtration and transfer, spray and drop casting, where the most critical parameter is the morphology control of the dispersed flakes. For other printing processes, such as flexographic, gravure, slot-die and ink-jet printing, the formulation of the ink is more complex, requiring the addition of many components in pre-defined steps. In the following, a few examples are given.

III.2.1. Tuning of rheological properties

The control of the ink rheology is key to ensure consistency and reproducibility. This is usually achieved by studying flow and deformation of the materials under external perturbation [485]. The complex structure of the ink determines a rheological behavior which is typical of non-Newtonian flow [486]. Thus, there is a non-linear relation between shear rate $\dot{\gamma}$ shear stress (τ), and apparent viscosity η ($\eta_{app} = \sigma\dot{\gamma}$) which depend on $\dot{\gamma}$ (or τ). This behavior is different from Newtonian liquids, where $\eta = \sigma\dot{\gamma}$ [487]. The shear rate determines the η behavior of inks and, thus, their range of application. Depending on their flow behavior, there are different classifications for non-Newtonian inks [488]: dilatant where η_{app} increases with increasing $\dot{\gamma}$ [488], pseudoplastic, where η_{app} decreases with increasing $\dot{\gamma}$ [488], and thixotropic, where η_{app} decreases with time under a constant deformation and will start to rebuild once the shear force η_{app} is removed [488], figure III.3. The ink rheology is strongly influenced by the GRM volume fraction, φ, with their shape and spatial arrangement [489], GRM flakes dispersed in a liquid affect its flow field resulting in an increase in energy dissipation due to fluid-flake and/or flake-flake interactions [489, 490]. These interactions increase with φ, restricting the flakes diffusion into small 'domains', formed by the nearest neighbors and η diverges. However, a theoretical model to predict η of fluids with dispersed GRMs does not exist yet. Such model is not even available for NPs in general, although a significant research effort has been carried out [491–493].

We now discuss the main ink requirements and the state of the art of the formulation for the of GRM-based inks for the main deposition/printing techniques.

Coating approaches, such as drop and spin coating, do not require a structured ink formulation, and, usually, the as-prepared dispersion can be directly

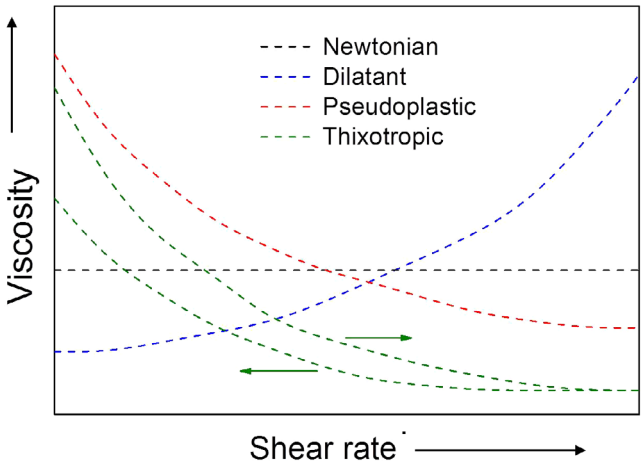


Figure III.3. Newtonian and non-Newtonian flow behavior of functional inks. Adapted from [166], © Wiley-VCH Verlag GmbH & Co. KGaA.

deposited onto the target substrates. On the contrary, although the ink for spray coating deposition does not require a high viscosity, the aerosol formation and the subsequent drying process need the control of several processing parameters [494] such as viscosity [495], flow rate [496], and the distance substrate/spray-nozzle [497]. The nature of the solvent, which determines its evaporation rate at the substrate surface [496], is also a critical point for a uniform deposition. The solvent vapor pressure is crucial. Solvents having low vapor pressure, such as NMP (0.5mm Hg @25 °C), one of the most common for LPE of graphite [164], promote long crystal formation time [496]. This allows a consistent structural arrangement prior to the transition to the solid phase of the deposited feature [496]. On the contrary, high vapor pressure solvents, such as, e.g. isopropyl alcohol (IPA, 33mm Hg @25 °C) and toluene (24 mm Hg @25 °C), promote faster solvent evaporation [1741]. This subsequently reduces the ability of the flakes to organize in a ordered manner. The consequence will be a decrease of the final device performance, such as, e.g. a reduction of the charge carriers mobility in FETs [496]. Other sources of instability for the coating are linked with the geometry of the spray coating system, i.e. small nozzle size, or the jetting pressure, i.e. low pressures reduce the flow rate, which produce scattered droplets on the substrate and eventually a non-uniform coating [496]. A continuous coating is obtained by high deposition rates [145, 496]. The uniformity of the coating is also determined by the appropriate substrate/nozzle distance [497]. If this too short, the ink previously deposited onto the substrate can be blown away by the incoming flow. If it is large, the solvent can evaporate during the flight time, i.e. before the droplets reach the substrate.

The formulation of the ink for an inkjet process requires the control and tuning of various liquid properties such as ρ, η, and γ [498], which are then summarized in the following dimensionless figures of merit (FOM): the Reynolds (N_{Re}) and Weber (N_{We}) [499, 500] and the inverse of the Ohnesorge number, Z ($1/N_{Oh}$) [500]. The Z number is independent on the drop velocity ($m \cdot s^{-1}$) and it is the most used FOM for inkjet printing [501–507]. Different Z values have been proposed, ranging from 1 to 91 with different functional materials [501–507].

Other parameters for the ink formulation have to be considered, such as, e.g. the physical dimensions of the flakes dispersed in the ink, that can agglomerate and clogg the print-head. Usually, it is required that flakes have lateral sizes smaller than ~1/50 of the nozzle diameter [508] (typically ~100 μm [509]). Other parameters to be optimized for the printing/deposition process are wetting and adhesion [510] to the substrate, as well as the distance between nozzle and substrate (typically 1–3 mm) [511].

An even more structured inkis needed for flexography and gravure printing. Although both require a high viscosity ink, there are several differences [166]. In flexography, there is a plate with a raised surface that spreads the ink onto the target substrate. Gravure is an intaglio process, where the ink is first transferred onto an image carrier and then printed on the target substrate. As summarised in table III.2 and Ref. [166], gravure printing is usually faster (~1000 m min^{-1}) than flexo (~500 m min^{-1}), with printed stripes thicker (~1 μm in gravure) than in flexography (<1 μm). The viscosity is also different: in flexography this is in the 50–500 mPa · s range, while in gravure it is higher 100–1000 mPa · s.

GRM-based inks for flexography and gravure were formulated [512, 513]. Ref. [512] reported a flexography ink by using CMC as a binder for FLG flakes in a water/isopropanol solution, obtaining a η ~20 mPa · s. The as-formulated ink was printed onto a flexible ITO substrate at 0.4 m s^{-1}, and used as counter electrode for the realization of a flexible dye-sensitized solar cell (DSSC) [512]. A FLG/terpineol ink (η ~0.2–3 Pa · s from the homogeneous dispersion of FLG-ethyl cellulose powder (5–10 wt%) in a mixture of ethanol/

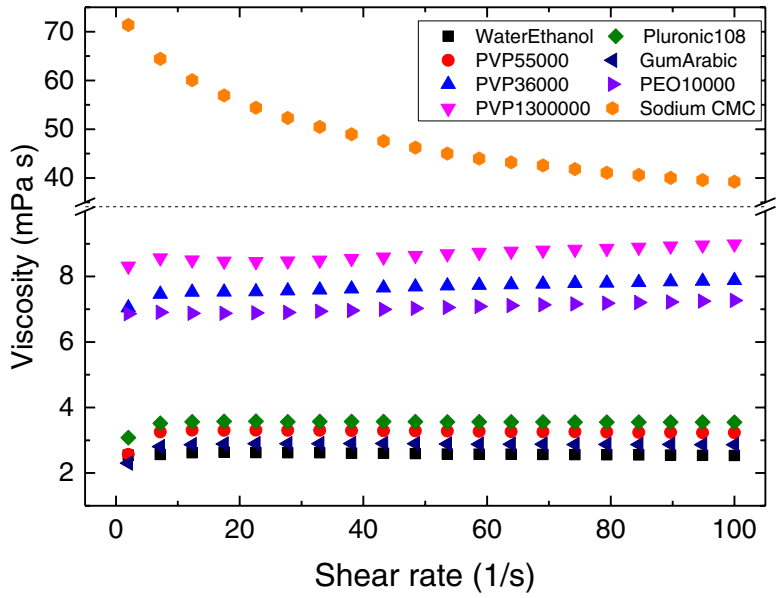


Figure III.4. Rheology modifiers in 50:50 water/ethanol solution at 1 wt% loading.

terpineol (2.5:1 volume%) was reported in Ref. [513]. For the formulation of high viscosity GRM-based inks, there are several issues to be addressed. First, the solvents used in LPE (e.g. NMP) are toxic and have very low η (<2 mPa · s). The use of alternatives such as volatile alcohols, e.g. ethanol [513] and isopropanol [512], is against the current environmental regulations, requiring the minimization of volatile organic compounds [514]. Second, the GRM concentration in these solvents is low (<1 g l^{-1}). Thus, in order to produce a functional (e.g. conductive) film, many print passes are required. The increase of GRM fillers could determine a problem with the solvent evaporation and in-series printability. In this context, the use of high boiling point solvents requires post-processing annealing for solvent removal [515], thus posing limitations on target substrate.

By increasing η, it is possible to obtain a paste, needed for screen printing. FLG-based conductive-pastes (i.e. FLG [516], RGO [517–519] and flakes [520, 521]) are emerging as possible alternatives to those based on metal NPs.

A paste based on FLG powder dispersed in terpineol, with ethylcellulose as a binder was prepared in [516]. The paste contained flakes at a concentration of ~80 g l^{-1}, having a η up to ~10 Pa·s at a shear rate of 10 s^{-1}. The as-deposited paste required a thermal treatment at 300 °C for 30 min to remove ethylcellulose. Another FLG-based paste, having shear thinning behaviour, was discussed in Ref. [522], which a gelation approach starting from the dispersion of expanded graphite in methyl ether dipropylene glycol in the presence of polyvinyl acetate and polyvinylpyrrolidone acting as binders. However, many parameters still need to be optimized for the development of optimal GRM-based inks/pastes for screen printing.

Figure III.4 shows a selection of polymers at 1 wt% loading that can be added to water or 50:50 water/ethanol solutions to modify the rheology. Polymers such as polyvinylpyrrolidone (PVP) can be added, with increased viscosity with increasing molecular weight (M_W). Celluloses which are commonly used, provide high viscosity at low loadings, and impart thixotropic behaviour. E.g. aqueous FLG-based inks produced by microfluidization [178] have FLG loading >100 g l^{-1} and are formulated using 1 wt% sodium carboxymethylcellulose (NaCMC) to provide η up to 1800 mPa · s.

NaCMC is not easily dissolved and its preparation can be affected by factors including the NaCMC particle size, rotational speed of the mixer, the rate at which solutes are introduced, and the solution T [523]. Heating the FLG dispersion should be avoided as this may promote flocculation. NaCMC is water-absorbent and has high water retention, therefore it clumps. To prevent this, NaCMC is added until dissolved completely and stirred to avoid bubbles. Bubbles and clumps need to be removed prior to printing.

The rheological properties of inks were investigated by monitoring the elastic modulus G'[J m^{-3} = Pa] [524], representing the elastic behavior of the material and a measure of the energy density stored under a shear process [524], and the loss modulus G''[J m^{-3} = Pa] [524], representing the viscous behavior and a measure of the energy density lost during a shear process due to friction and internal motions [524]. Flow curves measured by increasing $\dot{\gamma}$ from 1 to 1000 s^{-1} at a gap of 0.5 mm, because this $\dot{\gamma}$ range is applied during screen printing. Figure III.5(a) plots the steady state viscosity of an ink produced from microfluidization (100 cycles) containing 73 wt% flakes as a function of $\dot{\gamma}$. NaCMC imparts a drop in viscosity under shearing, from 570

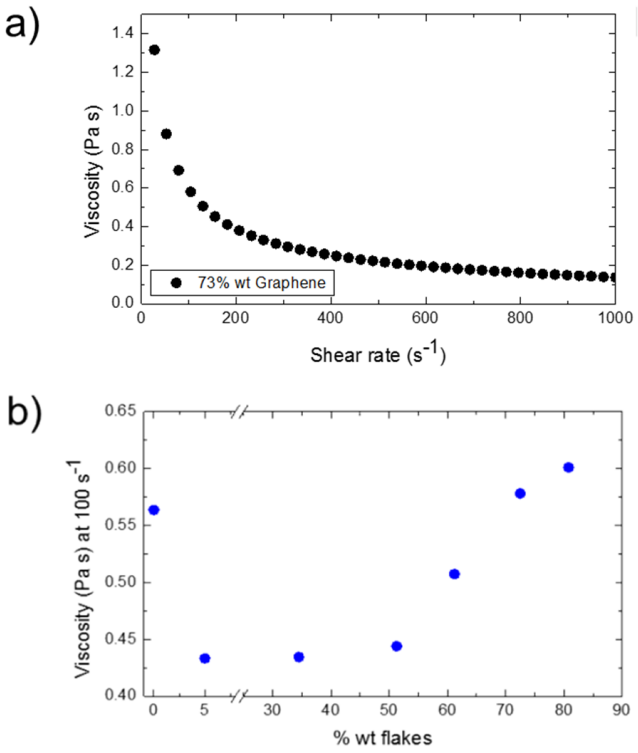


Figure III.5. (a) Viscosity as a function of shear rate for an ink with 73 wt% flakes, (b) viscosity at 100 s1 for different wt% of FLG flakes. Reproduced from [178].

mPa · s at 100 s^{-1} to 140 mPa · s at 1000 s^{-1}. This is thixotropic [525], since the viscosity reduces with $\dot{\gamma}$.

This behavior is shown by some non-Newtonian fluids, such as polymer solutions [526] and biological fluids [527]. It is caused by the disentanglement of polymer coils or increased orientation of polymer coils in the direction of the flow. In contrast, in Newtonian liquids, the viscosity does not change with $\dot{\gamma}$ [527]. Refs. [528, 529] reported that thixotropy in NaCMC solutions arises from the presence of unsubstituted (free) OH groups. Thixotropy decreases as the number of OH groups increases [528, 529]. Figure III.5(b) plots the viscosity at hundred s^{-1} as a function of wt%FLG flakes (70 microfluidic process cycles). The NaCMC polymer (10 g l^{-1} in water) has a μ ~0.56 Pa · s at hundred s^{-1}, and drops to 0.43 Pa · s with the addition of 5 wt% flakes. The loading wt% of flakes affects $\dot{\gamma}$, which increases at 51 wt% and reaches 0.6 Pa · s at 80 wt.%.

III.2.2. Hybrid inks

III.2.2.1. Graphene/polymer blends

We describe the formulation of a FLG-polymer-fullerene ink that can be processed by spin-coating to fabricate bulk heterojunction (BHJ) solar cells. The goal is to improve BHJ solar cells performance in terms of hole mobility, photocurrent efficiency and photoresponsivity [530]. Spin coating is commonly used to fabricate BHJ solar cells, allowing rapid deposition of thin films (~hundreds nm thickness) of different materials. In contrast to other printing techniques, it does not have any requirements in term of surface tension, viscosity, solute concentration and particle size for the ink to be deposited. Viscosity, volatility and concentration will affect the morphology and the thickness of the final film, which can be adjusted by tuning the angular velocity and the time of processing. The main advantages of spin coating are also the low amount of material required (μl) and the reproducibility of the film features for fixed working parameters.

Ref. [530] produced a FLG dispersion in 1,2-dichlorobenzene (ODCB) due to its compatibility with P3HT:PCBM by sonication and subsequent centrifugation to remove unexfoliated graphite. For the P3HT:PCBM dispersion, 10 g l^{-1} P3HT and 8 g l^{-1} PCBM are dissolved in ODCB and mixed with the FLG-ODCB supernatant. The P3HT:PCBM:FLG is then spin-coated on the substrate, which is a stack of glass, 100 nm ITO and PEDOT:PSS also deposited by spin coating. The BHJ solar cell is finalised by depositing a counter electrode of 20 nm Ca and 60 nm Al by evaporation. The critical step of the process is the mixing of the P3HT:PCBM to the ODCB-FLG supernatant, since the addition of the P3HT:PCBM could cause the destabilisation and flocculation of the ink. To prevent this destabilisation, the P3HT:PCBM should be added gradually and the dispersion immediately stirred after mixing. It is also important to not add an excess amount of FLG. In Ref. [530], only 2 wt%FLG is added; further increases cause aggregation of the FLG sheets, having a deleterious effect on exciton generation and charge separation/transport in the active layer.

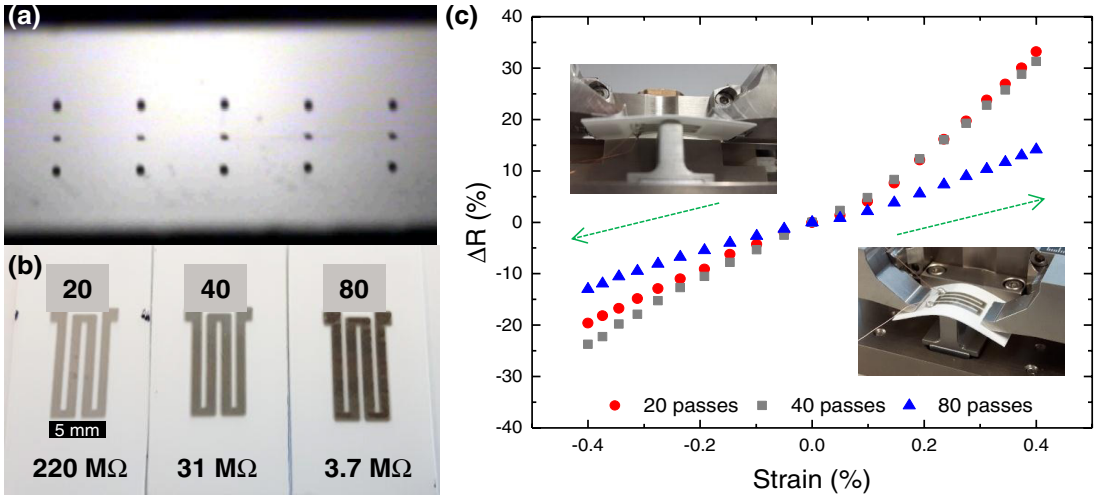


Figure III.6. Inkjet printing of microfluidized ink after 20 process cycles. (a) Typical jetting behaviour showing good droplet formation and the absence of satellite droplets. (b) Printed serpentine-type resistors after 20, 40 and 80 passes. (c) Resistance change whilst 3-point bending of three devices under tensile and compressive strain.

III.2.2.2. Graphene/CNT films

Transparent conductive films (TCFs) on flexible substrates require homogeneity, optical transparency and stability under mechanical stress. Composites of graphene and CNTs are promising in this regard. In this framework the deposition of films by rod coating [531] fulfils the above-mentioned requirements. The use of the so-called Meyer bar allows deposition at RT and is fully scalable over large areas. The diameter of the wound wire of the bar determines the size of the grooves and controls the thickness of the liquid film, as well as giving alignment to the material improving the percolation. The key parameters of the ink to ensure a homogenous coating are viscosity ~1 mPa · s and a small contact angle ~20–30° [532]. The speed of the deposition can affect the homogeneity creating aggregates. Aggregates can also arise from a fast drying of the liquid film.

In addition to published work [1742], we found that a suitable ink can be prepared by bath sonicating (9 h) natural graphite (0.1 g l^{-1}) in aqueous Triton X-100 (0.01 g l^{-1}) followed by centrifugation (10 000 rpm) to remove the unexfoliated flakes. A CNT dispersion was prepared by tip sonication (2 h) P3-SWNT powder (Carbon Solutions, Inc.) in 1.8 g l^{-1} aqueous Triton X-100 followed by centrifugation (25 000 rpm). These CNTs were purified with nitric acid, and left in highly functionalized form containing 1.0–3.0 atomic% carboxylic acid moieties which can be derivatized with a variety of functional groups [1743]. TCFs can then be conveniently fabricated on various flexible substrates such as PET, PEN etc by rod coating. Typically, for a 10 × 10 cm^2 substrate, 80 μl CNT ink is deposited and spread uniformly on the substrate using the Meyer bar. The wet film is allowed to dry in air before coating another layer. To remove the surfactant, after 2–3 coatings, the substrate is soaked in water-ethanol (50:50 in volume) solution at 60 °C and dried with nitrogen. The washing steps help to improve the final TCF conductivity. The same procedure is applied for the deposition of the FLG ink on the CNT film. Generally, for a 10 × 10 cm^2 PET film, 40 repetitions of both inks are required to get to tens of k$\Omega\,\square^{-1}$ at 80% transparency.

We find that these coatings can be applied in the fabrication of CNTs/FLG films as pixel electrodes directly on the backplane of an electrophoretic display. The CNT/FLG ratio is 40:60% in mass, assuring the uniformity of the film avoiding any aggregation. After every 3 coatings the film is washed to remove surfactants. For a 4 × 4 $inch^2$ backplane, 150 ml of the water-ethanol solution (50:50 in volume) are used.

III.2.2.3. Inks with conductive polymers

In order to overcome the obstacles of efficient micro-supercapacitors (MSCs) manufacturing, such as scalability, high cost, and flexibility, new strategies based on processing of FLG nanocomposite inks are appealing. Direct printing/transfer techniques, including spray deposition, inkjet printing, and filtration, offer a promising protocol for production of MSC arrays, which can be processed onto both plastic and paper substrates at low T and over large areas. As a key component for these techniques, the selected ink should be stable, low cost, and easily printable on appropriate substrates; it should display excellent electrical properties without the need for aggressive post-treatments. High quality FLG obtained from electrochemical exfoliation could meet the above requirements.

Two inks were developed based on electrochemically exfoliated FLG (EEG) and conductive polymers [533, 534]. In one, conducting polymers, such as PEDOT:PSS, are mechanically mixed (bath sonication and stirring) with EEG in isopropanol [533]. The other is a EEG/polyaniline (PANI) composite ink [534], based on *in situ* polymerization of aniline in the presence of EEG. First, EEG is prepared and dispersed in

DMF at the concentration of 2 g l^{-1}, followed by non-covalent functionalization with 1-pyrenesulfonic acid sodium salt to obtain water dispersion of EEG. Then the EEG/DMF dispersion is blended with aqueous aniline hydrochloride and gently stirred or sonicated. Afterwards, ammonium persulfate is added, followed by a vigorous stirring (10 000 rpm, 6 h) to form uniform dispersion of EEG/PANI. After washing through ultra-centrifugation with water and ethanol for 3 times, the composite is dispersed in ethylene glycol to get a stable EEG/PANI ink [534].

III.3. Printing and deposition of inks

To develop applications that make use of LPE GRMs, it is necessary to convert the dispersed material into structures suitable for further studies. In general, flakes may either be deposited on a supporting substrate (such as glass, metal foil, Si, or plastic film) or act as a filler within some host material (such as polymers, metals or other nanomaterials) to produce free-standing composites. To this end, numerous liquid-phase processing techniques have been developed for the deposition of GRM dispersions in combination with other dispersed nanomaterials or polymers. Here, we outline some approaches used to produce a range of GRM-containing structures and devices such as vacuum filtration, spray coating, ink-jet and screen printing.

III.3.1. Vacuum filtration

Vacuum filtration is a simple technique whereby a GRM dispersion can be filtered through an underlying porous membrane to obtain nm-to-several micron thick films [535, 536]. These can be removed from the underlying support to produce a freestanding film, or transferred to rigid and flexible substrates and the porous membrane removed e.g. by chemical dissolution [536]. Although this technique may be unsuitable for the production of GRM-containing structures for commercial purposes, its low cost and its simplicity makes it ideal for research purposes. The main advantage is the possibility to wash away surfactants and solvent residues that usually affect the performance (e.g. conductivity) of the final films. Films with different thicknesses and composition can be produced by tuning the amount of dispersion, the pore size of the membrane and the vacuum pressure. GRM dispersions can be filtered on to various membranes, selected based on their pore size and chemical compatibility. Membrane types include cellulose, polycarbonate, anodized alumina, PVDF or PTFE. This allows to produce composites such as layered oxides combined with SWNTs for supercapacitor electrodes [239, 537], and TMDs/SWNT composites for electrocatalysis [452, 538] can readily be fabricated.

A wide range of filtration membranes are available with different surface chemistries and pore-sizes, the choice of which depends on the nature of the dispersion media, the size of the dispersed materials to be filtered and the desired approach to carry out film transfer. As the flakes produced by LPE often have lateral dimensions in 10s-hundreds nm, it is often necessary to use filtration membranes with the smallest possible pore diameters. Mixed cellulose membranes with 25 nm pore size are compatible with aqueous/surfactant dispersion media and can be subsequently dissolved using acetone to achieve transfer of the filtered film.

FLG films with thickness ~150 nm, transmittance ~50%, roughness ~8 nm and R_s ~ 1–2 kΩ sq^{-1} were prepared as conductive electrodes for biological applications [432]. These were also exploited in photonic applications, demonstrating sub-50 fs compressed pulses from a FLG-mode locked fiber laser [539], power scaling lasers [540], and monolithic waveguide lasers [541]. To produce these, a 25 mm diameter membrane filtration setup was used. 500 μl of dispersion with concentration ~0.1 g l^{-1} was diluted in 1 ml DI water. The dilution is necessary when the amount of the filtered dispersion is less than 1 ml to ensure uniform coverage of the membrane. If the dispersion has a high surfactant concentration, the presence of foam on the liquid surface has to be avoided before vacuum filtration. FLG is filtered through a 100 nm pore-size nitrocellulose (NC) filter membranes (Millipore). In order to remove the residual surfactant, the film on the membrane can be rinsed by filtration of 20 ml DI water. The filtering process requires ~2 h, which will increase with the film thickness prepared.

These films can be transferred on to glass coverslips (25 mm diameter) using the following procedure: 1. the FLG/NC membrane is cut to the size required and soaked in deionized water. 2. The FLG/NC is placed on the glass substrate with the FLG side face down. 3. A sheet of cleanroom paper is pressed by hand on the back of the NC to remove the excess water and trapped air between the film and glass. This is a critical step, as trapped air can leave some FLG non-transferred and, therefore, holes or fractures in the final film. The substrate is then clamped with two bulldog clips between two glass slides (30 × 30 mm). 4. The sample is left to dry in an oven for ~2 h at 90 °C. 5. The glass slides are removed and the coverslip left to soak in a covered beaker of acetone to dissolve the NC (at least 24 h) then soaked in isopropyl alcohol (1 h) and in deionized water (1 h). 6. The final FLG/glass sample is then dried in an oven for 2 h at 90 °C. Transfer on flexible substrates can be done with the same procedure. For improved transfer it is possible to use a hydraulic press in step 3.

Another method to make large free-standing membranes is electrophoretic deposition [542]. A suspension of GO with a concentration of 3 mg ml^{-1} is prepared and used as the electrolyte. Two identical pieces of well-polished Cu sheets (30 × 50 × 2 mm) are used as anode and cathode. A constant current of 2 mA is applied between the two electrodes for 2 min.

The anode coated with GO is then dried under vacuum overnight, and then the free-standing GO membrane can be peeled off.

III.3.2. Inkjet printing

The printing of FLG inks is an attractive approach for developing electronic applications, such as transparent conductive films, printed electrodes and sensors. Inkjet printing is the ideal tool to produce prototype electronic devices at the lab scale. Indeed, it enables high resolution (~25 μm) of the pattern associated with the possibility of easily changing the pattern and the printed material. Several examples of inkjet printing of nanomaterials have been reported [201, 447, 543, 544]. In order to have a good jettability an ink has to satisfy particular requirements on Z, γ ρ, η and nozzle diameter. If Z is in the 4–14 range, satellite droplets recombine before reaching the substrate, but Ref. [447] demonstrated the possibility of having good printing also outside this range. Most lab-scale inkjet printers equipped with disposable cartridges, (e.g. Fujilm Dimatix 2800, Ceradrop X, LP50) mount cartridges with 50 μm diameter, so the flakes dispersed in the ink have to be at least 1/20 of the nozzle diameter to avoid printing instability and nozzle clogging. Dispersions produced by LPE followed by centrifugation are particularly suitable for inkjet printing, since they contain flakes with lateral sizes <2–3 μm [164]. Inks made by electrochemical exfoliation contain larger flakes even after centrifugation. These should be filtered before printing.

Inkjet printing can be performed on a variety of rigid (glass, Si/SiO_2) and flexible (PET, PEN, PI) substrates. However, the wettability of ink droplets, defined by the contact angle, varies significantly. The most common procedures for changing the surface properties is to reduce the contact angle (improve wettability) by treating substrates. To increase contact angles, the substrate can be silanized by spin coating hexamethyldisilazane (HMDS) (40 s at 1000 rpm, followed by annealing at 80 °C for 2 min) [447]. Silanization requires surface hydroxyl groups to bind to. For flexible substrates, a preliminary UV ozone or oxygen plasma treatment will help to generate surface oxides. This results in more confined droplets, less spreading of the ink and higher resolution [447].

Flexible substrates already optimized for inkjet can be found on the market i.e. glossy papers, Novele (PET/SiO_2/PVA) [545], etc which allow the quick wicking away of solvent, reducing the coffee ring effect thanks to their porosity.

Below, we report different examples for the production of strain sensors on flexible substrates from inkjet-pronted FLG. A flexible integrated platform, with four linear strain gauges 3 mm × 20 mm and a central Wheastone bridge strain gauge of 1.5 cm × 1.5 cm was printed on Novele substrate. A FLG-NMP ink with a concentration ~1 g l^{-1} and FLG flakes lateral size up to 600 nm was printed for 50 printing passes with an interdrop distance ~27 μm, inter-layer delay time ~ 120 s, and printer platform T ~60 °C. Annealing was performed at 80 °C in vacuum overnight. The strain gauges with a resistance ~100 kΩ show had gauge factor(GF ~20 at 25 mm bending radius with a change in resistance ~5% after 1000 bending cycles. FLG-based strain gauges with similar properties were printed on planarized PEN using a FLG-ethanol ink (2 g l^{-1}) to make fully flexible wearable devices. The sensors are aligned with the proximal inter-phalangeal joints of the first and second digit of the hand, allowing the extension-flexion movements of these digits to be monitored. 20 printing passes, 22 μm inter drop distance and RT were used with an additional annealing at 80 °C in vacuum for 2 h.

With aqueous-surfactant based inks, one problem is the formation of foam bubbles following agitation of the print-head. This is observed at surfactant concentrations >6 g l^{-1}. The presence of non-conductive species (surfactants, polymers) in the resulting printed films will reduce FLG network connectivity and, thus, conductivity. The ability for microfluidic processing to stabilize FLG at low surfactant concentrations (0.5 g l^{-1}) meant foaming does not occur. The suitability of 0.5 g l^{-1} SDC stabilized FLG inks after 20 process cycles and centrifuged at 10 krpm, 1 h can be tested for inkjet printing (figure III.6(6)). Serpentine-type FLG resistors are printed on to photo quality paper (HP Advanced) at room temperature using an interdrop distance of 18 μm, with 20, 40 and 80 printing passes (figure III.6(b)). Prints are left to dry at RT for 60 s between passes. Although minimum optimization is required, prints with over 20 layers suffer bleeding, due to insufficient drying time, and nozzles could become partially clogged. During printing, the head is cleaned by an automated Spit-Purge-Spit cycle every 180 s. Patterns are printed for 20 passes at a time and the nozzles wiped by hand with IPA prior to printing more layers. After 20, 40 and 80 passes the resistance of the patterns decreases from~220, to 31, 3.7 MΩ, respectively, over ~40 mm (track width ~0.9 mm) as shown in figure III.6(b). The resistance response of these devices is tested with strain (3-point bending) and in different gas environments.

Three-point bending is performed with a 300 N/2 kN Deben vertical three point tensile stage. The samples are bent with an extension rate of 0.5 mm min^{-1} and measured under tension (positive strain) and compression (negative strain), to a maximum of 5 mm displacement. The electrical resistance of the printed strain gauge varies, depending on the amount of axial bending strain in the device. Printed structures at 20 and 40 passes show very similar resistance versus strain curves (figure III.6(c)) with significant response to +0.4% strain (ΔR ~ +35%) and −0.4% strain ΔR ~ −25%). The 80 printed pass sample show significantly lower

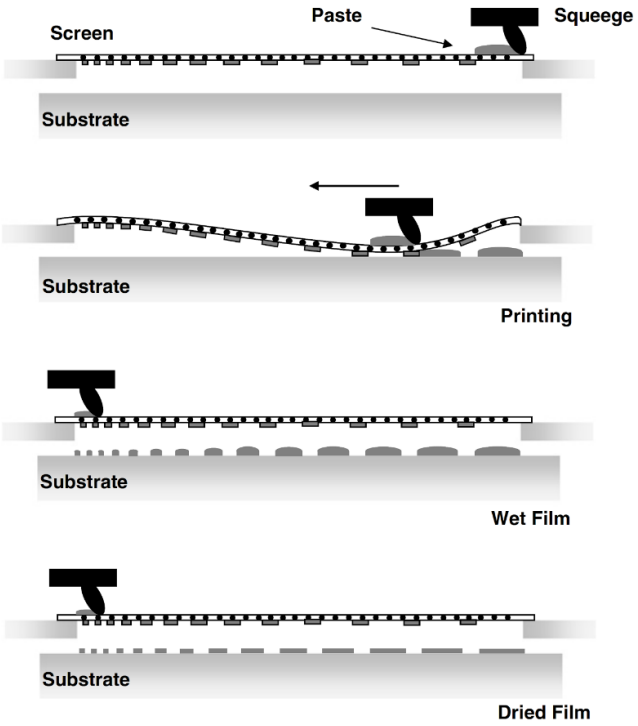


Figure III.7. Schematic of the screen printing process. FLG ink is applied to the screen and the squeegee is lightly passed over the screen to fill the mesh. This is then passed over the screen at a higher pressure, such that the ink is pushed through the mesh onto the substrate. The wet film is then left to dry to produce the final design. Reproduced from [553], with permission from Elsevier.

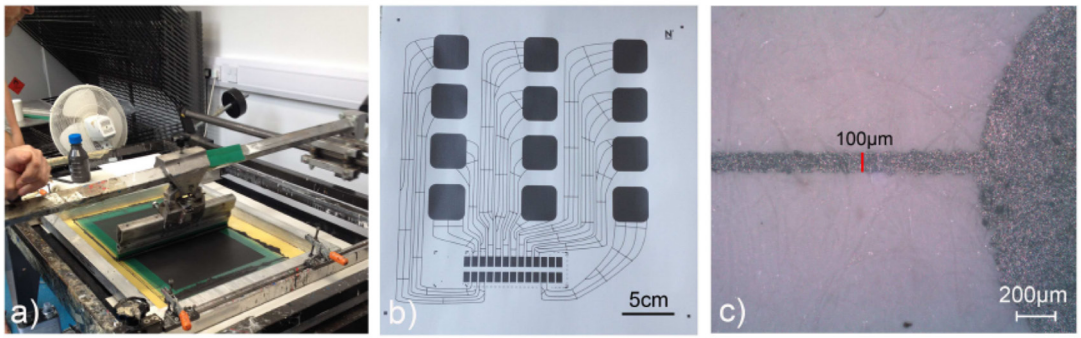


Figure III.8. (a) Demonstration of screen printing, (b) capacitive touchpad design (29 cm × 29 cm) printed on paper, (c) the line resolution is 100 μm. Reproduced from [178].

response ($\Delta R \sim \pm 10\%$) in line with the higher sample thickness. These changes are a result of conductivity variations, due to changes in length, as well as the distance between flakes. The relative change in electrical resistance ($\Delta R/R_0$) is related to the mechanical strain (ε) by the gauge factor ($G = (\Delta R/R_0)/\varepsilon$). These are 93, 85 and 39 for the 20, 40 and 80 print pass samples, respectively and thus comparable to other FLG devices produced by drop-casting or spray coating (G: 75–150 at 0.2% strain) [546]. These gauge factors are higher than graphite-based ink strain sensors (G: 19.3 ± 1.4) [547], and considerably higher than conventional strain gauges [548] or inkjet-printed metal strain gauges [549] in which $G_{\text{Factor}} \sim 2$.

In addition we used inkjet printing to print heterostructure devices by placing one material on top of the other. Inkjet printed MoS_2/FLG photodetectors (PDs) using LPE inks were demonstrated on PET. The devices were fabricated using a Dimatix 2800. A 40 μm MoS_2 channel contacted by two inkjet printed FLG electrodes on top. 100 passes of both FLG and MoS_2/NMP based inks were printed at 60 °C using 25 μm interdrop distance and 300 s interdelay time. MoS_2 was annealed at 90 °C in vacuum for 9 h before printing FLG. Finally the entire device was annealed overnight at the same conditions. The good performance of the PD showed that the MoS_2 properties could be retained after printing. Similar results were reported in Refs. [201, 550], confirming that inkjet-printing can become an efficient method to produce functional devices for a variety of applications including photonics, optoelectronics and energy storage.

III.3.3. Screen printing

For flexible electronic devices, e.g. organic photovoltaics (OPVs), $R_s < 10\ \Omega\ \square^{-1}$ is required [255], while for printed radio-frequency identification (RF-ID) antennas one needs a few $\Omega\ \square^{-1}$ [257]. To minimize R_s, μm range films are deposited using screen printing [551–554]. Screen printing is a commonly used industrial technique for fast, inexpensive deposition of films over large areas. It also allows patterning to define which areas of the substrate receive deposition. The screen is typically a polyester mesh with a cured lacquer stencil on top that provides the desired pattern. Mesh grades vary from ~10 up to 180 threads cm^{-1}. The film or emulsion stencils range from a minimum of 12 μm to >300 μm. The ink must have high viscosity (>500 mPa s) [555, 556], because lower viscosity inks run through the mesh rather than dispensing out of it [555]. To achieve this, typical formulations of screen inks contain a conductive filler, such as Ag particles,[557] and insulating additives [558]at a total concentration higher than 100 g l^{-1} [558]. Of this, >60 g l^{-1} consist of the conductive filler needed to achieve high $\sigma \sim 10^2$ S m^{-1} [557, 559]. A squeegee is used to fill the mesh with ink before a high pressure is applied to force the ink through the mesh onto the substrate [558]. Figure III.7 shows a schematic of the screen printing process. Ref. [560] provides a good introduction to screen printing.

The printability of inks with ~80 wt%FLG flakes after 70 microfluidic processing cycles formulated with 1 wt%NaCMC was tested using a semi-automatic flatbed screen printer (Kippax-2012-BU) and a Natgraph screen printer (figure III.8(a)), both equipped with screens with 120 mesh count per inch. Trials were made onto (PET) (125 μm thickness, PMX729 HiFi Industrial Film Ltd) and paper substrates. Figure III.8(b) shows a 29 cm × 29 cm print on paper with a line resolution ~100 μm (figure III.8(c)). The printed pattern (figure III.8(b)) can be used as a capacitive touch pad in a sound platform that translates touch into audio [561].

III.4. Applications

Proof of concept applications have been demonstrated for dispersions and inks produced from a range of LMs in diverse areas from nanocomposites, (opto) electronics and photonics to sensing and energy storage and conversion. A few examples will be given below. For a more detailed and comprehensive description, we referred to review articles [166, 562–564].

In nanocomposite applications, usually no complex ink formulations are required and dispersions can be used without tuning of rheological properties. FLG, GO and RGO can be used as filler in polymer [564], ceramic or metal composites [564, 565] to improve mechanical, electrical and thermal properties of the host material. Aligning the filler can be beneficial to further boost the performance [566]. FLG can also be used as additive in viscoelastic polymers to fabricate inexpensive, yet highly efficient strain sensors [567, 568]. E.g., when FLG is added to a lightly cross-linked polysilicone (often referred to as silly putty [1744]), electromechanical sensors with $G_F > 500$ have been realized that can measure pulse and blood pressure [567].

In (opto)electronics, the most widely pursued use of inks based on FLG and GRM is the fabrication of transparent conductors. The electrical conductivity of FLG-based conductive films is typically in the range of <2–4 S m^{-1} (corresponding to R_s of >20–10 $\Omega\ \square^{-1}$ for a 25 μm film) [166] much lower than the conductivity of films from metal inks which dominate the field of flexible transparent conductors due to their high conductivities of 10^7 S m^{-1} [569]. However, since graphite is a much cheaper starting material than noble metals, FLG inks might nonetheless be useful for applications that do not require very low Rs at high transparencies (e.g. <10 $\Omega\ \square^{-1}$ with transmittance >90% for photovoltaics). E.g., electrochromic windows, smart windows and electromagnetic shieldings used in every-day life can cope with Rs~ few hundreds of $\Omega\ \square^{-1}$) [166]. Significant improvements have been made with respect to improving both ink formulations and deposition techniques. E.g. Ref.[178] demonstrated the fabrication of blade-coated FLG films with Rs 2 $\Omega\ \square^{-1}$ for a 25 μm film (conductivity of 2×10^4 S m^{-1}) suitable for electrodes in organic photovoltaics. The highest conductivity (4×10^4 S m^{-1}) of an FLG film produced by inkjet printing [570] exploited nitrocellulose as stabilizer, which also improves the mechanical flexibility. These examples demonstrate that FLG-based inks might be suitable for low-end applications as transparent conductors if printing and ink formulation can be further improved and up-scaled.

Since graphene is not a semiconductor, it is not suitable as channel material in TFTs. While achievable mobilities can be as high as 200 $cm^2\ V^{-1}\ s^{-1}$, the on-off ratios are limited to <5 even in the state-of-the art [571]. In this regard, devices produced from inks of semiconducting LMs are more promising. Indeed, all electrolyte-gated TFTs were reported [572] using TMD as channel material. In this case, on/off ratios 600 were obtained, but mobilites were low (0.1 $cm^2\ V^{-1}\ s^{-1}$). A potential way forward to further improve the TFT device characteristics was suggested in Ref. [573]. By optimizing the electrochemical intercalation of quartery ammonium molecules, it was possible to produce phase-pure semiconducting flakes with uniform thickness and relatively large size (0.5–2 μm). This improved the stacking and thus charge transport, resulting in TFTs with on/off ratios and mobilities~ 10 $cm^2\ V^{-1}\ s^{-1}$ outperforming organic electronics.

Semiconducting flakes have also been exploited as active materials in PDs [562]. Ref. [201] uses inkjet printing to fabricate PDs with interdigitated FLG electrodes and a MoS_2 channel in a lateral heterostructures achieving a tenfold increase compared to the dark conductance. By optimizing the ink formulation and

printing of water-based dispersions, all inkjet-printed PDs were produced on plastic using graphene electrodes and WS_2 as semiconductor in a vertical heterostack with a responsivity ~1 mA W^{-1} at 514 nm [550]. NIR light detection was realised in BP integrated Schottky diodes (responsivity ~of 1.8 mA W^{-1} at 1550 nm) [574] inkjet-printed from an isopropanol/2-butanol mixture. The same device also showed good responsivity in the UV/Vis ~164 mA W^{-1} at 450 nm. Once encapsulated, the BP film showed good long-term stability (up to 30 days) also allowing the demonstration that the saturable absorption of BP can be exploited for the generation of ultrafast laser pulses through mode locking [574].

Due to their high surface-area to volume ratios and high surface sensitivity to the environment, GRMs can be used chemical sensing of various analytes, including gases, ions and biomolecules [575]. Since high-performance sensors have been demonstrated from MC or CVD GRMs [575], increasing research activities are now devoted to exploring printed sensors. Ref. [576] reported a graphene-based humidity sensor integrated on a CMOS platform and a gas sensor with high sensitivity (45%), fast response (12 s) and recovery (20 s) as well as selectivity to different chemicals based on gravure-printed RGO, was shown in Ref. [577]. BP was identified as promising material for sensing applications [190, 578]. However, the degradation under ambient conditions is a limiting factor [189].

The high SSA of GRMs also makes them promising as electrode materials in batteries or supercapacitors [563]. Many demonstrations with solution-processed graphene [563], MoS_2 [563] and MXenes were reported [579]. For such electrodes, advances in 3d printing can be exploited. E.g., free-standing anodes were produced from 3d printing a commercial FLG-based polylactic acid filament and employed in Li-ion batteries and solid-state supercapacitors [580]. In Ref. [581], a scalable, high-fidelity manufacturing of FLG micro-supercapacitors was demonstrated by a self-aligned printing process utilizing capillary action of liquid inks in microfluidic channels. An average specific capacitance ~221 μF cm^{-2} (at a cyclic voltammetry scan rate of 100 mV s^{-1}) was achieved. Many other examples exist where GRMs are explored as the electrode materials or additives for Li/Na-ion batteries, scaffold or interfacial layer for Li–metal anodes or cathode for Li/Na–O_2 batteries [582].

As illustrated by the examples above, printed structure from GRM-based inks are explored in many application areas. optimization of dispersions, ink formulations and printing can further boost device performance. Probably the greatest strength is that similar techniques can be applied to a whole host of often cheap and abundant starting materials. Bearing in mind that only a few material classes have been explored to date, while >1000 LM have been predicted (see chapter II.7), it is clear there are many opportunities associated with LPE and further processing of the inks. In addition to this intrinsic versatility, a number of advantages over inks from other nanomaterials have been identified. E.g., FLG and TMD inks can be biocompatible [550, 1717]. Furthermore, GRM only have dangling bonds on the edges, but usually not on the basal plane. As illustrated in Ref. [573], this has the potential to improve charge transport characteristics if clean and well-defined interfaces can be created. The accessibility of a range of material classes from insulators, conductors and semiconductors in layered structures allows one to combine various properties and functions in vertical and lateral heterostacks devices. A few examples have already been demonstrated, such as all inkjet-printed FLG-BN transistors on textiles [571], all-printed electrolyte-gated TFTs with TMDs as channel material, FLGs as electrode and BN as separator [572] or vertical PDs [550].

IV. Graphene growth on SiC

IV.1. Sublimation

The most commonly used SiC structures for growing graphene are hexagonal 4H-SiC and 6H-SiC polytypes [583]. Both polytypes are commercially available as single crystal wafer of up to 150 mm in diameter. Their (0 0 0 1) and $(0\,0\,0\,\bar{1})$-faces are polar [583], i.e. they are Si- or C-terminated surfaces. The name epitaxial graphene (or epigraphene—EG) is sometimes used [584] to reflect the idea that graphene has a quasi-epitaxial match with hexagonal SiC lattices, and an exact orientation relation with 4H/6H-SiC(0 0 0 1)-face. The (hetero)epitaxial orientation of EG on the Si-face relative to 4H-SiC is shown in figure IV.1. (For a review, see [585] and ref. therein).

The decomposition of SiC does not require an external source of C to produce graphene. C is provided by the SiC crystal itself when its surface decomposes at high T [586] ($T > 1000$ °C in vacuum [586]). SiC sublimation is intrinsically a wafer scale method [584, 587–589]. Since Si has the highest partial vapour pressure as shown in figure IV.2, Si leaves the surface, resulting in a C rich surface that forms SLG on the SiC substrate. For this reason, the second layer that forms grows under the first one, i.e. the top layer is always the first one to form on the SiC surface. Because SiC is stoichiometric, the amount of graphene formed is related to the amount of Si that leaves the surface by sublimation, and for the common SiC polytypes used, ~ 3 Si-C bilayers are required to provide enough C atoms to form a SLG. A schematic illustration of the graphene formation steps is in figure IV.2.

Graphene growth is driven by the same Si sublimation process on both the Si face and the C face. However, the surface reconstruction and growth kinetics for the Si terminated and C terminated faces are different, resulting in different graphene orientation relative to the substrate, different growth rates, morphologies and electronic properties, as schematically show in figure IV.1(c). The first C layer grown on the Si face of SiC polytypes is known as the buffer layer [590] (sometimes called the zeroth layer). It has the graphene atomic structure but it is in interaction with the SiC substrate, which is often described as a bonding between ~1/3 of the carbon atoms of the buffer layer to the Si dangling bond of the SiC substrate [591, 592]. However, the exact nature of the bonding is not fully understood as the SiC substrate and buffer layer have incommensurate structures [593] and the two lattices form a large superlattice unit cell $6\sqrt{3} \times 6\sqrt{3}$, making theoretical calculation difficult. The important point here is that the buffer layer has the graphene lattice structure, does not have the electronic dispersion of graphene [590]. Instead it is a semiconductor with an energy gap >0.5 eV, as shown by scanning tunneling spectroscopy (STS) and photoemission spectroscopy (see section IX.2.4/ARPES for an introduction to the technique) [592, 594, 595]. When the next graphene layer grows, under the buffer layer, the previously grown buffer layer is no longer in interaction with the SiC substrate and turns into a SLG (with a linear electronic dispersion), as the newly grown layer becomes the new buffer layer. Therefore, on the Si-face a SLG always rests on the buffer layer. SLG on the Si-face has a defined orientation relative to the SiC crystal (see figures IV.1(a) and (b))[585].

For the $(0\,0\,0\,\bar{1})$-face (C-face) no buffer layer has been observed [596]. The graphene layers grow much faster than on the Si-face with 5–10 L growing on the C-face compared to one the Si-face in standard Confinement Controlled Sublimation [597] (CCS) conditions [585]. Contrary to the Si-face where they are arranged in a graphite stacking (Bernal ABA, or sometimes rhombohedral ABC [598]), the layers on the C-face are stacked rotationally, alternating azimuthally rotated layers with 0° and 30° within ± few degrees [585, 599, 600]. The stacking explicitly is not turbostratic (random stacking of small grains). Graphite (AB) stacking in this case corresponds to stacking faults that have an occurrence of less than 15%–19% [596].

In the Si sublimation process, Si desorbs through steps [601–603] or from defects [604, 605] and terraces [606] and graphene growth results of a fine kinetic balance of different step evaporation rate, Si sublimation from and re- absorption onto the surface, and C diffusion [597, 601, 607]. When the SiC surface is in equilibrium with the Si vapour, the formation of graphene is arrested. The key to grow high quality graphene is a slow growth at high T, where the kinetic energy and the mobility of C and Si atoms are high. It is therefore necessary to slow down the Si escape rate that depends on the partial pressure of Si (PSi) in equilibrium with SiC.

Following figure IV.2, PSi increases by over three orders of magnitude in the range 1200 °C–1600 °C, which is a typical range for graphene growth.

Note that the partial pressure of C is less than 10^{-10} atm, at least five orders of magnitude lower than the Si vapour pressure (or that of the residual gasses in the vacuum chamber), so that the role of gas phase C is negligible in the graphitization process. It is reasonable to assume that each Si atom that escapes from the surface leaves a C atom on it to form graphene. Maintaining a background gas (either Ar [589] or Si [597] e.g.) reduces the diffusion out of Si and increases the return probability to the surface, thereby reducing the Si escape rate and consequently the graphene growth (see [597, 589] for details).

In order to better control the growth rate several methods have been employed, either by providing an external source of Si (by adding a flux of silane [609], a Si flux [610] or by sublimating a Si piece nearby), or by slowing the Si escape by diffusion through a neutral gas (Ar atmosphere) [589] or keeping the SiC as close as possible to equilibrium with its own vapour by confinement [597]. Alternatively, CVD methods were employed, where C species are brought externally [611, 612]. The last three methods are reviewed below.

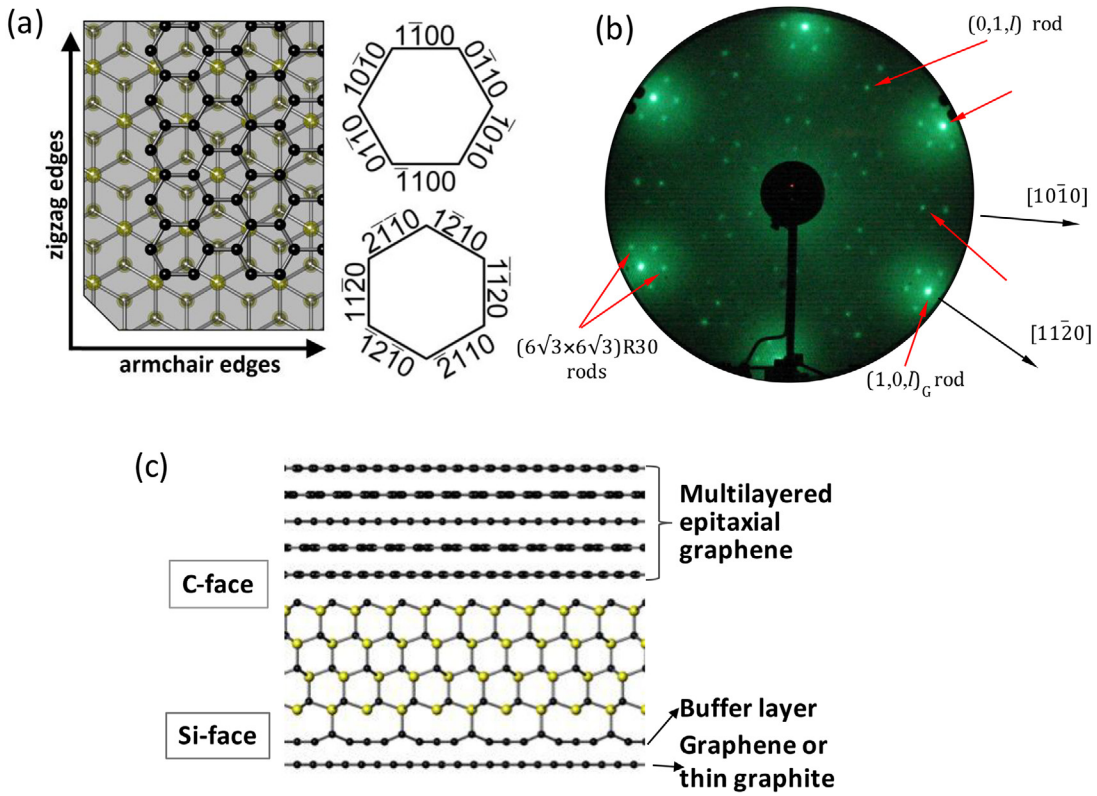


Figure IV.1. (a) Orientation of graphane on the Si-face relative to 4H-SiC. (b) LEED diffraction of MLG on 4H-SiC, showing the diffraction spots of SiC, SLG and the buffer layer $(6\sqrt{3}\times 6\sqrt{3})$R30. (c) Schematics of graphene growth on the top 6H/4H-SiC(0 0 0 1) and bottom$(0\,0\,0\,\bar{1})$ surfaces. Adapted from [585], © Springer Nature.

IV.1.1. Growth under argon

The vertical induction heated furnace shown in figure IV.3 consists of a coil to produce a uniform electro-magnetic field in the semi-close graphite platform called crucible on which the *T* is measured with an optical pyrometer, a quartz tube with a diameter of 100–200 mm depending on the size of the crucible, porous graphite insulation which is slightly smaller than the quartz tube [607]. The role of the radiofrequency (RF) field is to produce Eddy current in the crucible and that heat up the crucible (figure IV.3(b)). The long RF coil in the reactor provides a uniform electro-magnetic field distribution in order to ensure a uniform *T* on the substrate. This design allows treatment of SiC wafers up to 50 mm in diameter. Other furnace designs with fully automated T controls were also reported [613].

As the *T* distribution in the crucible influences the thickness uniformity, a symmetric crucible was designed for good T uniformity, with optimization by modelling the T distribution (figure IV.3(c)). The SiC substrate position should be in the centre of the RF coil. Prior to growth, the substrates are cleaned in organic solvents, then in solutions based on sequential oxidative desorption and complexing with H_2O_2–NH_4OH–H_2O (RCA1) followed by H_2O_2–NCl–H_2O (RCA-2) to remove organic contaminations and dipping in diluted HF. The substrates are then placed in the middle of the graphite crucible followed by the placement in the porous graphite insulation. After that, the whole assembly is loaded in the growth chamber (quartz tube), locked and pumped down. The chamber is ready for heating when the pressure reaches 5×10^{-7} mbar.

To slow the Si sublimation while being close to equilibrium conditions, growth was performed under 1 atm of Argon (Ar) [588, 589, 614]. At 2000 °C Si sublimation in 1 atm of Ar SLG on a large area and thickness uniformity [614]. Figures IV.4(a) and (b) show LEEM images of graphene layers (small domains of 1–2 μm size and thickness >5LG) grown in Ar atmosphere with a better thickness uniformity and quality for graphene grown in Ar [588]. Note that LEEM is performed instead of conventional SEM, because by counting the number of minima in the LEEM reflectivity as a function of the electron beam intensity, the N can be determined at the resolution of the LEEM image. Details about T-time profile can be described as setting T ramps (~20 per minute) up to at least 1150 °C and once the desired graphitization T (usually >1150 °C) is reached keeping this *T* during the growth time. Then decreasing it down to RT with a slow ramping ($70\,\mathrm{min}^{-1}$).

IV.1.2. Near equilibrium confinement controlled growth

CCS[597] relies on SiC being in near equilibrium conditions with the Si vapour. Graphene growth is

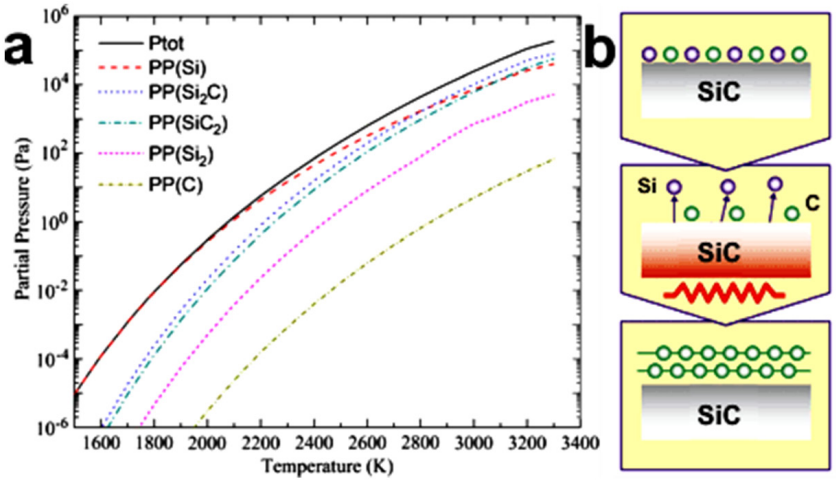


Figure IV.2. (a) Partial pressure of different vapour spices versus temperature in equilibrium with a crystal on SiC. (b) Schematics of graphene formation by Si sublimation [608] (reprinted with permission from Elsevier). For simplicity, the growth of graphene in (b) refers to the growth on the carbon face and, consequently, there is not buffer layer.

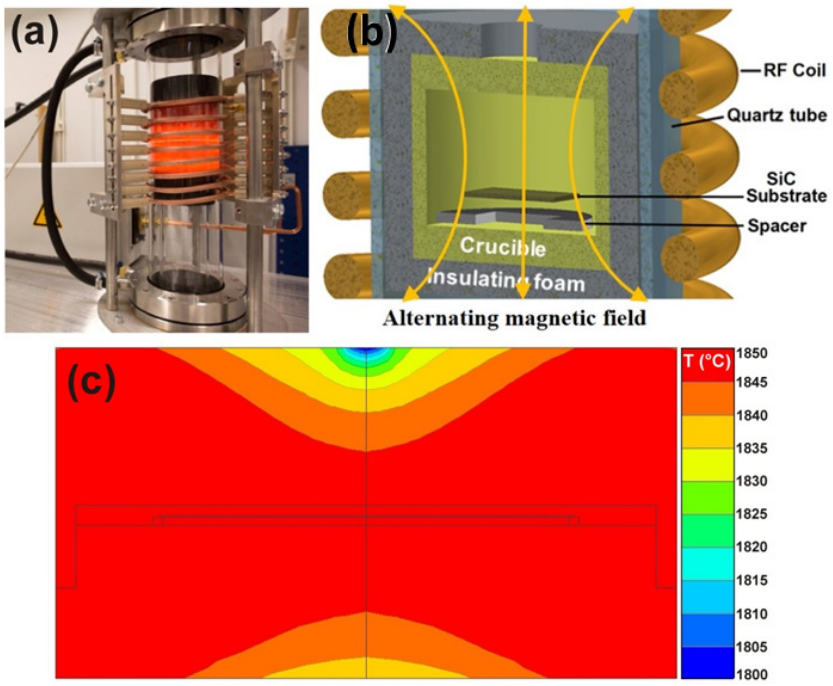


Figure IV.3. Sublimation reactor (a) Picture. (b) Sketch of the vertical RF-heated furnace in cross-section [607]. (c) distribution in the crucible. The diameter of the crucible in (c) is 50 mm and the height of the growth cavity (marked by black lines) is 5 mm. Adapted from [607].

controlled by encapsulating the SiC crystals in graphite so as to sequester the evaporated Si (see figure IV.5). A SiC crystal is placed in a closed graphite box (called crucible) provided with a very small calibrated hole of typical diameter 1 mm. As the T of the furnace is increased above 1200 °C and Si sublimates from SiC, the built-up Si vapour remains confined inside the crucible and escapes slowly through the hole (figure IV.5(b)). The SiC chip is therefore in a uniform Si vapour as defined by the PS_i versus T of figure IV.2, ensuring uniform graphene growth. Because the Si vapour is confined, the growth T is substantially increased (by ~300 K for CCS [597]) compared to vacuum growth. Details about the full furnace design and operating conditions can be found in Ref. [597, 615]. The Si escape rate that ultimately determines the growth rate, is defined by the geometry of the hole (diameter 0.5 to 2 mm) [597, 615]. The rate of graphene formation by CCS can be reduced by a factor >1000 compared to UHV sublimation, where 1LG grows on the C-face in ~1 min at $T = 1.200$ °C [597]. The graphene formation rates can be reduced by an additional factor of up to 10^3 by introducing 1 atm of Ar into the enclosed crucible [597]. The system is compact for fast pumping speed and small thermal inertia, allowing fast heating and cooling rate up 150 °C s^{-1} in the T range from RT to

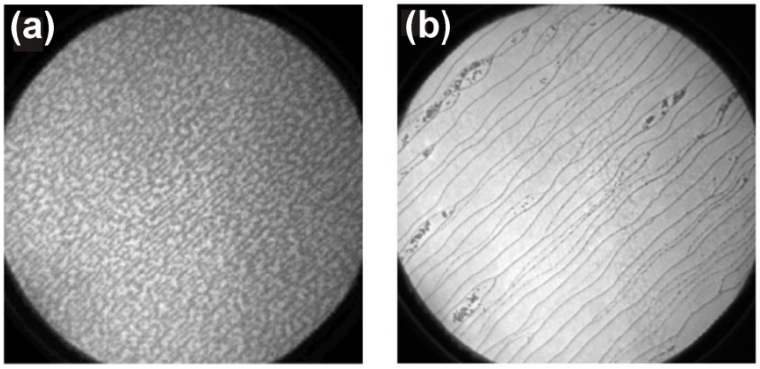


Figure IV.4. Graphene layers grown on the Si-face (a) in vacuum, (b) under Ar [588]. Field of view is 20 μm. The lines are identified as BLG by counting the number of minima in the LEEM reflectivity as a function of the electron beam intensity. Adapted from [588, 589].

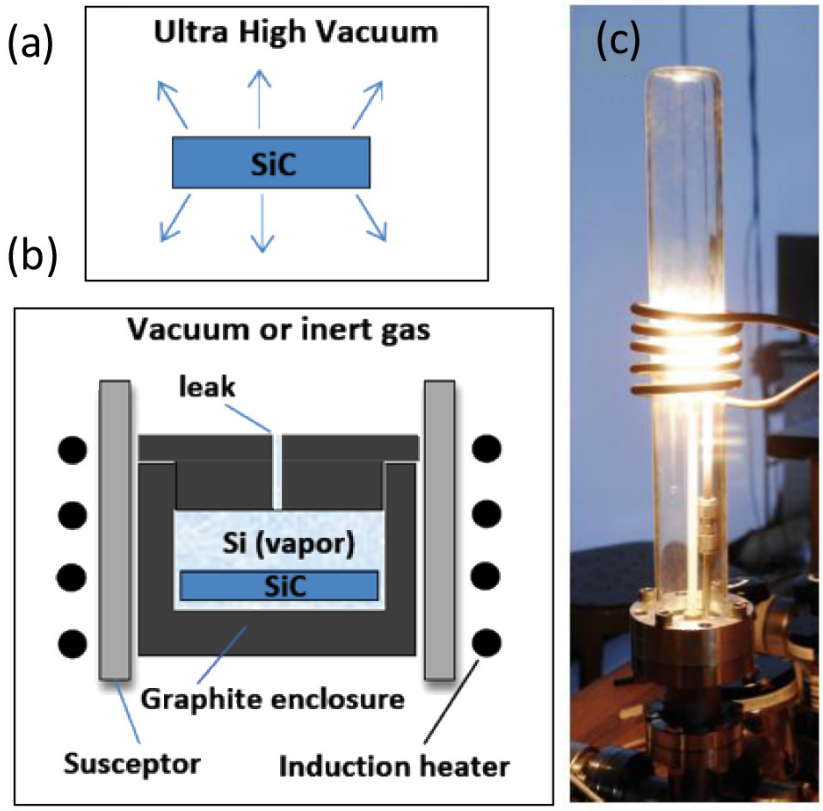


Figure IV.5. Confinement controlled sublimation. (a) In UHV Si that is sublimated from the SiC surface at high T escapes. (b) In the CCS method, SiC is in quasi-equilibrium with its own vapour (c) picture of the CCS furnace. Adapted from [597].

2100 °C. The T profile is computer automated [615, 616]. The whole process can be performed in less than two hours, being scalable to full wafer sizes.

An alternative method to CCS is to cover the SiC substrate with a piece of graphite, which provides some Si vapour confinement. The Si escapes on the side providing a non uniform Si vapour gradient that produces narrow tapered stripes of graphene [617].

To grow EG on hexagonal 4H- or 6H-SiC wafers by CCS [615] the key step after pumping out the cell to below 10^{-6} mbar, is the Si sublimation at high T (1400 °C–1650 °C). The exact T profile depends the geometry of the graphite crucible and geometry of the hole [615], and on the background pressure (with or without additional Ar backpressure). Optimum T and growth times are specific for each crucible adapted to each type of grown graphene. Typically, a 1LG in 20 min at 1520 °C [594] on the Si-face, a graphene buffer layer °C lower than the Si monolayer in the same crucible [594]. On the C-face, N is determined by both T (1450 °C–1525 °C) and time (1 min to several hours for very thick films) [597, 615] [606] (see section IV.1.3 and figures IV.5(a)–(c)). Templated graphene growth of nanostructures (e.g.SiC sidewalls [618–620]) on non-polar facets (i.e. other that (0 0 0 1) and $(0\,0\,0\,\bar{1})$) is finely tuned close to the buffer layer growth conditions.

IV.1.3. Carbon-face

The surface state of the substrate prior to growth is essential, because rough surfaces have multiple disordered nano-steps acting as nucleation centres for graphene growth. The first step is therefore SiC surface flattening. For SiC surfaces polished to optical quality, the deep polishing scratches can be removed by SiC etching at high T in a hydrogen environment [621]. Successful flattening is obtained at 1500 °C for 15 min in a flow rate of 200 sccm in 1 atm of a mixture of 5% H_2 in Ar [621], which produces a surface with no observable scratches in AFM section IX.1.2 and with a step-terrace structure with atomically flat terraces. However, on the 6H(0 0 0 1) face, the average width and step height of terraces after treatment do not have a clear correlation with hydrogen etching, T and time, but are related to the local miscut angle (the local angle θ of the surface relative to the on-axis orientation, generally $\theta < 0.2°$ for commercial wafers of on-axis wafer [621]. Commercial SiC wafers can be purchased with so-called 'epiready surfaces' treated by a chemical mechanical process. These provide excellent starting surfaces, with rms < 0.2–0.3 nm, with no need for etching prior to graphene growth.

On the 4H- or 6H-SiC carbon face, continuous MLG containing 5–10 LG [622] are grown by annealing for 15 min at T in the range 1450 °C–1525 °C. Repeated cycles produce much thicker films up to 50 LG [623, 624]. Shorter times and lower T are required to produce 1LG. They appear in patches on the SiC substrate (see inset of figure IV.7(a)) because of the rapid growth rates on the C-face and the multiple nucleation sites [604, 606, 615, 625].These 1LG have excellent electronic properties, despite draping over steps and making pleats [604].

Sample quality is revealed in AFM (see section IX.1.2) and STM images (see section IX.1.4) in multiple spectroscopy techniques (see section IX)), magneto-optical, photoemission, see (section IX), ultrafast optics and electronic transport (see section IX.3 Raman spectroscopy shows a vanishing D peak attesting the low defect density (see figure IV.7). All spectroscopy studies [622, 624, 627–629] confirm that the MLG behaves as electronically decoupled, i.e. as a stack of graphene layers with a non gapped linear dispersion down to a few meV from the Dirac point, not like graphite and exhibit the quantum Hall effect [604, 625, 630] and high mobility (up to $\mu = 39\,800\ \mathrm{cm^2\,V^{-1}\,s^{-1}}$ at charge density $n = 0.19 \times 10^{12}\ \mathrm{cm^{-2}}$ [604]). The se MLGare continuous over the entire SiC, drape over SiC steps and have rms < 5 pm as measured by x-ray diffraction [596]. STM shows extended moiré regions [600, 627] providing evidence that adjacently stacked graphene layers are rotated creating a superstructure. On a larger scale, smooth graphene pleats are observed, as seen as bright lines in figures IV.6(c) and (e), which originate from the differential contraction of graphene and SiC upon cooling.

MLGs have been used as a model system to study graphene properties [585]. This stems from a combination of factors: (i) Excellent structural quality (small Raman D peak observed, see figure IV.7 and [630]), (ii) Flatness of the layers (rms < 5 pm as measured by x-ray diffraction [596]) which excludes strain-related gauge field effects [632] and broadening effects in k-resolved spectroscopy measurements (see figure S1 in supp of [620]), (iii) Small interaction with the substrate and the environment, particularly for the layers in the middle of the stack that are quasi-neutral [629, 633] (charge density $n \sim 5 \times 10^9\ \mathrm{cm^{-2}}$, that is at most 8 meV away from the Dirac point) with high mobilities at RT [628, 633]. (iv) graphene electronic structure for all layers [634], due to the rotational stacking, providing a large signal intensity very much sought in optical measurements.

IV.1.4. Silicon-face

MLG on Si-face (see figure IV.4) is the most studied as for realization of quantum resistance standards (as multiples of $h/e^2 = 25.812\,807\ \mathrm{k\Omega}$) at 4.2 K in small (<1 Tesla) magnetic fields. With a quantum Hall resistance quantization accuracy of 3×10^{-9} that rivals the best 2d electron gas standards [612, 635]. As growth on the Si-face starts from the SiC steps [601, 603, 636], BLG (or MLG) tend to form at step edges when a 1LG fully covers the terrace (see figure IV.4), which makes it difficult to produce extended 1LG. Additionally, the step edges add electronic scattering due to the presence of BLG/MLGH, or to the reduction of the carrier concentration on the step [585], which is detrimental to the homogeneity of the quantum Hall effect [637]. Better control of growth on the Si-face was obtained by providing carefully balanced methane and H_2 [638]. Ref. [639] reported MEG draped continuously over the steps by graphitization of a polymer deposited on the bare SiC.

IV.1.5. Step bunching and graphene growth

During annealing above 1200 °C, the SiC surface undergoes microscopic restructuring by forming steps and terraces. This process, known as step bunching [1745], is different from atomic surface reconstruction and refers to surface morphology. Step bunching, i e. the bunching of straight steps on vicinal crystal surfaces, which is governed by energy minimization on different terraces is a fundamental phenomenon in SiC. Graphene formation has been analyzed with respect to step bunching of SiC, by studying the influence of the crystal structure at the atomic level for each SiC polytype [640]. As illustrated in figure IV.8(a), the 4H-SiC polytype has two decomposition energies, terraces $4H_1$ (−2.34 meV) and $4H_2$ (6.56 meV), respectively, and the 6H-SiC (figure IV.8(b)) has three distinct terraces, 6H1 (−1.33 meV), 6H2 (6.56 meV) and 6H3 (2.34 meV), while 3C-SiC (figure IV.8(c)) has only one kind of terrace, 3C1 (−1.33 meV) [640].

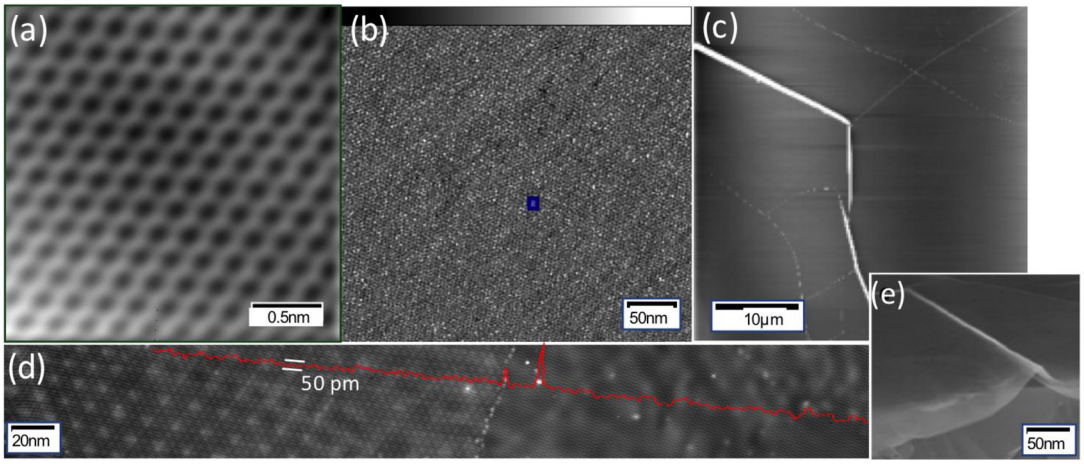


Figure IV.6. MLG on C-face topography images. (a) 4 × 4 nm STM image (reproduced with permission from [626]). (b) 400 × 400 nm STM image. The blue square represents the size of the STM scan in (a) [626]. (c) 40 μm × 40 μm AFM scan. The white lines are graphene pleats. (d) 400 nm long STEM image across areas of different moiré pattern, showing that the top layer is flat (rms < 50 pm) and continuous (from [627], with permission from AAAS). (e) SEM image of a graphene pleat (from [621], with permission from Elsevier).

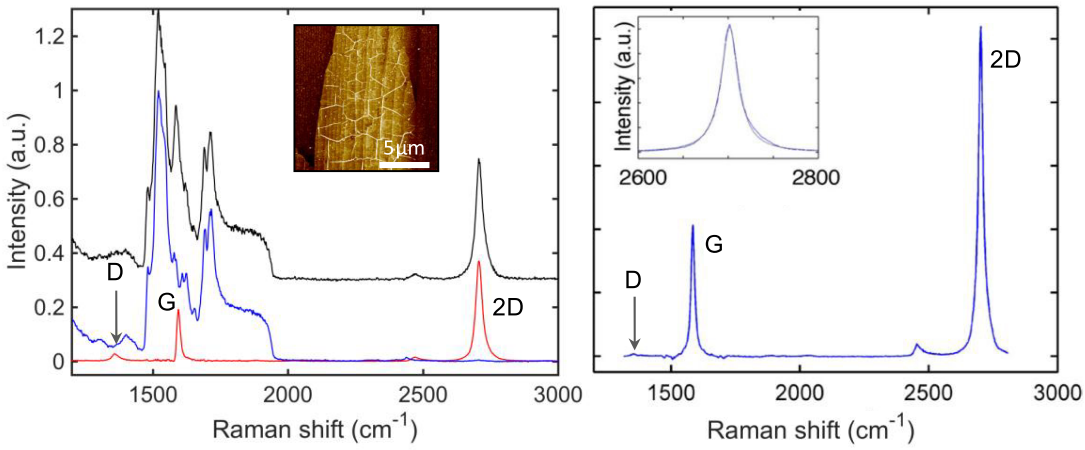


Figure IV.7. Raman spectroscopy for graphene layers on 4H-SiC C-face (a)SLG, inset AFM image. The black trace is the raw data (SiC + Graphene), blue is the bare SiC spectrum; the red trace is the graphene spectrum once the SiC Raman peaks are substracted [631] (b) MLG with the Raman contribution for SiC removed. The inset shows a Lorenzian 2*D* peak for this 10LG. Figure adapted from [630], © IOP Publishing.

The growth process is schematically shown for 4H-SiC in figure IV.8(d). Since Si and C atoms are bonded more weakly in the vicinity of step edges, Si desorbs from these areas faster in comparison with the terraces [601, 603, 636]. Based on the terrace energies, removing a 4H1 terrace costs less energy and the step decomposition velocity is faster (figure IV.8(a)). As shown in figure IV.8(d), from the edge of the 4H1 terrace on the graphene-free surface, C atoms are released onto the terrace as Si atoms leave the surface (stage 1). The C atoms coalesce and nucleate into graphene islands (stages 1 and 2), which act as a sink for subsequently released C atoms. After the 4H1 terrace step catches the 4H2 step, the newly formed two SiC bilayer step provides more C atoms as compared to the one-bilayer step and the first graphene layer extends along the step edge (stage 2). The large percentage of bunched steps with four Si-C bilayers, an increased source of C, will impose the formation of a second layer of graphene (figure IV.8(d), stage 3) since some extra C will be released. Therefore, a full coverage of the 4H-SiC substrate surface by just 1LG may be an issue.

A similar mechanism of energy minimization is expected in the 6H-SiC polytype (figure IV.8(b)). As a result, first the step 6H1 will catch step 6H2 and forms two Si-C bilayers. Then step 6H3 will advance and merge with the two-bilayer step. The growth process for 6H-SiC is the same as the 4H-SiC [640]. However, on 3C-SiC all terraces have the same decomposition energy [640] (figure IV.8(c)) and no energetically driven step bunching should be expected. In this polytype, a non-uniformity of sublimation may be induced by the presence of extended defects such as stacking faults, which are characteristic of this material [641].

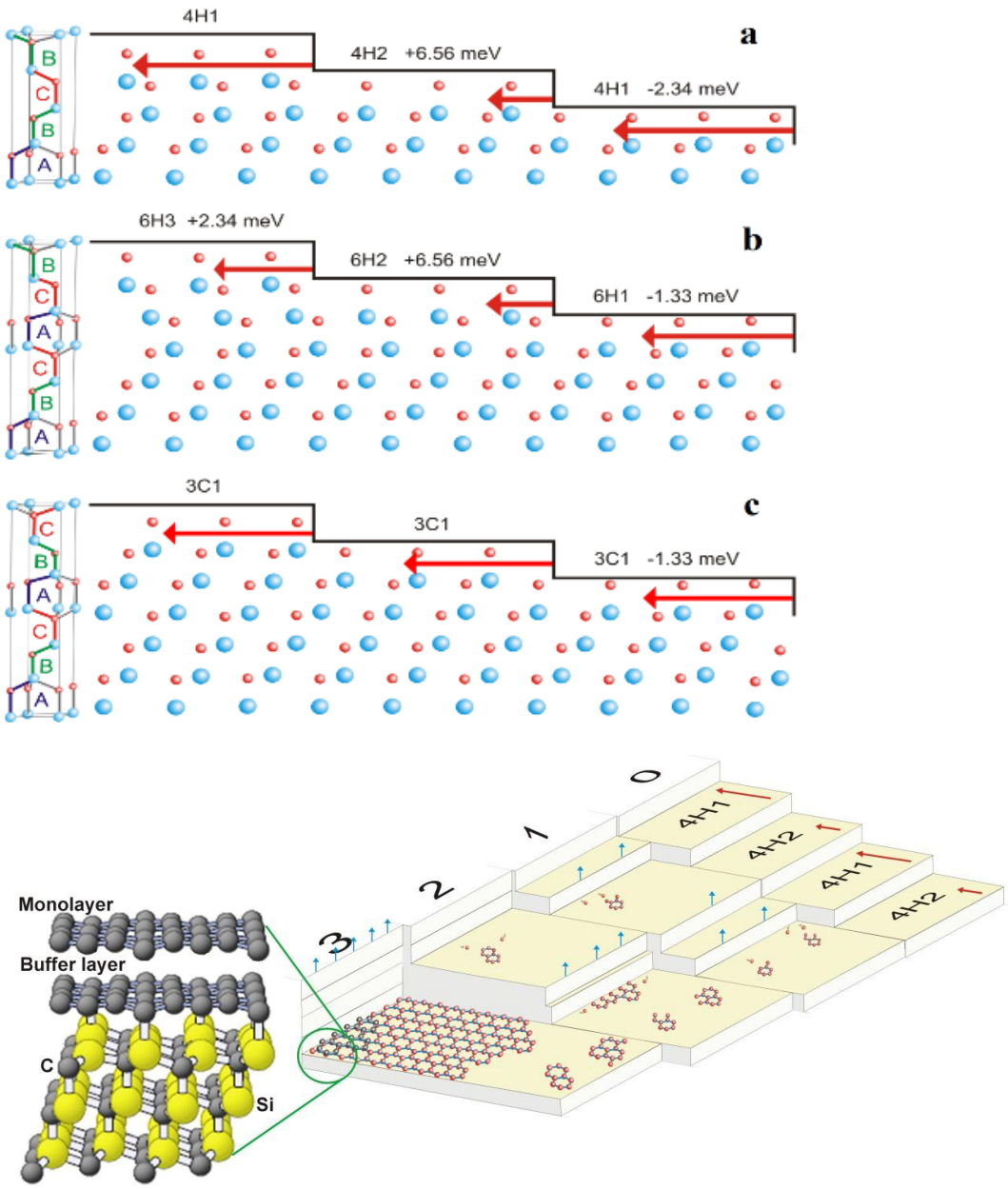


Figure IV.8. Stacking sequences and possible terraces on (a) 4H-SiC, (b) 6H-SiC, and (c) 3C-SiC surfaces. Large (blue) and small (red) circles represent Si and C atoms, respectively. Length of arrows indicates different step decomposition velocities. (d) Schematic depiction of the formation process of EG via sublimation of Si from the SiC surface. Adapted from [640], with permission from Elsevier.

A capping technique can be employed to localize the step bunching [642]. The cap consists of an amorphous carbon layer evaporated on the bare SiC grid evaporated on the bare SiC. Amorphous carbon is then patterned by plasma etching or lift-off to produce typically micron size structures. Upon annealing to produce graphene, the carbon layer pattern pins the SiC steps under it so that the SiC steps bunch against one enclosure wall and align along the amorphous C grid, as shown in figure IV.9(a). Several geometries have proven effective, and it is reasonable to position an edge of the cap perpendicular to the SiC substrate miscut to maximize step bunching against the cap wall. The slight SiC surface roughness induced by the mild plasma etch used to pattern the carbon layer (see figure IV.9(c) top) is smoothed out by the step bunching at the high T of the graphene growth (see figure IV.9(c) bottom). This technique provides large flat terraces (figure IV.9(c)-bottom) at a predefined location. The amorphous C is finally removable by plasma etching after annealing to access the graphene layer for further device patterning [642]. In that case a graphene protection layer is used (this can be the dielectric of a subsequent top grid).

IV.1.6. Optimization of growth process for scale up

Growth conditions can be developed to increase the size of the SiC substrate to 20 × 20 mm^2 and ultimately to 100 mm diameter wafers. The furnace is similar to that of figure IV.3, but with longer RF-coil with uniform distance between the pipes [643]. The coil can be moved up and down to change the T gradient if

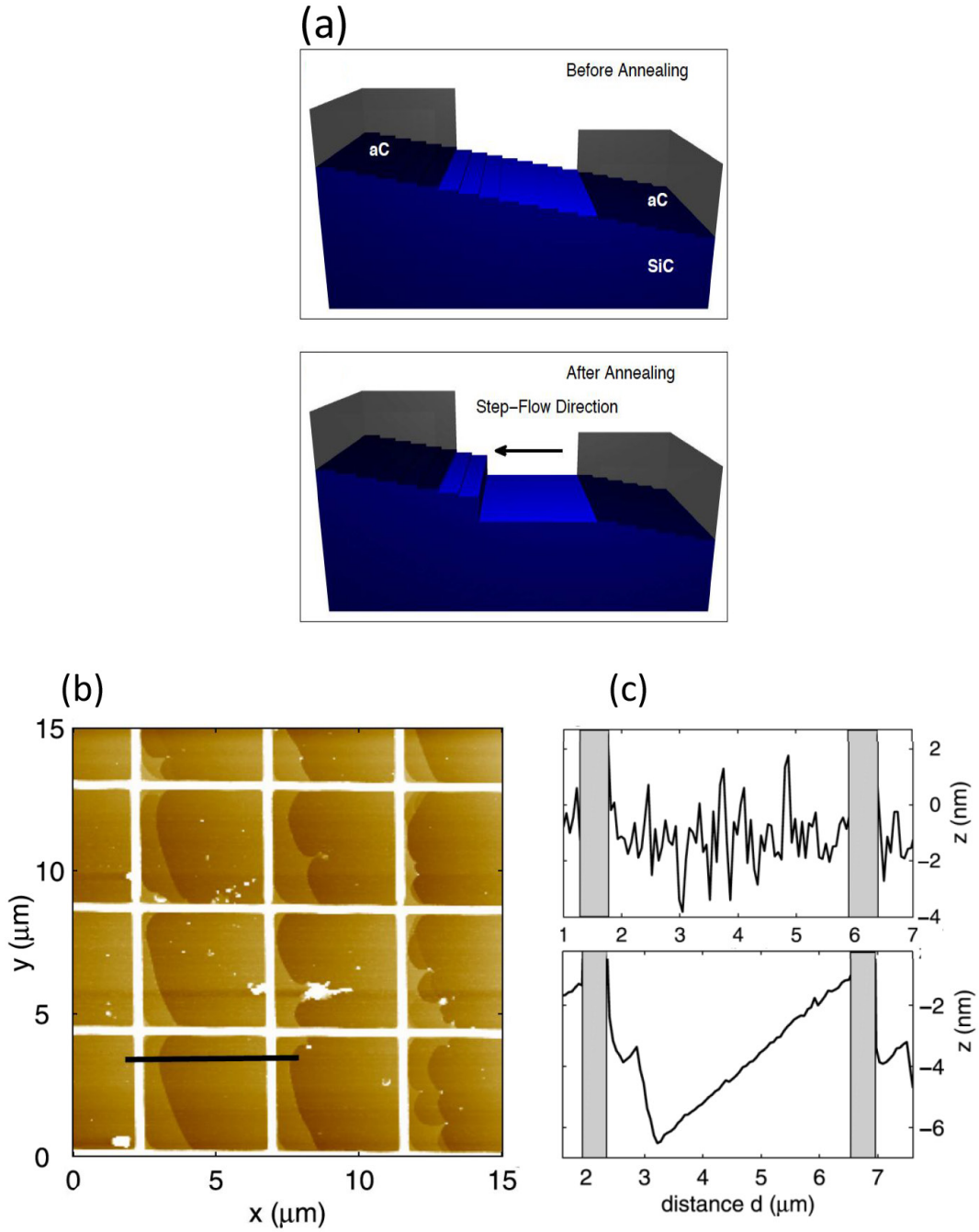


Figure IV.9. SiC Step pinning under an evaporated amorphous carbon grid. (a) Schematics of step pinning (before annealing, upper frame). After annealingat 1350 °C (lower frame), the steps accumulate at one side of the grid in each enclosure providing large terraces at a locations defined by the grid. The arrow point the direction of the flow. (b) AFM image after annealing and (c) topographic profile within the grid (top) before and (bottom) after step bunching annealing, showing that a large terrace has developed. Adapted from [642], with the permission of AIP Publishing.

necessary and it is fully automatic. The key to achieve large area 1LG on SiC is to (a) understand the role of the buffer layer [590, 592, 610] and of the step bunching [607] which takes place during its formation and to monitor the effect of (b) T (in the range 1700 °C–1950 °C); (c) Ar pressure (in the range 750–950 mbar) (d) and growth time (from 0 to 15 min). AFM topography and phase images show that the formation of the buffer layer (at 1850 °C and Ar pressure 950 mbar) can start at any place on the substrate, but preferably on the kink of steps, as shown in figure IV.10(a). The C atoms coalesce and nucleate into graphene islands on the step kinks (marked with a circle) and these islands act as a sink for other C atoms. As the step edges are the main source of C, the growth rate is two times higher along the step edge compared to that on terraces and for this reason a graphene layer first covers like a ribbon the sidewall of steps (figure IV.10(a)) [602, 618, 620, 644].Then growth continues from the edge of a step to the (0 0 0 1) terraces, where the graphene layer interacts with the surface and becomes the buffer layer. Studies show that the graphene layer first covers

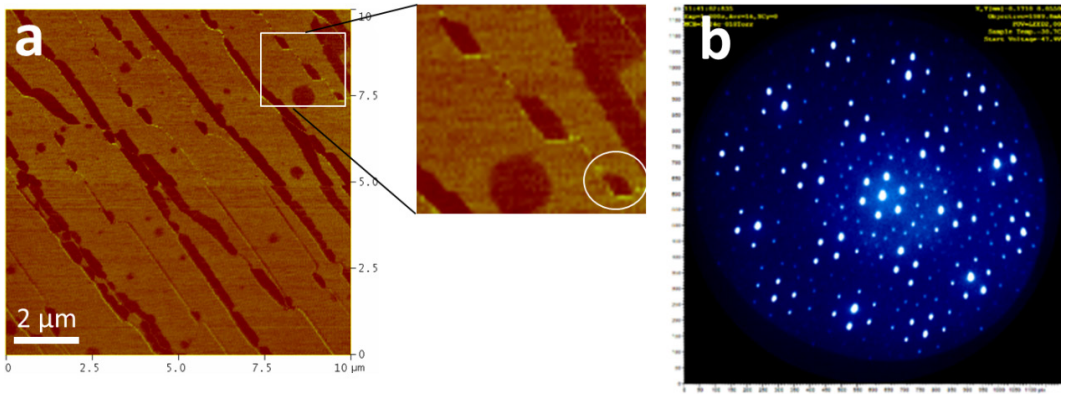


Figure IV.10. (a) AFM phase images of initial stage of the buffer layer formation, and (b) LEED pattern of the buffer layer (electron energy 60 eV) grown under Ar (in the reactor of figure IV.3) [643].

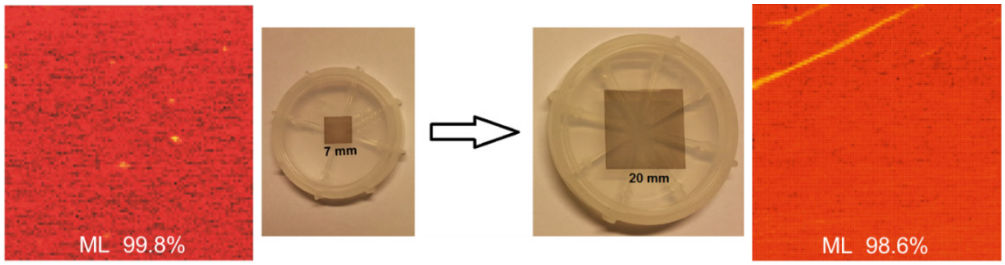


Figure IV.11. Size increase of 1LG from 7 × 7 mm^2 to 20 × 20 mm^2. The size of reflectance maps (red scale) are 30 μm × 30 μm [643].

the steps with larger terrace [643]. A critical issue is to fully cover the substrate surface by a buffer layer, before lifting it up as a 1LG by growing another buffer under it. A good quality buffer layer exhibits a particular pattern in LEED, as illustrated in figure IV.10(b) (see also figure IV.10(b), and [584, 592, 611, 645–647]. The pattern for a buffer layer grown in the reactor of figure IV.3 at 1850 °C and 850 mbar is similar over the whole surface.

Similarly to the amorphous C corral [642], the buffer layer can stop the step bunching process on 4H and 6H-SiC [648]. This means that the surface energy becomes uniform all over the substrate surface after the formation of the buffer layer subsequently resulting in a uniform and continuous 1LG coverage, which does not exclude the growth of BLG at the steps. The T dependence of the buffer layer formation and SLG coverage is sublinear (that is close to linear, not exponential [643]), which suggests that the synthesis is surface kinetics limited on both SiC polytypes [601, 643]. The results from graphene samples grown Ar indicate that there is an optimal Ar pressure (~850 mbar) yielding under this condition a high growth rate.

The time dependence of SLG and BLG growth under Ar pressure shows that graphene spreads faster on 4H-SiC substrates than on the 6H polytype from the start of the growth, and that 1LG coverage increases approximately linearly with time. After the SLG is complete, increasing annealing time does not significantly increase the BLG coverage for both 4H and 6H-SiC polytypes [643].

Based on the above results, a growth protocol was defined to optimized SLG coverage. The result, shown in figure IV.11 indicate the growth of ~99% 1LG on 20 × 20 mm^2 SiC substrates and 99.8% 1LG for 7 × 7 mm^2 substrate (figure IV.11). The SLG coverage is determined by optical reflectance maps. Experiments showed that the reflectance of graphene on SiC normalized to the reflectivity of bare substrate (the contrast) increases linearly ~1.7% per layer for up to 12L, which agrees with theory [649]. The wavelength dependence of the contrast in the visible is investigated using the concept of ideal Fermions and compared with existing experimental data for the optical constants of SLG [649].

The results for SLG on 4-inch SiC wafer showed that the growth rate on the edge of the wafer is higher than in the centre, due a faster Si escape at the wafer edges [597]. Quasi-equilibrium growth [597] provides a way to mitigate these problems. Figure IV.12 shows the recipe for growth of SLG on large area substrates, including on 4 inch SiC wafer. These operation conditions assume different T ramps up to 1150 °C and to the growth T, according to figure IV.12.

IV.1.7. Growth on SiC off-axis cut surfaces

Graphene layers are best grown on 4° and 8° off-axis 4H-SiC (0 0 0 1) substrates to have the right terrace width for performing step flow growth [650, 651].

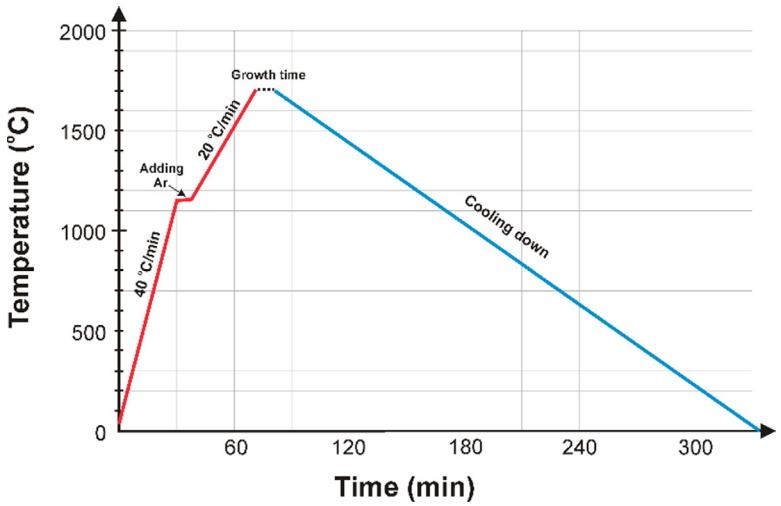


Figure IV.12. Temperature-time plot for the growth of SLG on 4 inch substrates under Ar [643].

A general recipe is provided in Ref. [652]. Figure IV.13 shows a side view of the off-axis SiC substrate used for graphene growth, where the off-axis surface is tilted at a specified angle (off-axis angle) from the basal plane surface toward the $[1\,1\,\bar{2}\,0]$ SiC direction. Controlling the tilt angle allows to change step heights, terrace widths and a growth rates.

A direct comparison of graphene formation on an 8°-off axis (0 0 0 1) 4H-SiC epitaxial layer and on-axis (0 0 0 1) 6H-SiC [653], performed by uniform graphitization of 1 cm × 1 cm SiC substrates at 2000 °C for 30 min (with a base pressure in the chamber ~5 × 10^{-6} mbar and an argon pressure ~1 atm during the growth) shows that the growth of graphene on off-axis SiC starts from the edge and follows the surface of the large terraces (0.5 to 1 μm width), running parallel to the original steps of the off-axis wafer.

Off-axis samples present significant step bunching after high T annealing (rms = 16 nm), while flatter surfaces (rms = 2.4 nm) are obtained on the on-axis sample. In comparison with on axis SiC wafers, off-axis SiC wafers contain a lot of steps due to their cuting angle. For this reaseon, during annealing they easily bunch. Step bunching is higher in off-axis samples with dense step edge, because etching or erosion start from on step edges, which is not the case in on-axis samples. A more uniform and homogeneous graphene coverage was found on on-axis 6H-SiC [653]. The 100 to 200 nm wide terraces of the 4H-SiC (0 0 0 1) 8° off-axis samples are covered by FLG spreading like a carpet for all growth T in the range 1600 °C to 2000 °C (growth under Ar) [654], with an increase in the N as a function of T (from 0 to 10 LG) (figure IV.14).

Similarly to the on –axis surface, the graphitization rate is much higher for the C-face off axis substrates while it is almost an order of magnitude smaller for the Si-face on-axis substrate compared to off axis substrates (figure IV.15). AFM analysis showed the presence of the steps with different heights. An ~0.35 nm and ~1.1 nm step height can be associated to 1 and 3LG, respectively, over the substrate or stacked over other graphene layers [601]. In fact, like for the (0 0 0 1) on-axis face, the graphitization starts from the step edges and propagates gradually to the centre of the terrace [601–603, 655]. In this case, the C atoms at terrace kinks and step edges have a lower coordination number, thereby leading to an easier breaking of the bonds at these sites. For this reason, the probability of SiC decomposition and further surface diffusion of C atoms is increased and graphitization of the SiC surface occurs [655]. Regarding the growth kinetics, anisotropy of the Si desorption rate is always present and, thus, different SiC steps have different evaporation rates [601]. In addition, increase in the miscut angle increases the step density, thereby leading to an increase in graphene thickness at this region [601].

Another interesting finding (see figure IV.14—right) is that the presence of the atomic steps leads to the formation of pleats similar to the MEG on the 4H/6H on-axis C- face (~1 to 2 nm high and 10 to 20 nm wide) preferentially oriented in the direction perpendicular to the step edges of the SiC terraces (figures IV.14(e) and (f)) [654]. Such a parallel orientation of pleats is particular to SLG grown on a vicinal SiC surface, while for SLG grown on on-axis 4H-SiC it is characterized by a preferentially hexagonal mesh-like network of pleats interconnected into (often) triangular nodes [585] (see figure IV.14(c)).

IV.1.8. Growth on non-polar surfaces SiC

The presence of the buffer layer on the Si-face is often argued to degrade the electronic properties of the SLG above it [656–659]. In quasi -free standing SLG the buffer layer is converted into SLG by intercalation. An alternative to intercalation is the direct graphitization of non-polar SiC surfaces where there is no buffer layer [660, 661], or to master the graphitization on 1LG on the C-face, where high mobilities are measured [604].

According to the crystallography of the hexagonal family of SiC, there are three non-polar planes

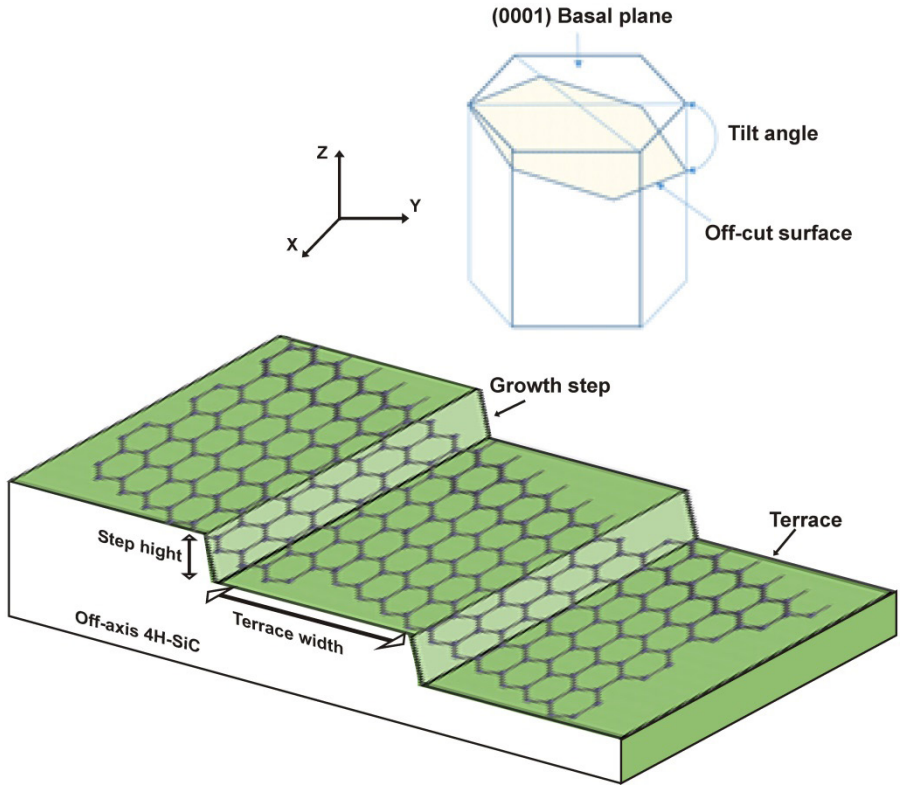


Figure IV.13. (Top panel) Diagram illustrating off-axis surfaces of 4H-SiC and (bottom panel) schematic drawing of the off-axis 4H-SiC surface after graphitization [643].

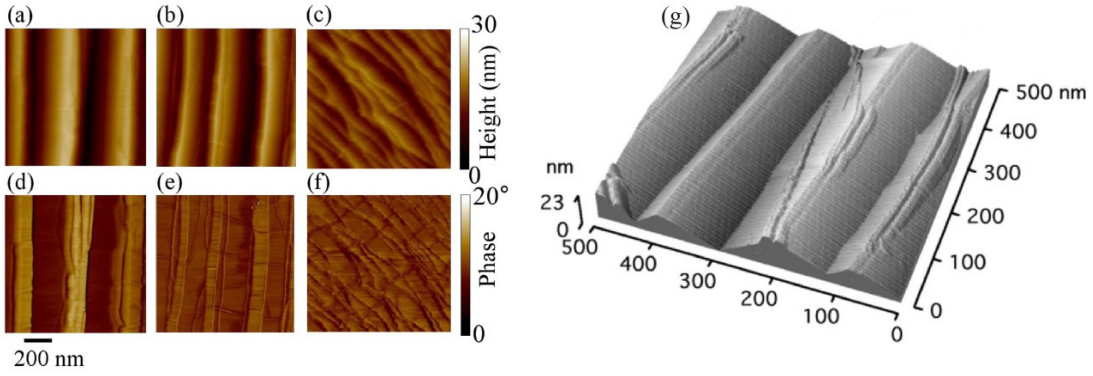


Figure IV.14. (Left panel) AFM images. Effect of graphitization temperature on the surface morphology of the sample 8°-off axis (0 0 0 1) 4H-SiC: 1600 °C (a), 1700 °C (b) and 2000 °C (c). The phase contrast maps on the same samples are also demonstrated ((d)–(f), respectively). (right panel) STM image of a sample annealed at 2000 °C. Adapted from [654], with permission of The Royal Society of Chemistry.

available for graphene formation: the *m*-plane $1\bar{1}00$, *a*-plane $11\bar{2}0$ and *r*-plane $10\bar{1}2$ [661]. Figures IV.16(a) and (b) show the possible polar and non-polar SiC planes for graphene growth. In addition, the growth of graphene can be performed using thermal decomposition of (0 0 1)-oriented cubic SiC [661]. However, the commercial production of 3C-SiC substrates is limited, and in contrast to 4H and 6H-SiC, large single crystals 3C-SiC are not available. Polycrystalline 3C-SiC are often grown as epilayers on SiC or on Si-wafers. Figures IV.16(c) and (d) demonstrates the important crystallographic planes in the cubic structure of SiC.

Synthesis of graphene on on-axis (0 0 1) cubic SiC substrates can be performed at $T > 1800$ °C for 20 min in a C rich atmosphere [661]. To provide reliable control of graphene formation a low growth rate (~1LG per five minutes) should be maintained, which is realized in a close crucible at a Ar gas pressure of 800 mbar.

Optimization of parameters (e.g., lowering T from 2000 °C to 1800 °C) can be effective for obtaining graphene layers with desired thicknesses and domain sizes ~100 nm. The optimizacion of the rest of parameters, like pressure, flow rate, step bunching, time, etc follow the same trend that for samples grown on non-polar faces and that are described in previous paragraphs.

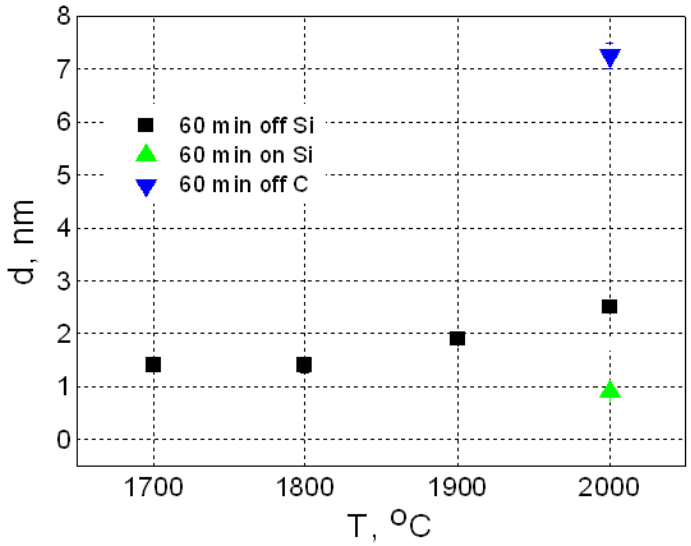


Figure IV.15. Graphitization thickness versus T at 60 min for 8° off cut Si- and C-face 4H SiC and for Si-face on axis 4H substrate (adapted with permission from [614]).

Figure IV.17 shows the LEEM images of graphene before and after optimization i.e at $T = 1800\,^{\circ}\mathrm{C}$ in the reactor of figure IV.3.

A (0 0 1) cubic SiC substrates with rather flat surface and low surface roughness (rms~2 nm) obtained by substrate polishing (rms ~0.6 nm) promotes growth of more homogeneous EG with large domain sizes as shown in figure IV.17. Growth on $(1\,\bar{1}\,0\,0)$ 6H-SiC resulted in non uniform coverage exhibiting areas of fragmented graphene and some micrometre large areas (figure IV.18—left). Similar results were reported in Ref. [662] for the $(1\,1\,\bar{2}\,0)$ plane (figure IV.18—right).

Growth on non-polar SiC surfaces is limited by the vertical growth rate (graphene growth on the polar face proceeds laterally) [641]. Such vertical growth produces scattered islands of graphene on the surface with higher density of grain boundaries (see figure IV.19). The latter causes a greater amount of Si outdiffusion from the substrate, leading to a thicker (up to 8LG) subsequent [607] MLG growth on the nonpolar faces in comparison to growth on polar faces [607]. As graphene growth on the low-packed non-polar planes is faster than that on the high densely packed non-polar planes, it is assumed that the surface density is a key factor limiting Si desorption and the graphene growth rate.

IV.1.9. Surface engineering by intercalation

Graphene grown on SiC(0 0 0 1), by sublimation resides on top of a buffer layer [590, 592], as schematically depicted in figure IV.20. The buffer layer (denoted also by $6\sqrt{3}$) is formed at the early stages of heating of the samples, i.e. before graphene is formed, and it has been observed in several experimental studies of of SiC(0 0 0 1) surfaces [586, 663–665] and also in an atomistic simulation of graphene formation on SiC(0 0 0 1) [590, 666]. The buffer layer has a $(6\sqrt{3} \times 6\sqrt{3})$R30° periodicity with respect to SiC(0 0 0 1) substrate surface.

This layer consists of C atoms in a graphene arrangement [590, 592, 668]. This means that the structure is has C hexagons with a C–C distance like in graphene. The $(6\sqrt{3} \times 6\sqrt{3})$R30° periodicity with respect to the SiC surface corresponds to a (13×13) super cell. Thus, the super cell contains 169 graphene unit cells. Due to a hybridization of states of the C atoms of the buffer layer with states from the SiC substrate surface, it lacks the typical π-bands of graphene and therefore has no Dirac cone [592]. On the other hand, the σ-bands of the buffer layer are fully developed and indistinguishable from those of graphene [592]. These observations are in agreement with theoretical studies [590, 669].

The buffer layer $(6\sqrt{3})$ induces electron doping in SLG. Typical values for the charge carrier density in SLG are $n \sim 1 \times 10^{13}\,\mathrm{cm}^{-2}$ [589, 671–674]. The buffer layer is also partly responsible for the relatively low μ and its T dependence [658]. Furthermore, the reduction in spin transport in SLG is attributed to the buffer layer [656]. Typical values for $\mu \sim 1000\,\mathrm{cm}^2\,\mathrm{V}^{-1}\,\mathrm{s}^{-1}$ at $n \sim 1 \times 10^{13}$ cm^{-2} and $T = 300\,\mathrm{K}$ and $\mu \sim 2000\,\mathrm{cm}^2\,\mathrm{V}^{-1}\,\mathrm{s}^{-1}$ at $n \sim 1 \times 10^{13}\,\mathrm{cm}^{-2}$ and $T = 25\,\mathrm{K}$ [584, 589, 658, 675, 676].

The structural similarities between the buffer layer and graphene suggest that it should be possible to convert the former one into the latter by cutting the bonds between buffer layer and substrate through intercalation, as depicted in figure IV.21 schematically for the case of hydrogen. Similar procedures have been studied before for SLG on metal surfaces like, e.g. Ni(1 1 1) [677]. In this case, different metals like Au, Yb, or Cu were intercalated between the metal substrate and graphene [677]. Several authors showed that different elements can be intercalated between the buffer layer and the SiC substrate. E.g., the intercalation of H [645–647, 658, 678–681], O [682–685], F [686, 687], N [688],

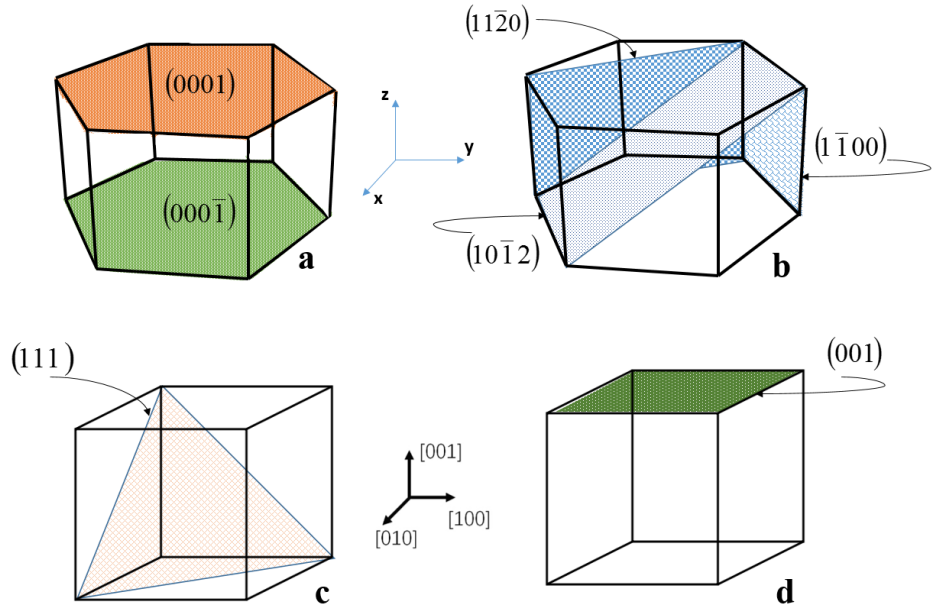


Figure IV.16. Principal crystallographic planes of (a,b)hexagonal and (c,d) cubic SiC.

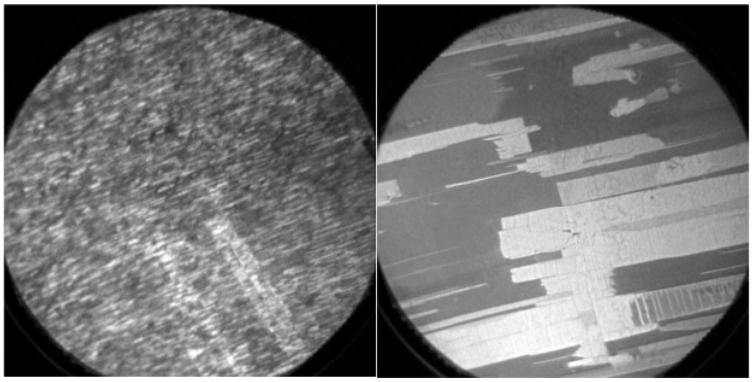


Figure IV.17. LEEM images of graphene grown on (0 0 1) cubic SiC before (left panel) and after optimization (right panel). In the first case, we have 4–5LG, while optimized growth allows to obtain 1–3 LG with increased domain size up to 10 μm.Field of view is 25 μm. Adapted from [661].

Si [689, 690], Ge [691, 692], Au [693–696], Cu[697], Li [698,699], Na [700] and subsequent transformation of the buffer layer into graphene have been confirmed.

For applications, it is important that the intercalated species does not give rise to electronic states at the Fermi level, since these would short-circuit the graphene layer on top of it. This is the case for hydrogen which saturates the SiC(0 0 0 1) surface with Si–H entities.

The doubly filled bonding and empty anti-bonding Si–H states are located below and above the valence band minimum and valence band maximum, respectively, leaving the surface electronically passivated [701–703]. A similar situation can be expected for oxygen and fluorine passivation of the SiC(0 0 0 1) surface.

The first study of the intercalation of hydrogen under the buffer layer on SiC(0 0 0 1) was reported in Refs. [645, 646] who annealed SiC(0 0 0 1) substrates covered by the buffer layer in one atmosphere of hydrogen at T between 600 °C and 1000 °C. Similar processes can be employed to intercalate hydrogen under the buffer layer even if an additional graphene layer already exists on top of it [645, 646, 657, 680, 704–706], although the exact conditions may vary. In this case, SLG becomes a quasi-freestanding BLG (see figure IV.21).

The successful decoupling of the buffer layer and conversion into so-called quasi-freestanding SLG was confirmed by LEED, ARPES, XPS and LEEM. Figure IV.22(a) shows typical XPS spectra of the C1s core level of various samples [707]. The spectrum of the buffer layer is has 3 components. S1 and S2 are caused by the C atoms of the buffer layer [592]. In addition, a component due to C atoms in the SiC substrate is visible. These are also seen in the spectra of SLG, BLG and TLG indicating that the buffer layer forms the interface. Upon H-intercalation, the buffer layer is converted to SLG which is evident from the disappearance of the components S1 and S2 and the formation of a graphene-related component. This

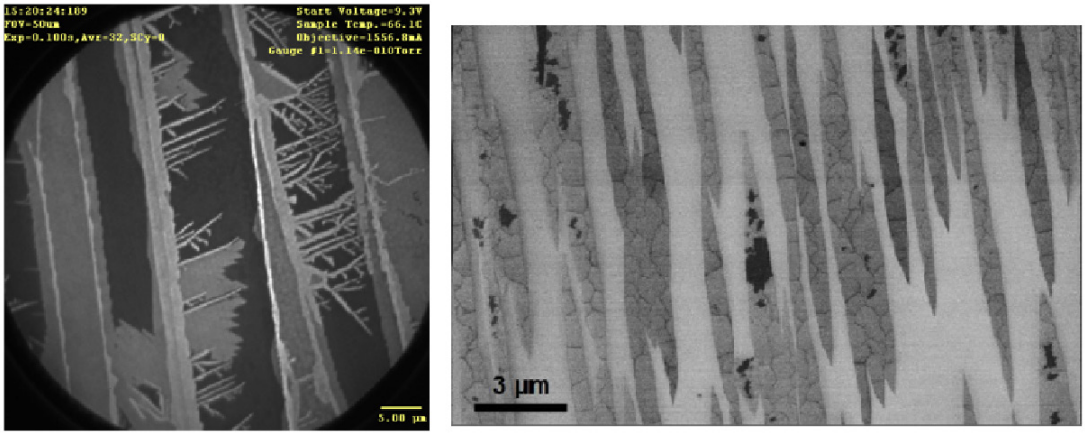


Figure IV.18. (left) LEEM image of graphene grown by thermal decomposition at 1900 °C on $(1\,\bar{1}\,0\,0)$ oriented 6H-SiC substrates, scale bar 5 micron, adapted from [643]. (right) SEM image of graphene grown on 6H-SiC, scale bar 3 micron $(1\,1\,\bar{2}\,0)$.

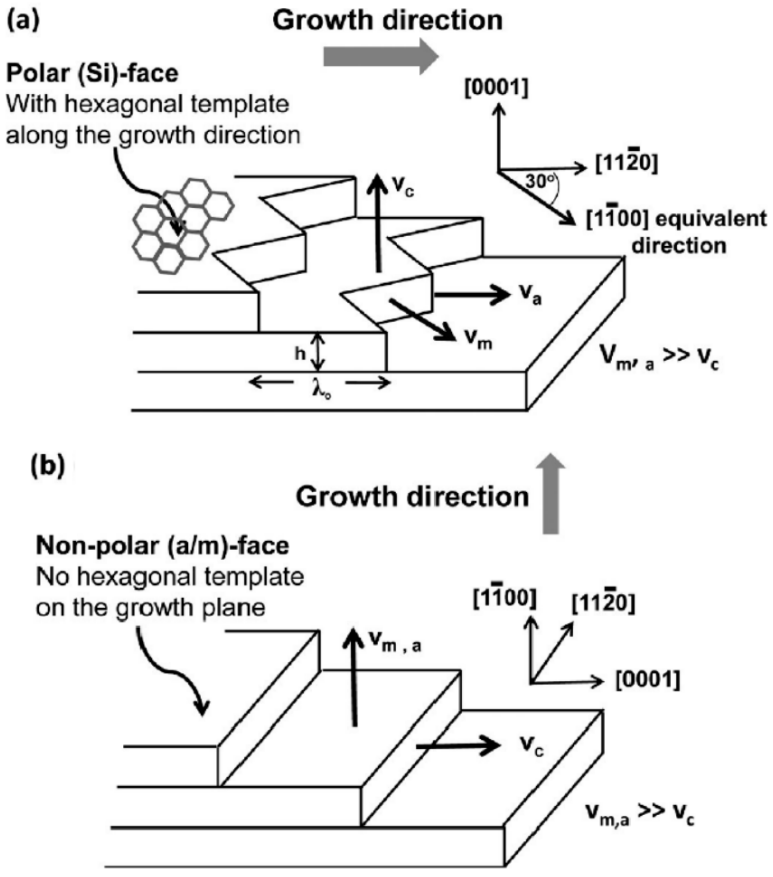


Figure IV.19. Graphene growth mechanism on (a) the polar (Si) face SiC with offcut toward $[1\,1\,\bar{2}\,0]$ and (b) the nonpolar a/m face with slight offcut along [0 0 0 1]. The growth on the polar face proceeds laterally while the growth on the nonpolar face is limited by the vertical growth rate. The zigzag structure shown on the polar face step edge is a consequence of two possible lateral growth directions. Adapted from [667], copyright American Chemical Society.

is also the case for SLG/BLG. The component of the SiC substrate is shifted to lower binding energy due to a change of surface band bending. Figure IV.22(a) shows examples of the band structure near the K-point of the hexagonal Brillouin zone as measured by ARPES [707] for SLG, BLG.

The charge carrier type is changed from electrons in SLG/BLG on the buffer layer to holes in QFSLG/QFBLG on the H-terminated (0 0 0 1) surface of hexagonal SiC polytypes [645, 646, 658, 704, 707, 708]. This is due to the spontaneous polarization of hexagonal SiC [708, 709], which varies with the polytype due to their different ratio of hexagonal to cubic stacking sequences [708–710]. For semi-insulating 6H- and 4H-SiC(0 0 0 1)-H substrates hole densities of 6.2×10^{12} cm^{-2} and 8.6×10^{12} cm^{-2}, respectively, as

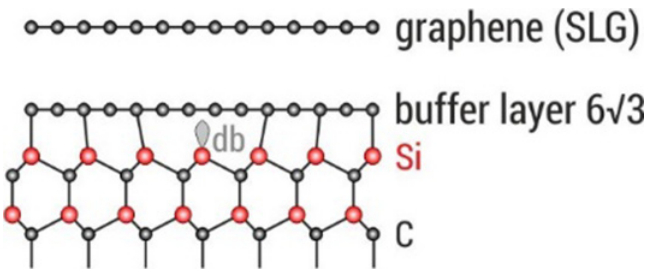


Figure IV.20. Schematic view of graphene on SiC(0 0 0 1). The graphene layer resides on top of the buffer layer. The buffer layer is structurally equivalent to graphene but strongly bound to the SiC substrate. Dangling bonds (db) are present due to the lattice mismatch between graphene and SiC. Drawing not to scale (after [645, 670]).

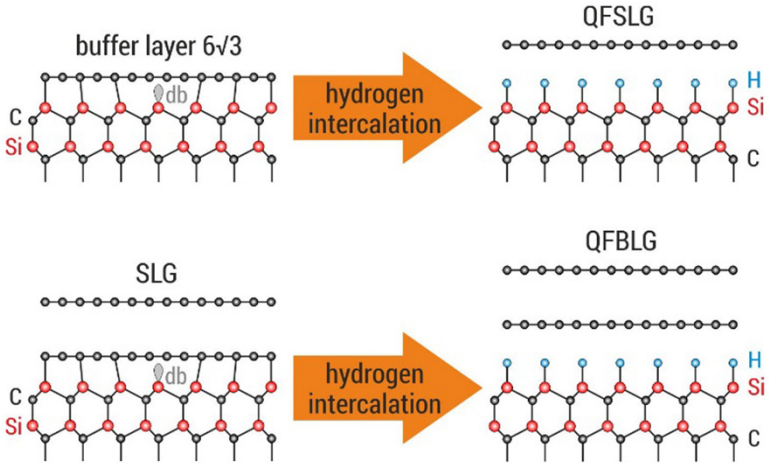


Figure IV.21. Schematic view of the conversion of the buffer layer into quasi-freestanding SLG on H-saturated SiC(0 0 0 1) (also referred to as SiC(0 0 0 1)-H) and of SLG on the buffer layer into quasi-freestanding BLG on SiC(0 0 0 1)-H. After [645, 670].

determined by ARPES in good agreement with theoretical predictions [708–710]. In the case of QFSLG on n-type doped cubic 3C-SiC(1 1 1)-H a slight electron doping is observed, which agrees with the fact that this SiC polytype has no spontaneous polarization. In this case the excess electrons in QFSLG is due to alignment of the Fermi levels as described by the Schottky model for metal–semiconductor interfaces [708]. Refs. [658, 704] have provided evidence for the hydrogen at the interface by measuring the Si–H stretch mode vibration using FTIR absorption spectroscopy as shown in figure IV.22(c). This was later confirmed by surface enhanced Raman spectroscopy [711, 712]. Raman spectroscopy also provided evidence for the conversion of the buffer layer to a QFSLG [658, 705, 711, 712]. In the case of QFSLG a narrow 2D line is observed while for QFBLG a broad 2*D* line indicative for AB stacking is found (see figure IV.22(d)). Electronic transport studies on simple Hall bar structures and FET have shown that QFSLG on 4H- of 6H-SiC(0 0 0 1)-H exhibits a higher charge carrier mobility (typically ~4000 $cm^2\ V^{-1}\ s^{-1}$) than SLG on the buffer layer and that it has a considerably reduced T dependence [658, 704, 705, 713–718].

Decoupling of the buffer layer from the SiC substrate and saturation of the SiC(0 0 0 1) surface with hydrogen can be carried out in an apparatus depicted in figure IV.23 [719], initially designed for the hydrogenation of SiC surfaces [703, 719, 720]. The system consists of a quartz tube in which the sample can be heated in an atmosphere of purified hydrogen in a contact-less manner by means of halogen lamps. In the hydrogenation process, the chamber is first filled with hydrogen and then the sample is raised to the desired value. Typical process parameters are listed in table IV.1.

Variations of the above procedure have been reported for the synthesis of quasi-freestanding graphene layers on SiC(0 0 0 1). Ref. [645], reported preparation *T* in the range from 600 to 1000 °C at atmospheric pressure without mentioning the annealing time. Ref. [713] annealed in molecular hydrogen to convert SLG to QFBLG. They reported a H_2 pressure of 800 mbar, *T* of 600 to 1200 °C, and process times between 30 and 120 min. Ref. [721] carried out the hydrogen annealing directly after the growth of graphene in a Hot-Wall CVD reactor. After graphene growth in Ar at 100 mbar at 1650 °C, the sample was cooled to 1050 °C. At this *T*, the gas a exchanged to H_2 and the pressure increased to 900 mbar. After 30 min, the sample was allowed to cool to 700 °C in H_2. Finally the system was evacuated and the sample allowed to cool to RT. Ref. [715] annealed their buffer layer samples in H_2 at 1013 mbar and temperatures between

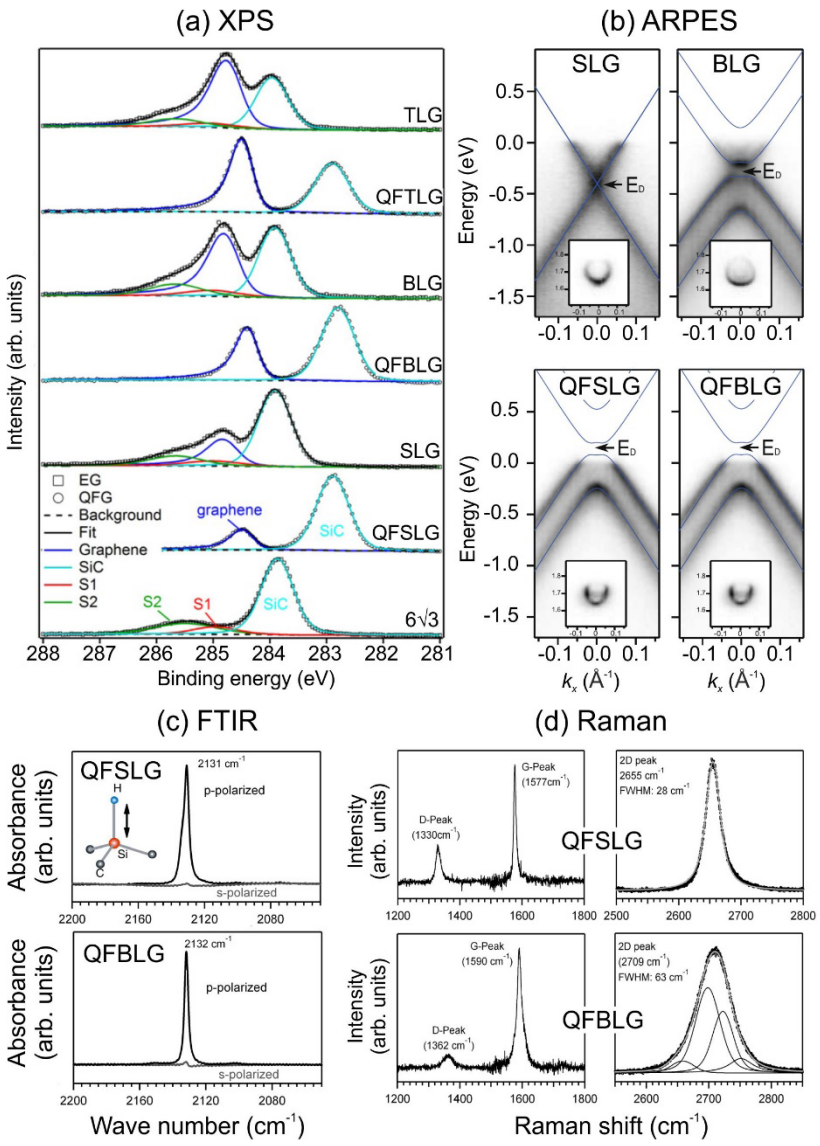


Figure IV.22. (a) C1s core level spectra of the buffer layer, SLG, BLG, =TLG and TLG, on substrated and quasi freestanding (QF). The H-intercalation leads to a disappearance of the buffer layer components (S1, S2) and an increase of the graphene-related component. The signal due to SiC shifts to lower binding energy due to a change of band bending. (b) ARPES intensity maps versus electron energy and momentum of SLG and BLG on the buffer layer as well as QFSLG and QFBLG on H-terminated 6H-SiC(0 0 0 1). (c) Si–H stretch mode of the H-saturated SiC(0 0 0 1) surface below QFSLG and QFBLG. (d) Representative Raman spectra of QDSLG and QFBLG. (a) adapted from [708] and (b) adapted from [707], both © IOP Publishing Ltd; (c) and (d) adapted with permission from [704].

600 and 1200 °C for 60 min. In Ref. [706], QFSLG was produced by annealing in a furnace at 800 °C and a H_2 flow of 0.2 slm for 1 h at an unspecified pressure. The process time was 60 min. The highest mobility was observed for at of 700 °C. In [706] QFBLG by annealing Hall-bars made from SLG at 1250 °C in H_2 at ~33 mbar was reported. Ref. [680] employed a plasma source as well as an atomic hydrogen source to convert SLG to QFBLG. They reported that the plasma treatment induces a disorder. Kinetic Monte Carlo simulations performed in Ref. [722] have shed light on the atomistic mechanism of H intercalation of the buffer layer, in good agreement with experiments.

Surface analytical tools such as LEED, XPS(see section IX.2/XPS for an introduction to the technique), ARPES (see section IX.2.3 for an introduction to the technique), LEEM and STM (see section IX.1.4 for an introduction to the technique) along with FTIR and Raman are ideally suited to characterize the quasi-freestanding graphene layers on H-terminated SiC(0 0 0 1). Table IV.2 lists several methods together with the expected observation and relevant references.

Oxygen intercalation was suggested a means for decoupling the buffer layer from the SiC(0 0 0 1) surface by annealing the buffer layer [682] in one atmosphere of molecular oxygen at 250 °C for 5 s, using a special oxidation chamber. In the first approach in Ref. [685] the buffer layer samples was annealed *in situ*, i.e. directly in the UHV chamber used for XPS and ARPES analysis, at 750 °C in ~10^{-4} mbar of molecular oxygen. The sec-

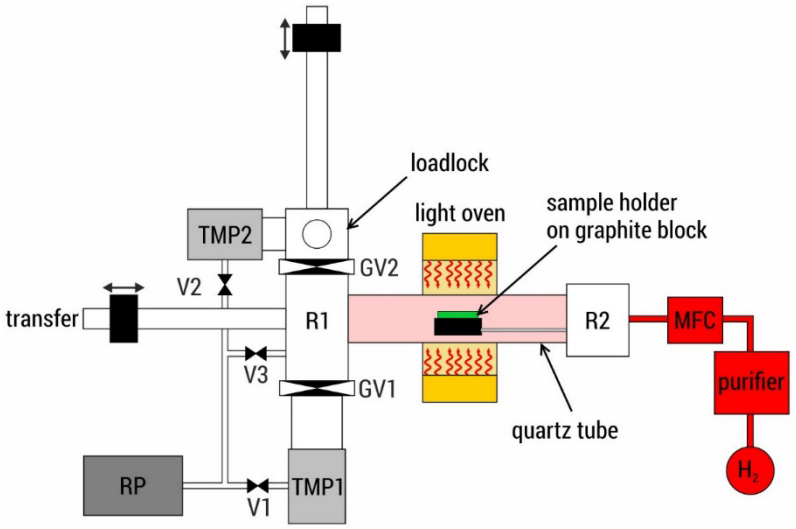


Figure IV.23. Sketch of the apparatus used for intercalating hydrogen between the buffer layer and the SiC(0 0 0 1) substrate [658, 704, 708]. After [719].

Table IV.1. Typical parameters for intercalating hydrogen under the buffer layer [658, 704, 708].

Process	Sample temperature in °C	Hydrogen pressure in mbar	Flow rate in slm	Time
6 $\sqrt{3}$ to QFSLG	540–560	900–960	0.9–1.0	60–90
SLG to QFBLG	840	900–960	0.9–1.0	60–90

ond procedure in Ref. [685] was carried out *ex-situ* by annealing in O_2 with best results at 270 °C at 200 mbar. The Raman spectra, however, demonstrated that both processes lead to the formation on numerous defects. In Ref. [683] the oxygen intercalation to transform SLG into a BLG was carried out by annealing in air at 600 °C for 40 min. A heat up ramp of 50° per minute was used. They confirmed the decoupling of the buffer layer and the formation of a high quality BLG.

In Ref. [684] buffer layer samples as well as SLG were annealed up to 500 °C and 650 °C, respectively, in a water vapour in order to decouple the buffer layer by oxidation of the SiC(0 0 0 1) substrate surface. Raman spectroscopy indicated numerous defects. However, like as for Ref. [683], the QFBLG formed by treating SLG showed a negligible *D* band. This was also evident from Hall effect measurements, which indicated $\mu \sim 790\ \mathrm{cm^2\ V^{-1}\ s^{-1}}$ at a rather high hole concentration of $2 \times 10^{13}\ \mathrm{cm^{-2}}$. While oxidation of the SiC interface by oxygen or water intercalation leads to highly defective QFSLG, this technique is promising for the synthesis of decoupled QFBLG on SiC(0 0 0 1). One may speculate that the buffer layer, which is highly corrugated and in which C atoms are partially sp^3 hybridized [723], is more prone to be attacked by the oxygen during intercalation. On the other hand, in the case of SLG, the buffer layer is protected by the graphene layer on top of it.

Intercalation with other elements was also studied. Contrary to Si, that intercalates only at T > 800 °C through migration at graphene domain boundaries and other defects, Li [698, 699] was found to penetrate into the C layer already at RT through the formation of Li-compounds. Na partial and inhomogeneous intercalation occurs already at RT directly after deposition, although most of the Na remained on the surface and formed Na droplets. Na intercalation is promoted both by electron/photon beam exposure and by moderate annealing at ~100 °C. Annealing at higher *T* results in de-intercalation and Na desorption from the surface [700]. Other elements intercalation would be appealing, such as nitrogen, that is predicted to provide charge neutral QFSLG [726]

Finally, we review studies on Ge [691, 692] and Au [693–696] intercalation between buffer layer and SiC(0 0 0 1) surface. In both cases, the preparation is performed using the following scheme. First, a thin layer (up to 5 monolayers) of the intercalant (Ge or Au) is deposited on the buffer layer using thermal evaporation. Then, the sample is annealed in UHV to induce intercalation. The properties of the QFSLG formed by intercalation depend on the amount of material present at the interface. For Au two phases were observed [693]: a highly n-type doped one with the Dirac point located ~0.9 eV below the E_F for 1 monolayer Au at the interface and a weakly p-type doped phase with the Dirac point at 0.1 eV above E_F for one third of a monolayer Au at the interface. Spin-resolved ARPES indicated a Rhasba-type spin–orbit coupling in the π-band of QFSLG at energies where it interacts with Au bands [696]. In the case of Ge [691], an n-type doped QFSLG is obtained when 1 monolayer of Ge resides at the interface while a p-type doped QFSLG is observed when 2 monolayers of Ge are intercalated. The hole and electron concentrations in the QFSLG were $\sim p = 4.1 \times 10^{12}\ \mathrm{cm^{-2}}$ and

Table IV.2. Characterization techniques for QFSLG and QFSLGon H-terminated SiC(0 0 0 1).

Method	Observation	References
Process: buffer layer 6 $\sqrt{3}$ to QFSLG		
LEED	Strong weakening of the superlattice diffraction spots caused by the buffer layer	[645–647]
XPS	Disappearance of the C1s signals related to the buffer layer and appearance of an asymmetric C1s signal due to QFSLG; Shift of the C1s signal related to the SiC bulk to lower binding energy due to a change of surface band bending (see figure IV.22(a))	[647, 704, 708]
XPS	Shift of the C1s signal related to the SiC bulk to lower binding energy	[647, 704, 708]
ARPES	Appearance of a graphene π-band at the K-point of the hex. Brillouin zone with the Dirac point located above the Fermi level (see figure IV.22(b))	[645–647, 703, 708]
LEEM	Transition from a flat LEEM-$I(V)$ curve to a spectrum with one dip	[647]
STM	Topography image without buffer layer moiré structure	[668, 707, 715]
FTIR	Appearance of a sharp Si–H stretch mode signal (see figure IV.22(c))	[658, 704]
Raman	Disappearance of the broad Raman spectrum of the buffer layer and appearance of sharp G and $2D$ bands; $2D$ band symmetric (see figure IV.22(d));	[658, 704, 713, 717, 724, 725]
Process: SLG to QFBLG		
XPS	Disappearance of the C1s signals related to the buffer layer and increase of the asymmetric C1s signal due to QFSLG(see figure IV.22(a))	[645, 680, 704, 708, 713, 721]
XPS	Shift of the C1s signal related to the SiC bulk to lower binding energy (see figure IV.22(a))	[645, 680, 704, 708]
ARPES	Disappearance of the linear π-band of graphene with the Dirac point below the Fermi level and appearance of the two parabolic π-bands of BLG with the Dirac point located above the Fermi level (see figure IV.22(b))	[645, 704, 708]
LEEM	Transition from a LEEM-$I(V)$ curve with one dip to a spectrum with two dips	[645, 646, 680]
STM	Topography image without buffer layer Moiré structure	[707]
FTIR	Appearance of a sharp Si–H stretch mode signal (see figure IV.22(c))	[704]
Raman	Disappearance of the broad Raman spectrum of the buffer layer and change of the symmetric $2D$ band to an asymmetric $2D$ band considerably broader than that of QFSLG	[704, 713]

$n = 4.8 \times 10^{12}$ cm^{-2}. This means that the shift of the Dirac point with respect to E_F is almost symmetric. Note that a mixed phase can also be prepared in which n- and p-type regions coexist.

This was employed by Baringhaus *et al* [692] to fabricate pn-, np-, pnp- and npn-junctions which were investigated by 4-point probe transport measurements. Evidence for Klein tunnelling of charge carries across such barriers was observed.

IV.1.10. Structured growth

The fact that growth starts at a step edges on the SiC(0 0 0 1) face (see above), can be used to produce graphene nanostructures for electronics. Masking methods, for selective growth using AlN [727], SiN [728] and amorphous C masks [642] with tens of nm precision have been proposed. The template growth method on sidewalls of SiC trenches [604, 615, 618, 619] is described below. It circumvents the detrimental effect of traditional plasma etching [729, 730] and resulting sidewall nanoribbons show RT ballistic transport properties [620].

The idea is to tune the parameters so to stop growth just as graphene covers the step sidewalls. Steps can be either natural steps obtained by step bunching at the SiC surface, or the sidewall of trenches of various shape etched in the SiC substrate. The width of the ribbon is then set by the step height and the angle with the basal (0 0 0 1) plane (~27°). Upon heating in the 1400 °C–1600 °C range for graphitization, the SiC steps flow to produce the equilibrium facets at that T. E.g., for ribbons oriented along the graphene armchair direction, stable facets are found at $(\bar{1}\,1\,0\,7)$, $(\bar{1}\,1\,0\,6)$, and symmetrically at $(1\,\bar{1}\,0\,7)$, $(1\,\bar{1}\,0\,6)$ [731].

For growing graphene on natural steps, SiC surface treatments are used to organize the step-terrace structure prior to graphene growth. These include [615] annealing the chemically and mechanically processed polished SiC substrate in vacuum, in Ar, in a face-to-face SiC configuration or with a refractory capping grid [642]. The key is to obtain a stable step configuration prior to graphene growth. The T for surface structuring are chosen according to the background pressure to prevent graphene growth, i.e. 1100 °C–1200 °C in vacuum, 1300 °C–1700 °C in Ar or face to face. Step bunching by annealing in these controlled conditions produces arrays of straight steps and terraces with uniform width and height (figure IV.24). The step structure depends on the polytype [732] the local miscut of on-axis SiC wafers (see above), which may vary up to ±0.1° across the whole wafer, and other factors such as the heating method. A complete systematic study is still lacking. After treatment, the terraces are up to 10–30 μm in width and extended over several hundreds μm in length (figure IV.24). Examples of ribbons grown on the sidewall of natu-

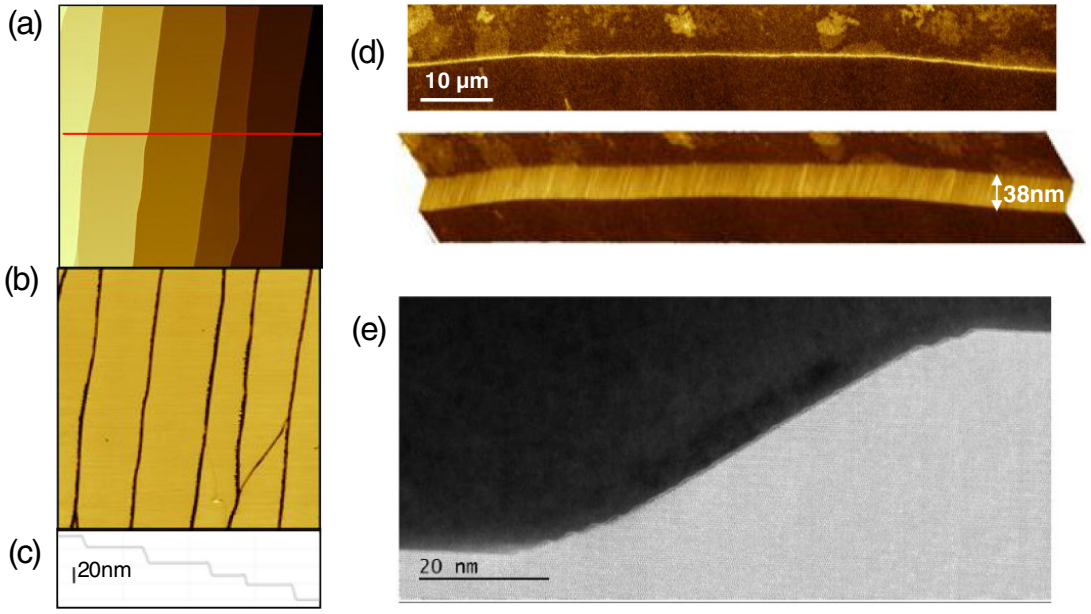


Figure IV.24. Examples of sidewall ribbons (a)–(d) on natural steps, 20 nm high. (a) Topographic AFM image, (b) lateral force AFM image, revealing graphene (dark) on the sidewall, (c) profile of the steps along the red line in (a) [615]. (d) Example of isolated ribbon more that 80 μm long, 38 nm high (top) lateral force AFM—the ribbon is bright; (bottom) 3d rendition by combining topography and lateral force. (e) Cross-sectional TEM high resolution image of a sidewall trench etched in SiC, recrystallized at a stable facet angle of ~30°, over which MLG is draped. Adapted from Ref. [734], copyright American Chemical Society.

ral sidewall steps (obtained by step bunching) and on etched trenches are shown in figure IV.24.

In a more controllable manner, nano-structured graphene can be grown on various shapes etched in SiC(0 0 0 1) [733]. Trenches can be etched along the 4H-SiC$(1\,\bar{1}\,2\,0)$, and 4H-SiC$(1\,\bar{1}\,0\,0)$ directions to produce GNRs along the zigzag or armchair orientation, owing to the epitaxial orientation of graphene on SiC (see figure IV.1(a)). For this, an e-beam or a photoresist is patterned on SiC(0 0 0 1). Plasma etching is used to etch SiC with the resist as a mask for shallow etching. Various recipes have been reported [615, 618–620]E.g., reactive ion etching (RIE) (using SF_6 and O_2 ratio 20:7) with etching rates ~0.3 nm s^{-1}, or 43% SF_6/23% O_2/33% Ar RIE operating at 30 mTorr where the radiofrequency power was tuned to give a SiC etch rate ~0.8 nm s^{-1} [616], allowing fine control of the etch depth. For deeper etching, a Ni mask can be used, that is evaporated on the resist and lifted up. The Ni mask is removed after RIE etching by an ultrasonic treatment in nitric acid [618].

The resist pattern is transferred to the SiC as a template for graphene growth, and complex interconnected graphene structures can be designed (see Refs. [604, 618, 733]), including pillars to produce nanometric graphene rings [604]. Although trenches of any height can be etched, well-formed graphene ribbons are best grown on sidewalls 15–35 nm deep. This is because shallow trenches ($\leqslant$10 nm) tend to get washed out upon annealing in the CCS furnace and deep trenches tend to break into multiple facets revealing multiple parallel ribbons [615].

In the CCS furnace, the structured SiC chip is then heated to 1100 °C to allow the vertical etched sidewalls to crystallize into the equilibrium facets [735] onto which the GNRs grow at~1500 °C–1600 °C [618]. The exact T and time depend on the specifics of system, such as the Si escape leak in the furnace CCS method [597, 620]. The sidewall ribbons produced this way are ballistic conductors at RT on micrometre distances [620]. Similar sidewall ballistic ribbons have been produced with the same technique, but by a dc current annealing of conducting SiC wafers (6H-SiC N-doped) in an Ar atmosphere of 4×10^{-5} mbar (sample clamped by graphite contacts) [620]. Well-ordered crystal facets from at~1150 °C, and further annealing to 1300 °C results in growth of extended GNRs [620, 736].

Because the steps in SiC are etched and annealed prior to graphene growth, the facets onto which graphene grows are smooth and atomically defined. This is demonstrated in cross-sectional transmission electron microscopy [734] (figure IV.24(d)), and in ARPES [731] where measurement integrating thousands of parallel GNRs show graphene electronic-bands.

GRNs of any nominal orientation can in principle be produced. By design, tens of thousands of sidewall nano-structures can be produced all at once, following the recipes above [604, 618, 731, 733], in particular long straight parallel GNRs [615]. However, sidewalls may in some cases show restructuring after annealing [604, 620, 733] with rounding and faceting [597, 615]. The effects are sensitive to a number of factors such as the step direction, growth condition (both T, time, and also possibly the type of heating), the pinning of steps (e.g. under amorphous C pads such as in, figure IV.9, or by defects), or the polytype. The most prominent feature of the GNRs, i.e. RT quantized ballistic transport, is however a very sturdy result and was observed for straight as well as curved GNRs [620].

IV.1.11. Integration with silicon wafers

As mainstream electronics and very large scale integration is based on Si technology, schemes to integrate graphene grown on SiC with Si wafers have been devised. Two routes have been investigated. The first is based on the standard SOI technology, where a thin monocrystalline Si layer ready for CMOS processing is bonded on top of graphene on SiC. Figure IV.25 shows the principle of the design. This 3d integration, inspired by the industrial development of 3d integration stacking thin-film electronic devices, realizes the interconnection of the SiC supported graphene platform, preserving the integrity of graphene, with a Si wafer, enabling, in principle, the full spectrum of CMOS processing. [737].

The main steps consist in the fabrication of graphene structures (either from patterned or from template growth on SiC sidewalls), evaporation of an alumina film by ALD as a bonding layer between the SiC and the oxidized Si wafer, wafer bonding in a pressure module and finally splitting of the Si wafer by annealing at 400 °C (smartcut) to leave a thin crystalline Si layer on top. The main advantage of the process is that the growth T (1400 °C and above) is not limited by the presence of Si (melting point 1414 °C). The Si wafer resides on top of SiC and is therefore fully accessible. Finally, the stacking of SiC and Si wafers increases the areal density inspired by the 3d stacked layers Very Large Scale Integration Technology.

The second strategy, so called graphene on-silicon (GOS), takes advantage of the heteroepitaxy growth of 3C-SiC on Si to produce graphane on SiC covered Si substrates (3C-SiC is the only SiC polytype known to grow on Si) [738–740] (see figure IV.25). The polar Si-terminated 3C-SiC(1 1 1)/Si(1 1 1) surface grown in UHV shows graphene Bernal stacking with an interfacial buffer layer, similarly to the 4H- or 6H-SiC(0 0 0 1) surfaces [738]. Conversely, the C-terminated 3C-SiC(1 1 1)/Si(1 1 0) shows a non-Bernal stacking, with the absence of an interfacial buffer layer, consistent with a C-face termination [738].

The quality of these graphene films is modest as shown by large Raman *D* peaks. The disorder results from Si diffusion through SiC grain boundaries (due to a large ~20% lattice mismatch between Si and 3C-SiC) and the lower *T* allowed for graphene growth (limited by the Si melting point) [741]. Process optimization is being developed. E.g., growing an epitaxial AlN layer on Si prior to SiC growth reduces Si out-diffusion and helps grow higher quality graphene [738]. Catalytic growth of SiC on Si with a NiCu coating [742] allows growth of graphene on predefined locations. For electronic application requiring high quality graphene, alternative schemes have been developed (see figure IV.25(a)).

Growing an epitaxial AlN layer on Si prior to SiC growth significantly reduces Si out-diffusion and helps grow higher quality graphene [738], as well as and interface NiCu layer [742].

IV.2. CVD growth on SiC

High quality graphene can be grown by CVD on insulating and conductive SiC substrates. In a CVD process, C atoms are provided externally by C gaseous precursors and deposited on the SiC substrate, which is different from Si sublimation. The method enables growth directly on the SiC surface on both Si and C-faces. A CVD process (see section V) typically involves hydrocarbon precursors: methane, propane or acetylene delivered to the reactor by a carrier gas (like Ar). It offers the precision of synthesizing a pre-defined number of C layers [611, 714], including a single layer (buffer layer) on the Si-face of SiC, and is less sensitive to SiC surface defects than the sublimation method [743]. With CVD the nucleation sites for graphene growth are located at the atomic steps, therefore enabling step-flow epitaxy. A CVD process requires high *T*. However, the lowest *T* must be higher that of thermal decomposition of the gaseous C precursor (~1000 °C). However, to form graphene of good structural quality requires $T \sim 1500$ °C to 1800 °C. At that *T*, SiC substrate decomposition (i.e. Si sublimation) takes place. Graphene growth by Si sublimation occurs (from ~1300 °C) before the *T* of CVD growth is achieved. Therefore, the first C layers will be formed by Si evaporation, not by CVD. Also, after the CVD growth is finished, uncontrolled sublimation may take place, causing additional carbon layers to grow.

The process presented below [611] is a method for manufacturing graphene by vapour phase epitaxy (VPE/CVD), in which SiC substrates may be used owing to a control of the Si sublimation process. Ref. [638] used a combination of hydrogen and propane to balance C supply and etching [638, 740], which provides excellent samples for quantum Hall effect resistance standards [612].

Ref. [744] relies on the creation of the flow conditions in the reactor that controls the Si sublimation rate and enables mass transport of hydrocarbon to the SiC substrate through the argon gas boundary layer. Laminar gas flow over the SiC surface consists of layers moving at different velocities, due to the shear stress between adjacent gas layers. The Reynolds number (Re) measures the ratio of inertial forces to viscous forces and consequently quantifies the relative importance of these two forces in a given gas flow [745]. Tuning Re (Vd/ν), where *V* is the gas velocity, *d* is the characteristic dimension of the reactor and ν is the kinematic viscosity, enables the formation of an Ar boundary layer thick enough to confine the Si vapour, and slow the Si escape that causes graphene to form. The Ar layer however allows the diffusion of hydrocarbon to the SiC surface and, in consequence, the CVD growth of graphene on the SiC surface.

When the velocity of Ar atoms above the substrate surface is sufficiently high, the flowing gas does not inhibit sublimation, because Si escapes in the Ar carrying gas [744]. If the velocity (related to the product of the pressure in the reactor by the flow through the reactor expressed in litre/min) is reduced below a critical value,

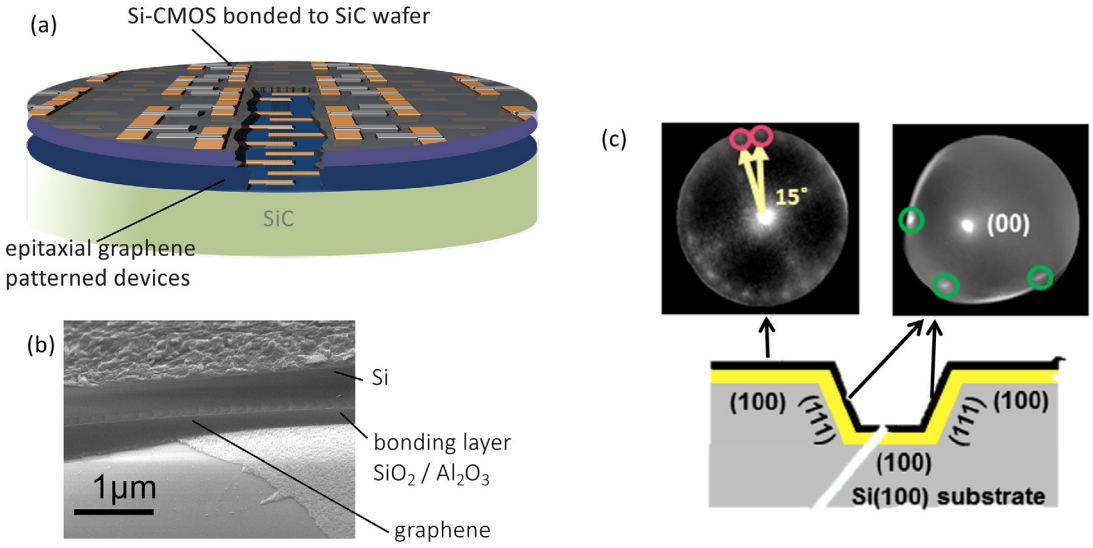


Figure IV.25. (a) Principle of Si-wafer to graphitized SiC-wafer bonding with the SOI technology, and (b) SEM image of the cross-sectional bonding showing graphene at the interface (after [737]). (c) Growth of graphene on an epilayer of SiC grown on Si(1 0 0), schematics and LEED diffraction, showing rotational order on 3C-SiC(1 0 0) compatible with C-termination, and Bernal stacking on 3C-SiC(1 1 1) compatible with Si-termination. Adapted from Ref. [738], © IOP Publishing Ltd.

a so-called 'stagnant layer' of Ar is created above the surface, while successive gas layers, starting from the substrate, move with increasing velocity [745]. The product of flow rate and pressure to obtain this critical condition depends on the reactor geometry and is adjusted experimentally. In the case of the Aixtron -VP508 reactor, an Ar flow rate ~6 l min^{-1} and a pressure ~100 mbar were used in order to completely inhibit sublimation. If the Ar flow is increased to ~26 l min^{-1}, the stagnant layer thickness decreases, enabling again Si sublimation. Therefore, by adjusting the Ar flow rate one can regulate the thickness of the gas layer inhibiting Si escape (the number of atomic gas layers of higher or lower velocity than a typical velocity to start/stop sublimation), thereby regulating the sublimation process efficiency.

Graphene was grown by CVD/VPE at 1600 °C on both Si-face and C-face of nominally on-axis 4H-SiC or 6H-SiC semi-insulating and conductive chemically mechanically processed substrates. SiC substrate are hydrogen etched prior to growth to remove a few tens of nm upper SiC, damaged in the polishing procedure. Etching is performed in the same conditions as applied for graphene deposition, i.e. $T = 16\,000$ C, $P = 100$ mbar. Hydrogen flow is not as critical as etching time, and was adjusted to 5 min.

The best graphene was grown at a pressure ~30 mbar under anAr laminar flow in hot-wall reactors, where graphene growth on the 4-inch SiC substrate was also developed. Application of CVD to graphene manufacturing enables to obtain thick rotated graphene films on the C-face $(0\,0\,0\,\bar{1})$SiC. It is also possible to obtain a several graphene layers on the Si-face, which is not easy in the case of Si sublimation.

CVD graphene has been studied for both the Si-terminated and C-terminated SiC. However, more attention was directed to SiC(0 0 0 1) since Si-face slower growth kinetics allows a better control of the N. Similarly to the sublimation growth method, the first layer to form on the Si-face is the buffer layer. Hydrogen intercalation decouples the CVD grown buffer layer from the SiC substrate forming a QFSLG. The use of CVD facilitates the formation of 3LG however, owing to its high structural quality, hydrogen diffusion through those layers is practically unattainable.

QFSLG exhibits much μ than SLG on the Si-face, and T independent μ. This is desirable for high-speed electronics. The carriers change from electrons for SLG on the buffer layer, to holes for QFSLG. H_2- intercalated SLG exhibits higher μ than the un-intercalated one.

QFSLG on the Si-face is also largely resistant to photoresists and solvents applied with standard processing techniques. Hydrogen presence is maintained up to 700 °C, high enough to meet the requirements of high-speed electronics and high-T sensing [746, 1746, 1747]. The intercalation of hydrogen was achieved *in situ* during the sample cool down, by switching Ar to hydrogen at 1100 °C at ~900 mbar. Cooling in H_2 keeps hydrogen atoms trapped between graphene and substrate. Prior to unloading the sample, the process gas is changed back to Ar.

X-ray and TEM experiments show an increase in interlayer spacing in hydrogenated graphene to 3.6 Å–3.8 Å, proving that hydrogen goes between the C layer and the SiC substrate and increases the separation distance between them, along with decorating Si dangling bonds on the Si face [747].

Raman maps are shown in figure IV.26. The I(G) and Pos(G) maps demonstrate that the SiC surface morphology has terraces and step edges, as expected from step bunching at high T. The single Lorentzian fitting and the FWHM (2D)~35 cm^{-1} indicate that the areas are SLG or decoupled multiple SLGs. On the steps, the I(G) is higher and the 2*D* peak is blue-shifted and broader (FWHM (2D)~62 cm^{-1}), consistent with BLG.

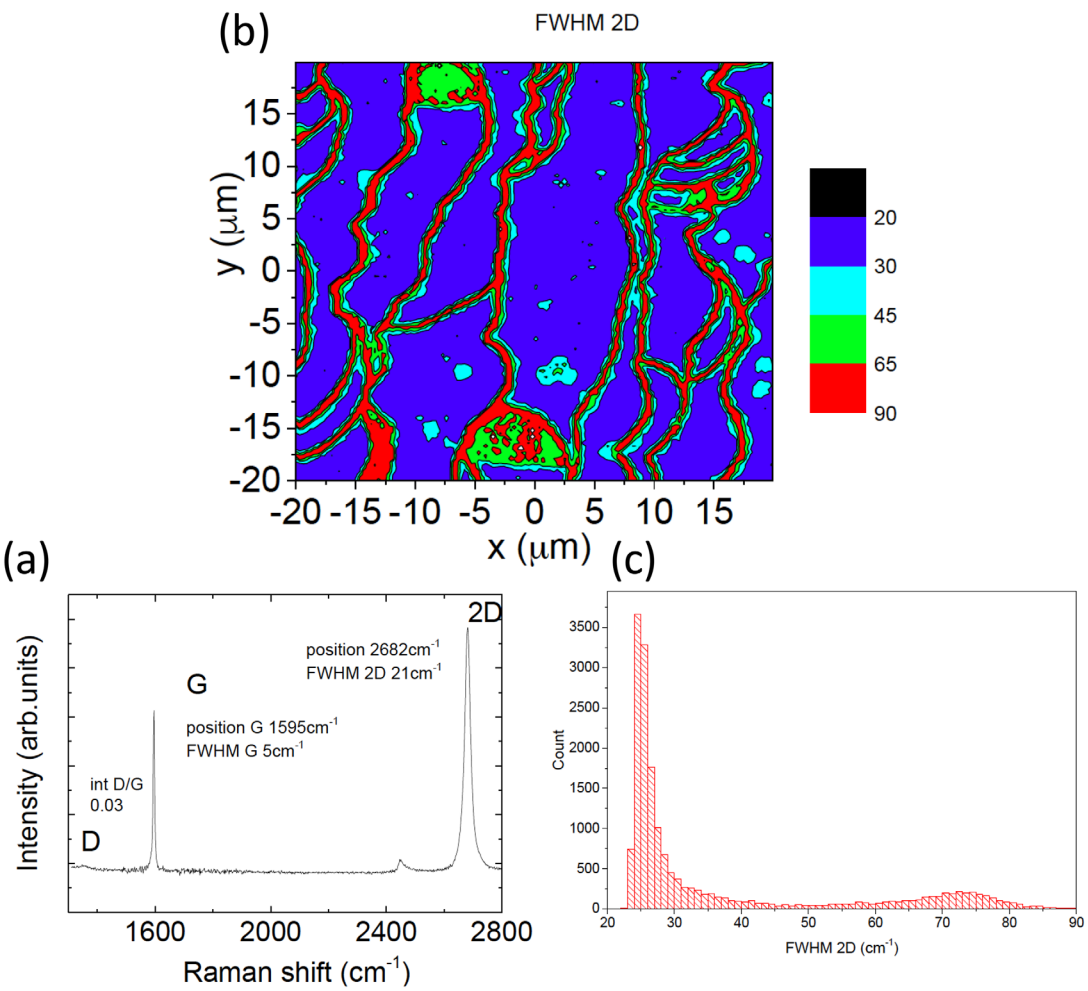


Figure IV.26. Raman measurements of SLG grown by CVD on SiC (SiC Raman peak subtracted) (a) spectrum, (b) map 20 mm × 20 mm (BLG on the step edges is depicted in red), (c) histogram of FWHM(2D) [751].

This process leads to the formation of a step-terraces structure. The steps remain within the nm range and are typically limited to 20 nm in height. The step edges follow a general parallel alignment. Regardless of N, there is an additional layer at the step underneath the primary layers. As a consequence, we get BLG at the step edges, [712, 748, 749].

Electrical parameters were measured focusing on large-scale and statistical parameters. The μ and n of multiple as-grown and hydrogen intercalated samples were characterized using Hall effect measurements on 10 mm × 10 mm in the van der Pauw geometry in ambient conditions. The n and μ were ~ 1.5×10^{13} cm^{-2} and ~ 1400^{-1}, 800 $cm^2 V^{-1} s^{-1}$, respectively. After intercalation with hydrogen: $n \sim 8 \times 10^{12}$ cm^{-2} and μ ~ 6500 $cm^2 V^{-1} s^{-1}$ for 10 mm × 10 mm MLG [747].

As expected, the electrical properties differ on the terraces and if there are step edges crossing the device. The step edges prove more resistive and, therefore, introduce a significant anisotropy [748]. CVD allows the fabrication of a large number of devices (here 320 Hall structures). Excellent performances were achieved, with $\mu > 7000$ $cm^2 V^{-1} s^{-1}$, measured for devices (sizes of 5 × 5 μm^2 and 10 × 10 μm^2) located on a single terrace, of widths ranging from 3 to 15 μm. Structures with a single transecting step exhibit μ~4500–6500 $cm^2 V^{-1} s^{-1}$, and structures with 2–3 transecting steps have μ~3500–5000 $cm^2 V^{-1} s^{-1}$. Improvements in μ are likely to be observed in SLG with large uniform terraces [750].

QFBLG is also p-type doped, typically in the range between $+8 \times 10^{12}$ cm^{-2} and $+1 \times 10^{13}$ cm^{-2} for 6H-SiC and between $+1.1 \times 10^{13}$ cm^{-2} and $+2.5 \times 10^{13}$ cm^{-2} for 4H-SiC. A correlation was observed between μ and n. The highest quality and μ are associated with the hole concentration approaching a well-defined substrate-dependent values, consistent with defects augmenting the doping level [714]. The scattering at the step is attributed to a lower n at the step (sidewall GNRs were reported to be charge neutral [620]), and to disorder near the step edge.

Because step edges are believed to result from SiC surface etching in hydrogen prior to graphene growth the anisotropy calls for a etch shortening. However, after a milder H_2 etching, the transport parameters were reported to be worse, in the reverse proportion to the steps height. This can be understood by a higher step density (for the same substrate miscut angle) interfering with the device size. There is thus a need to optimize the crystal surface with low step height (no higher than a SiC bi-layer).

V. CVD, PVD & MBE

V.1. Growth on metals

In this section we will discuss the growth of graphene on metals by : (1) CVD; (2) physical vapour deposition (PVD); (3) diffusion and precipitation; and (4) molecular beam epitaxy (MBE). In addition, we discuss the various growth techniques with respect to reactor design, precursor delivery, substrates heating options, and growth T. There have been many reports on growth on many elements and alloys and, while we understand many of the growth mechanism, there is still a lot more work to be done. Graphene film transfer is discussed in section VI.

The flexibility and pervasive success of CVD has made it a process of choice for the growth or deposition of many materials. Growth of graphite films, given its refractory nature, has been a challenge and many researchers have resorted to the use of catalysts [752–755]. These ideas have been expanded to the growth on metallic substrates by delivering hydrocarbon precursors in a CVD geometry [756, 757, 765]. One of the challenges in the growth of graphene on Ni and Co is the precise control of N [758]. SLG is difficult to grow Ni [756]. It is also difficult to grown MLG with a controlled N on Ni and Co, especially when CH_4 is delivered at low pressure. However, there are indications that when the Ni surface is exposed to CH_4 at atmospheric pressure and CH_4 dissociates into C on the surface of Ni, a more uniform graphitic film ensues upon cooling [762], growth on Cu led to the desired result of large SLG. The most striking results have been achieved on Cu using methane and hydrogen at low pressure, whereby where SLG was grown on over 95% of the metal surface at ~1000 °C in a few minutes [765]. This process is self-limiting due to the very low solubility of C in Cu [332].The transfer onto the substrate of interest is usually achieved by etching the metal subtrates [765] with various chemicals [763, 764] by electrochemical delamination allowing one to reuse Cu with a significant reduction in cost. Section VI provides a summary of the most commonly used methods.

There are many types of CVD systems. The selection of the specific system dependens on many factors. The ultimate objective is to produce a material at a competitive cost that meets the requirements. Here is a list of a few CVD approaches that can be considered/have been evaluated for the growth of graphene: (1) furnace system (horizontal or vertical) [765]; (2) single wafer cold wall reactor (resistively heated [766], flash lamps [767] (direct heating, top or bottom, or through a susceptor); (3) plasma PECVD [768]); (4) low-pressure CVD (LP-CVD); (5) atmospheric pressure CVD (APCVD) (continuous or single size substrate) [769–771]. In the case of graphene, the first and most common process is a furnace process [765]. The advantages are that the furnace is made of quartz which may be compatible with more precursors than a single wafer tool, multiple wafers can be loaded (e.g. more than 50 Si wafers) and low cost of ownership. The second most common growth system, is a single wafer tool [766] which has many advantages as well, flexibility in wafer to wafer processing, design of experiments in the development stage, heating system (lamps versus resistive and top versus bottom heating), base pressure control and clustering with other processes on a multi-chamber platform, rapid heating and cooling [767, 772, 773], etc. In applications where graphene grain size is not a critical factor, PECVD can also be used with the advantage of enabling lower growth T as well as much shorter growth times. This is particularly useful to grow graphene on insulators [774].

There are a few reports on the growth of graphene by photothermal CVD [772, 775] where, photochemical effects might be affecting growth. The principal advantage is fast heating and cooling that could be taken advantage of in the case of controlled layer growth of graphene on substrates with a higher C solubility than Cu.The rapid cooling can also benefit any effects that residual oxidants may have on graphene during cooling.

V.1.1. CVD growth on copper

The initial motivation to use Cu as a catalytic surface to grow graphene was to take advantage of the very low C solubility in Cu up to the melting point of Cu [776, 777]. This was expected to eliminate the need for a diffusion/precipitation mechanism[753, 778]. The binary phase diagram for Cu and C is shown in figure V.1. The solid solubility of carbon in Cu at 1100 °C is ~0.0076 w% at a T slightly above the melting point of Cu [777, 779, 780]. Mostly on this basis, it is argued that as CH_4 dissociates on the metal surface to form CH_x radicals at high T with the aid of the metal catalyst the resulting carbon atoms arrange in the form of graphene on the surface of Cu, thus creating SLG. This contrasts that on metals with a higher C solubility, where the C atoms dissolve and diffuse into the metal with subsequent segregation and precipitation at the metal surface upon cooling. Growth on Cu is limited largely to one monolayer [765, 781] for a low-pressure catalytic CVD process. The growth details were studied by using ^{12}C isotopes to try to understand whether graphene was growing directly on the Cu surface or precipitating from the bulk of the Cu substrate [781]. The Raman map of the isotopically labelled graphene transferred on a SiO_2 substrate showed that at least macroscopically graphene was growing directly on the surface at high T and not upon cooling as in the case of Ni [781]. The growth of single-crystal graphene domains with controlled edges with orientations that range from zig-zag to armchair via a CVD growth–etching–regrowth process was reported [782]. FLG are also observed on Cu. There are multiple sources of carbon that lead to the presence of the adlayers. First, some of the C dissociated on the surface of Cu dissolves into Cu and after growth at high T it diffuses to the Cu surface because of the lower solubility as the

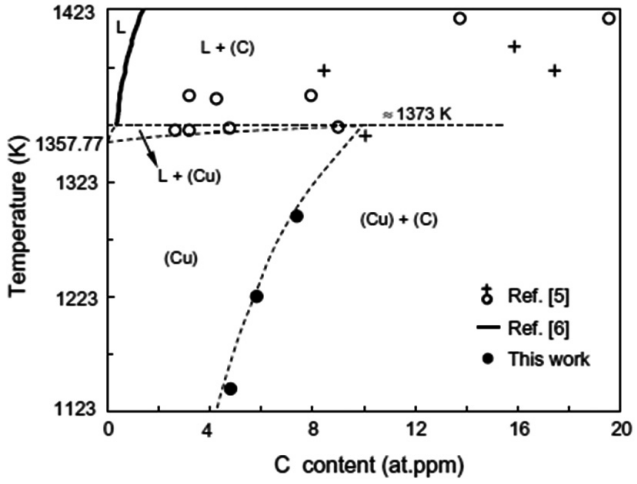


Figure V.1. Cu–C Equilibrium phase diagram at the Cu rich side, L is for Liquid Ref. [790].

Cu cools, and forms FLG under the already grown graphene [783]. These layers grow under the graphene on Cu as a result of precipitation upon cooling [783]. Even though it was reported that C might diffuse under the growing graphene to form FLG [784], it is more difficult to accept this mechanism since it does not take into account the C dissolved into Cu. If only the intentional C from the dissociation of methane were present, then a small percentage of the surface area would be covered with adlayers. However, in some cases many FLG have been observed across the surface of Cu/graphene and this can only be explained by the presence of other sources of C, and isothermal growth as a result of supersaturation [785]. It was also reported [791] that the surface of Cu can be covered with a high concentration of unwanted C from ambient, poor cleaning and cleaning using hydrocarbons.This can give rise to a high concentration of nuclei as well as FLG beyond the solubility limit of C in Cu [785]. The presence of the uncontrolled and unwanted C is also supported by anecdotal reports indicating that graphene can be grown on metal surfaces in the absence of a C precursor. Ref. [786], pointed out the importance of a high H_2/CH_4 ratio in the growth of SLG. The benefit of a high hydrogen concentration may arise from the details of the reactions at the metal surface, but also from the presence of excess oxygen in the growth chamber. This is highlighted by the fact, that graphene is etched during cooling in the absence of H_2 or CH_4 [787]. The effect of growth parameters such as T, and CH_4 flow rate and partial pressure on the growth rate, domain size, and surface coverage of graphene led to the definition of a 2-step CVD strategy for the growth of large single crystal graphene [788]. High-throughput growth of graphene on Cu foil was achieved at ambient pressure, interesting to reduce costs [789].

The graphene growth process on Cu surfaces to first order can be described by the following steps, [784, 786, 791–794]:

1. Cu surface cleaning/preparation prior to loading into the growth chamber
2. Surface cleaning and annealing in the growth chamber
3. Exposure to a hydrocarbon precursor with subsequent adsorption of the same on the Cu surface
4. Nucleation of graphene by the dissociating CH_x radicals and local supersaturation of C to form graphene nuclei
5. Surface diffusion of CH_x radicals and attachment onto the graphene edges
6. Dehydrogenation of the CH_x radicals attached to the graphene edges and dehydrogenation of some of the isolated CHx radicals with subsequent diffusion into the Cu
7. Coalescence of the growing graphene domains to form continuous polycrystalline films or single crystals.

Substrate selection, surface preparation, growth T and process are critical to achieve films that meet device requirements. Substrate surface quality, surface impurities, surface roughness and gas composition and pressure have large effects on the surface roughness, defects (Raman D-band), amount of FLG, and electrical properties. Graphene films of varying sizes, on Cu as well as other metal films have been grown in vertical single wafer cold wall reactors, horizontal furnaces [765], open continuous furnaces as well as in plasma enhanced single wafer systems [966]. Each one of these approaches requires optimization in order to achieve the desired results. Typically, growth conditions, such as reactor design, vertical versus horizontal, gas delivery system, precursor selection, heater, low versus high T growth, low pressure versus atmospheric pressure, must be considered and optimized. The aforementioned factors depend on material requirements as well as cost needed by a particular application.

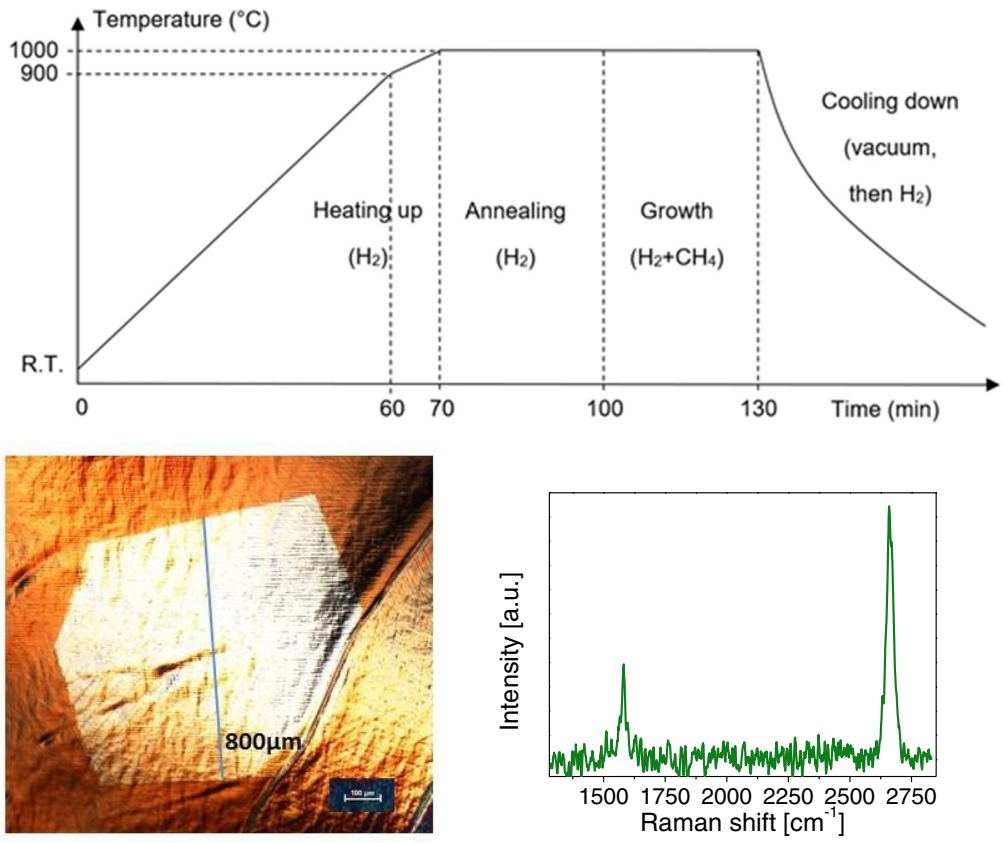


Figure V.2. (Upper) Schematic diagram of the thermal profile during graphene growth, type of gasses used and steps duration in case of growth SLG at 1000 °C, (Lower Left) Optical image of a graphene domain grown on molten Cu on a Mo substrate. Scale bar is 100 μm. (Lower Right) Raman spectrum of a graphene grown on molten Cu.

Typically, graphene is grown on Cu foils [332], Cu thin film on sapphire, and bulk Cu single crystal foils [782, 794–796]. The most commonly used Cu foils are of a high-purity 99.9999% in a variety of thicknesses and sizes. In addition, oxygen [783, 791], carbon and other impurities [785] in or on Cu are have large effects on the growth mechanism. The quality of graphene will depend on the quality of the Cu surface morphology and crystallographic orientation. The surface of the metal can be improved by electropolishing [769, 770, 786] Many experiments have been performed on Cu annealing [797, 798], heating the substrate to T above the melting point of Cu,[799, 800], Cu surface oxidation, [786, 790, 802], using Cu with controlled crystal orientation [786] and oxygen free Cu [791]. Growth of graphene on bulk single crystals or single thin films of Cu would be advantageous. It would be ideal to grow high quality graphene directly on a dielectric surface Ref. [802] diffused C on thin Cu on SiO_2 to grow graphene directly on the dielectric surface. However, at the films grown using this process are still not of high enough quality to compete with films grown directly on the metal surface. For a more extensive discussion on the growth of graphene on dielectrics, see section V.3.

Growth of graphene on Cu metal has been carried out in horizontal tube furnaces [765] as well as in cold walled single wafer tools [766, 803] and even at higher T [799, 804] than the Cu melting point, 1084 °C, using any one of several hydrocarbons (such as methane or ethylene), ethanol hydrogen and argon are also used [799, 804]. The effect of the H_2/CH_4 ratio on the shape of graphene domains has been widely reported [786, 800, 801]. Low pressure CVD with very low precursor flow rate has been effective in growing large area graphene filmsVarious other methods of heating the substrate have been use in addition to resistive heating, such as magnetic inductive heating [805] and a hybrid process combining hot filament and resistive (thermal) heating [806], but these techniques have not been widely adopted yet. Growth has also been carried out in the presence of a plasma in an attempt to reduce the growth T well below 800 °C.

A typical growth procedure is shown schematically in figure V.2. Prior to growth high purity Cu substrates (foils) having a thickness ranging from 25 to 35 μm and of a desired surface area are procured. The are then cleaned in acetic acid for ~10 min and then transferred in de-ionized water for additional 10 min and dried with N_2. After, the Cu foil is introduced in the growth chamber and the chamber is evacuated and back filled with H_2 to a desired pressure. CH_4 and H_2 are usually circulated to purge the lines (50:50 sccm) at pressure <4 mbar prior to substrate heating. The chamber *T* is then increased to 1000 °C under 20 sccm of H_2 in 70 min (see figure V.2 upper frame). *T* is then

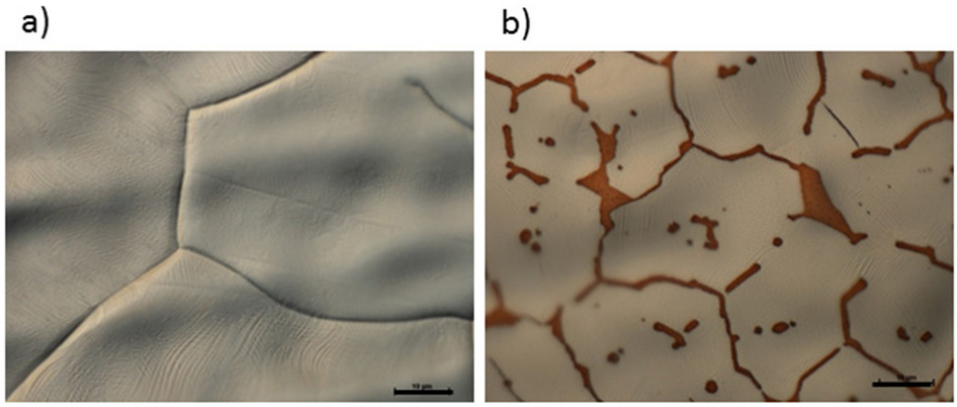


Figure V.3. Optical images of (a) continuous and (b) discontinuous graphene films on Cu.

kept constant at 1000 °C for an additional 30 min. During this last step, the Cu substrate T and microstructure are stabilized. Heating of the Cu foil to the growth T can be performed also in Ar and then in H_2 gas flow at a pressure $<$100 mbar. The purpose of this step is to promote grain growth of the Cu foil. A 'standard' graphene growth process follows: 5 sccm of CH_4 or C_3H_8 are then flowed for several minutes (typically ~30 min), after the growth phase, the substrate is cooled to RT by translating the furnace away from the substrate. The cooling can be done with the precursor flowing, hydrogen flow or under vacuum. The ambient during cooling is also critical especially in cases where the base pressure of the chamber is too high. In this case leaking oxygen can etch the graphene at the highest T. Once T is near RT, the gasses are closed off and the chamber is evacuated and back filled with an inert gas to one atmosphere. Growth of graphene on polycrystalline Cu foils using this process flow usually yields films with a grain size ~10 μm. By applying a longer annealing time, higher T, lower pressures, and by maintaining optimal hydrocarbon flow or melting the Cu, the domain size can reach several millimeters [807]. The lower frames in figure V.2 illustrate that domains ~800 μm can obtained systematically optimizing the CVD growth conditions and also show the corresponding Raman spectrum.

Optical microscopy with Nomarski contrast, i.e. differential interference contrast (DIC) microscopy, is very useful (see figure V.3) to explore the quality of the Cu substrate surface as well as the grown graphene. DIC microscopy can expose cracks and micro-holes in the graphene layer and can provide information on microstructural changes before and after anneal that can be correlated with graphene film quality.

Raman spectroscopy has been demonstrated to be the best characterization technique to confirm the presence of SLG on the Cu substrates [1748]. The technique is introduced in section IX.2.1, where representative spectra of SLG, BLG, etc are also given. Measurements performed by SEM plotted in figure V.4 can identify dark areas interpreted as adlayers of graphene. In addition, wrinkles formed during cooling from high T because of the large difference in the coefficient of thermal expansion between graphene and Cu are also visible as narrow lines criss-crossing the surface of the graphene. If Cu of lower quality (purity 99.9% or 99.999%) is used, e.g. Cu_5N and Cu_3N, the films are heterogeneous mainly in terms of their thickness. In figure V.4 light grey color represents areas with SLG.

Atomic resolution images of graphene on Cu as measured by STM (see section IX.1) presented in figure V.5 show the configuration of the carbon atoms in SLG. The corresponding Fourier transform of the STM image (upper right inset) indicates that the maxima correspond to the pattern formed as a result of the orientation of the SLG in relation to the substrate (lattice mismatch). The figure V.5 shows an area 3 $\times$ 2.2 nm with a graphene unit cell drawn upper left inset) exhibiting a lattice constant of 2.44 Å [812]. The shape, orientation, edge geometry, and thickness of CVD graphene domains can be controlled by the crystallographic orientations of Cu substrates [1749]. At the inception of the growth phase, during the nucleation stage, the Cu roughness plays a key role. The Cu-active sites are imperfections on the Cu surface, such as grain boundaries, irregularities or areas of coarseness, or surface impurities. It is at these defects that most of the graphene nuclei are formed. The higher the density of nucleation sites, the smaller the size of the graphene domains. The density of these grain boundaries is expected to affect electrical, chemical, and thermal properties, and it is thus necessary to optimize the graphene film properties according to the application requirements [808–811].

For some applications large (square meters) areas of graphene may be needed, as it is the case for the functional coating of large pieces of other materials. When growing graphene on 500 $\times$ 500 mm^2 Cu substrates, the T uniformity across the metal substrate must be controlled since the nucleation and growth characteristics has a large T component [755]. The control of the Cu metal foil T is critically important when growing films at T close to the Cu melting point as shown in figure V.6, where part of the Cu foil melted at the edges, due to an uneven T distribution across the Cu film. Ref.

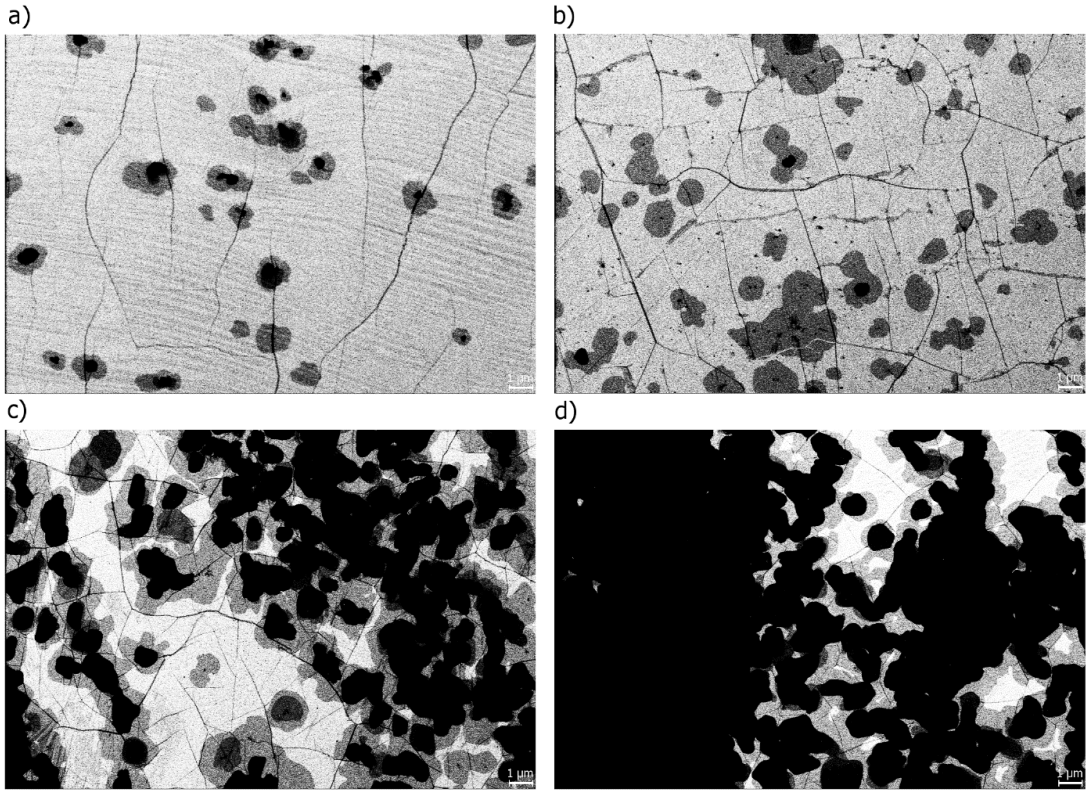


Figure V.4. SEM images of graphene layers on (a) Cu_mono, (b) Cu_6N, (c) Cu_5N and (d) Cu_3N substrates. Scale bars are 1 μm.

[794] reported the growth of 5 × 50 cm^2 single-crystal graphene on industrial Cu foils. They first transformed industrial polycrystalline Cu foils into single-crystal Cu(1 1 1) by thermal annealing using a T-gradient-driving technique. Then graphen grains growon the Cu(1 1 1) substrate and seamlessly mergeto form a large single-crystal graphene film.

This technique allows the synthesis of large-size single-crystal graphene films, with superior properties for various high-end applications, especially in electronics, such as large-scale fabrication of THz devices and transparent conductive film to replace ITO. It will also enable the growth of various other single-crystal LMson graphene

There are many alternatives for substrate heating, ranging from magnetic inductive heating [805] to hybrid processes, combining hot filament and resistive (thermal) heating [806]. Among them, photothermal heating (PT-CVD) provides up to 100 °C min^{-1} heating and cooling rates [767, 772] while keeping the chamber walls cold. The system is based on a halogen lamp-heated rapid thermal processing (RTP) (for up to 300 mm wafers), where gas lines (CH_4, H_2 and Ar) and their mixing manifolds are incorporated. While keeping the RTP chamber walls cold. This, together with the fast growth process, less than 1 min, helps to reduce the contamination from the walls. In this case, the cleaned Cu foil is placed between two silica plates on a photothermally heated Si- or SiC-coated graphite susceptor. Silica is needed between Cu and Si to prevent reactions between them. The growth process starts by annealing the Cu foil for 5 min at ~935 °C (as measured by a pirometer) and pressure ~7–20 mbar. Next, CH_4at a flow rate of 15 sccm (CH_4/H_2 mixture 4:1) is introduced into the chamber. Under this condition a continuous SLG film is grown on Cu in a few tens of seconds, one order of magnitude faster than in thermal CVD using similar growth parameters. The SLG coverage is ~94% in films grown in 60 s at 950 °C. The SLG contains very small adlayer flakes, and defects (~3 × 10^7 cm^{-2}) [775, 813]. The light from the RTP lamps enhances the catalytic effect of CH_4 on the Cu surface without generating defects. The grain size is in the μm range. Ref. [773] reported a rapid thermal CVD (RT-CVD) suitable for mass-production. In this setup, Cu foils are loaded vertically in the reactor, in which 24 lamps heat vertical graphite receptors around the Cu foil. They obtained a growth rate 7 times higher than thermal CVD using hydrogen-free N_2 carrier gas [773].

It would be desirable to grow graphene at low T for ease of process, equipment, contamination, as well as potential substrate melting issues. Ref. [814] reported growth of graphene on SiO_2/Si, plastic and glass at close to RT (25–160 °C). However, in most cases the reported reduction in growth T_g/T_{mp}(C) is very small ($\leqslant$0.30) and for most materials the quality of the grown crystals is higher when the growth T is close to the melting point. There have been some reports on the growth of graphitic films at low T by CVD [815], plasma assisted [816] and from solid sources [814, 817] on or under Ni films but not on Cu. Growth

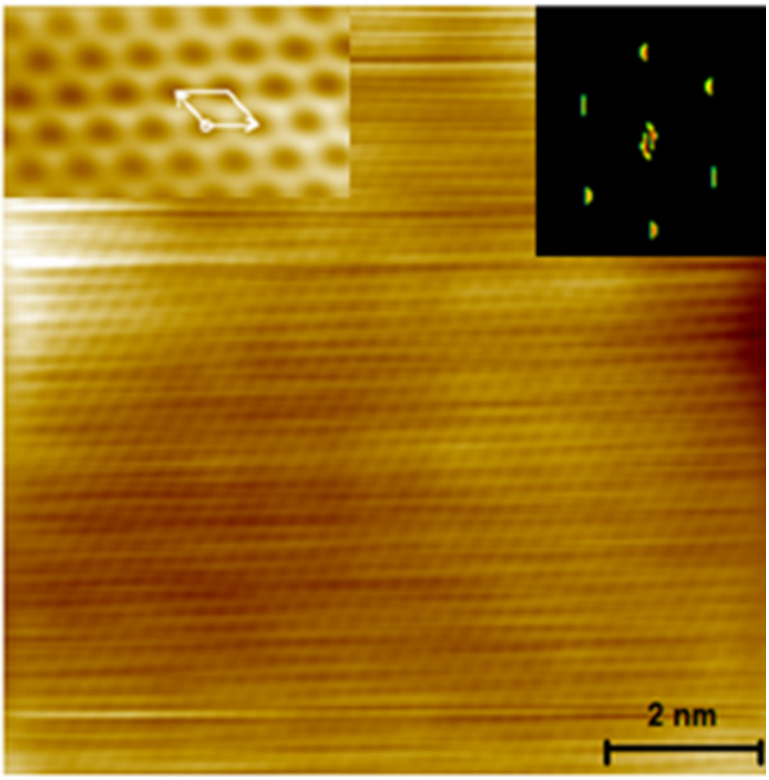


Figure V.5. Atomic resolution STM of graphene on a Cu mono-crystalline substrate with the Fourier transform (upper right inset). Adapted from [812] with the permission of AIP Publishing.

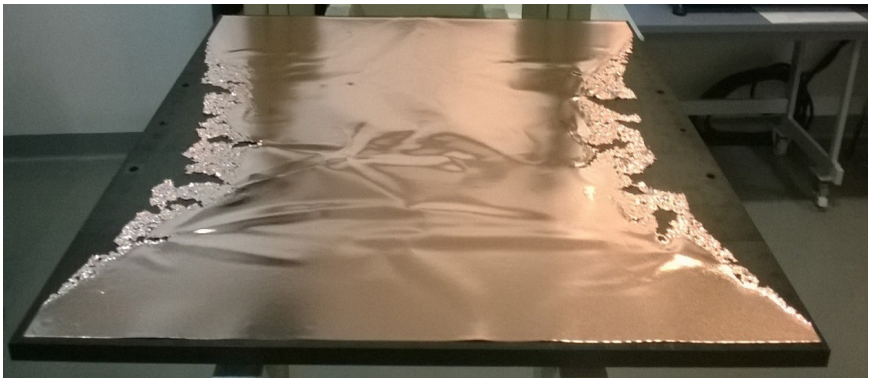


Figure V.6. Higher T near the edges of the substrate causes local Cu melting while the inner part is unaffected.

at low T on Cu, Ni or Cu-metal alloys could be of great interest, but the grown graphene could contain many defects, as in the case of low T crystal growth of many other electronic and optical materials.

V.1.2. CVD growth of large graphene single crystals

As in the case of crystalline semiconductor materials, it may be advantageous to grow single crystal graphene films in order to minimize scattering effects by pure grain boundaries and grain boundaries that may react with ambient species such as OH, hydrocarbons, etc. Also, the presence of grain boundaries and their tilting has been studied in relation to the mechanical properties of the synthesized graphene [811].

Graphene has been demonstrated to grow on Cu surfaces by a nucleation and growth mechanism [765, 781, 818] predominantly by a surface limited process, because of the low solubility of C in Cu. The films grown using this process are polycrystalline, with a grain size that depends on the specific growth process conditions and they can range from less than one micron to hundreds of microns. Therefore, in order to increase the grain size, one would have to reduce the nucleation density on the surface of the metal. Various approaches were developed to achieve this, such as reducing precursor flow by using a Cu pocket [128, 766, 819, 820]. An example of such pocket is shown in figure V.7(a).

The growth of large graphene single crystals led to the demonstration of very high μ in CVD graphene comparable to that of mechanically exfoliated flakes [821]. This is an important result since it has

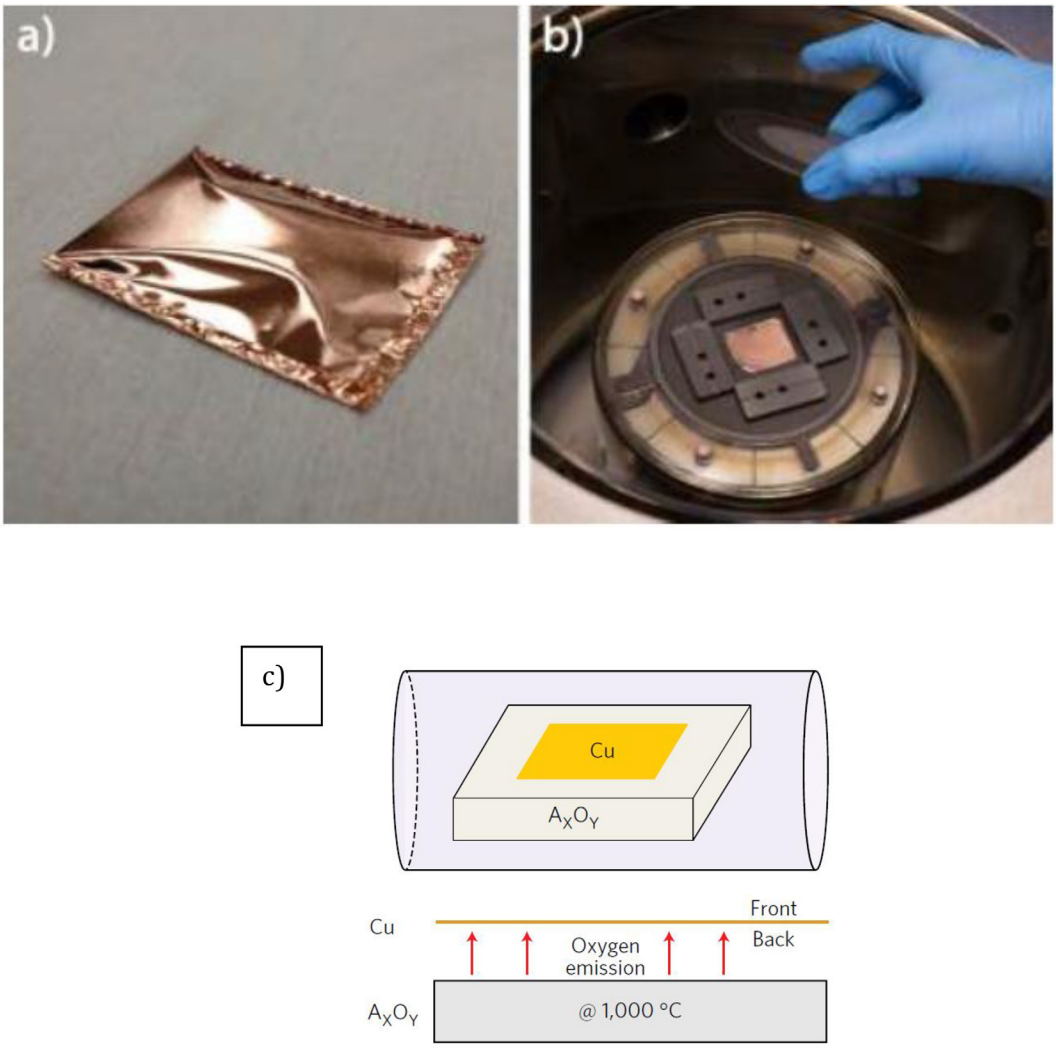


Figure V.7. (a) Cu 'pocket' enclosure. (b) Enclosing flat Cu foil with a quartz cover. (c) growth of graphene on Cu assisted by a continuous oxygen supply. Adapted from [766] (© IOP Publishing Ltd) and [825] (© Springer Nature).

led to focused efforts on further understanding of the graphene single crystal growth as well as transfer [807, 822–824].

Further reduction of graphene nucleation density was investigated by Ref. [783, 791], who showed that graphene single crystals on polycrystalline Cu of over 1 cm could be grown after treating the surface of Cu with oxygen. However, this process is time consuming, growth times of over 10 h were used to grow 1 cm single crystals. Oxygen not only passivates the Cu surface, leading to reduced nucleation density, it also significantly speeds up the growth of graphene crystals by changing the growth regime from diffusion to edge-attachment-limited. A further explanation on the decrease of the nucleation density on the surface of Cu was provided by Ref. [785], where they observed that the surface and the bulk of the Cu foils may be contaminated with impurities including C which can aid in the formation of graphene nuclei. In this case, Cu oxidation prior to graphene growth removes carbons from the Cu surface leading to a lower nucleation density. Following the Refs. [791, 826], Ref. [825] used a solid source of oxygen, A_xO_y—e.g. SiO_2/Si, to provide a continuous source of oxygen under the Cu substrate while providing the hydrocarbon precursor at atmospheric pressure (see figure V.7(c)). This process led to a growth rate~60 μm s^{-1} instead of~0.3 μm s^{-1} of Ref. [791]; this is a major improvement. Another approach to reducing the graphene nuclei density on the Cu surface was performed by treating the surface with melamine [827]. This process led to the growth of 1 cm graphene domains with μ reaching 25 000 $cm^2 V^{-1} s^{-1}$ for graphene transferred onto SiO_2/Si. Another method was proposed taking advantage of the residual oxygen in the CVD furnace for increasing the graphene domain size beyond one millimeter, and simultaneously promote recrystallization of a polycrystalline Cu foil in the (1 1 1) structure through a peculiar 'abnormal grain growth' mechanism [828]. The process yields aligned high-quality graphene single crystals smoothly merging together, with a crystal alignment maintained over few centimeters (in 1 hr).

In general, the following critical conditions should be met in order to grow large crystals: (1) suitable

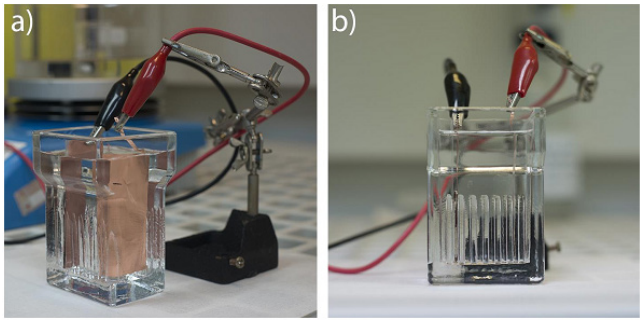


Figure V.8. Electropolishing set-up. (a) Three-quarter view. (b) Side view, showing the parallel orientation of the copper foil and the counter-electrode. Adapted from [766], © IOP Publishing Ltd.

substrate, (2) substrate surface cleaning and polishing prior to loading in growth chamber, (3) surface pre-treatment (oxidation, the use of melamine or other surface treatment), (4) enclosing the sample to limit precursor flow, and (5) a non-reducing surface treatment at high temperature prior to growth.

Substrate preparation is a very important first step in order to create a clean and flat surface. Many approaches can be found in literature [583, 819] on mild surface etching using acidic solutions [791, 820, 829]. However, the most reproducible surfaces have been prepared by electropolishing [766, 807]. The solution used for electropolishing has a volumetric composition of 45% water, 25% phosphoric acid, 25% ethanol and 5% isopropanol. To increase viscosity, 0.5% (weight) of urea is added. Electropolishing is performed by applying a voltage between the sample (anode) and a Cu plate cathode. A typical electropolishing procedure is 30 s at 12 V, with a cathode-anode distance of 4 cm. To ensure homogeneous polishing, it is important to keep the electrodes parallel. For this one can employ a Coplin glass staining jar as the electropolishing vessel (figure V.8(a)), which has grooves to keep the foil and the counter electrode in place, figure V.8(b). Following the electropolishing, it is important to rinse the samples under running DI water to completely remove the viscous electrolyte, followed by a quick rinse with isopropanol. Finally, the samples are dried with compressed nitrogen.

Owing to the catalytic nature of the Cu surface, it is important to reduce the carbon precursor flow impinging on the sample in order to reduce the nucleation density [755]. One of the most commonly-used approaches is to grow large SLG crystals inside 'pockets' formed from Cu foil, [128, 783, 791, 819, 820]. The discovery of large graphene crystals inside a Cu pocket led to the investigation of other methods to achieve similar results, for example a Cu tube [807], a sapphire cap over the Cu surface to minimize evaporation and the 'hydrocarbon' concentration [830], or placing a quartz plate on top of a flat Cu foil at a desired distance from the Cu surface [766]. The process conditions to achieve the largest single crystals will have to be optimized and perhaps combined with the use of Cu single crystals. Ref. [796] reported a comprehensive study of the evolution of the crystal morphologies grown inside Cu enclosures as a function surface orientation, absolute pressure, hydrogen-to-methane ratio (H_2:CH_4), and nucleation density At low pressure and low H_2:CH_4, circular graphene islands initially form. After exceeding ~1.0 μm, Mullins-Sekerka instabilities [1750] evolve into dendrites extending hundreds of micrometers in the ⟨1 0 0⟩, ⟨1 1 1⟩, and ⟨1 1 0⟩ directions on Cu(1 0 0), Cu(1 1 0), and Cu(1 1 1), respectively, indicating mass transport limited growth. Increasing H_2:CH_4 results in compact islands that reflect the Cu symmetry.

The nucleation density and growth rates are affected by the growth pressure and gas flow rates. While low pressure can help to radically reduce the nucleation density, it can also lead to extremely slow crystal growth. With a gas flow of~1 sccm CH_4, 900 sccm Ar and 100 sccm H_2, the graphene nucleation density is on the order of several crystals per mm^2 and typical growth rates are ~15 μm min^{-1}, allowing the synthesis of 1 mm-sized crystals in ~1 h. The use of Ni–Cu alloys will enable much higher growth rates due to the higher catalytic activity of Ni [831]. Figure V.9 illustrates the effect of using a nonreducing atmosphere and sample enclosure on oxidised Cu.

When hydrogen annealing is used, the nucleation density is ~10 000 cm^{-2} (a). Annealing in an Ar atmosphere reduces the nucleation density to ~1000 grains per cm^{-2} [128, 791]. Substrates annealed in argon and placed inside an enclosure have a nucleation density ~10 grains per mm^{-2} or lower, enabling the growth of large crystals. Figure V.10 shows a schematic diagram of the graphene growth process in a pocket and the image of a graphene single crystal grown inside the pocket. The interface between SLG and Cu (1 1 1) oxidises under ambient conditions within a few days, making SLG visible and decoupled from Cu. This is required for a reliable dry pick-up using h-BN [832].

There have been many observations on the shape of graphene domains on different Cu grains having varied crystallographic orientation [786, 1751]. The shape varies depending upon the Cu orientation as well as the growth conditions and Cu oxidation state [755, 791]. It has also been reported that growth of graphene domains on oriented Cu(1 1 1) foils [794] and Cu(1 1 1) thin films on sapphire [830] under

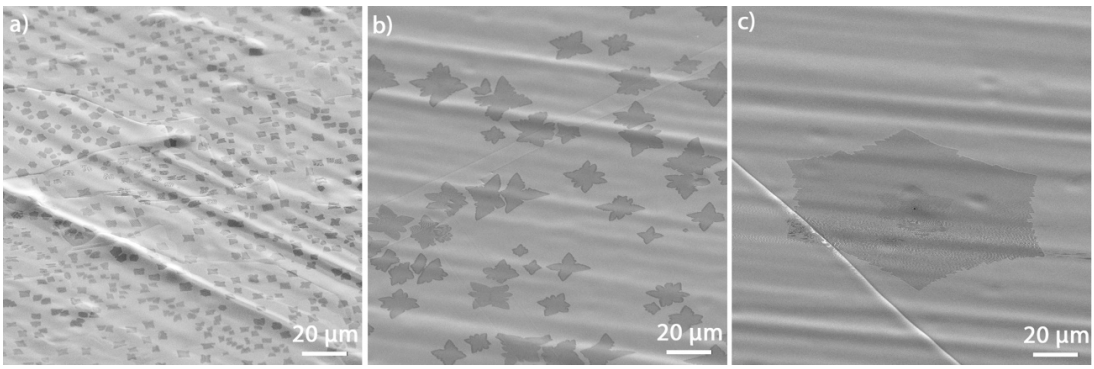


Figure V.9. Nucleation density of graphene when using (a) hydrogen annealing, (b) argon annealing (c) argon annealing and sample enclosure. Adapted from [766], © IOP Publishing Ltd.

certain process conditions are aligned. As the domain growth progresses, the domains merge to form single crystals as the Cu surface becomes fully covered by a boundary-free stitching. This is true in the case where the domains are aligned and the Cu surface is nearly atomically flat [583, 833]. The advantage of this process, if large area Cu(1 1 1) films or foils are available, is that the growth time can be significantly reduced in comparison to the single nuclei approach. Efforts have been dedicated to the growth large Cu single crystal foils [833] and [831]. More recently, a gas-flow-driven aligned growth of graphene on liquid Cu has been achieved [834]. Another method of preparing large area Cu(1 1 1) crystals is to take advantage of the epitaxial nature of Cu on c-plane sapphire and thicken the thin film using an electrodeposition process, after which Cu(1 1 1) can be peeled off from the sapphire substrate [835]. Significant activities are ongoing to optimize the growth of graphene on controlled Cu surfaces in an effort to grow high quality crystals in production worthy growth systems [836].

It would be advantageous to be able to grow single crystal graphene from a single nucleus as for bulk single crystals. Wu *et al* [837] used Ni–Cu alloys to increase the catalytic activity in conjunction with a localized precursor delivery technique to grow graphene single crystals over 3 cm in diameter. The growth mechanism of graphene on Ni–Cu is more complex than on Cu or Ni and further development would require precise composition identification/selection in order to ensure single layer growth and full coverage by a single graphene grain. Ref. [838] reported the synthesis of single-crystal-like SLG on polycrystalline substrates. The method relies on 'self-selection' of the fastest-growing domain orientation, which eventually overwhelms the slower-growing domains and yields a single-crystal continuous film.

In summary, the growth of high quality, large area, single crystal graphene can be performed in several ways on:

(1) Growth on conditioned Cu substrates (oxidized or treated with melamine) under low pressure conditions (slow growth rates, size up to 1 cm)
(2) Growth on Ni–Cu substrates with a localized precursor delivery (relatively high growth rates)
(3) oriented single crystal Cu(1 1 1) foils
(4) thin Cu(1 1 1) films on sapphire substrates
(5) thick predominantly Cu(1 1 1) on sapphire followed by a peeling process so as to facilitate sapphire re-use.

V.1.3. CVD Deterministic seeded growth on Cu

Seeded graphene growth was reported by Ref. [839] patterned and etched CVD graphene patches were used as nuclei for the subsequent single crystal graphene growth. However, because of the polycrystalline nature of the starting graphene film, the resulting crystallites were not aligned but each crystal was hexagonal. In a subsequent study [840] pre-annealed foils were patterned with arrays of crosslinked PMMA, then used as a carbon source for the growth of single-crystal arrays. In both cases the array periodicity was ~20 μm and crystal size of up to ~15 μm. Due to the much lower nucleation densities required for large-crystal graphene, carbon-based seeding was found not to be robust enough for controlled growth of large-periodicity arrays. Metallic nucleation seeds were chosen instead for large-crystal graphene arrays. Ref. [841] used Cr as the nucelation sites for localized single crystal growth of graphene.

The nucleation seeds can be patterned by performing optical lithography on electropolished Cu using positive photoresist, followed by thermal evaporation of 25 nm Cr and lift-off in acetone. Cr was chosen because of its high melting point [1752], ensuring that thin films are not evaporated during the annealing of the foil and instead form particles that can act as nucleation points on passivated Cu. Spots with a diameter ~5 μm and a thickness ~25 nm lead to the most reproducible results [841]. Smaller seeds or lower film thickness did not ensure reliable seeding, whereas larger spots were sometimes found to initiate the nucleation

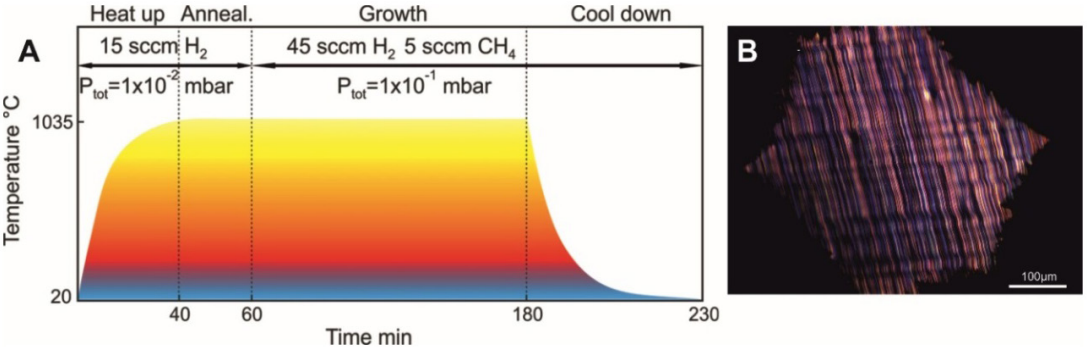


Figure V.10. (a) Typical growth scheme for a low pressure CVD process for SLG on Cu. (b) Optical dark field microscopy image of SLG on Cu foil using the process depicted in (a). Panel (B) is adapted from [832], with permission from AAAS.

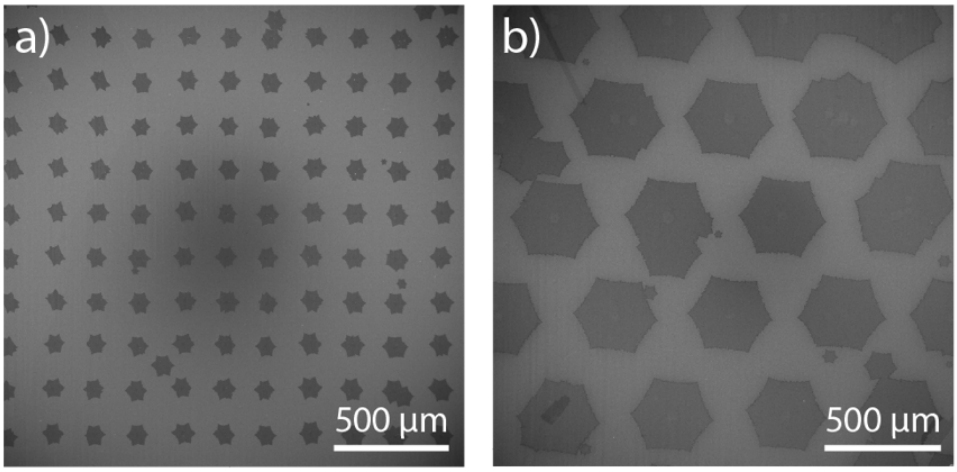


Figure V.11. Seeded arrays of large-crystal graphene. (a) Array with 200 μm periodicity and 100 μm crystal size. (b) Array with 500 μm periodicity and 350 μm crystal size Adapted from [841].

of several separate crystals. By changing such flow ratio, it is possible to control the presence of residual Cr seeds during the growth by changing the CH_4:H_2 flow ratio. After growing graphene using a H_2:CH_4 ratio of 20:1, particles of Cr are found at the centre of seeded crystals, whereas when using a H_2:CH_4 ratio of 100:1, Cr seeds are removed. Growth was carried out in a 4-inch Aixtron BM Pro. All gases used in the CVD process had purities of 99.9999%. As shown in figure V.11(a), arrays with a periodicity of 200 μm show high nucleation control, with less than 10% of non-seeded nucleation. At larger periodicities (see figure V.11(b)), sporadic nucleation was slightly higher. Well-ordered arrays of crystals with a diameter of several hundred microns can be synthesised [841].

We now discuss the growth of single crystal graphene with controlled edge structure. Two types of graphene crystals have been grown: (1) dendritic, and (2) hexagonal [791]. The shape of the graphene crystals was controlled by the presence (dendritic) or absence (hexagonal) of oxygen on the surface of the Cu for low pressure CVD. Ref. [842] reported the growth of 100 μm hexagonal graphene crystals on polished Cu foils at one atmosphere, with limited carbon flow, with the crystal edges dominated by the zigzag direction. Controlling the graphene edges may be important for some electronic applications and growth conditions to optimize quality and growth rate(cost) should be investigated. Another important point is the growth of edge-controlled graphene in the smallest dimensions (nm scale) and the treatment of graphene after patterning and etching to set the edge structure.

V.1.4. Low pressure & low temperature CVD

It is desirable to grow film at low T not only because of the integration device flows, but also to overcome problems associated with substrates like Cu. One issue with CVD of graphene on Cu from CH_4 is that the optimum growth conditions are typically at $T > 1000$ °C, very close to the Cu melting point of 1084 °C or even above its melting point. Cu has a vapor pressure ranging from 8.1×10^{-8} atm to 5.7×10^{-7} atm for the T range ~ 1000 –1084 °C [843]. During annealing and graphene growth at low background pressures a measurable amount of Cu is transported by the flowing gasses away from the Cu surfaces. The presence of Cu on the surface of the quartz tubes in the case of a furnace or the metal surfaces in the case of cold wall reactor can make the cost of ownership high, since the growth systems has to be cleaned on

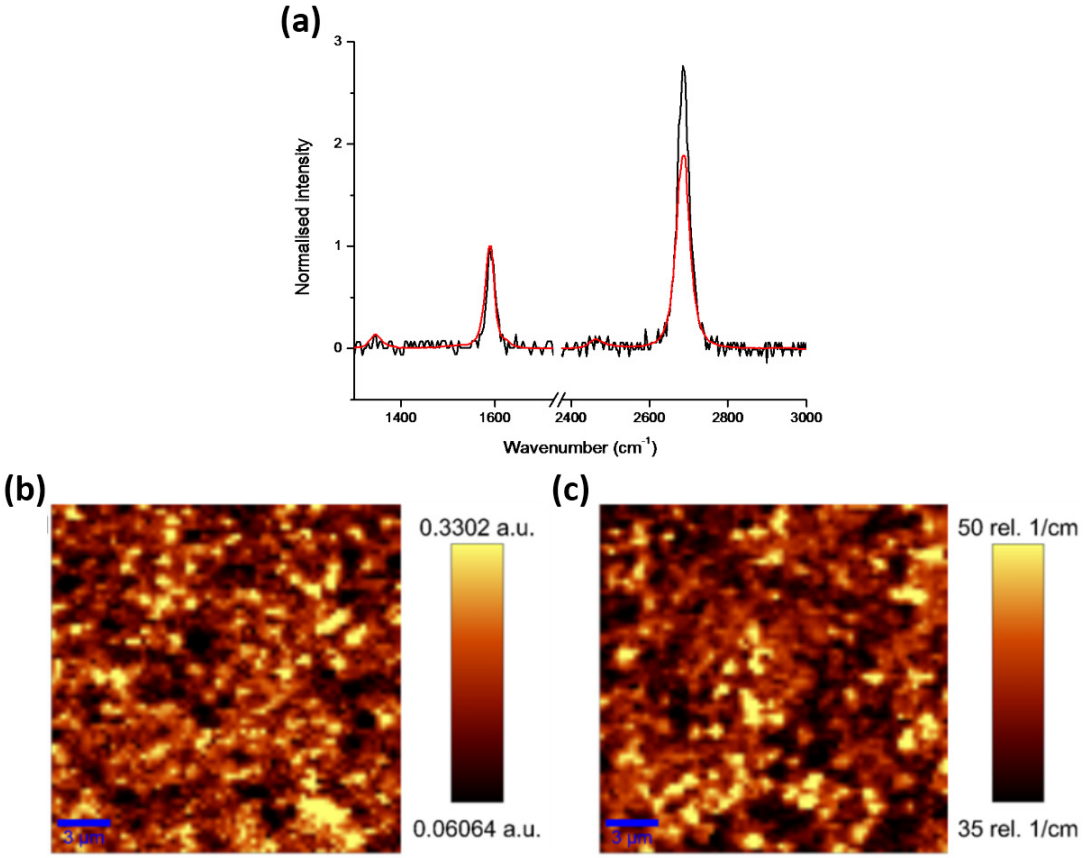


Figure V.12. Raman spectrum at the centre of a SLG domain (black) and averaged across a 20 × 20 μm region of the film (red). (b) I(D)/I(G)map. (c) FWHM(2D)map. Adapted from [850], with permission from Elsevier.

a regular basis to prevent Cu deposits flaking and particle formation. As a result there have been several activities to (1) reduce the growth T to address the evaporation and the potential integration of graphene directly in a device flow and (2) finding alternative metals or alloys as discussed above to minimize the Cu evaporation problem. It should be added that the cost and reliability of precursor delivery systems should also be considered when designing a CVD. in order of preference, gases are preferred over liquids and liquids are preferred over solids. In an effort to reduce the growth T researchers have used liquid precursors such as alcohols [844], or aromatic molecules, such as hexane [845, 846], benzene [847] and toluene [848]. In the case of benzene, high quality mostly monolayer graphene was synthesized at 300 °C with μ of 2500 $cm^2 \cdot V^{-1} \cdot s^{-1}$ by APCVD [849]. Evaporation of the catalyst was avoided and oxygen removed from the deposition chamber to minimize contamination or structural disorder of the film. Deposition of graphene at 100 °C was observed by this method but with lower quality [1753]. With extended time deposition, BLG or TLG started to form, indicating that the synthesis is not self-limiting [817]. At 160 °C continuous graphene films of reasonable quality (μ~667 $cm^2 \cdot V^{-1} \cdot s^{-1}$) were deposited on SiO_2, however N was barely controlled. At lower T (from 60 to 160 °C) the deposition of continuous films was not achieved, being the coverage from 60% to 98% and the grain size and quality of the deposits deteriorated. At 60 °C on glass and PMMA the Raman signal showed the deposition of highly defective graphene layers with nanometric grain size.

Thus, the quality of the films is inferior to that grown on Cu at higher T using CH_4. In addition, the delivery system for the liquids may be more complicated and more costly, not to mention the toxicity issues. Ref. [850] reported on the CVD growth of high-quality, large-area predominantly SLG films with domains o~1 μm^2 and FWHM(2D)~35 cm^{-1} on Cu foils using C_2H_4at 850 °C. Spectroscopic and electrical measurements show that these films display high uniformity and crystalline quality with reasonable μ~1000 $cm^2\ V^{-1}\ s^{-1}$ [850]. Figure V.12(a) shows the average Raman spectrum of a ~20 × 20 μm^2 area (red) and a discrete spectrum taken at the centre of a SLG domain. I(2D)/I(G) is lower for the averaged spectrum as this includes the regions of secondary island growth. Figure V.12(b) plots a I(D)/I(G) map with brighter areas corresponding to regions of higher defect levels, highlighting the low defect levels throughout the film. The defects that are present here are attributed to domain boundaries. Figure V.12(c) plots FWHM(2D) across the same area of the film with brighter regions corresponding to wider FWHM(2D). The majority of the film FWHM(2D) ~35 cm^{-1}, typical of SLG [96, 105].

Further characterization was carried out by fabricating GFETs. Al_2O_3 pre-patterning of the Cu foil passivates the areas, giving a patterned graphene film on the final substrate. Electrical measurements were performed with source-drain voltage (V_{SD}) ~20 mV while the gate voltage was swept to +60 V and −60 V. I_{DS} versus V_{GS} curves in figure V.13 give hole and electron μ~1100 and 700 $cm^2\ V^{-1}\ s^{-1}$ at RT. These fall short of the best reported values for CVD graphene [851], due to the smaller domains (~1 μm) compared to films grown at higher T.

Ref. [849] investigated the growth process of graphene at ~300 °C, using C_6H_6as precursor at ambient pressure. They used a pump purge process multiple times to minimize residual oxidizing species in the growth chamber and annealed the Cu substrates at 1000 °C under H_2 and Ar gasses for 30 min to grow the Cu grains as well as clean the surface through evaporation of potentially damaged surfaces as well as surface adsorbates. This process produced films with 100% surface coverage, 97.6% transmittance, and μ~1900 to 2500 $cm^2\ V^{-1}\ s^{-1}$. This may become useful for back-end-of-line (BEOL) integration of graphene.

Another approach is the use of PECVD. However, the typical quality of graphene has not been significantly better than thermal CVD. PECVD synthesis on Cu foil was reported via simultaneous removal of native Cu oxide and film growth (<420 °C) [852]. This shows the importance of smoothing Cu and the differences in the deposition on top and bottom sides. The bottom side near the sample holder suffers a confinement that allows preparing smooth Cu metallic surface and growth of mostly SLG continuous films in one step. However the process is not self-limiting and the thickness was time dependent. Contamination of the process tube with Cu affects the lifetime of furnace as well as reproducibility.

V.1.5. CVD graphene growth on Ni

Growth of graphitic carbon on Ni was achieved asfar back as the 1960s [746] and to the 1970s [753, 853]. Using PECVD, vertically oriented graphene nanosheets (VOGNs) on Ni can be prepared [854–856]. Carbon on metals is either soluble or it reacts to form a carbide. The majority of efforts on growth on metals have focussed on the use of non-carbide forming metals such as Cu, Ni, Co, Pt, Ru, Ir, and Au. There have been interesting reports on the growth of graphene on carbide forming as well [1754]. In this section we focus on the growth of graphene on Ni and Co, and similar metals. The solubility of C in Ni and Co is fairly high in comparison to that of C in Cu [857, 858], and it is much higher than that in Cu [790] ~1 at% (C in Ni) versus 8–10 ppm (C in Cu). The higher solubility makes it difficult to grow uniform SLG on the metal surface [756, 761]. In both growth on Ni and Co, one can grow produce patchy SLGs. Even by decreasing the Ni or Co thickness and growth T, single layer control is very challenging. This also does not solve the equivalent challenging problem of coefficient of thermal expansion difference between metal and graphene [859].The growth of graphitic C on Ni, Co, Pt and other elements that have high C solubility occurs principally by a diffusion and precipitation mechanism from the bulk of the metal [753, 754, 788]. Depending upon T and microstructure the C diffusion can be dominated by grain boundaries or bulk diffusion. Ref. [781] showed using C isotope labeling that while in the case of Cu, graphene growth is dominated by surface growth, on Ni this takes place by dissolution followed by diffusion and precipitation upon cooling to RT. Growth on Ni and Co alloys of Cu on the other hand has given better results, including growth of large area single crystals [1755]. This is due to a number of reasons, the principal being that at low Ni concentrations in Cu, the catalytic activity of the metal surface is much higher than just on Cu, leading to a higher surface growth rate [837]. While growth on elemental Ni and Co resulted in uncontrollable graphene layers, growth on Cu alloys (Ni_Cu, Co–Cu, etc) may lead to controlled larger single crystals of graphene [837]. The presence of metals with higher catalytic activity could also enable growth at lower T.

V.1.6. CVD growth on metal foams

The integration of graphene into accessible and scalable 3d materials is an issue that is inspiring a growing field of research [860]. Free-standing interconnected porous graphene materials, called graphene foams (GF), attract interest due to their ability to transfer many of the unique properties of graphene to a larger scale, with high surface area >850 $m^2\ g^{-1}$ high electrical conductivity (>10 S cm^{-1}) and good structural integrity, retaining the form of the metallic template on which they were synthesized [861]. Applications include variable geometry elastic conductors [861], lithium ion batteries [862], EMI shielding [863], supercapacitors [864, 865] and lithium sulphur batteries [866, 867].

Structures such as papers [542] and hydrogels [343] can be prepared starting from chemically exfoliated graphene and/or GO [304]. These often suffer from poor electrical conductivities (e.g. only 5×10^{-3} S cm^{-1}) [343] and thermal properties, mainly because of defects and their non-continuous nature. Graphene may be grown on templates of virtually any shape by CVD and continuous structures can be obtained starting from custom porous templates. Synthesis of graphene foams by CVD on metal foam templates was reported in Ref. [861]. The authors used commercially-available Ni foam templates to fabricate tunable, macroscopic structures consisting of high quality interconnected graphene sheets. The resulting materials were highly conductive, light and flexible with high surface area, and subsequent infiltration with PDMS led to robust composites that exhibited a resistance change when subjected to mechanical deformation, such as bending or stretching, indicating their

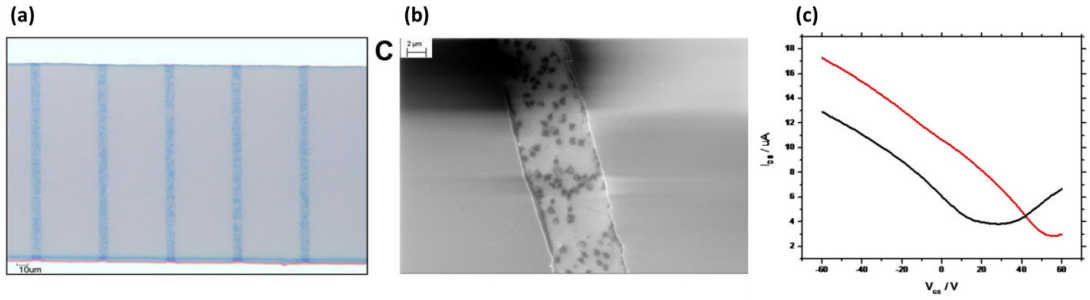


Figure V.13. (a) Optical micrograph of GNRs on SiO_2 used for GFET devices. (b) SEM image of an individual GNR ribbon with second layer islands visible as darker spots. (c) I_{DS} versus V_{GS} curves for GFETs (red) as-fabricated and (black) after vacuum annealing. Adapted from [850], with permission from Elsevier.

potential in the field of stretchable electronics. This work inspired a lot of new research around graphene foams, for many different applications, such as lithium storage [347], high sensitivity detection of NH_3 (ppm in air at RT and NO_2)[868] supercapacitors [869], conductive scaffolds for the proliferation of neural stem cells [870], superhydrophobic coatings [871] combined with Teflon, or stretchable strain sensors [872] combined with PDMS.

The growth process depends on the metal catalyst. In the case of Cu, the process is self-limited, i.e. growth mostly ceases as soon as the Cu surface is fully covered with graphene principally because of the negligible C solubility and C diffusivity in Cu [781]. In the case of Ni, the carbon atoms diffuse into the bulk of the metal due to the high carbon solubility, ~0.9% at 900 °C [781], and graphene is formed both by the isothermal growth on the surface and carbon precipitation from the bulk upon cooling [115]. The shortcoming of graphene growth on Ni is the poor control on N, which is strongly influenced by the Ni thickness, T and exposure time to the hydrocarbon, and the cooling rate, not yielding uniform SLG but rather FLG [791]

In Ref. [873] GF were grown on commercially-available Ni foam templates by CVD in a hot-wall tube furnace (diameter 5 cm) using CH_4.The templates were washed by ultrasonication in dilute hydrochloric acid, then de-ionised water, and finally acetone, before being placed inside the furnace and heated to 1000 °C under a H_2 flow of 50 sccm. After annealing under these conditions for 30 min, the flow of H_2 was increased and CH_4 introduced (H_2:CH_4 = 500:50 sccm). Following a 10 min deposition time, the sample was removed from the furnace and allowed to cool in flowing Ar or N_2 for at least 2 h. To remove the sacrificial Ni templates, the samples were immersed overnight either in 17 vol% nitric acid (HNO_3) or in 4.5 vol% iron (III) chloride ($FeCl_3$) followed by 10% hydrochloric acid (HCl) heated to 80 °C. Finally, they were thoroughly rinsed in deionised (DI) water then allowed to dry completely before further handling.

Figure V.14 shows the characterization of the synthesized GF. From SEM observations, the wall thickness is estimated to be 10–20 nm, characteristic wrinkles are observed in the foam, arising from the mismatch in thermal expansion coefficients between Ni and graphene [874].The interior is hollow, indicating that Ni etching was successful. XRD measurements on foams etched with HNO_3 showed residual Ni (figure V.14(g)), most likely due to the produced by the reaction of Ni with HNO_3. These gas bubbles could block the infiltration of etchant to some channels of the internal structure. To overcome this, etching was instead performed in $FeCl_3$, which has no gaseous products on reaction with Ni, only soluble salts. These were [873] washed away in hot HCl, which also served to complete the etching process. XRD measurements confirmed that the resulting GF had few traces of Ni when $FeCl_3$ was used at RT (figure V.14(g)), and no traces of Ni when it was at 80 °C. However, in this case there was some residual Fe (figure IV.14(g)).

TEM diffraction measurements confirmed the polycrystalline graphite nature although the thickness of the walls was too large to observe the individual layers of graphene (figures V.14(e)–(f)). The quality of the sample was further investigated by Raman spectroscopy (figure V.14(h) The small D peak indicates negligible defects. The 2D is consistent with that of FLG. Thinner GF featuring fewer layers of graphene may also be grown by varying parameters such as the amount of CH_4, the growth time and/or T and the cooling rate. However, thinner foams are less robust and require a PMMA support during etching, so that they do not collapse [861].

The structures described above are limited by the commercially-available templates, which typically have pore sizes in the range of 200–400 μm. In this case, most of the volume is occupied by void space rather than graphene, which is a disadvantage in applications such as energy storage, where a high volumetric energy density is required. Thus, a smaller pore size is often desirable.

High density scaffolding have been produced, as described in [875] as follows: Ni and Cu metal powders with typical particle sizes between 0.5 and 150 μm were purchased from Sigma Aldrich (figure V.15(a)). In the case of Cu powder below 1 μm, the powder was additionally mixed with $MgCO_3$ powder to prevent the

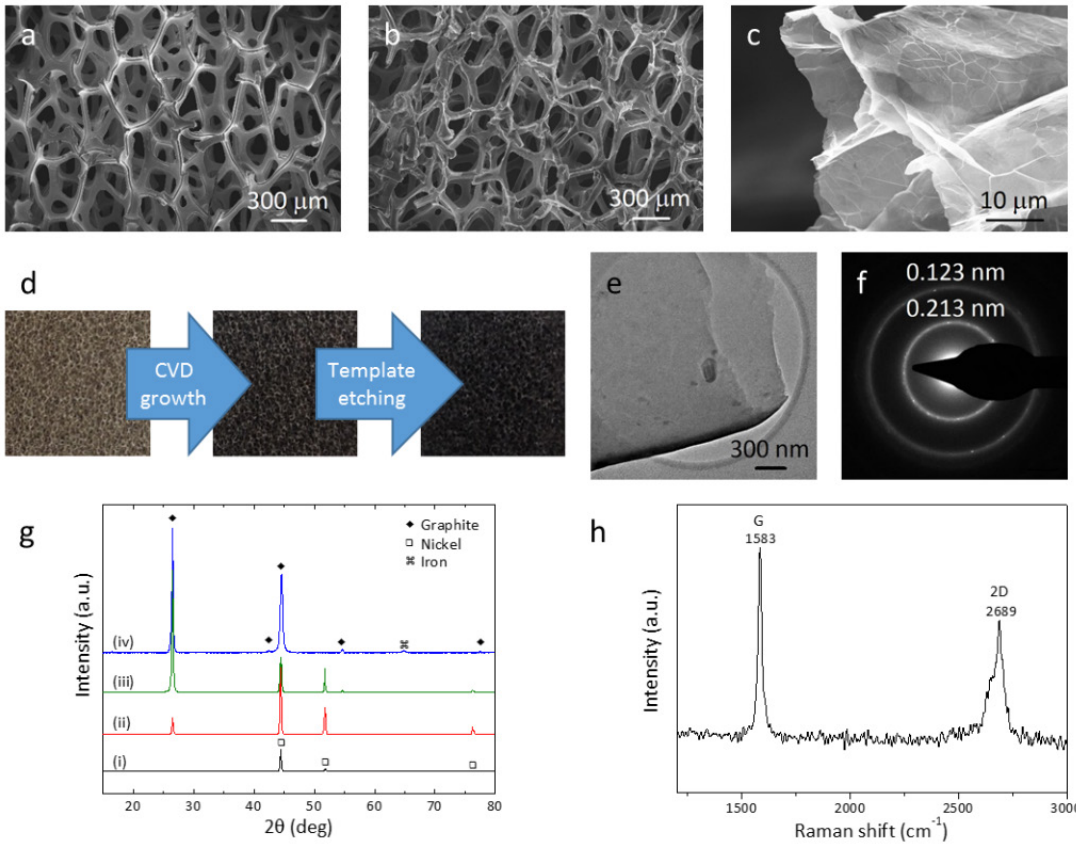


Figure V.14. Characterization of GF from Ni foam precursor. SEM images of (a) Ni foam as received, (b) and (c) GF. (d) Photographs of foam at different stages of the synthesis process. (e) TEM image of GF. (f) Electron diffraction pattern from the foam area in (e). (g) XRD patterns of (i) Ni foam, GF etched with (ii) HNO_3, (iii) $FeCl_3$ followed by hot HCl and (iv) hot $FeCl_3$ followed by hot HCl. (h) Raman spectrum of GF, adapted from [873], with permission of Springer.

agglomeration of the metal particles and compressed. The powder was placed into a quartz combustion vessel inserted into a quartz tube in a horizontal tube furnace. An annealing step with a flow of 400 sccm argon and 100 sccm hydrogen at high T for 45 min was used to connect the metal particles (thus forming the metal scaffold, see figure V.15(b)) as well as to remove metal oxides and contamination. The minimum T for preparing the scaffold was 600 °C for Ni and 800 °C for Cu. Carbon feedstock was provided by a CH_4 flow of 10 sccm under a constant Ar flow of 400 sccm and a total pressure of 50 mbar and 400 mbar for the case of the growth on Ni and Cu, respectively. These were the minimum pressures yielding closed graphene layers on the metal templates for all the investigated temperatures (figure V.15(c)).

Figure V.16(a) plots a typical Raman spectrum at 532 nm of GFs grown on Cu at 900 °C and Ni at 600 °C. This gives Pos(2D) ~2695 cm^{-1} and 2699 cm^{-1} for GFs (Cu) and GFs (Ni), respectively, with FWHM(2D) ~61 cm^{-1} and 80 cm^{-1} for Cu and Ni-grown GFs, respectively, indicating FLG. $I(D)/I(G)$ ~ 0.16 and ~0.25 for Cu- and Ni-grown GFs, indicating defects.

For SEM analysis the GFs were freeze-dried at low pressure in liquid N_2 for several hours in order to prevent the collapse of the foam. A SEM picture of a GF is in figures V.16(b) and (c) depicts an optical image of two Ni foams fabricated at different T.

A similar process was described in Ref. [873], in which a combination of Ni and NiO NPs compressed into a pellet were used as the template. Despite the presence of NiO, the mechanism for the subsequent growth of graphene did not change, since during the annealing process in a high-T (1000 °C) H_2 atmosphere NiO was reduced to Ni, leading to the same behaviour as for Ni templates. After growth, the sacrificial template was removed. A long period (several days) of immersion in the etching solution was required before no more colour change was observed, indicating that all the Ni had been removed.

Figure V.17 reports the characterization of the GF produced in this way. The pellet subjected to high pressure (~440 kg cm^{-2}) was too compact (figure V.17(a)), while the GF synthesized from pellets subjected to low pressure (~50 kg cm^{-2}) shows a well-controlled particle size distribution (figures V.17(b) and (c)), with a network of interconnected hollow branches of graphene. The pores are in the 1–10 μm range, around 2 orders of magnitude less than the GF grown on commercially-available Ni foam templates. As estimated from the SEM images, the thickness of graphene is less than 10 nm. Indeed, by TEM, 10–30 layers of graphene could be observed (figures V.17(e)–(f)) and the polycrystalline graphite nature was confirmed as before by diffraction measurements (figure V.17(g)). To analyze the quality of the graphene, Raman spectroscopy was

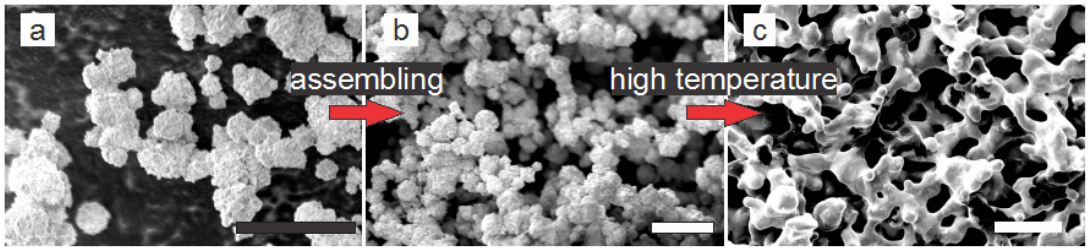


Figure V.15. Fabrication principle of graphene foams illustrated by SEM images. (a) Metal particles, in this case Ni, are assembled in a vessel to get (b) a 3d structure. (c) At high T (~600 °C) interconnected metal foams are created; this process is implemented in the CVD annealing step. The scale bars are 20 μm. Adapted from [875], © IOP Publishing Ltd.

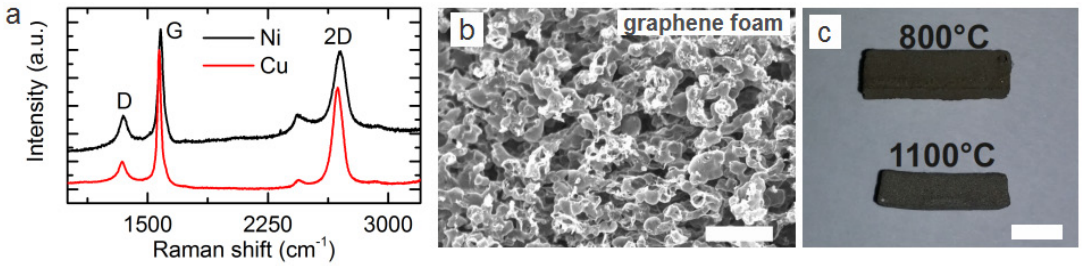


Figure V.16. (a) Raman spectra of GF grown on Cu (red curve) at 900 °C and Ni (black curve) at 600 °C. (b) SEM micrograph of GF grown at 800 °C after metal etch. (c) Optical image of Ni foams fabricated at 800 °C and 1100 °C using a Ni powder. Scale bar in (b) is 20 μm and in (c) 5 mm. Adapted with permission from [873, 875].

employed at 632.8 nm (figure V.17(d)). The sample was first fragmented slightly to ensure that measurements were taken from the inside of the foam. No significant *D* peak was visible in the Raman spectrum, indicating negligible defects and the 2*D* peak was consistent with FLG.

V.1.7. CVD growth of graphene on metal alloys

Selection of the proper alloy could address some of the shortcomings of Cu. Ref. [876] studied the use of Mo-Ni alloys to grow SLG without the precipitation of diffused C into the bulk, because Mo traps C by forming a Mo-carbide. In principle, this approach could be extended to other metal alloys with the objective of finding a substrate with better CTE matching with graphene than Cu, and lower vapor pressure at the growth T. Another widely studied alloy is Ni–Cu in order to take advantage of the low solubility of C in Cu, the higher catalytic activity of Ni and the non-linear behavior of C solubility on Ni concentration in $Cu_{1-x}Ni_x$ [857]. Additionally, some of the metal alloys could be much better catalysts than Cu, enabling growth at much lower T [877, 878]. Refs. [877, 878] grew predominantely SLG by an admixture of Au to polycrystalline Ni. This allows a controlled decrease in graphene nucleation density, at low T ~450 °C. The graphene films exhibit an average I(D)/I(G)~0.24 and domain sizes >220 μm^2 were reported via the design of alloy catalysts.

Carbide forming metals were also suggested to to grow SLG [879, 880]. Commercially available polycrystalline groups IVB-VIB metals (Ti, Zr, Hf, V, Nb, Ta, Mo and W) were used to grow graphene by CVD at ~1050 °C. However, the Raman spectra showed many defects, as exhibited by the presence of a high intensity D-band.

V.1.8. Mechanisms of graphene CVD growth on Cu and Ni

To get some insights into the atomic mechanisms ruling the growth of on metals by CVD, understanding the specific CVD kinetics [881] is crucial for advancing graphene processing and achieving a better control of graphene thickness and properties. Although the thermodynamics of the synthesis system remains the same, based on whether the process is performed at atmospheric pressure (AP), low pressure (LP) (0.1 − 1 Torr) or under ultrahigh vacuum (UHV), the kinetics are different, leading to a variation in uniformity. Graphene synthesis using a Cu catalyst in APCVD processes at higher CH_4concentrations revealed that the growth is not self-limiting, which is in contrast to previous observations for the LPCVD case [1756]. Hydrogen acts as an inhibitor for CH_4 (and for other widely used precursors like C_2H_4) on Cu and other metals, supressing deposition onto the surface [882]. Besides, hydrogen plays a key role in forming form C—H out of plane defects (as efficient nucleation points) in CVD graphene on Cu, defining an optimal (and desired) CH_4/H_2 ratio [882].

Several theoretical studies predicted that carbon atoms are thermodynamically unfavourable on the Cu surface under typical experimental conditions, and the active species for graphene growth should thus mainly

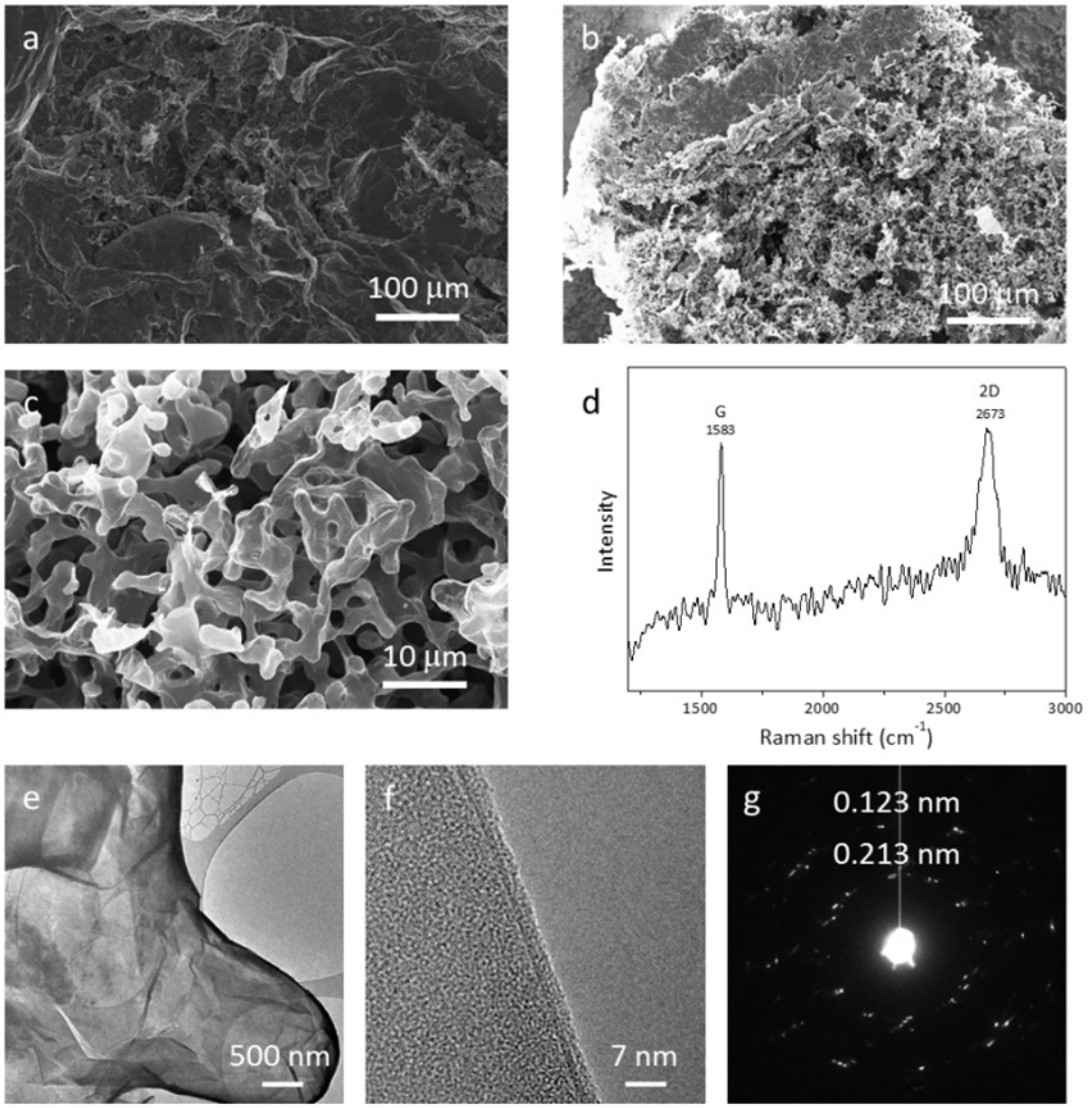


Figure V.17. (a) SEM image of GF from pellet of Ni/NiO NPs pressed under ~440 kg cm^{-2}. The resulting pellets are too compact, with only small areas of porosity where NPs resist tight packing. (b) and (c) SEM images of the GF from pellet of Ni/NiO NPs pressed under ~50 kg cm^{-2}. (d) Raman spectrum from HD-GF sample. (e) and (f) TEM images of the HD-GF foam. (g) Electron diffraction pattern from the area in (f). Adapted from [873], with permission of Springer.

be CH_x instead of atomic carbon [883]. Based on this [882, 883] the nucleation behaviour could be understood (see figures V.18(A) and (B)), explaining many experimental observations and providing a guide to improve graphene simple quality [883]. Other studies were conducted combining ideas from step flow growth augmented by detailed first-principles calculations [792]

A combination of *in situ* LT-STM experiments and DFT-based calculations (see figure V.18(C)), revealed the growth intermediates of CVD graphene on Cu(1 1 1) via thermal decomposition of CH_4at different growth stages, comprising various carbon clusters (i.e. carbon dimers, carbon rectangles, 'zigzag' and 'armchair'-like carbon chains) and defective graphene [884]. Saturation of these carbon clusters on Cu(1 1 1) resulted in the transformation into defective graphene, with pseudo-ordered corrugations and vacancies due to lattice mismatching. These defects were healed by high T annealing in the presence of CH_4 and transformed into vacancy-free SLG. Such atomic insights of the structural evolution at different stages of graphene grown on Cu(1 1 1) can help better understand the growth mechanism of CVD graphene, and provide design rules for large scale growth of single crystalline graphene films.

The kinetics of graphene growth on Cu were also studied using Raman spectroscopy taking advantage of the mass difference of ^{12}C and ^{13}C [781, 791] where the time dependence of graphene growth on the surface of Cu was presented as shown for oxygen rich and oxygen free Cu surfaces in figure V.19

On Ni another interesting growth mechanism can take place. This arises from the decomposed on-surface C atoms, catalytically produced from the CVD CH_4 [888] (or other precursors like C_2H_4, among others) at high T (see figure V.20(A)). The favourable solubility and diffusivity permits the decomposed C atoms

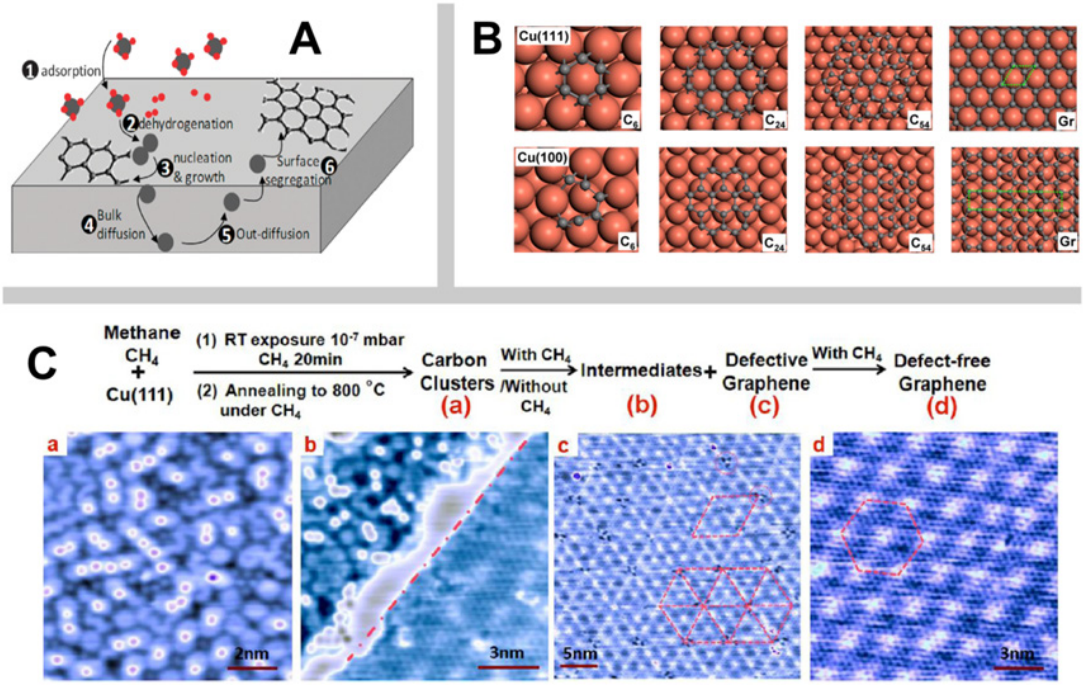


Figure V.18. (a) Sketch of graphene formation by both direct chemisorption/deposition on Cu (and precipitation/segregation on Ni) [882] (with permission of the PCCP Owner Societies). (b) Computed optimized structures of representative carbon clusters along the graphene growth-by-aggregation on Cu(1 1 1) and (1 0 0) surfaces [883] (copyright American Chemical Society). (c) Evolution of graphene grown via thermal decomposition of methane on Cu(1 1 1). Top: Schematic illustration of the surface intermediates at different reaction conditions. Bottom: overview of STM images showing (C.a) carbon clusters, (C.b) the boundary between carbon cluster (left) and defective graphene (right), (C.c) defective graphene, and (C.d) vacancy-free graphene, at different reaction stages [884] (copyright American Chemical Society).

to diffuse into the Ni bulk during the annealing stage at high T [889]. Then, the inward carbon atoms precipitate (segregate) on the catalyst during the cooling period due to supersaturation of the diluted carbon into Ni. This supersaturation-by-cooling leads to the segregation of carbon atoms on the cooled Ni surface, which will promote the formation of the graphene domains. It is worth mentioning that this mechanism has been validated by a complex theoretical computer modelling protocol accounting for a large variety factors affecting the CVD graphene synthesis (solubility in Ni, growth time, growth T, cooling rate, Ni thin film thickness, among others) [886], and will naturally lead to the formation of MLG easier than in other metal substrates by the nature of the segregation mechanism. Another growth mechanism of graphene on Ni(1 1 1) was suggested in Ref. [887] at T $<$ 460 °C. A surface-confined nickel-carbide phase coexists with SLG (see figure V.20(B)). This grows by in-plane transformation of the carbide along a phase-boundary, unlike other growth processes on other transition metals and on Ni above 460 °C, where carbon atoms attach to 'free' edges of graphene islands [887].

V.1.9. Graphene growth on noble metals

Other low-interacting substrates have been explored. Ref. [108] reported the growth of graphene on Pt. This hand high crystal quality with lowest wrinkle height ~0.8 nm and $\mu > 7100\,\mathrm{cm^2\ V^{-1}\ s^{-1}}$ under ambient conditions. The repeatable growth of graphene with large single-crystal grains on Pt is nondestructive after electrochemical delamination of the grown graphene [108]. The growth of can be designed to control the graphene edges that range from zigzag to armchair orientations via growth-etching-regrowth by CVD on Pt [782]. Ref. [890] reported the nucleation and growth of graphene islands on Pt(1 1 1) at $T \sim 1000$ K by CVD of ethylene. Using a CVD method followed by a repeated etching-regrowth process on Pt Ref. [891], single-crystal graphene domains were reported up to $13\,000\,\mathrm{cm^2\ V^{-1}\ s^{-1}}$ under ambient conditions. Ref. [892] engineered the grain size of SLG grown on Pt with a limitted carbon solubility, by a segregation–adsorption CVD yielding a grain size ranging from ~200 nm to ~1 μm, which enabled the determination of the scaling laws of thermal and electrical conductivities as a function of grain size. They concluded that the thermal conductivity of graphene decreases with grain size, while the electrical conductivity slowly decreases with a small grain boundary transport gap ~0.01 eV and resistivity ~0.3 kΩ μm. CVD-graphene growth on Pt substrates can provide an extra added-value, as it may exhibit catalytic properties towards H_2 dissociation [893]. Pt is one of most commonly used materials for electrodes due to its thermal stability and chemical resistance.

The thermal expansion coefficient difference of Pt with graphene is smaller than for other transition metals [894]it is possible to tune the edge termination

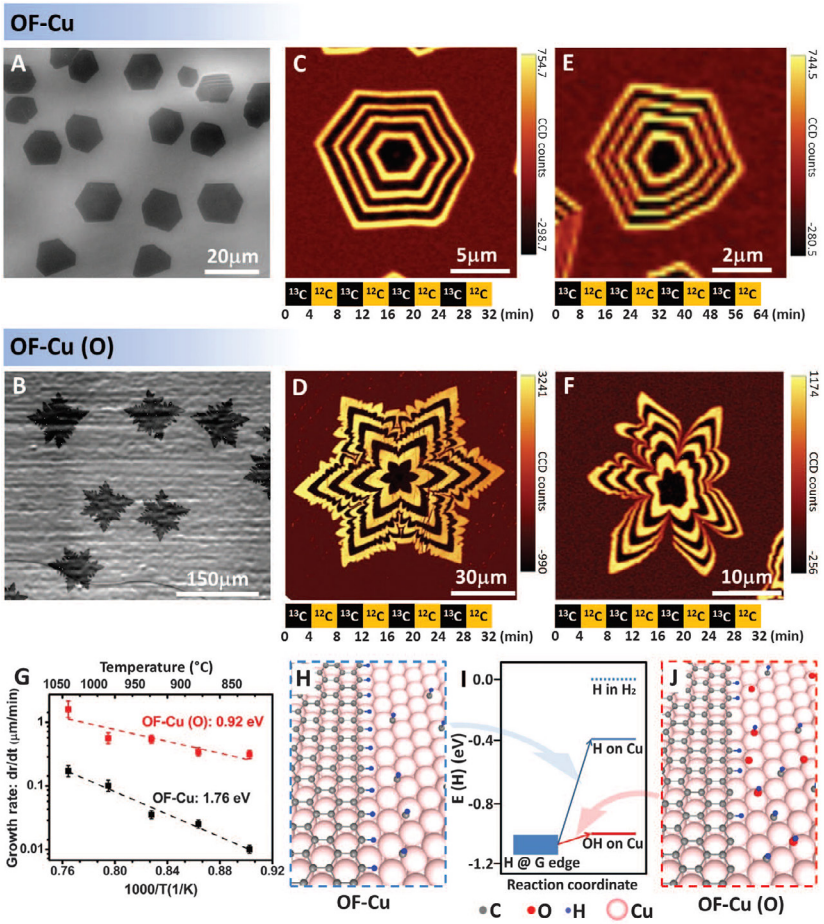


Figure V.19. Effect of O on graphene growth kinetics. SEM images of graphene domains grown on (A) OF-Cu and (B) OF-Cu (O). Isotope-labeled Raman maps of I(2D) on Si for growth at (C) and (D) 1035 °C and (E) and (F) 885 °C. The isotope switching intervals are indicated below each image. (G) Logarithmic plots of graphene domain growth rate d*r*/d*t* versus 1/*T*. The error bars are from calculations of different domains for each case, and the activation energy Ea is extracted from the slope of the linear fit. (J) and (H) Atomic-scale schematics of graphene edge growth on Cu with and without the assistance of O, respectively. (I) DFT calculated energies of different configurations of H attachment, in reference to H in H_2. The energy spread of H at the graphene edge is due to the computational uncertainty resulting from the lattice mismatch between graphene and Cu. Adapted from [791] with permission from AAAS.

of the crystals via growth–etching–regrowth [108, 782, 793].

Efforts have been made not only in the growth of millimetre-sized hexagonal single-crystal graphene films on Pt but also in developping transfer methodologies. A bubbling method, was used to transfer SLG grown on Pt to arbitrary substrates, using a nondestructive process not only to graphene, but also to the expensive Pt substrates [108]. There are also studies focused on the growth on other noble metals, such as Ir [895], Ru [896] and Rh [896]. Moiré patterns have been explored on graphene on Rh(1 1 1) using *in situ* STM [897]. The synthesis of large-scale uniform graphene films on high carbon solubility substrates of Rh foils at ambient-pressure CVD was reported [898]. The thickness of graphene can be tuned from multilayer to monolayer by increasing the cooling rate in the growth process graphene prefers to stack deviating from the Bernal geometry, with the formation of moiré patterns. Ref. [899] grew SLG on Ir(1 1 1) by LP CVD. The graphene layer had a very low density of defects. These are edge dislocation cores consisting of heptagon–pentagon pairs of carbon atom rings, related to small-angle in-plane tilt boundaries. Using Ir(1 1 1) as substrate at 750 °C–900 °C, growing rotated islands are more faceted than islands aligned with the substrate [895]. Further, the growth velocity of rotated islands depends not only on the C adatom supersaturation but also on the geometry of the island edge. Different growth mechanisms were proposed to explain the differences in the graphene edge binding strength to the substrate. Graphene growth by CVD of ethylene on a Ru(0 0 0 1) surface was also explored. At low pressures and high T the metal surface facets into large terraces, leading to ordered graphene layers [900]. Engineering of Ru surfaces with Ar^+ sputtering to produce subsurface bubbles led to a tailored growth of graphene on Ru(0 0 0 1) and to anysitropic oxygen interacalation [896].

V.1.10. CVD growth on Ir (1 1 1)

The substrate Ir(1 1 1)/YSZ/Si(1 1 1) in principle allows integration with Si technology. However, the growth is ruled by the outermost Ir atoms, and therefore the

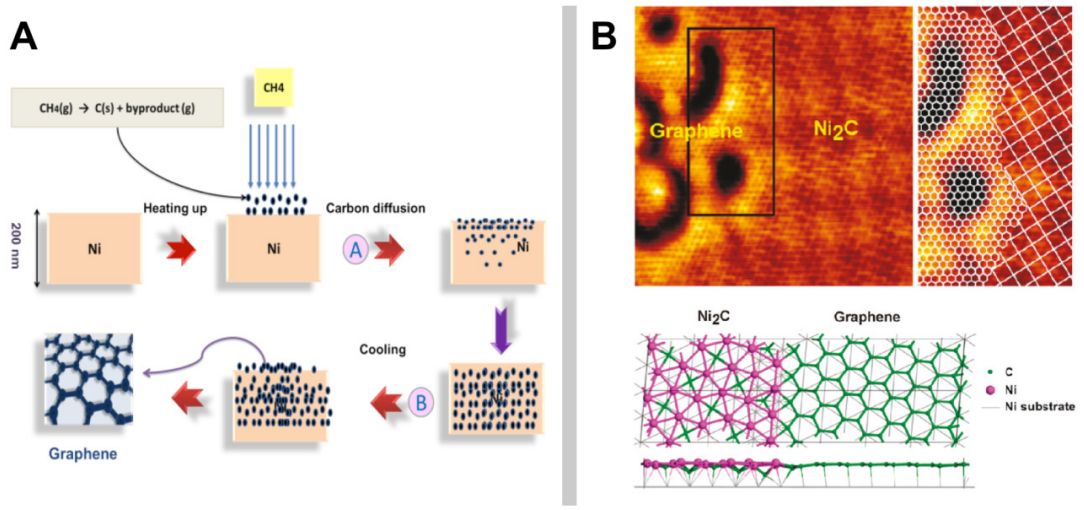


Figure V.20. (A) sketch of graphene CVD growth on a Ni surface [885, 886] through the carbon diffusion and cooling processes. (B) (Top-left) the hexagonal structure of the graphene domain can be identified in the STM image, while the right side shows the quasi-square structure of the carbide Ni_2C. The domain boundary between the two phases is in the same atomic plane and without any defect pattern. This indicates that the two phases form a line interface. (Top-right) the carbide and graphene lattices are superimposed in the region indicated by the rectangle in the top-left panel. (Bottom) Top and side views of the optimized atomic structure of the graphene/Ni_2C interface [887] (copyright American Chemical Society).

process may be generalized to many other transition metals like Ir [895], Ru [896] or Rh [896].

In the case of Ir and Pt, the interaction with the substrate is rather low, and this presents pros and cons. As an advantage graphene can be transferred to other substrates. However, the main disadvantage is the small domain size, as many rotational domains can be generated [901, 902]. Work is underway in the search of optimization methods for enlarging domain sizes, even to millimeter scales. Ru and Rh are substrates were the graphene-substrate interaction is very strong and it is possible to grow large grains on single-crystal substrates, however transfer is difficult [1757, 1758].

SLG on Ir(1 1 1) thin films on YSZ-buffered Si(1 1 1) wafers [903] was reported [905]. The substrate was first cleaned by Ar sputtering (0.8 keV, 5 μA, 15 min) and annealing to 900 °C followed by an oxygen treatment ($p(O_2) = 5 \times 10^{-8}$ to 1×10^{-7} mbar, T between 400 °C and 550 °C) and a final flash annealing (to desorb the oxygen) up to 900 °C.

SLG was grown using ethylene as a precursor CVD at $T = 850$ °C, starting from very low ethylene partial pressures (ideally $<1 \times 10^{-8}$ mbar for the first 20–30 min), then progressively increasing the pressure up to 2×10^{-7} mbar. This approach prevents the formation of multiple nucleation centers, which would result in the appearance of many rotational domains (mosaicity). The substrate should first be heated to the setpoint T and only then should ethylene be admitted into the chamber[905]. Surface processes such as oxidation and overlayer (including graphene) formation modify the work function of the metal substrate, the photoelectron yield measured while irradiating the sample with a pulsed UV source can be used to track the onset of the surface process under study and to monitor its evolution until saturation is reached [905].

V.1.11. MBE growth on Pt(1 1 1)

Several physical evaporation methods employing sublimation from a carbon source have been used, like electron beam evaporator [906, 907], or a resistively-heated piece of graphite [790, 908]. The growth of nanometer-sized SLG on hBNby MBE was reported [909].

Ref. [910] used a solid carbon source consisting of a glassy carbon filament connected by two refractory metal bars to a DC current source. Thanks to a 10 times higher resistivity of glassy carbon versus graphite, it is possible to use moderate electrical current ~14–18 A [911]. This makes this method simple and easy to install in a UHV system, significantly reducing contamination. Ref. [910] showed that for MBE growth of graphene, the substrate can be at lower T than in other methods [912, 915, 916]. This enables growth on dielectric substrates in an inherent transfer free process. Also, *in situ* surface science analysis techniques (LEED, RHEED, STM, XPS) can be used in a highly controllable growth environment (growth rate, substrate type, substrate temperature, *in situ* doping).

The evaporation growth rates are generally very as low as 3×10^{-4} ML s^{-1} to avoid a rapid degeneration of the glassy carbon filament. This requires a sample-to-source distance of tens of millimeters. At this distance the sample is radiatively heated.

An evaporation carbon source can be fabricated [913], using a resistively heated piece of glassy carbon [914], [915].

Using a 0.3 mm thick glassy carbon plate cut in the desired shape (see figure V.21) by laser or water-jet cutting, one gets the carbon source as shown in figure V.21(b). The glassy carbon filament is mounted on a standard UHV feedthrough, terminated with Ta rods, and fixed with Mo screws.

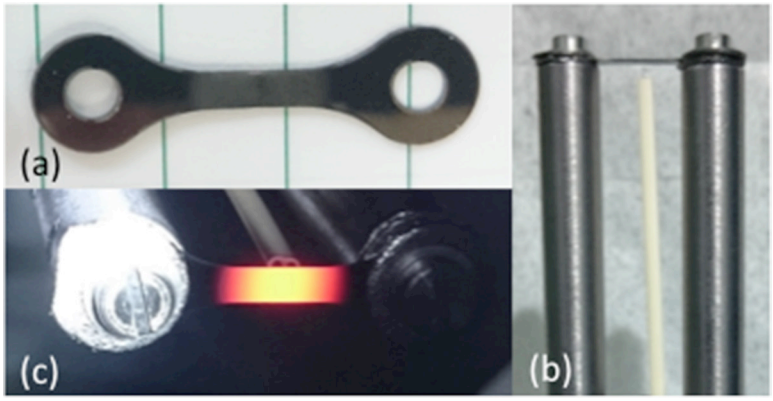


Figure V.21. A glassy carbon filament (a) is mounted on an UHV electrical feedthough (b) and resistively heated (c). *T* is simultaneously measured with an optical pyrometer and a type-C thermocouple located on the back side.

The C Source is placed in a deposition UHV system, base pressure 1×10^{-10} mbar heated using a DC current. The *T* calibration of the cell is performed in a separate UHV system with a base pressure 1×10^{-8} mbar. The *T* in the hottest spot of the filament is measured using a dual-color optical pyrometer through an optical window located in front of the cell. Evaporation of carbon starts above 2000 °C. Using a DC current ~14 A (~100 W) the filament is at 2014 °C. A clear correlation of the increase of the partial pressure of atomic mass unit number 12 (a.m.u.) is observed in a residual gas analyzer (quadrupole) with source temperature. The presence of amu 12 can be associated to the evaporation of monoatomic carbon. The deposition rate is 3×10^{-4} SLG s^{-1}.

By exposing a clean Pt(1 1 1) substrate to the carbon source the formation of carbon structures is observed [910]. First, the glassy carbon filament his held at $T > 2000$ °C for degassing for 15 min. The pressure is kept $<1 \times 10^{-8}$ mbar. Before growth, the Pt single crystal is cleaned by cycles of Ar^+ sputtering and annealing at 850 °C. The cycles are repeated until a sharp LEED pattern is observed, where only Pt peaks appears and/or STM images showing clean and flat extended regions. Then, one places the Pt (1 1 1) substrate at ~650 °C in front of the carbon source at 2000 °C with a distance between them of 20 mm. After 30 min 0.5 ML SLG is attained. During the process the pressure is $\sim 7 \times 10^{-9}$ mbar. The procedure works equally well if the sample is annealed after growth. The graphene formation is demonstrated by *in situ* LEED and STM. The LEED diagram in figure V.22(a) shows the spots corresponding to the Pt(1 1 1) plus a surrounding ring characteristic of graphene. Brighter spots along the ring are indicative of the preferential orientations of the carbon periodicity with respect to the Pt crystal orientation. Figure V.22(b) shows an STM image measured on the graphene areas. The bigger periodicity (bright bumps) of the image corresponds to one of the possible moirés. The smaller periodicity (diagonal lines) is the atomic corrugation of the graphene. Graphene covers extended regions of the surface with a surface morphology similar to growth from decomposition of hydrocarbons or aromatic molecules.

The MBE growth mechanism on Pt(1 1 1) by the evaporation of C atoms can be understood on the basis that the evaporated C atoms will not interact with each other or with gases until they reach the surface. This guarantees a continuum flux of atomic C on the surface, heated up to the desired T. The synergistic effect of surface T with the kinetic energy of the C atoms reaching the surface catalyses the initial graphene nucleation by atomic on-surface aggregation: C atoms reaching the surface are free to move until finding correct (stable) positions on the surface crystal lattice to bond and the epitaxial graphene growth undergoes by aggregation of on-surface diffusing C atoms or nucleated nanostructures (see figure V.23).

T-assisted on-surface diffusion of C nucleation centers, able to collide with others, favours graphene formation, which will epitaxially grow in their most stable graphene domains. The CI-NEB approach [916, 917] yields a minimum diffusion barrier of a C atom on Pt(1 1 1) of 0.45 eV, and a $C + C \rightarrow C2$ on-surface aggregation reaction barrier <0.8 eV (with a net enthalpy gain ~3 eV), to be compared with barriers of 0.6 and 1.1 eV, respectively, reported for the Cu(1 1 1) surface [918], or the 0.58 eV for the atomic O diffusion barrier on Pt(1 1 1) [919]. These energy barrier values are easy to overcome in seconds at the typical surface temperatures in the MBE process on Pt(1 1 1). In addition, the graphene epitaxial growth-by-aggregation will be favoured as the nanopatches increase their size, which will be able to stabilize the incorporation of new diffusing C atoms and larger nucleated C nanostructures.

V.1.12. MBE growth on Au

The use of Au as a substrate is difficult, since the *T* needed to obtain graphene is too close to Au melting point [906, 907]. A solid-carbon source can be used to decrease the *T*.

The Au (1 1 1) substrate is kept at 550 °C, with a well degassed carbon filament. This step can last for

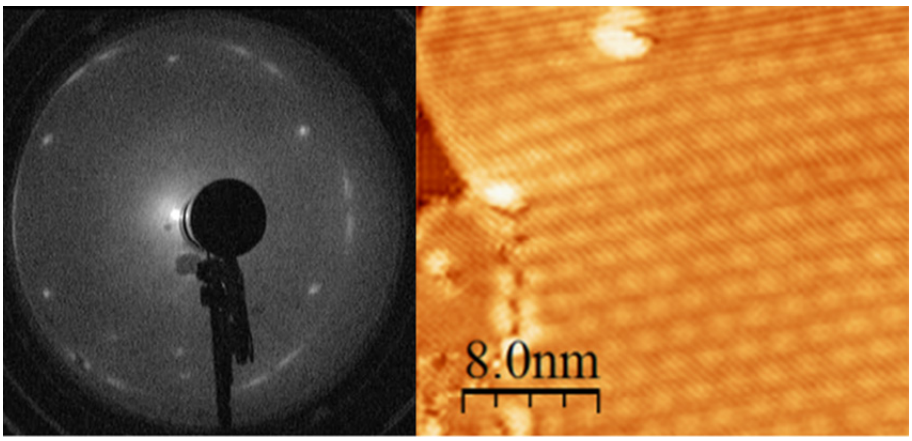


Figure V.22. (a) LEED pattern on SLG/Pt(1 1 1). (b) STM image showing a moiré and the atomic corrugation of graphene. Adapted from [910], with permission from Elsevier.

days because the freshly new filaments are porous containing many impurities. The degas pressure needs to be $<5 \times 10^{-9}$ mbar when the glassy carbon filament is at ~1600 °C (12 A, 83 W).If this step is not performed correctly, the samples get covered by an amorphous layer and the substrate has to be cleaned again.

In case of graphene growth by supersonic molecular beam epitaxy (SuMBE) from C_{60} [920, 921], the two major issues to take into account are the substrate type and kinetic energy (KE). The main steps are the following:

- *Surface preparation*. Numerous (up to 40) Ar ion sputtering (0.5 keV) and annealing cycles of the Cu substrate ($T > 700$ °C for optimal LEED diffraction pattern) to avoid the presence of unwanted contaminants, such as oxygen, sulphur or remaining carbons, during growth.
- *Carrier gas choice*. He or H_2The use of noble gases prevents strong interactions between carrier gas and the substrate and does not affect C_{60} internal dynamics, which is frozen unlike ordinary heating that increases the molecular vibrations.
- *Aerodynamical acceleration* of the highly diluted (less than 1% of the mixture) C_{60} beam by isentropic expansion of the flux out of the injection cell into vacuum through a nozzle. By changing the carrier gas and the seeding parameters (source T, gas inlet pressure), fullerene KE can be tuned, being inversely proportional to the carrier gas mass. KE ~ 10–15 eV using He carrier gas up to 30–40 eV using H_2.
- *Collimation* of the expanded flux and impact of the organic molecules on the Cu reconstructed surface, keeping the substrate at RT.
- *Thermal activated* growth of graphene islands by increasing T to 645 °C.

Refs. [922, 923] showed that substrate T must be raised to 645 °C to synthesize graphene islands as C_{60} high-energy deposition on Cu, even at the highest KE reachable by SuMBE, does not lead to immediate C_{60} cage rupture.

The ultimate evidence of the presence of defected nanometric graphene islands comes both STM and Raman spectroscopy [923]. This process is expected to be self-limiting and to stop completely as soon as the Cu surface is entirely covered by a monolayer of carbon atoms [923].

Ref. [923] reported a coating of graphene-like material at 645 °C using H_2 as carrier gas. These nanoislands also contain pentagons, which come from the original buckyball structures. Thus, at this stage this is just a proof of principle approach. The technique might be applied to a wide range of substrates, such as semiconductors and insulators, avoiding transfer.

V.1.13. UHV-thermal decomposition on Cu foil, Cu(1 1 1), Pt(1 1 1) and Ir(1 1 1)

This method consists in the growth of graphene in a UHV environment, using surface decomposition of C_{60} [924] as a carbon source. The same method applies to Pt(1 1 1) and Ir (1 1 1), Cu(1 1 1)single crystals [901, 912, 925] and Cu foil [926].

The combination of a UHV environment together with the use of C_{60} molecules provides some advantages with respect to conventional CVD [927, 928]. On one hand, this procedure is self-limited, which assures the growth of SLG. On the other hand, the controlled and clean environment (UHV chamber with a base pressure ~10^{-10} mbar) results in samples almost free of impurities with a lower growth T than CVD.

Ref. [926] used commercial C_{60} (Sigma, 98% purity). To control the evaporation rate, a molecular evaporator is needed, that can be either commercial or homemade, as in this case. Figure V.24 shows a homemade one with a Ta crucible on which a type-K thermocouple is spot-welded. The molecules are placed inside the crucible. Acurrent is passed through the Cu rods and the molecules are evaporated at 450 °C–500 °C. Molecules are outgassed in UHV conditions prior to growth. To this aim, C_{60} is heated 10 °C

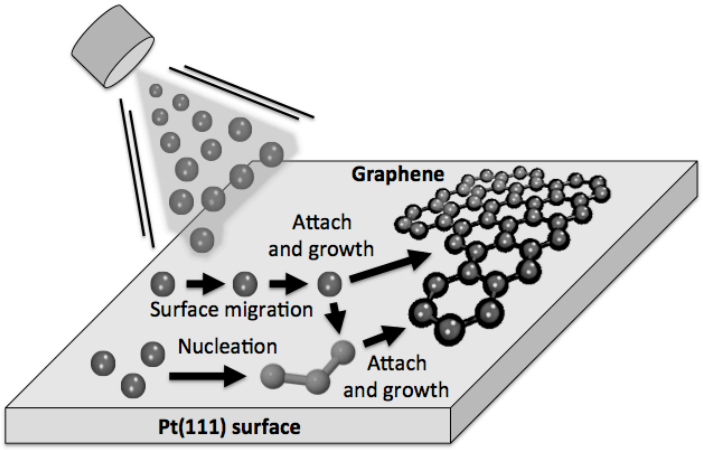


Figure V.23. Sketch of the coexisting processes leading to the growth of graphene on a Pt(1 1 1) surface by MBE.

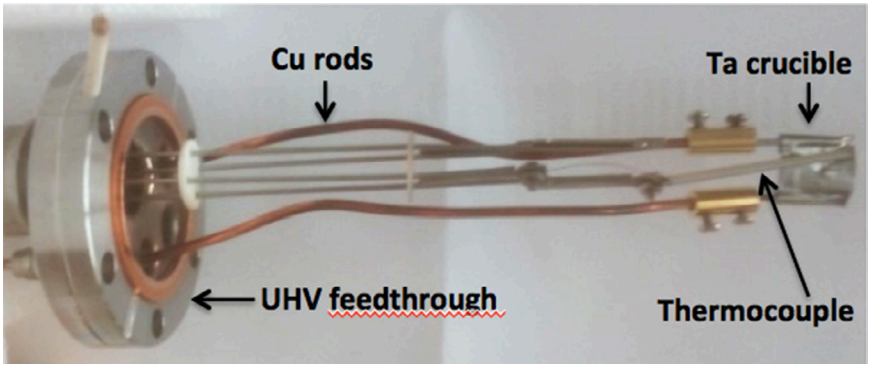


Figure V.24. Homemade C_{60} evaporator.

above the growth T, until the initial pressure is restored ($\sim 10^{-10}$ mbar) after elimination of impurities (water, CO, CO_2). Usually the crucible is spot welded to two pieces of steel that are clamped to Cu rods. It is important to have a good electrical contact between Ta crucible and rods, otherwise the whole evaporator will be heated and the result will be a rise in the base pressure of the chamber and, therefore, a dirty evaporation.

Cu, used as a substrate, is cleaned with several sputtering and annealing cycles. A standard preparation consists in five cycles of 10 min Ar sputtering and 10 min annealing by electron bombardment at 800 °C. For the first cycle the sample current is 10 μA. For the last cycle, the sample current is reduced to 5 μA to prevent large surface roughness. With this sample current value a surface roughness of 0.4 nm is obtained. $T > 800$ °C may promote the diffusion of impurities from the bulk to the surface as well as an excessive Cu sublimation, leading to higher roughness.

Figure V.25(a) shows a Cu foil mounted on a typical sample holder by using two lateral Ta wires to support it. Other fixing procedures, like the use of glue or carbon tape, are not possible in UHV. The way the sample is mounted is important because the sample might bend during annealing if the thermal contact with the sample holder is not homogenous (figure V.25(b)). The simplest and more efficient way of improving the thermal contact is the use of thicker Cu substrates.

In situ surface techniques such as LEED, AES or STM can provide valuable information with no need to expose the sample to the air, thus avoiding surface contamination. Figure V.26 is a LEED pattern of a Cu foil after cleaning, where multiple spots, corresponding to different grain orientations, are observed.

Once the substrate is clean and the molecules purified, the growth consists in exposing the substrate to the molecules at the chosen growth T. Typical parameters are: evaporation $T \sim 450$ °C, substrate size $\sim 15 \times 20\,mm^2$, 10 cm evaporator/sample distance and growth time ~90 min. Coverage can be tuned by changing the exposure time. An important step is to have initially the substrate at the growth T before the C_{60} molecules start to sublimate, avoiding any C_{60} arriving to the sample surface when this is still cold. Different growth trials have been made by first depositing the molecules on the cold surface and making a post-annealing, but this procedure shows less satisfactory results. Once the evaporation is finished, it is important to keep the sample hot until the evaporator gets cold.

This procedure provides polycrystalline SLG on Cu. The next step involves sample characterization. Figures V.27(a) and (b) exhibit LEED patterns taken at

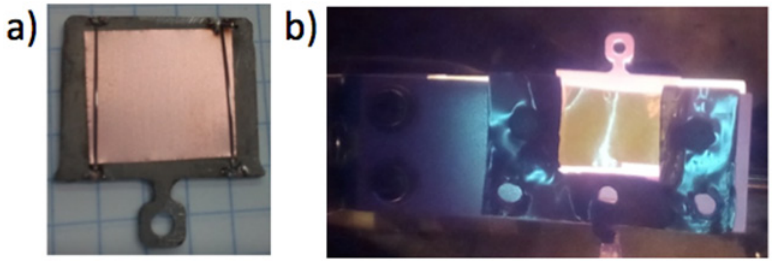


Figure V.25. (a) Mounting of a Cu foil in a Ta sample holder. (b) Bending of the 25 μm Cu foil produced by Cu thermal expansion.

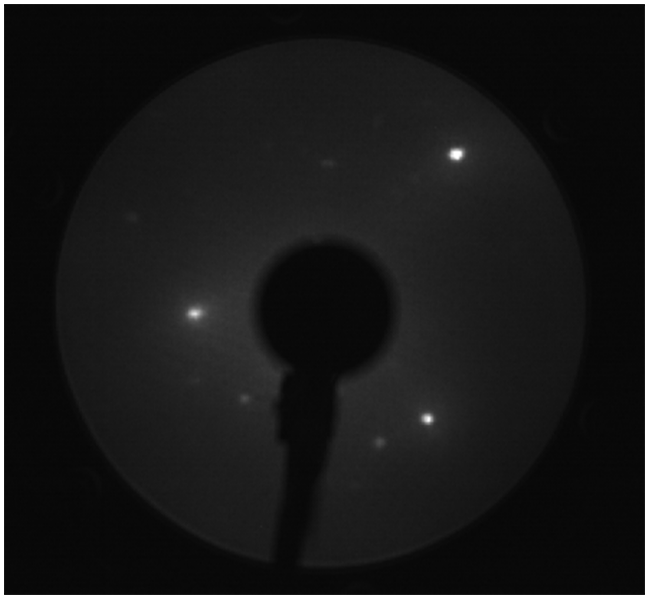


Figure V.26. LEED pattern at 107 eV of a Cu foil after cleaning and prior to the C_{60} evaporation.

of 50 and 56 eV with a typical ring of a polycrystalline graphene surface. AFM images (figures V.27(c) and (d)) show very large and flat Cu terraces (hundreds of nanometers) free of contaminants where graphene wrinkles cross all over the area, assuring a complete coverage. Figure V.27(e) shows a Raman spectrum at 532 nm, after background subtraction, taken in the area delimited in the optical image that appears in the inset. The spectrum exhibits a symmetric and narrow 2D peak located at ~2703 cm^{-1} with FWHM(2D) ~28 cm^{-1}, compatible with SLG [105], with a significant *D* peak that could be due to grain boundaries and defects.

As the solubility of carbon in Cu decreases with decreasing T with this method the solubility is reduced four times with respect to CVD [790]. For this reason, with this process mainly SLG is growth, without contribution of BLG.

The growth of graphene on single crystals by thermal decomposition of C_{60} does not differ much from the polycrystalline ones. All surfaces must be clean, several sputtering and annealing cycles are mandatory, otherwise defective samples are obtained. Figure V.28 shows three STM images of graphene grown by on Cu(1 1 1) and Pt(1 1 1), Ir(1 1 1) for comparison. Some of the typical moiré patterns that depend on the substrate can be seen. These appear due to the mismatch of the graphene and metal network, meaning that only SLG has grown. This leads to a clean graphene not only because it takes place in a UHV environment but also because the precursor contains only C atoms.

The same method works for other metals like Pt or Ir. Table V.1 shows the differences between the growths on the various substrates.

There is still a lack of a precise atomic mechanism rationalizing the thermally-assisted on-surface decomposition of fullerenes on metals, whose foundations still remain unclear. The process needs the synergistic effect of surface T and availability of enhanced reactivity sites on the metal surface: such as atomic metal vacancies, kink/add surface metal atoms or metal surface steps. The combination of these factors favours the anchoring of the C_{60} molecules to the surface strongly enough to disrupt their stable geometrical arrangement (see figure V.29). A strong interaction of C_{60} with the sites with enhanced-reactivity could lead to an efficient weakening of the C–C bonds within the cage-like configuration contacting with the surface, in particular, of the C–C bridges participating in pentagon-rings of the C_{60} molecules, which store less

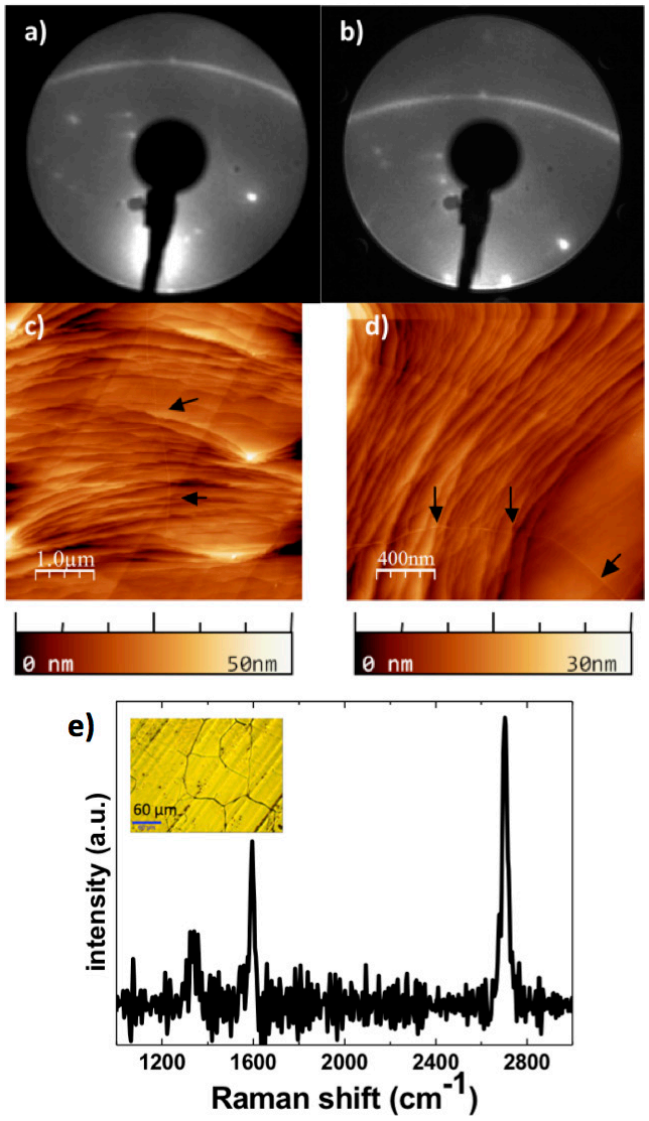


Figure V.27. LEED patterns with a beam energy of (a) 50 eV and (b) 56 eV, where the ring of polycrystalline graphene is observed. (c) and (d) AFM topography images where Cu flat terraces are observed. Wrinkles crossing the terraces (pointed by black arrows). (e) Raman spectrum at 532 nm. The inset shows an optical image with Cu grains visible.

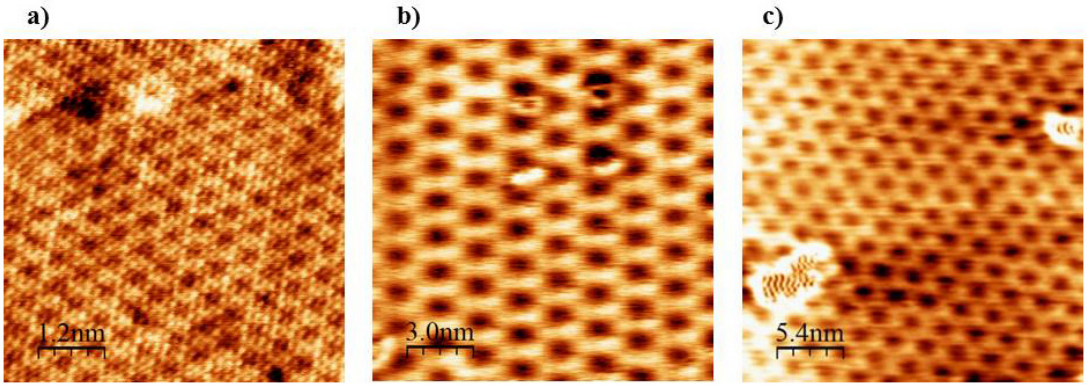


Figure V.28. STM images of SLG grown from C_{60} on: (a) Pt(1 1 1), (6 × 6)nm, 0.11 V, 2.3 nA. (b) Ir(1 1 1), (15 × 15)nm, 1.2 V, 2.6 pA and (c) Cu(1 1 1), (27 × 27 nm), −0.4 V, 2.7 pA. In every image different moiré superstructures are shown.

energy than those connecting hexagon-rings. The process will start with the molecular cage rupture toward the on-surface disaggregation of the molecules into C atoms or other flatter C-based structures, free to diffuse on the metal surface by effect of the T.The epitaxial graphene growth will undergo by aggregation of the mentioned on-surface diffusing C atoms or C-based nanostructures (see figure V.29), which will lead to the

formation of the most stable graphene domains on the metal substrates.

V.2. Graphene growth on semiconductors

Working conditions in CMOS fabs are extremely restrictive in particular regarding metal contamination [1718] Transfer technologies are being improved to provide a very clean environmentDirect growth on semiconductors would be the ideal alternative.

V.2.1. Graphene growth on Ge

It would be desirable to grow graphene on high quality single crystals. Graphene on SiC is of high quality and may satisfy some applications. However, these are limited to the use of SiC as a substrate. Other than on SiC, most of the high-quality isolated graphene has been grown on metal surfaces because of their high catalytic activity and limited C solubility. While as a single crystal is not widely used in the semiconductor industry, it is used as an alloy with Si (SiGe) in the sources and drain of advanced transistors and it could also be deposited selectively onto Si. With respect to its ability to be a good graphene substrate, Ge like Cu has an extremely low C solubility and it does not form a carbide, [930] thus potentially making it a good candidate for graphene growth. Ref. [931] took advantage of this and found CVD growth conditions for SLG. Additional work was performed on the growth of graphene using other techniques such as APCVD, [932] and MBE, [933] on Ge(1 1 0), Ge(1 0 0) and Ge(1 1 0)/Si(1 1 0) and Ge(1 0 0)/Si(1 0 0). Although Ge is more 'compatible' in Si device flows, there are still challenges: transfer and crystallinity. These could be overcome by developing growth selective techniques on isolated Ge/Si post transistor fabrication. Ref. [934, 935] reported the CVD growth of graphene on monocrystalline Ge(1 0 0) on Si(1 0 0), the preferred orientation of Si for CMOS technology. The growth took place between 900 and 930 °C with a ramp-up rate of 1–20 °C min^{-1} and CH_4 flow in the (0.4–5 sccm) range. The optimal roughness of the substrate was achieved when the step growth was preceded by annealing at 750 °C–800 °C in pure H_2 to reduce native oxides *in situ* [936, 937]. Ref. [934, 935] also grew SLG on Ge(1 0 0)/Si(1 0 0) under laminar conditions with a Aixtron VP508 horizontal CVD hot wall reactor. The SLG growth was perfromed at 890 °C–910 °C with a ramp-up rate ~1 –10 °C min^{-1} and a pressure ~850–990 mbar. CH_4 at flow rate ~0.1–0.5 sccm was used in an Ar flow ~3 l min^{-1}. The step growth was preceded by substrate annealing at 800 °C–850 °C in H_2.

V.3. Graphene growth on insulators

V.3.1. High temperature CVD growth

The production of large area polycrystalline graphene and graphene single crystals has been demonstrated via chemical vapor deposition (CVD) on metal catalyst. Currently, the major drawback is the transference of the large area graphene film to the desired substrate for applications that normally induces contamination, wrinkles or even breakage of graphene. In this scenario, the game changing breakthrough would be the development of processes to deposit directly high quality graphene films and single crystals on arbitrary substrates avoiding the transference step and, if possible, at lower T than catalytic approaches. The first route involves the direct CVD synthesis on insulators or dielectrics at T > 1000 °C with examples of synthesis surpassing 1500 °C [943]. Along the high T, atmospheric pressure and CH_4 as precursor diluted typically in Ar and/or H_2 are the most common parameters. Synthesis of SLG and FLG films was on reported on Si_3N_4 [938, 939], sapphire (Al_2O_3) [940–943] and silicon oxides in different structures [944–946] with final R_s between 5 kΩ [944] and 800 Ω [945]. FLG grains were also deposited on h-BN flakes at 1000 °C in atmospheric pressure CVD [947] and on MgO nanocrystal powder by LP CVD at lower T between 325 and 875 °C [948]. Other substrates include SiC [611] and $SrTiO_3$ [949] with μ ~1800 and 1050 $cm^2 \cdot V^{-1} \cdot s^{-1}$. Even though, the typical grain size is smaller (between 0.5 and 10 μm) and the amount of defects higher in comparison with the graphene synthesized with the catalytic approach, the final properties of the deposited graphene resemble transferred material grown on catalytic metals [945].

Table V.1. *T* and typical evaporation times needed to grow SLG from thermal decomposition of C_{60} for different substrates (at a sample-evaporator distance ~10 cm).

Substrate	T sample during evaporation (°C)	Time to have SLG
Cu foil	800	90′
Cu(1 1 1)	900	30′
Pt(1 1 1)	850	30′
Ir(1 1 1)	900	30′

V.3.2. SiO_2

SiO_2 whether in bulk form as transparent quartz or fused silica or on thin films grown on Si wafers (SiO_2/Si), are the most frequently used insulators to directly growth graphene. In the case of the transparent substrates, the typical features of these films include transparency from 80% to 95%, nearly maintaining the transmittance of the substrate itself in some cases, and tunable R_s depending on process parameters [950–954] with values ranging from 1 kΩ sq^{-1} [954] to few kΩ sq^{-1} [952]. Those transparent materials have demonstrated potential for a broad range of daily life applications as heating elements in smart windows, high performance defoggers with fast response (one minute) [951], anti-icing glasses or as mechanical strain or rupture sensors (demonstrated G_F ~600 [955]), to name a few. The main limitation to transfer this knowledge to the industrial environment is the high growth T.

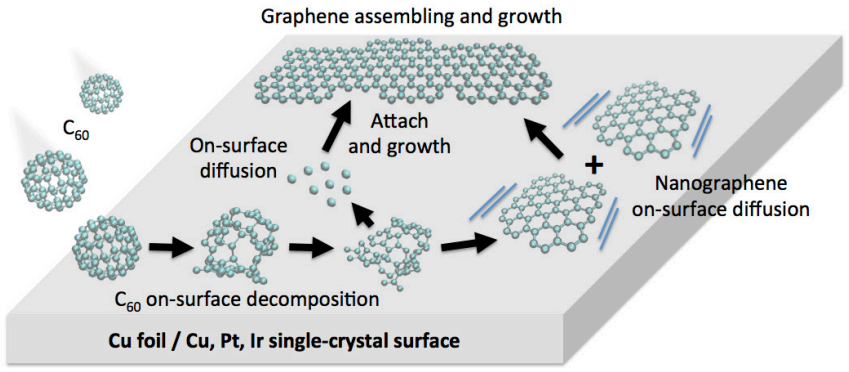


Figure V.29. Pictorial sketch corresponding to the thermal PVD decomposition of C_{60} on the mentioned Cu foils, and Cu, Pt and Ir single-crystal surfaces, as well as the coexisting subsequent processes leading to the growth of graphene.

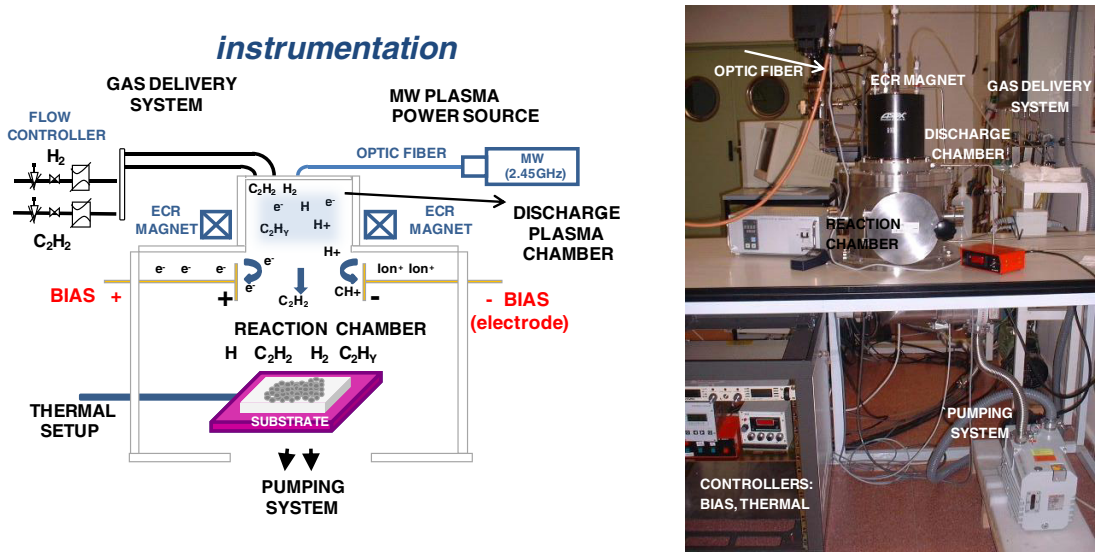


Figure V.30. Schematic illustration (left) and picture (right) of a r-(ECR-CVD) Plasma system. This consists of a gas delivery system with flow controllers, an ASTEX AX 2000 microwave power source with optic fiber coupling the power to the discharge plasma chamber with an ECR magnet surrounding it. The activated gases are transported by forced convection, with two electrodes attracting electrons and ions. The substrate is independently heated. A two stage pumping system generates the vacuum. Adapted from [816], © IOP Publishing Ltd.

Given that Si based electronic technology is the established standard, it would be also extremely interesting to grow graphene on SiO_2/Si wafers so as to integrate graphene in Si-based devices. Many approaches have been developed in this area, but the temperature required, typically over 1100 °C [944, 945, 951, 954, 956–958], poses some problems derived from the poor thermal stability of SiO_2. Among them, desorption of SiO_x from the exposed surface [956] and diffusion of carbon or silicon species from the interface) [951] are well known phenomena that play an undesirable role during synthesis, affecting the structure and quality of the deposited graphene. These effects are more pronounced in thin oxide layers (less than 90 nm) [951] that, in turn, are an important issue in CMOS technologies [959]. Confinement of the substrate was suggested to eliminate desorption [956]. Even so, the final μ ranged from 410 to 760 $cm^2 \cdot V^{-1} \cdot s^{-1}$much lower than catalytic CVD. In order to manage the stability issue, PECVD has been considered as an alternative approach to direct deposit graphene at lower T [962].

V.3.3. PE CVD on SiO_x and Si/SiO_2

PECVD enables catalyst free direct growth by the activation of molecules in gas phase and reduces the high T in conventional CVD or in attempts to use pyrolysis [938, 939, 941, 942, 944–948]. The most important drawback is the resulting small grain size.

PECVD has been reported on non-metallic substrates, resulting in films with small grain sizes -from 2 to 30 nm-, and amorphous carbon [816, 960, 961]. Ref. [774] reported an enlargement of grain size by a 'two-step' growth strategy in remote electron cyclotron resonance plasma assisted chemical vapor deposition, r-(ECR-CVD), figure V.30. The entire protocol is shown in figure V.31.

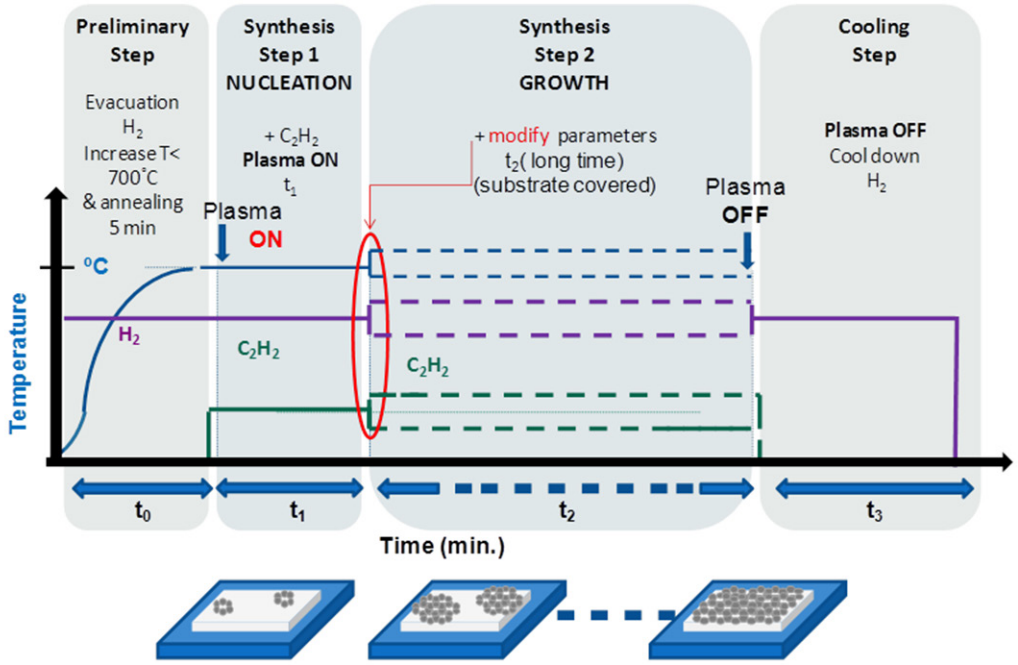


Figure V.31. 'Two step' synthesis protocol schematics.

The various parameters (time (t), T and partial pressures of C_2H_2 and H_2, PC_2H_2 and PH_2) were tuned '*in situ*' in the nucleation (t_1, T_1, $P_1C_2H_2/P_1H_2$) of high quality graphitic seeds and growth from the seeds edges (t_2, T_2, $P_2C_2H_2/P_2H_2$) stages. A post-growth annealing is applied in UHV, improving the final properties of the film. The detailed procedure is usually as follows:

- Evacuation down to 10^{-5} mbar, introduction molecular H_2 at a $P_1H_2 = 10^{-2}$ mbar (typical flow of $H_2 = 55$ sccm) and increase T up to $T_1 = 500$ °C–700 °C in 40–60 min (t_0, figure V.31) for stabilization. Subsequently, annealing the substrate for 5 min. In some cases is interesting to bias the substrate with a positive potential (0 V–50 V) if the auto polarization due to the plasma is not positive.
- Step 1 (NUCLEATION): Introduction of C_2H_2, at a $P_1C_2H_2 = 10^{-4}$ mbar, typical flow = 0.25:0.20 sccm and turn on the plasma (100 W) during 5 min (t_1, figure V.31).
- Step 2 (GROWTH): Modify T_2 in a range of 30 °C–100 °C or $P_2C_2H_2/P_2H_2$ in the $0.1–0.9 \cdot 10^{-4}$ mbar range (between 10%–20%), maintaining it for few hours (t_2, figure V.31), until the substrate is completely covered. As a general rule, $P_2C_2H_2$ is modified, due to its minimal relevance in the final pressure.
- Turn the plasma and bias off and cut the flow of precursor ($P_2C_2H_2$), cooling down in hydrogen atmosphere (P_2H_2) during 40 min (t_3, figure V.31) preventing oxidation. Post growth annealing in UHV at 650 °C, to desorb some chemical species attached to grain boundaries and to improve the coalescence among the grains.

V.3.4. PECVD on quartz substrates

Following the above protocol graphene was deposited on quartz as depicted in figure V.32. AFM images of lateral force contrast are shown in figures V.32(a)–(c). Raman analysis indicates the formation of predominantly highly defective SLG at 650 °C, figure V.32(d).

Figure V.33 presents an AFM characterization of continuous film, confirmed by four point probe measurements, with a $R_S \sim 3.4$ kΩ·sq^{-1}. The coalescence of graphene grains follows two different trends (figures V.33(a) and (b)). Hexagonal graphene domains of similar orientation often generate a smooth lateral merging, presenting boundaries without linear defects (figure V.33(b), black arrows) [611, 931, 962–965]. On the other hand, rough lateral merging also takes place at many points, where linear defects occur (figure V.33(d), pink line). On these defects, carbon species accumulate as in vertical graphene deposition [966] that indicates that the process is not completely self-limiting. From UV–vis-NIR spectrophotometry transmittance (figure V.33(c)), it is also clear that there is an influence of this accumulation (values ~95%).

After growth, the sample can be annealed in UHV to improve the final properties. Ref. [774] increased T stepwise up to 600 °C. The height and density of the linear defects is lower after annealing. R_S decreased from ~3.4 kΩ·sq^{-1} to ~900 Ω·sq^{-1}, with transmittance > 92%. The protocol is scalable it is likely accelerated by changing plasma power and pressure.

The r-(ECR-CVD) mode activated by microwave (MW) source provides higher efficiency in the dissociation of gases than other plasma and it is especially efficient in the dissociation of H_2. It is one order of magnitude more efficient than other DC (continu-

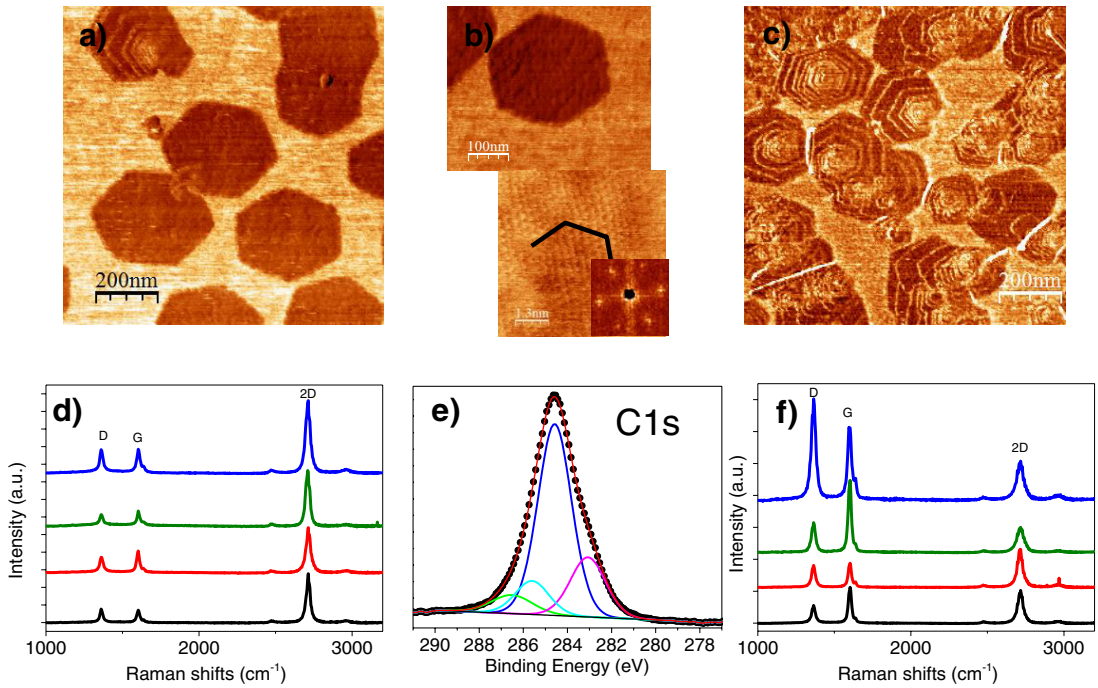


Figure V.32. Graphene on quartz at $H_2/C_2H_2 = 55/0.25{:}0.20$ (sccm), PT $= 5.4 \times 10^{-2}$ mbar, $P = 100$ W for 5 min nucleation time, 9 h growth. AFM lateral force image of the sample grown at (a) $T = 650$ °C and, (b) high magnification lateral force image of a single flake from sample and below the corresponding atomic lattice periodicity of the flake along with the Fast-Fourier transform in the inset of the periodicity image in (a)–(c) AFM lateral force image of the sample grown at $T = 700°$. (d) and (f) Individual Raman spectra acquired at grain positions, for samples in (a) and (c), respectively. (e) High resolution XPS C1s core level spectrum (black dots) of the sample grown at 650 °C. The C-sp^2 graphitic component (blue, 284.6 eV), C–H (green, 285.6 eV) likely from H-terminated edges, and C–O (cyan, 286.5 eV) species. The component at (magenta, 283 eV) can be ascribed to remainders of the growth process (e.g. C_2H_4Si at 282.5 eV) or to the interaction with substrate (e.g. SiC C(1s) is 282.5–283.5 eV). Adapted from [774], © IOP Publishing Ltd.

ous polarization) and RF (radiofrequency) plasma sources. Along with the activated species and neutral radicals, ions and electrons coexist, being mostly the highly energetic ions a potential cause of etching of films. From a geometric point of view, a minimum distance between the plasma zone and the substrate (20 cm) should be respected ('remote plasma activation'). Moreover, the inhomogeneous plasma activation (plasma ball) results in different deposition rates on different sites. For this reason, to make de process reproducible the position of the sample in the holder is critical and must be respected. Apart from geometric considerations, one parameter that can minimize the presence of remaining ions reaching the sample is the positive bias of the substrate [967–969]. The activation of the substrate is also minimized preventing high nucleation density. The last fundamental plasma parameter is the power; the higher the power, the grater is the gas activation. However, as this protocol is a competitive process between etching and growth, assessing the role of power is not straightforward. The increase of power itself does not reflect a proportional increase of all species.

A T increase keeping the other parameters fixed, results in an increase of the reaction rate but at the expense of an enhanced nucleation density due to the present dangling bonds in freshly activated oxide surfaces. As a minimum $T > 400$ °C is needed for graphitization, the key is to favor the reaction at the graphene edge instead of reaction with substrate by carefully playing with the local saturation of carbon. In figure V.32, a deviation in T from the established recipe affects the nucleation density, growth rate, microstructure and N. Figure V.32(a) shows single layer grains at 650 °C. At 700 °C, figure V.32(c) more flakes of few layers are predominant. Side chemical and topological effects take place, as covalent bonding with substrate or etching, hindering the desired van der Waals interaction. Formation of carbide phases or volatilization of oxide species (CO, H_2O, OH, SiO...) can be produced. There are interdependence between pressure and T, as the unbalanced pressure has similar effects, as observed in figure V.34 (variation of 20% of gas flow). If hydrocarbon flow is below the critical value at a given T, there is no deposition in the nucleation step. If it is over, the deposited nuclei suffer from amorphization. In the second step, a similar effect occurs with (T_2) or partial pressures relation, $P_2(C_2H_2)/(P_2H_2)$, resulting in secondary nucleation or etching of the deposited material. In figures V.34(a) and (c) a deposition of submonolayer graphene can be seen in topography and friction images. In figures V.34(b)–(d) more few layer flakes are deposited increasing pressure.

The precursors and atomic hydrogen, also play a critical role. An appropriate H/C_xH_y ratio in the atmosphere is necessary to grow crystalline material

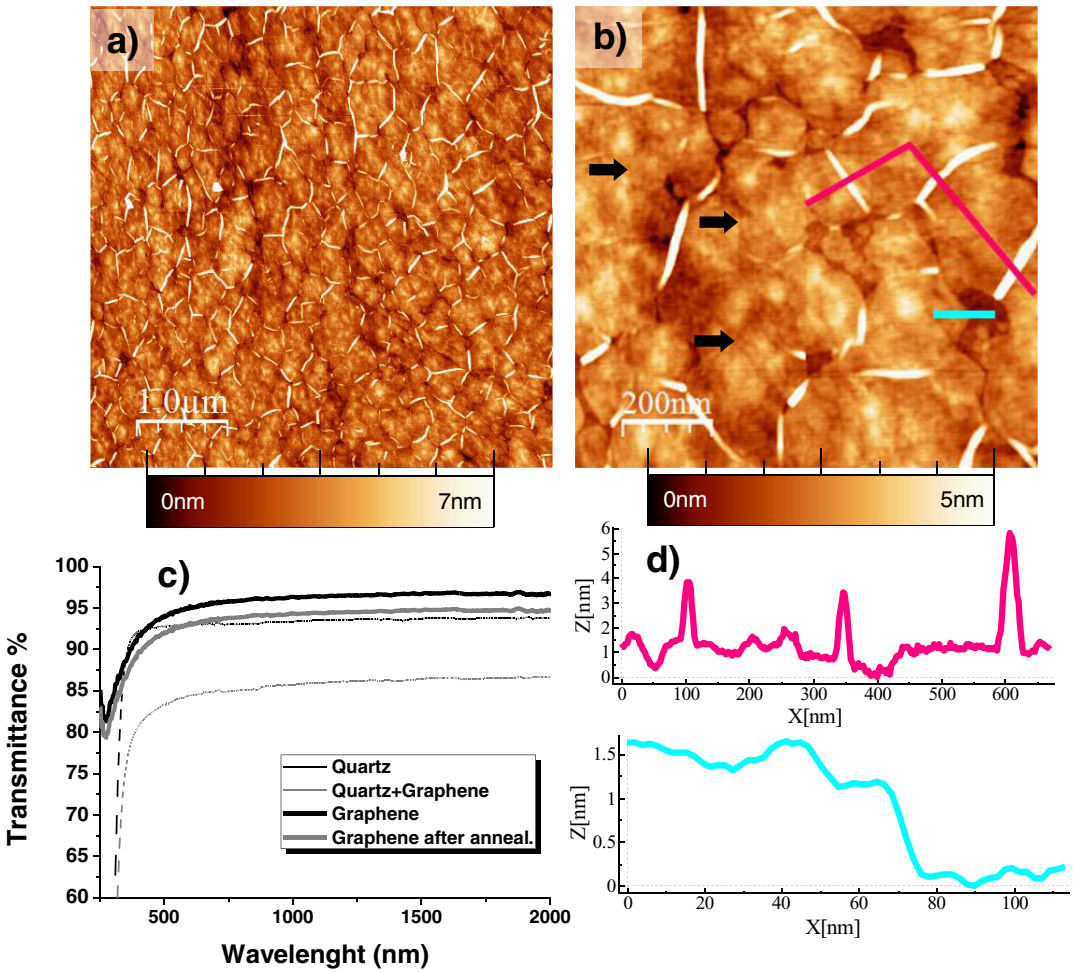


Figure V.33. Characterization of continuous film $T = 650$ °C, $H_2/C_2H_2 = 55/0.25{:}0.20$ (sccm), PT $= 5.4 \times 10^{-2}$ mbar: P $= 100$ W. (a) and (b) AFM topographic images of graphene deposition on quartz for 5 min nucleation time and 10 h growth. (c) Transmittance spectra before (95%) and after (92%) post-growth annealing. (d) Height profiles taken along the corresponding lines in (b) (film thickness, cyan).

[970]. There is a competition between growth from C_xH_y radicals and etching of amorphous deposits by atomic H [971, 972]. The etching rate depends on T and N.

Ref. [774] found that C_2H_2 is a suitable precursor for low T, and no relevant differences between the films deposited with CH_4 and C_2H_2 diluted in hydrogen, once the appropriate H/C_xH_y relation and T) settings are selected. For C_2H_2 the activation is much higher due to combination of plasma and thermal activation (that does not happen with CH_4) [973]. This enhances the reaction rate because the plasma environment is full of activated carbon dimmers, postulated as the main precursor, or at least the main intermediate product, in the case of the synthesis of graphene, due to their higher mobility [974, 975].

Ref. [774] used fused silica at high T up to 700 °C. However, some kind of modification was detected in the surface and changed to quartz.

Dangling bonds in freshly activated surfaces (oxides or insulators) promote strong chemical interaction between the surface and gases. To overcome this limitation the two step process was developed Ref. [774] where the edge growth from seeds is highly favored over the nucleation on substrate. Even so, some limitations continue as the process is slow and not completely self-limiting as can be seen in figure V.34(d) where several layers conforming a multilayer deposit (rose petals shape) is apparent. The origin of this multilayer deposits is the slight reduction of the quartz surface.

The reduction process of the quartz surface has been computationally simulated by modelling the quartz [1 1 − 2 0] facet (x-cut), assessing the activation energies for the most probable reaction paths within the CI-NEB approach [916, 917] (see figure V.35(a)). Protonation of surface oxygen with atomic hydrogen from plasma and subsequent water vapour release are highly probable in this surface at Si synthesis T[774]. The passivation of the silicon enriched surface with hydrogen prior growth is also favoured because the Si detachment is more energy demanding. Simultaneously to the different steps along the reduction of the quartz surface (figure V.35(a)), plasma products, acting as reaction precursors toward the formation of graphene, start to adsorb on the surface, which will lead to their decomposition and dehydrogenation, favouring the nucleation at specific enhanced-reac-

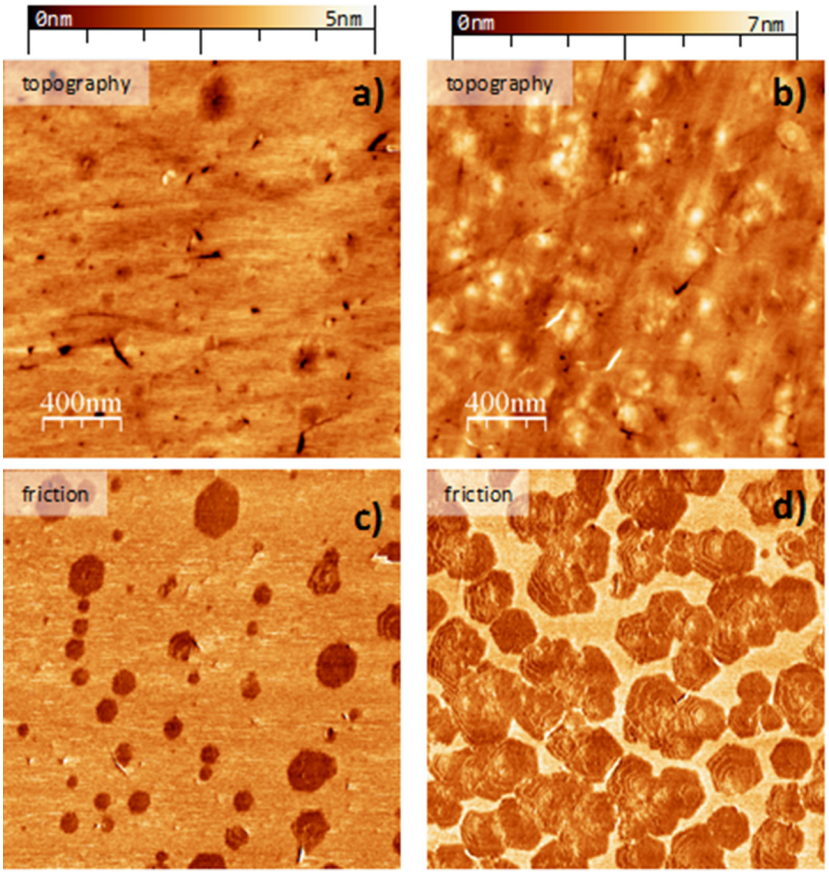


Figure V.34. Graphene on quartz $T = 650$ °C, PT $= 5.4 \times 10^{-2}$ mbar: $P = 100$ W. $t_1 = 5$ min. $t_2 = 690$ min. Topographic (top row) and corresponding lateral force (bottom row) AFM images of samples grown at increasing pressure from (a) and (c) $H_2/C_2H_2 = 55$ 0.25:0.20 (sccm) to (b) and (d) $H_2/C_2H_2 = 55/0.30{:}0.25$ (sccm). The increase in the number of FLG with increasing pressure is seen.

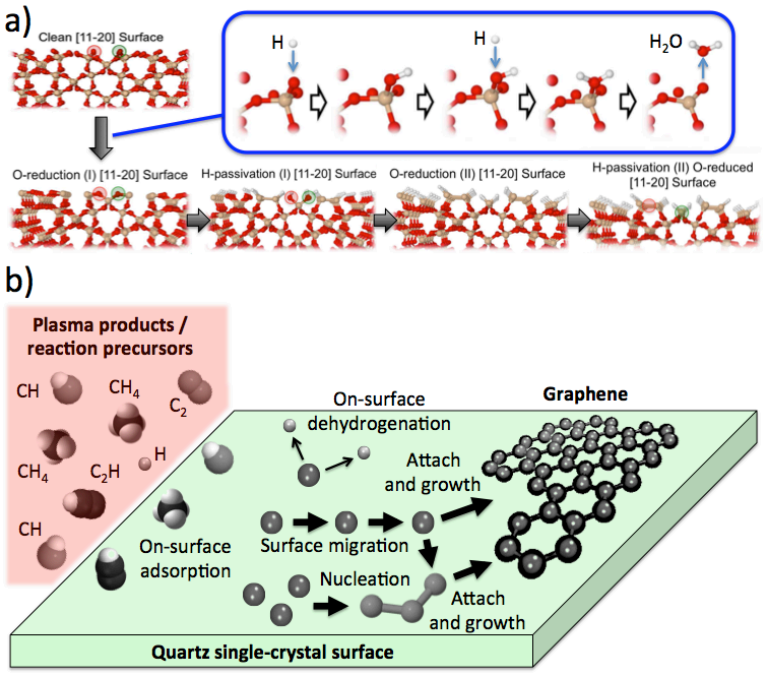


Figure V.35. (a) Side view of the different DFT-computed steps along the reduction process of the [1 1 − 2 0] quartz surface (adapted from [774], © IOP Publishing Ltd): starting from the clean hydroxylated surface [976] across subsequent protonation barrierless steps and detachment of H_2O molecules (see inset), which lead to slight surface reconstructions, and H-passivation of the surface. (b) sketch corresponding to the coexisting processes leading to the growth of graphene on a quartz single-crystal surface from the different plasma products by PECVD: adsorption, decomposition and dehydrogenation of the reaction precursors, toward graphene nucleation and formation.

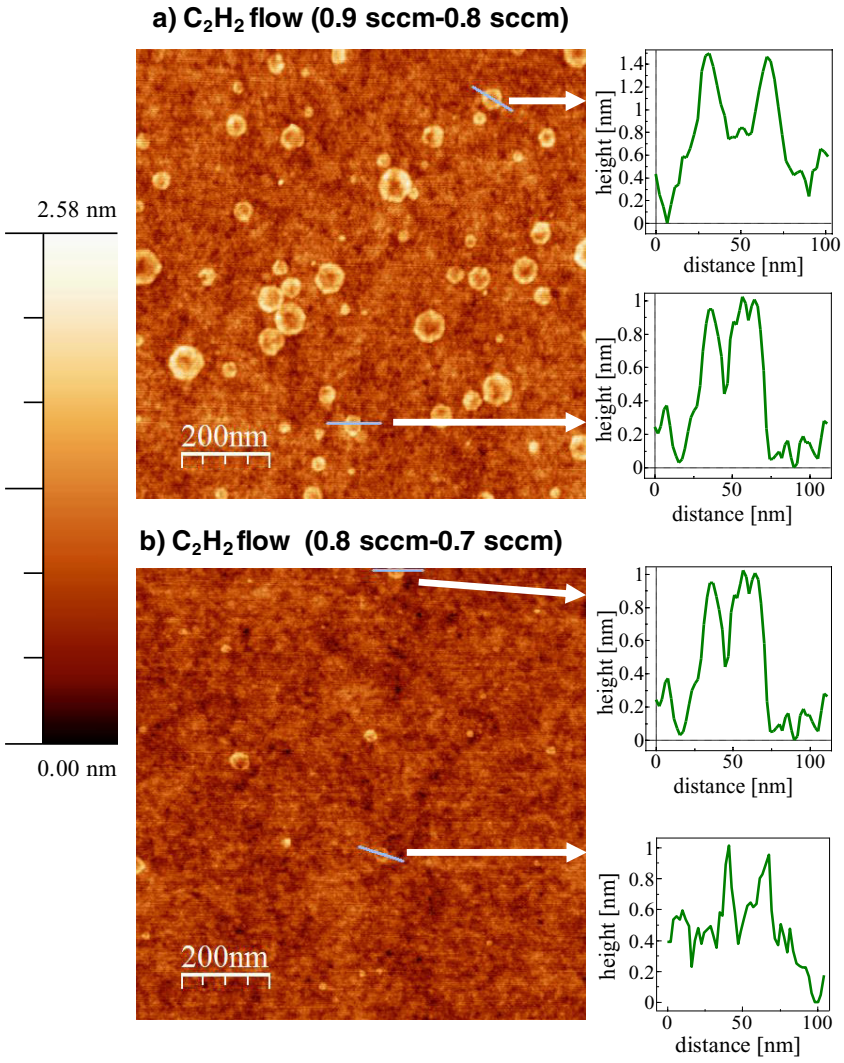


Figure V.36. AFM topographic images of graphene nuclei and corresponding profiles at 550 °C, PT = 5.4 × 10^{-2} mbar, P = 200 W, H_2 = 50 sccm, t_1 = 5 min, t_2 = 150 min. (a) C_2H_2 flow: 0.9 sccm in the nucleation and 0.8 sccm in the growth step. (b) C_2H_2 flow: 0.8 sccm in the nucleation and 0.7 sccm in the growth step. Adapted from [981], with permission of The Royal Society of Chemistry.

tivity sites, depending on the surface reduction stage (see figure V.35(b)). Graphene nanopatches will grow from the incorporation of dehydrogenated carbon atoms, as well as from nucleation centers catalysed by the surface. The coexistence of these processes with the plasma atomic hydrogen maintains the H-passivation and de-passivation (by surface-assisted H_2 formation) equilibrium in the surface promoting the plasma precursors into graphene.

V.3.5. PECVD on Si/SiO$_2$

PECVDis as an alternative approach to directly deposit graphene at low T. Several studies were reported on the grown of graphene by PECVD over Si/SiO_2 with thick (250–300 nm) and medium oxide layers [977, 978], resulting in BLG or FLG [979, 980]. Ref. [981] addressed the direct growth of graphene on Siwafers with ultrathin native oxide by r-(ECR-CVD) using the two-step protocol discussed throughout this section to separately control nucleation and growth stages [977, 774], enabling tuning of grain size and thickness.

Figure V.36 is one example of graphene nuclei obtained at 550 °C following the two step protocol using two C_2H_2 flows. The increase of C_2H_2 flow in the nucleation step from 0.8 to 0.9 promotes a moderately increase of the nucleation density for a particular nucleation time (~30 nuclei μm^{-2}). Also, the increase of C_2H_2 flow from 0.7 to 0.8 sccm increases the grain size during a given growth time. The height profiles in figures V.36(a) and (b) evidenced that, despite the different graphene nuclei sizes, for both experimental conditions, the thickness of the nuclei remained below 1 nm, resembling the features of SLG on quartz [774]. During the synthesis, the SiO_x surface is not affected in terms of surface roughness.

After nucleation, the enlargement of the nuclei in figure V.37(a) follows to complete the deposition of a continuous film. Figure V.37(a) shows the submonolayer coverage of the substrate. Longer t_2 (seven hours) enables the creation of graphene domains up to 300 nm in lateral size. Flake thickness, as shown in figure V.37(b), corresponds typically to SLG. The coalescence of the domains occurred without vertical

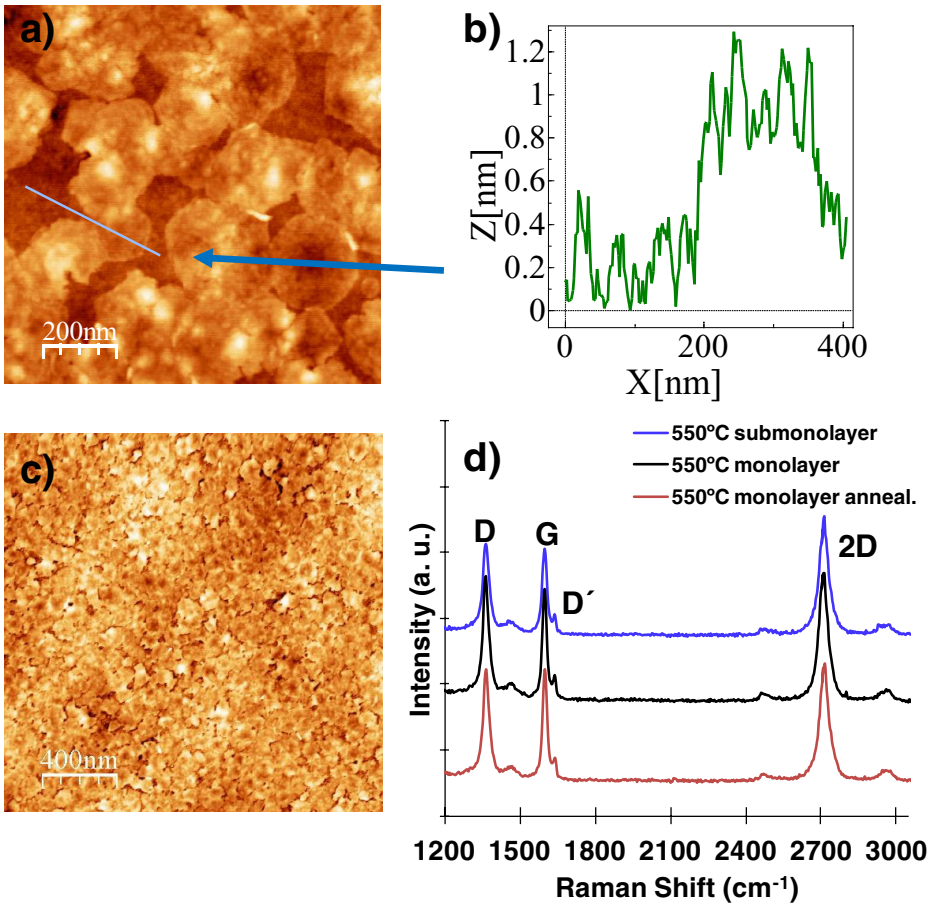


Figure V.37. (a) AFM topographic image of graphene nuclei at 550 °C, $H_2/2H_2 = 50/0.9{:}0.8$ (sccm), PT $= 5.4 \times 10^{-2}$ mbar: $P = 200$ W, $t_1 = 5$ min $t_2 = 7$ h. Vertical scale: 0–5 nm (b) Corresponding profile from a graphene flake in (a). (c) Continuous film, $t_2 = 10$ h and same conditions than (a). Vertical scale: 0–5 nm. (d) Corresponding Raman spectrum of sample (a) (blue) and (c) before (black) and after annealing (red).

growth at the grain boundaries as seen in figure V.37(c) but the surface of the film is not completely flat. Inhomogeneous stitching between grains is apparent, along with lack of continuity in some others (darker contrast). Figure V.37(d) presents the corresponding Raman spectra before and after annealing. The Raman spectrum from submonolayer coverage shows the characteristic graphene peaks. I(2D)/I(G)~1 and 2 and FWHM(2D) 38 cm^{-1}. The high I(D)/I(G)~ 1 is due to the high density of grain boundaries and defects. Along with grain boundaries, another source of defects could arise from the hydrogen enriched atmosphere during deposition, which functionalizes the graphene grains and boundaries, inducing some re-hybridization in the corresponding carbon atoms [982]. The Raman spectrum in black from the continuous film in figure V.37(c) shows similar results. The continuity of the film in figure V.37(c) was also confirmed by four point probe measurements (R_s~15 kΩ·sq^{-1}) This high value can be related to these aspects mentioned: incomplete stitching in some grain boundaries due to randomly oriented grains and functionalization [972]. Thisdecreased to 8 kΩ·sq^{-1} after annealing at 650 °C in vacuum at 10^{-6} mbar, lower than reported for low T procedures [977]. After annealing, I(D)/I(G)decreases from ~1.1 to 0.9. This could be related to H desorption from the film inducing sp^2 hybridization in the carbon atoms [774]. The decrease of $R_s$after annealing could be also related to the same reason: H desorption from grains and boundaries and conversion of carbon hybridization [774, 982, 983].

V.3.6. PECVD of vertical structures

PECVD can be used to synthesize graphene on insulators. In Ref. [854–856] a cold wall chamber was pumped by a turbo pump and an RF plasma power of up to 1000 W is applied on top of the chamber, through a matching network. H_2 and CH_4 are used as precursors (figure V.38(a)). Different growth conditions were investigated and the highest film uniformity was achieved by using a 1000 W RF plasma, a $T = 750$ °C and a growth time of 20 s. Figure V.38(b) shows an AFM image of the grown film directly on Si/SiO_2, highlighting a film roughness of 0.624 nm. The film thickness was 3.33 nm (figure V.38(c)), indicating MLG.

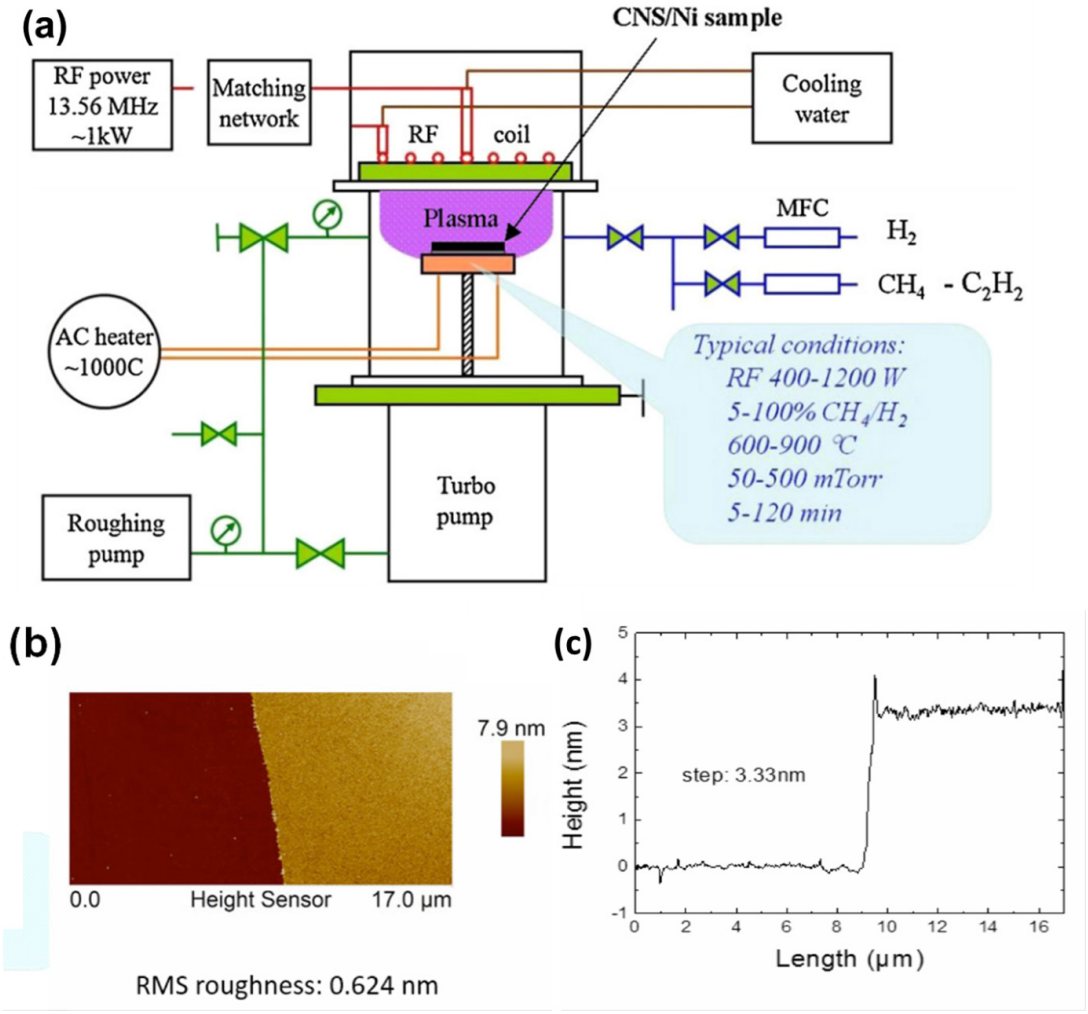


Figure V.38. (a) Schematic PECVD system used to grow graphene on Si/SiO_2. Figure reproduced from [856], with permission from Elsevier. (b) AFM image of the grown graphene film (c) Height profile.

V.3.7. CVD graphene by sacrificial metal layers on Si/ SiO_2

By replacing Cu foil with a thin sacrificial metallic film one may arrive at an alternative route for graphene deposition on dielectrics. The proposed approach is based on the fact that in the CVD process, graphene grows on the Cu-substrate interface provided that carbon precursors have access to it [802, 984]. Thus, by removing graphene from the Cu surface by RIE and then removing the Cu catalyst by wet etching, one can obtain graphene on a silica substrate [802, 984].

Ref. [984] used up to 300 nm thick thermally evaporated sacrificial layers of 99.999% pure Cu on silica or Si/ SiO_2. Cu evaporation does not require UHV, although the higher vacuum reduces the oxidation of the deposited Cu film. Ref. [984] indicated that a vacuum level ~10^{-5} Bar is sufficient. Since the surface of the deposited Cu layer rapidly oxidizes in an ambient atmosphere [985], it is advisable to start the CVD process soon after evaporation to minimize the amount of Cu oxide. Otherwise, Cu oxide can be removed by treatment of the deposited layer in acetic acid [985, 986]. Ref. [984] placed the substrate into the CVD chamber immediately after Cu deposition and pumped down the chamber for an hour. While pumping, 5 sccm H_2 is admitted to remove moist and air remains from the chamber. Thereafter, the chamber is heated up to 700 °C in H_2 (5 sccm, 0.5 mBar, 20 °C min^{-1}). At 700 °C the CVD chamber is vacuumed and CH_4:H_2 (1:1) gas mix injected (8 mBar, static atmosphere). *T* is risen (10 °C min^{-1}) up to 950 °C and kept for 5 min and then the chamber is cooled down to 700 °C in one hour. At 700 °C the CH_4–H_2 gas mix is replaced with H_2 (10 mBar) and the chamber is cooled down to RT overnight (see also [984, 987]).

Surface melting is a key process that governs the deposition of graphene [984]. Although the melting *T* of bulk Cu is 1084 °C, the melting of low dimensional systems takes place in a much lower range [988]. Therefore, although the hydrocarbon catalysis starts ~800 °C–900 °C [989, 990], in Ref. [984], CH_4 was injected into the chamber at 700 °C. At this T, catalytic decomposition of CH_4involves mobile atoms of molten Cu. Since the carbon solubility in Cu is very low (<10 ppm at 950 °C) [790], the migration of the carbon atoms bound to Cu atoms is mainly restricted to the surface [802, 881, 882]. When a few hundred nm thick Cu film melts, melting of each Cu grain results

in well-defined grain boundaries [802]. Highly mobile Cu atoms carry carbon atoms along the molten grain boundaries allowing them to penetrate into the Cu film and arrive at the substrate surface [802, 984]. This effect eventually results in graphene synthesis on substrate-Cu interface. After reaching the maximum $T \sim$ 950 °C the reactor cools down very slowly, i.e. the carbon precursor (CH_4–H_2 mixture) is available for graphene synthesis at the surface of the molten Cu grains until the Cu solidifies at 700 °C.

The Cu film thickness is an important parameter [984]. When the thickness of an original Cu film is <100 nm the molten Cu film recedes forming mainly round droplets of submicron radii covered by graphene, with no graphene between those Cu droplets. When the thickness is ~300 nm the Cu film remains solid after the process, resulting in a grainy but continuous graphene film to the Cu-substrate interface [984].

The topmost layer of graphene can be removed from Cu by oxygen plasma (20 sccm/100 W/1 min), while the remaining Cu protects the graphene layer at the Cu-substrate interface. The remaining Cu is etched by ferric chloride solution. If the topmost graphene is not removed, it will usually stay on the substrate surface as small, arbitrary ribbons and fragments.

Raman characterization in figures V.39(c) and (d) shows a small D-peak and the absence of amorphous carbon [991]. The SEM image in figure V.39(b) indicates that the material is grainy and consist of μm and sub μm flakes. Ref. [802] reported a rather poor $\mu \sim 300\,cm^2\,V^{-1}\,s^{-1}$. However, the linear and nonlinear optical properties of directly deposited graphene are somewhat comparable to graphene grown on Cu foil [992].

One major part of the process is that of the substrate surface. Similarly to controlling the water droplet behaviour by modifying the surface wettability [993], surface modifications can be used to control molten Cu [987]. In figures V.40(a)–(c) one can observe a grating structure that has been under the Cu film during CVD. The continuous Cu film has first molten and receded in between grating lines. Under those Cu lines, graphene lines are located. When the width of the grating lines is sub-μm, the lines are no more discrete but sometimes merge together [987].

Deposition on thin Cu film does not offer an ideal route for graphene synthesis. An important drawback is the very high, 900 –1000 °C deposition T. This makes graphene deposition impossible on some substrates because (i) substrate melting (e.g. polymer substrates), (ii) recrystallization of a thin film (e.g. amorphous titanium dioxide) or (iii) thin film-substrate thermal expansion mismatch, which may cause thin film material to crack out from the substrate surface. Moreover, high synthesis T may start a chemical reaction between the metal and the substrate (e.g. Si may react with Cu or Ni).

Another approach demonstrated that even at near RT (60 –160 °C) graphene can be deposited from graphite powder by using Ni as catalyst [814]. A thick Ni polycrystalline film was firstly deposited over the substrates (SiO_2/Si, glass and PMMA). Then the stack heated at low T. Ref. [814] suggested that carbon diffuses through the Ni film boundaries to the interface. At 160 °C continuous graphene films of reasonable quality ($\sim 667\,cm^2 \cdot V^{-1} \cdot s^{-1}$) was deposited on SiO_2, however N was barely controlled. At lower T (from 60 °C to 160 °C) the deposition of continuous films is avoided being the coverage from 60% to 98% and the grain size and quality of the deposits deteriorate. At 60 °C on glass and PMMA the Raman signal shows the deposition of highly deteriorate graphene layers with nanometric grain size.

Another route is the use of alloys as catalysts, an approach well-known in heterogeneous catalysis to tune the reactivity and selectivity of precursor molecules. Low T (~450 °C) SLG (74%) was demonstrated via the catalysts alloying (sputter deposited polycrystalline Ni films covered with evaporated Au. The initial Au top-layer dissolves into the Ni upon annealing) [878]. The nucleation density is reduced and the graphene domains exhibit lateral dimensions >15 μm. The main limitation is the lack of control in the deposition of monolayer films without multilayer areas [877].

Pd–Coas a catalyst was introduced to realize low T graphene growth on glass substrate by using remote RF PECVD [877]. FLG films were formed with high transmittance ~88.8% and R_s~66 $k\Omega \cdot sq^{-1}$ at T as low as 400 °C, in contrast with Ni catalyst in which no graphitic layer was formed. High decomposition rate of hydrocarbon gases and formation of nanosize aggregates enhances the carbon incorporation into PdCo alloys and as a consequence, a graphene layer is formed at low T. The graphene may be further improved by optimizing Co composition and CVD conditions.

V.3.8. Conversion of amorphous carbon and other carbon sources on sacrificial layers

For this purpose, one can employ liquid and solid carbon precursors for graphene synthesis [814, 847, 994–997]. Regarding the substrate, due to higher carbon solubility and lower reaction T, Ni can be considered a more aggressive catalyst in comparison to Cu. Its use may be advantageous when solid carbon precursors are chosen. Ni-catalysis is activated at a few hundred degrees lower T than Cu [182, 802, 814, 984, 994–997] and may open pathway for direct deposition on bendable substrates [881, 882, 995, 998]. The drawback of Ni is the high C solubility (~0.6 w% Ni at 1326 °C [999] that makes difficult to control the deposition process.

Typically, the amount of carbon precursors determines number of carbon atoms available for the catalysis, while the temporal evolution of the process T governs N [1000]. The cooling rate is important since it defines either the dissolved C will stay inside Ni or be squeezed on a Ni surface forming SLG or FLG films [1000], while the amount C dissolved in the Ni is determined by catalyst amount. Ref. [1001] minimized the thickness of Ni to decrease the amount of dissolved

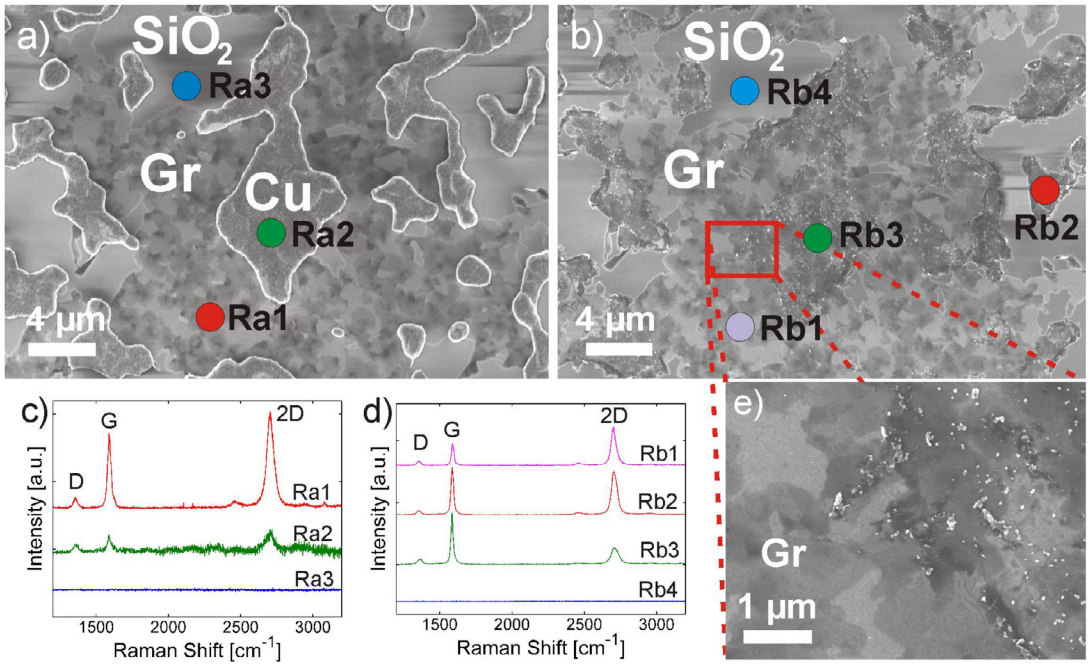


Figure V.39. SEM images of sample with (a) and without (b) and (c) Cu catalyst remains after CVD. Raman spectra with (c) and without (d) Cu catalyst. (e) High resolution SEM image from border area where Cu remains are removed. Adapted from [984], with permission from Elsevier.

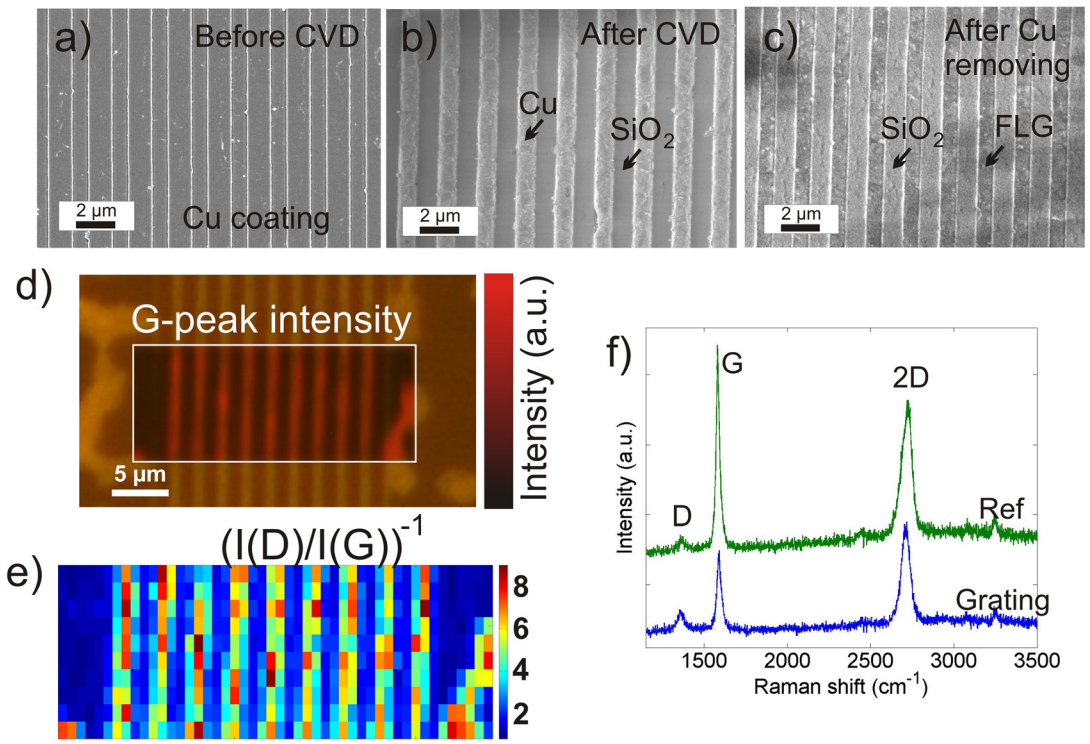


Figure V.40. (a)–(c) SEM images of sample before CVD, after CVD and after Cu removal in $FeCl_3$. (d) and (e) Raman mapping reveals graphene on the grating. (f) Raman spectrum of the grating area is comparable to that grown outside. Adapted from [987], with permission from Elsevier.

carbon because precise *T* control of the bulky hot wall CVD of was hardly possible. Ref. [1001] used 10 nm thick Ni film on a silica substrate as a catalyst and the carbon precursor was nLOF photoresist (AZ nLOF 2070, negative tone resist diluted with AZ EBR 70 thinner). The pyrolysis *T* of the photoresist film in the CVD chamber varied from 600 to 900 °C and resulted pyrolyzed photoresist film (PPF) with and without Ni [1001]. Since during the CVD process some part of the resist layer is expected to evaporate, the Ni film was deposited under the nLOF layer. Thus the Ni layer did not prevent the evaporation from the resist layer.

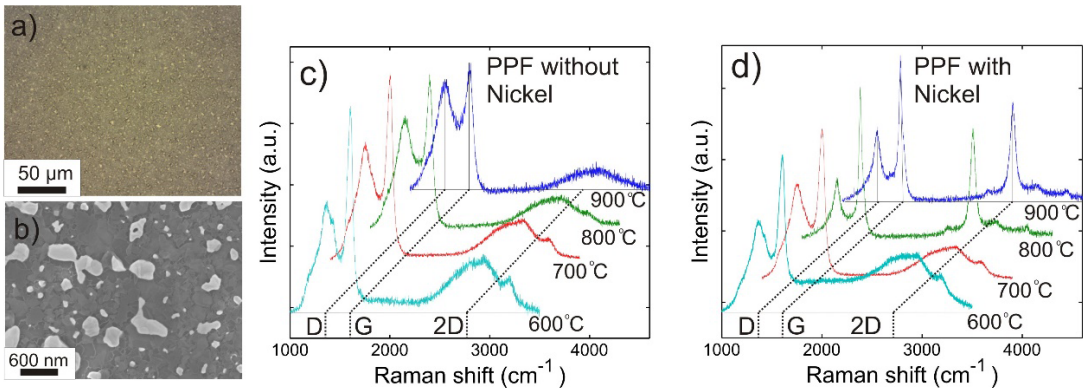


Figure V.41. (a) optical microscope and (b) SEM image of PPF with Ni particles fabricated at 800 °C. SEM reveals non-uniform size and shape of Ni particles (bright particles). Raman spectra shows the evolution of the carbon film as a function of temperature (c) without and (d) with Ni in the process. Adapted from [1001].

Table V.2. Methods, substrates, precursors and optimal growth conditions.

Method	Substrate	Precursor	Temperature	Pressure	Lateral grain size
CVD	• Cu Foil • Partially oxidized Cu foil enclosed	CH_4, C_3H_8	1000 °C < T < 1084 °C	0.5 mbar–1 bar	10 μm Few mm-cm
CVD	Cu foil	C_2H_4	850 °C	2 mbar	1 μm
CVD	Ir(1 1 1)/YSZ/Si(1 1 1)	C_2H_4	850 °C	$1 \cdot 10^{-8}$—$2 \cdot 10^{-7}$ mbar	Up to a few mm
CVD	Ge(1 1 0) on Si(1 1 0)	CH_4	900 °C–930 °C	850–990 mbar	<1 μm
CVD	Ni Foam	CH_4	1000 °C	50 mbar	Depends on metal foam structure
CVD	Cu Foam	CH_4	1000 °C	400 mbar	Depends on metal foam structure
CVD	Cu film on Silica wafer	CH_4	950 °C	8 mbar	<1 μm
PT-CVD	Cu	CH_4	950 °C	7–20 mbar	1 μm
MBE	Au (1 1 1)	Glassy carbon filament	550 °C	UHV	Tens of nm
PVD	Cu (1 1 1), Pt(1 1 1), Rh(1 1 1) single crystal or polycrystalline	C_{60}	800 °C–900 °C	UHV	Tens of nm
PECVD	Glass or quartz	C_2H_2	600 °C–720 °C	$0.1–0.9 \cdot 10^{-4}$ mbar	500 nm

Similarly to Cu, Ni will also melt and recede during CVD. Since the thickness of the original Ni film was only 10 nm the particle size is in sub-μm range. Figures V.41(a) and (b) show the appearance of the Ni particles on PPF pyrolyzed in 800 °C. In Ref. [1001] the T dependence to the PPF graphitization was observed by Raman spectroscopy. Most significant changes in the structure of the PPF with Ni took place For T = 800 °C or above (see figures V.41(c) and (d)) [1001]. A 2D peak appeared at 2705 cm^{-1}. The D and G peaks became narrower, indicating higher degree of crystallization in to comparison to PPF pyrolyzed in 700 °C and lower T or without Ni catalyst.

One approach to control the growth process and improve the quality of graphene grown by catalytic transformation of solid carbon sources was the introduction of a carbon diffusion barrier (Al_2O_3) between Ni catalyst and carbon layer [817]. At thin Al_2O_3 barrier enabled the growth of SLG at 600 °C, with domain size >50 μm and quality that equals the CVD grown films at similar T.

The direct formation of graphene on various dielectric surfaces via a single-step rapid thermal processing (RTP) of substrates coated with amorphous carbon and nickel (Ni) thin films has been reported [1002]. Here, high-quality graphene was obtained uniformly on the whole surface of wafers with a controlled N. SLGshoewd a low R_s and a high optical transmittance in the visible.

V.4. Brief comparison of all methods

There is a wealth of methods to grow graphene on a variety of substrates. Some are more suitable to grow on catalytic substrates while others are better for insulators. Most of them exploit a variety of precursors. Table V.2 summarizes methods, substrates, precursors and optimal growth conditions.

VI. Graphene transfer, placement and decoupling from substrate

VI.1. Wet transfer

Many advances have been reported on the transfer of nanolayered materials such as graphene since the isolation of graphene on silicon dioxide and the growth of graphene on metal substrates [759, 765, 1003, 1004]. In 2007, Gölzhäuser *et al* were first to disclose a method to transfer nanolayers. Patents for this method were issued in 2013 and 2017 (Gölzhäuser; Armin, Nottbohm; Christoph, and Beyer; Andre, US Patent No. 8,377,243 B2 (19 February 2013), A. Gölzhäuser, C.T. Nottbohm, and A. Beyer, European Patent No. EP2144711B1 (31 May 2017)); this process is a wet transfer procedure very similar to the one published in the papers above. The nanolayer can be a single layer (SLG), bilayer (BLG) or multilayer (MLG) graphene but this aspect is not substantial for the purpose of the description of the transfer process. GRMs are covered with a polymeric layer that acts as surface protection as well as a carrier after the metallic substrate is removed by a chemical etchant. The polymeric layer, PMMA, with a thickness of several hundred nm, is used to coat the surface of GRM. One of the advantages of this process is that the polymeric layer conforms with the GRM surface without macroscopic damage. The resulting polymer/GRM/substrate structure is then dipped into a liquid etchant to dissolve the substrate or, alternatively, detached from the substrate. The latter can be achieved by electrochemical methods. After the substrate is removed/etched away or 'detached' an optically visible, several hundred nm thick polymer, with the GRM is left floating on the etchant surface. This 'hybrid layer' is then transferred onto a second desired substrate, typically a dielectric surface. Finally, the thick polymeric layer is dissolved or removed and the GRM remains on the target substrate.

VI.1.1. Etching of a metallic substrate

VI.1.1.1. Cu foil substrate

The wet transfer of CVD graphene on metals like Cu and Ni or its alloys by etching the metal is now broadly used [759, 764, 1003, 1004].

Once the graphene is grown on a large Cu metal substrate (foil) by CVD, the desired sample size is cut and transferred onto a 125 μm-thick PET foil, which acts as a mechanical support. Then a A4-950K polymethyl methacrylate (PMMA) resist is spin coated on the GRM/Cu/PET stack at 4000 rpm for 40 s to achieve the desired thickness, up to ~400 nm, after which the PET support is removed. Since graphene grows on both sides of the Cu foil, that on the uncoated by PMMA has to be removed to prevent it from being combined with graphene under the PMMA. This graphene can be removed from the Cu surface using a reactive ion etch (RIE) process, typically using O_2plasma at 20 W for 20 s and at 200 mTorr. The PMMA/graphene/Cu stack is then immersed/placed on the surface of a metal etching solution such as ammonium persulfate (APS), ~2.0 g in 150 ml of DI H_2O, to etch Cu as shown in figure VI.1 and enable transfer of graphene onto a dielectric substrate. After Cu is dissolved, the remaining PMMA/graphene stack is lifted with the desired substrate (PET, SiO_2/Si, or other) substrate and transferred to a container with DI H_2O for washing. The procedure is repeated a few times to ensure that all of the etching solution is removed. After washing, the PMMA/graphene stack is removed from the water bath and left to dry. There are many implementations of this process and thus a lot of room for improvement as the processes are transferred to a pilot line or production environments. The PMMA/graphene/target substrate is then first transferred in a beaker with acetone for PMMA removal for 1 h, second to a beaker with isopropyl alcohol for 5 min and then dried with nitrogen, leaving the GRM on the target substrate.

VI.1.1.2. Au coated mica substrate

The transfer of a CNM grown on a Au coated mica substrate follows a slightly different path and can be applied also to the transfer to many target substrate [75, 76, 78, 1006]. The procedure is as follows: PMMA (950 K, AR-P 671.04, Allresist) is spincoated at 4000 rpm for 30 s, followed by a soft bake at 90 °C for 5 min. Optionally, a double layer of PMMA can be applied: (i) a first layer (50 K, AR-P 631.09, Allresist) is spun to a thickness of 130 nm at 2000 rpm for 30 s and baked on a hotplate at 90 °C for 5 min; (ii) a second layer of PMMA (950 K, AR-P 671.04, Allresist) has a higher molecular weight to provide mechanical stability. The latter is spun to a nominal thickness of 310 nm at 4000 rpm for 30 s and also baked at 90 °C for 5 min. The advantage of the additional PMMA layer with '50 K' is that it can be removed more cleanly than PMMA with a higher molecular weight in direct contact with the GRM. After the formation of the PMMA transfer medium, the edges of the sample are cut in order to ease the release of the PMMA/GRM from the mica substrate. Then, the sample floats on the liquid level of I_2/KI etching bath (I_2:KI:H_2O with ratio of 1 g:2 g:10 ml) for ~10 min. Au is slightly etched from its lateral interface The separation of polymer/GRM/Au from mica is attained by dipping into water. To remove the Au layer, PMMA/GRM/Au floats on the liquid level of I_2/KI etching bath for ~20 min. After wards the Au layer is completely removed, the polymer/GRM is transferred to a fresh water bath for rinsing. The hybrid transfer layer can be taken out of solution and placed onto a target substrate following the same protocols used to rinse it as detailed in the previous paragraph.

If the new host substrate is not solid and the GRM is to be free-standing on a grid-like substrate, removal of PMMA can be done by critical point drying [78, 1009] (CPD-) that avoiding the damaging effects of surface tension. The mounted sample is immersed into acetone. After 60 min, the chamber is cooled with

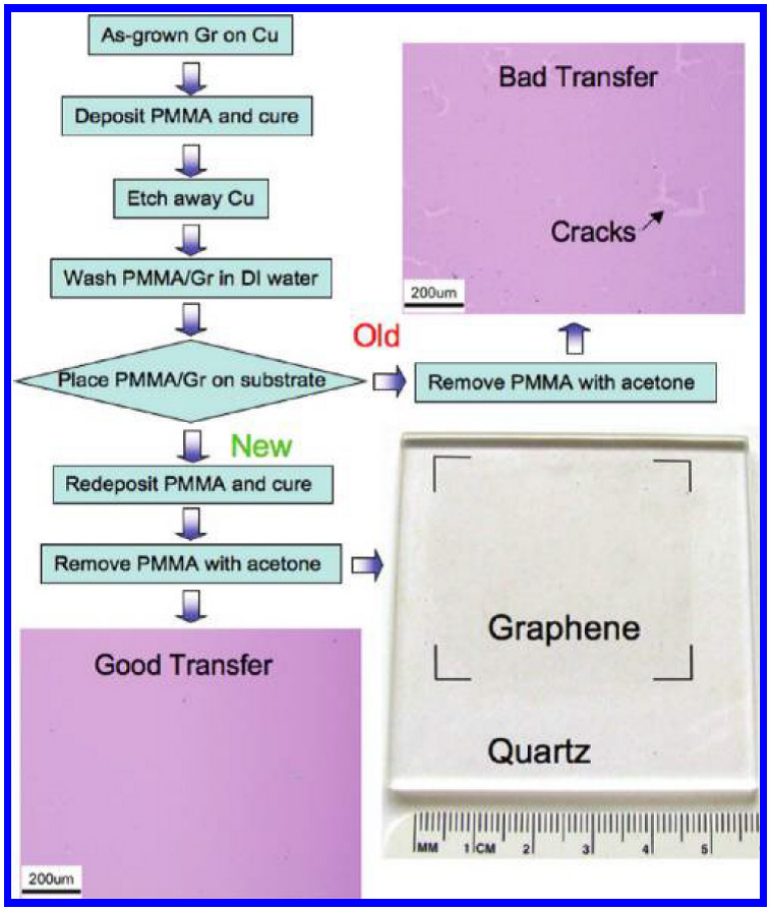


Figure VI.1. Transfer of SLG from a Cu substrate to a dielectric surface. The top-right and bottom-left insets are the optical micrographs of SLG transferred on SiO_2/Si with 'bad' and 'good' transfer, respectively. The bottom-right is a photograph of a 4.5 × 4.5 cm^2 SLG on quartz substrate. Adapted from [1005], copyright American Chemical Society.

liquid CO_2 and then liquid CO_2 is introduced into the avoiding turbulence. Liquid CO_2 substitutes acetone according to a predefined time (15 or 20 min). Finally the dryer heats and pressurizes CO_2 to its critical point, and gas CO_2 bleeds off to leave nanolayer dry. A scheme of the procedure is shown in figure VI.2.

A HIM [1007] image of a CNM, placed onto a Cu grid with hexagonal pores of 40 μm, after removing PMMA without CPD, is show in figure VI.2. Note the appearance of wrinkles. The effect of critical point drying can be seen in figure VI.3(a) that shows a flat CNM on a grid with 40 μm openings. Figure VI.4(b) shows a very large free-standing CNM transferred onto a hexagonal grid with openings of ~0.5 mm [1007]. In both images, no folds and wrinkles are visible.

An additional option of removing the PMMA is the inverted floating method (IFM) [1008]. Therein, only the PMMA covered side of the sample is in contact with acetone. Large graphene membranes were reported, covering circular holes in SiO_2 substrates. This approach is most effective in circular support structures and it requires full coverage of the substrate openings. In contrast to IFM, CPD avoids surface tension related forces on the membrane. Therefore, if available, CPD seems to be a better choice for removing the PMMA layer.

Ref. [1009] systematically studied the effect of annealing of transferred graphene by PMMA by FTIR and XPS in oxidative environments (CO_2, O_2 and NO_2) and found it more effective than in reducing ambients, such as forming gas or vacuum [1010]. More specifically, they found that annealing in an atmosphere of CO_2 at 500 °C in a few minutes is very effective in removing PMMA (mainly carbon) without damage to the graphene. Atomic level cleaning of PMMA was also performed using radiolized water at high T. The cleaning process was studied by [1011]. The radiolized water was obtained via interaction of the electron beam in the TEM with water at high T. In this process of radiolysis, as the electron beam interacts with water and the graphene surface forms atomic hydrogen and hydroxyl radicals at high T. This process was reported at the submicron scale and will have to be demonstrated at much higher scales before considering it as a viable practical process, although it is contributing to the basic understanding of graphene surface cleaning.

VI.1.2. Electrochemical delamination

The use of PMMA as a carrier layer followed by chemical etching of the metal substrate is an effective way of graphene transfer. This process, however, can be time consuming and the whole metal substrate is

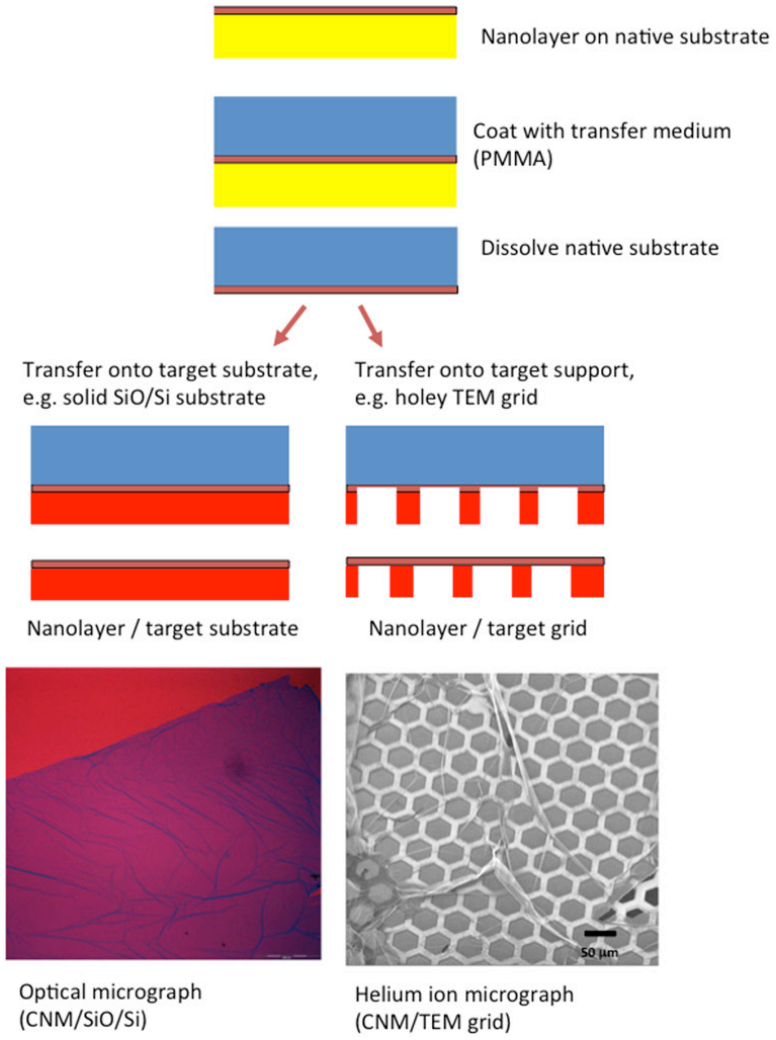


Figure VI.2. Top: Schematic of GRM transfer using polymeric media. Bottom, left: Optical micrograph of CNM transferred onto SiO_2/Si showing interference contrast; bottom right: HIM of CNM transferred onto a metal grid without critical point drying. Ruptures and faults, as well as large intact areas of the freestanding nanolayer are visible. Adapted from [75, 1009].

etched away. The latter makes the process costly and environmentally unfriendly. It would be desirable to use a process whereby the graphene film is removed from the substrate without significant metal loss and without damaging the overlying graphene layer. Electrochemical delamination was introduced to accomplish this task. Ref. [779] reported this processes for graphene transfer from Cu substrates and in Ref. [108] for the delamination of graphene from Pt. This technique is nondestructive not only to graphene but also for the metal and preserves the quality of the substrate so that it can be reused [108, 779, 780, 896, 1012]. After the growth process, the Cu foil with graphene on top is spin-coated with a thin layer of PMMA (4% in anisole, layer thickness ~350 nm) and cut into suitable pieces. PMMA also serves as a support preventing the graphene film from collapsing during Cu removal. A cleaner support for graphene transfer was suggested:rosin [1012]. As shown in figure VI.4, this technique takes advantage of the electrochemical process of metals in various solutions of e.g. (1) KOH [1013],(2) NaOH [1014], (3) $K_2S_2O_8$ etc to dissociate the weakly bound graphene from the metal substrate, Cu, Pt, etc [779, 1013, 1015]. $K_2S_2O_8$also etches Cu and thus is not totally non-destructive. However, at low concentrations one might be able to use it and still reuse the Cu substrate.

Using a custom-made mechanism (figure VI.4) (utility model P.411053) the Cu/Graphene/PMMA stack is placed in KCl, 1 mol dm^{-3}, at a rate of 1 mm s^{-1} or an aqueous solution of $K_2S_2O_8$ (0.05 mM) to perform the delamination. The graphene/Cu cathode is kept as the negatively polarized (from 4 to 10 V) and the anode can be made of a number of materials including glassy carbon. Hydrogen bubbles appear then at the graphene/Cu interface due to the reduction of water molecules and allow graphene to gently detach. The current depends on the Cu foil size and can be adjusted to control the delamination rate to ~1 mm s^{-1}.

In order to obtain the best results, the samples are gradually immersed in the electrolyte solution at an angle ~45° as in figure VI.5. At this angle the graphene/PMMA stack slowly moves towards (floats) the top of

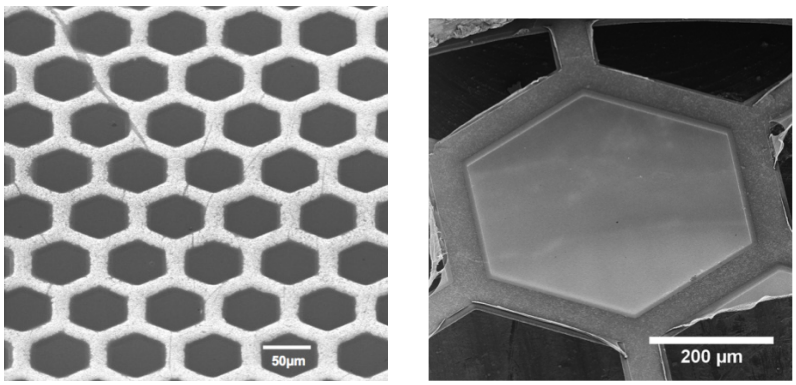


Figure VI.3. HIM image of large freestanding CNMs transferred onto hexagonal TEM grids. (left) The size of each hexagon is 50 μm and the grid is uniformly covered by the CNM.Scale bar is 50 μm. Right) The size of the hexagon is 500 μm and it is completely covered by CNM, no wrinkles or folds seen. Scale bar is 200 μm. Adapted from [1007].

the solution and the Cu foil moves toward the bottom of the glass container. After the delamination process, the detached Graphene/PMMA stack is rinsed with DI water, transferred onto the substrate, heated to 130 °C, and treated with acetone to remove PMMA. Next, graphene samples are dried for 1 h at high T (~350 °C) in high vacuum [851, 1010] or high pressure [1016] furnace to be sure that the organic residues and impurities are removed, although other methods claim no polymer residue [851, 1017]. After the delamination process, the detached Graphene/PMMA is rinsed with DI (deionized) water [1011], transferred onto the substrate, heated to 130 °C, and treated with acetone to remove PMMA. Additionally, UV-irradiation was suggested to facilitate PMMA rinsing [1018]. When substrates other than Cu are used to grown graphene, such as Ir, an additional step before the main electrochemical delamination process is needed. It was shown that an effective transfer could be achieved in SLG/Ir samples after treatment with a 0.1 M tetraoctylammonium-bromide TOABr/acetonitrile solution prior to the electrochemical delamination [1019, 1020]. Figure VI.5 presents the scheme of the graphene transfer process. Figure VI.6, shows the iteration of the transfer process to place MLG on PMMA [1021]. Ref. [1015] found that the delamination of graphene from Pt and Cu electrodes (substrates) increases with Na(OH) concentration, making this attractive as practical process to remove graphene from metal surfaces. More work is needed to bring this process from laboratory to 'production'.

One of the most difficult challenges are residues left by the PMMA used as the carrier μ. Ref. [1022] studied the surface of CVD graphene before and after transfer and compared it to HOPG. They found that there are significant organic residues that limit μ [851]. It is difficult to completely remove all impurities using only the organic solvent and the PMMA residue from the graphene surface. High-T treatment in high-vacuum is additionally needed for a more effective and cleaner transfer. To examine the effect of T during this treatment, x-ray photoelectron spectroscopy was used (see section IX.2/ARPES) to determine the chemical composition of graphene surface before and after heat treatment. A large O1s [812] peak on the XPS graphene spectrum before the heating is apparent in figure VI.7. An enhancement of the intensity of the characteristic C1s XPS peak located at 288.9 eV, which represents the C–C=O and O=C–O groups [812], is a signature of an incomplete PMMA removal. After heat treatment in 350 °C in high-vacuum, the C1s and O1s XPS peaks in figure VI.7 are the same as those corresponding to graphene samples that had never had been into contact with PMMA, confirming that the removal of the polymers is complete.

An additional method for the confirmation of the PMMA residue removal is scanning near-field optical microscopy (s-SNOM) [1023, 1024] (see section IX.1/AFM for an introduction to the technique). Topography and near-field images recorded on graphene samples on SiO_2/Si before and after heat treatment are shown in figure VI.8. After heating the graphene surface looks much cleaner, the wrinkles smoothen and the particles derived probably from PMMA are fewer. As the probing depth of s-SNOM is larger compared to the graphene thickness, the recorded optical contrasts show not only the local defects in the graphene layer but also differences in the substrate composition and in the distribution of the PMMA contamination

A spectroscopic method based on imaging an area at different wavelengths was used to test whether the contamination particles randomly spread across the graphene samples are indeed PMMA molecules. As the dielectric function depends on the wavelength [1025], the scattering coefficients (amplitude and phase) of the investigated materials varies with the tuning of the laser wavelength [1026]. Imaging at 1150 cm^{-1} illumination frequency, on resonance with the SiO_2 vibration (asymmetric stretching vibration of the oxygen atoms bridging the Si-O tetrahedral groups) the optical contrast between graphene/SiO_2 and PMMA particles is the largest. The near-field IR images recorded on a PMMA particle in figure VI.9 show a stronger phase at 1740 cm^{-1} due to the carbonyl band absorption at this

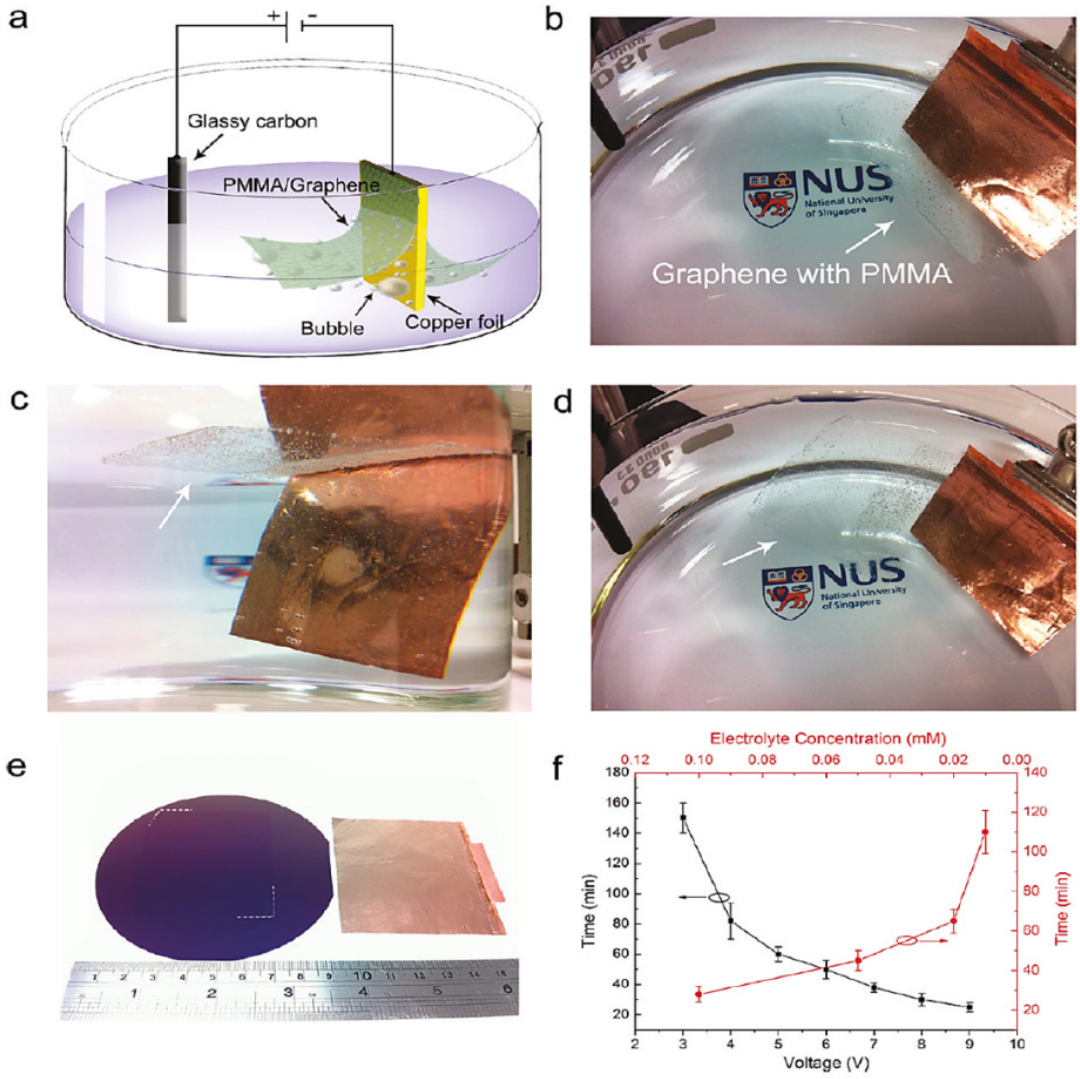


Figure VI.4. Electrochemical exfoliation of graphene from Cu. (a) Schematic diagram of electrochemical cell used for exfoliation, (b)–(d) optical images showing the 'whole film' peeling of PMMA-covered graphene form Cu. (e) Graphene film wet transferred onto a 4 inch wafer. (f) Time needed for complete film exfoliation of a 5 cm × 5 cm foil as a function of voltage and electrolyte concentration (at 5 V, red line). Adapted from [779], copyright American Chemical Society.

wavelength [1027], while the optical phase on the graphene and substrate is larger at 1150 cm^{-1}, matching the SiO_2 phonon absorption [1028]. For both wavelengths, the optical amplitude (scattering efficiency) is stronger on the inorganic materials compared to PMMA, due to the lower reflectivity coefficient on the polymer [1029]. These measurement together with the XPS strongly suggest that the particle residue is PMMA.

Ref. [1012] studied the use of rosin ($C_{19}H_{29}COOH$) as a support layer. The advantage is a high solubility in organic solvents, weak interaction with graphene, yet strong enough to enable support and transfer. These potentially make it a more suitable support in comparison to PMMA, as for the XPS data comparison of the transferred graphene using the two different materials [1012]. Therefore, through a combination of support material selection and surface treatment process/cleaning one can in principle create a graphene surface that is clean enough for many applications. The cleanliness needed will depend on the application.

Another way to ensure a clean graphene surface is to coat it with a metal or an oxide to eliminate the adhesion of any organic compounds. Ref. [1017] used Au as interface layer between graphene and PMMA and demonstrated a decrease in contact resistance of a factor of two. Ref. [1030] used Ti as an interface material to clean the graphene surface after transfer. Ti reacts with the residues on the graphene upon deposition. The 'reacted' Ti is then removed using a dilute HF solution. This also led to a decrease in contact resistance.

VI.1.2.1. Chemical delamination

There are two main techniques that have been evaluated to delaminate graphene from metals chemically: (1) Tetraalkylammonium (TOA)-assisted electrochemical delamination and (2) water delamination. The first is is a modified electrochemical delamination ('bubbling') method which enables the exfoliation of SLG and FLG or h-BN from substrates which are more strongly interacting than

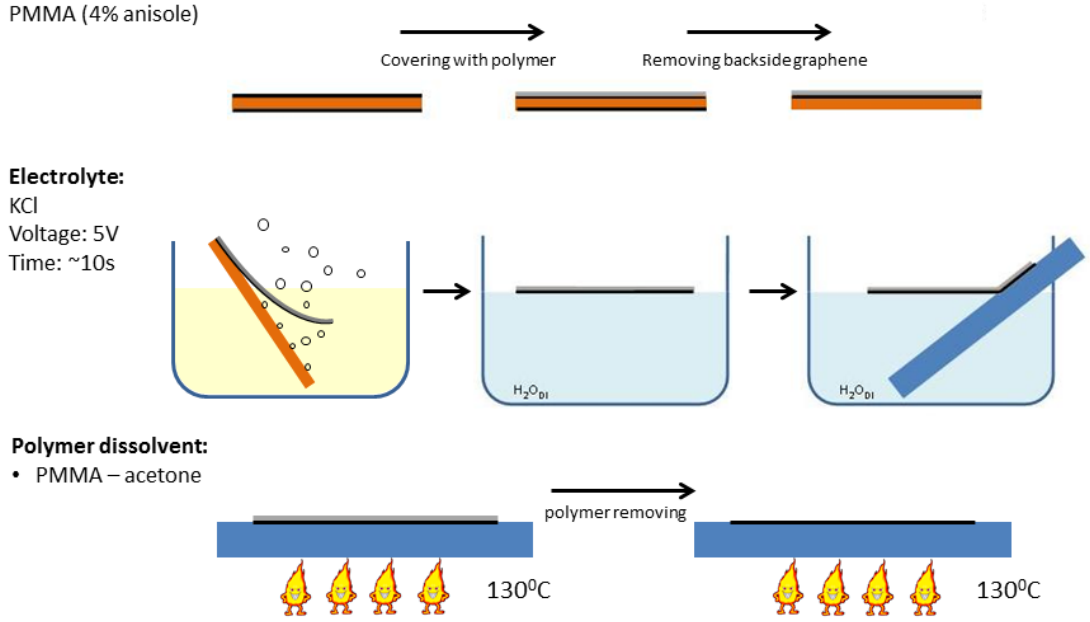


Figure VI.5. High-speed electrochemical delamination graphene transfer. Adapted from [1021], with the permission of AIP Publishing.

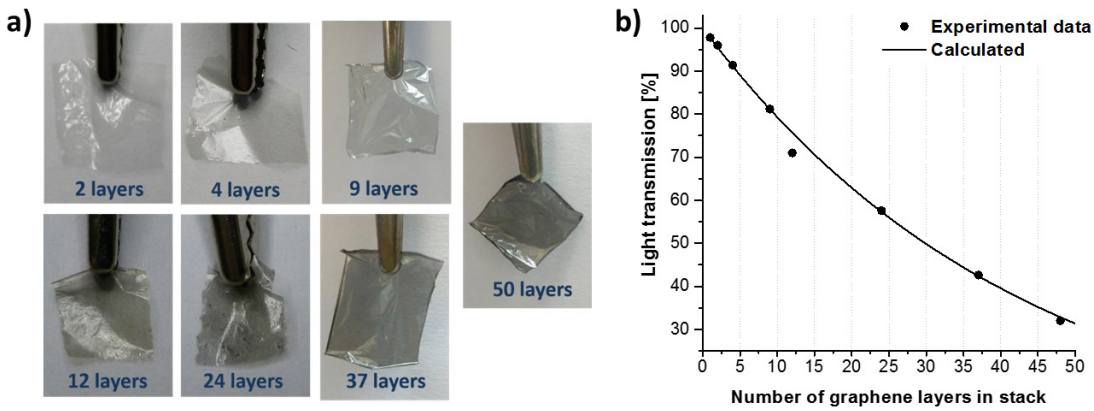


Figure VI.6. (a) Images of stacks of 2, 4, 9, 12, 24, 37, 50 LGs on PMMA. (b) Optical transmittance of MLG stack.

Cu [1031]. The TOA pretreatment was introduced in Ref. [1019] to enable the subsequent delamination of Graphene on Ir. Tetraalkylammonium compounds are weaken the interactions of sp^2 materials with the underlying metal [1019, 1020, 1032], thus facilitating the subsequent detachment from the substrate. TOA^+ intercalation is a 3-electrode electrochemical procedure which requires the use of a potentiostate to ensure a fine control on the bias between working and reference electrode. In the following, reference will be made to graphene grown on Ir, but the same protocol applies to many other LMs, including h-BN/Rh and $MoSe_2$.

The experimental set up of the electrochemical cell can be seen in figure VI.10. The cell is open to the air or Ar atmosphere. The Working Electrode (WE) is the graphene/Ir sample. It is fixed to one corner by an alligator clip. The reference electrode (RE) is an Ag wire (alternatively one can use a standard Ag/AgCl or any other reference electrode, in which case one needs to correct the bias between WE and RE to account for the potential offset of the RE). The Counter Electrode (CE) is a Pt wire. The WE and the RE should be placed as close as possible facing each other (avoiding contact); the CE should be facing the WE (with the RE between the two) and should be immersed in such a way to expose a large area. The operation of the vessel follows several steps. Fill the vessel with 10–20 ml of TOABr/acetonitrile solution (0.1 M concentration, i.e. 5.46 g of TOABr every 100 ml of solution). Subsequently, degassing the solution with Ar or N_2 for 15 min is required. After, leave the Ar/N_2 capillary tube above the vessel, in order to maintain an Ar or N_2 atmosphere and prevent air from dissolving into the solution. Then, apply −1.9 V between WE and CE for 10 min to promote TOA^+ to the graphene/metal interface. A partial discharge of the sample for 20 s at −0.2 V follows to obtain Ir/TOA/graphene stack. This step is needed to prevent the

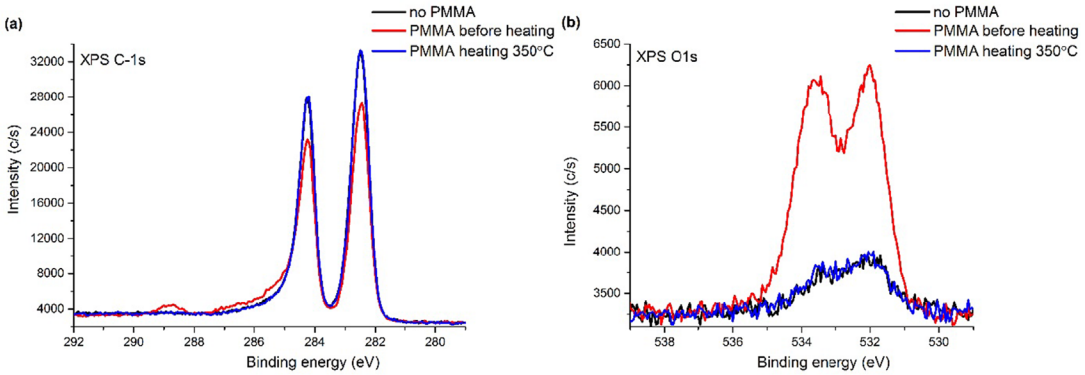


Figure VI.7. High resolution XPS C1s (a) and O1s (b) spectrum of transferred graphene samples before heating (red line), after heating (blue line) and graphene samples without contact with PMMA (black line).

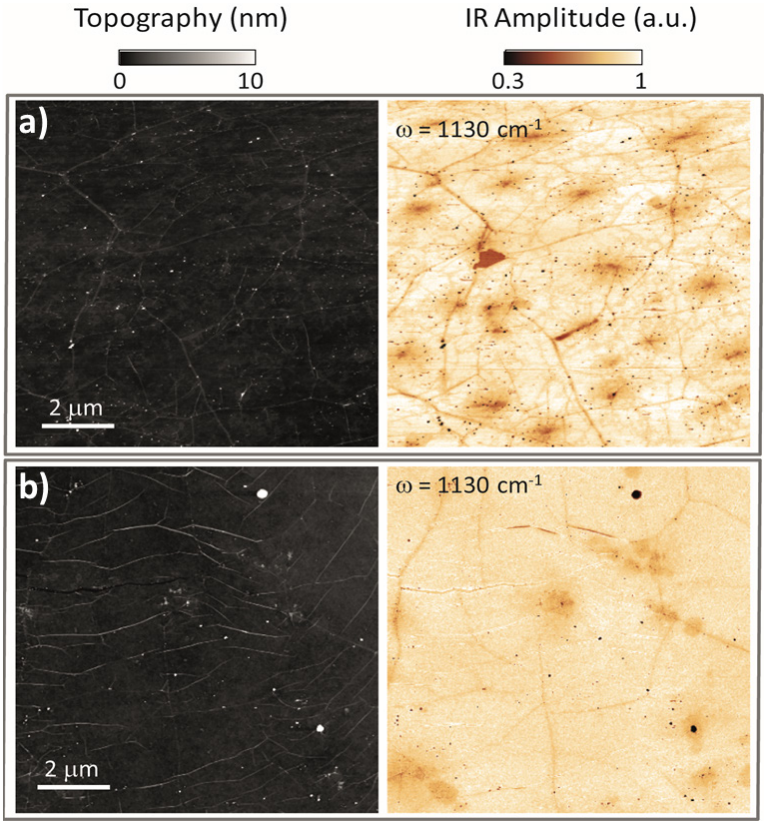


Figure VI.8. AFM and near-field IR images recorded from samples before (a) and after (b) heat treatment. Scan size for each measurement was $10 \times 10\ \mu m^2$.

negatively charged graphene from reacting with the PMMA and facilitate subsequent PMMA removal.

After TOA-pretreatment, the samples must be rinsed in acetonitrile, dried in N_2 atmosphere, and spin-coated (or drop-coated) with PMMA. The samples can be then exfoliated according to the electrochemical delamination explained above [1021].

Water intercalation has also been found to be an effective method of decreasing the bonding between graphene and underlying metal substrate [1033]. In this process, water is intercalated between metal substrate, e.g. Pt, and graphene. The intercalated graphene film/metal substrates is then placed on a hydrophilic SAM surface, dry bonded and transferred through an electrolysis process. This process enables the reuse of the growth substrate without significant metal loss.

VI.1.3. Electrochemical oxidation by cyclic voltammetry

Electrochemical oxidation can be described in terms of the formation of a metal-oxide layer at the interface between graphene and metal. A rational optimization of the parameters of this process follows the methodology described below. The voltammetric profile of Pt in a non-adsorbing electrolytes is known [1034], but the conclusions can be extended to other metals. It was reported [1035] that the processes that occur at the metal surface can be described by the reaction

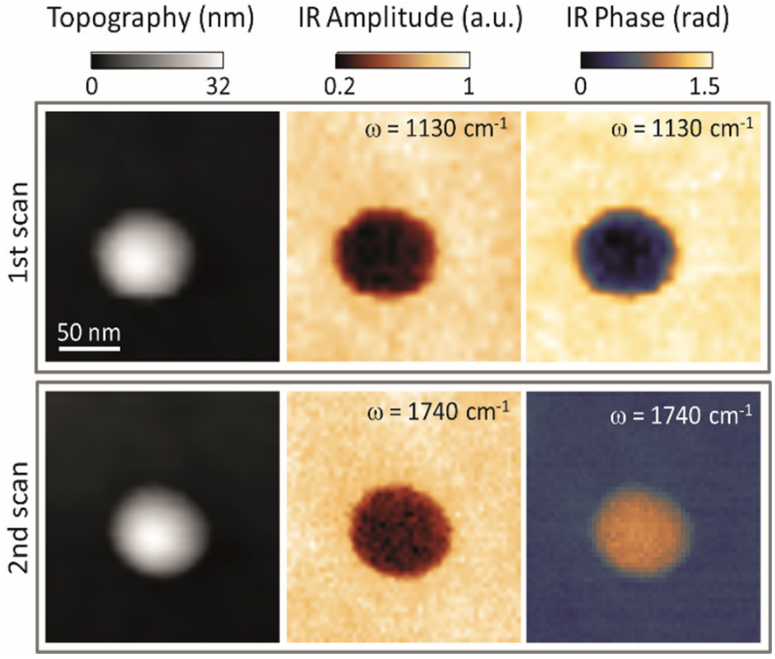


Figure VI.9. Sequential imaging of a PMMA particle at 1130 cm^{-1} and 1740 cm^{-1}. Scan size: 200 × 200 nm.

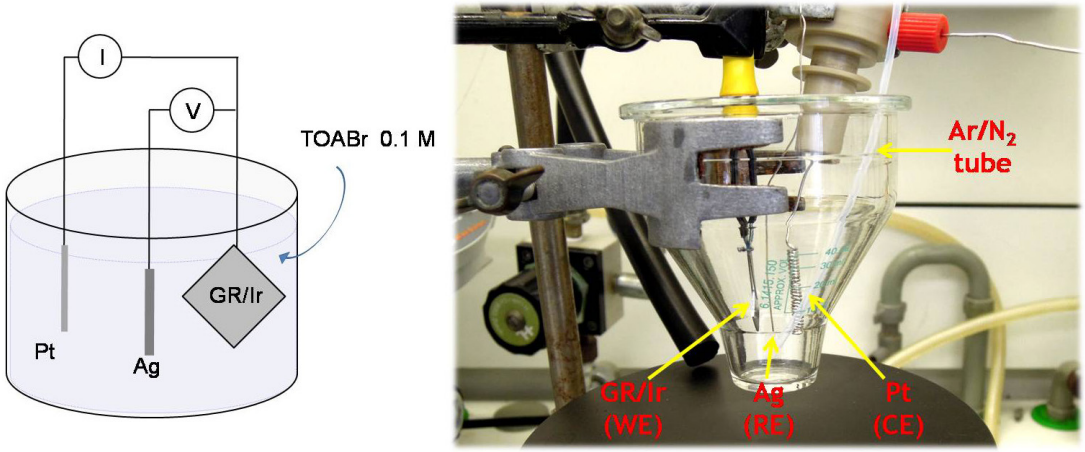


Figure VI.10. 3-electrode setup used in TOA intercalation and voltammetry experiments. Adapted from [1020], with permission from AAAS.

$$H_2O + (*) \leftrightarrow OH_{ads}\,(*) + H^+ + 1e^-$$

where ∗ stands for a free Pt adsorption site. In a first step, the water molecules interact with the graphene/Pt electrode, intercalating through graphene, then dissociate in the Pt surface forming $Pt_2(OH_{ads})$. A charge ~101.50 $\mu C\,cm^{-2}$ is transferred, corresponding to the formation of $Pt_2(OH_{ads})$ with a coverage close to 1 monolayer. Even though SLG presents a barrier to direct access to the metal surface, the water molecules are able to diffuse onto the metallic substrate via surface defects [1036]. The intercalated water between SLG and metal surface is responsible for the oxidation of the outermost Pt atoms when an appropriate potential is applied.

Voltammetric measurements were performed under N_2 in a three-electrode set up (figure VI.11) [1037]. There is a N_2 gas inlet and outlet to assure an inert environment during the electrochemical oxidation. A Pt wire (99.99% purity) serves CEand all the potentials are quoted with respect to the Ag/AgCl (RE. The Ag electrode is specific for the cell (Ag/AgCl electrode driref-25H, WPI). The WE is the Pt(1 1 1) sample covered with a SLG. The WE area exposed to the solution is 0.33 cm^2 in all experiments. The electrochemical cell is set into a Faraday cage in order to reduce the signal-noise ratio. The electrolyte employed is 0.1 M $HClO_4$ and the water is purified with a Millipore Milli-Q purification system. A scan rate of 0.05 $V \cdot s^{-1}$ is selected to control the oxidation reaction. The anodic potential is varied to obtain the optimal conditions to decouple graphene from Pt avoiding side reactions, such as the evolution of CO_2 and O_2, and defects in the graphene network. The sample is placed on the electrochemical

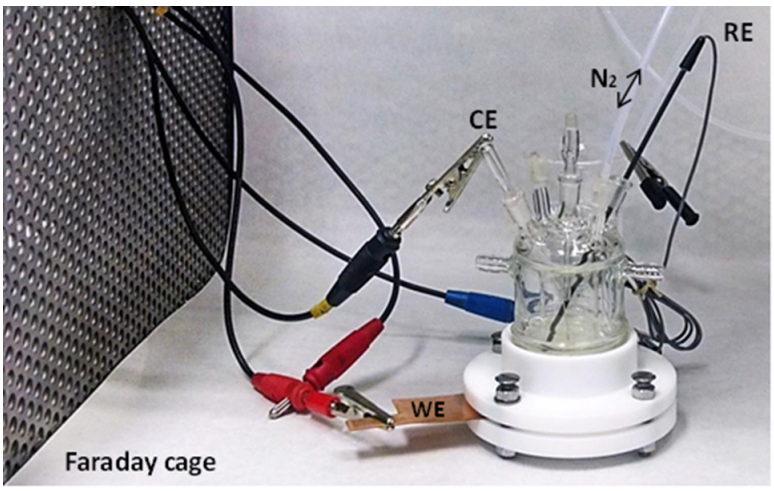


Figure VI.11. Electrochemical cell used for the electrochemical oxidation of Pt in the Graphene /Pt (1 1 1) stack. RE, is the Ag/AgCl reference electrode, CE the Pt counter electrode and WE the working electrode (i.e. stack graphene/ Pt(1 1 1). The cell is purged with N_2 and installed inside a Faraday cage.

cell for 1.5 h soaked into the previously deoxygenated acid solution so water molecules are able to diffuse onto the metallic substrate via surface defects [1036]. Figure VI.12 shows four cyclic voltammograms with different experimental conditions used to decouple an area ~0.33 cm^2 of graphene from Pt(1 1 1).The first protocol (A, figure VI.12(a)) is an anodic potential scan from 0.36 to 1 V followed by a cathodic potential scan between 1 V to 0.7 V. The second B, figure VI.12(b)) is similar, but with a higher applied potential (1.05 V). In the third cycle (C, figure VI.12(c)) the potential is even higher (1.45 V). In the last one (D, figure VI.12(d)) two cycles are involved: a complete oxidation-reduction in the range 0.45–1.1 V and a subsequent oxidation up to 1.1 V, followed by reversing the potential finishing at 0.7 V. The applied potential in A is not high enough to decouple graphene. D is the most aggressive and the sample is decoupled but also damaged. B and C accomplishthe best decoupling, meaning that every method in between those ranges will be appropriate to decouple graphene from Pt.

Table VI.1 summarizes the potentials and scan rates for the shown cyclic voltammograms. It also includes the parameters to oxidize Pt and the charge involved in the oxidation process, as well as the charge to get 1 monolayer of Pt_2OH. The presence of SLG delays the oxidation process compared with the clean Pt(1 1 1) sample, requiring higher overpotentials to attain a comparable oxidation charge. The charge obtained by integrating the anodic peaks for the other treatments is lower in comparison with the target. The process starts when the oxide coverage is much less than one monolayer (~0.25 of monolayer). Table VI.1 also includes the parameters to decouple graphene from Ir(1 1 1).

VI.2. Semi-dry transfer: hot press lamination and UV assisted transfer

UV adhesive (UVA) and hot-press lamination (HPL) [1040], which can be broadly classified as semi-dry transfer. This is the process of transferring graphene without complete immersion of substrate and graphene in an aqueous environment [115]. In particular this refers to the use of melt techniques whereby a liquid interfacial layer is solidified by various means [1759]. Both methods are large-area-compatible [115], and are capable of producing transferred layers that are optically transparent and electrically conductive whilst retaining areal uniformity with only a few percent variation. UVA and HPL are stable under bending stress and fatigue with a resistance towards micro-crack formation compared to ITO and FTO platforms [1760].

Figure VI.13(a) outlines the HPL process [1040]. Thermally activated ethylene vinyl acetate (EVA) treated PETsubstrate were used, however other supports such as thermal release tape (TRT), with different adhesive strengths ranging from 2.5 to 7.0 (N/20 mm), can be also used. First, the as-synthesized graphene-on-Cu stack is sandwiched between the polymer and a 125 μm-thick PET substrate, the acting as mechanical support. The sandwich structure then traverses a dual roller laminator, which is, contingent on the laminate used, either cold [1761] or heated to ~100 °C [1040]. Following lamination, the backside laminate, i.e. the side in contact with the heated stage during CVD, is mechanically detached. This exposed graphene-coated-Cu face can then be ashed to remove residual organics along with the defective graphene layer. The Cu catalyst is then etched, in this case, using $(NH_4)_2S_2O_8$ in de-ionised (DI) water (1 M) for 12 h. The transferred films are subsequently rinsed in DI water and dried in high-purity N_2. Up to 0.1 m^2 areas were transferred using this method, though larger areas and subsequent integration into roll-to-roll process lines are easily accommodated. EVA is also suitable for flexible substrates, which cannot withstand solvents such as acetone and/or isopropyl alcohol [1762]. Following transfer, the resulting polymer/graphene stack

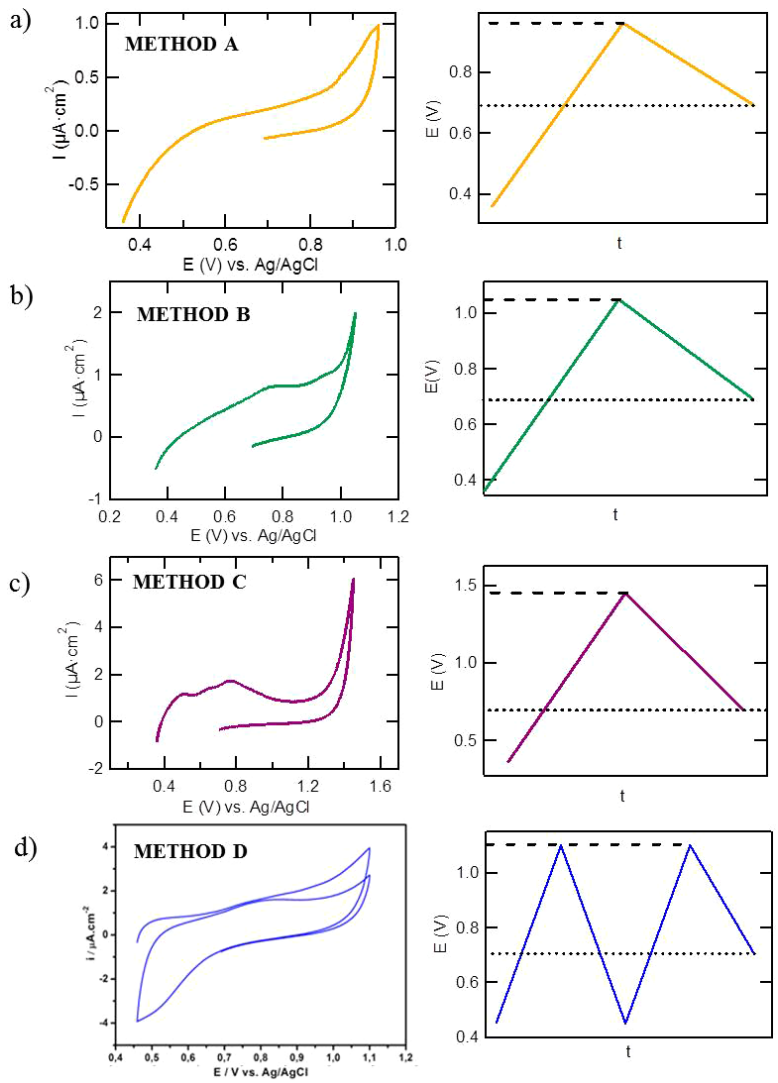


Figure VI.12. Cyclic voltammetries for graphene on Pt(1 1 1) in 0.1M aqueous $HClO_4$ solution. Four different voltammetric treatments have been applied (A, B, C, D), being the scan rate 0.05 V · s^{-1} in all the cases. The right panels plot the potential programs applied to the SLG/Pt electrodes, producing the corresponding cyclic voltammograms of the left panels.

Table VI.1. Parameters for potential-controlled electrochemical oxidation of Pt(1 1 1) and Ir(1 1 1) with SLG on top. Ei stands for the initial potential, Esup for the upper limit of the potential, Ef for the final potential, v for the scan rate and Q for the charge.

		E_i (V)	E_{sup} (V)	E_f (V)	v (V · s^{-1})	Q (μC · cm^2)
				1 ML Pt_2OH		120
SLG/Pt(1 1 1)	A	0.36	1	0.7	0.05	10
	B	0.36	1.05	0.7	0.05	32
	C	0.36	1.45	0.7	0.05	106
	D	0.46	1.1	0.7 (cycle and a half)	0.05	24
Pt(1 1 1)	B	0.36	1.05	0.6	0.05	101.5
Gr/Ir(1 1 1)		0.2	1.0	0.9	0.05	140.8

remains attached to the target substrate. Repeated lamination, at RT or elevated T, can be undertaken to further remove absorbates, bubbles, voids and non-conformalities in the transfer [1719, 1720]. In the case of TRT, the support-coated substrate is finally baked at 120 °C to remove the TRT.

Figure VI.14(b) outlines the UVA transfer [1040]. The UV adhesive is first coated onto a polymer substrate by spin coating at 5000–8000 rpm for 30–60 s, following a preliminary casting at 500 rpm for 10–20 s. This coated substrate is then placed in contact with the as-grown graphene-on-catalyst. This sandwich is subsequently compressed at 0.2 MPa using a cold-roll laminator, to avoid air pocket formation at the interface. The UVA is subsequently cured by exposing the backside of the PET to a UV optical source (365 nm, 20–25 mW m^{-2}) for 10–15 min. The Cu foil is etched in aqueous ammonia persulfate for 12 h, rinsed in DI

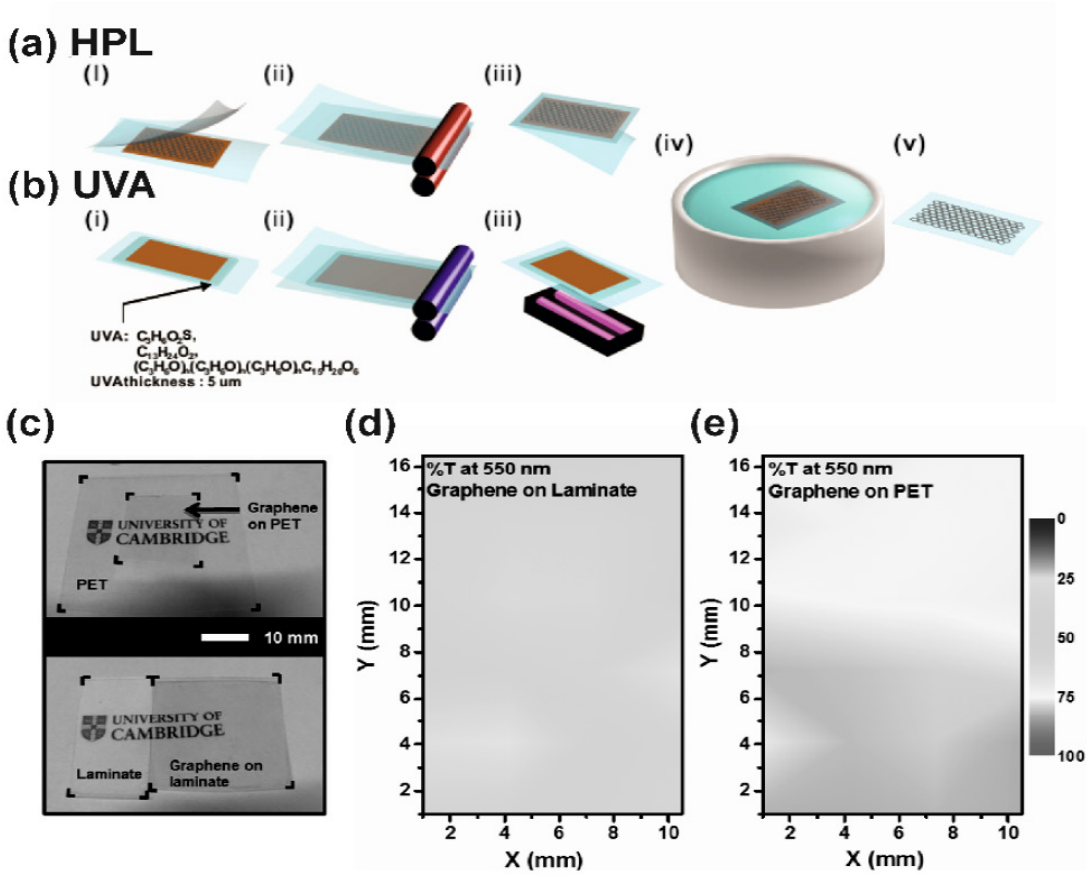


Figure VI.13. Graphene transfer by (a) HPL and (b) UVA, and (b) corresponding optical images and (c) and (d) 550 nm optical transmission maps. Adapted from [1038–1040].

water and dried in high-purity N_2. All at RT, making the approach applicable to a wide range of polymer substrates. Figure VI.14(c) shows typical optical micrographs of transferred samples that exhibit long-lasting adhesion between substrate and graphene[1040].

VI.2.1. Benchmarking and ageing effects

Ref. [1040] reported that the optical transmittance (%T) for HPL and UVA transfers was ~10% and 12% lower than the uncoated substrates. This was assigned [1038–1040] to the transferred graphene and the augmented optical properties of the interfacial binding layer. The spatially averaged 550 nm transmittance of HPL and UVA is ~58.6% ± 3.6% and 76.5% ± 3.8%, respectively [1040]. Both techniques result in equivalent areal uniformity with <4.0% variation. The increase in absorption is likely due to folding and wrinkling of graphene during transfer. Ref. [1040] reported a rms of HPL ~26% higher than UVA. The agglomerates, 5.5 ± 5.6 μm (UVA) and 7.9 ± 3.9 μm (HPL), are most likely adhesive residues.

Using PMMA transferred graphene on quartz, with Cr/Au van der Pauw structures on the order of tens of micron in channel size, graphene showed R_s~5.47 ± 1.20 kΩ sq^{-1}. R_s for HPL transfers was ~9.9 ± 3.8 kΩ sq^{-1}, whereas UVA showed lower values ~3.5 ± 2.3 kΩ sq^{-1} [1040]. Elemental analysis revealed significant (S) and (O) peaks in UVA transfer, attributed to Cu etchant exposure [1763]. Such peaks were absent for HPL transfers [1764]. S is a strong dopant of graphitic carbons [1765].

The 550 nmtransmittance of UVA transfers tends to increase with time (~80%) [1040]. No observable change was reported for HPL transfers, likely due to the absence of doping. The metallic component of may be central to the doping temporal stability [1039].

HPL transfers were reported with a time invariant R_s (5.0 → 5.2 kΩ sq^{-1}), whereas R_s of the UVA transfers increased from an initial 2.2 kΩ sq^{-1} to 3.5 kΩ sq^{-1}, after 200 h, suggesting the need for an hermetic capping layer [1766]. Such deleterious increase in R_s in due to time and ambient unstable Sdoping associated with the necessary Cu-etching. R_s doped graphene remains approximately one order of magnitude larger than achieved by doping strategies reported elsewhere [1051, 1041, 1042]. This may be, in part, associated with the macroscale measurements undertaken, and the necessarily higher areal density of defects within the measured channels.

To attain a robust mechanical interface, graphene requires proximal contact to the substrate [1767]. In both transfer approaches, the as-grown graphene-on-catalyst achieves contact the EVA melt and to low-viscosity UVA prior to curing. Graphene transferred in this way showed lower surface energy and higher adhesion (UVA: 4.40 ± 1.09 N m^{-1}, HPL: 0.60 ± 0.26 N m^{-1})

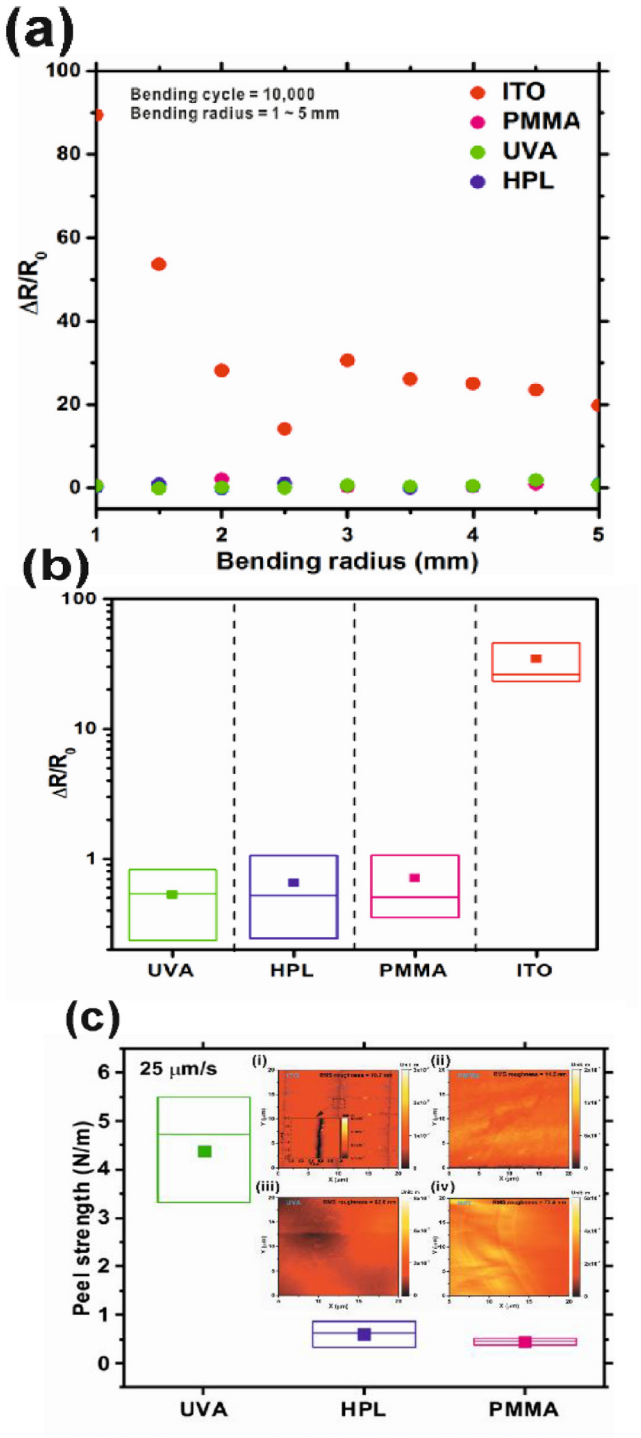


Figure VI.14. (a) Change in normalised resistance ($\Delta R/R_0$) with bend radius. (b) $\langle \Delta R/R0 \rangle$ for all bending diameters for UVA, HPL, PMMA and ITO. (c) peel strengths for transfer methods. Inset: Typical AFM height maps of fatigued transfers. Adapted from [1038–1040].

compared to PMMA transfers (PMMA: 0.44 ± 0.06 N m^{-1}) [1040].

To assess the bending fatigue performance, transfers were assessed during 10^4 bend cycles with the differential resistance extracted after each (figure VI.14(b)) [1040]. ITO on PET showed a 95-fold increase in differential resistance, up to ~190 kΩ. After such testing, the fatigued ITO showed a significant difference in resistance between its bent and relaxed state. The differential resistance of graphene, in both UVA and HPL increased from ~46 kΩ to 74 kΩ, with less than ±0.5 kΩ difference between bent and relaxed states [1040], highlighting the robustness in maintaining electrical continuity even after many thousands cycles. The is was~60 times higher than ITO/PET.

The differential resistance as a function of angle and bend radius was also investigated (figure VI.14(b)) [1040]. All transfers demonstrated a low normalized resistance even at bend angles ~100° (1.05, PMMA; 0.94, UVA; and 1.04, HPL), almost two orders of mag-

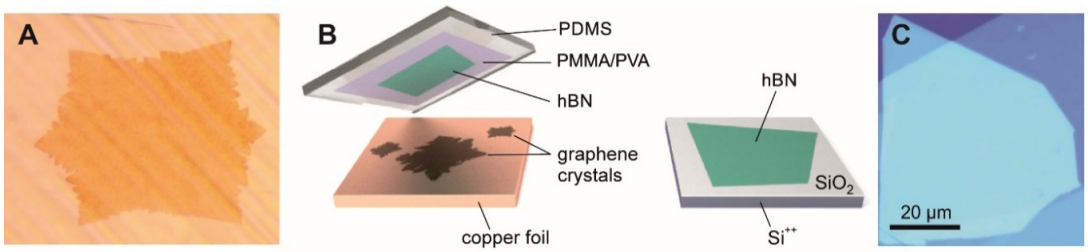


Figure VI.15. (A) Graphene crystal onCu grown as described in section VI.1.2. after exposure to ambient conditions for several days. (B) Schematic of dry transfer. (C) h-BN/Graphene/h-BN fabricated using contamination free dry transfer. Panel (B) is adapted from [832], with permission from AAAS. Panel (C) is adapted from [823], copyright American Chemical Society.

nitude less than optoelectronically comparable ITO on PET (79.8) [1768]. The mechanical robustness of transferred graphene is, regardless of the transfer method, much improved over ITO. UVA transfer showed consistently lower resistance for all bend angles, though HPL graphene repeatedly showed the lowest for bend angles >40°. These bend angle experiments suggest that UVA and HPL are somewhat more robust than PMMA in high-bend-angle applications, such as e-paper and wearable sensors. For bend radii $R_b = 1 - 5$ mm Ref. [1039] reported that ITO normalised resistance increased ~20/90 at $R_b = 5/1$ mm. Conversely, the change in the normalised resistance of all graphene transfers, including PMMA, were much smaller (PMMA: 0.5 − 0.9, UVA: 0.5 − 0.8, and HPL: 0.2 − 1.2) and showed no measurable dependence on R_b for the bend radii considered. UVA and HPL approaches seem to offer a viable solution to the limited flexibility, with maintained conductivity, of transparent electrodes used in flexible electronics.

T-peel tests were also conducted to explore the level of adhesion between graphene and flexible substrate [1769]. A low peel strength represents weak adhesion between laminate and substrate, while a high peel strength suggests that graphene is strongly adhering. As depicted in figure VI.14(c), UVA-transfers showed the highest peel strength (4.39 ± 1.09 N m^{-1}), followed by HPL (0.60 ± 0.26 N m^{-1}) and PMMA (0.44 ± 0.06 N m^{-1}).

VI.3. Dry transfer using h-BN

A contamination- free transfer process utilizes exfoliated hBN flakes to pick up graphene from Cu [823, 832]. Figure VI.16(a) is an optical microscopy image of a graphene crystal on Cu, exposed to ambient conditions for a few days, resulting in the oxidation of the interface between Cu and graphene. The oxidation of the interface does not only make the graphene optically visible, but also decouples it from the substrate.

For the transfer process, a polymer stack consisting of PDMS, PVA and PMMA is prepared. First, a glass slide is covered with scotch tape and drop coated with a 13% aqueous solution of PVA and baked at 95 °C for 5 min. Subsequently, the slide is spin coated with PMMA (4%, 50 k, in ethyl lactate) at 1000 rpm and baked for 10 min at 110 °C. Then, h-BN is exfoliated on the PVA and large, thin and defect free flakes are selected and cut out in a 5 mm × 5 mm square. The polymer stack can be lifted off the scotch tape using tweezers and placed on a 3 mm thick cushion of PDMS, resting on a glass slide. As depicted in figure VI.15(b), the h-BN is aligned with a graphene flake brought into contact and heated to 125 °C. During the cool down (at ~75 °C), the polymer and Cu foil are separated again, resulting in an h-BN flake covered with graphene on the polymer stamp. Next, an arbitrary substrate, e.g. an h-BN flake on Si/SiO_2, is aligned with the h-BN/graphene stack, brought into contact at 125 °C and peeled off the PDMS. Subsequently, stack of SiO_2/h-BN/graphene/h-BN/PMMA/PVA is placed in hot water, acetone and isopropanol, in order to dissolve the polymers. Figure VI.15(c) depicts such an h-BN/graphene/h-BN sandwich on a SiO_2 substrate.

VI.4. Graphene/PMMA sandwich structures

Removing PMMA after transfer is not allways necessary as there are potential benefits of building graphene/PMMA heterostructures [1040]. PMMA is a colorless polymer, commonly used as a glass replacement (acryl glass). Very thin, transparent PMMA could be beneficial. The dielectric constant of PMMA is 2.6 and comparable to fused silica (~3.5) [895], making PMMA a decent insulating layer between multiple graphene layers. PMMA has been used to prevent the contact of graphene with water during transfer, therefore enabling the use of water-sensitives substrate and in applications to fabricate flexible, air-stable, low-voltage GFETs [1043]. A polymeric bilayer consisting of PBU (bottom) and PMMA (top) can be used as a supporting layer for graphene transfer without affecting its promising intrinsic characteristics [1770]. The Dirac voltage and field-effect μ of GFETs with the polymeric layers kept the intrinsic properties of graphene unaltered in air for more than 130 days, whereas GFETs without polymers underwent significant and rapid degradation. High resolution positive tone electron beam resists, ARP-661.08 and ARP-672.08 (by Allresist(tm)), have been used to build PMMA/Graphene heterostructures [1044, 1045]. ARP-661.08 has molecular mass ~600 000 g mol^{-1} and requires chlorobenzene as a solvent or a thinner, while

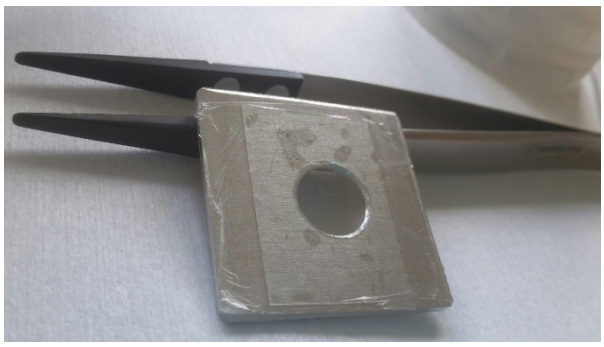


Figure VI.16. Free standing 500 nm thick and 10 mm in diameter graphene/PMMA structure. The film is transparent and thus convenient for optical experiments.

ARP-672.08 has molecular mass ~950 000 g mol^{-1} and requires anisole as a thinner. Both thinners consists of a benzene like structure and are small size weight ~110 g mol^{-1}). The higher molecular mass of ARP-672.08 can increase the resist film durability, which can be beneficial if the resist film needs to be transferred or made free standing. When the PMMA/Graphene film is deposited on a substrate, long PMMA molecules can be reduced in size by electron beam lithography [904, 1046]. This may open up an interesting route for graphene patterning [1046].

PMMA layers with thickness ~600–800 nm have been used in heterostructures [1044]. After spin coating, Cu/graphene/PMMA was baked at 60 °C for 10 min to evaporate most solvents. The transition temperature of PMMA from soft polymer to acryl glass is ~100 °C [904]. Similar recipes can be used to transfer the PMMA/Graphene hybrid or as a free standing. Elastic and thin graphene/PMMA films can be stacked [1044]. Figure VI.16 shows a free standing 500 nm graphene/PMMA sandwich placed on an Al aluminum plate with 10 mm diameter hole. The sample is prepared by using ARP-672.08 resist (4.5% diluted with anisole). Similar 1 μm thick free standing films were fabricated using ARP-661.08 (4.5% diluted with chlorobenzene) [1045].

Multi-layered structures, where graphene is sandwiched between two PMMA layers, can be prepared and used as EMI shielding layer by absorbing >50% of electromagnetic waves at 30 GHz [1044].

VII. Growth and transfer of other layered materials

VII.1. Hexagonal BN

BN, has been extensively studied as a dielectric material for LM-based devices It has a large bandgap (>6 eV), atomic flatness, chemical inertness and small lattice mismatch (1.8% larger) with respect to graphene [1047]. H-BN is a natural dielectric to GRMs as SiO_2 and Si_3 N_4 are to Si-based devices. The quality and structural characteristics of the hBN film can impact the performances of GRM-based devices. h-BN bulk single crystals, are very small, millimiters at most, and do not satisfy manufacturing requirements. In order to meet future, GRM based device manufacturing requirements, it is necessary to develop processes capable of providing large area single crystal or polycrystalline films that can meet both device and high volume production needs. The growth process selection depends on the materials requirements. Up to now most devices have used multilayer h-BN with only a few using monolayer films. It is likely that many applications will require multilayer films rather than 1L-h-BN, and some applications can use use polycrystalline films. The exact requirements will guide the selection of the film growth/deposition process.

Hexagonal hBN has been grown on metals, dielectrics and graphitic surfaces by various techniques and under different conditions. The basic growth techniques used so far are the following: (1) growth on dielectrics and graphitic surfaces by CVD and PA-MBE; (2) growth on metals by a diffusion and precipitation as well a surface limited processes; (3) Growth by ion beam assisted deposition and by physical vapor deposition. Each of these have advantages and disadvantages. When considering the use of any material for devices it would be desirable to deposit or grow it at low T on a desired surface as done for materials integrated in Si-based devices. In the case of GRMs it has been difficult so far to integrate/grow/deposit the m directly on the desired surface in a fully integrated flow. This issue has necessitated the development of specific film transfer processes which will be discussed a the end of this section. Therefore, the selection of a growth process will depend on whether the materials requirements can be met to satisfy the specifications of the individual application and on whether the material will be transferred or grown/deposited on the device being fabricated.

VII.1.1. Growth of h-BN on metal surfaces

h-BN was grown on Cu foils by LPCVD in a horizontal reactor using ammonia borane as BN source and H_2 as carrier gas [1049]. The growth of h-BN on metals can be carried out in a hot-wall low-pressure ~10^{-3} mbar reactor, vertical or horizontal, as for figure VII.1. This process can be redesigned to a vertical furnace batch type reactor commonly used by the semiconductor industry. Borazine is a volatile liquid with a relatively high vapor pressure (280 mbar at 25 °C), and is air and moisture sensitive [1050]. Therefore, its use requires a specific set-up to have an accurate control of the gas flow. To avoid gas flash in the CVD chamber and have good control the flow rate, borazine is maintained at 0 °C with a chiller to control the vapor pressure and a system of mass flow controllers is used to transport the gas to the growth chamber. A cold trap was installed to prevent the damage of the scroll pump with potentially non-decomposed borazine. The process follows the typical cycle of heating, pre-annealing (30 min under H_2 at 1000 °C) of the metallic substrate, usually polycrystalline Cu or Ni, growth at 1000 °C, a regulated pressure of 0.3 mbar, under 50 sccm of H_2, with $P_{borazine} = 10^{-2}$ mbar, for a time between 10 min and 2 h, and slow cooling under H_2 flow.

The role of the underlying metal, Ni and Cu, microstructure on the BN film morphology was studied. Figure VII.2(a) shows an optical image of a BN film grown on Cu and transferred onto a 90 nm SiO_2/Si. Yellow and pink areas correspond to folded edges of BN. The thickness of the film determined from the AFM profile is ~70 nm, with a 20 nm roughness (figure VII.2(b)). This behaviour is confirmed by TEM observation of the sample (figure VII.2(c)). The electron diffraction pattern, figure VII.2(d), shows several six-fold symmetry patterns and diffuse rings, indicating that the film is crystalline and turbostratic. This result is in agreement literature in the same range of T and borazine partial pressure [1051, 1052], for which a non self-limited growth, with a turbostratic stacking is expected. Due to its non-flatness and turbostratic structure, this hBN useful as a graphene substrate, as well as being good candidate to be used as dielectric compatible with GRMs as capping material in a device.

Higher crystallinity is achieved if h- BN is grown on Ni [1053–1056] as compared to the growth on Cu. Few investigations were performed to elucidate the influence of the underlying Ni grain orientation on the BN growth kinetics and coverage but there is hardly any record in terms of crystallinity, morphology and thickness of the BN film [1057, 1058]. In order to fully characterize the influence of the grain orientations of the substrate on the BN film structure, combined SEM and TEM imaging and electron diffraction of both BN film and underlying Ni substrate are used. Figure VII.3(a) is a SEM image of the as-grown BN on its substrate showing an area at the intersection of three differently oriented Ni grains. Their respective crystalline orientation is determined by Electron Back Scattering Diffraction (EBSD) in figure VII.3(b). Two different surface aspects of the film can be identified and are dependent on the Ni orientation. In the blue grain with a (1 1 1) orientation, the film surface structure is striated and nearly smooth, while for other orientations (0 0 1), red grain, the surface appears to be very rough. Direct transfer on the TEM grid enabled TEM observations of the same area. The TEM image

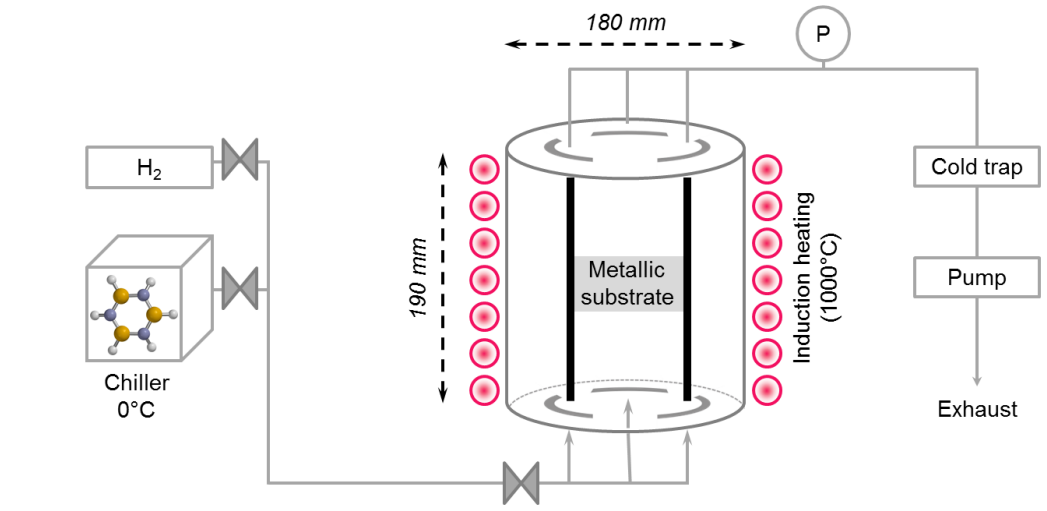


Figure VII.1. Schematic diagram of vertical CVD growth chamber for hBN growth on metal.

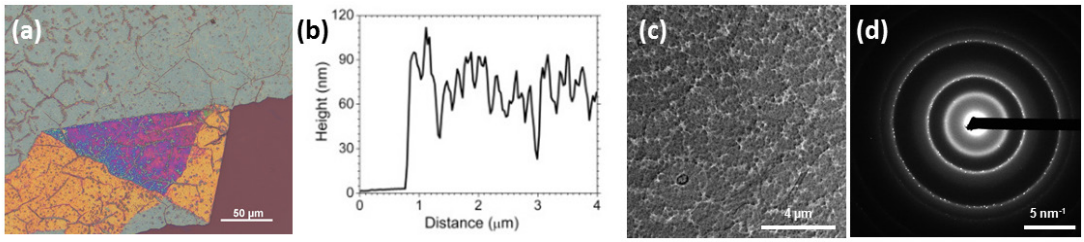


Figure VII.2. (a) Optical image of BN film grown on Cu and transfer red onto 90 nm SiO_2/Si, scale bar is 50 μm. (b) AFM profile showing the 90 nm thickness and the high roughness. (c) TEM image with scale bar 4 μm and (d) electron diffraction pattern showing the rough/turbostratic nature of the ML-h BN film grown on Cu with scale bar 5 nm.

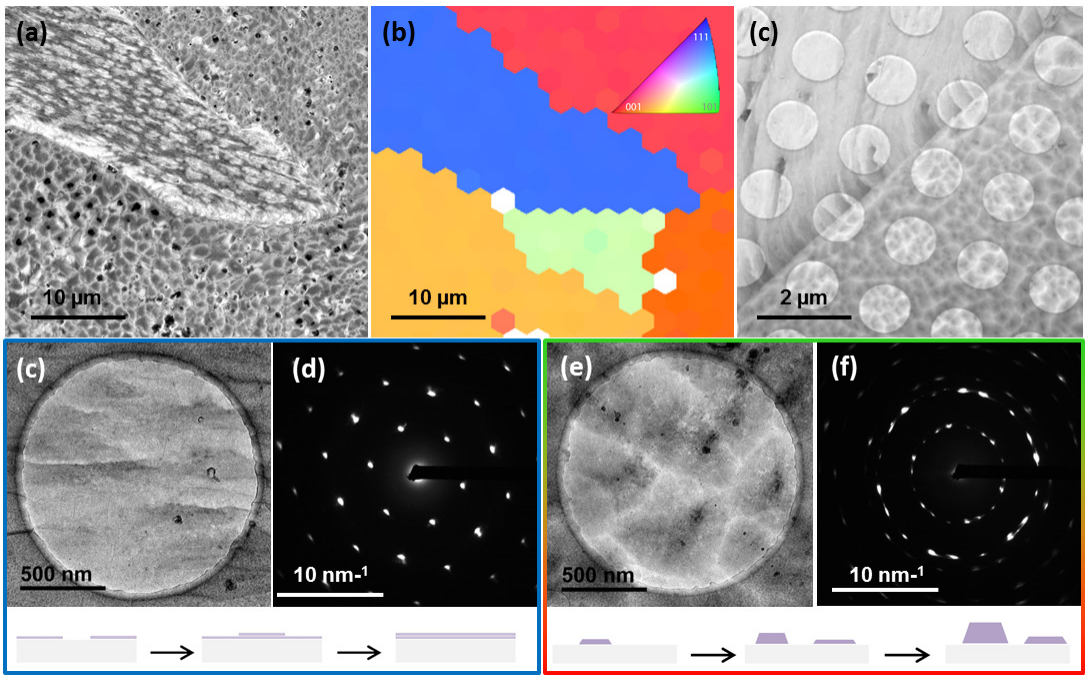


Figure VII.3. (a) SEM image and (b) corresponding EBSD mapping of BN on Ni. (b) TEM image of the BN film transferred polymer-free on holey amorphous carbon TEM grid. HR TEM images and corresponding electron diffractions of (c) and (d) a flat BN area and (e) and (f) a rough BN area with the schematic of the growth process: Van der Merwe for Ni(1 1 1) and Volmer Weber for Ni(1 1 0) and Ni(0 0 1).

of figure VII.3(c) reveals the effect of Ni grain boundaries on the BN film and confirms the presence of different BN morphologies depending on the underlying Ni grain orientation: flat and rough [1059]. As on Ni (1 1 1) hBN displays an almost perfect lattice match, the BN growth is highly oriented resulting in the formation of a flat h-BN as shown in figure VII.3(c). By recording electron diffraction patterns in different areas as shown in figure VII.3(d), the single crystalline character of the h-BN film over the whole Ni (1 1 1) grain is assessed. For (0 0 1) Ni grain orientations, the h-BN growth domains nucleate at different places on the Ni surface and grow independently from each other. This process is responsible for the island morphology characterized by thickness variations from an island to another, discontinuity between the islands (darker and brighter contrast on TEM image figure VII.3(e)) and multiple orientation domains (several rotated electron diffraction patterns, figure VII.3(f)).

This detailed analysis presented above on the growth of h-BN on polycrystalline Cu and Ni provides insights and guidelines for further optimization of the h-BN conditions leading to planar and single crystal layers needed for many applications.

The growth of h-BN at atmospheric pressure CVD (APCVD) may reduce the production costs of h-BN. Ref. [1062] synthesized h-BN by APCVD on polycrystalline Ni. Depending on growth conditions, the thickness of the obtained h-BN film is between ~5 and 50 nm with grain size limited by the size of the Ni single crystal grains. The controlled growth of h-BN on polycrystalline Pt foils by APCVD with ammonia borane as the precursor was also reported [1061]. 1L, 2L and FL-h-BN domains and large-area films were selectively obtained on Pt by changing the concentration of ammonia borane. 1L and 2L h-BN obtained are uniform with high quality and smooth surfaces.

In principle the quality of h-BN can be significantly improved by growing on single crystal metals. h-BN on Rh(1 1 1) (h-BN nanomesh) was first reported [1062]as well as on Rh(1 1 1)/YSZ-buffered/Si(1 1 1) [1063]. This substrate formation strategy may also be considered as a model system for growth of 1L- h-BN on transition metals (catalyst) surfaces at $T < 1000$ K. BN nanomesh has been extensively studied, starting from pure surface science [1062] to applications as electrodes in electrochemistry [1064, 1065] and exfoliation [1066]. It was used as a template for molecular assemblies in vacuum [1067], and is stable in air and in liquids [1065, 1067]. It was furthermore used to study the effects of hydrogen [1064, 1068] and metal intercalation [1069].

The h-BN nanomesh is a corrugated honeycomb superstructure and is the product of a high T CVD growth using $(HBNH)_3$ as a precursor. The highly regularly corrugated structure with a lateral periodicity of 3.2 nm is determined by the mismatch between hBN and Rh. The unit cell consists of 13×13 BN units on 12×12 Rh atoms. It has one 'pore' with 2 nm diameter, and is surrounded by 'wire' regions [1062, 1067] (figure VII.4(c)).The high T CVD growth of h-BN nanomesh on Rh(1 1 1) single crystal or Rh(1 1 1) single crystalline films on YSZ-buffered Si(1 1 1) wafers [1063] proceeds as follows. The substrate is first cleaned in UHV by Ar^+ sputtering (1.0 keV, 3.5 μA cm^{-2} sputter current) for ~30 min, and annealed to 700 °C. The substrate is kept at 700 °C for 5 min, and oxygen ($P(O_2) = 5$–8×10^{-7} mbar) is dosed for 10 min. This is followed by a flash-annealing treatment up to 900 °C for 5 min. The substrate is then cooled to RT. The whole preparation cycle (sputtering + annealing + O_2 dosing + flash-annealing) must be repeated twice to ensure high quality of 1L-h-BN on Rh(1 1 1). At the third treatment cycle, no O_2 dosing is needed. The substrate is directly flashed to 900 °C for 5 min after annealing. Then the substrate T is stabilized at 800 °C, and borazine is dosed at $P = 5 \times 10^{-4}$ mbar for 5 min. Afterwards the sample is cooled to RT with an initial cooling rate of 10 °C min^{-1}. The YSZ/Si(1 1 1) substrates may be coated with a large number of unary [903] and binary transition metals, which allows the tailoring of the growth products. The intercalation of other metals, such as like Au, was studied [1069]. On the binary transition metal PtRh it was found that the nanomesh unit cell may be tuned from 3.2 to 2.7 nm when increasing the substrate lattice constant from Rh to PtRh [1070].

VII.1.2. Growth of h-BN on graphitic and dielectric surfaces

It would be advantageous to to grow h-BN on dielectrics or graphitic surfaces in the absence of a metal catalyst to satisfy device integration requirements for many applications. Direct growth of h-BN layers on graphite substrates was achieved using high T plasma-assisted MBE [1071]. The h-BN grown on HOPG is hexagonal with no chemical intermixing with the graphitic carbon layers. This processes seems to provide high qualtiy commensurated growth of h-BN on graphite.

There are reports on the direct growth of Graphene/h-BN heterostrutures. Ref. [1072, 1073] took advantage of the solubility of C in Ni to grow a graphene/h-BN heterostructure by a combination of C precipitation and MBE of h-BN on Ni/MgO(1 1 1). The growth process was performed first by saturating Ni(1 1 1)/Mg(1 1 1) with C, then growing h-BN on the exposed surface at high T (>730 C). The process can yield FLG/FLG-hBN heterostructures. The greatest difficulty is the control of thickness of both graphene and h-BN at the 1L level. While h-BN may be desired as a FL film, in most applications the graphene layer number would have to be precisely controlled ($N = 1 \pm 0, N = 2 \pm 0$, etc).

Ref. [1074] grew wafer-scale and high-quality ML-h-BN on sapphire by LPCVD. Spectroscopic and microscopic measureements revealed that the h-BN film had a wrinkle-free surface and AA′ stacking, with a single orientation and a well-oriented superstructure with respect to sapphire. The electron transport in a

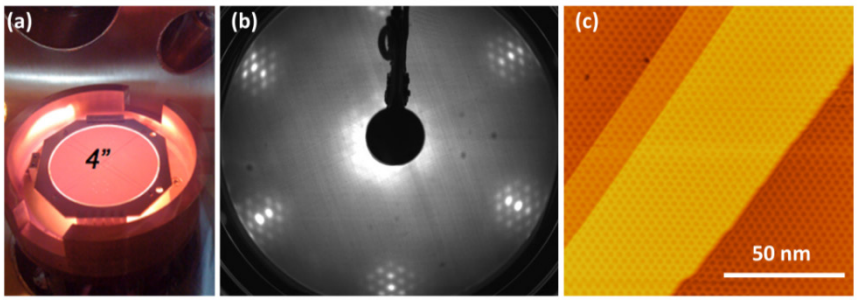


Figure VII.4. (a) 800 °C hot 4 inch wafer in the growth chamber. (b) Low energy electron diffraction (LEED) pattern of h-BN/Rh(1 1 1) at 60 eV kinetic energy. (c) STM image of the same surface with $U_t = -1.2$ V and $I_t = 0.5$ nA.

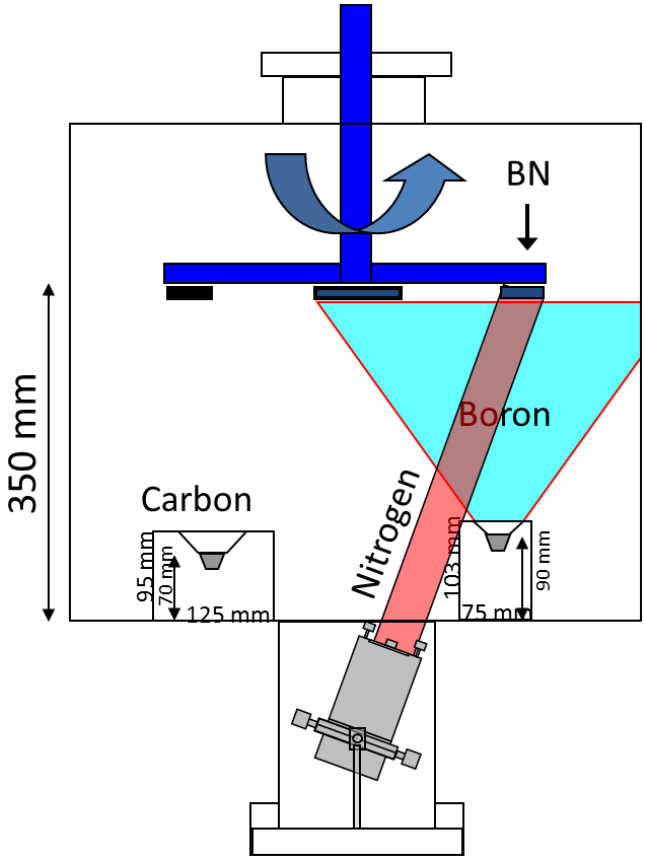


Figure VII.5. IBAD set up.

GFET on h-BN/SiO_2 was improved compared to SiO_2. Ref. [1076] claims that these h-BN films can be transferred to any substrate making LMhs and LM-based electronic devices possible.

h-BNfilms were also successfully grown on (0 0 0 1) sapphire by metalorganic vapor phase epitaxy (MOVPE) [1075]. These were grown using triethylboron, $B(C_2H_5)_3$, and ammonia (NH_3) at various V/III ratios, ranging from 210 to 2100. The films grown at V/III ratios above 1280 showed two XRDpeaks, one from the (0 0 0 2) plane and the other from the (0 0 0 4) plane. These films also exhibited a Raman hBN peak at 1366 cm^{-1}. In contrast, the films grown using V/III below 640 revealed an XRD pattern consistent with a turbostratic structure.

VII.1.3. Growth of h-BN by ion beam assisted deposition on metals and dielectrics

An alternative method of hBN growth is the physical vapor deposition (PVD) using a solid boron and nitrogen gas. This is not self-limiting, therefore the h-BN thickness can be controlled through the deposition time. This technique allows the deposition of thick layers of amorphous BN or cubic BN with different orientations and textures on almost any type of substrate, both metallic or insulator.

Among the possible PVD techniques, ion beam assisted deposition (IBAD) is specially versatile because it permits independent control of B and N fluxes, and fine tuning of the ion energy. The technique relies on electron beam evaporation of boron in vac-

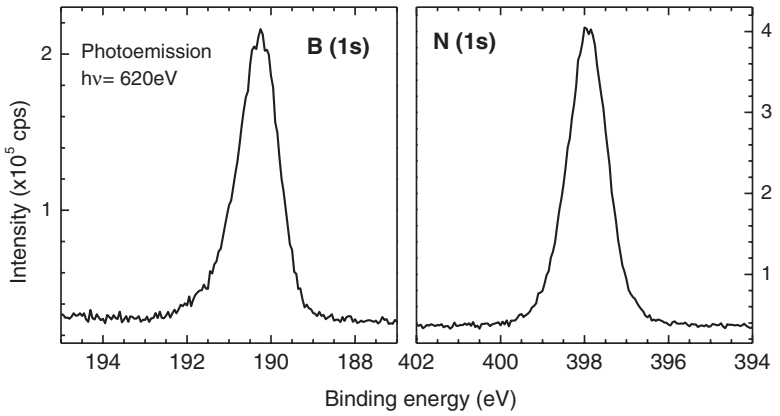


Figure VII.6. XPS from a stoichiometric h-BN produced by IBAD.

uum and the simultaneous bombardment with N ions, [1076–1080]. Figure VII.5, depicts a typical experimental set up. BN is obtained in a vacuum by reaction between the evaporated B and the N_2^+ ions. By using this technique, one can control the quality, texture and thickness of the h-BN layer by proper selection of growth parameters such as B/N impinging ratio, evaporation rate, deposition time, ion energy and substrate T. The composition of BN is adjusted by controlling the incoming B and N fluxes. The B/N ratio can then be measured by EDX, XPS, as shown in figure VII.6, and XANES,

Typical growth rates range from 0.1 to 10 nm min^{-1}. Since the growth is not self limited in this process the thickness is controlled by the various deposition variables including deposition time. The quality of BN is determined principally by the substrate T and the ion energy, which controls the orientation of the basal planes, the defect density and surface roughness. A review of these parameters with regards to the formation of high quality h-BN: orientation, crystallite size and density of defects is given in Ref. [1081]. The deposited materials have been thoroughly characterized using spectroscopic analytical tools [1079, 1082–1085]. One of the most important properties is the extreme flatness, with a surface roughness ~0.1 nm for any film thickness.

VII.1.4. Transfer of h-BN

The goal of the transfer process is to get GRMs on suitable host substrates.

Transfer processes are based on the use of a temporary support, most of the time a polymer, as described in section VI for graphene. Several methods have been developed: (1) wet transfer, involving the use of a liquid aqueous solution, and (2) dry transfer, relying on solid adhesive layers. The second approach ensures the absence of water between layers, which can be detrimental to device properties. Table VII.1 scrutinizes advantages and drawbacks or difficulties inherent to both kinds of transfer processes.

Several parameters can impact the feasibility and quality of transfer, including the roughness and the thickness of the film, its homogeneity, the interaction with the substrate, and roughness and surface termination of the host substrate. These parameters determine best suited transfer for a particular growth on an specific substrate as it rules the basic properties of the grown film, (mechanical, defect density…) and interaction of film with growth surface and temporary support.

VII.1.5. Wet transfer

Wet transfer includes chemical etching, and electrochemical delamination, aided or not by a chemical intercalation

VII.1.6. Electrochemical

Using the bubbling method, Ref. [1061] achieved nondestructive transfer of h-BN from Pt to arbitrary substrates and the repeated use of Pt for h-BN growth, which not only reduces environmental pollution but also decreases the production cost of h-BN.

A PMMA layer is first spin coated on BN/Cu. For electrochemical delamination process, an aqueous solution of KCl (1M) is employed as electrolyte, with a glassy Pt anode and the PMMA/BN/Cu cathode is negatively polarized (5 V). The formation of H_2 bubbles at the BN/Cu interface leads to the separation of PMMA/BN and Cu substrate. The film is then rinsed with DI water, deposited on the target substrate and, at 20 °C/10 min, heated to 120 °C to remove excess water and to stretch it. After one night, the PMMA film is removed with acetone at RT. An example of BN transfer from Cu onto SiO_2/Si and TEM grid is shown in figures VII.7(a) and (b). Sizes 1 × 1 cm^2 are achieved.

VII.1.7. Chemical intercalation

The previously described electrochemical delamination does not work on Ni due to the stronger BN/Ni interaction compared to BN/Cu TOA-assisted chemical delamination, described in section VI for graphene, was tested and new strategies are required in order to remove the ions residues. In this particular case, chemical etching (see section VI.1) is used to remove the Ni substrate, without any polymer [763]. The Ni substrate is etched

Table VII.1. Comparison of the various procedures developed to date for transferring CVD grown BN.

Method		Metals	Potential contamination	Special equipment	Re-use of the substrate	Time	Key parameters	Other
WET	Chemical etching	Cu [1049, 1087], Ni [1054, 1058, 1062]	Etchant, polymer, metal residues, interfacial water		No	Several hours	Etchant nature and concentration	
	Electrochemical delamination (ECD)	Cu [1088], Pt [1061, 1189], [108, 1090] Fe [1091]	Electrolyte, polymer, metal residues, interfacial water	5 V DC generator	Yes (smoothed)	A few minutes	Voltage, electrolyte nature and concentration	Possible damage due to gas bubbles produced at the interface
	TOA treatment + ECD	Rh [1066], Ni	ions, electrolyte, polymer, metal residues, interfacial water	3 electrodes set-up	Yes	~20 min	Voltage, electrolyte nature and concentration	
	Lift-off transfer	Cu [1092]	NaOH residues, polymer, metal residues, interfacial water		Yes	2–3 h at 60 °C	Interface oxidation	
DRY	PMMA/PVA [832]	Potentially any (depends on the interaction BN—substrate)	PMMA	Heating plate	Yes (if no BN remaining)	~2 h	PMMA adhesion	Semi-dry transfer: water at the very end
	Scotch tape		Adhesive residues			A few minutes	Scotch tape choice	Difficult release/deposition

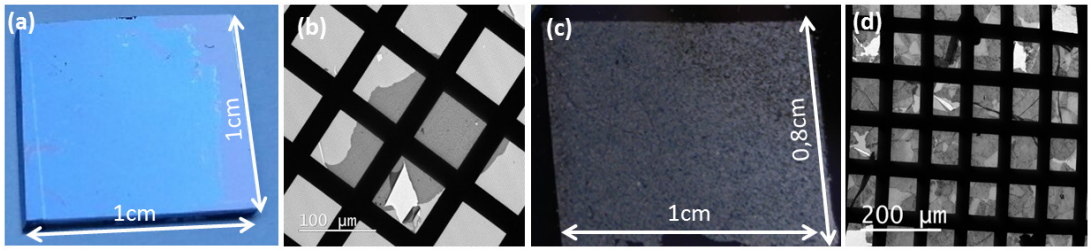


Figure VII.7. Examples of large areas BN film transferred on (a) 90 nm SiO_2/Si, (b, c) TEM grid, fromCu and Ni growth substrates.

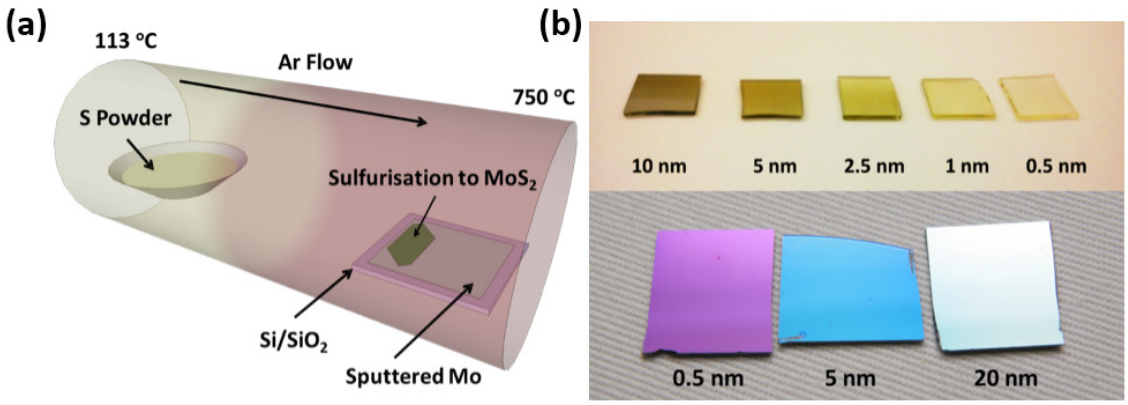


Figure VII.8. (a) Two zone furnace for TAC of Mo to MoS_2. (b) Photographs showing different thicknesses MoS_2 films on fused quartz (top) and SiO_2 (bottom) substrates. Adapted from [1093], with permission from Elsevier.

with a commercial solution (TFB Nickel Etchant, Transene) for one night. The BN film is rinsed with DI water, deposited on the target substrate and slowly heated to 120 °C to remove excess water. This polymer-free technique does not create any contamination andpreserves the film integrity. An example of BN transfer from Ni substrate onto SiO_2/Si and TEM grid is show in figures VII.7(c) and (d), respectively. A size ~1 × 1 cm^2 is achieved, and a full TEM grid coverage.

VII.1.8. Dry transfer

Dry transfer uses PVA/PMMA or scotch tape as the adhesive material. Most of the time using an adhesive strong enough to pick up the film is necessary but not sufficient, as the redeposition on the targeted substrate may be hard to achieve. If the adhesive material is transparent, it can be done under a microscope, which permits to target precisely the area to pick up and where to deposit it.

Ref. [1086] proposed a method for wafer scale dry transfer of thick h-BN films and other LMs and LMHs. The is based on controlled crack propagation between thick layer and saffire growth substrate. For that purpose a Ni film was deposited onto the h-BN film. An adhesive material is then placed on top of the Ni layer and the Ni and h-BN film are detached from the saffire wafer. Then another Ni layer is grown on fresh h-BN surface after the removal of the saffire wafer. Another adhesive tape is then placed onto the new Ni film and repeated splitting of the Ni-h-BN-Ni proceeds up to reaching a single layer h-BN.

VII.2. Layered semiconductors

VII.2.1. Thermal assisted conversion

While CVD provides a feasible route towards deposition of GRMs, other approaches offer simpler, scalable methods to grow thin films, at the expense of crystallinity. Thermally Assisted Conversion (TAC) [1093] of transition metals is one such technique. Figure VII.8 a shows a typical TAC set up. Thin films of the appropriate transition metal are deposited via sputter coating or electron beam evaporation onto appropriate substrates (often SiO_2 or sapphire) and then exposed to chalcogen vapour at elevated T (400 –1000 °C). Controlling the thickness of the initial metal layer allows some control of the thickness of the final TMD film, but achieving consistent 1L remains a problem. Additionally, TAC films are polycrystalline in nature [1093, 1094]. Thinner films preferably align parallel to the substrates while thicker films form vertically standing grains, with crossover point roughly at 10 nm [1095]. These features limit the practical usage of TAC in certain applications such as electronic devices, as the abundance of grain boundaries compromises the electrical properties. However, they are suited to other areas, such as gas sensing and electrochemical applications [1093, 1094, 1096–1099].

A variety of TMD films via TAC have been grown and employed across a wide range of applications [1093, 1094, 1096–1099]. Thin films of Mo or W of varying thickness (typically 0.5–20 nm) were deposited on to SiO_2 and heated to 750 °C in a quartz tube

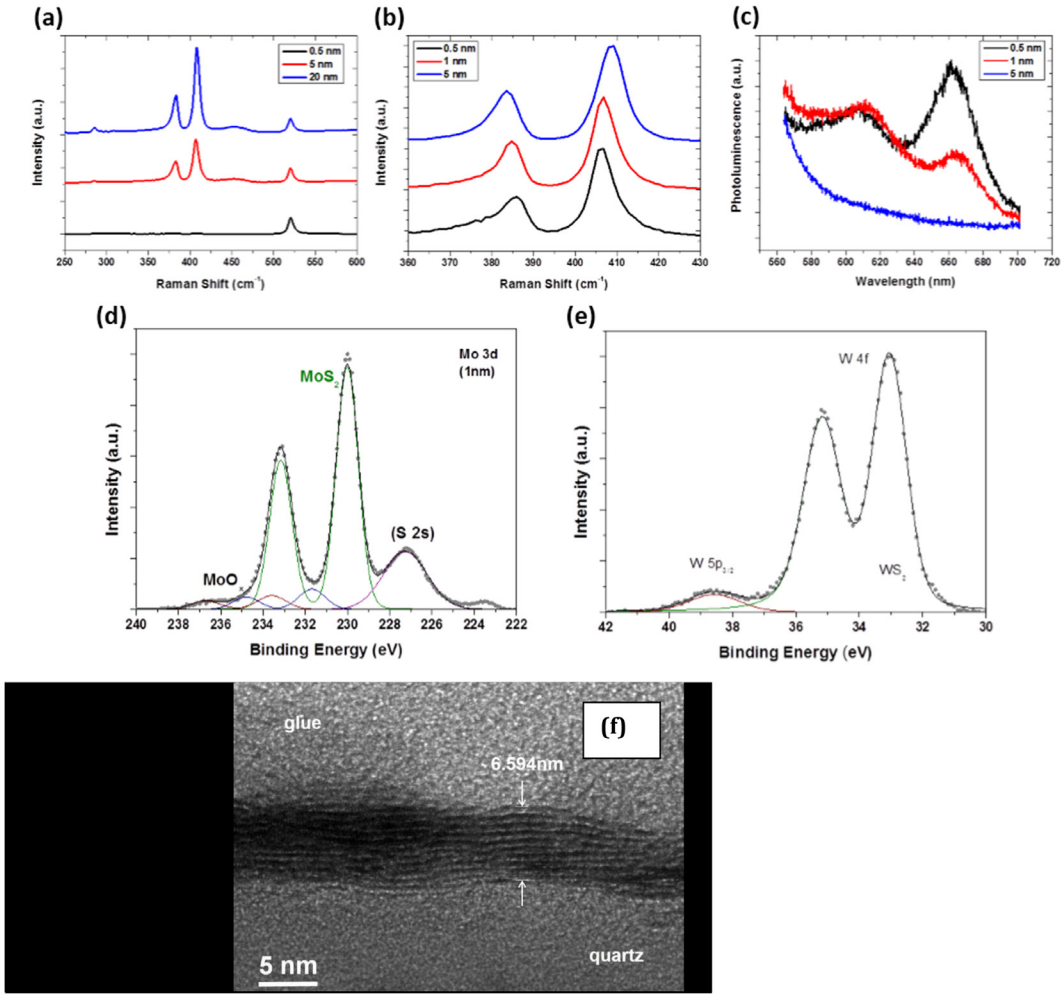


Figure VII.9. (a) and (b) Raman spectra and (c) PL of TAC MoS_2 grown from Mo films of differing thickness. (d) Mo 3d peak for MoS_2 grown from 1 nm Mo. (e) W 4f peak for WS_2 grown from a 20 nm W film. Adapted from [1093], with permission from Elsevier. (f) HRTEM image of WS_2 polycrystalline film. Adapted from [1100], copyright American Chemical Society.

furnace under Ar flow (150 sccm), see figure VII.8(b), and annealed under these conditions for 30 min. Following this, S powder was heated to 113 °C in a separate heating zone upstream of the samples to generate S vapour. Sulphurization was carried out for 20 min, after which the supply of S vapour was shut off and the samples were annealed for a further 20 min. They were then cooled to RT by switching off the heating over several hours under Ar flow.

Raman spectra and PL (see section IX.2 for an introduction to these techniques) of MoS_2 films grown via TAC from different initial thicknesses (0.5–20 nm) of Mo are shown in figure VII.9(a)–(c). Of note is the decreasing separation between the characteristic A_1' and E' peaks and increasing PL intensity with decreasing film thickness. This might suggest that, although these samples are polycrystalline few layer films, thinner samples exhibit significantly more monolayer character [1093]. This is of particular interest if one wishes to tune the characteristics of such TAC films to suit a particular application. Figures VII.9(d) and (e) show the Mo 3d and W 4f spectral regions for MoS_2 and WS_2 films. The Mo 3d core level exhibits spectral features consistent with a M:S stoichiometric ration of 1:1.9, indicating signifying an almost ideal MoS_2 film. A small amount (<5%) of surface oxide was also present in the form of MoO_2 and MoO_3. The W 4f core level is typical of WS_2 with minimal oxides or unreacted S on the surface.

One strength of TAC production of TMD films is the ability to pre-pattern the starting metal prior to conversion. This eliminates subsequent processing steps which would be necessary if one were to use lithography to pattern a pre-existing TMD film. MoS_2 devices were fabricated by sputter-coating of Mo through a shadow mask, conversion to MoS_2 and then contacting with a second metal deposition with a second shadow mask defining the contacts [1093, 1096]. A photograph of the resultant device is shown in figure VII.10(a). This device was employed as a gas sensor for NH_3 (figure VII.10(b)), whereby adsorption of NH_3 onto the MoS_2 film surface causes a change in resistance, figure VII.10(c). This was used to generate a calibration curve, demonstrating the sensor response of the device in figure VII.10(d) [1096].

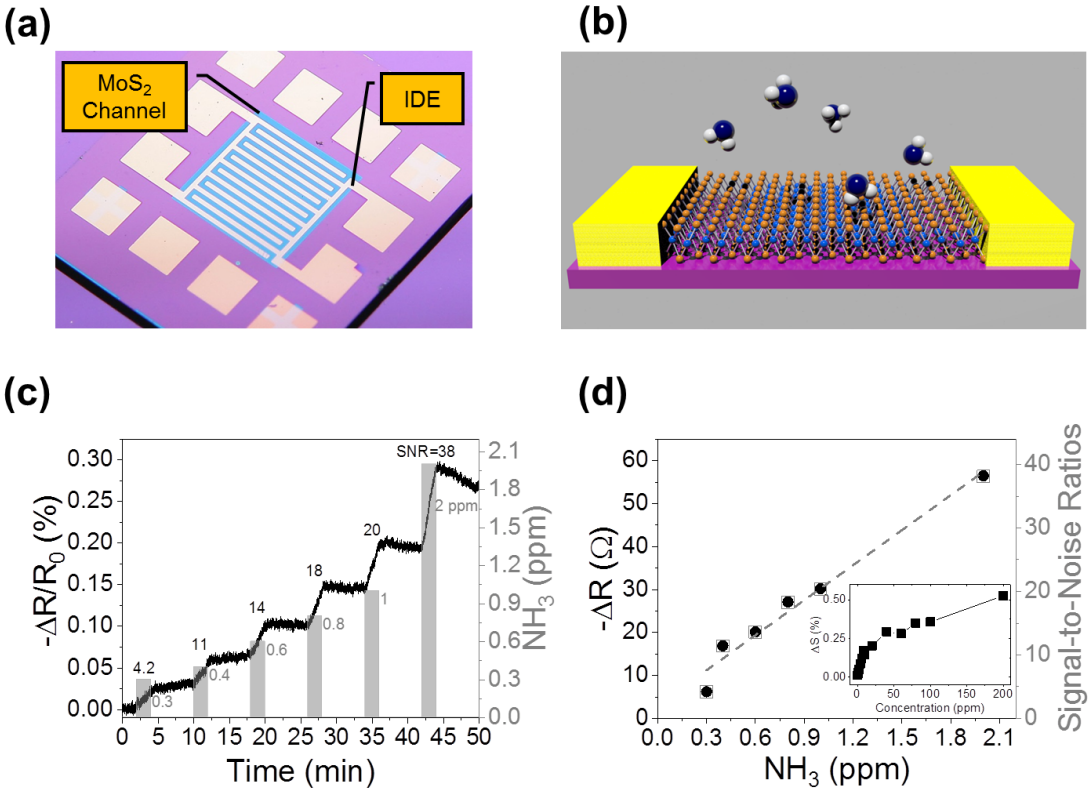


Figure VII.10. (a) MoS_2 device with Ti/Au contacts. (b) NH_3 gas sensing device. (c) Sensor response plot showing percentile resistance change versus time for the MoS_2 film with a bias voltage of 0.5 V. NH_3 exposures range from 300 ppb to 2 ppm. (d) Resistance change (black solid circles) and signal-to-noise ratios (gray open boxes) as a function of NH_3 concentration. Inset: full calibration curve ranging from 300 ppb to 200 ppm. Adapted from [1096], © Wiley-VCH Verlag GmbH & Co. KGaA.

Heterojunction devices with large (>tens mm) active layers were fabricated from TAC films for a range of applications [1099–1103].

VII.2.2. Physical vapour transport

InSe is attracting increasing interest for its desirable electronic and optical properties [1104]. More generally, compounds with different stoichiometry, In_xSe_y, and their different polytype phases, e.g. α, β, γ, have physical properties relevant for several applications in electronics, thermoelectrics and optoelectronics [1105–1108]. They have band gaps in the NIR to visible range, 1.25–2 eV, high μ at RT (>0.1 $m^2\ V^{-1}\ s^{-1}$) and an interesting 'Mexican hat' valence band energy dispersion [1109–1113], sensitive to the layer thickness [1110, 1111, 1113] and/or an externally applied electric field [1109].

Several methods have been employed for the synthesis of In-Se compounds with different stoichiometric ratios, such as InSe, In_2Se_3, and In_4Se_3, and their polytype phases [1114]. The synthesis of 1L was demonstrated for the α-[1115, 1116] and β-phase [1117, 1118] of In_2Se_3, and for γ-InSe [1119, 1120].

Figure VII.11 shows the crystal structures of α- and β-In_2Se_3 and γ-InSe. Electronic, thermal and optical properties of these flakes are still largely unknown [1118, 1121], although crucial to the implementation in several technologies, including molecular sensing [1106], high-performance thermoelectric devices with low thermal conductivity [1112], phase-change memories [1122], and high-gain photodetectors [1123].

The grown layers by physical vapour transport are β-In2Se3. The presence of β-In_2Se_3 is confirmed using a combination of Raman spectroscopy XRD, elemental analysis and PL. In general, Raman spectroscopy can help identify the crystalline phase of In_2Se_3 due to the presence of distinct vibrational modes for the different phases [1120]. β-In_2Se_3 flakes grown by physical vapor transport are optically active with a RT PL emission that is blue-shifted relative to that of exfoliated layers of α-In_2Se_3 and γ-InSe [1117, 1124]. Also, the grown layers have distinct Raman lines [1117, 1120, 1121]. More importantly, the RT PL peak of β-In_2Se_3 is strongly sensitive to the thickness due to quantum confinement of carriers by the boundary of the layers and light electron mass [1117].

The synthesis of the In_2Se_3 layers by physical vapor transport involves three separate steps

For the growth of β-In_2Se_3 layers by PVT, ground powder of Bridgman-grown [1125] γ-polytype InSe was used as source material, see figure VII.12(a). Bulk Bridgman-grown γ-InSe crystals were ground into fine-grained powder using a pestle and a porcelain mortar. Then the powder was loaded into a quartz beaker and mixed with ethanol (96% purity) in a 1:4 weight ratio of InSe:ethanol, which acted as a dispersing liquid environment. The obtained suspension was sonicated for 18 h at RT ($f = 21.2$ kHz and $P = 100$

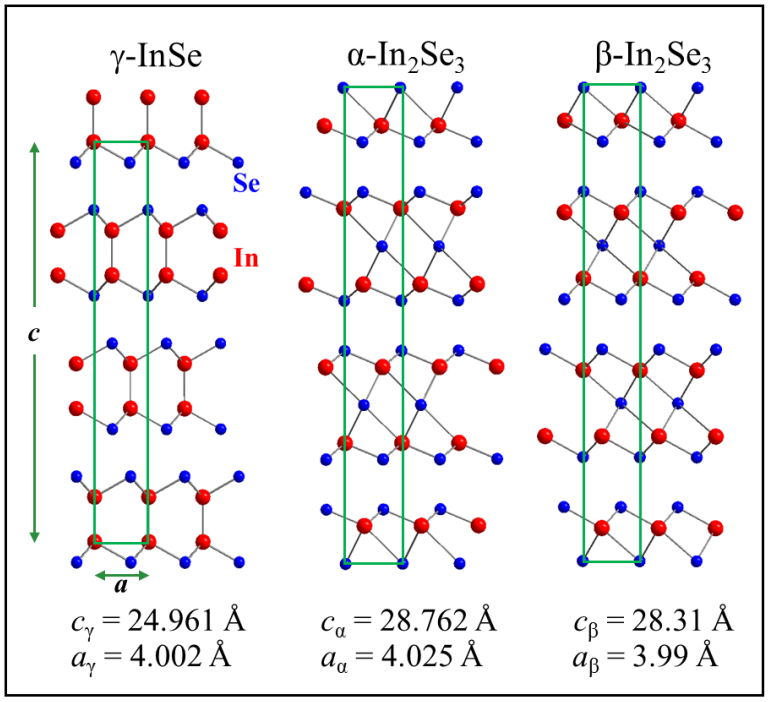


Figure VII.11. Side view of the crystal lattice and unit cell of γ-InSe (left), α-In_2Se_3 (middle) and β-In_2Se_3 (right). Blue and red spheres correspond to Se- and In-atoms, respectively. The primitive unit cell of γ-InSe contains three layers, each consisting of four closely-packed, covalently bonded, atomic sheets in the sequence Se–In–In–Se. For both α- and β-In_2Se_3 phases, the unit cell contains three layers, each consisting of five closely-packed, covalently bonded, atomic sheets in the sequence Se–In–Se–In–Se. In α-In_2Se_3 the outer Se-atoms in each layer are aligned, whereas in β-In_2Se_3 they are located into the interstitial sites of the Se-atoms in the neighboring layers, thus leading to a smaller volume in β-In_2Se_3.

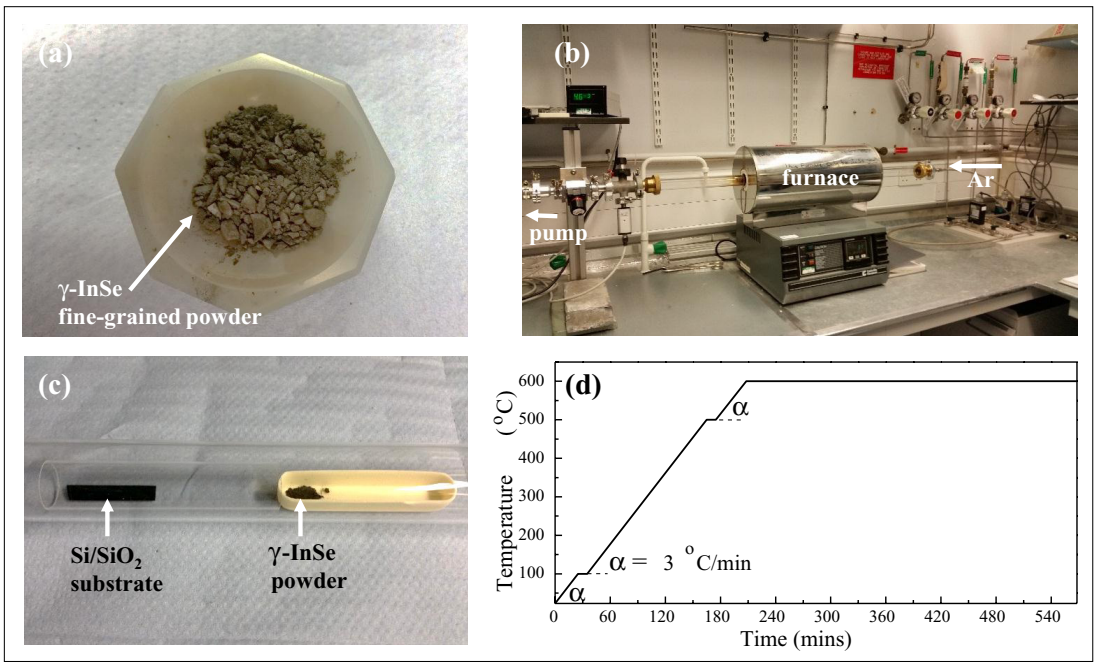


Figure VII.12. (a) Optical image of fine-grained powder of γ-InSe. (b) Tube furnace system used for the growth of In_2Se_3. (c) The source material and the substrate in the quartz tube. (d) Program profile of the furnace heater.

dB). The resulting solution was dried in a porcelain beaker at RT. The dried powder was rinsed with DI water five times and finally dried at 50 °C for 24 h. Then the powder was ground again using a pestle and a porcelain mortar. Finally, the InSe powder was sieved ($200 \times 200\ \mu m^2$).

The β-In_2Se_3 layers were grown on different substrates such as Si/SiO_2, mica and HOPG [1117]. Prior to growth, the Si/SiO_2 substrate (7 mm wide and 3 cm long) was cleaned in hot acetone ($T = 60$ °C) and ultrasonicated in methanol and isopropanol (10 min in each solvent) and then cleaned by oxygen plasma at

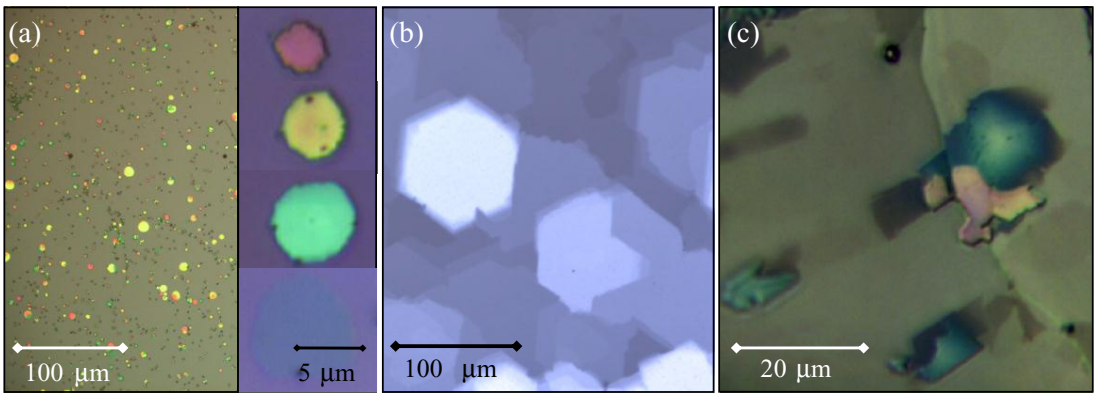


Figure VII.13. Optical micrographs of β-In_2Se_3 layers grown on (a) SiO_2/Si, (b) mica, and (c) graphite ($T = 600$ °C, $t = 9$ h and Ar flow rate ~150 sccm). Different colors correspond to different thicknesses of the layers. This ranges from hundreds of nanometers down to 2.8 nm. Adapted from [1117], © IOP Publishing Ltd.

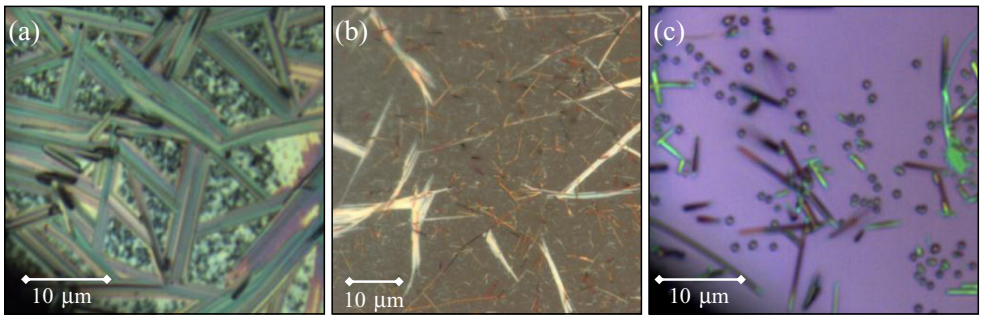


Figure VII.14. Optical micrographs of β-In_2Se_3 rods (a) grown on mica at $T = 620$ °C for $t = 9$ h under an Ar flow rate of 150 sccm, (b) grown on mica at $T = 570$ °C for $t = 6$ h under an Ar flow rate of 150 sccm, and (c) grown on Si/SiO_2 at $T = 600$ °C for $t = 6$ h under an Ar flow rate of 170 sccm.

$T = 100$ °C for $t = 10$ min to remove ambient adsorbates from its surface. The cleaned substrate was immediately loaded into the tube furnace for the growth. Mica and graphite were cleaved prior to growth and the fresh surface was used as substrate.

A tube furnace system was used to grow the In_2Se_3 layers (figure VII.12(b)). The system comprised a Carbolite furnace, a 1 m long quartz tube, a rotary pump and an Ar flow controller (Hastings mass flow controller). γ-InSe powder (~300 mg) was loaded into a ceramic boat and placed at the center of the tube furnace. The substrate was placed in the downstream side 6–10 cm away from the source material, see figure VII.12(c). The pressure was lowered $\sim 6 \times 10^{-3}$ mbar using the rotary pump. Then an Ar gas was intoduced at a rate of 150 sccm for 2 h providing $P = 1.6$ mbar. Thereafter, the system was heated from $T = 22$ to 600 °C at a rate of 3 °C per minute and kept at 600 °C for 6 h or longer (up to 9 h), see figure VII.12(d). The vaporized In- and Se-atoms were carried by the Ar gas and deposited on the substrate. The system was then allowed to cool naturally to RT. Typically, the source material can be reused for a second cycle of growth.

Figures VII.13(a)–(c) show the as-grown β-In_2Se_3 layers on Si/SiO_2, mica and graphite, respectively. The growth on Si/SiO_2 substrates produces near-circular, slightly facetted films with lateral size between 1 and 15 μm (figure VII.13(a)), while highly facetted hexagonal films with lateral size ~100 μm grew on mica, see figure VII.13(b). On graphite, films with arbitrary shape grew (figure VII.13(c)) with preferential growth at step edge bunches on the substrate. The thickness, t, was measured by AFM. It ranges from hundreds of nanometers down to 2.8 nm on Si/SiO_2.

For the same growth conditions ($T = 600$ °C, $t = 9$ h and Ar flow = 150 sccm) β-In_2Se_3 layers were grown on mica with layer thickness between 80 and 5 nm and on graphite from hundreds nanometer down to 10 nm, (see figure VII.13(c)). Figures VII.14(a)–(c) show some examples of growth under different conditions. 'Hay'-like growth was obtained on mica at $T = 620$ °C for $t = 9$ h for an Ar flow of 150 sccm, see figure VII.14(a). Nano rods were grown on mica and Si/SiO_2, respectively, at 570 °C or under 170 sccm Ar flow rates (figures VII.14(b) and (c)). The growth of different polytype phases of In-Se is highly dependent on the growth T [1114]. This results in a significant advantage of this method since, due to the T gradient within the tube furnace, it is possible to grow different phases and stoichiometries, including γ-InSe, during a single run [1120].

The electronic and vibrational properties of the as-grown films of different t were compared with those

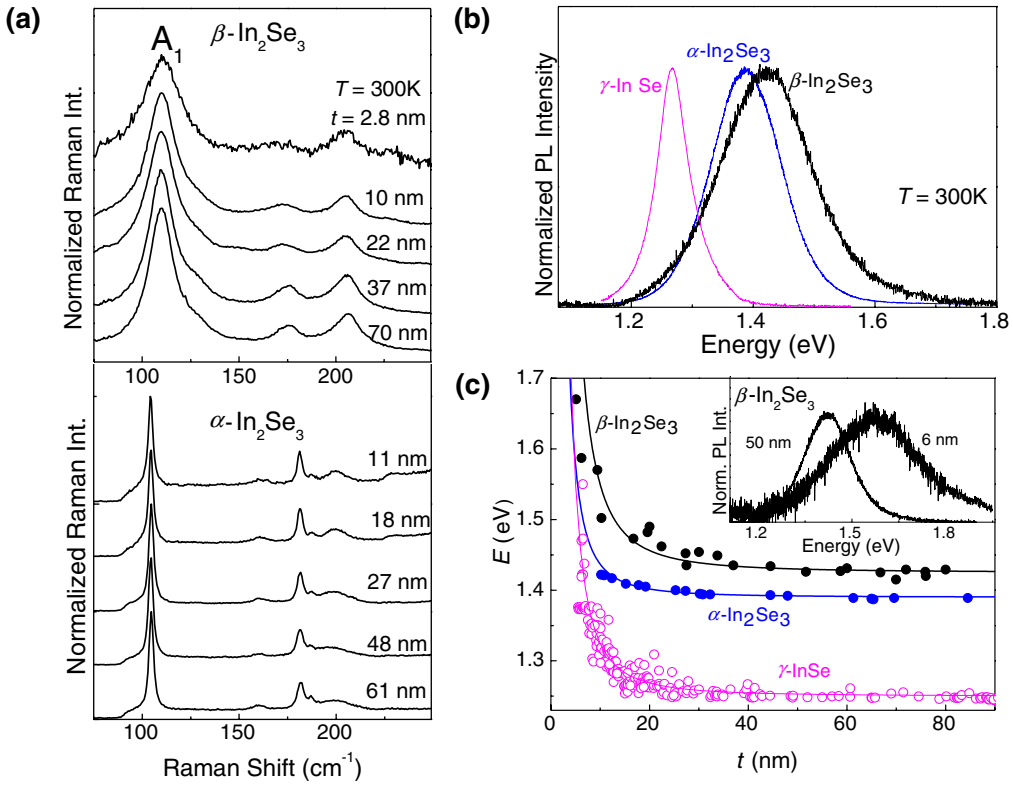


Figure VII.15. (a) Normalized Raman spectra of as-grown β-In_2Se_3 layers (top) and exfoliated flakes of α-In_2Se_3 (bottom) at $T = 300$ K ($P = 0.1$ mW and $\lambda = 633$ nm). (b) Normalized μPL spectra of bulk γ-InSe, β-In_2Se_3 and α-In_2Se_3 at $T = 300$ K ($\lambda = 633$ nm and $P = 0.1$ mW). (c) Measured and calculated dependence of the peak energy, E, of the PL emission on layer thickness t of as-grown β-In_2Se_3 (black dots) and exfoliated Bridgman-grown α-In_2Se_3 (blue dots) and γ-InSe (magenta dots) flakes. Inset: Normalized PL spectra of β-In_2Se_3 with $t \sim 50$ nm and 6 nm at $T = 300$ K. Adapted from [1117], © IOP Publishing Ltd.

of thin α-In_2Se_3 and γ-InSe layers exfoliated with adhesive tape from Bridgman-grown ingots [1125, 1126]. The α- and β-phases of In_2Se_3 are characterized by distinct Raman modes [1117, 1120, 1121]. For the as-grown β-In_2Se_3 films, the Raman peaks are centered at ~110, 175, and 205 cm^{-1} at $T = 300$ K (figure VII.15(a)), corresponding to the intralayer vibrational A_1-modes (110 and 205 cm^{-1}) and the Eg-mode (175 cm^{-1}) of bulk β-In_2Se_3 [1118, 1127]. For exfoliated flakes of α-In_2Se_3 the Raman modes are narrower and centered at ~104, 181, and 200 cm^{-1} at $T = 300$ K. β-In_2Se_3 flakes exhibit RT PL. RT normalized PL spectra of as-grown β-In_2Se_3 with $t \sim 50$ nm are compared with bulk α-In_2Se_3 and γ-InSe in figure VII.15(b). The PL emission for the β-In_2Se_3 films is peaked at higher energy compared to α-In_2Se_3 and γ-InSe, and it blue-shifts with decreasing layer thickness (inset of figure VII.15(c)).

Figure VII.15(c) shows the dependence of the PL peak energy, E, at RT on t, as obtained from several PL and AFM studies of as-grown β-In_2Se_3 layers (black dots) and α-In_2Se_3 and γ-InSe flakes [1124] exfoliated from Bridgman-grown crystals [1117, 1125] (blue and magenta dots). The PL peak energy undergoes a blue-shift to higher photon energies with decreasing layer thickness consistent with quantum confinement of photo-excited carriers along the c-axis [1117]. This energy shift can be modelled by a quantum well potential of infinite height, i.e. $E = E_{3d} + \pi^2\hbar^2/2t^2\mu_{\|c}$, where E_{3d} is the band gap for the bulk and $\mu_{\|c}$ is the electron–hole reduced mass for motion along the c-axis. For β-In_2Se_3, the best fit to the measured E versus t, gives $\mu_{\|c} = 0.04\ m_e$ and $E_{3d} = 1.428$ eV, where m_e is the electron mass in vacuum. These values differ from α-In_2Se_3, i.e. $\mu_{\|c} = 0.08 m_e$ and $E_{3d} = 1.390$ eV, and γ-InSe, i.e. $\mu_{\|c} = 0.05 m_e$ and $E_{3d} = 1.250$ eV.

The comparison of the PL peak energies for the β-In_2Se_3 layers with those for α-In_2Se_3, and γ-InSe [1116, 1119, 1124] indicates distinct spectral ranges for these In-Se compounds and a wider spectral tunability for β-In_2Se_3 and γ-InSe, among the largest within the wide family of LMs. The larger quantum shift and lighter electron–hole reduced mass for the β-phase compared to the α-phase are assigned to the closer spacing of the layers in the β-phase ($\Delta c/c \sim -1.5\%$) (figure VII.11), leading to a stronger inter-layer coupling. On the other hand, the larger value of E_{3d} in β-In_2Se_3 compared to α-In_2Se_3 cannot be accounted for by a simple argument and may involve a redistribution of electronic charge between the Se- and In-atoms in neighboring vdW layers [1114]. This may be also affected by the presence of crystal defects, such as In- and Se-vacancies (V_{In} and V_{Se}), which tend to form in In_2Se_3 due to the misvalency between the III- and VI-atoms [1114]. Vacancy ordering and bond relaxation due to vacancies are expected to modify atomic orbit-

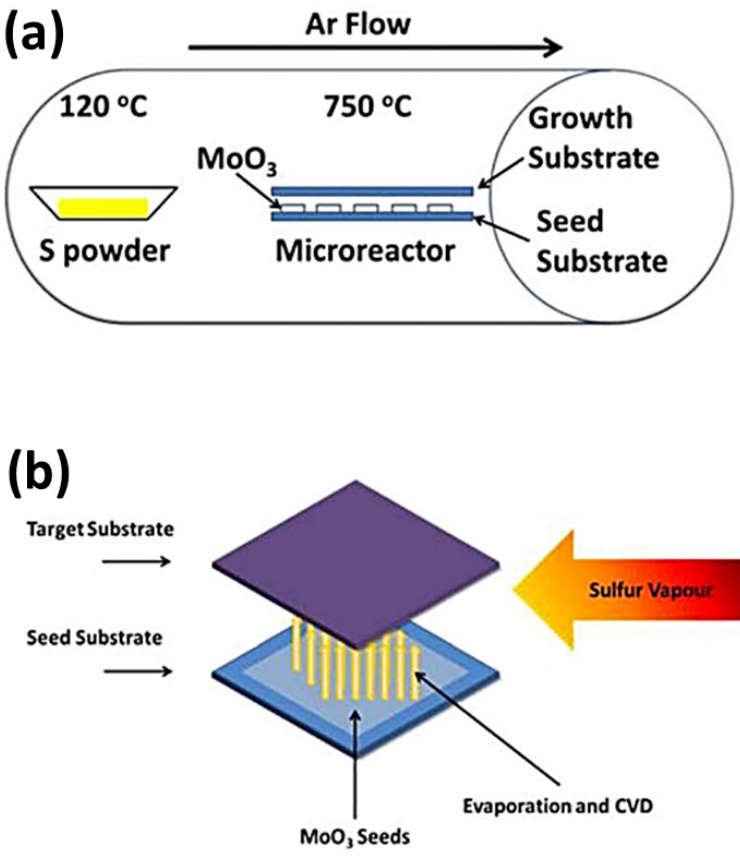


Figure VII.16. (a) Schematic set-up for CVD of MoS_2. (b) mechanism by which MoS_2 is deposited on the target substrate. Adapted from [1098] CC BY 4.0.

als and increase the band gap of bulk layers [1128], and may play a more important role in LMs [1129].

VII.2.3. CVD growth

As is the case with graphene, CVD of LMs is a synthesis route which offers a compromise between film quality and large area coverage and uses techniques compatible with CMOS processing. CVD of LMs other than graphene typically requires two precursor materials which adds to the complexity of depositing uniform, 1L films. Precursors can be sourced as solids which sublime under heating with these vapours then reacting to complete the CVD process, or as gaseous. Gaseous precursors allow much greater control of parameters, such as flow rate, but are often toxic or highly flammable, such as H_2S and H_2Se [1008].

VII.2.4. Solid precursors

Figure VII.16 describes the microreactor set-up for CVD of MoS_2 in which flakes of MoO_3 and S powder are used as solid precursors to supply Mo and S, respectively. LPE MoO_3 flakes in IPA were drop-cast on a SiO_2 chip placed face-down on top. This assembly was heated to 750 °C in a quartz tube furnace under Ar flow (150 sccm) with S powder heated to 120 °C in a separate heating zone upstream of the microreactor. The samples were exposed to the resulting S vapour for 20 min before annealing at 750 °C under just Ar flow (150 sccm) for a further 20 min.

Imaging of the resultant deposit shows a film consisting of single crystal domains joined together to form a continuous film (figure VII.17(a)). Raman spectroscopy shows the A_1' and E' peaks characteristic of MoS_2 [1098] (Figure VII.17(b)), while the spectral contributions to the Mo 3d region of the XPS spectrum are consistent with that of MoS_2 with a small amount of oxide present [1098] (Figure VII.17(c)). The A_1' to E' peak separation ~18 cm^{-1} and the strong PL (Figure VII.17(d)) are evidence for 1L-MoS_2 [1098].

CVD of MoS_2 on c-plane sapphire using solid inorganic precursors [1130–1132] has enabled an efficient route toward producing high quality 1L-MoS_2 films with lateral dimensions (>cm^2) beyond that of the mechanically exfoliated flakes (less than 100 μm) with electronic properties matching those of mechanically exfoliated samples [1133].

However, solid precursors such as S and MoO_3 exhibit negligible vapor pressure at RT. This leads to the requirement of positioning the precursors inside the heated zone of the reaction chamber to reach T usually above 200 °C for S and 500 °C for MoO_3 with fixed distances from the position of the substrates as shown in figure VII.18 with unseeded or seeded substrates. Since the available composition of the precursors in

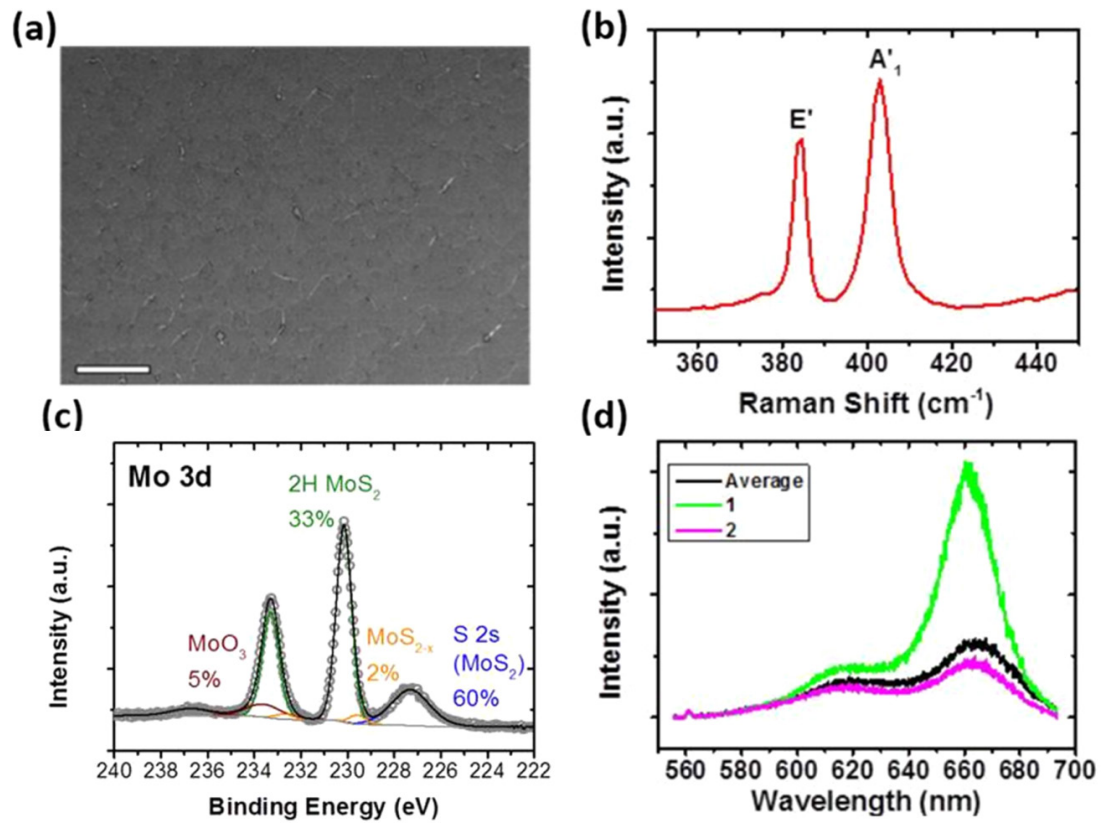


Figure VII.17. (a) SEM image showing continuous MoS_2 film. Scale bar is 2 μm. (b) Average Raman spectrum measured across a 20 $\times$ 20 μm area of the film. (c) Mo 3d core level showing contributions consistent with MoS_2. (d) PL measured across a 1L region (green) and 2L island (pink). Adapted from [1098].

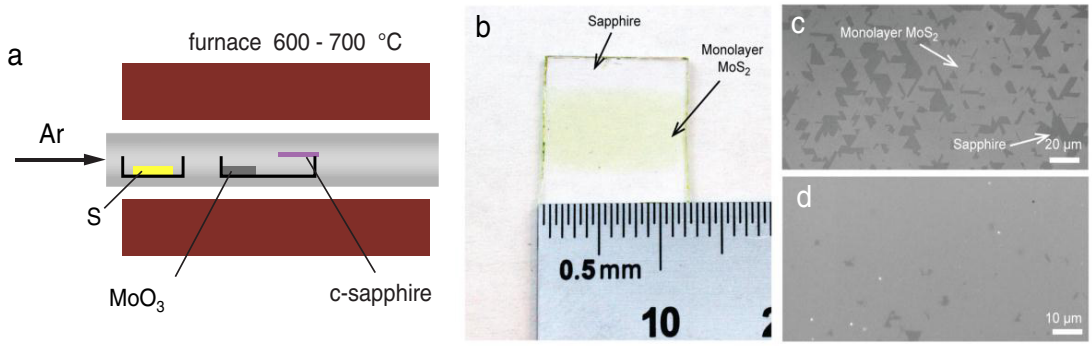


Figure VII.18. (a) CVD setup for deposition of 1L MoS_2 using solid precursors, MoO_3 and S. (b) MoS_2 deposited on c-plane sapphire. (c) 1L-MoS_2 covering c-plane sapphire without complete coverage, scale bar is 20 μm. (d) 1L MoS_2 with complete coverage, bar is 10 μm. Adapted from [1130], copyright American Chemical Society.

the atmosphere of the reaction chamber depends on the evaporation from the time-dependent masses and surface areas of the solid precursors, it is challenging to consistently control the flow of the precursor vapours reaching the substrates over the period that affects the uniformity and stoichiometry of the resulting film. There is also a practical issue of over-consumption of the precursor materials that may lead to unwanted deposition of residual by-products on the substrates and walls of the reaction chamber which also hinders the growth uniformity and technological feasibility.

VII.2.5. Gas precursors

In order to achieve a better control over the gas phase composition of the precursors in the chamber, gas sources with high RT vapor pressures (>0.1 mbar) can be used, which allow the precursors to be stored in a T-and pressure-controlled bubbler, outside the heated zoned of the reaction chamber where the vapour pressure and mass flow rate can be controlled independently, see figures VII.19 and VII.20.

A large range of gas precursors containing Mo and S were developed for semiconductor and cata-

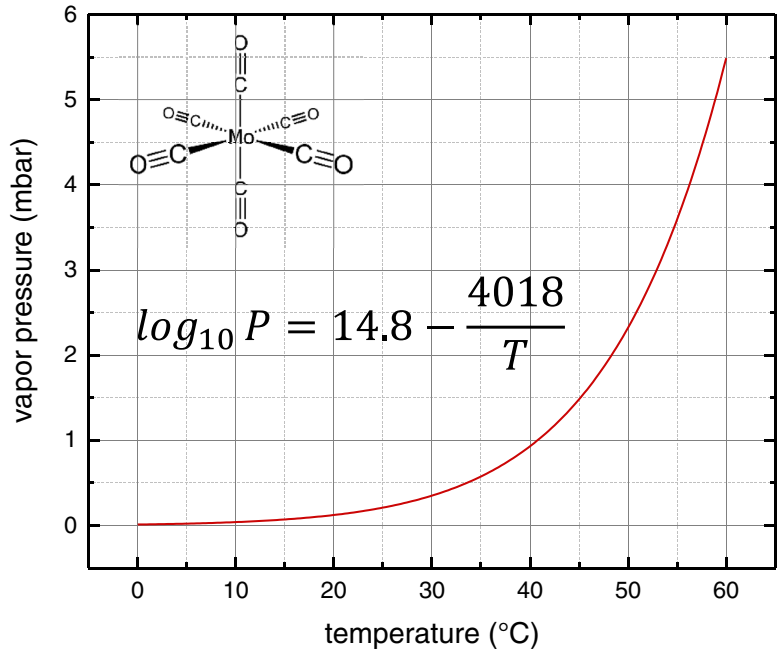


Figure VII.19. Equilibrium vapor pressure of $Mo(CO)_6$ as a function of T based on the measured thermodynamic constants in Ref. [1134].

lyst industries. They include $Mo(CO)_6$ [1135], $MoCl_5$ [1136], $(NH_4)_2MoS_4$ [1137] for molybdenum and H_2S [1136], diethyl sulphide [1138] for S. Often these techniques using gas precursors are named Metal organic CVD, MOCVD, even if the precursors cannot be considered proper metal organics.

Significant progress has been made using MOCVD in the growth of large-area, reproducible, high-quality TMDs. However, we still have to overcome the challenge of single crystal continuous film growth of MoS_2 by MOCVD in a reasonable growth time (~1 h). Basic nucleation and growth processes will have to be developed and understood in more detail before this problem can be solved. More work needs to be done on understanding the basic growth mechanisms which may include *in situ* growth observations to determine the kinetics and rate limiting steps for systematic MOCVD control of film morphology and micro-nanostructures. Ref. [1139] reported the diffusion-controlled growth of WSe_2 on sapphire, where a two-step process was used to nucleate WSe_2 followed by growth from the seeds using process conditions to minimize additional nuclei while growing single layers. This is an example of many growth studies that need to be performed in order to achieve large area single-crystal TMDs. While this study has shed some light on WSe_2 growth process, single 1L crystals across the whole wafer have not been achieved yet. Another growth process that could be used is atomic layer epitaxy, however at this time there does seem to be a significant effort in this direction, perhaps because a proper substrate has not been identified yet.

So far, the growth of 1L-MoS_2 by MOCVD was demonstrated by a few groups with a varying degree of coverage, crystallinity, thickness uniformity, and scalability. Ref. [1140] developed a method to grow a wafer scale polycrystalline 1L-MoS_2 films on SiO_2/Si with $Mo(CO)_6$ and $(C_2H_5)_2S$ (Diethyl sulfide; DES) with relatively low growth T (~550 °C), albeit with a rather long growth time to achieve a continuous film (~26 h) in low vacuum conditions (7.5 Torr). Ref. [1141] produced average-thickness controlled MoS_2 1L-to-ML on cm scale SiO_2/Si and sapphire after a thermodynamic modelling of vapor phase equilibrium reaction of the precursors $Mo(CO)_6$ and H_2S. The growth pressure (~1 atm to 1 Torr) and T (400 –850 °C) were considered as a main factor in determining the range of growth parameters for the synthesis of high quality MoS_2 films of a good stoichiometry without any carbon residues originating from the carbon-containing Mo precursor.

$Mo(CO)_6$ and H_2S were used in Ref. [1142] as model precursors. The choice was based on the fact that both are readily available, well-established high purity (>99.9%) MOCVD sources with know thermochemical properties [1141, 1143–1147].

In designing how the sources are delivered, a solid precursor such as $Mo(CO)_6$ is to be loaded into an inert, stainless-steel bubbler immersed inside a T controlled bath. Ideally, the evaporation of $Mo(CO)_6$ is considered to be fast enough to always completely saturate the bubbler with equilibrium vapor pressure (figure VII.19) which would determine the concentration of the precursor exiting the bubbler with the carrier gas. However, the common problem with solid precursors is that the actual vapor transported out of the bubbler quickly decreases over multiple growth runs because of increased dead volume of the precursor and decrease in the available precursor surface area for an efficient evaporation (at least ~1 μl $(min \cdot g)^{-1}$).

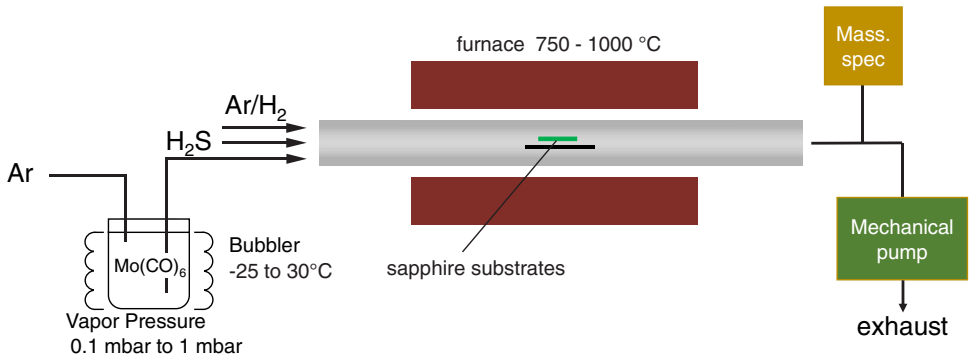


Figure VII.20. MOCVD setup, with a reverse bubbler configuration for $Mo(CO)_6$.

In order to tackle this issue, a reverse bubbler configuration (see figure VII.20) and packing of precursor with an inert silica beads ~2 mm are used to increase effective dwell time of the carrier gas and the precursor surface area [1148] by an order of magnitude. These approaches have been previously employed for solid metalorganic precursors to ensure efficient evaporation [1148]. The evaporation rate of the $Mo(CO)_6$ precursor should now be fast (at least ~1 μl $(\text{min} \cdot \text{g})^{-1}$) enough to assume an instantaneous phase equilibrium between gas and solid phases of $Mo(CO)_6$ within the bubbler while the $Mo(CO)_6$ precursor vapour is carried into the reaction zone of the system by an inert gas (specifically Ar). In this case, the partial pressure of $Mo(CO)_6$ exiting the bubbler can be estimated by the vapour pressure of $Mo(CO)_6$ at the T of the bubbler (T_b). T_b is preferably kept below the RT to prevent unwanted condensation of the precursor material upstream, before reaching the heated zone. Typically, a bubbler equipped with a chiller can reach a minimum bubbler T~–30 °C.

The actual amount of $Mo(CO)_6$ introduced to the reaction chamber can be monitored by mass spectroscopy of the atmosphere inside the chamber. Although calibration of the absolute concentration of the precursor is somewhat challenging, the relative concentration can be obtained for every run of the experiment serving as an indicator for the amount of the precursor remaining in the bubbler. At the outlet of the bubbler, in order to abruptly turn on and off the flow of $Mo(CO)_6$, a solenoid valve was installed, which can be automatically controlled, so that the precursor mass flow from the beginning to the end of the MOCVD growth cycle is timed precisely.

As for the S source, mass flow control is more straight-forward as H_2S is in gaseous state at ambient conditions and high purity (99.999%) gas can be provided readily from commercially available compressed gas cylinders. However, extreme caution should be exercised since the H_2S gas is a highly flammable and toxic gas with an acceptable exposure limit of 20 ppm (set by the Agency for Toxic Substances and Disease Registry, USA). In this regard, H_2S gas level detectors both in the ventilated gas cabinet storing the H_2S gas cylinder and near the CVD furnace are installed. They are connected to a sound alarm to alert the appropriate emergency services immediately. In addition, experiments thorough He leak test of the assembled CVD system need to the conducted before performing the experiments involving H_2S to prevent anyone in the work area from exposure.

The CVD system used, as illustrated in figure VII.20, consists of a horizontal hot wall filament three-zone, quartz tube system (Carbolite HZS 12/-/600) commonly used for laboratory scale CVD synthesis as one of the most economical ways to produce cm scale thin films. The quartz tube is coupled to KF-standard (DIN 28403, ISO 2861) high-vacuum compatible flanges which can be evacuated by a mechanical pump to ~10^{-3} mbar. All the gas lines are made of stainless connections that prevent any outgassing and extraneous chemical reactions. The size of the sample is limited by the diameter of the tube and length of the heating zone.

MOCVD MoS_2 was deposited onto single crystal c-plane sapphire substrates pre-annealed in air at 1000 °C for 1 h to yield atomically flat terraces [1130]. This substrate has yielded much better growth morphology than other amorphous substrates, such as SiO_2/Si. The presence of an atomically flat surface is likely to be one of the prerequisites layer-by-layer epitaxy of LMs [1130, 1149, 1150]. Typically, c-plane sapphire substrates are cut into square pieces of 1 by 1 cm by first scratching them with a diamond tipped pen and snapping them into separate pieces by hand. Before the pre-annealing procedure at 1000 °C in air, they are subsequently cleaned in the IPA, acetone, and DI bathes inside a bath sonicator for at least 10 min.

Ref. [1141] computed the thermodynamic 'map' of all possible phases resulting from the vapor reactions for different compositions of $Mo(CO)_6$:H_2S:H_2, T, and pressures. They found a set of growth parameters with a high growth T ~850 °C, presence of H_2(99%), and high growth pressure ~1 atm leading to a good morphology with a large 1L domain size >1 μm and stoichiometry predicted from the equilibrium thermodynamic modelling of the vapor phase. However, vapour phase reactions may not translate very

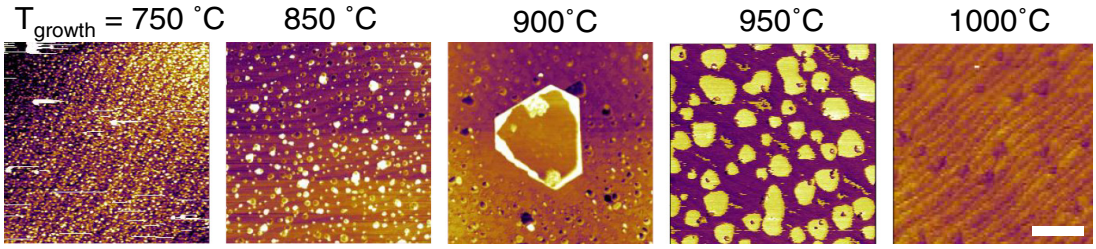


Figure VII.21. Dependent growth morphology illustrated by AFM height images of as-grown MoS_2 on sapphire samples produced at different using $Mo(CO)_6$ and H_2S as model precursors. Scale bar, 250 nm. Adapted from [1142], copyright American Chemical Society.

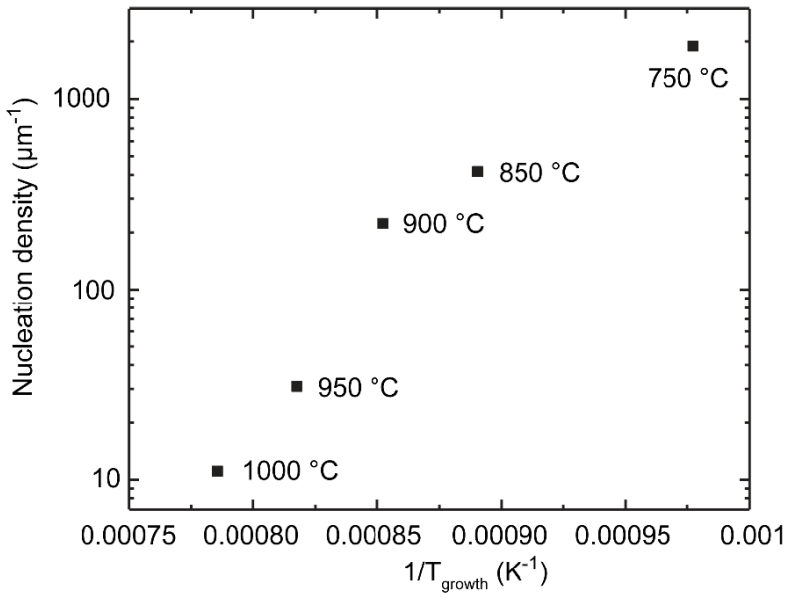


Figure VII.22. Nucleation density versus $1/T$ for the samples in figure VII.11. Adapted from [1142], copyright American Chemical Society.

well to what takes place at the substrate surface level, as the non-equilibrium dynamics, mass-transport, presence of boundary layers due to the fluid dynamic condition, and surface reactivity also play an important role in the final surface mediated growth mechanism [171, 765, 1151].

E.g. excessive vapour phase reactions must be avoided, as they may lead to a significant formation of MoS_2 particles rather than substrate assisted epitaxy of atomically thin layers [1152–1155]. In order to enhance the heterogeneous, surface reaction over the vapour phase ones, generally speaking, higher T (>800 °C) and pressure (>850 Torr) are preferred [1151].

H_2 during MOCVD is used as a reducing agent to prevent the oxidation of MoS_2 and deposition of carbon based species. However, H_2 is detrimental to the grain size, as the nucleation concentration could increase by an order of magnitude increasing H_2 [1140]. Performing the growth at high T, low vacuum environment (~800 °C and 10 mbar) in the presence of H_2 would lead to Si contamination of substrate hindering the growth.

In turn, the growth conditions based on Ref. [1141] were used for initial growth studies. The saturated vapour of $Mo(CO)_6$ at the bubbler T~30 °C was introduced into the CVD system (a quartz tube three-zone hot-wall furnace) through Ar carrier gas. c-plane (1 0 0 0) monocrystalline sapphire substrates were placed in the center of the furnace by loading them onto a larger sapphire plate (which serves as a boat) and were heated to the growth T (750 °C–1000 °C) and annealed for 15 min in Ar (75 sccm), followed by added flow of the S precursor, H_2S (1.5–20 sccm), before introducing $Mo(CO)_6$ to initiate the MoS_2 growth in the S rich conditions that prevent the creation of vacancies due to S removal within the as-grown MoS_2. At the end of the growth (typical growth time ~30 min), the $Mo(CO)_6$ flow was shut-off by a solenoid valve and the sample was cooled naturally to RT with Ar and H_2S gases still flowing through the quartz tube. All the stages of the MOCVD growth were performed under atmospheric pressure.

After each growth run, the inner wall of the quartz tube was rinsed with DI water and IPA and blow-dried with N_2. Afterwards, it was annealed at 1100 °C in Ar (100 sccm) for 2 h and in air for 2 h order to eliminate all the residual precursor and by-product materials.

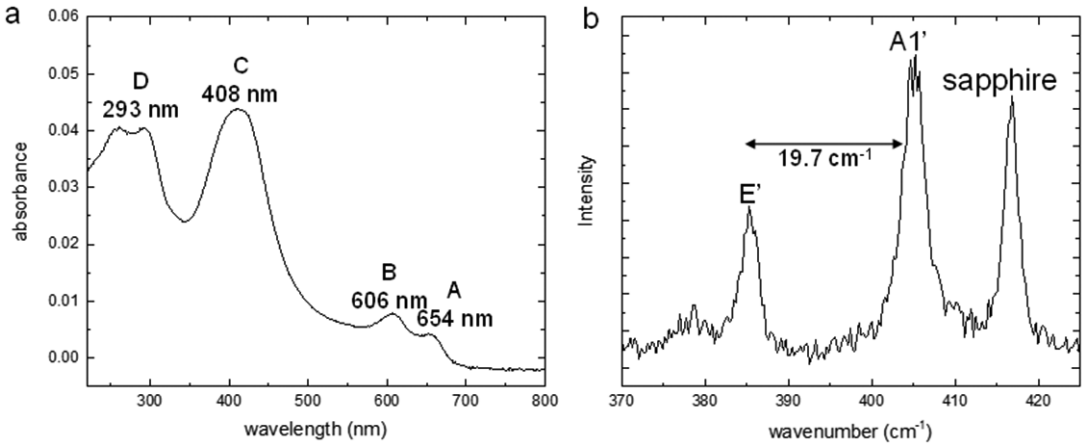


Figure VII.23. (a) Optical absorption and (b) Raman spectra at 532nm from 1L-MoS_2 grown at 950° C. Adapted from [1142], copyright American Chemical Society.

In order to optimize the growth morphology toward large lateral size (>1 μm) and crystalline 1L-MoS_2, the growth parameter space was explored. The T dependent growth of MoS_2 on sapphire in figure VII.21 shows the AFM height images of for the conditions that yield low overall coverage without merging of individual nuclei. The MoS_2 nuclei form randomly over the surface.

The nucleation concentration exponentially decreases with increasing temperature in an Arrhenius fashion (figure VII.22). This is consistent with a surface-mediated process, where the apparent activation energy is linked with various activated surface reactions such as adsorption, attachment, and diffusion [793, 1156].

Raman and absorption spectroscopy (figure VII.23) demonstrate the high optical quality of the as-grown 1L-MoS_2, comparable to exfoliated and CVD deposited MoS_2 [1130]. E.g. the A, B, C, and D excitonic peaks are visible [1130, 1142], a clear optical signature of MoS_2. Moreover, the wavenumber difference between the two prominent Raman peaks, relating to E' and A_1' modes is ~19.7 cm^{-1}, close to the standard value of 1L- MoS_2. Nevertheless, the grain sizes even for high growth T (1000 °C) are less than hundreds of nm for these growth conditions. This makes further characterization of individual flakes difficult and the polycrystallinity of the film may lead to a significant degradation and non-uniformity in electronic quality for wafer-scale applications.

The effect of partial and overall pressures of the gas species, $Mo(CO)_6$:H_2S:H_2 on grain size was investigated. Using XPS, it was found that for low growth pressure (10 mbar or below), the MoS_2 film becomes contaminated with Si (figure VII.24) likely originating from the quartz tube, with the reducing environment originating from H_2 in the carrier gas and from the decomposition of H_2S, not ideal for a clean, growth of 1L-MoS_2. In addition, larger amounts of $Mo(CO)_6$ compared to H_2 tend to yield bulk particles of non-sulphurized, Mo oxides as probed by XPS (figure VII.25).

Figures VII.25(a) and (b) showoptical microscopy images of MoS_2 films grown on sapphire, for two different $Mo(CO)_6$:H_2S ratios, 4:1 and 1:1 respectively. The core-level XPS spectra of Mo 3d, S 2s, and S 2p demonstrate that the low $Mo(CO)_6$:H_2S condition provides a good stoichiometric film of MoS_2 with only small (<1%) amount Mo in different chemical state (Mo^{5+}) than MoS_2 (Mo^{4+}), while the high $Mo(CO)_6$:H_2S condition leads to undesired deposition of thick Mo particles likely oxidized in 5+ state, with a poor Mo:S stoichiometry consistent with the thermochemistry of the Mo, O, S, H system [1147].

VII.2.6. Reduction of the nucleation density using alkali metal halides

So far MOCVD has produced 1L-MoS_2 with average domain size <1 μm[1157, 1158]. This presents a challenge towards production of single-crystal 1L-MoS_2 over the length scale of the substrates. In order to improve the domain size, one could employ alkali metal halide salts such as NaCl, KI, and KBr. The use of thes salts was documented in MOCVD experiments to improve domain sizes, involving precursor combinations of $Mo(CO)_6$ and $(C_2H_5)_2S$ [1140], $MoCl_5$, and $(CH_3)_2S$, [1159] and conventional CVD [1160] on SiO_2/Si. A metal halide, such as NaCl or KI powders (~0.01–1 mg), was placed in the upstream area of the furnace either in a boat or plate of alumina [1142]. $Mo(CO)_6$ was introduced at ~600 °C for 30 min before introducing H_2S at higher T (750 °C–1050 °C). A nucleation suppression effect is observed [1140], where 1L-flakes > 10 μm can be achieved. Analysis by optical absorption, Raman, PL spectroscopy and XPS in figure VII.26 indicate that this MoS_2 exhibits a direct-band gap without significant defects, strain, impurities and doping comparable to those of 1L-MoS_2 grown by conventional CVD. Furthermore, the crystal facets are highly aligned in one direction, demonstrating a successful lattice-orientation matched epitaxial deposition of MoS_2 on single-crystal sapphire. T dependent field-effect

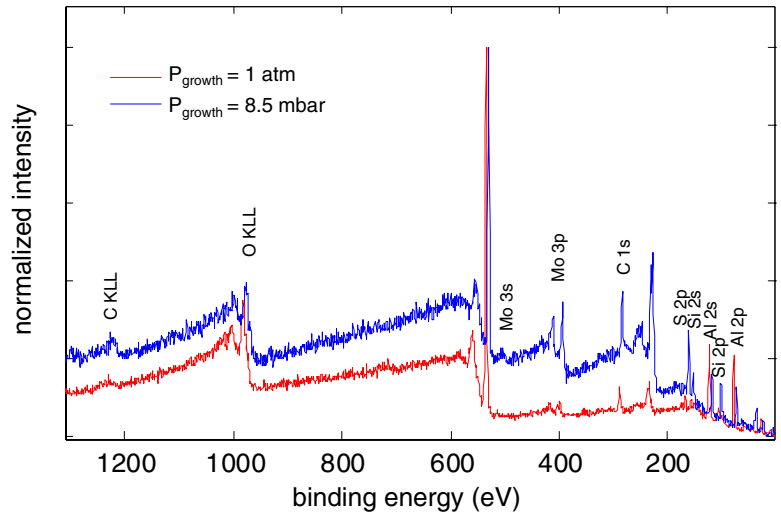


Figure VII.24. XPS survey spectra of MoS_2/sapphire samples from the two growth runs with different chamber pressures (1 atm and 8.5 mbar). XPS measurements were performed with PHI Versaprobe II equipped with x-ray source, Al Kα; $h\nu = 1486.6$ eV.

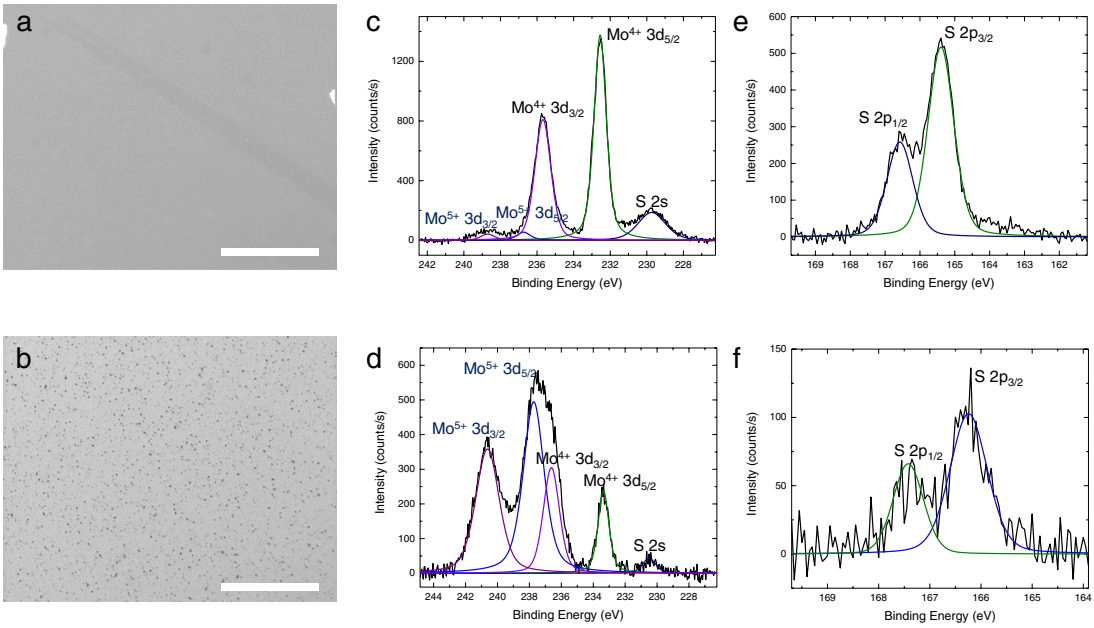


Figure VII.25. Influence of Mo(CO)6:H2S flow rate ratio on MoS2 film composition. (a) and (b) Optical images of two different Mo(CO)6 Ar carrier and H2S mass flow rates of (a) 15 (Mo(CO)6 flow rate of 0.0053 sccm) and 15 sccm, and (b) 5 (Mo(CO)6 flow rate of 0.0018 sccm) and 20 sccm with growth T~ 950 °C, bubbler T~ 30 °C, H2 ~10 sccm, growth pressure ~1 atm, and growth time ~30 min. Scale bar, 25 μm. (c) and (d) Mo 3d and S 2s core-level XPS spectra for the corresponding growth conditions of (a) and (b). (f) S 2p core-level XPS spectra for the corresponding growth conditions of (a) and (b). XPS measurements were performed with PHI Versaprobe II equipped with a Al Kα x-ray source; hv = 1486.6 eV.

transistor characterization using polymer electrolyte gating demonstrated a promising n-type μ~100 cm^2 V^{-1} s^{-1}, similar to 1L-MoS_2 deposited by conventional CVD [1149].

It is currently not clear exactly how the domain enlargement or the suppression of nucleation by the metal halides occurs. The desiccating effect of NaCl salt as suggested by Ref. [1140] is not likely to be the dominant factor since even a very small amount of salt (<10 μg) could be used, where it would decompose before the growth reaction. Ref. [1159] suggested that salt helps to reduce the carbon contaminant, which might hinder crystallization, from organic parts of the MOCVD precursor. Refs. [1161, 1162] suggested that the presence of alkali metals leads to decrease in the melting point of oxide-based Mo precursors and even the melting point of a substrate [1163], increasing the reactivity. This in turn could lead to the increased diffusion and reduction in the nucleation density. Na oxides or compounds of sodium and molybdenum oxides (NaxMoyOz) [1160, 1162, 1164] may also play a role, as they were found at the interface between as-grown 1L-MoS_2 and substrate [1164]. It was also found that after growth, where the salt was initially present, the halogen atoms evaporated away from the substrate surface while the alkali metals remained

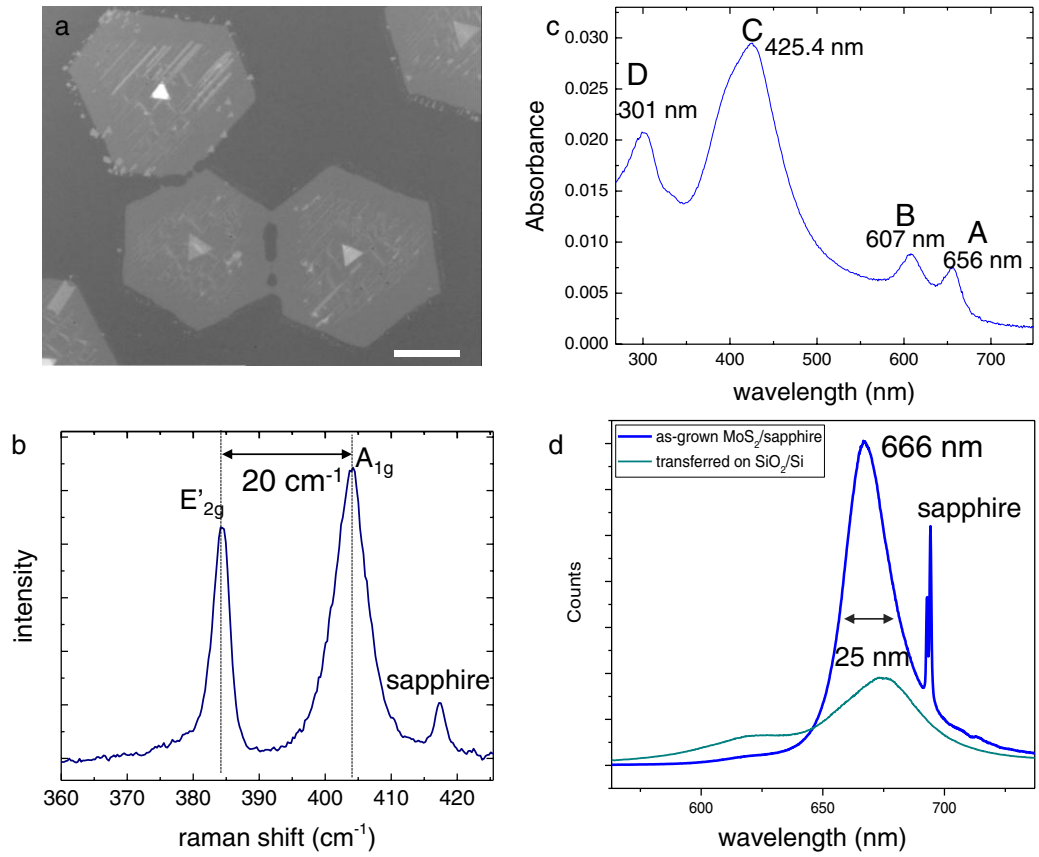


Figure VII.26. (a) Optical microscopy of 1L-MoS_2 with NaCl placed upstream. Scale bar: 25 μm. (b) Raman spectroscopy on a single crystalline 1L-MoS_2 area (c) optical absorbance. (d) PL spectra from single crystalline 1L-MoS_2 flake as-grown on sapphire and transferred onto SiO_2/Si. Adapted from [1142], copyright American Chemical Society.

[1142]. Na_2MoO_4 alone (without any halogens) is effective precursor for growth of large domain sizes [1165]. Large area MoS_2 growth of large domain sizes was acieved on Na doped glass substrates [1164, 1167]. Na especially impacts the growth of large crystalline domains at a wide range of growth T (720–1050 C). The exact role of the alkali metals remains to be investigated, as there are numerous competing atomistic processes, such as surface diffusion, nucleation site activation, attachment kinetics that control nucleation and growth, which all can influence the nucleation density and domain size.

This be extended to perform MOCVD of vertical and horizontal heterostructures of TMDs, such as $MoWS_2$ and $MoWSe_2$, using currently available metalorganic sources, such as $W(CO)_6$, and dimethyl selenide [1168]. In addition, doping of TMDs may also be achieved by introducing dopant precursors, as done for MOCVD of other materials systems [1169, 1170]. Low toxicity, low-cost precursors should also be considered, in order to achieve a safer and more accessible production of TMDs.

VII.2.7. ALD

Atomic layer deposition (ALD) techniques were presented as a modified CVD to produce thin layers of MoS_2 using the precursor pairs—$MoCl_5$ and H_2S [1171], $Mo(CO)_6$ and H_2S [1157], $Mo(CO)_6$, and dimethyl disulphide [1172], $Mo(NMe_2)_4$ and 1,2-ethanedithiol [1173], on various insulating substrates such as SiO_2/Si, sapphire, and mica. However, often the end products are misaligned nanocrystalline MoS_2, with varying degree of thickness likely resulting from the low growth T ~300 – 600 °C). Although it is more challenging to prepare and control the stoichiometry of the product, MOCVD of MoS_2 using single-source precursors, tetrakis(diethyldithiocarbamato)molybdenum(IV) [1174] and Mo(S-t-Bu)4 [1175] were also investigated.

7.2.8. Brief comparison methods for the growth 2D semiconductors

In the table VII.2, we summarize the methods for the growth of LM semiconductors presented in this chapter.

VII.3. Layered materials heterostructures

Typically, heterostructures of semiconductor compounds have been fabricated using isostructural substrates with nearly lattice matched substrates. One of the advantages of LMs is that the lattice matching requirements needed for cubic materials systems is relaxed [1149]. Lateral heterostructures are also a focus of research [1176]. Growth of lateral and vertical heterostructure could enable a number of devices [1177]. Many groups have fabricated and studied

Table VII.2. Basic conditions for growth of TMDs.

Method	Material	Substrate	Precursors	Temperature	Pressure	Reference
CVD	MoS_2	SiO_2	MoO_3 and S	750 °C	Atmospheric	[1008]
MOCVD	MoS_2	Sapphire	$Mo(CO)_6$ and H_2S	600 °C–700 °C	Atmospheric	[1142]
TAC	MoS_2, WS_2	Quartz, SiO_2	Mo, W, S	750 °C	Atmospheric	[1093]
PVT	β-In_2Se_3	SiO_2, mica, graphite	γ-InSe	600 °C	1.6 mbar	[1117]

aligned and unaligned LMHs with the objective of making new devices and scale transistors beyond the CMOS limit [1178–1183]. Many of these LMHs were fabricated using exfoliation and transfer rather than direct growth. It would be desirable to use CVD to fabricate them. In the case of h-BN and graphene, because of their refractory nature, a catalyst is used to grow them. HBN or graphene would be ideal substrates for other LMs. Thanks to its atomically flat surface, low interlayer electronic coupling and almost perfect reticular matching, h-BN is an ideal substrate for graphene [1184]. Many of the researched LMH devices also include TMD semiconductors [112, 1185]. However, these materials have challenges of their own as discussed in section VII.2 In order to create LMHs containing semiconducting TMDsor BLG, metals (TMD and graphene), and dielectrics (h-BN), a significant amount of effort is needed either via repeated transfer of the individual LMs or direct growth [1177].

LMHs of cubic systems were grown by MBE and CVD, MBE being the work horse for bulk III-V heterostructures today. Both CVD and MBE were used for the growth of TMDs [1186–1189] while CVD [765, 1038] has advantages for graphene [765, 1038] and h-BN [836, 1054, 1055, 1087, 1190, 1191]. CVD may be the most suitable technique for the scalable synthesis of highly-crystalline LMHs even though the selection of the final deposition equipment and preferred precursor types have not been finalized yet. Such CVD approach is not trivial as weak interlayer interactions favor 3d island growth [1192]. The formation of multilayer islands is typically avoided by using high chalcogenide to metal ratios adopting short reaction times, which leads, however, to isolated crystals [1192–1196]. Growth LMHs, vertical or lateral, is challenging. In this section we will discuss a few materials options[1192].

There are several reports targeting the Controlled lateral and vertical TMDs heterostructure growth [1197–1199]. Controlled grown of lateral heterostructures of TMDs would enable quantum engineered devices, through band alignments, enabling new generation of electronic devices [1177, 1200]. 1L-TMDs can be grown sequentially to construct in-plane LMHs, otherwise not achievable through other processes such as transfer of grown or exfoliated films. Ref. [1200] demonstrated a direct synthesis of lateral LMHs of $MoS_2 - WS_2$ and $MoSe_2 - WSe_2$ by using ambient-pressure CVD with aromatic molecules as seeding promoters. Vertical LMHs, while simpler, will require significant effort is reducing 3d growth [1201, 1202].

VII.3.1. Graphene/h-BN stacks

There are several types of LMHs that can be envisioned for future devices: (1) vertical, (2) lateral, (3) twisted (controlled and uncontrolled). Graphene and h-BN have been grown by a number of catalytic CVD [1203, 1204] and plasma enhanced techniques [963]. Catalyst-free graphene growth yields poor crystal shapes and crystallinity, with low rates [947, 1204, 1205]. Ref. [836] used a catalyst-free CVD approach to synthetize crystalline graphene on exfoliated h-BN, with noticeable growth rates on single-crystal on-axis SiC substrates (either Si- or C-face). SiC was selected because of its high thermal stability [1206], in view of the high growth T, typically >1200 °C, needed for a non-catalytic growth approach. The SiC(0 0 0 1) samples were diced from commercially available wafers and then cleaned via wet chemistry, prior to mechanical exfoliation of h-BN. They were immersed in an ultrasonic bath of acetone and then IPA for 3 min each followed by a DI water. They were then cleaned in HF (48% solution) diluted in DI water (1:10 HF: DI-H_2O) for 1 min to remove the native oxide and thoroughly rinsed in DI water. The samples were then subjected to an oxygen plasma (O_2 flow, 80 W, 5 min) to completely remove the organic or carbonaceous contaminants. The SiC surfaces, which had polishing scratches in the as purchased form, were hydrogen etched in the same vertical cold-wall reactor (Aixtron, HT-BM) for 4 min in an atmosphere of high purity (6N) H_2 and Ar at 1230 °C and a total pressure of 450 mbar using 500 sccm flow rate for each gas. AFM was used to measure the SiC surface roughness and only substrates with atomically flat surfaces were used for growth. PDMS stamps were used for mechanical exfoliation of h-BN on the hydrogen etched SiC. To this end, two PDMS stamps with dimension of $2 \times 2\,cm^2$ were adopted and the mechanical exfoliation process was repeated more than 40 times. The clean SiC substrate was then pressed on the PDMS stamp for 20s. This process yielded h-BN flakes with lateral size up to 150 μm. The PDMS residue on top of the h-BN/SiC was removed by using first acetone for 3 min and then IPA while gently shaking the beakers. Ultra-sonication was not adopted, since it causes detachment of the mechanically exfoliated h-BN flakes from the SiC substrate. Finally, the samples were treated with a 25 W oxygen plasma for 30 min. This last step was found to be crucial for obtaining single crystal graphene on h-BN as it allows for removal of adventitious carbon contaminations [836]. The h-BN/SiC substrate was then placed in the Aixtron HT-BM system and

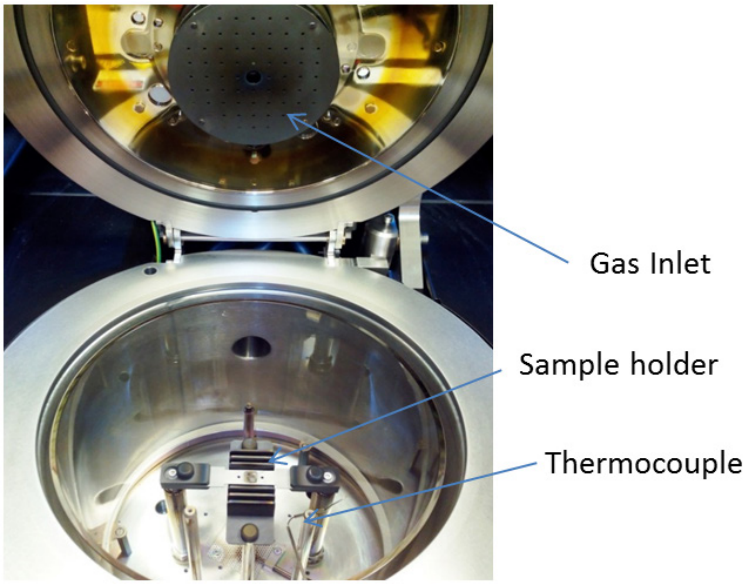


Figure VII.27. Growth chamber of the Aixtron HT-BM vertical cold-wall reactor used for growth of graphene on h-BN.

positioned in the central recess of the heater (see figure VII.27) for subsequent graphene growth.

The h-BN films on SiC were then annealed in an 8 mbar H_2 pressure, with hydrogen flow of 1000 sccm at 1150 °C for 10 min. [836]. Single crystal graphene was then grown under the following conditions: 150 sccm H_2, 1000 sccm Ar and 5 sccm of methane (CH_4) for 30 min. The H_2:CH_4 ratio was found to be a critical parameter for the growth of high quality graphene. H_2:CH_4 ratios of 1:1 yielded polycrystalline graphene with rounded edges, and a ratio of 1:30 yielded hexagonally shaped single-crystal graphene domains. The optimum growth T was found to be 1150 °C. Lower growth rates were achieved at 1000 °C [836], but little to no growth was observed below this T. Above 1150 °C, growth was also achieved, but clustering of amorphous carbon was also often observed [836]. Growth was performed at different pressures ranging from 7 to 150 mbar. This yielded smaller (<0.5 μm) and bigger (>2.0 μm) domains for low and high pressure conditions respectively. Carbonaceous clusters were occasionally observed at the higher pressures (150 mbar). For this reason, the growth pressure should be limited to 25 mbar to prevent the formation of such clusters. Lower hydrogen flows (i.e. 100 sccm) and longer growth times were also be used to obtain continuous films. With hydrogen flows >150 sccm only partial growth of hexagonal single-crystals could be achieved. At the end of the growth process at high T, the system was cooled (300 °C min^{-1}) in the same atmosphere of Ar and H_2 used during growth. The sample was unloaded from the chamber for T < 120 °C.

VII.3.2. TMD/h-BN and TMD/grapheneLMHs

There are many reports on growth of sulfides [1196, 1197, 1207–1210] and selenide [1139, 1176, 1211–1213] TMDs using a variety of precursors using similar CVD systems, although this is far from the optimal or desired approach. Direct growth of WS_2 on other LMs resulted in isolated grains at the micron scale [1194] or uncontrollable growth of FL-WS_2 on graphene [1195] and isolated grains on h-BN [1196]. What is critical in the initial crystal growth process development, in addition to identification of the materials and the equipment and precursor selection and design, is the understanding of nucleation and growth of controlled TMD layers. Some inroads in the basic understanding for both MBE as well as CVD were reported in Refs. [1201, 1202, 1214].

A CVD approach to obtain continuous 1L-WS_2 on h-BN and graphene was reported [1209] following similar growth procedure used for MoS_2 [1189, 1215]. Ref. [1216] used a similar method to grow MoS_2/h-BN LMHs, as well as growing h-BN by CVD as shown in figure VII.28.

Sulfurization of WO3 powder (Sigma Aldrich, 99.995%), was carried out within a horizontal hot-wall furnace. This is is basically a two-zone system with WO3 within a high T zone, and Sulphur (Sigma Aldrich, 99.99%) in a quartz crucible in a cooler zone, of the furnace as shown in figure VII.29. The system is connected to a scroll pump, which ensures a base vacuum ~5×10^{-2} mbar. The h-BN and graphene substrates are prepared through MC on either quartz or SiCwith variable (up to 1 cm^2) surface area. Quartz substrates are cleaned with a piranha solution (3:1 H_2SO_4:H_2O_2) for 15 min and acetone and 2-propanol semiconductor grade for 3 min each before flake exfoliation. SiC substrates are also threated with 5% HF in water for 1 min to remove the SiO_x on the surface. After the exfoliation of h-BN, the substrates (either quartz or SiC) are treated with an oxygen plasma (5 min, 80 Watt) to remove possible scotch tape residue.

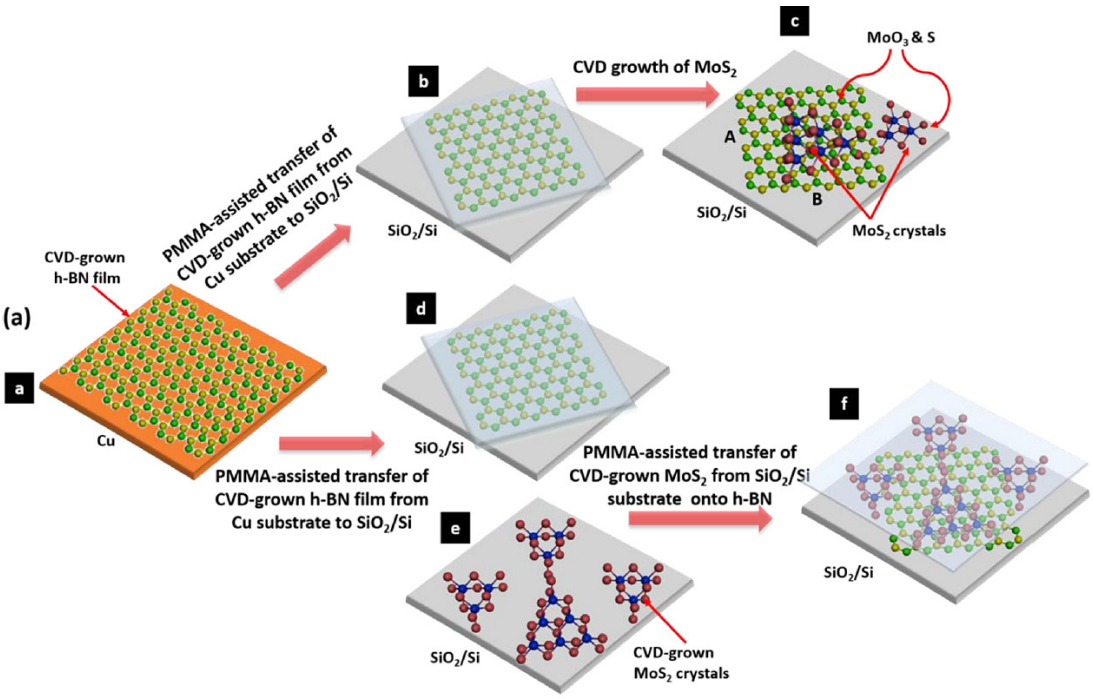


Figure VII.28. Schematic of two fabrication processes of MoS_2/h-BN LMHs. The first consists in transferring the CVD grown film from a Cu foil to the center of a Si/SiO_2 chip, leaving four corners of the substrate to be bare SiO_2. This substrate is then loaded face up into the CVD system to grow MoS_2 on it. The MoS_2 domains will cover both h-BN and SiO_2 areas. The second approach is through a two step PMMA assisted process. The CVD grown h-BN film is first transferred onto the center of a SiO_2/Si chip, followed by stacking another layer of CVD grown MoS_2 on the whole substrate surface, obtaining transferred MoS_2 domains on h-BN in the central area. Two of the transferred bundaries of h-BN on the SiO_2 surface in the first fabrication method are labeled A and B. Adapted from [1216], copyright American Chemical Society.

WS_2 can also be grown on polycrystalline or single crystal CVD graphene [766, 841] transferred on quartz or SiC cleaned as described above. For WS_2 growth on graphene on SiC, fresh as-grown samples are used. Both are cleaned for 3 min in acetone and for 3 min in 2-propanol. Crucibles are cleaned with 2-propanol wet tissue and subsequently annealed in the furnace used for the growth at 1100 °C for 60 min in 200 sccm Ar before each growth. This 'empty run' ensures having both a reactor and clean crucibles. After annealing usually the crucibles are electrostatically charged. This can alter the weighing of the reactants. The electric field interacts with the WO_3 powder, which sticks to the crucible and spreads around in a not reproducible way. Hence, the crucible needs to be grounded before weighing.

There are many important details related to oxide powder preparation, loading and placement in the horizontal furnace. The substrate and WO3 are placed in the same flat 1-inch wide crucible, next to each other, but well separated to avoid accidental deposition of the powder on the substrate. The WO3 powder has to be spread uniformly on the quartz crucible after weighing in order to maximize the reaction surface. The distance, typically ~1 cm, between substrate and WO3 powder is also important to control the surface coverage. The S powder is placed outside the hot zone of the oven in the Ar upstream part, ~20 cm away from the furnace (see figure VII.29). A heating belt is wrapped around the tube region where the S is placed to control evaporation. It is important that the growth reaction occurs under S rich conditions. To ensure this, two aspects are crucial:

1) S and WO_3 powders have to be in a ratio between 50:1 and 100:1. If not, the reaction typically stops at the intermediate step of WO_2 cluster formation. Optimum weights ~100 mg of S and 1 mg of WO3 were reported.
2) S has to be delivered when WO3 has reached a stable optimal T. To achieve this, this process can be followed. Once crucibles and target sample are in place within the reactor as shown in figure VII.29(b), the growth can start. The ramp-up phase has two steps: (i) ramping up to 350 °C at 10 °C min^{-1} with no gas flowing to favor sample outgassing; (ii) ramping up to 900 °C (still at 10 °C min^{-1}) while the Ar flow is set at 500 sccm (tube pressure equals 4 mbar) in order to keep the S powder solid. The purity of the Ar gas is 99.9999%. Once the hot zone reaches the working T~ 900 °C, the Ar flow is reduced to 8 sccm (i.e. tube pressure ~0.5 mbar) to ensure S delivery. The heating belt wrapped around the S zone has to be turned on in order to reach 200 °C when the hot zone reaches the working T. This ensures S feeding for ~30 min. The total process is ~1 h long to anneal the surface of the sample after the growth reaction. The sample is then cooled

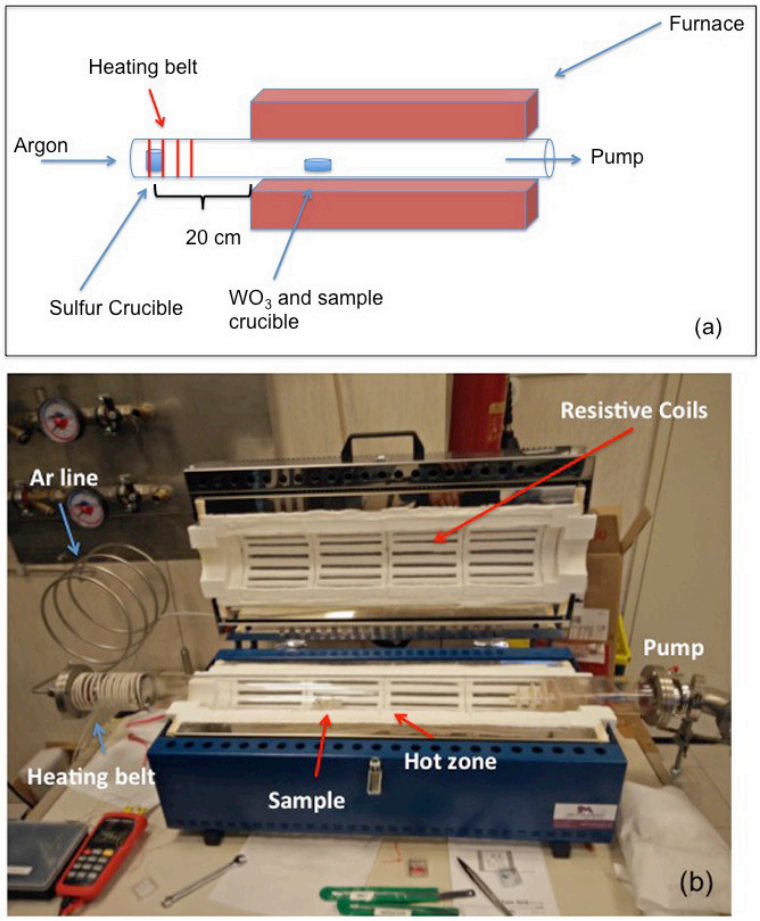


Figure VII.29. (a) Scheme of the furnace used to grow continuous films of WS_2 on graphene and h-BN; (b) picture of the furnace. Adapted from [1217], with permission of The Royal Society of Chemistry.

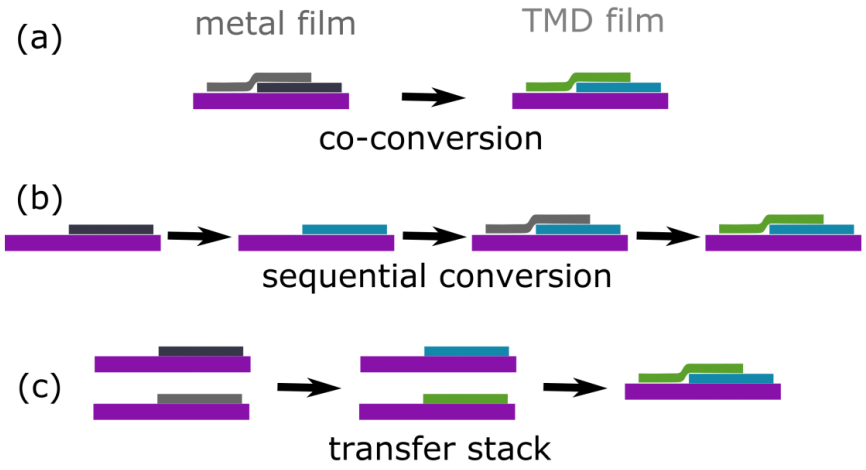


Figure VII.30. Different method used to create TMD LMHs, (a) Co- conversion of both metal films together to form TMDs. (b) Sequential conversion of metal films. (c) LMH formation through stacking pre-converted films.

to RT by shutting the power to the furnace and, once 400 °C are reached, the furnace lid is opened to speed up cooling.

VII.3.3. TMD/TMD LMHs

CVD and MOCVD can also be used for growing different types of TMD LMHs [1176, 1198, 1199, 1218]. Lateral LMHs between different TMDs show atomically sharp interfaces with an abrupt transition between constituent materials, without voids and other defects. Using direct growth instead of material transfer has the benefit of a residue-free LMHs and scalability to large areas.

Lateral and also vertical 1L-LMHs both based on the same metal such as MoS_2 and $MoSe_2$ [1218], WS_2

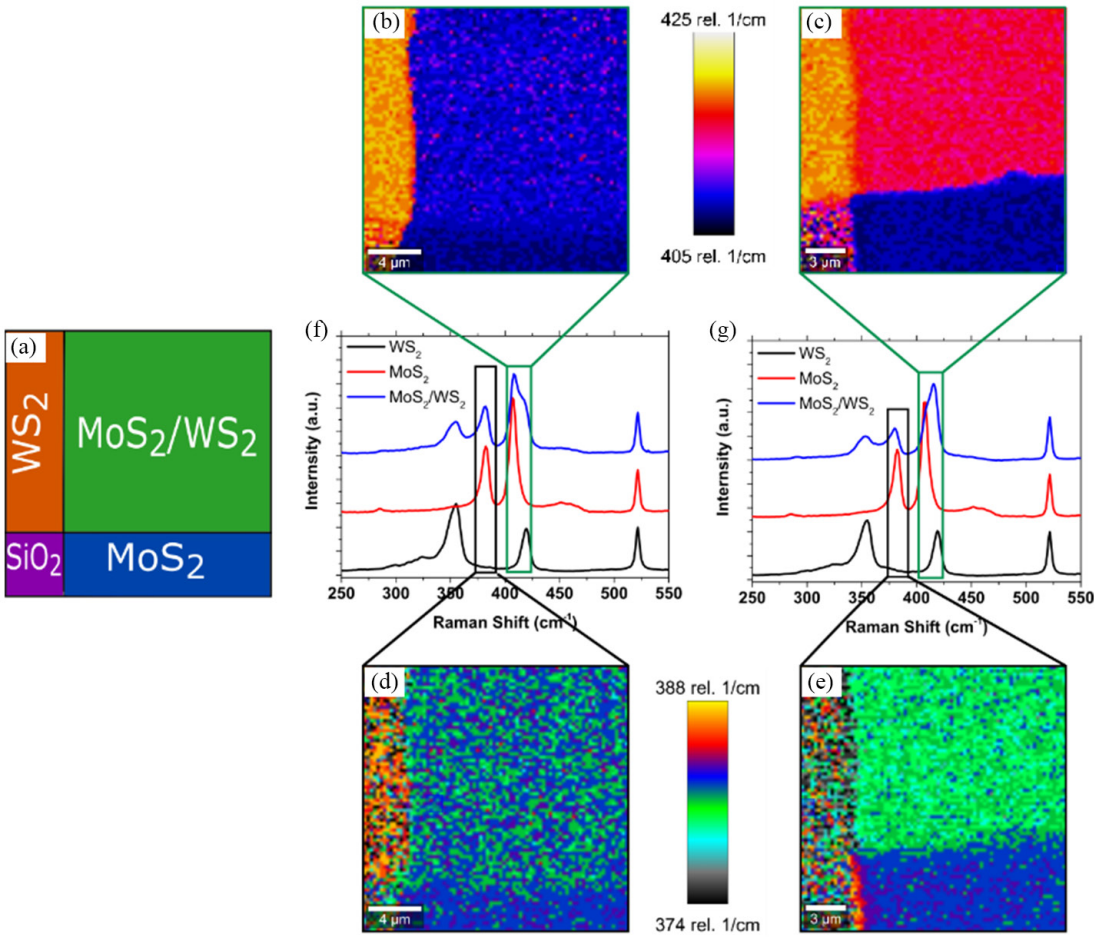


Figure VII.31. (a) Legend for Raman maps. (b) and (c) Raman map of MoS_2/WS_2 A_{1g} peak position for sequentially and co-converted films. (c) and (d) Raman map of MoS_2/WS_2 E^1_{2g} peak position for sequentially and co-converted films. (e) and (f) Raman spectra of MoS_2/WS_2 for sequentially and co-converted films respectively.

and WSe_2 [1218], as well as different metals, such as WSe_2 and $MoSe_2$ [1176], MoS_2 and WS_2 [1198], $MoSe_2$ and WSe_2 [1176], and WSe_2 and MoS_2 [1199] have reported using CVD based on solid sources. Control over gas flow during the CVD process can also allow the growth of superlattices with well-controlled spatial modulation [1220, 1221].

Some of these materials can be used as lateral p-n junctions without employing *in situ* doping, as e.g. in the case of MoS_2 and WSe_2, where the boundary between the two materials serves as a p-n junction [1222] and can be used as a LED. Theory also predicted novel behaviours, such as efficient charge separation [1222] and spin/valley filtering [1223].

While these methods yielded perfectly stacked materials, they are limited to very small lateral dimensions and a few selected material sets. TAC methods are an alternative for large scale production of TMD/TMD heterostacks. TAC opens various avenues for the formations of large scale LMHs as in figure VII.30. Figure VII.30(a)) shows the subsequent deposition of two different metals by PVD followed by TAC. This works for sulfides or selenides of metal in which the conversion takes place at a similar T. The second example in figure VII.30(b) is the growth of a TMD by TAC followed by a second metal deposition and TAC. The third is the large scale mechanical transfer of one TAC film on top of another (figure VII.30(c)

Raman spectroscopy was employed to analyse the interface between the two TAC films in a LMH. It was used to analyse the effect of co-converting the two metal films versus sequentially converting them. This experiment was performed with MoS_2 and WS_2 as they both can be sulfurised in the same T range, 800 °C. The co-sulphurized sample had both metals sputtered and converted to the equivalent TMD together, while the sequential sample had the Mo deposited and converted, then the W deposited and converted. Shadow masks were used to give the cross structure indicated in figure VII.31(a). Both samples were then Raman mapped, with a spectrum taken every 300 nm over a 10 μm × 10 μm area. All spectra are normalised to the SiO_2 peak ~520 cm^{-1}. This data was then used in figures VII.31(d) and (e), which show the frequency position map of the MoS_2 E^1_{2g} peak. For the MoS_2 area the peak is at ~383 cm^{-1} (blue) in both maps. The WS_2 and SiO_2 areas, with no peak in this frequency region, show only random noise. In the overlap region, for the sequentially sulphurized sample figure VII.31(d), the maximum intensity is very close to the same frequency

as the MoS_2 area. However, in the co-sulphurized sample figure VII.31(e), there is a noticeable shift to a lower wavenumber as shown by the green colour. This is an indication of increased alloying at the interface in the co-sulphurized sample. A similar effect was seen in Ref. [1224] where they saw increasing shift of the MoS E^1_{2g} to lower wavenumber with increasing alloying with W.

To confirm this, the A_{1g} peaks of MoS_2 and WS_2 were analysed, position maps are shown in figures VII.31(b) and (c). These peaks are both in the same frequency region ~400–430 cm^{-1} so to distinguish between changing peak intensities and peaks shifting frequency, these peaks were fitted. What is expected in the case of alloying between the layers is that the A_{1g} peak of MoS_2 and WS_2 will both shift towards an intermediate value, as observed. For the sequential conversion there is a small shift of both peaks towards each other by ~1 cm^{-1}. For the co-conversion the peaks each shift by ~4 cm^{-1} towards each other, indicating more alloying in the co-conversion case.

Even though large scale LMH formation by co-conversion was successful [1224], the electrical performance was poor probably due to the roughness of the films and some level of alloying during the TAC process. Co-sulfurisation (figure VII.31(a)) was used to create catalyst for hydrogen evolution, [1225] while the subsequent sulphurization of Mo and W (figure (b)) was employed to create PDs [1226].

VIII. Functionalization of GRMs

A number of strategies have been developed for the functionalization of GRMs. On one hand, this is driven by the curiosity of chemists to master controlled surface modification. On the other hand, functionalization is of great practical importance, as it has the potential to tune the properties according to the needs of specific applications. In this section, an overiew is given in particular focusing on the practical requirements for successful modification of GRMs. A broader overview, is also given in Refs. [160, 165, 1227–1229].

Typically, functionalization is classified as noncovalent or covalent as outlined in Ref. [160] and brifly summarized below. Noncovalent involves the adsorption of other species without covalent bond formation. It is therefore often considered as 'non-destructive', since the lattice is not altered, or referred to as physisorption. However, physisoprtion is not a precise term for noncovalent functionalization. This is because not only van der Waals interactions can occur. Often, more specific, stronger noncovalent interactions are exploited, e.g. dipole and ionic interactions [1771], or π–π stacking, which is specific to graphene with a conjugated sp^2 carbon network. The term covalent modification is used when covalent bonds are formed [1329]. Often, this is referred to as chemisorption. For graphene this includes various cases: from new C–C bonds on the basal plane leading to a rehybridization from sp^2 to sp^3 [1772, 1773], to modifications of defects (e.g. edges [1773–1776]) or the production and derivatization of GO [156, 160, 1799].

In all cases, the properties of the parent material are modified, but in a different way and to a different extent. E.g., the grafting of other species on the surface can be used to form functional architectures or to adjust the compatibility with other materials in composites. Functionalized GRMs typically also display a better dispersibility (higher concentration), especially in solvents that can otherwise not be used. In terms of electronic properties, noncovalent functionalization can be considered as a 'milder approach': while it can be used to controllably dope graphene, it does not harm the conjugated basal plane network and thus does not alter the intrinsic electronic properties dramatically. In turn, covalent functionalization of GRMs essentially creates new materials with distinct properties. E.g., covalent functionalization of graphene is a tool to open a band gap, but at the cost of reducing μ [1780, 1781].

VIII.1. Covalent functionalization of graphene

VIII.1.1. Reductive bulk functionalization

The covalent functionalization of carbon allotropes, especially graphene, is a major research topic in the growing field of functional nanomaterials. The development of novel architectures built-up from graphene requires the availability of a cheap source with low polydispersity. Chemical bulk functionalization of graphene using graphite as starting material has gained significant interest since it allows (i) the generation of exfoliated graphite sheets in large quantities compared to other exfoliation techniques [375, 377, 1230], (ii) access to solution-processable graphene [373, 374], (iii) access to modified physical properties compared to pristine graphite [1231, 1232], and (iv) the investigation of the intrinsic chemical and physical properties of graphane [160, 1230]. Graphite can be activated by reductive charging using an alkai metal, which subsequently leads to a Coulomb driven, solvent-based exfoliation [160, 373, 375], as sketched in figure VIII.1. The intermediately generated material is negatively charged and commonly referred to graphenide [1233]. It can be reoxidized by benzonitrile or other chemical agents [1234], yielding SLG and FLG [375], or trapped by a variety of different electrophiles, yielding covalently functionalized graphene with a variety of functional entities. By this route, hydrogenated [369, 1235, 1236], alkylated [368, 1237–1239] and arylated graphene [370, 1240, 1241] are accessible in a one pot synthesis.

The entire functionalization sequence has to be carried out without oxygen and moisture under inert gas atmosphere in a glove box, otherwise a substantial amount of side products is formed [375, 1247, 1242, 1243]. Reductive graphene functionalization represents a versatile protocol which can be applied to graphene in dispersion as well as to SLG on substrates. The latter approach can be used to elucidate topological and mechanistic details of the reaction [1237, 1244].

A variety of experimental conditions are reported in the literature [160, 1777–1779]. From the starting graphite sources, to the composition of the GICs, the employed solvents and/or the used equivalent number of the organic addends, to name a few. We will overview different aspects of fundamental importance for the successful covalent functionalization of graphene, starting from reductively activated bulk graphite: (a) Type of starting graphite, (b) solvents used for the exfoliation, and (c) type of GIC and electrophilic trapping reagent [371, 1238]. Covalently functionalized graphene, without initial reductive activation of graphite, can be accessed by a variety of other synthesis approaches [1245–1247].

VIII.1.1.1. Type of starting graphite

In the context of the reductive graphite exfoliation/functionalization protocol, almost any type of graphite, can be used. A variety of graphite starting materials with different physical and morphological properties were screened [1248] and based on that their covalent functionalization studies focused on 3 types of graphite [1238]: (a) Natural flake graphite (Kropfmühl AG, Passau) with a particle size of 18 μm and a low intrinsic density of defects as expressed by $I(D)/I(G) \sim 0.2$, with a regular stacking order, (b) PEX 10 (Future Carbon AG)—an expended powder graphite with grain size of ~3–5 μm and $I(D)/I(G) \sim$

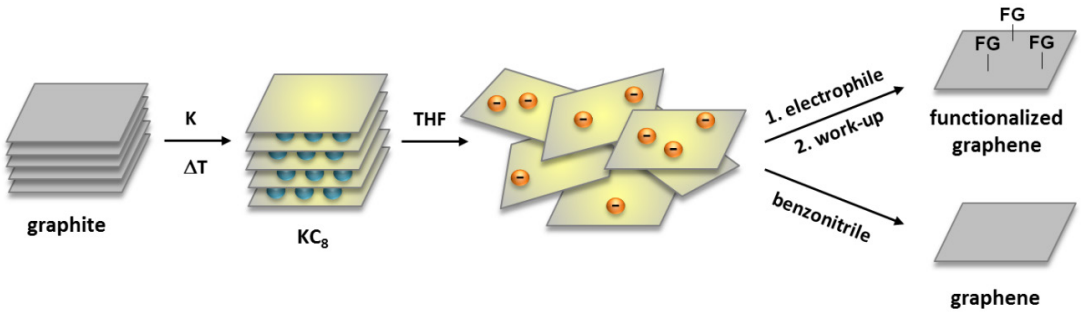


Figure VIII.1. Reductive exfoliation/functionalization of graphite.

0.3 and, (c) SGN18 (Future Carbon AG)—a spherical, defect-rich graphite with $I(D)/I(G) \sim 0.4$, with a grain size ~20 μm.

In general, the chemical reactivity of graphite with respect to a reductive covalent functionalization scenario strongly depends on the nature and in particular the morphology of the starting material. It is key that the starting material is dry and free of oxygen. Therefore, a thermal annealing step (300 °C, vacuum, 4–5 d), is used to remove any oxygen inclusion. For materials with intrinsically large graphene basal planes (e.g. natural flake graphites) a reductive charging/exfoliation is very difficult. The intrinsic flake size can be reduced by grinding with NaCl, in particular, the graphite is ground with 5 times the amount of NaCl in a mortar for 20 min. After the elution of NaCl with distilled water and drying in vacuum, smaller and easier dispersible flakes can be obtained.

For the reductive charging/activation of graphite, 4 approaches can be pursued: (a) Electron transfer reagents [1239], (b) *Birch*-type based reduction [1249–1252] in liquid ammonia with alkali metals [374], (c) reduction with sodium/potassium alloy [1253], and (d) the generation of alkali metal/GICs [373, 1254]. In the latter two cases, the balanced combination of intercalation-driven layer expansion in combination with a Coulomb-repulsion-driven interaction facilitates exfoliation and the wet chemical functionalization of the electronically activated graphene sheets. The solid-state-based graphite intercalation process (d) allows for a fine tuning of the different alkali metal to carbon stoichiometries from KC_4 to KC_{24} [370]. K is used to reduce graphite and to generate the respective GICs. The metal is directly mixed with graphite in an inert gas atmosphere (glove box <0.1 ppm O_2, <0.1 ppm H_2O) at 150 °C overnight. By changing the alkali metal amount, different intercalation compound stages can be obtained e.g. KC_4, KC_8, KC_{16}, and KC_{24}. The reductive activation of flakes, deposited on substrates, or CVD SLG can be carried out by applying of a droplet of liquid Na/K alloy (1:3) in 1,2-dimethoxymethane (DME). The deep-blue Na/K alloy solution can be prepared inside a glovebox and stirred for 3 d in an Ar atmosphere. After the graphene activationfollowed by the addition of the trapping electrophile, the remaining reagents can be rinsed off by dry and degassed DME.

The type of graphite activation used prior to the addition of the trapping electrophile has a significant influence on the outcome of the functionalization sequence and the obtained graphene architectures [1235]. The hydrogenation of graphite the GIC (d) yields polyhydrogenated graphene with the highest hydrogen content when alcohols are used as trapping reagents [1235], whereas for the *Birch*-type reductive activation (b) the highest hydrogen content is obtained for water [369]. This can be explained by the nature of the solvent. In the latter case, ammonia is used at −75 °C and interacts with the trapping water (formation of ammonium hydroxide in an equilibrium reaction). This underlines that the applied reductive activation conditions of graphite have a fundamental influence on the outcome of the reaction.

VIII.1.1.2. Solvent preparation

Water- and oxygen-free solvents are mandatory for the successful exfoliation of the reductively activated graphite starting material and in order to suppress side reactions during the functionalization sequence [375, 1242, 1243]. The solvent has to be stable against the intermediately generated negatively charged graphene sheets (graphenides). The most suitable solvents with respect to these prerequisites are tetrahydrofuran (THF) [1242], 1,2-dimethoxymethane (DME) [1255] and *N*,*N*′-dimethylacetamide (DMAc) [1256]. Although widely used for the dispersion of negatively charged CNTs and graphene, DMSO is thought to partially quench the respective negatively charged carbon allotrope, yielding methylated side products [1242, 1256].

Regardless of solvent used, the most crucial step for the wet-chemical reductive functionalization of graphite is the initial solvent purification. Stabilizers, water and/or oxygen traces can influence the reaction outcome and may lead to undesired and uncontrollable side reactions [1242]. Ref. [1257] established a multistep solvent purification protocol using molecular sieve. Ethers (THF, DME) must be stored under light exclusion in order to suppress any auto oxidation processes. The water content of the solvent can be determined by a Karl-Fischer titration. A sufficiently low water content value, THF: < 2 ppm, DME: < 0.5 ppm, allows to proceed with the next solvent treatment step:

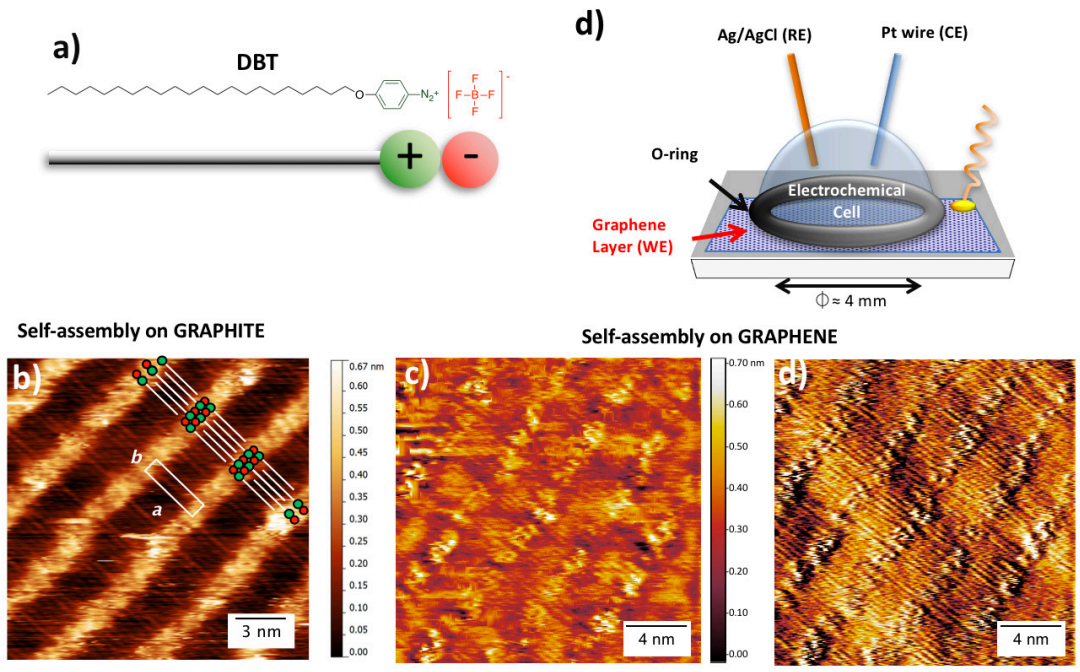


Figure VIII.2. (a) Molecular structure of DBT. (b) STM image of DBT assembly on graphite, showing also the unit cell; the possible molecular packing is also schematized. The position of BF4-counterions is indicative. Lattice parameters: $a = 3.9 \pm 0.1$ nm: $b = 1.0 \pm 0.1$ nm: $a = 89° \pm 2°$: $A = 3.9 \pm 0.1$ nm^2. (c) and (d) STM height (c) and current (d) images of DBT self-assembled on SLG. The quality of the image is not as good as on graphite, as a result of the few Å roughness of the underlying SiOx, causing a blurring effect. (e) Schematic representation of the electrochemical setup used for grafting. WE = graphene; CE = Pt; RE = Ag/AgCl (3 M KCl). Adapted from [1263], copyright American Chemical Society.

the removal of oxygen traces by a freeze-pump-thaw degassing. For this purpose, the solvent is transferred into a Schlenk flask and frozen by the aid of liquid nitrogen. The flask is connected to a vacuum line in order to remove the gas phase. Afterwards, the solvent is allowed to warm to RT (gas bubble evolution from the solution). Subsequently, the solvent is frozen again and the gas phase is removed *in vacuo* (~10^{-2} mbar). This procedure is iteratively repeated several times (4–6 cycles) until no gas evolution is detected during the thawing process. In order to remove any residual water traces, a distillation over Na/K alloy is carried out. Here, a Na/K alloy (1:3) is freshly prepared and added dropwisely to the solvent. A water separator connected to the distillation apparatus and filled with dried molecular sieves allows additional drying of the solvent. Preferably, the solvent is stored in an Arfilled glove box in order to prevent any further contamination. The purity of the solvent can be checked upon addition of GIC. Here, the bronze color of the GIC must be preserved.

VIII.1.1.3. Type of GIC and electrophilic trapping reagent

Several electrophiles have been utilized in solid support and in homogeneous dispersion functionalization of graphenides, like the diazo coupling [1253], iodonium coupling [1240, 1258], alkylation [368, 1237–1239], arylation [370, 1241], hydrogenation [369, 1235, 1236], halogenation [1259], and silylation [1255]. In addition, by an iterative repetition of the charging/functionalization step, mixed functionalized graphene derivatives are accessible [1244]. However, there is a huge dispersion of the experimental conditions in literature [368, 1239, 1258, 1777, 1778]. In this sense, a complete study surveying all the reaction parameters and determining the most effective synthetic routes is highly desired. Even more important, a deeper understanding of the correlation between bulk approaches, aiming at functionalized SLG and direct functionalization is of utmost interest [368, 370, 371, 1227, 1238, 1253]. Ref. [371] compared 3 reductive functionalization pathways (phenyldiazonium- and bis-(phenyl)-iodonium salts as well as aryliodide) and the reductive alkylation route using hexyl- and dodecyliodide. The use of iodide derivatives with spherical graphite as starting materials is the most efficient to achieve functionalized materials. A single electron transfer (SET) process from the charged graphenides towards the electrophilic trapping reagent can be expected as the primary reaction step. This leads to the generation of radicals in the proximity of the graphene sheet, with subsequent covalent bond formation [1260, 1261]. In this line, the diazonium/iodonium coupling reactions are more expedite than the alkylation, because the generated phenyl radicals are significantly less stable than the alkyl ones due to the much higher bond strength of aromatic C–H bonds [1262]. This higher stability, as well as improved solubility, of the resulting functionalized graphene in DME, plays the major role during the functionalization process, favoring the reaction of hexyliodide with

new graphenide activated surfaces, leading to higher functionalization and explaining the narrow Raman $I(D)/I(G)$ distributions [371]. In contrast, faster reactions (i.e. diazonium) lead to broader distributions, probably related with a clustering of the functionalities [371]. The open question regarding the role of remaining negative charges after the initial electrophile addition step was also addressed [1242]. According to Ref. [371] the role of the remaining negative charges can be neglected. This is in contrast to unfunctionalized graphenides. The exposure of these air-sensitive intermediates towards air, leads to a covalent framework modification with an attachment of OH- and H- groups [375, 1243].

Refs. [368–374] demonstrated that GICs are suitable for the covalent functionalization of graphene. In typical covalent functionalization sequences, the negatively charged graphene layers first act as reductants for electrophiles, subsequently attacked by the intermediately generated organic radicals or H-atoms, yielding the covalently modified graphene architectures. This wet-chemical functionalization concept is facilitated by the fact that, due to Coulomb repulsion, the negatively charged graphenide layers within the solid GICs can be dispersed in suitable organic solvents [373]. One fundamental question is whether all negative charges of the graphenide intermediates can be controlled or completely removed in such redox reactions [376]. Only complete oxidation is expected to avoid reactions with moisture and oxygen during workup, leading to side products with undesired and additional oxygen- and hydrogen functionalities. More importantly, the controlled removal of all negative charges from the solvent-exfoliated graphenide intermediates with a suitable oxidation reagent allows for the bulk production of defect-free graphene. Ref. [375] reported that the treatment of K intercalated graphite with benzonitrile (PhCN), leads to a quantitative discharging of the individual graphenide sheets upon the formation of the colored radical anion $PhCN^{\bullet-}$ (figure II.18), which can be monitored by the accompanying exhaustive and Coulomb force-driven migration of the interlayer potassium counterions (K^+) from GICs into the surrounding benzonitrile phase. The suppression of any reactions of dispersed graphenides with moisture and air takes place when no treatment with benzonitrile is provided, followed by generation of SLG. This could be confirmed by Raman spectroscopy and AFM of exfoliated material on Si/SiO_2, treated with benzonitrile, leading to SLG flakes over a lateral grain size of 10–18 μm. This represents a rather mild and inexpensive method for the wet-chemical graphene production on a small scale. This exfoliation approach was also extended to water as solvent [377].

VIII.1.2. Electrochemical functionalization

The high chemical stability of the SLG basal plane requires highly reactive conditions for its covalent modification. While reductive functionalization can be achieved after intercalation/activation of graphite via GICs, thermal or photo-induced cycloadditions of SLG with nitrene and carbene intermediates are employed [1263]. However their long (~3 h) reaction time and/or low yield (<10% surface functionalization) hinders a facile and useful covalent functionalization.

Functionalization can be enhanced using electrochemistry [1263]. The electrochemical potential applied can shift the E_F of graphene, graphite, glassy carbon or any conductive substrate, increasing their reactivity as compared to a direct attack of the covalent sp^2 bonds with aggressive chemicals. Ref. [1263] demonstrated that electrochemistry can also be used to functionalize SLG with organic molecules, and that the functionalization can be controlled on the nm scale. In contrast to earlier work on electrochemical functionalization of graphite/graphene using diazonium salts [1264, 1265], a two-steps process was used that allows the independent control over the adsorption of the molecules on graphene as ruled by supramolecular interactions, and their successive covalent grafting (figure VIII.2). The molecule used is 4-docosyloxybenzenediazonium tetrafluoroborate (DBT), an aryl diazonium salt comprising a long (C12) aliphatic chain and a diazonium grafting unit. The alkoxy chains promote the physisorption of DBT forming ordered patterns. Meanwhile, the highly reactive diazonium salt head group allows the covalent attachment of DBT onto graphene, disrupting its sp^2 lattice, modifying its optical and electronic properties [1263].

In Ref. [1263], DBT was physisorbed from solution onto SLG, allowing the molecules to self-assemble on the surface into ordered monolayers. The maximal amount of molecules deposited on the SLG surface depends on the packing density of the DBT monolayer, and could be as low as few ng cm^{-2}. After drying in air, a polydimethylsiloxane (PDMS) circular mask was fixed on the top of SLG along with an electrochemical setup composed of a three-electrode cell: a Pt wire as CE, Ag/AgCl as RE, and the target substrate used as WE. The substrate was high-quality SLG obtained by CVD on Si, or on polymeric substrates. The PDMS mask confined the electrolytic solution laterally giving a fixed reaction area ~0.1 cm^2 on the CVD graphene, making it possible to perform electrochemical treatments with very small amounts of solution (10 μl). An acidic solution (0.1 M H_2SO_4) was then deposited inside the mask as the electrolyte, and DBT molecules were not soluble in this acidic aqueous solution. The grafting process was done by ramping the voltage from +0.2 to −0.7 V at 100 mV s^{-1}. After the electrochemical reaction, functionalized SLG was sequentially washed by DI water and dried under a gentle flow of nitrogen gas.

The versatility of this approach was demonstrated by using it on different carbon-based materials, graphite, glassy carbon and SLG on SiO_2, PET, or quartz [1263] utilizing a homemade electrochemical setup (figure VIII.2(d)). Besides the easy packing of aliphatic chains, the two-step approach could be used in

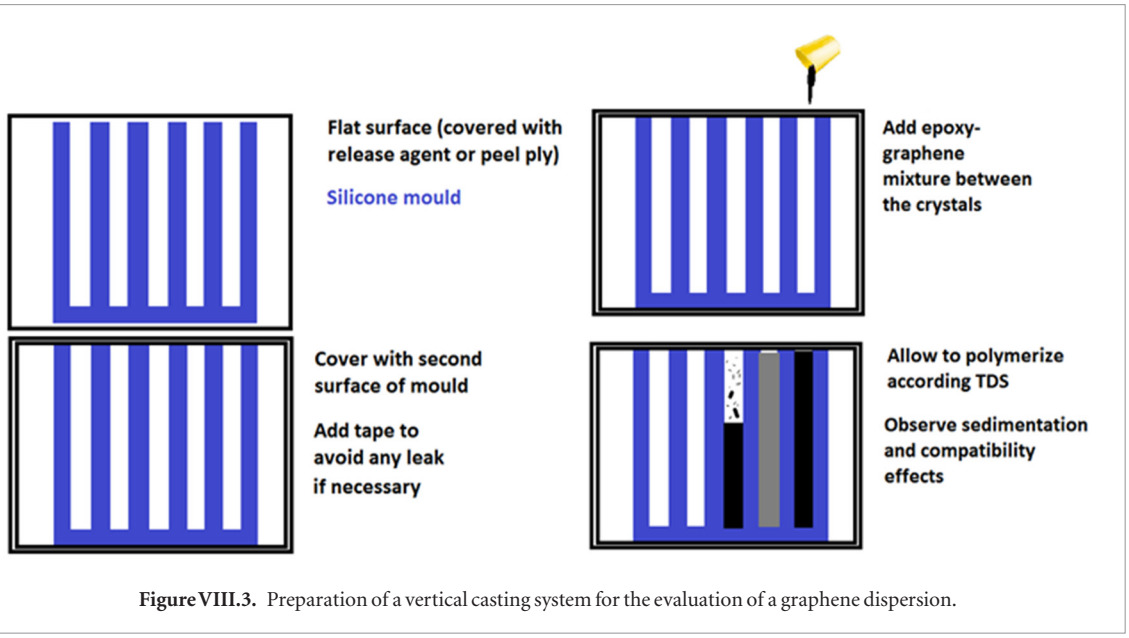


Figure VIII.3. Preparation of a vertical casting system for the evaluation of a graphene dispersion.

principle also with more complex patterns, e.g. based on arrays formed by adsorption of alternating complementary building blocks, or nanoporous organic frameworks, paving the way to a versatile, ordered and simple route to functionalize such a technologically important, yet poorly reactive material. The maximal amount of molecules deposited on the graphene surface depends on the packing density of the DBT monolayer and can be tuned using molecules of different packing density [193]. Combining the DBT surface density (as measured by STM) and the DBT molecular weight of 401 g/mol (with no diazonium group), a DBT coating ~35 ng cm^{-2} could be estimated for a uniform, perfect coverage, although the defects observed in the grafted layer will significantly modify this theoretical value [193].

Other examples of electrochemical functionalization have been reported. E.g., Ref. [1266] showed that amidation can be achieved directly after electrochemical exfoliation in nitrogen containing electrolytes such as $(NH_4)_2SO_4$, and NH_4NO_3. RGO was also functionalized electrochemically with catechol derivatives [1267]. Electrodeposition of Au NPs selectively at edges of CVD graphene was demonstrated [1268]. In Ref. [1269], it is highlighted that arylmethyl groups can be reversibly grafted electrochemically onto graphene with controlled functionalization by adjusting the electrochemical conditions, rather than the concentration of the reagent α-naphthylacetic acid.

VIII.1.3. Reductive bulk versus electrochemical functionalization

Reductive bulk and electrochemical functionalization of graphene both rely on the principle that the reactivity of graphite can be enhanced though activation introducing negative charges on the lattice which then readily react with electrophiles [160]. Negatively charged graphene/graphite is highly reactive, so that it is difficult to suppress side-reactions [375]. In both cases, it is important to work under dry and inert conditions to achieve maximum control over the grafted functional groups. Both functionalization strategies can in principle be applied to a range of graphite/graphene precursors, even though electrochemical functionalization is often used for CVD-grown graphene or graphene grown from SiC [1778], while reductive bulk functionalization is mostly employed for graphite powders [1238].

A challenge is the control over the degree of functionalization and the homogeneity of surface modification. In the case of reductive bulk functionalization via GICs and graphenide dispersions, the functionalized flakes are extremely polydisperse, in particular when using natural graphite as starting material [1238]. Electrochemical functionalization should in principle offer a better control since the charge density can be controlled via the applied potential. However, as discussed in Ref. [1263], in practice, sp^3 defects and functional groups are spatially poorly controlled resulting in a highly disordered morphology. This has been overcome by combining electrochemical functionalization with self-assembly of the addends [1263], a strategy that has not yet been successfully shown in reductive bulk functionalization. A downside of electrochemical functionalization is that the parameter space that can be explored is even wider than in reductive bulk functionalization, including parameters such as applied potential in combination with the electrolyte. Due to the required presence of the electrolytes, it is probably even more challenging to suppress unwanted side-reactions than in reductive bulk functionalization.

In summary, both of the discussed covalent reductive functionalization routes have seen remarkable progress. Currently, reductive bulk functionalization through chemically charged species is more widely used and the more versatile strategy enabling grafting of a range of functional groups via electrophilic addi-

tion reactions [160]. Compared to this, electrochemical functionalization is still in its infancy, but definitely holds great promise due to the better control of the charge density on the graphite/graphene.

VIII.2. Functionalization of GO

VIII.2.1. Covalent derivatization

GO is rich in polar oxygen-containing functional groups that make it highly soluble in a wide range of solvents [216]. The different functional groups (i.e. hydroxyl, epoxy, carboxylic, lactones, phenols, etc) can be exploited to prepare chemically functionalized GO for a wide range of applications [160, 1270]. Due to the presence of the different oxygenated functional groups and their high chemical reactivity, simultaneous reactions of these functions may occur, leading to uncontrolled GO derivatives. Most of the reactions reported in literature concern functionalization of carboxylic functions via amidation, using a variety of amine derivatives [1226, 1271]. However, other functional groups can participate. E.g., epoxy ring opening can take place in the conditions of amidation, as epoxides are highly reactive towards nucleophiles like amines [1272–1278] so that precise control is lacking. To clarify the chemical reactivity of carboxylic acids and epoxides, Ref. [1279] elucidated the structure of GO in the presence of amines and the reactivity of the functional groups towards amines. Magic angle spinning solid state NMR allowed to prove the absence of reactive COOH groups. As a consequence, the amidation reaction of carboxylic groups with amine derivatives did occur to a negligible extent, while the main reaction consists in epoxide ring opening. This is also the case in the presence of coupling reagents necessary to form the amide bonds. Therefore, the reaction between GO and amine functions involves mostly epoxy groups, and not carboxylic acids, present in a small amount. This situation cannot be generalized to all types of GO. Ref. [1279] underlined the importance to well characterize the starting material and use the appropriate controls (e.g. the conditions for amidation versus the epoxide ring opening reaction) to prove the reactivity of the different oxygenated functions on the surface of GO. A better understanding of the reactivity of GO is essential for controlled derivatization.

Although polymerization on the GO surface in polar solvents, e.g. water, has been widely studied, it remains a great challenge to achieve polymerization reactions on RGO in organic solvents due to the limited functional groups for dispersing RGO in organic solvents. RGO was produced from the reduction of GO by hydrazine hydrate [1280]. We found that RGO can then be functionalized using *p*-bromobenzene diazonium salt under aqueous conditions to produce *p*-bromobenzene functionalized RGO (RGO-Br). This was dispersible in DMF for further reaction. Afterwards, conjugated microporous polymers (CMPs) were prepared through the Sonogashira-Hagihara coupling reaction [1281] of 1,3,5-triethynylbenzene and halogenated aromatic monomers, by using RGO-Br as structural-directing template. 1,3,5-triethynylbenzene was selected as key monomer, mixed with another monomer of aryl halides (such as 2,5-dibromothiophene, 2,5-dibromo- 1,3-thiazole, and 2,6-dibromopyridine) or halogenated BODIPY (2,6-diiodo-1,3,5,7-tetramethyl-8-phenyl-4,4-difluoroboradiazaindacene) in the RGO-Br dispersion. The above mixture polymerized at 80 °C for 72 h catalyzed by tetrakis-(triphenylphosphine) palladium ($[Pd(PPh_3)_4]$), copper iodide (CuI), and triethylamin (Et_3N), forming a series of CMPs on graphene-based template (RGO@CMPs). The as-prepared insoluble precipitated polymer networks were filtered and washed several times with chloroform, water, and acetone to remove any unreacted monomers or catalyst residues. Further purification of the polymer networks was carried out by Soxhlet extraction with acetone for 48 h. The powder was dried in vacuum (0.1 mbar) for 24 h at 60 °C to obtain the final product.

This method not only offers a new way to polymerize on RGO surfaces through the Sonogashira-Hagihara coupling reaction, but also paves the way for versatile reactions on the RGO surface in organic solvent.

GRMs are ideal for energy applications because of their large accessible specific surface areas and high electrical conductivity [563].The SLG theoretical specific surface area is ~2600 $m^2\ g^{-1}$ [1282]. However, a common problem is the restacking of SLG sheets, i.e. the aggregation during wet-processing, resulting in a decrease of accessible specific surface area [1283]. E.g. the reduction of unmodified GO typically leads to the irreversible aggregation of RGO sheets [1284]. In order to overcome this issue, the bridging of GO layers into macroscopic porous structures is a key step to modify SLG-based multifunctional materials, which could preserve many of the unique properties of the individual SLGs [1285]. In particular, the high specific surface area and porous structures can provide space for hosting electrolyte ions, therefore increasing the performance in supercapacitors [1286]. In this context, graphene-based networks through covalent linkage between individual SLGs is one among the greatest challenges, with the aim to achieve a high control over the structures with a nanoscale precision and consequently tuning of the material's physical properties [1287–1289].

A method for the facile preparation of graphene-based covalent networks (G3DCNs) with adjustable interlayer distance upon covalent functionalization of GO has been reported [1290]. This relies on the condensation and ring-opening reactions of the carbonyl and epoxy groups on GO with benzidine (B_Z) at different T. In Ref. [1290] the controlled polymerization of B_Z with GO, to obtain the G3DCNs, was performed under catalyst- and template-free conditions. By varying the reaction temperature, BZ monomers or polymerized B_Z units can bridge GO sheets to form

covalent networks with tunable interlayer spacing. The reduced form of G3DCNs (RG3DCNs) was used to develop high-performance supercapacitors, taking advantage of the high specific surface areas (280 $m^2\ g^{-1}$) combined with N doping obtained through chemical functionalization. A three-electrode configuration gave~460 F g^{-1} at a current density ~0.5 A g^{-1}, while a two-electrode configuration resulted in ~156 F g^{-1} at a current density ~1 A g^{-1} in combination with a stability over 5000 cycles. This combination of physicochemical stability and high supercapacitor performance demonstrates that integration of GO into covalent tuneable structures is a promising route to obtain multifunctional graphene based hybrids.

Most methods towards porous carbons mainly focused on a hard template and activation approaches [1782], which suffer from poor rational design of the micropores and heteroatom components. In general, the preparation of layered porous carbon remains a challenge. In Ref. [1291, 1292] the as-prepared porous polymers (RGO@CMPs) were directly pyrolyzed at X °C (X = 700, 800, 900 and 1000) for 2 h under inert atmosphere, resulting in heteroatom-doped (B, N or S) porous carbon materials. This method not only provides a new way for preparation of porous carbons without using any inorganic templates, but also offers a rational approach to control the heteroatoms by choosing different heteroatom-contained monomers.

Chemical functionalization of GO is a key step to prepare covalent conjugates that can be exploited not only in for energy applications or in the biomedical field, but also in the studies related to the impact of such materials on health (i.e. biodistribution and biodegradation). In the context of pharmacokinetic studies, GO needs to be labelled with molecules that can be traced once the conjugates are injected into a body [289]. For this purpose, radiolabeling is extremely powerful, as the material can be followed using different imaging techniques and many radionuclei can be exploited. GO has been modified with the chelating agent DOTA (1,4,7,10-tetraazacyclododecane-1,4,7,10-tetraacetic acid) for complexation of the radionuclide [1 1 1]In to assess the *in vivo* biodistribution in mice [1293]. GO was initially functionalized with triethylene glycol diamine to open the epoxy rings and introduce amino functions on its surface. Then, the amino groups were derivatized with an isothiocyanate DOTA reagent. Structural characterization of both GO and GO-DOTA revealed that the thickness of GO was increased from 1L to FL after functionalization. GO-DOTA was subsequently radiolabelled with [1 1 1]In and injected into mice to follow its organ distribution, accumulation and elimination. An appropriate functionalization of GO can also be useful to modulate its biodegradability. Covalent functionalization was conceived by designing surface-functionalized GO with the capacity to be degraded more effectively compared to unmodified GO [463] The surface of GO was tailored with different ligands able to enhance the catalytic activity of horseradish peroxidase (HRP). GO was functionalized with two reducing substrates of HRP: coumarin (7-hydroxy azido coumarin) and catechol (3,4-dihydroxy benzoic acid) derivatives. The kinetic of the biodegradation process was enhanced in comparison to unmodified GO.

VIII.2.2. Noncovalent derivatization of GO for thermoplastics

When GRMs are incorporated into a polymer matrix, one of the most important problems is the lack of affinity between them, due to differences in polarity [1294]. Just a few polymers, such as polyaniline and Kevlar, contain aromatic rings in their structure [1783, 1784]. π–π interactions between these chains and SLG/GO can take place [1295], however most of the polymers do not have these moieties that facilitate interaction with SLG/GO.

Re-agglomeration or bad interaction between them and polymer chains leads to creation of defects and discontinuity regions, and loss of mechanical performance, such as a decrease of the elastic modulus at break [1695]. This affects the properties of the SLG/GO and the composite does not show the desired performance, i.e. electrical conductivity, thermal management, gas barrier properties, flame retardance or other due to the creation of these agglomerates.

To solve these problems, functionalization is needed to change the surface chemistry and improve the compatibility with the polymeric matrix. Another effect of functionalization is the reduction of agglomeration during the preparation of composites, due to the electrostatic repulsion that can be produced [1296, 1297]. Non-covalent functionalization can enhance dispersability, compatibility and binding capacity with the matrices, with less impact on the structural properties of the graphitic sheets than covalent functionalization, as this creates sp^3 carbon centers [160]. Non-covalent functionalization helps in networking or connecting the molecules without forming covalent bonds. This process requires physical adsorption of suitable molecules by forming van der Waals bonds between functional groups and SLG, such as π–π interactions, electrostatic attraction, adsorption of surfactants and polymer wrapping [1298].

When organic molecules or hydrophobic character polymers are the functionalities, van der Waal forces are created between them and SLG/GO [282, 1785]. When the functional groups are molecules with an extended π-system, the predominant interactions are π-π based. Besides, hydrogen bonds and ionic interactions can be involved due to the presence of oxygen groups, especially in the case of GO, and in minimum percentage in the case of RGO or SLG [282].

For the design of the non-covalent functionalization strategies, an important decision regards the polymer matrix and the processing method. In the case of thermosets, most of the processes consist on liquid phase polymerization [1786]. For thermoplastic

matrixes, most of the polymers are processed by melt mixing, and just in a few cases *in situ* polymerization can be an alternative [1786]. The polarity of the matrix, from very nonpolar such as the polyolephines, to polar such as polycarbonate needs to be taken into account. Besides, the groups on the surface of GO or RGO are of crucial importance for the functionalization strategy. In this regards, XPS is a useful tool to understand the distribution and binding of the moieties and functional groups over the GRM surface.

Many different organic molecules were used in literature [194, 218, 282, 1284, 1299–1302]. The selection is based on availability on the market, or ease to synthetize them and scale up. For the preparation of thermoplastics and thermoset composites, even at lab-scale, at least hundred g are needed. For scale-up at lab or pilot level, few kgs are needed. A typical amphiphilic non-ionic surfactant, commercially available as Triton X-100 (polyoxyethylene octyl phenyl ether, POPE) can be used to increase the compatibility of GRMs and the polymer matrix [1294].

Aqueous surfactant solutions of RGO above the critical micelle concentration (CMC) are enough to ensure physical adsorption and non-covalent adsorption. Aqueous dispersions of functionalized materials remain stable during long (more than one month) periods, while pristine graphene suspensions may sediment in less than one day [1303], due to low viscous and agglomeration problems. For laterally large (>20 μm) RGO, sonication is needed, in bath or tip, or even a combination of both processes. For RGO of lateral dimension >50 mm, two cycles of 10 min of tip and 10 min in bath is our recommended process to achieve dispersion without significant decrease in lateral size. After filtration and drying of the non-covalently functionalized RGO, the GRM can be dispersed in the polymeric matrix.

Polyvinylpyrrolidone, SDS, SBDS, CTAB and other surfactants can be added to water suspensions of GRMs to stabilize them thanks to the electrostatic repulsions created [1294, 1304]. In most cases, interaction occurs in the absence of ultrasound, which is required to increase the accessible surface area and it is especially helpful when lateral size is medium or large (>20 μm). The same strategy has been used to improve the dispersion of RGO in plasticized polymers and in epoxy resins before curing [1297, 1305]. The results of the dispersion have a strong influence on the final properties of the composites. Epoxy composites prepared with this functionalized graphene materials have shown better interaction to the matrix in SEM micrographs and improved mechanical behavior at very low loadings [1294, 1300, 1306, 1307].

Silanes can also be used for non-covalent functionalization of GO. From our experience, mild conditions [i.e. ethanol dispersions of GO and selected silane are mixed under bath sonication, and filtered in air, or oven dried <80 °C] are favoured to avoid covalent reactions with GO between the alkoxy groups of silane molecules and the hydroxyl groups of the graphene surface. It is also important to select a graphene material with lower number of hydroxyl moieties. Several silanes can be used, e.g. 3-(aminopropyl) triethoxysilane, 3-glycidoxypropyltrimethoxy silane, tris[3-(trimethoxysilyl)propyl]isocyanurate. Covalent silanization is a common strategy for the functionalization of GRMs for their use in polymers [1308]. For this, the GRMs need a high number of hydroxyl groups. This functionalization usually is done at RT, or under reflux conditions in organic solvents such as toluene, ethanol [1309]. Silanization of OH groups can also be accelerated using microwaves: coupling microwaves (energy source) with graphite (support) is responsible for a high T gradient leading to increased reaction rates as compared to conventional procedures.

The most commonly used strategy for noncovalent functionalization exploits π-π interactions. This has been discussed in several reviews and books [1327, 1310]. Some organic molecules can be used for non-covalent functionalization to improve the dispersion in polymers: i.e. melamine [1311], chitosan [1312], glycidyl 2-methylphenyl ether, anisole, 4-ethynylanisole among others [282]. These were dissolved in organic solvents of slightly acidic solutions in the presence of GRMs and agitated under bath sonication for 15–30 min, then filtered and dried [282].

To establish the success of the functionalization in the dispersion of GRMs in thermoset composites, a fast method is vertical casting (figure VIII.3). This employs two polished surfaces (e.g. glass) treated with release agent or covered with peel ply. Few silicone double tapes of 1 mm are glued at the same distance (e.g. 2 cm) to the polished surface. Another silicone tape is glued perpendicular to the other tapes to the bottom surfaces. This system is used as the mould, and the epoxy-graphene dispersions are introduced.

In the case of thermoplastics, a polymer adapted microtome which allows to obtain flat and smooth slices or ultrathin slices of the composite is needed [1311] and cryo-microtomography, working at temperatures between −15 to −185 °C, to avoid disturbing the positions or relocating NPs along the sample [1313, 1316]. The analysis of the graphene composites' mechanical and electrical properties is key to understand if the functionalization works properly, to improve the dispersion and interface.

By optical microscopy, even at low resolution, it is possible to characterize the effectiveness of functionalization, i.e. the homogeneity of the dispersion of GO in an epoxy composite, and the rate of decrease of large size aggregates.

VIII.3. Noncovalent functionalization of graphene

VIII.3.1. Functionalization in dispersion

Graphene can be exfoliated in water with the help of amphiphilic surfactants [182, 184]. Most published works use 'conventional' aliphatic surfactants (i.e. soaps) [182, 184]. However, stable dispersions can

also be obtained using small polyaromatic dyes as surfactants [194, 214, 215]. Thanks to their aromatic core, these molecules can adsorb strongly on the graphene surface, forming also ordered layers [193], noncovalently functionalizing SLG/FLG. They have also a strong and unique absorption (molar absorption coefficient $\varepsilon > 15\,000$ l g^{-1} m^{-1}) and emission spectrum in the visible range, which allows to monitor their interaction with graphene in solution and in solid [216, 217]. Many of these molecules are also low cost dyes, already widely used in large-scale compounding of polymers, e.g. as industrial additives and colorants [218]. These molecules can exfoliate not only graphene but also a wide range of LMs, such as BN, WS_2, MoS_2, selenides and tellurides with concentrations up to 0.54 g l^{-1} [219].

Several pyrene derivatives with a varying number of polar functionalities were used as exfoliation agents [194]. A significant part of the solubilized material was composed of SLG (up to 22%), with most of the remaining material composed of FLG (50% to 60% <7L). The total concentration depends on the polar functionalization present on the pyrene core. Molecular dynamics calculations revealed that a critical factor is a one molecule thick solvent layer present between dye and SLG [194]. The amphiphilic molecule changes its orientation when approaching the surface to slide into this layer, and the asymmetric shape of the dyes facilitates this step. In these graphene organic hybrid systems, colloidal stabilization is achieved through electrostatic repulsion between charges introduced by the surfactant, and can be overcome by changing pH or adding salts [194].

VIII.3.2. Exfoliation in organic solvents

The use of small organic molecules acting as stabilizing agents is expected to promote LPE of graphite when molecules have a stronger affinity to graphite/graphene than the solvent/graphene interactions. A good starting point in terms of molecular design relies on the use of alkanes, which exhibit a high affinity (~2 kcal mol^{-1} per each methylene unit) for the basal plane of graphite/graphene [1315]. Ref. [230] reported that arachidic acid (C19CA) can promote the exfoliation of graphite in NMP. The addition of C19CA does not affect the quality and structure of the resulting graphene, as compared to NMP alone, highlighting the non-invasive nature of the process, but alkyl chain based stabilizers led to an increase of SLG (25%) and FLG (70% for 2–6 layers) [230].

The use of α-functionalized alkanes as stabilizers during LPE allows one to increase Y_W in liquid media. To understand the role of the functional group in α-substituted alkanes, Ref. [235] used the $C_{21}H_{43}$ alkyl chain as a scaffold and decorated it with simple, yet chemically distinctive groups: methyl, alcohol, amine, and carboxylic acid. The most effective exfoliation was obtained with docosanoic acid, with Y_W ~ 1.6%, with a ~100% increase when compared to control samples (0.8%). Y_W of LPE in docosane is ~1.35%, while docosanol and docosan-1-amine have lower performance (1% and 1.1%, respectively). The thermodynamic analysis in Ref. [235] suggests that aliphatic chains functionalized with carboxylic acid groups promote the stabilization of exfoliated SLG and FLG in NMP due to synergistic interactions between DSAs, surface, and polar solvent.

Ref. [231] also reported that the performance of linear alkanes exposing a carboxylic acid head group as stabilizers directly depends on the length of the linear alkane chain. 5 linear modules were explored: hexanoic acid (C6CA), lauric acid (C12CA), stearic acid (C18CA), lignoceric acid (C24CA) and melissic acid (C30CA), whose different adsorption energies on graphene and tendency to form tightly packed self-assembled monolayers on such a surface affect their performances as stabilizers. The analysis of carboxylic acid assisted LPE revealed that the concentration of graphene dispersions prepared in NMP, ODCB and TCB increases linearly with the length of the aliphatic chain. The dependence of Y_W with the length of the aliphatic chain was interpreted by means of a thermodynamic model of molecular self-assembly on graphene [231]. This showed that the shorter the aliphatic chain, the larger is the (rotational and translational) entropic cost of forming a 2d layered structure. These results suggest that a model based on molecular mechanics for the energetics and a statistical mechanic treatment of entropy, could be used to predict the efficiency of supramolecular building blocks as stabilizers and guide the chemical design of next generation stabilizers. Nevertheless, the role of kinetics cannot be fully ruled out.

Ref. [234] reported that alkoxy-substituted photochromic molecules can act as photo-addressable stabilizers to enhance Y_W in an upscalable molecule-assisted LPE-based method. The large conformational change associated with the *trans–cis* photochemical isomerization of alkyl-substituted azobenzenes can be used to improve Y_W. The simultaneous use of UV light, promoting the trans-to-cis isomerization, as well as thermal annealing at 40 °C and mechanical forces generated by sonication, both favoring *cis*-to-*trans* isomerization of 4-(decyloxy)azobenzenes, promotes the exfoliation of graphite in liquid media. The most effective exfoliation is obtained with azobenzene molecules irradiated with UV light in NMP at 40 °C, with a concentration of exfoliated graphene ~110 mg ml^{-1}. This corresponds to an ~80% increase in Y_W when compared with pure NMP (63 mg ml^{-1}). By depositing the hybrid film onto Au pre-patterned SiO_2 substrates, light- responsive thin hybrid films, formed in a one-step co-deposition process, can be realized, whose conductivity can be reversibly modulated by the trans-to–cis photoisomerization of the azobenzenes. By combining this approach with cost-effective techniques, such as ink-jet printing, more complex responsive device designs and architectures may be realized.

VIII.3.3. Exfoliation with aromatic dyes in chloroform and THF, and further processing in polymers

Graphene can be exfoliated in water, using surfactants, or in high-boiling solvents such as DMF or NMP. For an effective, technologically competitive application of GRMs as additives in (nano)composites for electronics or structural applications it may be preferable to solubilize graphene in low-boiling volatile solvents, like $CHCl_3$ or THF. However, the use of amphiphilic surfactants is not suitable to solubilize graphene in organic solvents whose polarity is low [193].

Ref. [193] used perylene diimide (PDI) molecules soluble in organic solvents as 'apolar surfactant' for exfoliation and successive processing in polymeric commercial films of poly(vinyl chloride) (PVC), to make them conductive. The PDI has an extended polyaromatic core (which can interact via π–π stacking with the GRM) and flexible side groups, with low, but tunable polarity that make these molecules soluble in a range of organic solvents (figure VIII.4).

Transparent sheets of PVC (thickness 182 $\pm$ 4 μm) were dipped into chloroform dispersions of FLG and PDI at RT, a procedure already used for rubber [568]. They were then dried in air, to let the chloroform evaporate. The swelling process was completed in <3 min, and gave an increase of ~80% in volume. No further change of the swollen area/size was observed when the polymer films were left in the dispersions for >3 min. After the swelling treatment, the PVC samples showed a dark color due to the presence of the FLG as well as a bright fluorescence due to the PDI.

SEM images showed a dense coating of rectangular and polygonal shapes covering the surface. The sheets were not just deposited on the surface, but embedded into it, in some case reaching some microns (<10 μm). Control experiments by swelling in PDI only gave surface covered by PDI crystals, and no improvement of electrical conductivity. Typically, when deposited by conventional solution processing, GRM flakes tend to lay flat on a substrate [272, 277]. Due to the swelling, the flakes penetrate into the polymer in an isotropic way, in some cases protruding out of the surface [193]. An improvement of material hydrophobicity by ~40% was observed in all cases, with measurements of water contact angle increasing from 72° (blank PVC) to >100°. R_s decreased significantly, going from completely insulating to ~105 Ω sq^{-1}, a value useful, e.g. for applications in antistatic coatings [1787].

VIII.3.4. Functionalization on substrate

VIII.3.4.1. Doping of CVD graphene via noncovalent interaction with thionylchloride

Halogenation, i.e. doping of graphene with halogens, is a process in which halogens, such as fluorine, chlorine, bromine and iodine, are either used to replace one of the carbon atoms or are attached to the graphene surface [1316–1320]. As for all doping or chemical modification, processes stability is of importance. Here the focus is on chlorination, as this has proven to be a reliable, stable way of halogenation, allowing SLG doping without losing transparency [1316].

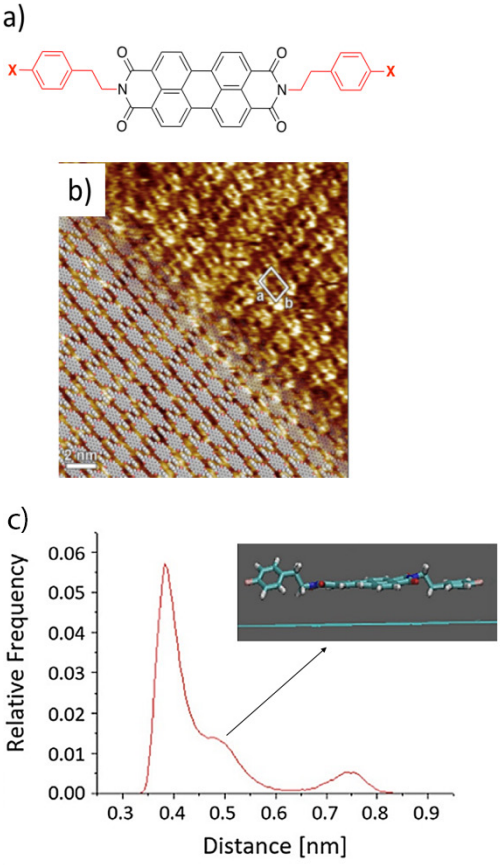


Figure VIII.4. (a) General formula of the PDI used for exfoliation. (b) STM image of the typical packing of PDI adsorbed on graphite. (c) Average distance of the side groups of the PDI from SLG, from molecular modeling. In the inset, a typical snapshot of the simulation. Adapted from [193], © 2016 WILEY-VCH Verlag GmbH & Co. KGaA.

In Ref. [1316] R_s ~ 30 Ω sq^{-1} using up to 5LG was achieved, while keeping a high transparency ⩾85%. Depending on whether the doping agent is an electron acceptor or donor, p- or n-type doping can be attained. To achieve a high doping level in the range 10^{13} cm^{-2}, thionyl chloride ($SOCl_2$) is recommended. $SOCl_2$ induces p-type doping due to the higher electronegativity of Cl compared to C.

CVD-grown graphene is first transferred on glass. Thermal release tape was used for the transfer process [1316]. Different approaches for doping with thionyl chloride have been tested: last layer doping, where the last or top layer of 1 to 5LG was doped after all layers were transferred in a staggered fashion, or interlayer doping, where the top layer after each transfer of SLG/FLG is doped creating a doped surface in between the layers. The doping is achieved as follows [1316]: $SOCl_2$ treatments are performed in a dry chamber by placing graphene/glass and 1 ml of liquid $SOCl_2$ (avoiding direct contact) at 105 °C for 60 min. Doping of multilayer samples was performed by repeating the $SOCl_2$ treatment after transferring and stacking each SLG/FLG.

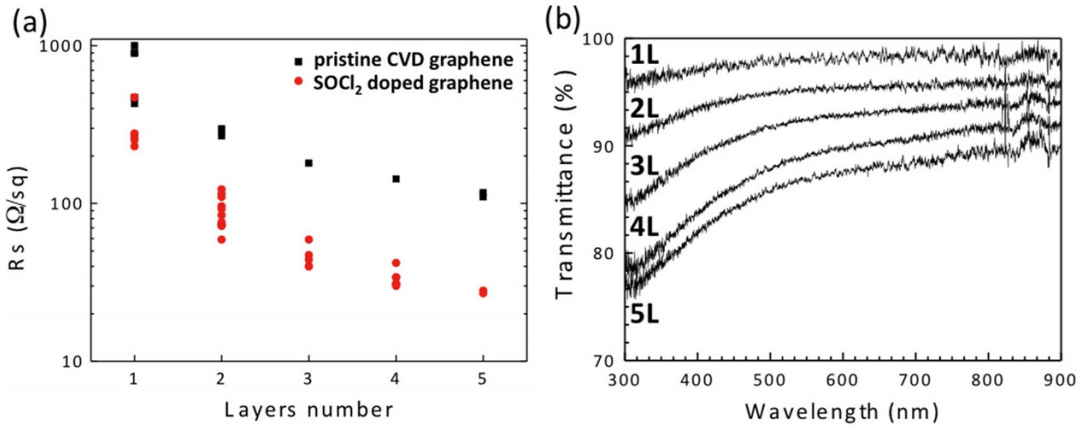


Figure VIII.5. (a) Comparison of R_s of chlorinated and non-chlorinated CVD graphene as function ofN. (b) Transmittance for 1 to 5L G. Adapted from [1316].

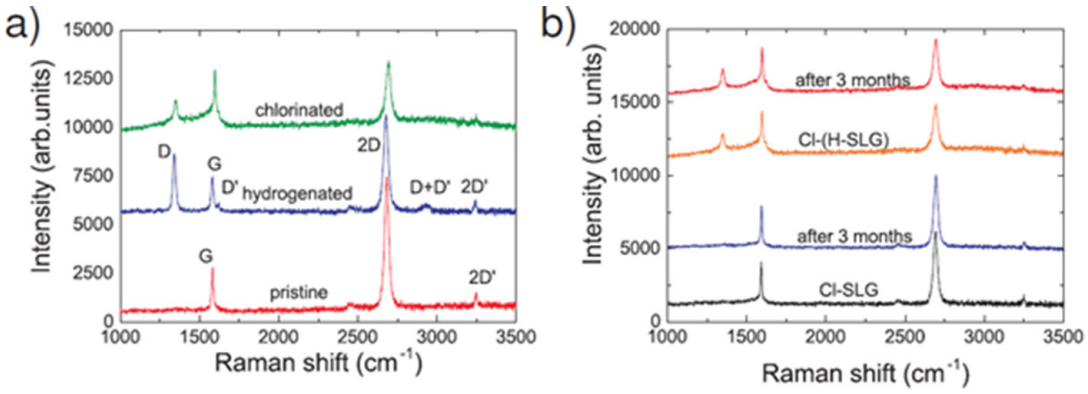


Figure VIII.6. (a) 514.5nm Raman spectra of pristine, hydrogenated and chlorinated graphene after hydrogenation. (b) 514.5nm Raman spectra of chlorinated, Cl-SLG, and hydrogenated and chlorinated graphene (Cl-(H-SLG)) directly and after doping and after three months in ambient conditions.

R_s is then measured in a van der Pauw configuration (see section IX.3). Ref. [1316] suggested to use a large sample area ~4 × 4 mm^2 to obtain a representative R_s. Figure VIII.5(a) plots R_s as function of N for interlayer doped and undoped samples. $R_s = 1/ne\mu$, where n is the doping level, e the elementary charge and μ the mobility. The mobility is affected by defects, therefore $\mu \sim 1/n_D$, where n_D is the defect concentration. It is thus important to know doping and defect concentration. $SOCl_2$ allows a nucleophilic substitution by Cl atoms, which selectively occurs on defective sites, without affecting the existing sp^2 carbon bonds, therefore, without introducing any new defects [1316]. In order to verify this doping mechanism a controlled amount of defects was introduced in graphene by H plasma [1316].

The quality of graphene after doping can be assessed by Raman spectroscopy. It is important to follow the correct procedure to extract the correct doping level and defect density [1321, 1322]. Graphene with controlled amount of defects induced by mild H plasma showed a higher doping compared to a pristine, reference sample doped with $SOCl_2$ under the same conditions, but without being subjected to H plasma. This shows that $SOCl_2$ molecules selectively chlorinate defective sites in graphene. However, defects are always counter-productive for achieving low R_s and high μ. Thus, a compromise between doping and R_s has to be made. It is therefore more favorable to abstain from the introduction of defects by mild H plasma in order to achieve lower R_s, instead of inducing structural defects to which Cl will attach and increase the doping level.

The most critical point is the doping stability with time. Figure VIII.6 shows the Raman spectra of pristine, chlorinated and defective graphene (induced by H plasma) measured directly after chlorination and after 3 months. Pristine graphene shows a Pos(G) and FWHM(G) ~1583 cm^{-1} and 14 cm^{-1}, while FWHM($2D$) ~31 cm^{-1}. $I(D)/I(G) < 0.1$. Therefore, the doping level is estimated ~100 meV. Hydrogenated graphene on the other hand shows D, D' and $D + D'$ peaks as result of defect introduction via H plasma treatment with $I(D)/I(G) \sim 1.65$. The doping is estimated ~107 meV. This gives $n_D = 4 * 10^{11}$ cm^{-2}. This confirms the presence of defects introduced by the plasma treatment with no change in doping. After chlorination of the plasma treated sample the doping is ~380 meV. This is higher compared to that achieved

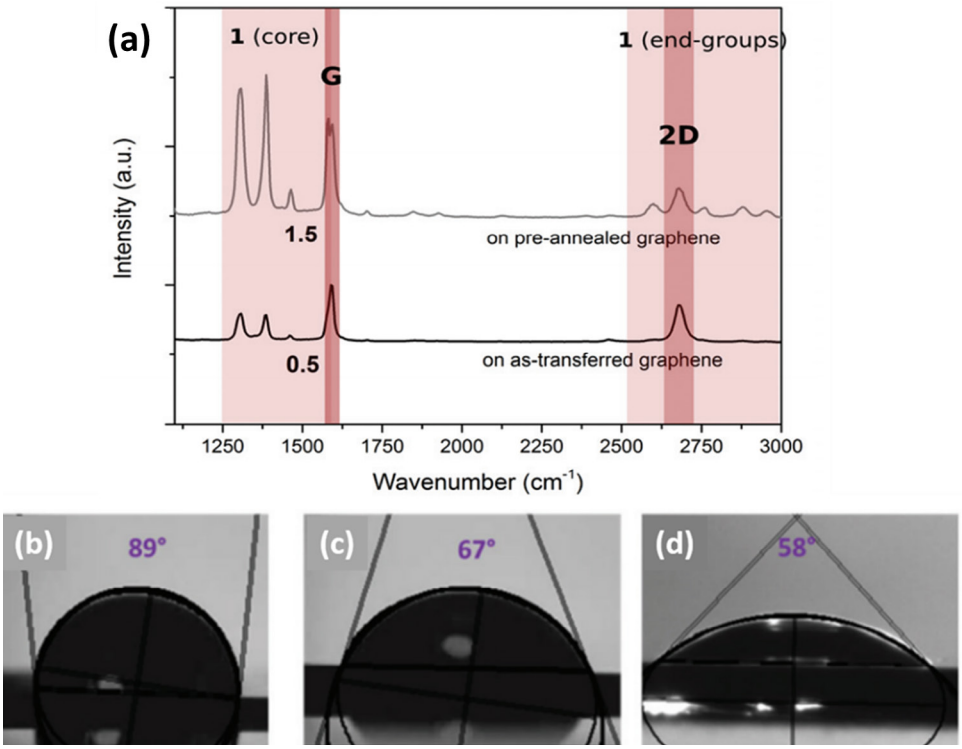


Figure VIII.7. (a) Raman spectra for high and low packing density perylene1 SAMs on as-transferred and pre-annealed SLG. Inset: Structure of perylene1. Water contact angles on (b) bare SLG, (c) low and (d) high packing density of perylene1 on SLG. Adapted from [1323] with permission of The Royal Society of Chemistry.

by doping pristine SLG, suggesting that $SOCl_2$ molecules selectively chlorinate defective sites. The Raman spectrum of chlorinated graphene after plasma treatment shows a reduction I(D). This can be explained by the doping dependence of the *D* peak [1321]. This gives $n_D \sim 3 * 10^{11}$ cm^{-2} consistent with that of the hydrogenated sample before chlorination. Therefore, although the chlorination process is able to increase doping, the defect density remains unchanged, in agreement with the chemistry of the $SOCl_2$ doping process.

Considering that after chlorination, one chlorine atom is attached to each defect and taking a charge transfer of 0.57 electrons [1317], i.e. each Cl takes 0.57 electrons from graphene to induce p-doping, the doping can be estimated from the defect concentration. As a result, the estimated defect density evaluated in hydrogenated graphene corresponds to a doping ~65 meV. This is the doping level introduced via additional defects by plasma etching. The doping of a chlorinated pristine graphene sample was ~304 meV. This is the doping introduced directly via chlorination. Adding these two contributions to the doping coming from only chlorination, the final doping level is ~370 meV, in agreement with the ~380 meV of the hydrogenated and chlorinated sample estimated from the Raman spectra measured directly after plasma treatment and doping with $SOCl_2$.

To check stability, figure VIII.6(b) compares the spectra of chlorinated (Cl-SLG) and chlorinated hydrogenated graphene (Cl-(H-SLG)) recorded after three months. The initial doping levels are ~304 meV for doped pristine graphene and ~380 meV for doped hydrogenated graphene. After three months these are ~250 meV and ~350 meV. This shows that doping is stable over time.

UV–vis spectroscopy can be used to assess the optical properties of the chlorinated samples. Figure VIII.5(b) reports the transmittance of 1 to 5LG interlayer doped graphene using thionyl chloride. The transmittance is still ~85% even for the 5LG interlayer doped sample, making this attractive for applications where low R_s and high transparency are needed.

Solution based processes for halogenation of graphene were also proposed (see e.g. [1318, 1319]), Ref. [1320] used CVD grown FLG on Ni and transferred it on a glass substrate to induce doping by bromine vapor at RT in inert atmosphere: a glovebox with <0.1 ppm of O_2 and H_2O and nitrogen filled glovebag with 2000 ppm of O_2 and 2500 ppm of H_2O. Ref. [1320] reported $R_s \sim 180\ \Omega\ sq^{-1}$ with a reduction in transmittance ~2%–3% with respect to pristine SLG. A drop of R_s from 1548 Ω sq^{-1} to 602 Ω sq^{-1} after exposure to Br for 60 min was reported [1320].

VIII.3.4.2. Functionalization with polycyclic aromatic hydrocarbons

Non-covalent functionalization of CVD graphene transferred to SiO_2 was achieved via drop-casting of an aqueous solution of perylene bisimide 1 [1323]. The packing density of the perylene self-assembled monolayer (SAM) was related to the cleanliness of the SLG surface. Vacuum annealing prior to

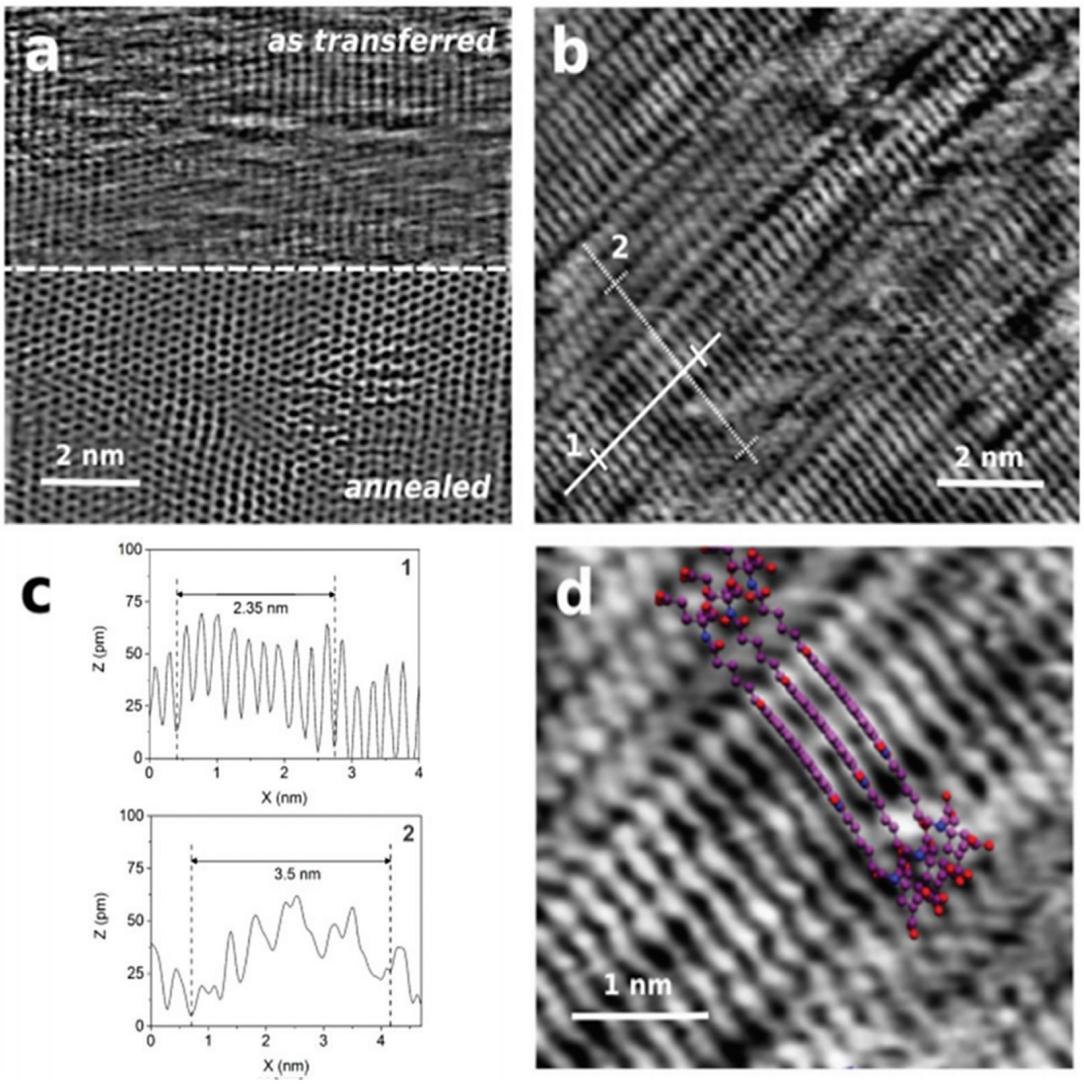


Figure VIII.8. STM images of (a) as-transferred (top) and subsequently annealed (bottom) CVD-SLG on SiO_2 and (b) after wet-chemical deposition of perylene1 on the same annealed substrate. (c) line profiles from (b) and (d) zoomed in area with molecular structure overlay. Adapted from [1323] with permission of The Royal Society of Chemistry.

functionalization removes polymer and leads to a much higher denser perylene packing density than on untreated SLG [1323]. This is illustrated when the Raman spectrum and water contact angle measurements are considered (figure VIII.7). The increased relative intensity of the perylene Raman peaks (pale shading) when compared to the SLG peaks (dark shading) for the pre-annealed SLG versus the as-transferred one is indicative of a greater quantity of perylene on the surface. Likewise, high density packed perylene on graphene has the smallest water contact angle (58 °) compared to the as-transferred graphene sample (89 °) and low density perlylene sample (67 °). Again, this increased hydrophilicity indicates a greater number of molecules on the SLG surface for the pre-annealed film.

STM can be used to estimate the SLG cleanliness before and after annealing, figure VIII.8. An image of the resultant high packing density perylene SAM is in figure VIII.8(b). Analysis of the periodicity of the line profiles indicates that the perylene molecules pack together with the perylene cores perpendicular to the SLG surface, figure VIII.8. This is at odds with the common belief [1324–1326] that organic molecules with large conjugates systems will adsorb via π–π interactions between the conjugates core and SLG/FLG. This suggests that the method of deposition has a large bearing on the adsorption mechanism, as the liquid deposition process discussed here results in significantly more neighboring molecule-molecule interactions [1323] than another techniques, such as thermal evaporation.

This non-covalent functionalization was taken a step further by chemically modifying the functional end groups, as well as showing that perylene functionalization can successfully be carried out prior to polymer transfer to arbitrary substrates, creating a functional layer transfer (FLaT) [1327]. The latter finding is important, as it allows perylene SAMs of very high packing density to assemble on pristine SLG without having to anneal the as-transferred SLG to remove any polymer residues as depicted in

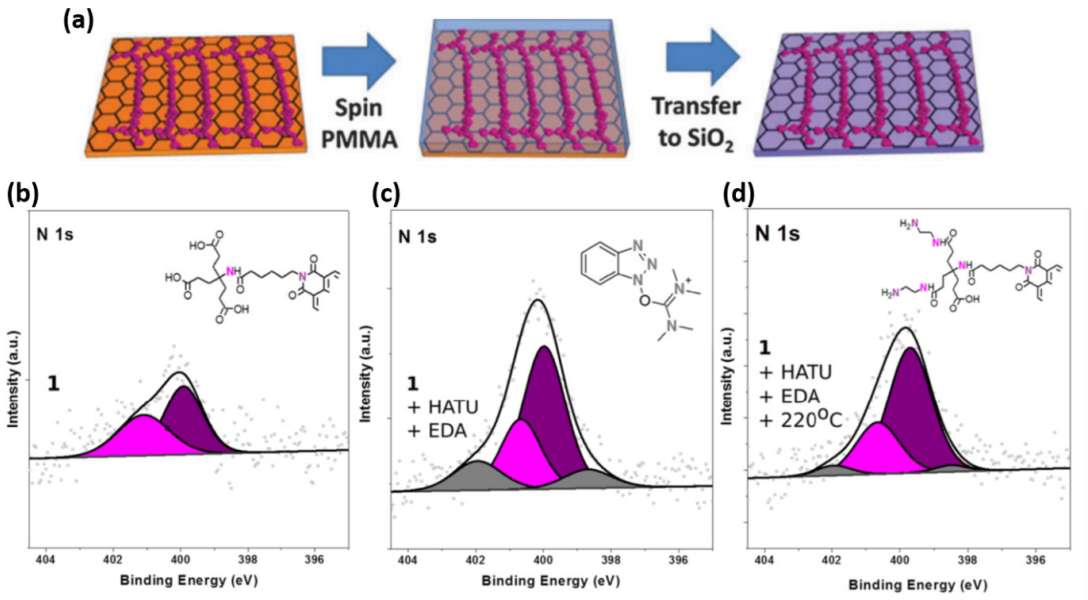


Figure VIII.9. (a) Schematic FLaT, in which perylene fucntionalised graphene is transferred b-d) XPS spectra of perylene on CVD-SLG for each derivitization step. (b) As-transferred perylene1 on SLG. Inset: Partial structure of perylene1 with corresponding nitrogen contributions. (c) Perylene1 on SLG after reaction with HATU and EDA. The two new contributions are from HATU residue. Inset: Chemical structure of HATU. (d) After annealing of derivatized sample at 220 °C. The HATU contributions reduce, but the amine signal increases. Inset: Partial structure of perylene1 after reaction, depicting corresponding nitrogen contributions. Adapted from [1327] with permission of The Royal Society of Chemistry.

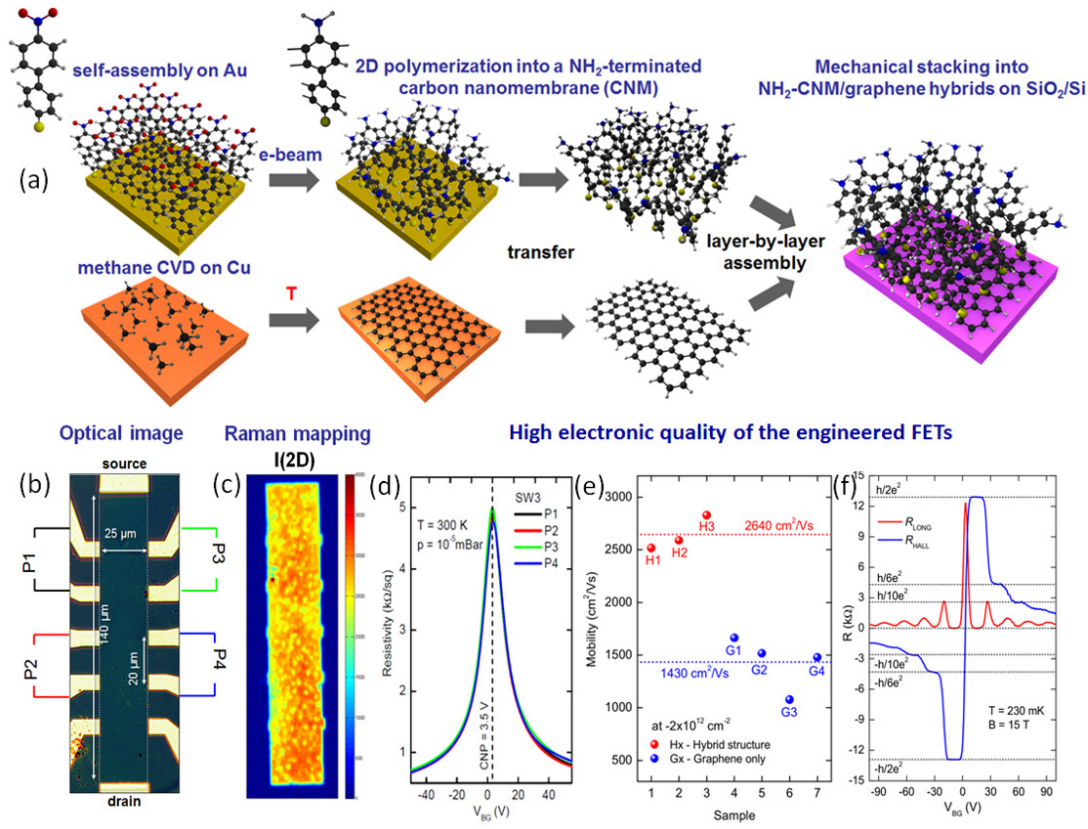


Figure VIII.10. Noncovalent chemical functionalization of SLG. (a) Schematic of the fabrication of NH_2-CNM/SLG heterostructures via mechanical stacking of the individual sheets. (b) Microscope image of the fabricated FET with Au contacts in the Hall bar geometry. (c) Mapping of the Raman 2*D* peak on the active device area. (d) RT homogeneous electrical field effect at different side contacts of the FET as a function of V_G. (e) μ of heterostructure and reference devices. (f) Quantum oscillations in a magnetic field at low *T* confirming high electronic quality of SLG in the heterostructures. Adapted from [1328] © Wiley-VCH Verlag GmbH & Co. KGaA.

figure VIII.9(a). Reacting ethylene-diamine (EDA) with the carboxylic acid groups of the perylene1 SAM using O-(7-azabenzotriazole-1-yl)-*N*,*N*,*N*,*N*′-tetramethyluronium hexafluorophosphate (HATU) was carried out to investigate the possibility of converting the carboxylic acid groups to amines [1327]. This would allow the use of perylene bisimide 1 as anchor in SLG-based biosensing.

Figures VIII.9(b)–(d) show that after reacting perylene molecules with HATU and EDA new contributions can be seen in the N1s core level XPS spectra. The relative intensity of the peak component arising due to the presence of amine groups increases (pink), along with other contributions likely due to HATU residues (grey). Annealing the derivitized sample at 220 °C was found to reduce the relative intensity of these peaks, indicating that the any unreacted physisorbed surface contaminants are removed [1327]. These results show that it is possible to use perylene functionalized graphene as the basis for further chemical modification, towards biosensing applications.

The non-covalent functionalization, can then be, if needed, transformed also in covalent functionalization, triggering the covalent grafting of molecules self-assembled on graphene using, e.g., an electrochemical pulse (see section VIII.1 Electrochemical Functionalization) [1263].

VIII.3.4.3. Noncovalent functionalization with CNMs

Noncovalent functionalization can be used to fabricate heterostructures of graphene and CNMs [1328]. Figure VIII.10(a) shows a route to noncovalent chemical functionalization via assembly of all-carbon vertical heterostructures consisting of amino-terminated CNMs (NH_2-CNM) on SLG produced by CVD on Cu foils [1328]. The chemically active amino groups of NH_2-CNMs are located in these heterostructures in close vicinity to the SLG plane, as they are separated from it only by the ~1 nm dielectric CNM [81]. As shown by complementary spectroscopy, microscopy and electric transport measurements, the pristine SLG properties in these heterostructures remain unaffected [1328], which opens avenues for implementations in graphene-based electronic devices. In figure VIII.10(b), an optical microscope image of an NH_2-CNM/graphene FET in the Hall bar geometry is presented. The structural quality of the device characterized by Raman mapping (figure VIII.10(c)) shows homogeneity. Figure VIII.10(d) presents RT electric-field effect measurements as a function of back-gate voltage, V_{BG}, at 4 side contacts, figure VIII.10(b), P1–P4. The electrical characteristics are homogeneous on the scale ~3500 μm^2. μ is nearly a factor of two higher (~3000 $cm^2\ V^{-1}\ s^{-1}$) in the heterostructure devices in comparison to the starting SLG (~1500 $cm^2\ V^{-1}\ s^{-1}$), figure VIII.10. This may results from a reduction of charge impurities at the SLG/SiO_2 and SLG/ambient interfaces. Shubnikov–de Haas oscillations accompanied with resistivity plateaus of the quantum Hall effect at low T, figure VIII.10(f), demonstrate the high electronic quality in the engineered NH_2-CNM/graphene heterostructures [107, 1328].

The NH_2-CNM/graphene FETs are promising for biosensors. As amino groups can further be functionalized with respective receptors, one could use NH_2-CNM/SLG FETs as analyte-specific electrochemical sensors. GFET biosensors have a very high sensitivity up to the fM level [285]. However, this is difficult to achieve in combination with high selectivity and specificity of the biomolecular binding events. While any covalent SLG functionalization may affect the electronic quality, a functionalization via physisorption typically involves larger distances leading to the reduced sensitivity. Woszczyna *et al* [1329] used 1 nm dielectric and specifically functionalized CNMs to overcome these problems. It is also promising to use them in graphene-based electronics as a complementary dielectric, similar to hBN, for engineering top-gate electrodes, for field-effect tunneling transistors or in flexible electronic applications.

VIII.4. Defect functionalization of GRM

VIII.4.1. Edge modification of GRM in dispersion

Edge selective functionalization would be of particular interest to obtain engineered samples able to further react or assemble in a controlled way. Edge functionalization is in principle driven by the reactivity of the carbon atoms localized at the peripheral edges, which differs from the inertness of the C atoms on the basal plane due to the stability of the extended delocalized π-system. In fact, edges may be regarded as defects in the graphene structure, which can be exploited for its functionalization without severely disrupting the π-conjugated network [1329, 1330]. Edge functionalization may also be carried out on non graphene LMs in general [1246, 1331].

The diazonium chemistry of carbon nanostructures is one of the most convenient methods to covalently functionalize the edges of graphitic materials [1332–1335]. This reaction proceeds through a free-radical mechanism as a result of transfer of a delocalized electron from a graphitic substrate to the aryl diazonium cation to form an aryl radical after the release of nitrogen [1246] (figure VIII.11).

The standard protocol [1330], which generates the reactive diazonium species *in situ* from a stable anilinic compound in the presence of an alkyl nitrite (radical initiator), was followed by performing the reaction in DMF with different equivalents of the aniline derivative per carbon atom. In Ref. [1337], graphite flakes with lateral size ~10–50 μm and thickness ~10 nm, were first dispersed in DMF by bath sonication. Then, 4-aminophenol was added and the mixture sonicated. After that, isopentyl nitrite (6 equiv. per carbon atom) was slowly added to the dispersion and the reaction mixture was kept at 80 °C for two different reaction times, 24 and 48 h. After cooling to RT, the reaction was

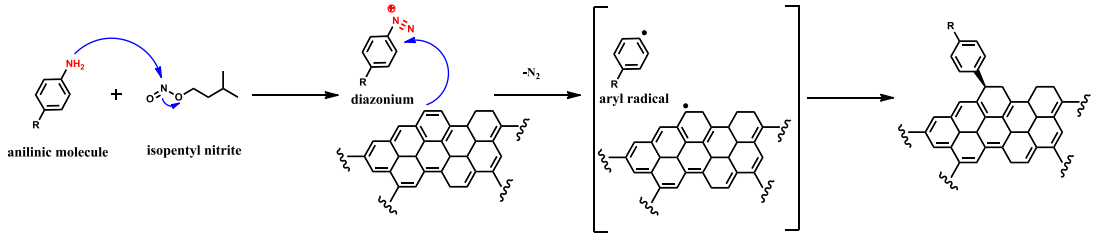


Figure VIII.11. Free-radical mechanism for edge-selective functionalization using diazonium species. Adapted from [1336], copyright American Chemical Society.

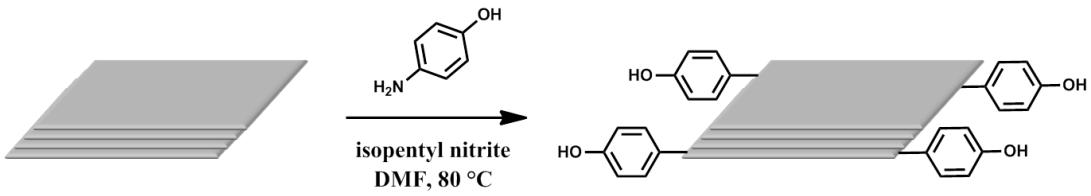


Figure VIII.12. Edge-selective functionalization with 4-aminophenol.

quenched by pouring the mixture into distilled water and filtration of the GRM dispersion through a PTFE membrane. The filtered cake was redispersed in DMF by ultrasonication and filtered through a PTFE membrane. This sequence was repeated twice with DMF, distilled water, methanol and diethyl ether, before obtaining the product after drying (figure VIII.12) [1337].

Functionalization of the flakes was confirmed by a dispersibility test in an organic solvent, where the functional groups present good solubility. Pristine and functionalized flakes were dispersed in IPA at a concentration of 0.1 mg ml^{-1} and sonicated for 30 min. After 2 days, chemically modified flakes with 2 and 4 equiv. of 4-aminophenol during 24 and 48 h, respectively, precipitated from the dispersion. The functionalized sample prepared with 4 equiv. of the anilinic compound using a reaction time of 24 h displayed better dispersibility and was the only sample that did not precipitate after a few days in IPA, which suggests the presence of a higher concentration of hydroxyl groups.

The chemical composition of pristine and chemically modified flakes was investigated by XPS. Upon functionalization, both the C–C sp^2 content and the π-$\pi*$ shake-up band decrease due to the disruption of the delocalized π conjugation in the graphitic structure, while the content of C–OH/C–N and >C=O/C = N increased. The O/C ratio increases from 1.7% to 8.2%, while the N concentration is ~3%–5%, ascribed to adsorbed molecules or residual solvents [1332, 1338].

The degree and selectivity of edge functionalization is influenced by N, edge states, degree of exposure of the interior basal planes and defects [1330, 1332]. In Ref. [1337], edge selective functionalization was maximized for 4-aminophenol and these conditions can be extended to *para*-substituted aniline derivatives. This opens new possibilities to modulate physical and electronic properties for diverse applications, such as catalysis and opto-electronics [1335, 1339]. Similar functionalization can be used to obtain building blocks for the design and manufacturing of functional materials.

VIII.4.2. Functionalization of SLG on substrate after introduction of defects

Ref. [1340] functionalized graphene on SiC with organic molecules forming covalent bonds. This is alternative to wet-chemistry protocols that reported covalent modification methodologies incompatible with some functional groups due to harsh conditions (such as high thermodynamic force, generally exceeding 20 kcal mol^{-1}, or long reaction times, even more than 12 h) used e.g. diazonium salt, click chemistry or surface reactions [1227, 1232, 1244, 1253, 1341–1344].

Ref. [1340] reported the controlled atom-molecule substitution in ultra high vacuum (UHV, $P < 2 \times 10^{-10}$ mbar) by using p-aminophenol molecules, consisting of an aromatic ring with an amino and a hydroxyl group, linking the amino group to the graphene network and leaving free the hydroxyl group. This method was also successfully carried out on graphene grown on Ir.

The substrate was degassed by UHV annealing at 200 –400 °C (details depending on the type of sample) in order to remove physisorbed contaminations [1340]. This thermal treatment was performed by electron irradiation in a heating stage placed at the manipulator, while the annealing T was monitored with an IR pyrometer (emissivity ~0.9). After degassing, the cleanness of the sample was confirmed by STM [1340].

The next step consists in creating single atom vacancies (SAV) by bombarding SLG with low energy ions (Ar^+). For this procedure, the sample needs to

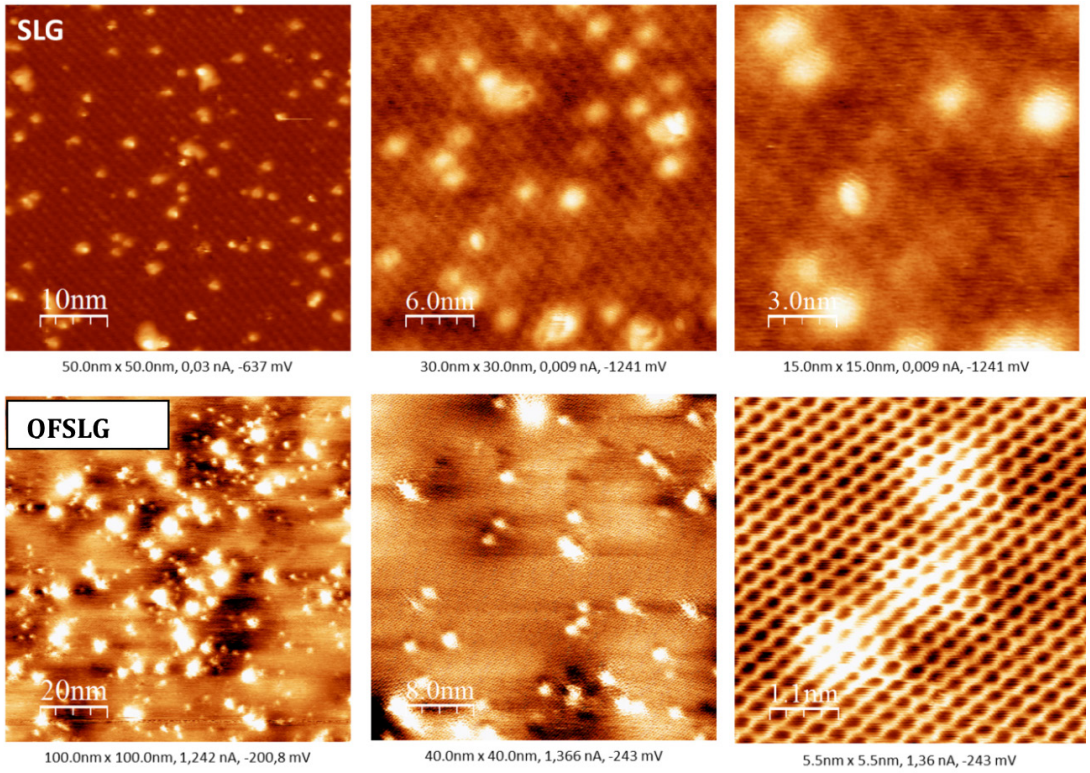


Figure VIII.13. STM images of the p-aminophenol molecules covalently anchored to the monovacancies created by the soft irradiation of the surface with argon ions in both types of samples: SLG (upper panel) and QFSLG (lower panel). The graphene on SiC was grown as for Ref. [611]. Note that in the images of the SLG sample one can see the $(6\sqrt{3} \times 6\sqrt{3})R30°$ reconstruction from the SiC buffer layer, whereas in the QFSLG sample only the graphene network is seen since intercalated hydrogen has decoupled the buffer layer. The molecules appear as protuberances inserted into the graphene network. Partially adapted from [1340].

be placed close to the ion gun (10 cm maximum) at a 0°–15° incidence. The acceleration of the electrons inside the Specs IQE 11/35 ion gun should be 100–140 eV, 10 mA, having a controlled Ar pressure $\sim 1 \times 10^{-7}$ mbar. The most important parameter is the exposure time, that varies between 30 s^{-2} min for producing the desired density of mono-vacancies [1345–1348].

After irradiation, the sample is subjected to a thermal flash to remove the physisorbed Ar. This flash should not be longer than 5 min, reaching different T for each type of sample: 550 °C for SLG and 250 °C for QFSLG. It is important to check the mono-vacancies by STM as soon as possible. Defects are very reactive and they could get passivated with air contamination [1349, 1350].

After modifying the graphene network, the evaporation of organic molecules (P-aminophenol) followed. They need to be purified by turbo pumping for at least 6 h to remove impurities. Following this strategy, Ref. [1340] tested by STM that the organic molecules filled most of the SAV defects, as for figure VIII.13.

VIII.4.3. QFSLG

In order to check the covalent nature of the bonding of the organic molecules to the graphene lattice several experiments were conducted. Figure VIII.14(a) shows the XPS N 1s peaks corresponding to a p-aminophenol dosing of a sample with and without previous SAV defects. This points out the covalent nature of the bonding in the latter case. The thermal stability of the bond was tested up to $T = 250$ °C, figure VIII.14(b)). Even after annealing at this T, the XPS N 1s does not shift indicating the absence of breaking up of the A-AP molecule and that the covalent linked N remains in the graphene network.

Functionalization reaction mechanisms have been computed when the p-AP approaches the SAV either by the –OH or $–NH_2$ terminating groups [1340] within the CI-NEB approach [916, 917] to get a converged minimum energy path. For approach by the $–NH_2$ group, the molecular incorporation undergoes by a double ($–NH_2$) dehydrogenation (see figure VIII.15). This process is efficiently catalysed by the SAV on the surface yielding energy barriers ~ 1.3 and 0.7 eV for the first and the subsequent second dehydrogenation, respectively, and a total enthalpy gain ~ 3 eV. The net enthalpy in the double ($–NH_2$) dehydrogenation (~1.5 eV) is significantly higher than that corresponding to a single dehydrogenation of the OH group, pointing to a favoured incorporation of N atoms in graphene.

VIII.5. Decoration with nanoparticles

The large surface area, electrical conductivity and mechanical strength make SLG a promising substrate to be coupled with NPsfor synergistic benefits in applications such as catalysis, energy storage, plasmonics and optoelectronics or solid state hydrogen

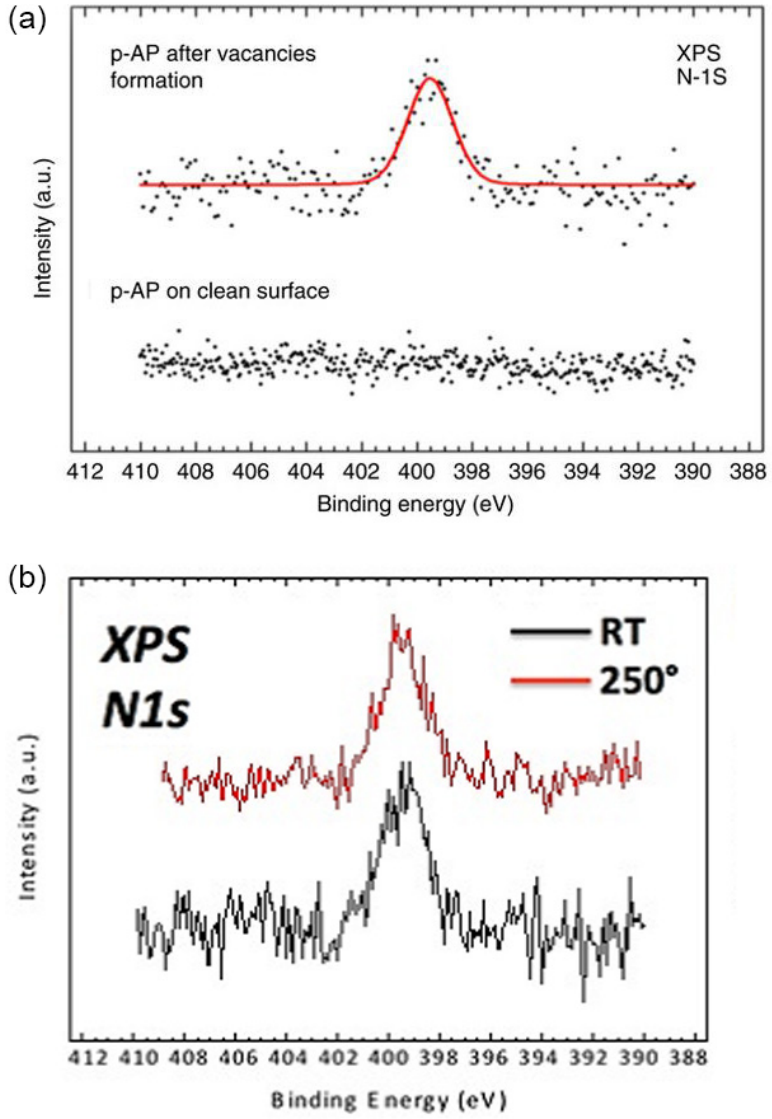


Figure VIII.14. (a) N 1s core level spectra after dosing p-AP on a SLG surface without and with atomic vacancies. The N 1s binding energy corresponds to that of a C atom substitutional in the graphene-network. (b) thermal estability of the N 1s peak at RT and after annealing at ~250 °C.

storage [1351]. Depending on the Fermi level/work function of SLG and metal NPs, interfacial charge transfer can occur from SLG to NPs or vice versa. Hence, decorating with NPs is an efficient method for graphene doping with electrons or holes. To enhance interfacial charge transfer, a strong interaction between graphene and NPs is required [1351]. SLG can be decorated with NPs either by growing NPs directly on its surface, by mixing it with NPs, or by depositing NPs produced in the gas phase in UHV conditions.

VIII.5.1. Graphene-metal NPs

Graphene and other surfaces can be decorated with NPs via electroless plating [1352]. CNTs/SLG act as reducing agents towards metal salts. The Fermi level of nanocarbons allows them to spontaneously reduce Au^{3+} and Pt^{2+} salt solutions to form their respective M0(metal) NPs on the nanocarbon surface [1352]. To extend this to other metal NPs, reductive charging protocols can be used to increase the reducing strength of the nanocarbons. Fulleride, nanotubide and graphenide can be generated following reduction using alkali metal/liquid NH_3 [1233, 1353, 1354] alkali metal naphthalide/THF [1355, 1356], or electrochemically in non-aqueous electrolytes [1357]. All reductive charging techniques insert electrons into the carbon $\pi*$ orbitals, shifting E_F, resulting in increased reactivity. Subsequent chemical reaction may take place via redox or electrophilic addition reactions that are believed to involve SET (i.e. radical based reactions) [1261, 1358–1362]. Due to the high reactivity of reduced nanocarbons towards oxygen and moisture in the atmosphere, these materials should be handled using inert gas filled glove boxes or Schlenk techniques [1363].

Ref. [376] used graphenides to reduce a series of Cu, Zn and Mg salts/complexes, to generate metal NPs on the SLG surface. KC_8 and KC_{24} potassium-graphite intercalation compounds (K-GICs) were produced via the vapor transport [1363] from natural graphite,

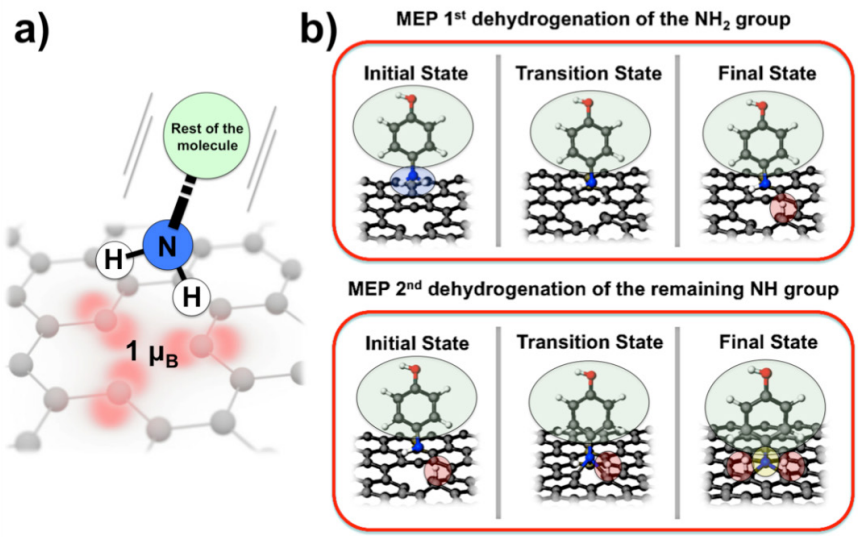


Figure VIII.15. (a) Schematic representation of the approaching of a generic NH_2-terminated organic molecule towards a graphene SAV (with a magnetic moment of 1 μB). (b) For the case of p-AP molecule, most representative geometries for initial state, transition state and final state along the minimum energy path (MEP) for: (top) the first single dehydrogenation of the molecular –NH_2 group, and (bottom) the second single dehydrogenation of the remaining molecular –NH group and the subsequent incorporation of the molecule via the N atom into the graphene lattice via the graphene SAV.

giving the corresponding characteristic bronze stage 1 KC_8 and steel blue stage 2 KC_{24} compounds. For each experiment, anhydrous NMP was added to 10 mg K-GIC in a Young's tap Schlenk tube. The sample was removed from the glove box, mildly sonicated for 30 min and returned to the glove box for subsequent reactions.

MX_2 (M = Mn, Zn and Cu) salts and Cu mesitylene (CuMes) were dissolved in NMP to yield 0.1 M stock solutions. Aliquots were added to the KC_x dispersion to give the desired stoichiometry of metal to K. Typically, reactions are performed using the exact stoichiometry as the number of charges that are available for the reduction, e.g. for M^{2+} salts, M^{2+}:K = 0.5:1, M^+ salts, M^+:K = 1:1, etc. It should be noted that the reduction potential of the metal salt/complex is shifted dependent on its concentration as defined by the Nernst equation [1364], $E_{M^{n+}/M}/M = E^0_{M^{n+}/M} + ((RT/nF)\ln[M^{n+}])$, where E^0 is the standard reduction potential, and n is the number of electrons involved. The reaction was left to stir for 72 h before being removed from the glove box, washed and filtered under vacuum with 100 ml each of NMP, water, chloroform and ethanol, and left to dry in air [376].

Another approach for NP decoration is anchoring them to a polymer matrix surrounding SLG/FLG [1365]. EEG was prepared in Ref. [1365] with a sodium methanesulfonate aqueous solution as electrolyte. It was then dispersed in DMF and mixed with polyaniline (PANi, emeraldine base). The strong π–π interaction between PANi and EEG facilitated anchoring of PANi, achieving controlled surface functionalization. Subsequently, various colloidal NPs (Si, Fe_3O_4 and Pt) were added into the above PANi-functionalized EEG dispersion. During this process, NPs were bound to the amine/imine groups of PANi and assembled into EEG-PANi via electrostatic interaction and hydrogen bonding. Protonic acid doping of PANi with HCl generated EEG-NPs with sandwich-like nanostructures.

Plasmonic coupling of AuNP creates intense hot spots with large electromagnetic field-enhancements within the cavity formed by the two metallic surfaces [1721]. However, this localized field is extremely sensitive to morphological fluctuations and subtle changes in the dielectric properties of the cavity contents. SLG was used as an ultrathin spacer between AuNPs and a Au substrate to create plasmonic field enhancements [1721]. By gating, the possibility to produce plasmon tuning was demonstrated.

NPs can also be grown on SLG by gas phase synthesis [1366]. This approach was used to grow clusters (hence the name Ion Cluster Source or ICS [1367]). The ability to control the mean NP size (from 1 nm to few tens nm) with a quite narrow size distribution while keeping a high chemical composition has made ICS a versatile tool for the fabrication of NPs [1366]. The replacement of the single magnetron of the ICS by multiple magnetrons (Multiple Ion Cluster Source or MICS), offers the advantage of the synthesis of complex highly crystalline NPs with core–shell and core–shell–shell structures [1368–1370], hence providing multiple functionalities to the decorated material [1371, 1372].

One of the important issues in this fabrication method is the vacuum quality in terms of base pressure and purity of the injected gases. A good base pressure is needed ($<5\cdot10^{-9}$ mbar–$5\cdot10^{-7}$ Pa) in order to avoid contaminations. Ref. [1373] showed that small amounts of oxygen could modify the atomic structure of Au clusters. One can assume that other contaminants, such as C, N, He, etc could also affect the

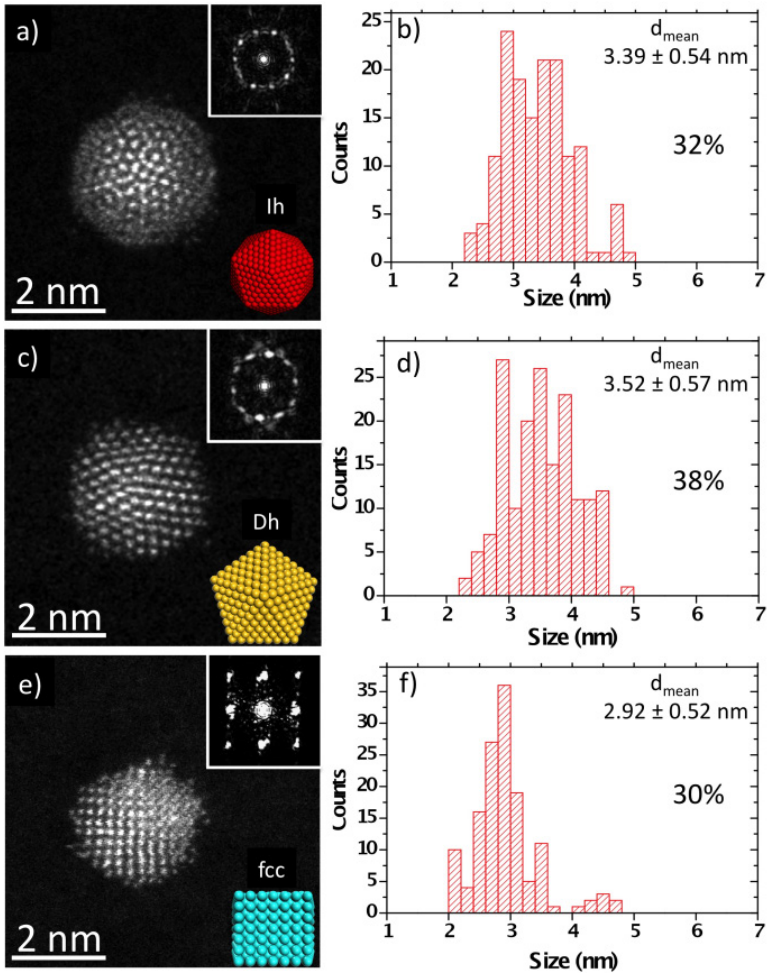


Figure VIII.16. Representative Cs-corrected STEM-HAADF images of (a) Ih, (c) Dh and (e) fcc NPs and (b–f) their corresponding size distributions for Ih, Dh and fcc, for Au NPs grown by MICS. The FFT and the model of each structure are shown as insets. The mean diameters are also given.

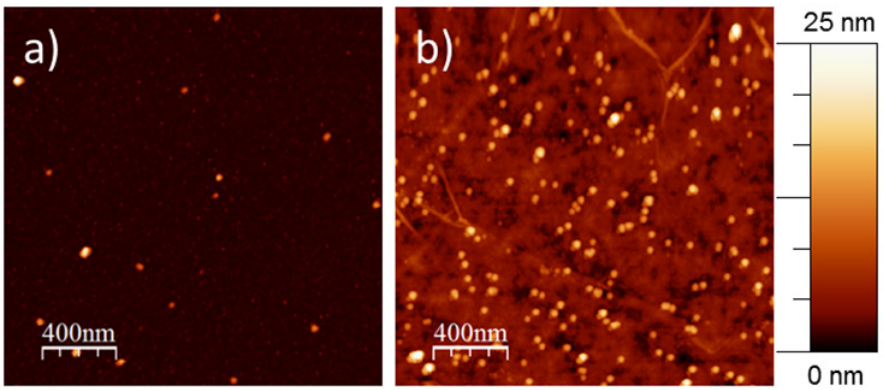


Figure VIII.17. AFM of Au NPs (a) on SiO_x and (b) on SLG after a deposition time of 4 s and 3 s, respectively, to illustrate the importance of the sticking coefficient.

growth and properties of NPs. Therefore, it is crucial to obtain the best base pressure in the vacuum vessel. For the fabrication of the NPs in figure VIII.16, a base pressure below $5 \cdot 10^{-10}$ in the MICS set-up was measured [1368–1370]. To ensure a minimum contamination, all gas pipes used to inject Ar and He are made of stainless steel and vacuum sealed. The purity of Ar and He was ~99.5% and >99.5% respectively. Additionally, the purity of Au was ~99.99% and a systematic pre-sputtering of the targets was performed for 4 min to remove possible contaminants adsorbed on the target surfaces. The samples were handled following basic precautions like using plastic tools, to avoid metallic contamination, [1374] flushing the fresh Si substrates with nitrogen, to remove dust, and depositing <4% of a monolayer of NPs to avoid NPs interactions [1375].

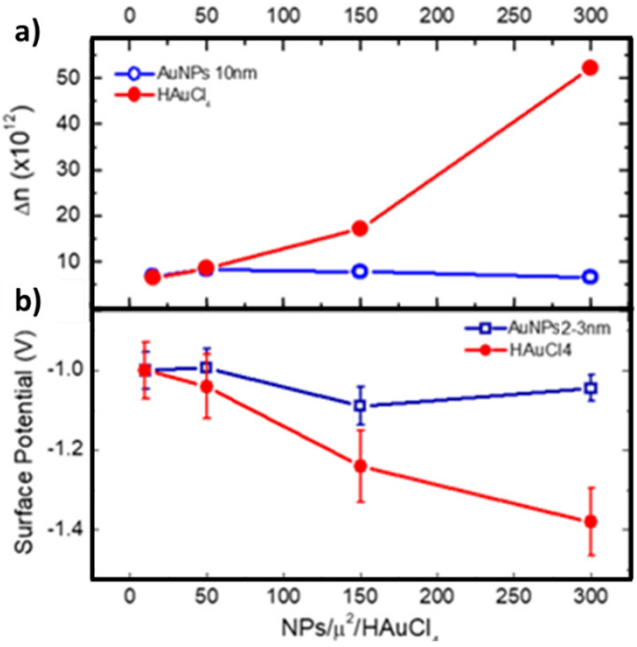


Figure VIII.18. (a) Increment of carriers versus NPs density using UHV and wet chemistry Au salts methods, (b) surface potential versus density of Au, NPs using the UHV method or the wet chemistry Au salts method. After [1378].

The structure and properties of NPs grown by gas phase synthesis is dependent on the parameters used in the cluster sources. Ref. [1376] reported that the power applied to the magnetron and the positioning of the magnetron inside the cluster source that defines the residence time of the NPs in the cluster source (and hence their size) can be used to tune the proportion of icosahedral (Ih), decahedral (Dh) and face-centered cubic (fcc) isomer structures. Therefore, a detailed description of the parameters is mandatory for any attempt to reproduce the growth of NPs by using the gas phase synthesis route.

The next step is the deposition of the NPs on SLG. a series of samples with different coverages are needed to evaluate the evolution of the SLG properties with increasing amounts of NPs. When using gas aggregation sources, the NP density is controlled by the deposition time. Once the number of NPs per time unit is known, one can calculate the time needed for a given coverage. However, if the calibrations are made on a different substrate, the different sticking coefficient will modify this value. The sticking coefficient of metallic NPs on SLG is 3 times SiOx as depicted in figure VIII.17).

Charge transfer effects were explored between the AuNPs and graphene and compared with the doping achieved using other methods [1377], figure VIII.18. Depending on the functionalization method, different results are observed. When the decoration is driven through direct growth of NPs by chemical methods (red line, HAuCl4 [1377]) an increase of charge carrier concentration and a decrease in the surface potential as a function of the coverage is observed. This trend is not observed when the decoration is carried out with AuNPs deposited in UHV conditions (blue line). The effect of the latter method, where the AuNPS arrive already formed, is much subtler. This is the result of a smaller contact area between the UHV generated NPs campared to those synthesized by wet chemistry, since the cleaner UHV synthesis does not result in debris any debris in the NPs neibourhood.

VIII.5.2. GRM as support to grow Mg NPs

For the synthesis MgH_2NP a support is needed to better control the NP dimensions. GRMs are a possible alternative to other substrates such as porous carbon, CNTs or other carbon nanostructures [280, 1379–1386]. Ref. [1387] used graphite flakes as support and anhydrous tetrahydrofuran (>99%) and *n*-dibutyl-Mg. High purity hydrogen gas (99.999%) and graphite flakes with 12, 6 and 1.6 nm thicknesses and tens of microns in lateral size were used. Material processing was performed in a glove box filled with high purity argon (O_2 and $H_2O < 1$ ppm) to avoid oxygen contamination of the reactants preventing the formation of the Mg hydride.

MgH_2 was synthesized by decomposition of *n*-dibutyl-Mg leading to the direct formation of MgH_2 and under an inert atmosphere [1252] at 110 °C. A rapid formation of MgH_2 is expected for higher T following the reaction [1388]:

$$(C_4H_9)_2Mg \rightarrow 2C_4H_8 + MgH_2. \quad \text{(VIII.1)}$$

In a typical synthesis protocol, *n*-dibutyl-Mg was mixed to THF or C_6H_{12} in different proportions. The mixture was placed in a stainless steel reactor and porous carbon, MWNTs or FLGs added. THF is slightly polar (0.207), while C_6H_{12} non-polar (0.0006). For this reason, different solubility in relation to the solvent used are expected. In addition, MgH_2 is highly reactive toward organic molecules [1389]. Then the process of thermal degradation of *n*-dibutyl-Mg rea-

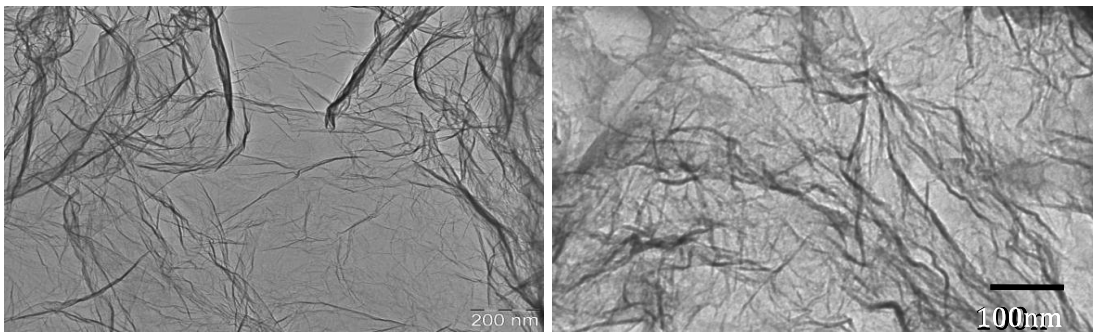


Figure VIII.19. TEM images showing wrinkles and crumpling.

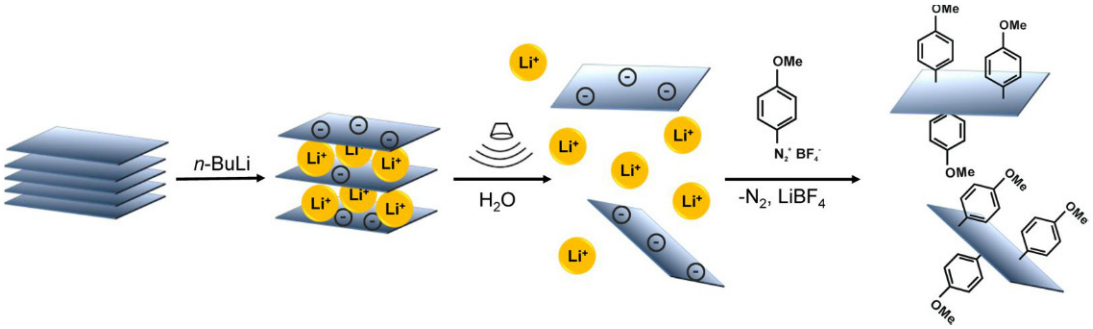


Figure VIII.20. Schematic of basal-plane functionalization of MoS_2. After intercalation with n-butyllithium, the negatively charged MoS_2 is dispersed in water by mild bath-type sonication leading to an efficient exfoliation into individual sheets. The charges on the MoS_2 are quenched by the addition of 4-methoxyphenyldiazonium tetrafluoroborate obtaining the functionalized product. Adapted from [379], copyright American Chemical Society.

gent is expected to be susceptible to the synthetic solvent utilized. Hence the use of different solvents in principle should lead to different MgH_2 structures and hydrogen performances [1390].

Hydrogen was introduced in the reactor at a pressure of 10 or 20 bar and the solution heated at 170 °C and stirred at 50 rpm overnight [1391]. After 12 h, a black/gray precipitate was obtained from the decomposition of *n*-dibutyl-Mg. The suspension was then transferred in appropriate vessels under inert atmosphere and the main part of the solvent was removed by using a centrifuge at 5000 rpm (~2000 g). To further dry the material and remove the remaining organic residuals, the material was placed in a dynamic vacuum ~10^{-2} mbar for ~5 h. The exsiccated material was placed in sealed vials, to avoid Mg oxidation, for the characterization [1387, 1392].

Stabilization of MgH_2NPs depends on the interaction between NPs and the support surface [1393–1395]. Defects and functional groups play an important role and a description of synthesis recipes should always be accompanied by a detailed description of the material. The TEM analysis showed crumpled surfaces (figure VIII.19). Curvature leads to higher reactivity of FLG towards chemical elements such as hydrogen or Mg [1394, 1396, 1397]. Wrinkles may then play an active role in limiting the formation of MgH_2NPs in the solvent and enhancing the decoration of the graphene surface.

The XPS analysis showed Mg in a completely oxidized form, because it difficult to introduce the sample in the XPS instrument avoiding exposure to atmosphere. The oxygen is ~34%. However, if oxygen is considered as exogenous due to atmosphere exposure, the quantification can be limited to C and Mg core lines. The Mg concentration corresponds to ~27%.

Lower reactant concentrations led to better results in terms of NP size. MgH_2 NPs with size >5 nm were obtained after optimization. Nowadays the use of hydrogen for fuel cells is limited by the difficulties of synthesizing efficient storage materials. Mg offers a compromise between good hydrogen storage (7.6 wt%) and desorption T if compared to other materials. In addition, Mg is an interesting material because it is low cost and non-toxic. For Mg/MgH_2 the enthalpy of reaction is ~75 kJ mol^{-1} H_2, corresponding to a H desorption T ~350 °C [1398, 1399]. However the thermodynamic properties of this material can be improved lowering the Mg-H bond formation enthalpy. For practical application in automotive, the metal-hydrogen formation enthalpy should be ~30 kJ mol^{-1} H_2 [1400, 1401]. It has been demonstrated both theoretically and experimentally that the reduction of the Mg particles affects the bond energy with hydrogen [280, 1402], although it is not easy to confine the Mg particle size to the nanometer scale. The possibility to synthesize Mg NPs on the nanometer size is then of great interest for both automotive and stationary

applications. Materials on these size exhibit hydrogen desorption T ~ 160, 140 °C [1387].

VIII.6. Functionalization of other LMs

VIII.6.1. Covalent functionalization of MoS_2

VIII.6.1.1. Reductive covalent functionalization

Functionalization of MoS_2 can be achieved by ligand conjugation of thiols at S vacancy sites either introduced by ion irradiation [1403] or naturally occurring after chemical exfoliation [1404, 1405]. Such methods are interesting but limited in their utility. Ref. [380] reported the first step toward a general route to functionalize TMDs by grafting functional groups to the exposed S atoms, with a sequence, based on intercalation, chemical-exfoliation and subsequent quenching of the negative charges on the MoS_2 by organic halides or other strong electrophiles [379, 380]. In this functionalization sequence intercalated, chemically exfoliated MoS_2 is reacted with electrophiles such as halides and diazonium salts (figure VIII.20). The use of chemically exfoliated MoS_2 is beneficial due to the good exfoliation in water making LM both sides accessible. Chemically-exfoliated MoS_2 can be obtained by reacting it with *n*-butyllithium (*n*-BuLi). This leads to the formation of a Li intercalation compound associated with a widening of the interlayer distance between the individual MoS_2 layers and a charge transfer from *n*-BuLi to the MoS_2. As a result of the charges residing on the MoS_2 flakes, a destablilization of the semiconducting 2H-polytype is observed due to an effective change of electron density in the *d* orbitals of the transition metal [1406]. Chemical exfoliation after Li intercalation thus usually results in the formation of the 1T-polytype of MoS_2 [1406]. It depends on the intercalation conditions to which extent this transformation occurs [379, 1407].

In contrast to negatively charged graphenides, the resultant material is reasonably stable under ambient conditions and can be dispersed in water [1406]. Due to this, the preparation of solvents used for the initial intercalation process is easier compared to graphene. Solvents only have to be dried and not necessarily freed from oxygen. For this purpose, it is recommended to distil and reflux the solvents (e.g. *n*-hexane and cyclohexane) two times over a Na wire under Ar atmosphere, prior to the use of the intercalation reagent.

Since MoS_2 has long been considered to be unreactive and almost inert even after intercalation [159], Ref. [379] used very aggressive electrophiles: diazonium salts to quench the negative charges on the MoS_2 and functionalize the material. After the final sonication step of the purified intercalate 4-methoxyphenyldiazonium tetrafluoroborate was dissolved in distilled water and added to the dilute yellowish/brownish MoS_2 dispersion dropwisely under exposure to light. After addition of only a few drops of reagent, a black precipitate formed. The reaction mixture was stirred overnight and filtered. Material which passed through the membrane in the first step was collected and filtered again.

Washing with ~100 ml isopropanol to remove organic side-products, such as the correspondent biphenyl, and washing with distilled water yielded the functionalized MoS_2 product after drying under vacuum (~ 10^{-2} mbar) at RT. The formation of a covalent C-S bond was evidenced by the appearance of a C-S stretching vibration in the IR spectra [379, 380], a new component in the S XPS core level spectra at higher binding energy [379, 380] and solid state NMR [380]. By XPS [379, 380] and thermogravmetric analysis coupled to mass spectrometry [379], it was possible to estimate the degree of functionalization. Typically, 10–20 atom% S bears a functionality [379, 380]. The degree of functionalization was shown to depend on the initial intercalation conditions: when a milder intercalation with a low *n*-BuLi to MoS_2 stoichiometry ratio is used (three-fold molar excess of MoS_2), the degree of functionalization is ~ 10 atom% [379], whereas it can reach up to ~ 20 atom% when *n*-BuLi is used in excess (three-fold molar excess of *n*-BuLi) [379, 380].

Here we provide a protocol for the fabrication of MoS_2-templated conjugated microporous polymers (M-CMPs) by growing nitrogen-rich CMPs shells on both sides of 4-iodophenyl-functionalized MoS_2 templates [1408]. The synthesis strategy for M-CMPs is illustrated in figure VIII.21. First, chemically-exfoliated MoS_2 (CE-MoS_2) was achieved by reacting bulk MoS_2 with n-butyllithium (*n*-BuLi) [379, 380, 1408]. Then, it was functionalized with 4-iodophenyl diazonium salt under aqueous conditions [379, 380, 1408]. The obtained 4-iodophenyl-functionalized MoS_2 (MoS_2-I) can be well-dispersed in various organic solvents, such as toluene and DMF. Next, the arylacetylene building block 1,3,5-triethynylbenzene mixed with an aryl di- or trihalide was reacted with MoS_2-I in anhydrous DMF in the presence of $Pd(PPh_3)_4$, CuI and Et_3N under inert atmosphere. This Sonogashira-Hagihara cross-coupling reaction was carried out at 100 °C for 3 days under vigorous stirring and yielded an insoluble, crude product that was collected by filtration and purified by Soxhlet extraction with THF for 2 days. Sandwich-like M-CMPs with high specific surface areas and hierarchically porous structure were obtained after vacuum drying. As-prepared porous polymer-MoS_2 sandwiches can be converted into the corresponding hierarchically porous MoS_2/nitrogen-doped porous carbon hybrids by direct pyrolysis of the M-CMPs flakes. The hybrids are characterized by high specific surface areas and aspect ratios and showed a promising oxygen reduction reaction (ORR) and supercapacitor performance, due to the maximized interfacial interaction between nitrogen-doped porous carbon and MoS_2 layers.

A pathway towards covalent functionalization of TMDs was established through the reaction between liquid-exfoliated MoS_2 and various metal acetate salts [1409]. This involves functionalization of the semiconducting 2H-MoS_2 polytype. Generating it requires treatment of the 2H material with *n*-butyllithium,

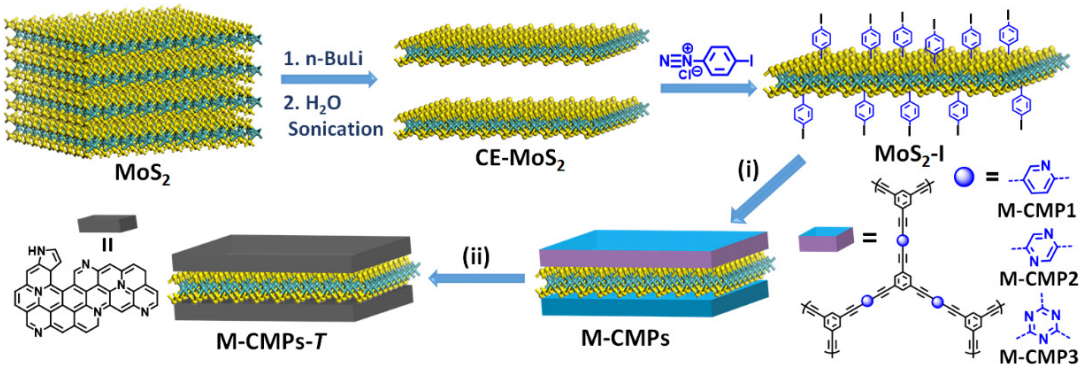


Figure VIII.21. Idealized formula scheme depicting the chemical exfoliation of bulk MoS_2 and subsequent functionalization with 4-iodophenyl substituents under formation of MoS_2-I, as well as the preparation of MoS_2-templated conjugated microporous polymers (M-CMPs) and the corresponding MoS_2/nitrogen-doped porous carbon (M-CMPs-T) hybrids. (i) monomers: 1,3,5-triethynylbenzene and 2,5-dibromopyridine, 2,5-dibromopyrazine, or 2,4,6-trichloro-1,3,5-triazine, argon, $Pd(PPh_3)_4$, CuI, Et_3N, DMF, 100 °C, 3 d; (ii) argon, heating rate: 10 °C min^{-1}, pyrolysis temperature: 700, 800, or 900 °C, 2 h.

necessitating safety steps when handling this harsh substance. Direct functionalization of 2H-TMDs removes the requirement to use this treatment. Acetate functionalization of LPE MoS_2 was shown to stabilize the exfoliated flakes in IPA and acetone, rather than having to use toxic solvents such as NMP and CHP [1409]. Dispersions of exfoliated 2H-MoS_2 in IPA were mixed with a given metal acetate dissolved in IPA. This mixture was then sonicated for 30 min and the functionalized 2H-MoS_2 was separated and collected by centrifugation and washing [1409].

XPS analysis was performed on the thin films of material formed via vacuum filtration [1409]. The Mo 3d and S 2p spectral regions shown in figure VIII.22 demonstrate functionalization of the flakes after treatment with $Cu(OAc)_2$. The Mo 3d core level displays a new doublet associated with MoS_2, shifted to higher binding energies than the unfunctionalized 2H-MoS_2 polytype, due to functionalization. The S2p core level exhibits a new spectral feature for the same reasons. Re-dispersing dried functionalized 2H-MoS_2 flakes in NMP removed the functional groups [1409]. Figures VIII.22(c) and (f) show that the material returns to its original state without any permanent changes in the spectral features, indicating no permanent structural or chemical modification during functionalization with M(OAc)2.

The most critical step is to provide sufficient energy when the liquid exfoliated MoS_2 in IPA is mixed with the acetate salts. This was achieved by additional sonication using a tapered microtip with high local energy input [243]. When using a larger diameter tip (required to produce larger quantities), the degree of functionalization (i.e. the number of S atoms on the surface decorated by the functional group) drops to <20%. Furthermore, depending on the purity of starting MoS_2 and water content in the IPA, the initial MoS_2 dispersion is sometimes not colloidally stable and the MoS_2 precipitates from the dispersion while leaving a deep blue colored supernatant. This is currently not understood, but likely related to MoO_x impurities in the powder that form complexes with the IPA/H_2O solvent. From our experience, a stable dispersion can be obtained by sonicating this precipitated MoS_2 a second time. However, in such cases, the degree of functionalization was again lower than reported.

The number of functionalization procedures available is limited. These mainly use exfoliated metallic 1T-MoS_2 and in some cases ligand conjugation to semiconducting 2H-MoS_2. All these works [1229, 1404, 1788] do not focus and discuss on the location and how the functionalization takes place. To get this information a different approach has been developed for functionalizing exfoliated 2H-MoS_2 with the organic electron donor of 1,2-dithiolane-based pyrene derivative [1412]. These works demonstrated the possibility of obtaining MoS_2-pyrene nanohybrids, showing a preferential edge functionalization [1412]. This primarily occurs via sulphur addition along partially saturated zig-zag MoS_2-S edges, preserving intact the basal structure of functionalized MoS_2. A natural consequence of this finding is that chemical functionalization of exfoliated MoS_2 should be similar to that of bulk material, where edge functionalization is likely to be predominant [1412, 1732]. Thus, this offers the possibility of direct transfer of functionalization strategies from bulk to exfoliated MoS_2, e.g. transition metal doping of edge sites to improve catalytic behavior.

The interfacing of TMDs with photoactive species via robust covalent bonding needs to be exploited via the formation of hybrid materials. This is particularly true in the context of their ability to function as donor–acceptor systems upon photoillumination. This goal has been achieved via the realization of novel donor–acceptor hybrids based on the covalent functionalization of MoS_2 and WS_2 with 1,2-dithiolane-modified carbon nanodots (CNDs) [1413]. The excitation of CND-MoS_2 and CND-WS_2 at 370 nm showed ultrafast energy transfer from CNDs to both MoS_2 and WS_2, while at 425 nm, charge transfer in CND-MoS_2 but not in CND-WS_2 was detected [1413]. These excited state electron-transfer processes offer good opportunities for donor–acceptor-type hybrids for energy harvesting applications.

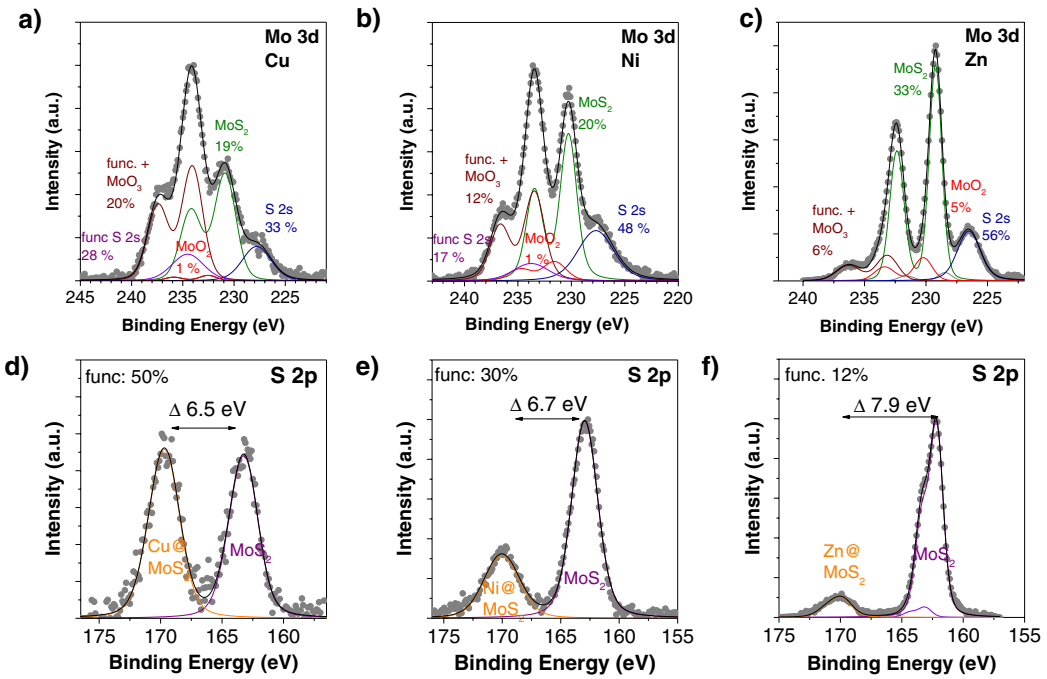


Figure VIII.22. Fitted XPS Mo 3d and S 2p core level peaks for (a, d) 2H-MoS_2 (a), (b, e) 2H-MoS_2-$Cu(OAc)_2$, and (c,f) defunctionalized 2H-MoS_2-$Cu(OAc)_2$. Adapted from [1409], © Wiley-VCH Verlag GmbH & Co. KGaA.

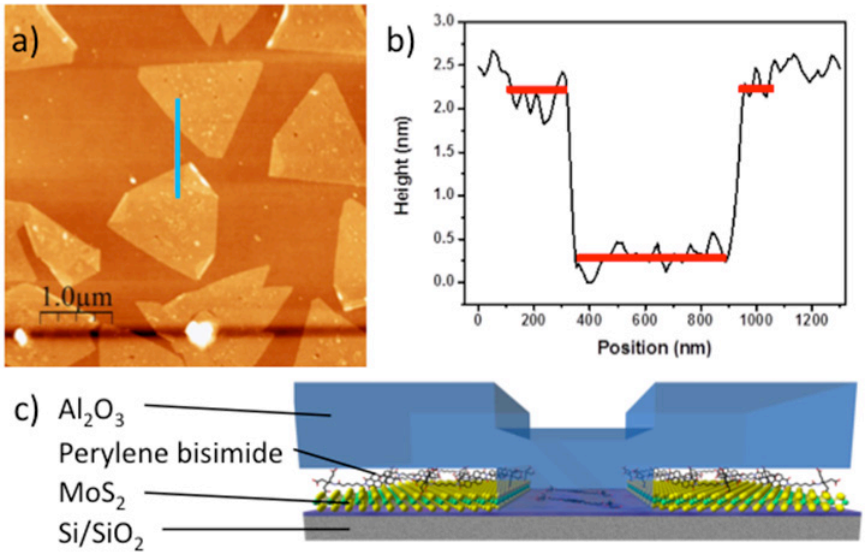


Figure VIII.23. (a) Topography of MoS_2 triangles after 27 cycles of ALD after seeding with a perylene bisimide derivative. The flakes are higher than the surrounding substrate. (b) Line profile along the line marked in (a). The step height is 1.9 nm. (c) Schematic representation of the structure of (a) as indicated by the scan. Adapted from [1414] with permission of The Royal Society of Chemistry.

VIII.6.2. Noncovalent functionalization of MoS_2

Perylene functionalization of CVD-grown MoS_2 and WS_2 was carried out in a similar manner as for SLG [1323, 1327]. MoS_2 and WS_2 grown on SiO_2 were coated with aqueous perylene solutions creating a non-covalent functionalization. It was reported that the resulting perylene layer was suited to seed ALD growth of Al_2O_3 on 1L TMD flakes (figure VIII.23) [1414]. ALD directly on TMD flakes, while successful for $N > 2$, was unsuccessful on 1L. This was attributed to the electronic structure of 1L-TMDs, and their cleanliness [1414]. After functionalization with perylene1 the ALD growth of Al_2O_3 takes place uniformly across the sample. Thus the non-covalent functionalization provides a robust mechanism to seed thin films of dielectric materials on 1L-TMDs, a requirement for many device applications and for further functionalization.

IX. Characterization methods

IX.1. Microscopies

IX.1.1. Optical microscopy

IX.1.1.1. Quantitative analysis of the optical microscopy images

Many optical characterization methods rely on the quantitative analysis of optical microscopy images [1, 1375, 1417–1419, 1421]. One can extract the contrast difference between GRM and substrate by analysing the red, green and blue channels of the digital images. For each camera channel the reflected intensity at the substrate and GRM can be measured and the contrast difference can be directly calculated.

Figure IX.1(a(l)) shows an example of a collection of epi-illumination (light reflected by the surface of the sample and then detected) mode optical microscopy images of MoS_2 flakes with different N (previously determined by AFM) where the thickness dependent colour is evident. The contrast difference requires an initial calibration, using an alternative thickness determination method, and it might slightly change from one experimental setup to another one as it relies on the spectral response of the employed digital camera, the microscope lamp emission spectrum, and the numerical aperture of the microscope objective.

IX.1.1.2. Multispectral imaging

Multi-spectral imaging characterization of GRMs was introduced by Refs. [1418, 1419, 1420] to identify N for graphene flakes on SiO_2/Si substrates and it has been rapidly adapted to characterize and identify other GRMs [1416, 1421–1425]. The method involves the acquisition of optical images using narrow bandpass filters to select the illumination wavelength. The optical contrast, C_T, is typically extracted from these images in order to obtain a quantity that does not depend on the illumination intensity. C_T is typically defined as:

$$C = \frac{I_{\mathrm{GRM}} - I_{\mathrm{substrate}}}{I_{\mathrm{GRM}} + I_{\mathrm{substrate}}} \qquad \text{(IX.1)}$$

where I_{GRM} and $I_{\mathrm{substrate}}$ are the reflected intensities from GRM and substrate. A quantitative analysis can be done on the basis of a Fresnel law based model, where the system is modelled as a stack of different optical media under monochromatic illumination in a normal incidence configuration [1418, 1419, 1426]. Hereafter the subscripts 0, 1, 2 and 3 will be used to refer to air, GRM, SiO_2 and Si. First we focus on the case where only air, SiO_2 and Si are considered. The Si layer is modelled as a semi-infinite slab whose optical properties are determined by its complex refractive index $\tilde{n}_3(\lambda)$ that strongly depends on the wavelength (λ) [1431, 1432, 1426]. The SiO_2 layer, with a thickness d_2, is modelled with its refractive index $n_2(\lambda)$ that also depends on the wavelength [1418, 1419, 1426].

The total amplitude of the light beam reflected by the SiO_2/Si substrate (r) can be obtained from the infinite sum of light beams coming from the multiple reflections in the central SiO_2 layer (see figure IX.2). Anytime that a light beam reaches an interface the Fresnel equations are applied, considering both the real and the imaginary part of the refractive index and accounting for the phase shift between the different light beams. E.g. the phase shift between the reflected beams at the air/SiO_2 and those transmitted through the air/SiO_2 (going across the SiO_2 then getting reflected at the SiO_2/Si interface then going across the SiO_2 and finally being transmitted at the SiO_2/air interface) is $2\Phi_2$ (see the sketch in figure IX.2) with $\Phi_2 = 2\pi n_2 d_2 \cdot \cos(\theta_2)/\lambda$. All this being considered, the total amplitude of the reflected light by the SiO_2/Si substrate (r) is:

$$r = r_{02} + t_{02}e^{-2i\Phi_2}r_{23}t_{20}\left[1 + \sum_{m=1}^{\infty}\left(r_{23}r_{20}e^{-2i\Phi_2}\right)^m\right] \qquad \text{(IX.2)}$$

where r_{ij} and t_{ij} are the amplitude of the beam reflected and transmitted at the interface between the media i and j. These coefficients r_{ij} and t_{ij} can be obtained directly from the Fresnel law. Considering that $r_{ij} = -r_{ji}$ and $t_{ij}t_{ji} - r_{ij}r_{ji} = 1$ and summing the geometrical series

$$r = \frac{r_{02} + r_{23}e^{-2i\Phi_2}}{1 + r_{02}r_{23}e^{-2i\Phi_2}}. \qquad \text{(IX.3)}$$

Then the intensity of the light reflected by the SiO_2/Si is $I_{\mathrm{substrate}} = |r|^2$.

$$I_{\mathrm{substrate}} = \left|\frac{r_{02} + r_{23}e^{-2i\Phi_2}}{1 + r_{02}r_{23}e^{-2i\Phi_2}}\right|^2. \qquad \text{(IX.4)}$$

Under normal incidence assumption this expression is simplified because $r_{ij} = (\tilde{n}_i - \tilde{n}_j)/(\tilde{n}_i + \tilde{n}_j)$ and $\Phi_2 = 2\pi n_2 d_2/\lambda$. When a GRM is placed on the SiO_2/Si substrate, the intensity of the light reflected by the stack can be calculated in a similar way as $I_{\mathrm{substrate}}$:

$$I_{\mathrm{GRM}} = \left|\frac{r_{01}e^{i(\Phi_1+\Phi_2)} + r_{12}e^{-i(\Phi_1-\Phi_2)} + r_{23}e^{-i(\Phi_1+\Phi_2)} + r_{01}r_{12}r_{23}e^{i(\Phi_1-\Phi_2)}}{e^{i(\Phi_1+\Phi_2)} + r_{01}r_{12}e^{-i(\Phi_1-\Phi_2)} + r_{01}r_{23}e^{-i(\Phi_1+\Phi_2)} + r_{12}r_{23}e^{i(\Phi_1-\Phi_2)}}\right|^2. \qquad \text{(IX.5)}$$

Although the previous approach is general and it can be applied to stacks with an arbitrary number of media, it might become cumbersome to calculate the intensity of the light reflected by stacks with more than 3 media. The transfer matrix formalism is the most appropriate approach to analyse the light propagation in systems formed by a stack of many different media. From the previous expressions one can deduce that if one determines the GRM thickness (e.g. with AFM) it is possible to use the optical contrast measured at different illumination wavelengths to determine the GRM refractive $\tilde{n} = n - i\kappa$ [1419, 1421, 1424, 1428–1430]. On the other hand, if the GRM refractive index is known one could determine its thickness directly from the measurement of the optical contrast acquired at different wavelengths with no need of AFM (figure IX.3).

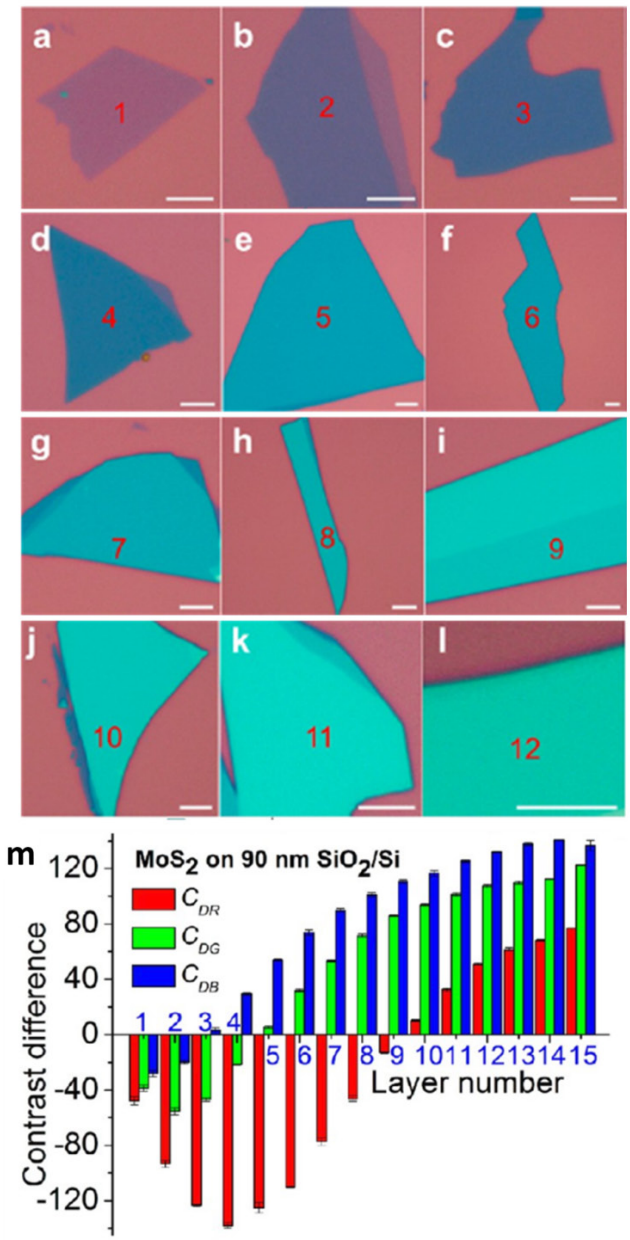


Figure IX.1. (a)–(l) Color optical images in epi-illumination mode of MoS_2 flakes with N = 1–12 a 300 nm SiO_2/+ Si. The scale bar is 5 μm. (m) Thickness dependent contrast difference extracted from the red, green and blue channels. Figure reproduced from [1416], © Tsinghua University Press and Springer.

IX.1.1.3. Hyper-spectral imaging

In this technique the illumination wavelength is selected with a tuneable light source, e.g. based on a halogen lamp and a monochromator, instead of using narrow band pass filters [1431]. Figure IX.4 shows a schematic setup for transmission mode hyperspectral imaging. Epi-illumination hyperspectral imaging (or reflection mode hyperspectral imaging) can be also done with minimum modifications of the setup [1432].

Hyperspectral imaging is carried out by sweeping the excitation wavelength in steps and acquiring a microscope image of the sample for each wavelength. The acquired images are then arranged forming a 3d matrix, being the first two matrix indexes the X and Y spatial coordinates and the third index (λ) the wavelength (figure IX.4(b)). Spectral information of a certain sample region can be directly obtained by plotting all the elements of the matrix along the wavelength dimension λ for fixed X and Y coordinates (figure IX.4(b)). Figure IX.4(c) shows a sketch of two spectra extracted from two regions in the sample: substrate (red) and GRM (blue). The GRM transmittance (T_r) can be obtained by dividing both spectra: $T_r = I_{GRM}/I_{subs}$ (inset in figure IX.4(c)), where I_{GRM} is the intensity acquired on the GRM and Isubs that of the substrate. The absorbance A can be obtained from as: $A = -\log10\,(T_r)$.

Figure IX.8 shows an example of characterization of GRM by means of hyperspectral imaging. The panels (a) to (f) show transmission mode optical images of a MoS_2 flake for different wavelengths. From the

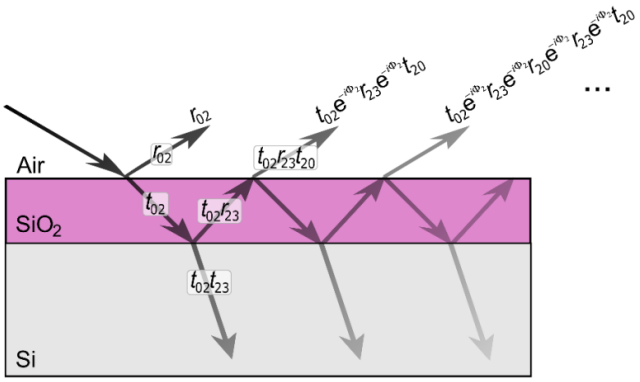


Figure IX.2. Sketch of the optical beam path transmitted and reflected at the different interfaces in a multilayer structure air/SiO_2/Si to understand the role of the different optical paths on the optical contrast. Adapted with permission from [1427].

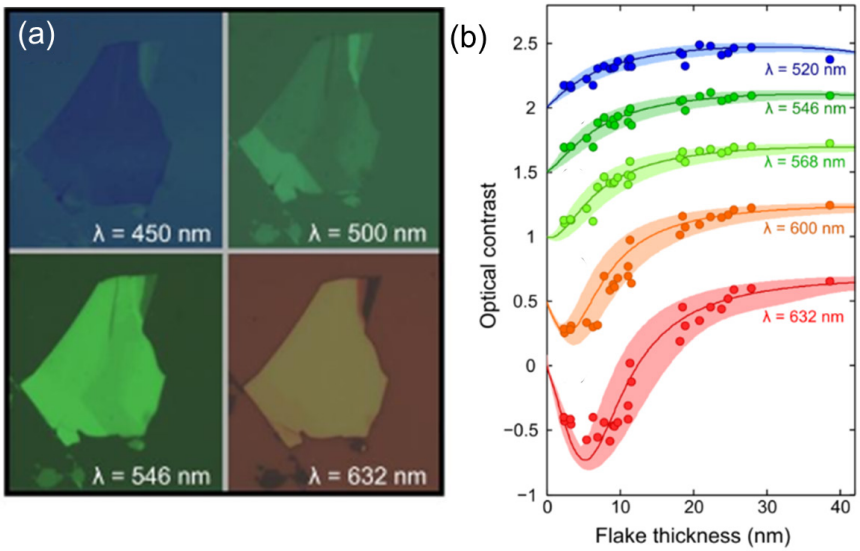


Figure IX.3. (a) Optical images of a $TaSe_2$ flakes with regions with different thicknesses, acquired at different wavelengths. (b) Optical contrast as a function of thickness for different wavelengths. The experimental data (circles) can be reproduced by the Fresnel law based model by using the refractive index for bulk $TaSe_2$ (solid lines). Reproduced from [1416], © Tsinghua University Press and Springer.

collection of hundreds of images from 400 to 1000 nm one can extract the absorbance, figure IX.5(g).

IX.1.1.4. Micro reflectance/transmittance spectroscopy
In this method one illuminates the sample with white light and the reflected/transmitted light is analysed with a spectrometer (see figure IX.6) [1198, 1310, 1428, 1429, 1433, 1434]. The acquired reflection/transmission spectra can be analysed with the Fresnel law to extract information on the GRM optical properties. In figure IX.7 the refractive index of 1L-MoS_2 is determined by fitting the measured optical contrast on different SiO_2/Si substrates to the Fresnel law based model, using the refractive index of 1L-MoS_2 as a fitting parameter (panel a) [1428]. The resulting values of the real and imaginary part of the refractive index are displayed in figure IX.7(b) and compared with bulk MoS_2.

One can also obtain the dielectric functions from the measured reflectance spectra by means of a Kramers-Kronig constrained analysis of the spectra of GRMs on transparent substrates [1198]. From the resulting dielectric function, the refractive index can be calculated [1198]. Figure IX.8 shows an example of determination of the dielectric function from the reflectance spectra of 1-4L TMDs. From the resulting dielectric function, the absorption spectra refractive index can be calculated [1198].

Another feature of micro-reflectance/transmittance measurements is their speed, each spectrum can be acquired in ~1 s, allowing one to characterize large scale samples (e.g. films grown by CVD, cm^2 area) at hundreds of different locations to get an insight about uniformity [1429]. Figure IX.9 shows a differential reflectance spectrum acquired at one position on a 1L-MoS_2 grown on sapphire. It also plots the histograms of the energy and FWHM of the A and B excitons measured at 550 different locations to characterize the sample homogeneity.

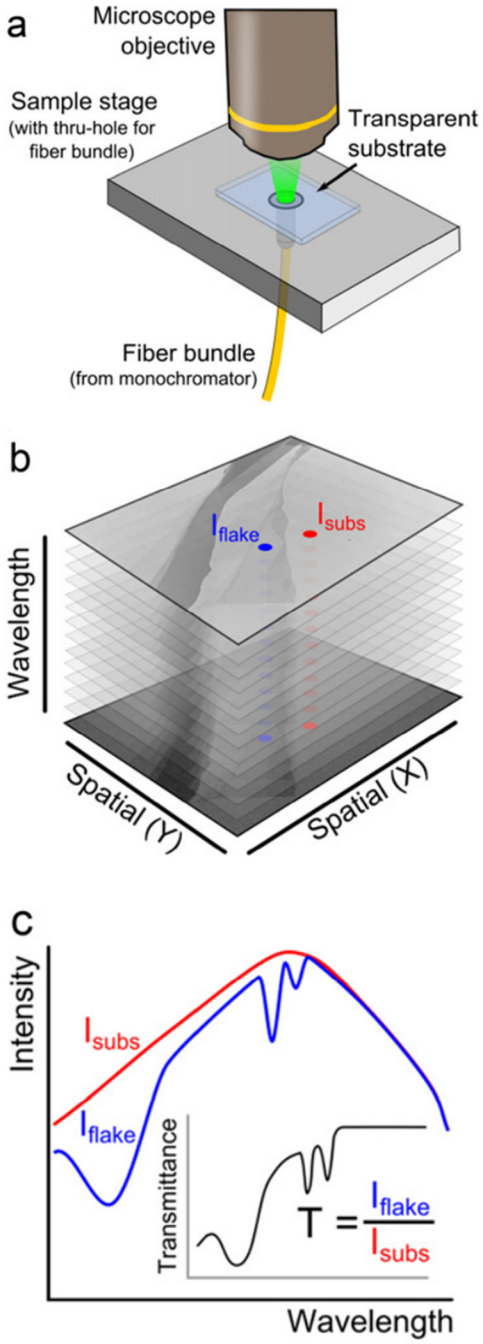


Figure IX.4. (a) Schematic setup for transmission mode hyperspectral imaging. (b) Data acquisition process: optical images are acquired while the wavelength is varied. The resulting dataset is arranged in a 3d matrix. (c) Spectral information extracted from the dataset. The inset shows a transmittance spectrum obtained by normalizing the GRM spectrum to that of the substrate. Adapted from [1431], © IOP Publishing Ltd.

IX.1.1.5. Comparison between multispectral, hyperspectral and micro-transmittance

Figure IX.10 compares different optical microscopy characterization methods, studying the same system: multi-spectral, hyper-spectral and micro transmittance of 1-3L-MoS_2 [1421, 1431, 1434]. Table IX.1 compares the area characterized, the spectral resolution, and the time to carry out one measurement. This shows that micro transmittance/reflectance is a powerful tool to perform fast measurements in one spot, due to its high spectral resolution and low measurement time. The short measurement time allows one to perform point measurements at hundreds of different locations[1429]. Multi-spectral and hyperspectral imaging are very interesting to study large areas as in one shot ~10 000 μm^2 can be measured at once, allowing for the acquisition of spatially resolved maps with diffraction limited spatial resolution [1435].

IX.1.2. AFM

IX.1.2.1. LPE GRMs

AFM provides fast (<10 min/measurement) and reliable characterization of the lateral size and thickness distribution of flakes deposited on different substrates, allowing one to investigate large areas (hundreds of μm^2) and to collect data from hundreds of flakes (figure IX.11(c)). The size distribution can be roughly modelled using a log-normal distribution, as observed for a range of GRMs exfoliated in the liquid including graphene [178], hBN [1437], MoS_2 [185], WS_2 [186], GaS [188] and black phosphorus [190]. More extensive statistical studies, performed on GO flakes using AFM, SEM and fluorescent microscopy, demonstrated that the fragmentation process can be described by a series of rupture-like breakup events, yielding two different populations of flakes featuring different size distributions [136].

When working with LPE samples for AFM analysis, it is critical to avoid re-aggregation during solvent evaporation. For this, drop-casting the dispersion on pre-heated wafers (10 μl per 0.5 × 0.5 cm^2 wafer) is often used [245]. The solvent evaporates and bubbles are formed, resulting in more uniform deposition compared to drop casting at lower T. The wafer should be heated to ~50 °C–70 °C above the boiling point of the solvent.

In the case of surfactant-based dispersions, it is recommended to dilute the sample with water (rather than surfactant) prior to deposition and wash the wafer thoroughly with water and isopropanol (~5 ml each) to remove residual surfactant. Residual surfactant can make thickness measurements very tedious, especially for very small flakes that are more difficult to distinguish from the surfactant. In this case, phase images can provide a guide as they usually give a good contrast between different materials. If problems with residual surfactant persist, the substrates can be soaked in water overnight without significant loss of flakes. Deposition from high boiling point solvents, such as NMP, may be challenging, and re-aggregation, residual solvent, or polymerized NMP covering flakes are observed. In order to overcome this problem, it is advisable to transfer the material exfoliated in NMP to IPA by centrifugation prior to AFM [190].

Si substrates with a 200–300 nm SiO_2 enable flakes to be seen with an optical microscope/optical [1419]. This is a useful guide to identify regions of interest for

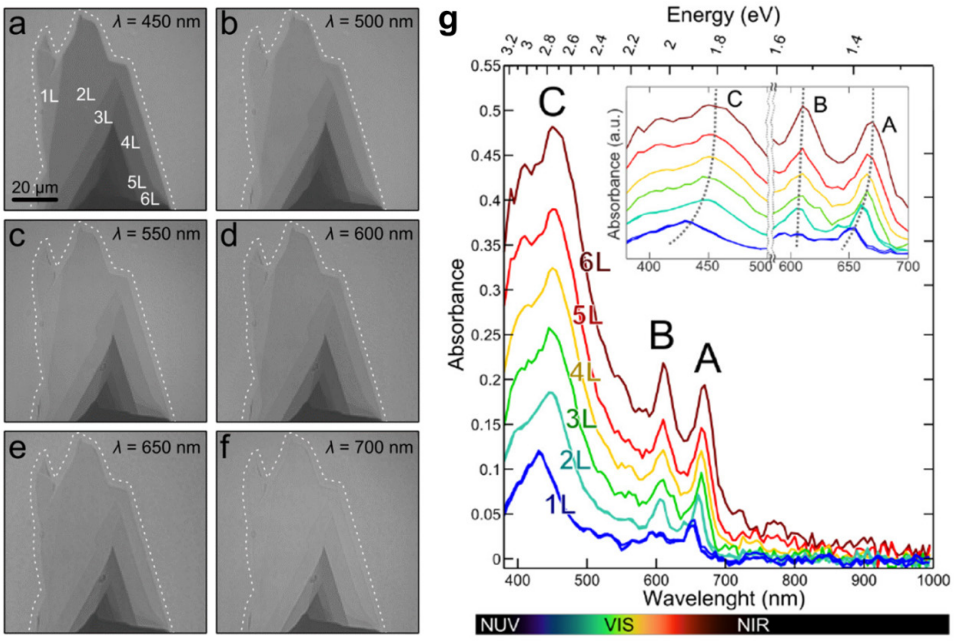


Figure IX.5. (a)–(f) Transmission mode images of a MoS_2 flake acquired at different wavelengths, selected with a tuneable monochromatic light source. (g) Absorbance versus wavelength, extracted from the sequence of MoS_2 images on a flake with regions of different thicknesses ($N = 1$–6), for different wavelengths. Adapted from [1431], © IOP Publishing Ltd.

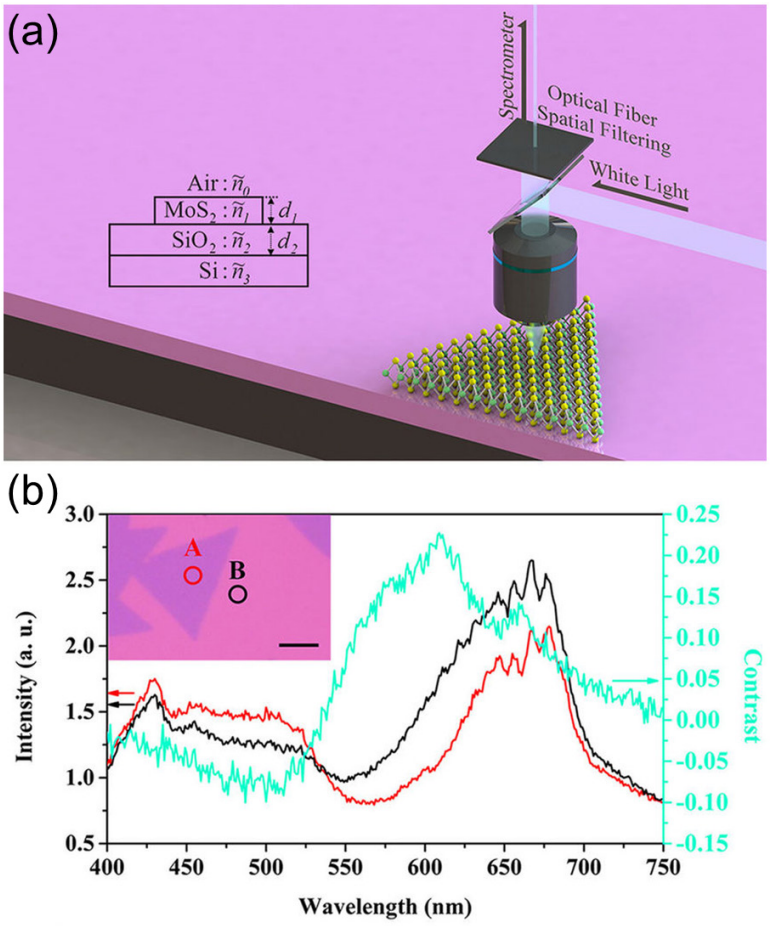


Figure IX.6. (a) Setup to characterize GRMs with micro-reflectance. (b) CVD grown MoS_2 studied by micro-reflectance. Two spectra are acquired on (A) MoS_2 and on (B) the SiO_2/Si substrate and the optical contrast is extracted from them. Adapted from [1428], CC BY 4.0.

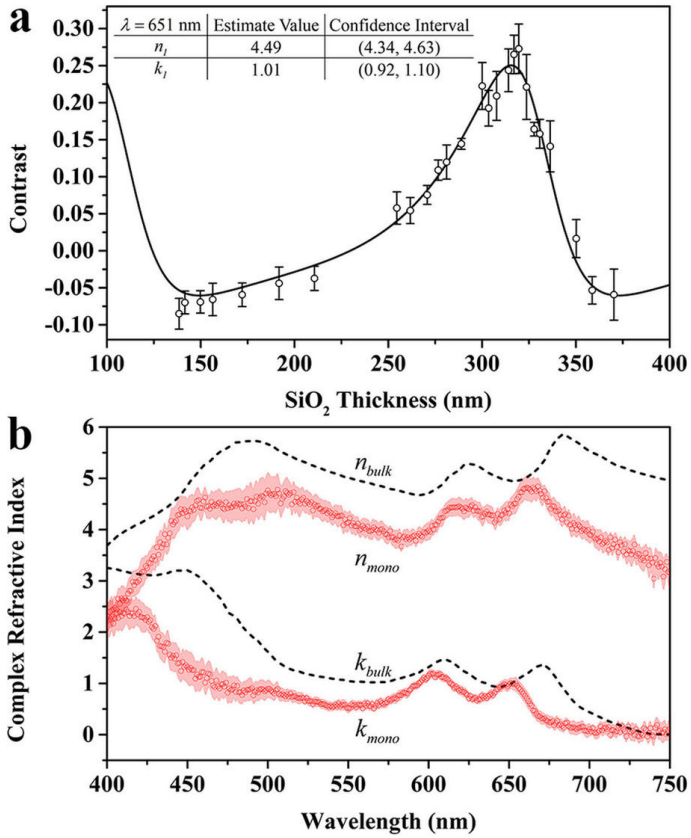


Figure IX.7. (a) Optical contrast for 1L-MoS_2 on SiO_2/Si with different SiO_2 thicknesses. The datapoints are fitted to a Fresnel law using the refractive index of 1L-MoS_2 as fitting parameter. (b) refractive index of 1L-MoS_2, compared with the bulk value. Adapted from [1428].

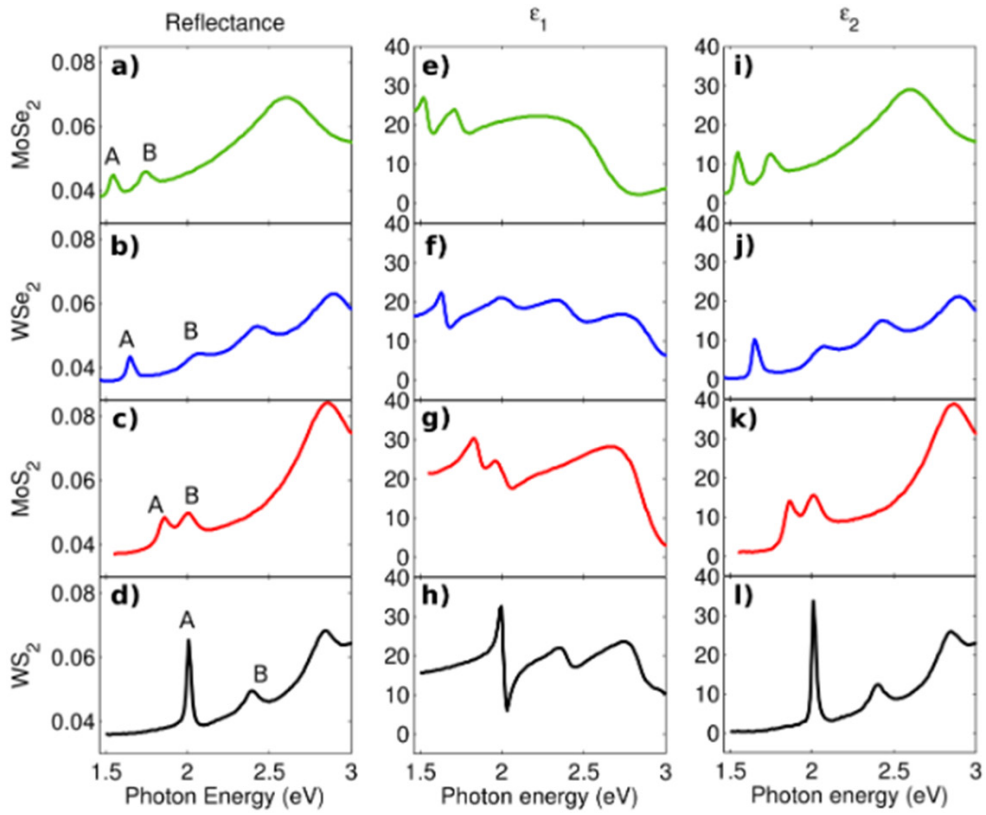


Figure IX.8. (a)–(d) Reflectance spectra for 1L-$MoSe_2$, WSe_2, MoS_2, WS_2. (e)–(h) Real part and (i)–(l) imaginary part of the dielectric function. Adapted from [1198], © Springer Nature.

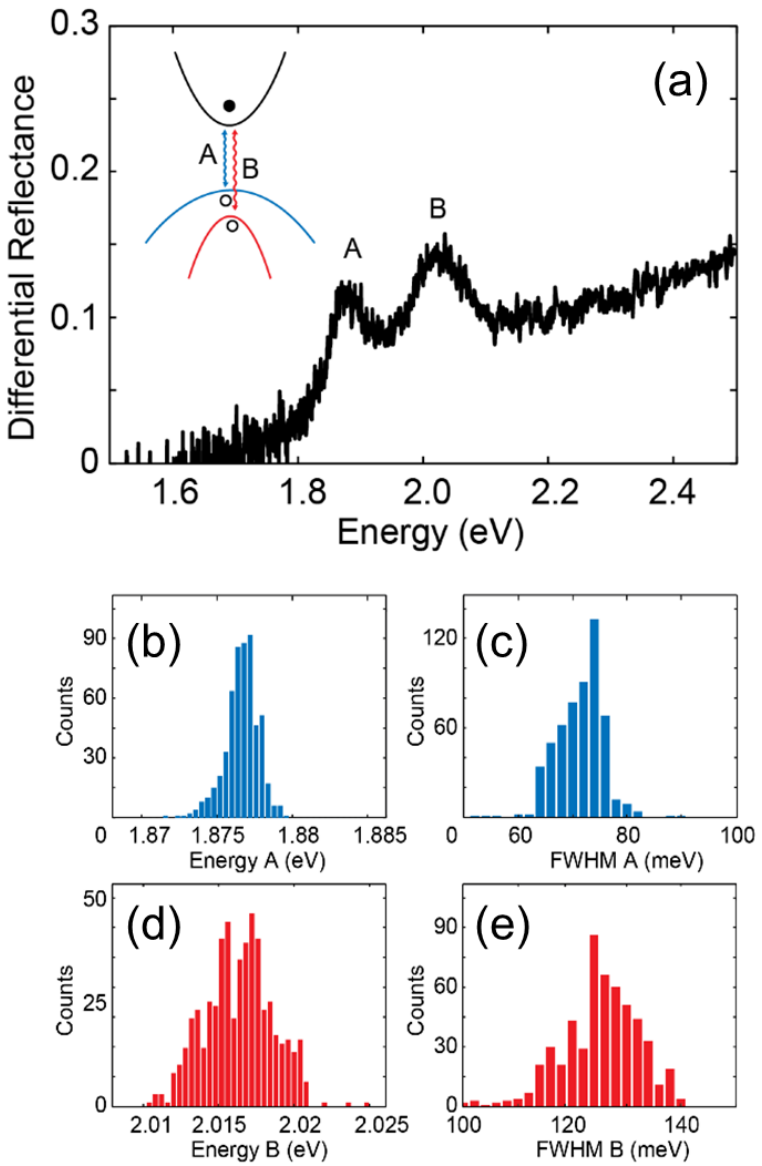


Figure IX.9. (a) Differential reflectance of 1L-MoS_2 grown on Sa. (b) and (c) Histograms of A and B exciton energy for 550 flakes. (d) and (e) Histograms of FWHM of A and B excitons. Adapted from [1429], CC BY 4.0.

imaging. Measured, apparent AFM heights of LPE GRMs are overestimated due to the presence of residual solvent. In general, accurate height measurements on inhomogeneous surfaces (such as flakes deposited on a substrate) are challenging due to contributions from capillary forces and adhesion, which depend on the material and measurement parameters [1438, 1439]. In addition, crosstalk between electrostatic and topographic signals [1214, 1215] can occur, leading to a bias of the height.To overcome these problems and obtain N from apparent height values, a step height analysis procedure was developed in Refs. [176, 185, 186, 190]. Incompletely exfoliated flakes showing clear terraces are first examined and the height of a various steps are recorded. These terrace step heights will always be a multiple of the apparent 1L thickness. The apparent measured SLG height can be 1–2 nm, much greater than the theoretical thickness [176, 185, 188, 190, 240, 1407]. Raman and PL analysis can be conducted in order to make sure that the thinnest objects measured are really SLG [176, 185]. The apparent SLG height can then be used to convert the apparent measured AFM thickness to N. For statistical analysis, it is recommended to record the height of at least 100–150 flakes. If the thickness varies across the flake, the mean value should be taken. From such statistical analysis, population histograms can be constructed. These are typically log-normal [185, 186, 188, 190, 1437] (also in the case of flake length). If this is not the case, the counting and/or imaging may be biased. e.g., if reaggregated rather than individually deposited flakes are included in the counting, this will lead to a deviation from the log-normal shape at the thicker end of the thickness distribution histogram. On the contrary, if surfactant and solvent residues are included in the counting, a deviation is obtained on the smaller end of the length distribution histograms. From these histograms and the statistical analysis, the

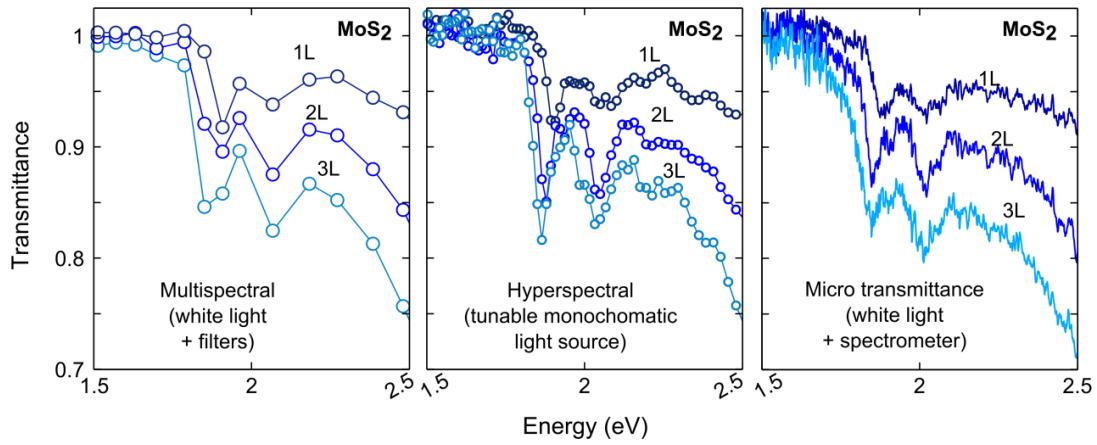


Figure IX.10. Comparison between different methods to measure the optical properties of 1L, 2L,3L-MoS_2. In multispectral imaging narrow bandwidth filters (10 nm FWHM) are used to select the wavelength (the wavelength resolution is limited by the number of filters). In hyperspectral imaging, the illumination is provided through a white light source connected to a monochromator (2–3 nm resolution). In micro-transmittance, white light is collected through an optical fiber (acting as a confocal pinhole) and sent to a CCD spectrometer (~1 nm resolution). Adapted from [1436].

Table IX.1. Comparison between different optical microscopy methods.

Method	Area	Spectral resolution	Measurement time
Multi-spectral	~10 000 μm^2	~20–100 nm	10–30 min
Hyper-spectral	~10 000 μm^2	~1–5 nm	30–60 min
Micro transmittance	~1–4 μm^2	~1 nm	~0.1–5 s

arithmetic number mean for length and thickness is obtained.

Since AFM can be used to measure both flake thickness and lateral dimensions, for each flake of a given thickness, the volume can be estimated as thickness (N) × length(L) × width(w). This allows for the calculation of the volume-fraction-weighted mean layer number, $\langle N\rangle_{Vf} = \sum N^2LW / \sum NLW$, where the summations are over all flakes. This is an alternative measure of thickness which reflects the fact that mass the tends to be concentrated in thicker flakes (the difference between arithmetic and volume fraction weighted mean is akin to the difference between number-average-molecular-weight and weight-average-molecular-weight in polymer physics [1440]). Arithmetic and volume fraction weighted mean values are typically related linearly, therefore both are an adequate measure of thickness [236].

Conductive SPM, like Kelvin probe microscopy (KPM), beside imaging capabilities, can be used to investigate charge transfer in exfoliated GRMs [277], while conductive AFM, providing localized current injections, can be used to locally modify the GRM chemistry, e.g. directly drawing conducive paths in GO films on SiO_2 [1441].This can also be used to probe other electronic properties, such as piezoelectric effects [1442].

IX.1.2.2. Grown and transferred GRMs

When referring to grown materials measured heights can be affected by artefacts, i.e. crosstalk between electrostatic and topographic signals [1443, 1444], or can be overestimated due to the presence of adsorbates between substrate and 1L-GRMs [1445]. By combining two of the most employed measuring modes (contact and dynamic), these can be minimized and more accurate height values obtained. Recording secondary signal channels such as phase (in dynamic mode) or lateral force (in contact mode) is useful in revealing information such as different local mechanical and/or electrical properties [1446] or different polymorphic structures [1447] sometimes difficult to detect, or even hidden, in topographic images [1443–1445, 1447]. Dynamic and contact modes measurements can be performed at RT, purging the chamber with N_2 to decrease the relative humidity and minimize capillary forces between tip and sample surface. Details about measuring modes in AFM can be found in Refs. [1448, 1449].

Figure IX.12 shows representative images of graphene layers grown on different substrates acquired in dynamic mode. In this mode, which employs the oscillation amplitude as feedback parameter [1448], the durability of the AFM probes (i.e. tip sharpness) is usually larger than in contact mode, since the tip gently [1450] taps the surface during the scanning [1446, 1451]. Probes with nominal force constant values ~3 nN nm^{-1} and resonance frequencies ~75 kHz are used. The most characteristic features are the pleats, commonly referred to as wrinkles, figure IX.12. These correspond to pleated/folded SLG due to released stress caused by the differences in the thermal expansion coefficients between SLG and the substrate, during cooling after growth [1452, 1453], or to local accumulation of carbon material at defects between coalescing

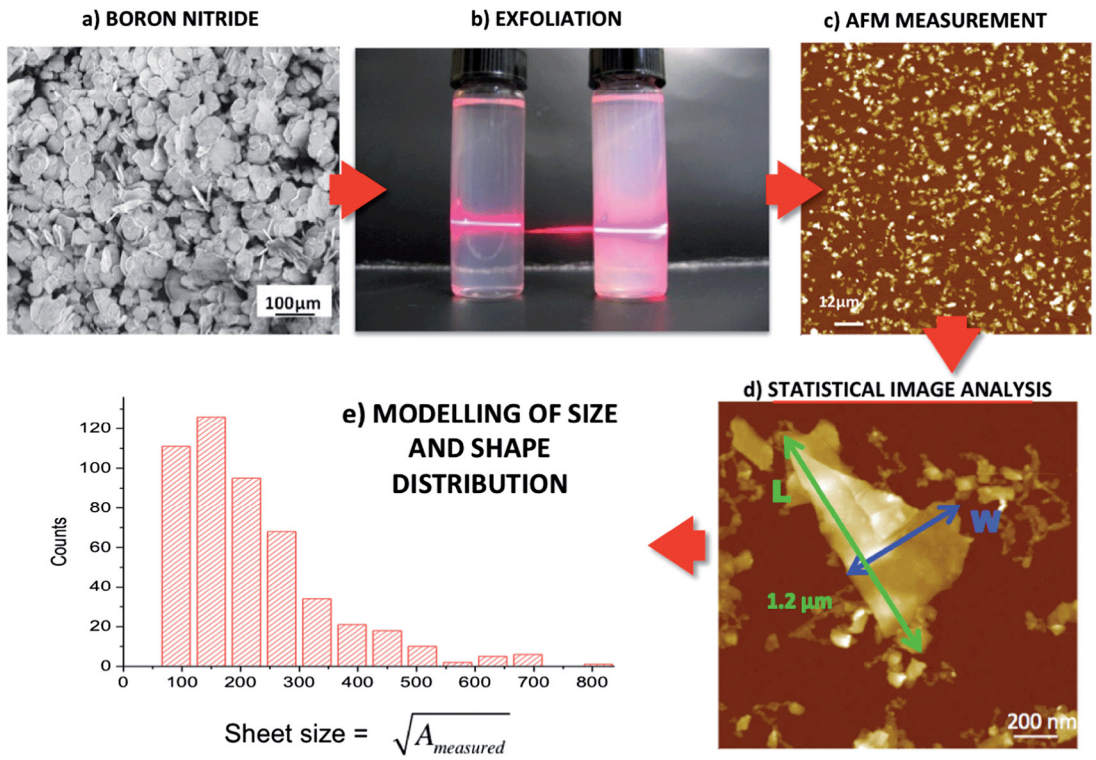


Figure IX.11. (a) SEM micrograph of bulk BN flakes. (b) Solutions of exfoliated BN in isopropanol. (c) AFM image of BN flakes on SiO_2. (d) Individual BN flake. (e) Histogram distribution of flake sizes. From [1437], with permission of The Royal Society of Chemistry.

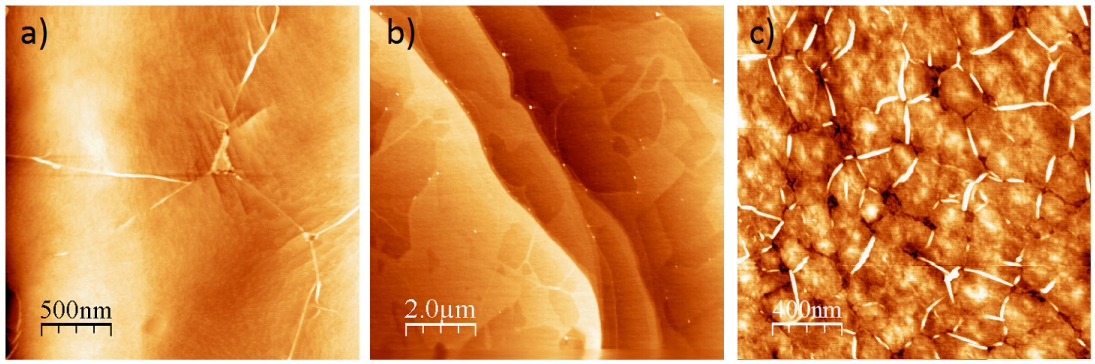


Figure IX.12. AFM topographic images measured in dynamic mode of SLG grown on (a) Cu foil by PDV, (b) SiC(0 0 0 1 by CVD, (c) quartz by r-(ECR-CVD) [774] z-scale: 0–12 nm.

grains of different orientation [630]. The maximum scanned areas are limited by the morphology of the substrate. For Cu foils this is usually $<5 \times 5\ \mu m^2$, due to the high overall roughness that can exceed several hundreds of nm for those areas. For graphene on SiC, the scanned area is only limited by the piezo range thanks to the flatness of the SiC wafer [627, 630] (for chemical mechanical polished on-axis wafers).

In dynamic mode, phase images can be acquired simultaneously with topography. Phase contrast is generally ascribed to differences in local energy dissipation and can reveal local mechanical and/or electrical properties [1446, 1451]. As shown in figure IX.13, this signal can be very useful to identify areas of different thickness. Top and bottom images in figure IX.13(a) illustrate this case, where circular brighter patches corresponding to BLG areas and are distinguished in phase imaging due to their different dissipative properties arising from mechanical and electrostatic difference as a function of N [1454]. Damaged areas in transferred layers (figure IX.13(b)) or covered areas in sub-SLG growth (figure IX.13(c)) can be identified in phase images. However, phase images can also be misleading since the contrast is very sensitive to the measuring parameters (oscillation amplitude and control setpoint [1455, 1456]). This is shown in figure IX.14, where phase contrast can be turned on and off at will, and even reversed, by changing the measured amplitude. There is no fixed recipe that ensures a good phase contrast, and tuning of the

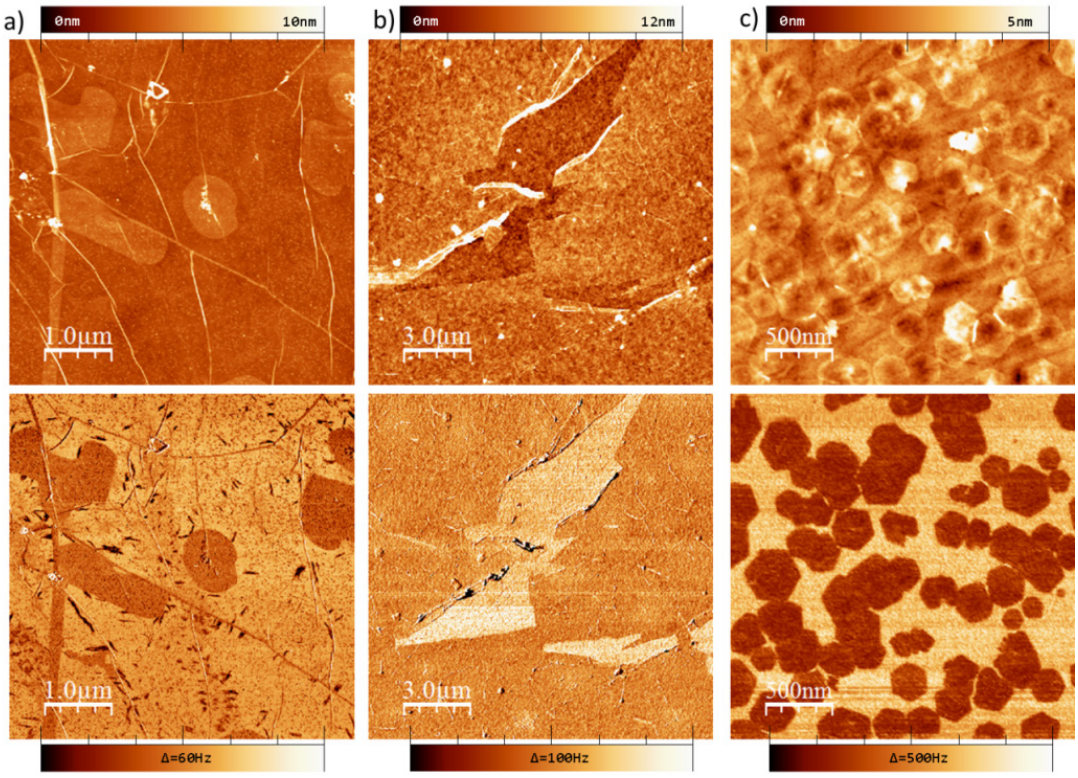


Figure IX.13. Simultaneous topographic (top row) and phase (bottom row) AFM images in dynamic mode of (a) and (b) CVD-graphene transferred to SiO_2. (c) Flakes grown by r-(ECR-CVD) on quartz at submonolayer coverage.

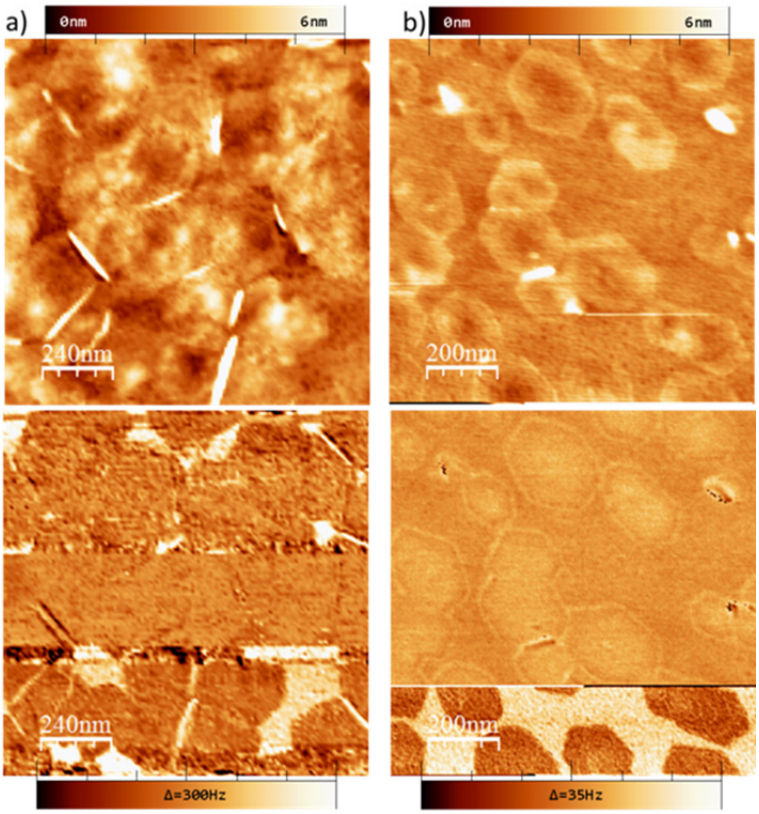


Figure IX.14. Simultaneous topographic (top row) and phase (bottom row) AFM images measured in dynamic mode of graphene flakes grown by r-(ECR-CVD) on quartz at submonolayer coverage. (a) Phase contrast between graphene and substrate disappears in the center of the image after changing the amplitude setpoint. (b) Phase contrast between graphene and substrate is reversed at the bottom of the image by increasing the amplitude setpoint.

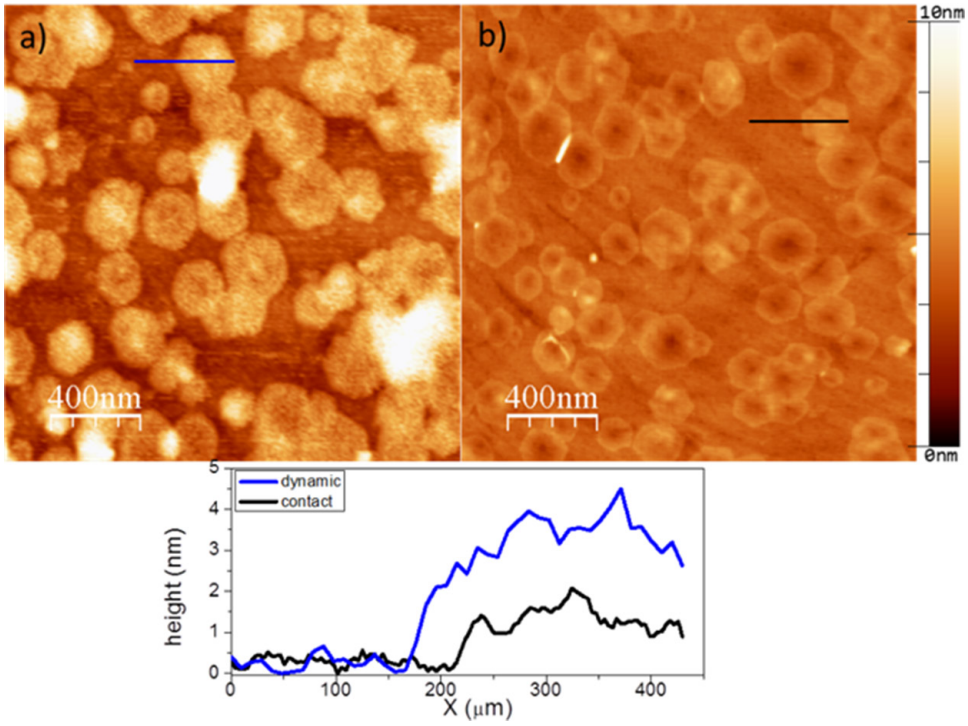


Figure IX.15. Topographic images of graphene flakes on quartz measured in (a) dynamic and (b) contact mode. Bottom: height profiles from the corresponding lines marked in the above images. The thickness measured on the same sample is different, depending on the mode used.

measuring parameters is necessary. Small amplitudes and amplitude set-points $>$ 50% of the cantilever free amplitude usually enhance the phase contrast [1456]. The main disadvantage of using dynamic mode stems from the possible crosstalk between tip and sample surface. This is particularly critical in heterogeneous surfaces, with areas presenting different mechanical, electrostatic and/or hydrophobic/hydrophilic nature, and can lead to wrong N determination [1443, 1457]. This is illustrated in figure IX.15 graphene on quartz at submonolayer coverage. The thickness of the flakes measured in dynamic mode is ~3 nm, almost twice that in contact mode. This is due to the influence of uncompensated electrostatic forces, particularly affecting samples grown on insulating substrates. Ref. [1443] suggested to use KPM to avoid this problem [1452]. However, when dealing with insulating substrates, like in figure IX.15, it is not so straightforward, and the alternative is switching to contact mode (figure IX.15(b)). In contact mode, the lifetime of the probes is usually shortened compared to dynamic mode [1448] (tip radius increases after successive scans and resolution worsens), but height artefacts as those shown in figure IX.15 are seldom encountered. Commercial probes of low force constant (0.05–1 nN nm^{-1}) are used to minimize damage to the sample. Similar to the dynamic mode, secondary signals can be recorded when measuring in contact [1458]. Lateral force imaging can reveal differences in friction between tip and surface [1458]. This is particularly interesting GRMs since they usually present a low ($<$0.1) friction coefficient [1459], which yields images like figure IX.16.

The SLG areas are distinguished in lateral force images, facilitating flakes location, coverage quantification and size analysis. With lateral force images it is also possible to visualize the internal structure of SLG grains, masked in topographic images due to surface roughness. In figure IX.16, lateral force images reveal the multilayer structure of some flakes.

To better visualize these internal features in graphene flakes, soft tips (0.05 nN nm^{-1}) and forces between 5 and 10 nN are recommended to avoid wear [1455]. Lattice-resolved lateral force images can also reveal the lattice periodicity, figure IX.17. To acquire these images, small scans are performed (5–20 nm lateral sizes), at frequencies ~2–3 Hz, with low feedback parameters. Applied forces are ~5–15 nN. These images do not correspond to true atomic resolution like routinely measured in STM, but lattice orientation and average lattice parameters can be determined.

The AFM tip can also be used to displace the samples. Ref. [774] swept the tip to determine N in fully covered samples. This should be used as last resort, after morphological characterization, since the tip can be irreversibly damaged due to the high ($>$100 nN) forces needed to remove the material. This damage can be visualized by recording force-distance curves prior and after sweeping. Figure IX.18(a) compares these two curves, and shows that adhesion is one order of magnitude larger after the experiment. This is mainly due

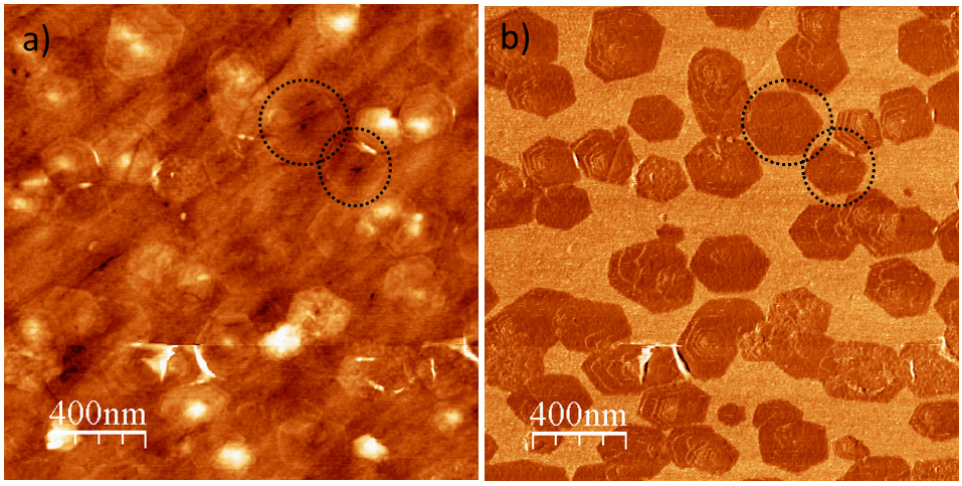


Figure IX.16. Simultaneous (a) topographic and (b) lateral force images of graphene flakes on quartz measured in contact mode. Dotted circles mark flakes location, hardly distinguishable in topography, but resolved in lateral force images.

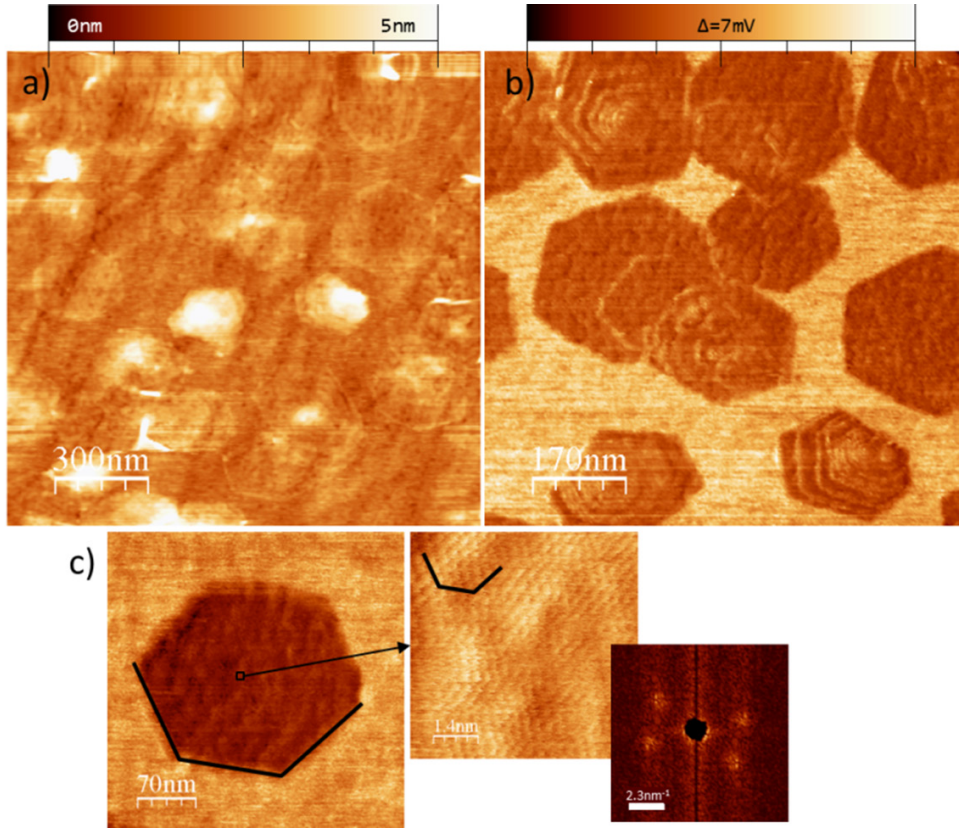


Figure IX.17. Simultaneous (a) topographic and (b) lateral force images of graphene flakes on quartz in contact mode. The multilayer structure of some flakes can be distinguished in lateral force images. (c) High resolution lateral force image. Right: high resolution image acquired at the marked area. Inset: fast Fourier transform (FFT) of the high-resolution image to better observe the lattice periodicity.

to the increase in tip radius, which translates in a worsening of the resolution [1460, 1461]. Taking this into account, sweeping experiments should performed as follows. 1) an area is scanned either in dynamic or contact mode to check the morphology prior to sweeping. 2) contact mode is selected, and the same area (2–5 μm lateral size) is repeatedly scanned while increasing the scan rate (5–10 Hz), decreasing the number of points (256/128) and increasing gradually the applied force. By controlling the topography and lateral force signals, one can detect the onset of the removal of the material. Once the critical applied force is reached, the scanning is repeated during several images to ensure the complete displacement of the material. 3) To visualize the swept area it is recommended to switch to dynamic mode, to avoid spreading the accumulated material at

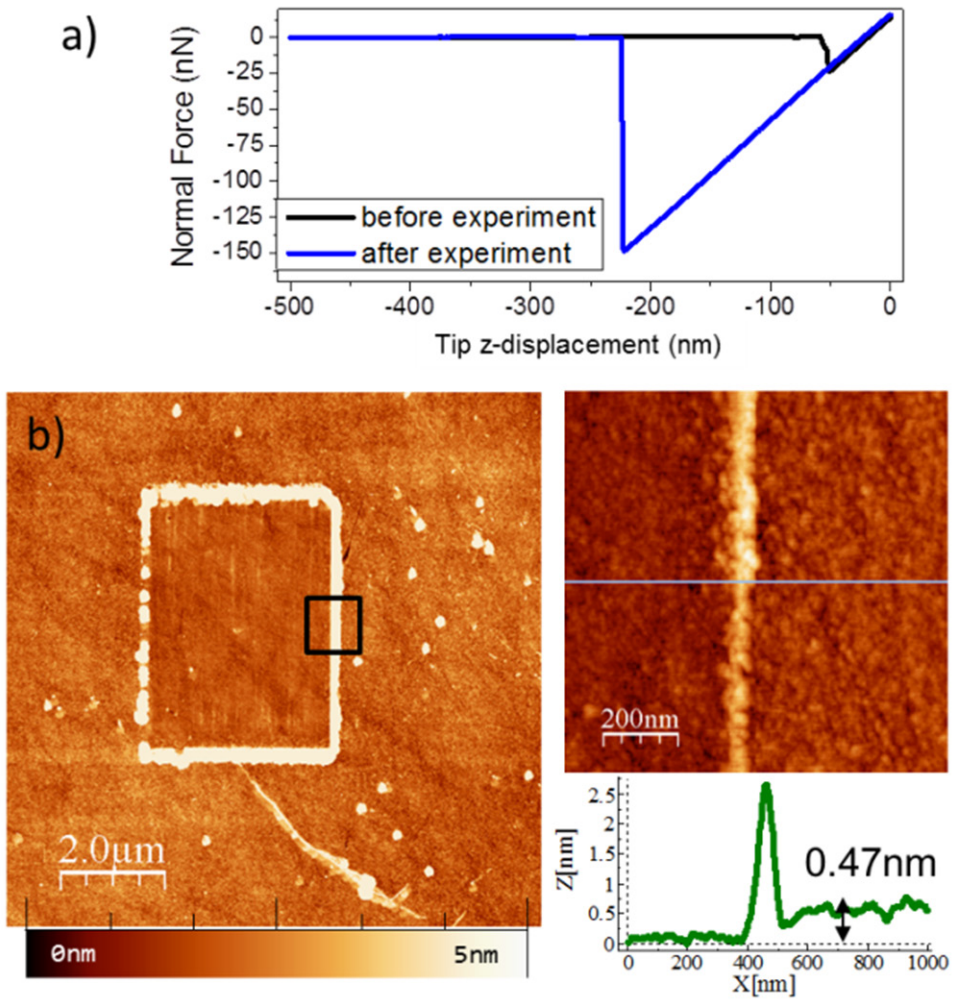


Figure IX.18. (a) Force versus distance curves acquired before (black) and after (blue) sweeping. Only the retract branch is plotted to better visualize the increase in the adhesion force. (b) Topographic image showing the rectangular area with SLG removed. From line profiles taken across the edge, the thickness can be obtained as in as pointed out scanning the inset in (b).

the edges of the scanned area. To acquire final image is better if the scan is performed at 90°, since debris are accumulated at the lateral edges (fast scan direction). Figure IX.18 (b) summarizes the results of this procedure.

Depending on applied force, the material swept by the tip can be either the contaminant layer adsorbed on SLG exposed to air, if forces are restricted to few nN, or the complete layer for forces up to hundreds nN.

KPM can give information on thickness, layer-dependent distribution of charges, electrical potential and work function [1462]. Measurements are performed in dynamic mode, using the amplitude as feedback channel for topographic determination, and the retrace mode for surface potential acquisition, at a lift distance between 15–20 nm. NT-KP tips from Next-Tip S.L. provide very good resolution for KPM [1463].

Surface potential maps can be used to discriminate between N, figure IX.19, for graphene grown on SiC. While the topography image (figure IX.19(a) top) is dominated by SiC terraces, a contrast is observed at the step bunches in surface potential images (figure IX.19(a) bottom), a fingerprint of the presence of BLG [1462, 1464]. The dark contrast corresponds to SLG and the brighter contrast areas, at the step bunches, indicate BLG. Small islands (300–500 nm in diameter) decorating the terraces are assigned to BLG from their contrast. This contrast observed in surface potential as a function of N is ascribed to different work function values for different N, due to different substrate induced doping and different energy dispersions of SLG and BLG [749, 1465, 1466].

When measuring in ambient conditions, aging of the sample can affect the contrast in surface potential. This is shown in figure IX.19(b), where the same sample is measured after growth and several days later. In addition to the presence of small clusters (2–5 nm high) in the topographic image, due to adsorbates, the corresponding surface potential image shows negligible contrast between terraces and steps bunches. This is due to the passivation layer that screens any electrostatic difference between SLG and BLG areas. Annealing in controlled atmosphere above 150 °C is enough to recover the original KPM signal.

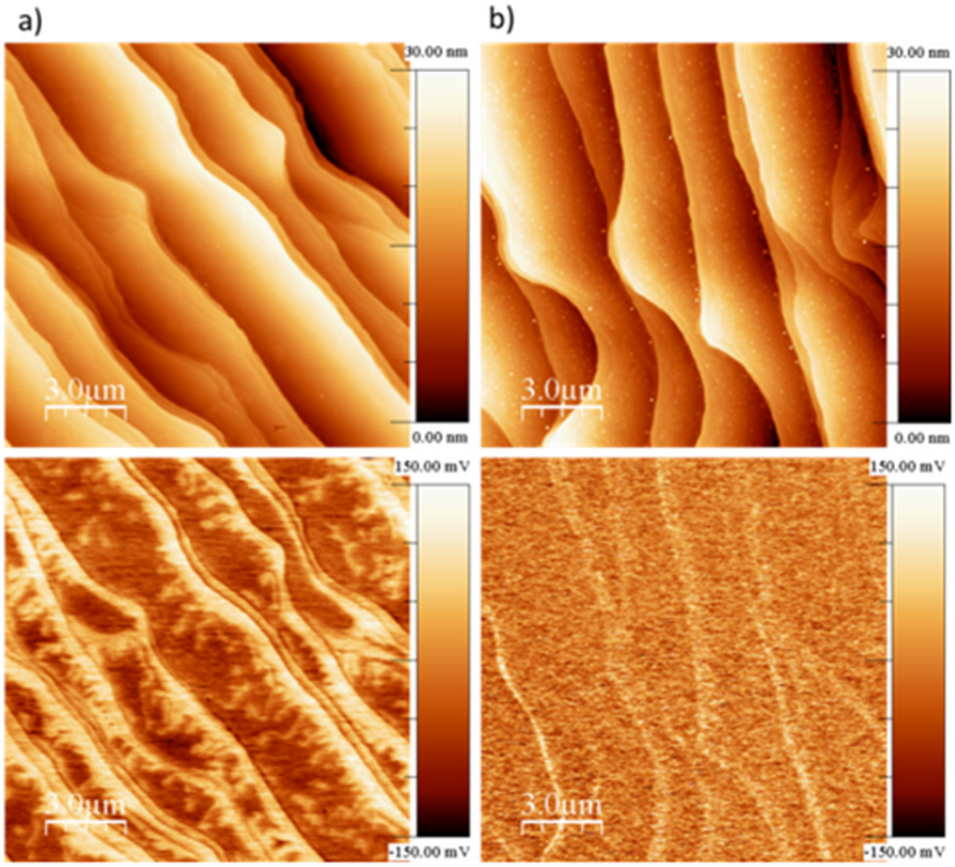


Figure IX.19. Simultaneous topographic (top) and surface potential (bottom) images acquired on graphene on SiC. (a) Measurements performed after sample growth. (b) After several days, with the sample kept in ambient conditions.

KPM was also employed to investigate the changes in work function upon controlled doping [1377]. By definition, the measured surface potential (V_{SP}) is related to the work function (Φ_S) [1467] as:

$$eV_{SP} = \Phi_T - \Phi_S \qquad \text{(IX.6)}$$

where Φ_T is the work function of the tip, and e is the electron charge. Therefore, changes V_{SP} potential for differently doped samples reflect changes in Φ_S. The critical point in these studies is ensuring that the tip conditions (particularly, Φ_T) do not change. To monitor this, a reference sample of known Φ_S (i.e. HOPG, Au) is measured between samples.

To preserve tip conditions, these comparative studies can be done using Kelvin probe force spectroscopy (KPFS) instead imaging acquisition [1468, 1469]. KPFS consists of applying a varying DC bias, to the tip, located above a single spatial location, while monitoring the dynamic response of the cantilever using heterodyne detection [1469]. The force-voltage or frequency-voltage (depending on the detection mode used [1457]) curves have parabolic voltage dependence, and the position of the maximum of the fitted parabola yields V_{SP}. Two representative curves are shown in figure IX.20(a), for SLG doped with Au NPs, for different NP concentration [1377]. The difference in the maximum position of the curves corresponds to a difference in the E_F[1377]. For comparison, several curves are acquired on different locations, and measurements are repeated altering the sample order, to ensure reproducibility of measured differences in surface potential. Similar curves are measured in the reference sample after each round. Figure IX.20(b) compares the results of gradual doping with Au NPs, reflected in a gradual variation of the surface potential measured by KPM [1377].

IX.1.3. Transmission electron microscopy

TEM techniques can be used to investigate individual flakes from solutions, measuring their lateral size and thickness, the characterization of their crystal structure and chemical composition. Cross section TEM can also be used to give information about N and their interaction with the substrate [688] (see e.g. figure IV.25(e). Since TEM provides a higher resolution compared with SEM and higher throughput compared with AFM, low resolution TEM is frequently used to analyse the shape and lateral size of LPE GRMs statistically [131, 174, 176, 177, 184–186, 188, 190, 239–242, 244, 1470]. To perform these measurements the dispersion is drop-cast onto a TEM grid. Here, it is important to use dilute dispersions (i.e. optically transparent if the material absorbs in the visible) to avoid reaggregation. For statistical length analysis, the longest dimension is measured and denoted as length and the direction

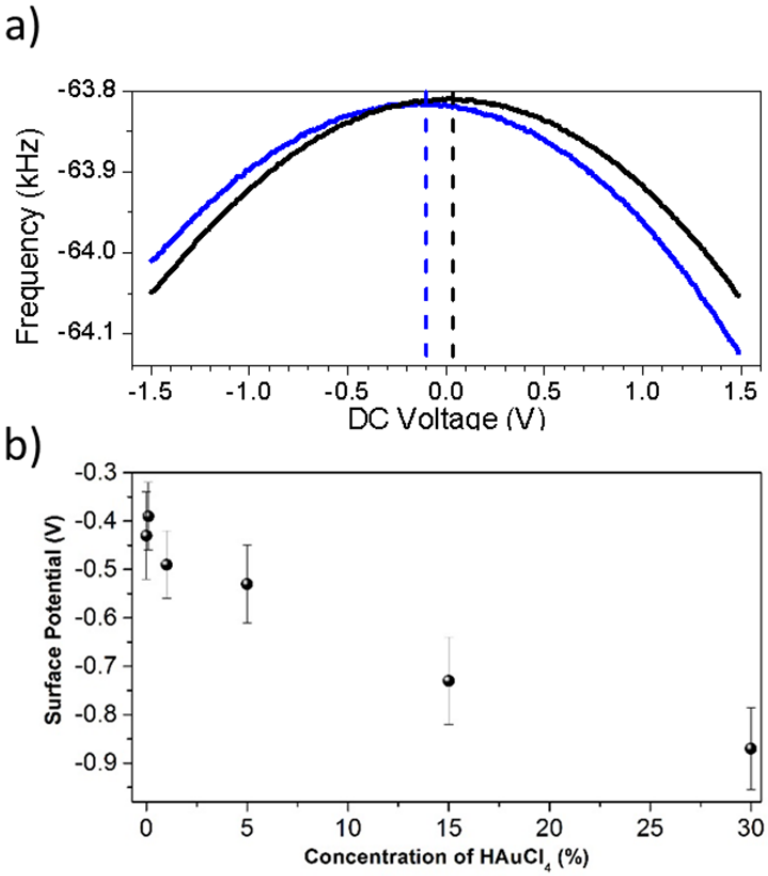


Figure IX.20. (a) Frequency versus voltage curves acquired on SLG on SiO_2 doped with HAuCl4 for two concentrations [1377]. V_{SP} corresponds to the maximum of the parabolas, marked with dashed vertical lines. (b) The variation of the measured V_{SP} reflects the tuning of E_F upon doping with Au NPs nanoparticles. (Reproduced from [1377], with permission from Elsevier.)

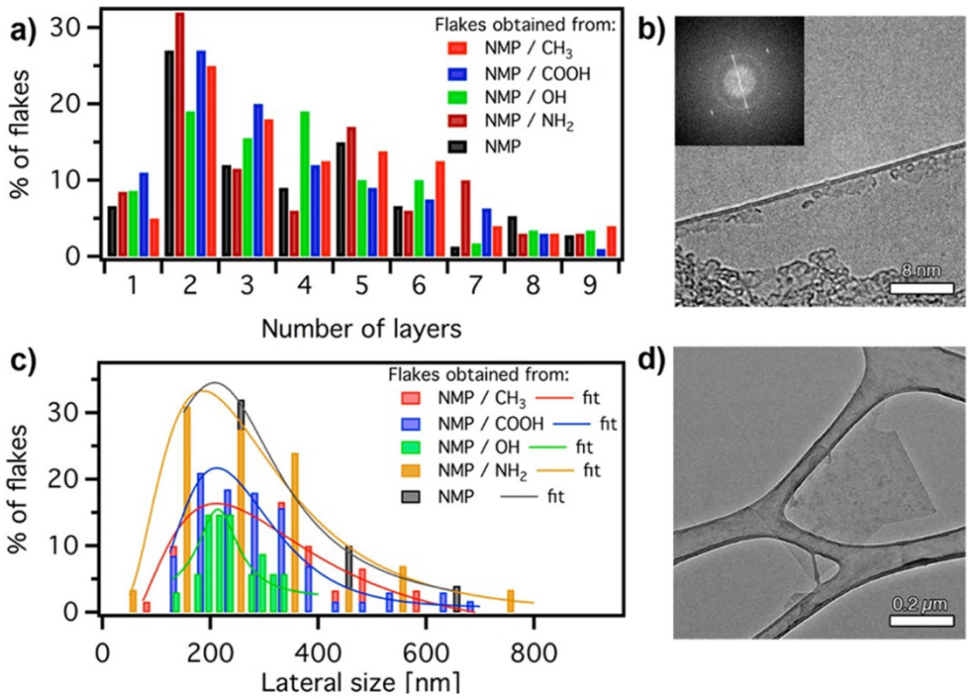


Figure IX.21. TEM analysis of graphene flakes exfoliated in NMP and different Alkanes. (a) Histogram of N. (b) HREM of folded edge. (c) Flake size distribution; data fitted with a log normal function. (d) TEM micrograph of graphene flake. From [235], with permission of The Royal Society of Chemistry.

perpendicular is denoted as width [131, 174, 176, 177, 184–186, 188, 190, 239–242, 244, 1470]. Depending on the expected flake size, continuous film grids can be beneficial to avoid small flakes falling through the holes. When drop-casting, the best results are obtained when the grid is placed on a filter paper to wick away access solvent [131, 174, 176, 177, 184–186, 188, 190, 239–242, 244, 1470]. During image acquisition, it is important to adjust the field of view according to flake size. Without size selection, samples can be very polydisperse with lateral sizes ranging from 20 nm-a few μm. This is extremely challenging and requires recording higher magnification images as to not bias the statistics towards larger, more easily discernible flakes in wide-view images. Similar to the AFM statistics, the log-normal shape of the histogram can be used as a guide whether counting/imaging are biased [186, 188, 190]. In such cases, a comparison of the statistically determined mean length from AFM and TEM [186, 188, 190] suggests that ~150 counts are sufficient to obtain robust mean values.

In addition, thickness determination can be achieved from high-resolution electron microscopy (HREM) images. This is done by counting the number of (0 0 0 2) lattice fringes (see figure IX.21(b)) exposed in folded flakes [235] or by analyzing the electron diffraction pattern intensities from individual crystal [235], providing statistical qualification of the exfoliation process [235]. Additional functional properties can be engineered by decoration with either organic moieties or NPs. In this case, STEM imaging and elemental mapping can provide nanoscale characterization of the decoration and of the interface between NPs and GRMs [235, 288]. Electron beam damage can be limited by reducing the accelerating voltage, making it possible to use TEM for the characterization of blends between GRMs and organic complexes [288].

IX.1.3.1. Low-energy HRTEM

For structural characterization on the atomic level, aberration-corrected high-resolution transmission electron microscopy (HRTEM) is the method of choice. However, for very thin samples such 1L-GRMs, the interactions of energetic electrons with the material during imaging may result in permanent changes in the structure, also referred to as radiation damage. This can be both an obstacle for imaging, as well as a useful tool for manipulating matter at the atomic scales [1471–1474]. The best investigated damage mechanism is the so-called knock-on damage [1475], where the impact of fast electrons gradually removes atoms from the sample. From kinematic considerations [1476], it follows that these alterations can be prevented if a certain threshold energy is undercut [1477]. Depending on the GRM, acceleration voltages of 80 kV and less are required [1478]. At such voltages, in conventional TEMs without aberration correction, atomic resolution is not achievable as the resolution is worse than 0.35 nm already at 80 kV. Today's high-end TEMs are equipped with a corrector for the spherical aberration (Cs), and usually operate at acceleration voltages between 300 kV and 80kV. The resolution is ~0.8 Å at 300 kV and ~1.9 Å at 80 kV, which allows to resolve single atomic columns of many bulk crystalline samples. For SLG, the pristine lattice withstands 80 kV for a sufficiently high electron dose for HRTEM imaging with good signal-to-noise ratio (SNR), however edges and pores will be more quickly altered and much lower voltages are required [1478]. At voltages below 80 kV, the resolving power of Cs-corrected microscopes is however not sufficient as it is limited by the chromatic aberration Cc of the objective lens. In recent years this limitation has been tackled by two approaches: either the effect of chromatic aberration is reduced due to a reduced energy width of the primary electron beam by a cold field emission gun [1479] or by a monochromator (e.g. [1480, 1481]), or, most efficiently, by a chromatic aberration corrector [1482]. Ref. [1482] reported a microscope, the so-called Sub-Angstroem Low-Voltage Electron microscope (SALVE), equipped with a Cc/Cs corrector optimized for voltages between 80 and 20 kV. Even at 20 kV, this microscope can resolve individual C atoms with a resolution < 0.14 nm [1482] over a wide field of view of 4096 $\times$ 4096 pixel. With the SALVE microscope, sub-Å resolution resolution is achieved for voltages between 40 kV (0.92 Å) and 80 kV (0.76 Å), and the achievable contrast for the same electron dose is increased [1473, 1484].

Example low-voltage HRTEM images of GRMs are shown in figure IX.22. The diffractograms of SLG and MoS_2 (30 kV images) feature reflections up to the third and fourth order. A good agreement between image calculation and experiments can be seen (see linescans A6/B6).

The tunable low acceleration voltage allows for its optimal choice for each sample. The chosen one is a compromise between the resolving power (which is higher at higher voltages) and knock-on damage. In addition, especially non-conducting material, suffer from ionization effects, which usually increase at lower voltages [1473, 1484]. Sophisticated sample preparation methods are then needed to reduce these effects. The following techniques provide good results: the production of clean surfaces [1485], sandwiching the radiation-sensitive material between two SLGs [1486], and isotope substitution [1487]. To summarize, the choice of the acceleration voltage depends on the trade-off between resolution, knock-on damage and ionization. Appropriate sample preparation is crucial for reaching the voltage-dependent resolution limits. The Cc/Cs-corrected technology for TEM is regarded as a major improvement of the current technology which can be judged from the single-shot images of SLG in figure IX.23, at 80 and 30 kV from the new (Cc/Cs) technology compared with the old (Cs) technology (all single-shot images). Reliable information from HRTEM images about pore sizes distribu-

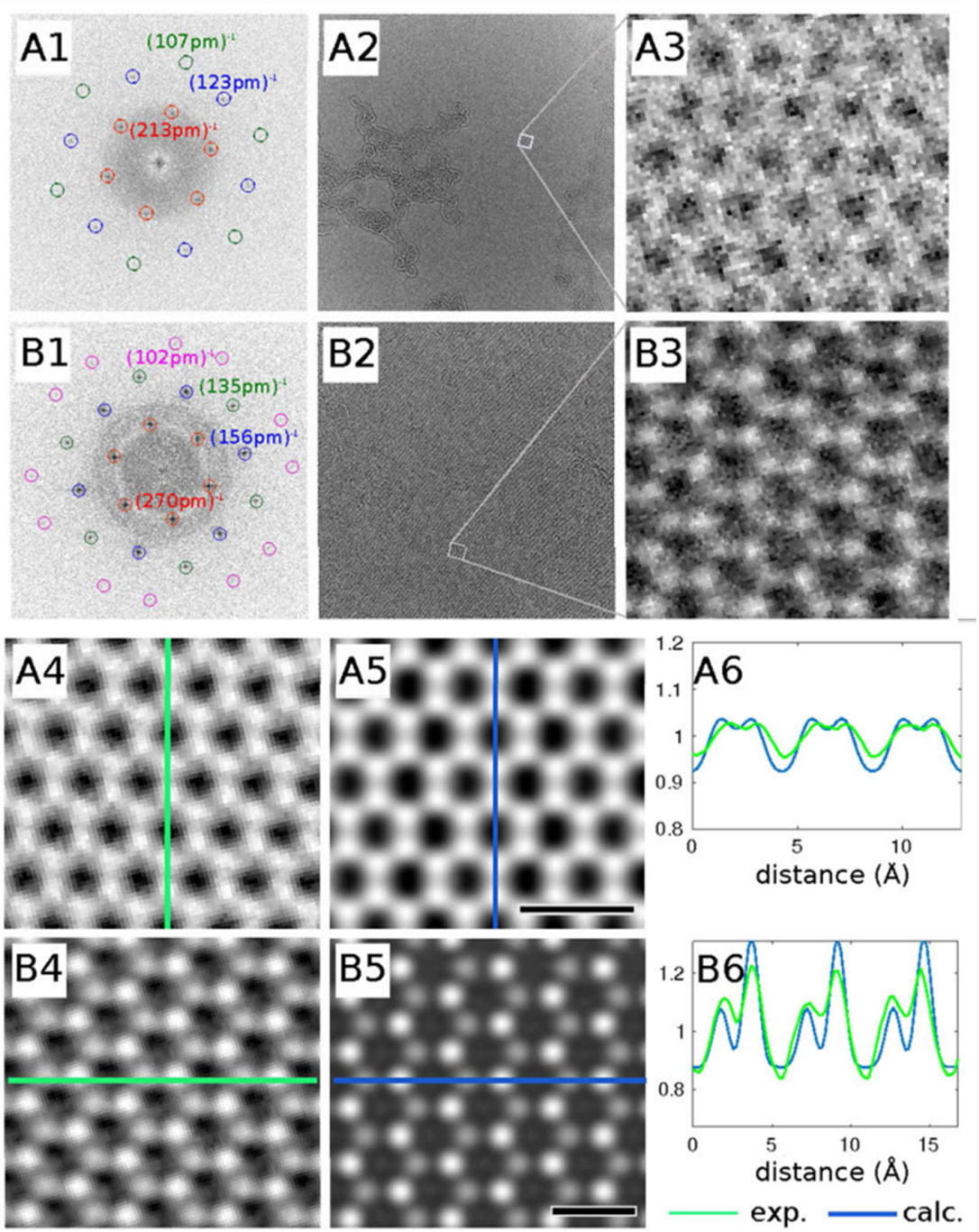


Figure IX.22. Experimental and calculated Cc/Cs-corrected HRTEM images of (A) SLG [1482] and (B) MoS_2 at 30 kV. (A1) and (B1) show the Fourier transforms of (A2) and (B2). The outmost reflections demonstrate a resolution ~1 Å. (A3) and (B3) show atomic resolution with magnified areas. The SNR can be improved by averaging the experimental images (A4) and (B4). The results are in good agreement with simulated HRTEM images (A5) and (B5) [1483]. The line scans (A6) and (B6) show the intensity profiles along the marked lines in the experimental and the simulated images. Adapted from [1482], copyright by the American Physical Society.

tions in GRMs, or edge structures can now be obtained at lower voltages with higher resolution and higher contrast [1482]. In addition, due to the wide field of view of 4096 × 4096 pixels, this microscope is also very useful for dynamic studies and manipulations at the atomic scale.

IX.1.4. STM

STM is a powerful tool for graphene characterization. It is generally used inside UHV chambers for *in situ* structural and electronic studies at the atomic level. When the graphene samples are measured in ambient conditions or after *ex situ* manipulations, AFM is a preferred tool as force maps are more directly interpreted in terms of topographic features of the sample. STM images, in contrast, are proportional to the tunnel current which is sensitive to the electronic structure of the tip and surface [1488, 1489]. When samples are characterized in ambient conditions, data acquisition can be quite difficult as atmospheric

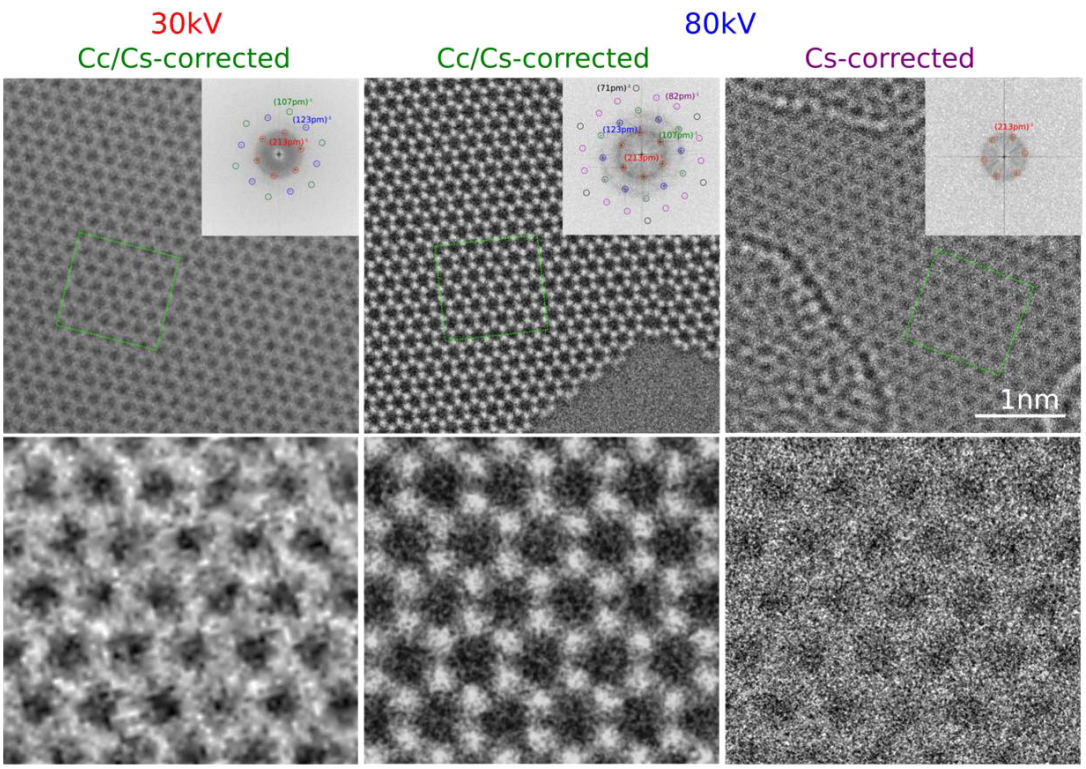


Figure IX.23. SLG HRTEM images obtained at 30 kV (left) and 80 kV (middle) in the Cc/Cs-corrected SALVE microscope and at 80 kV (right) in the Cs-corrected TITAN-microscope. The inserts show the corresponding Fourier transform patterns. The $(\bar{1}\,\bar{1}\,2\,0)$, $(0\,\bar{2}\,2\,0)$ and $(1\,\bar{3}\,2\,0)$ reflections are encircled in red, blue, green, and purple, respectively. Adapted from [1482], copyright by the American Physical Society.

contaminants may intrude between tip and surface as they diffuse, thus provoking current instabilities and hindering high-quality data acquisition. After graphene exposure to ambient conditions, annealing in vacuum for a short period of time at ~ 250 °C before measurement is recommended in order to remove possible adventitious adsorbates. With respect to the acquisition mode, topography images at constant current are preferred as they are typically more stable and avoid tip crashes during measurements. Nevertheless, the use of constant-height or current-error images can also be useful in some cases for obtaining atomically-resolved images of local features [1490, 1491].

The atomic lattice of graphene can routinely be resolved with STM. A hexagonal lattice with a periodicity of 2.44 Å is normally observed for graphene and graphite samples. When imaging graphene, the smaller periodicity (1.42 Å) of the honeycomb lattice can sometimes also be resolved. Low voltages and high currents (short tip-sample distances) are recommended for obtaining atomic resolution images, with typical values ranging between 50–200 mV and 1–4 nA, respectively. Graphene superlattices of larger scale (1–2 nm) can also be resolved with STM images STM is the ideal tool for local measurements needing ultrahigh spatial resolution. STM has demonstrated its capabilities for resolving low-dimensional structural defects with unmatched atomic resolution. There are several defective structures that have been described by STM images. The most important 1d defective structures are wrinkles and graphene edges between different (rotational) domains. Figure IX.24 shows a representative STM image of a graphene on Pt(1 1 1) sample together with a representative LEED pattern of the same system [1035]. In the constant-current topographic image, a graphene pleat and some graphene nanobubbles can be seen. Profiles along this pleat show an apparent height ~ 2–2.5 nm. The origin of these structures is the difference between thermal expansion coefficients of graphene and Pt, which results in compressive strain during cooling. Graphene nanoscale dome-like structures, also known as nanobubbles, can also be resolved with STM images. In figure IX.24 (a) one is encircled in yellow and in figure IX.24(b) one is shown with atomic resolution. Structures submitted to compressive strain, like graphene pleats and nanobubbles, have been proposed to induce high pseudomagnetic fields, which lead to Landau quantization of the electrons when measured with STM at cryogenic T [632].

In figure IX.25 different point defects of a SLG/Pt(1 1 1) system are depicted. Figure IX.25(a) shows a single atom defect which can be explained in terms of an in-lattice heteroatom inclusion,–most likely a N impurity coming from the residual gas in the chamber [1492] Figure IX.25(b) displays a multiatomic vacancy which induced a reconstruction of a region ~ 1–2 nm. Although a dome-like local configuration can be expected one must take with caution the fact that

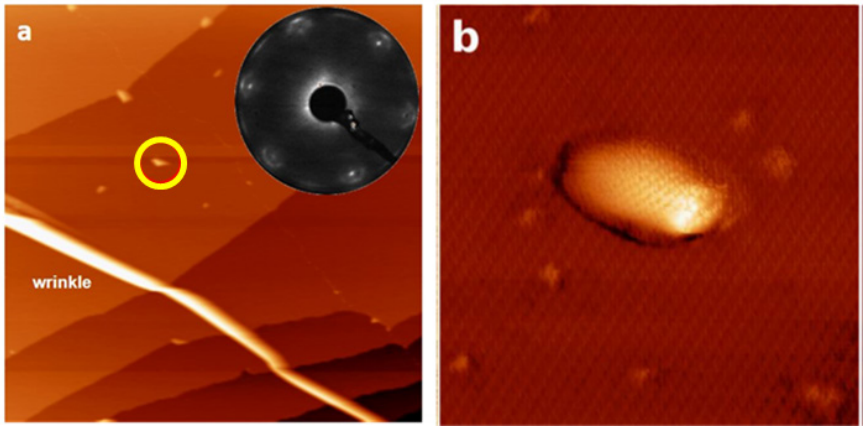


Figure IX.24. (a) STM image of a 200 × 200 nm^2 area of graphene grown on Pt(1 1 1), $I = 0.15$ nA, $V = 750$ mV. A SLG covers the whole surface. In the image a wrinkle/pleat and several nanobubbles, one of them is encircled in yelow, can be seen. The inset shows the characteristic LEED pattern of SLG on Pt(1 1 1). (b) High resolution STM image of a graphene nanobubble (20 × 20 nm^2, $I = 0.6$ nA, $V = 310$ mV) and few point-like atomic defects with atomic resolution. Figure a is adapted from [1035], with permission from Elsevier.

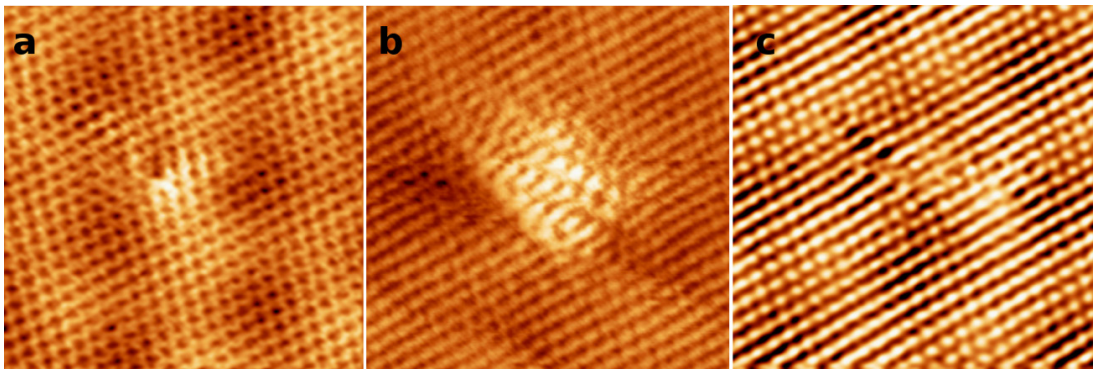


Figure IX.25. 5 × 5 nm^2 images showing graphene point defects on Pt(1 1 1). (a) 10 mV, 3.9 nA. (b) 10 mV, 2 nA. (c) 10 mV, 3.9 nA.

this region appears brighter, thus higher, in the STM images as electronic effects are normally occurring in the defective regions of graphene. Figure IX.25(c) shows a strain-induced lattice dislocation involving at least two unit cells of graphene.

IX.1.4.1. Graphene on metals

The formation of graphene has been mostly studied by STM on hexagonal metal surfaces, like the (0 0 0 1) for the HCP crystallographic structures, Ru, Co, Re, and the (1 1 1) for the FCC metals, Ni, Cu, Rh, Pd, Ir, Pt and Au, but it has also been observed to grow on non-hexagonal crystallographic surfaces such as Pt(1 0 0) [1031].

Moiré superstructures [902] arise from the electronic interference between two periodicities with a difference in lattice parameter and/or angle. In the present case moirés are originated by the interference between graphene lattice and metal surface beneath it. Figure IX.26 shows a ball and stick model of a moiré pattern for describing the different distances and angles occurring in moiré superstructures. With these parameters, models minimizing lattice mismatch can be used for describing the structure of graphene with respect to the metal substrate. Figure IX.27 presents the STM images of four moiré superstructures on SLG/Pt(1 1 1) that can be described with these structural parameters (see blue hexagons overlaid onto it). In every STM image, two periodicities can be seen: a short one, corresponding to atomic resolution, and a long one, corresponding to the moiré superstructure.

Depending on the reactivity of the metal, the interaction between graphene and metal substrate can range from van der Waals physisorption to strong bonded chemisorption. The interaction between substrate and graphene overlayer drives the measured STM corrugation and the mean distance from the substrate [901]. Typical corrugations of moiré supperlattices range between 0.2–1.2 Å for graphene grown on metal surfaces, and typical corrugations for the atomic lattice range between 0.1–0.3 Å [901].

Figure IX.28 presents a series of defective structures appearing on the SLG/Pt(1 1 1). This figure shows how graphene adjusts itself to the lowest energy conformation when grown on surfaces, thus deforming its atomic structure to fit to the substrate and other graphene grains in the vicinities. Figure IX.28(a) shows two moiré domains lying in the same Pt(1 1 1) terrace,

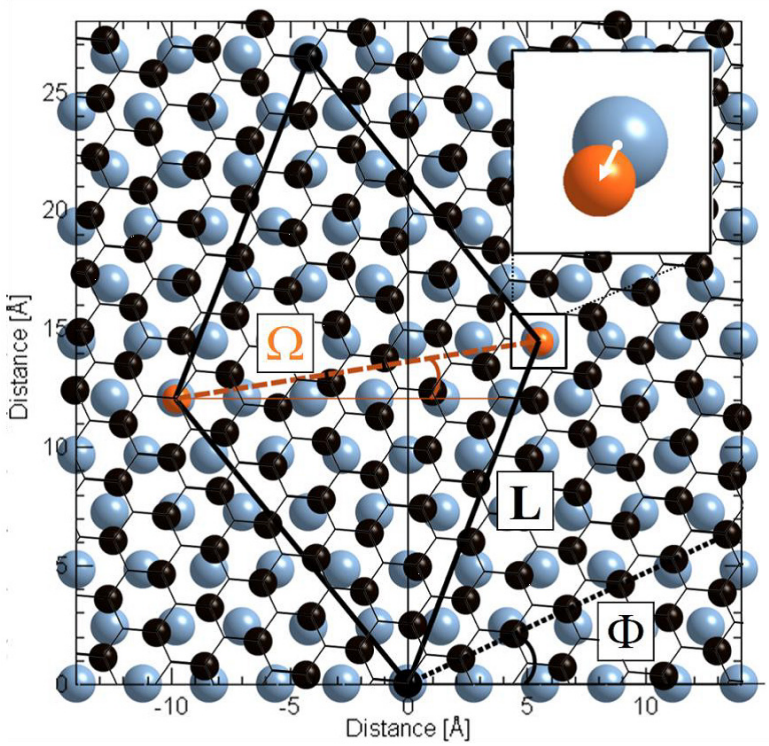


Figure IX.26. Diagram of the model represented for a moiré superstructure. Pt atoms are represented by blue spheres, whereas the hexagonal lattice of graphene is represented by black spheres. The angle between the black dotted line and the Pt$[1\,\bar{1}\,0]$surface direction (x axis) represents the crystallographic angle, $\Phi = 25.1°$ for this case. The orange spheres are C atoms with the lowest mismatch for a given Φ, which define the moiré unit cell indicated by the black rhombus. The angle between the orange dashed line and the Pt$[1\,\bar{1}\,0]$direction is the moiré apparent angle (Ω). The white arrow in the inset represents the mismatch. Adapted from [902], copyright American Chemical Society.

connected by an amorphous grain boundary. The strain accumulated between the two domains induces the appearance of an edge. Figure IX.28(b) shows that graphene can, in some cases, run across an atomic step without forming a grain boundary in a 'carpet-like' fashion (covering unperturbed the higher and lower part of the step while running through it). In this case the only effect is an out-of-plane bending of SLG. In figure IX.28(c) a pseudo-periodic graphene grain boundary is presented. The structure involves several, unresolved, vacancies and lattice deformations. Interestingly, in cases like this, the grain boundary can be pseudocrystalline (contrary to figure IX.28(a)) and adopt the periodicity of one of the two moirés that reaches the interface.

Figure IX.29 presents a different 1d structure occurring on graphene on metals: the interface between graphene and a metal step (in particular a Pt(1 1 1) surface). In this case a crystalline structure emerges permitting to perform a combined experimental-theoretical approach to study the contact region formed along the interface at the atomic scale. Figure IX.29(a) shows a high-resolution STM image of atomically resolved border-like edge of $(\sqrt{7} \times \sqrt{7})$ R19° graphene with a Pt(1 1 1) step. Combining STM images with DFT simulations, the atomic and electronic structure of Pt-graphene edges can be fully characterized (see figure IX.29(b)). This approach reveals electronic highly localized states in one of the graphene sublattices, and thus the brighter aspect in the STM images of the contact region. Theory predicts, and STM images confirm, that this state is mainly confined on the first C atomic lines of the edge [1590].

IX.1.4.2. Silicon carbide

Graphene grown on SiC(0 0 0 1) shows very interesting electronic properties at the nanoscale. When inspected with STM, it can appear transparent, depending on the bias voltage. Used: The honeycomb graphene structure is 'visible' only within a small range of scanning conditions which typically involve voltages bias near E_F (see figure IX.30) [659]. SLG/SiC(0 0 0 1) present quantum interferences between electrons of different sublattices, which result in a $\sqrt{3} \times \sqrt{3}$R30° lattice appearance of graphene lattice near defective structures. All these characteristics makes G/SiC(0 0 0 1) an ideal system to test the fundamental electronic properties of this pure sp^2 compound with STM, although typically low T STM is needed to decrease electronic broadening effects. The, so called, C-terminated SiC face or SiC(0 0 0 $\bar{1}$) develops MLG. Its layers are weakly bound and stacked in different orientations forming graphene-graphene moirés with different orientations and periodicities [600, 659].

Graphene grown on the Si terminated surface SiC(0 0 0 1) can show different surface reconstruc-

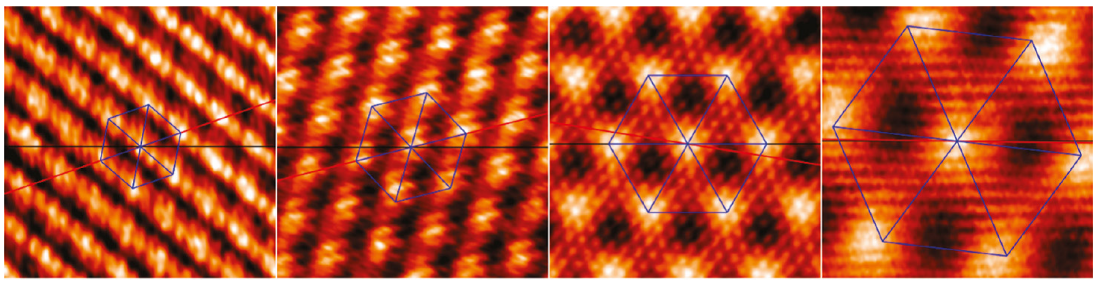


Figure IX.27. High resolution atomically resolved STM images of periodically modulated graphene structures. The red line indicates the graphene orientation with respect to the black line, which indicates the Pt [1 1 0] surface direction. The blue hexagon denotes the resulting moiré structure. All images are $5 \times 5\,\mathrm{nm}^2$. $V \sim -250, +250$ mV; $I \sim 1, 3$ nA. Adapted from [902], copyright American Chemical Society.

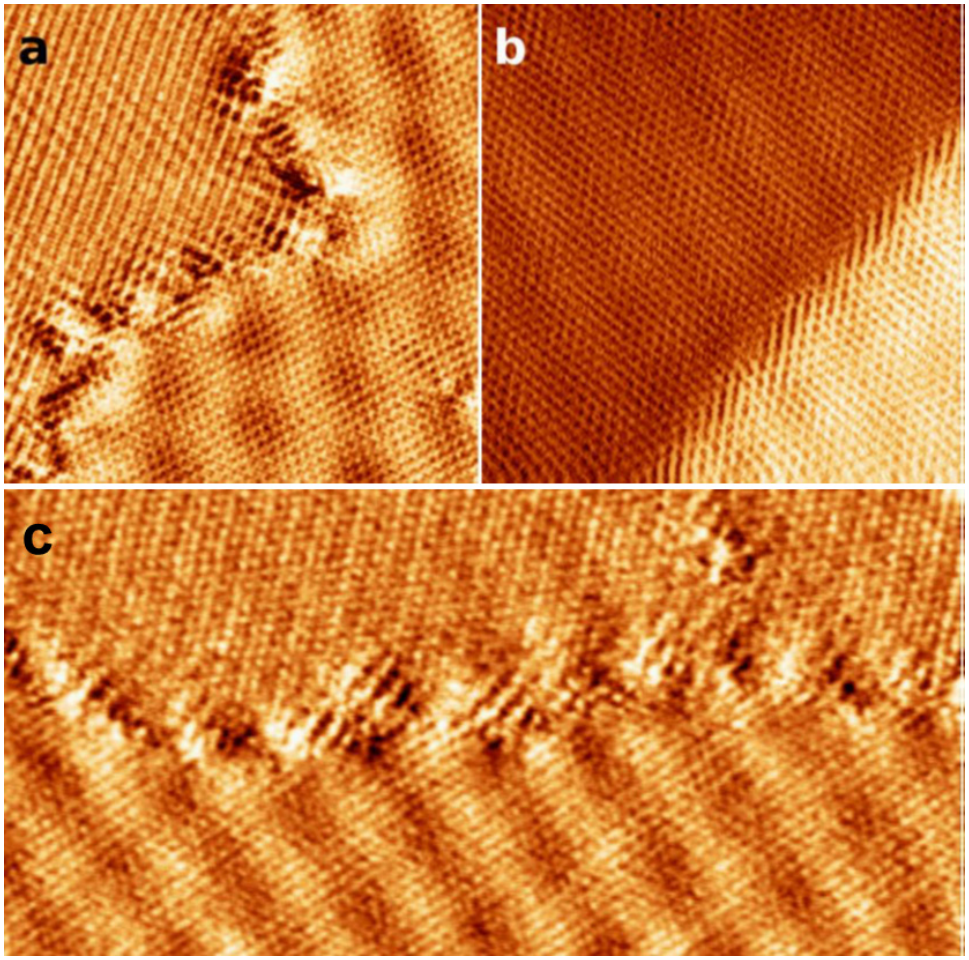


Figure IX.28. Examples of defective structures of graphene. (a) edge between two rotational domains (moirés) $10 \times 10\,\mathrm{nm}^2$ 1.9 nA, 10 mV. (b) Graphene running through a Pt step in a carpetlike fashion $7.5 \times 7.5\,\mathrm{nm}^2$, 8 nA, 2 mV. (c) Pseudo periodic edge, the grain boundary follows the periodicity of the moiré appearing in the lower part of the image. $18.4 \times 9\,\mathrm{nm}^2$, 2 nA, 10 mV.

tions (see section IV). There are three main surface terminations that can be distinguished by STM. First, $(6\sqrt{3} \times 6\sqrt{3})$R30°/SiC(0 0 0 1) or buffer layer (figure IX.31(a)) is a carbon rich termination which is usually described as sp^2 carbon lattice covalently bound to the uppermost SiC slab. Second, SLG, figure IX.31(b), is characterized by a $(6\sqrt{3} \times 6\sqrt{3})$R30° superperiodicity overlaid with an atomic scale graphene lattice. When measuring SLG at high voltage bias one can normally measure the atomic features of the SiC beneath graphene [1493]. Third, BLG and, more generally, MLG. When SiC samples are annealed at very high T, Si depletion can be high and promote MLG growth. STM measurements of MLG (figure IX.31(c)) have lower corrugation and, in some cases, the underlying superperiodicity disappears and a graphene–graphene moiré superlattice dominates. Similar MLG are also found in the SiC(0 0 0 $-$ 1) surface [1494]. SLG can be decoupled from the SiC substrate by H intercalation. Figure IX.31(d) shows a STM image of hydro-

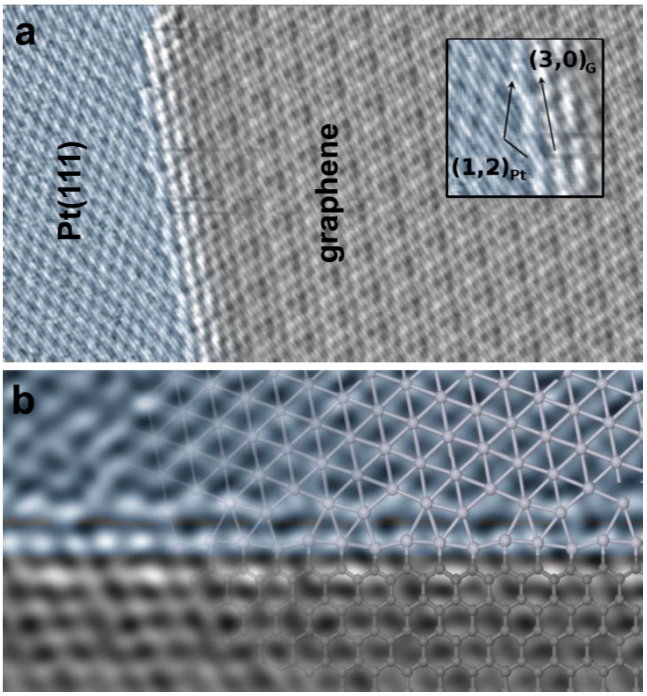


Figure IX.29. Graphene-metal interface. (a) High resolution, atomically resolved, STM images of SLG/Pt(1 1 1)-Pt(1 1 1) interface. These crystalline edges are energetically favoured and have the same orientation as the graphene moiré superstructures. $12.6 \times 6.8\,\mathrm{nm}^2$, $V = 40.2$ mV, $I = 5.2$ nA. The inset shows the chiral vectors of this particular edge. (b) Ball and stick model of the DFT relaxed structure (right-hand part of the image) compared with the STM image of the SLG-Pt(1 1 1) edge boundary. The atomic positions of the calculations reproduce with great accuracy the protrusions in the STM images. Adapted from [1490], copyright American Chemical Society.

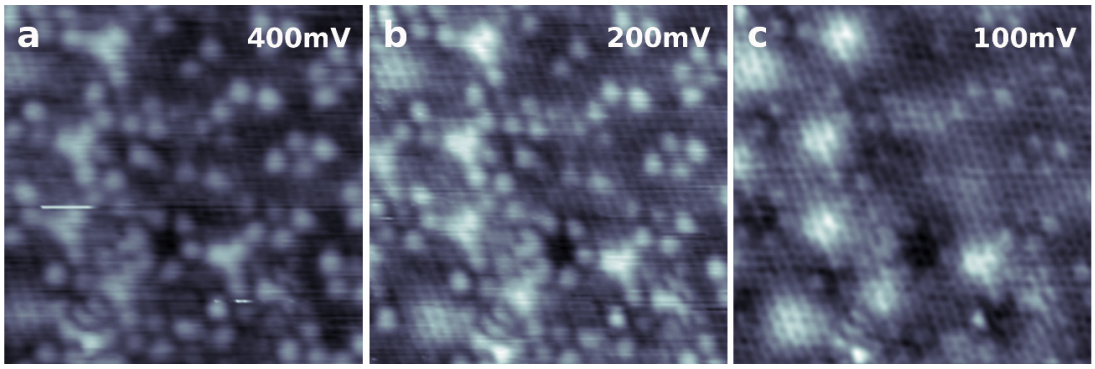


Figure IX.30. STM images of the same region showing the bias dependence of SLG/SiC(0 0 0 1). When scanned at bias near E_F (100 mV) the main feature is the graphene lattice, while scanned at higher bias (400 mV) the subsurface buffer layer structure is revealed. $7 \times 7\,\mathrm{nm}^2$.

gen intercalated graphene. In this case, the underlying $(6\sqrt{3} \times 6\sqrt{3})$R30° superperiodicity is not appearing in the STM images and only the graphene lattice can be resolved. The low surface corrugation measured with STM on the hydrogen intercalated samples might be related to the high μ reported for these samples.

The (0 0 0 −1) face shows ordered graphene over mm scales, easily observed by STM on doped SiC. This allows atomic moiré and spectroscopic studies at low T and high magnetic field [595, 600, 627, 630].

IX.1.5. Scanning thermal microscopy

Heat transfer properties of graphene are a topic of high interest [1495–1498] based on calculations and measurements of its thermal conductivity in the range of a few thousands W/mK [1499]. Due to the strong covalent sp^2 bonding, heat transport in carbon materials is usually dominated by phonons [1498]. However, lattice defects, impurities, interfaces as well as the presence of sp^3 bonds can limit heat conduction [1498]. Several techniques have been proposed for characterizing the GRM thermal properties [1500]. However, accurate and reliable measurements remain challenging. Electrical methods and the Raman optothermal measurements were used to determine the thermal conductivity of both suspended and supported SLG [1498, 1501, 1502]. The main limitations are the rather complex setup and limited

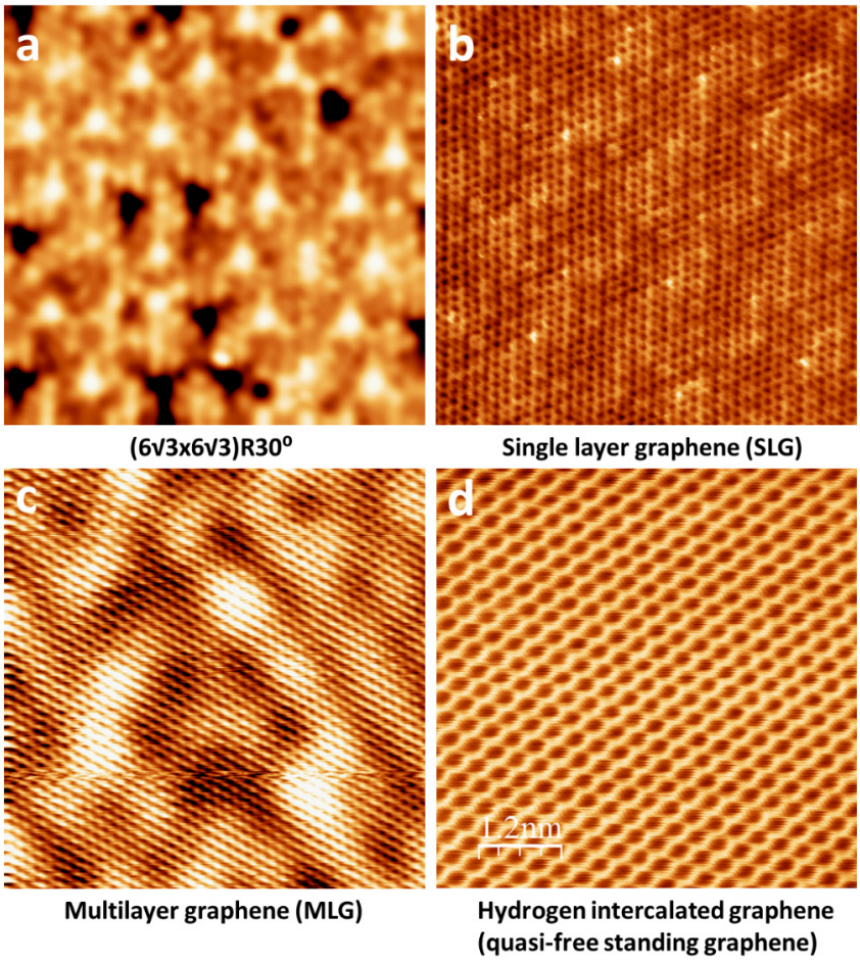


Figure IX.31. Atomically resolved STM images of the SiC surface with different terminations. (a) $6\sqrt{3} \times 6\sqrt{3}$)R30°1000 mV, 200 pA. (b) SLG −100 mV, 200 pA. (c) MLG, −100 mV, 100 pA. (d) Hydrogen intercalated graphene. $V = 243$ mv; $I = 1.33$ nA. Images (a)–(c) are $10 \times 10\,\mathrm{nm}^2$. *d* is $6 \times 6\,\mathrm{nm}^2$.

spatial resolution. Optical techniques are limited to a few hundreds nm by the diffraction limit of the incident light, while electrical measurements provide a result representing the average of the conductivity on the whole specimen.

Scanning thermal microscopy (SThM) [1503, 1504] is an interesting technique to measure heat transfer in GRMs, requiring limited sample preparation and with lateral resolution of some tens nm or less. Although a quantitative determination of the thermal conductivity of GRMs by SThM [334, 1504] is very challenging, it was demonstrated to be possible in at least some specific cases and with particular probes, e.g. by electrically heating a suspended SLG and by using the so called null point technique, adopting probes integrated with a thermocouple junction [1505].

SThM can be performed by using resistive probes, where a Pd film acts both as heater and T sensor (the so-called Pd probes) [1504]. A 40 nm [1506] Pd film, deposited near the apex of the Si_3N_4 tip, acts as the element of a Wheatstone bridge. The resistor is heated by Joule effect and, when the tip is in contact with more thermally conducting regions of the sample, its *T* (and therefore resistance) decreases, while it increases when scanning on less conductive areas, since less heat is carried away by the material under investigation. The change in the sensor resistance is monitored by measuring the bridge voltage, which is sent to the controller to display the thermal maps, subsequently converted into T by using the Wheatstone bridge formula [1789], and the temperature coefficient of the probe $\sim 8.92 \times 10^{-4}\,\mathrm{K}^{-1}$. [1790]

RGO flakes were studied by SThM [334]. These were measured both 'as-received' (RGO) or after a annealing at 1700 °C in vacuum for 1 h (referred to as RGO_1700) to gain insight into the evolution of the heat dissipation properties, due to the simultaneous reduction of disorder and defectiveness upon annealing [334]. SEM and AFM analyses did not evidence significant changes in the morphology upon annealing. XPS showed a strong reduction of oxygen, by the elimination of carboxylic and carbonyl groups. A considerable reduction of defects was observed by Raman spectroscopy which also indicated an increase of the graphitic stacking order [334]. This result was further confirmed by x-ray diffraction experiments which revealed an increased ordering both along and perpendicular to the planes. Figure IX.32 plots the SThM maps for (a) RGO and (b) RGO_1700 on Si/SiO_2. Topography artefacts are observable owing

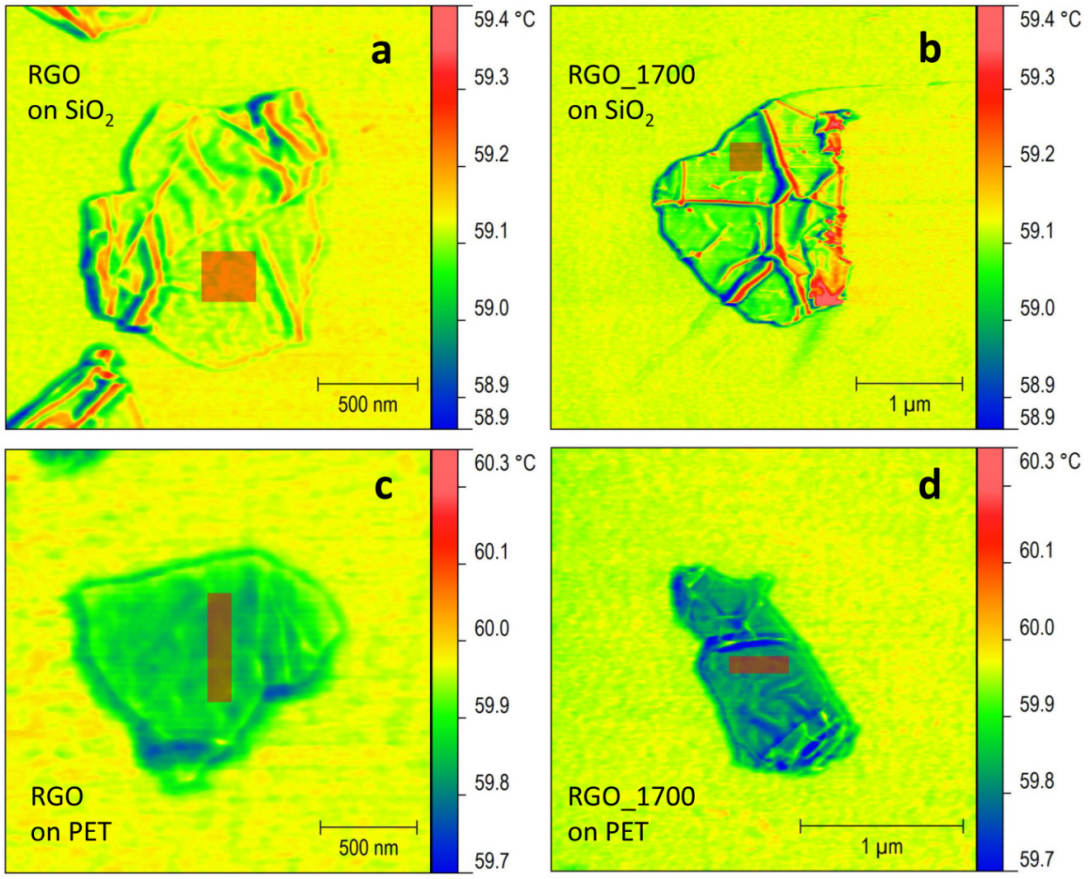


Figure IX.32. SThM maps of (a) RGO and (b) RGO_1700 on Si/SiO_2 and (c) RGO and (d) RGO_1700 on PET. Adapted from [334], with permission from Elsevier.

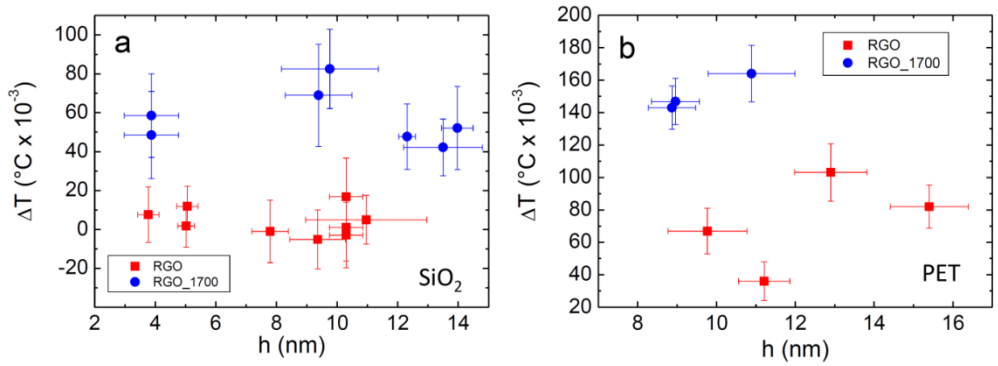


Figure IX.33. (a) Summary of T difference between Si/SiO_2 and RGO (red) or RGO_1700 (blue). (b) The same as in (a) but for PET substrate. Adapted from [334], with permission from Elsevier.

to the dependence of the tip-sample contact on steep edges, wrinkles and bulges on the surface [334, 1507]. The tip heater T in panel (a) shows that on the flat areas of the sample (see e.g. the masked region), T is basically the same as when the tip is scanning the substrate ($T_{sub} - T_{RGO} = \Delta T = (8 \pm 14) \times 10^{-3}$ K). This does not mean that the two materials have the same thermal conductivity, but only that their apparent thermal conductance is the same. On the other hand, in panel (b) it can seen that for the annealed flakes T is now *lower* when the tip is on the flake than when it is on the substrate, $\Delta T = (42 \pm 15) \times 10^{-3}$ K. Thus, by comparing (a) and (b), Ref. [334] concluded that the annealed flake features a *higher* thermal conductivity than the as-received ones, due to the reduced disorder and defectiveness upon annealing. Panel (c) and (d) show an analogous result, but with the flakes supported by the less (one order of magnitude) thermally conducting PET. In this case, the heater T on the RGO flake is now lower than that of the substrate ($\Delta T = (103 \pm 18) \times 10^{-3}$ K) and also in this case ΔT increases when looking at the RGO_1700 sample, where it goes to $\Delta T = (143 \pm 13) \times 10^{-3}$ K. The results on PET confirm that RGO_1700 flakes are more thermally

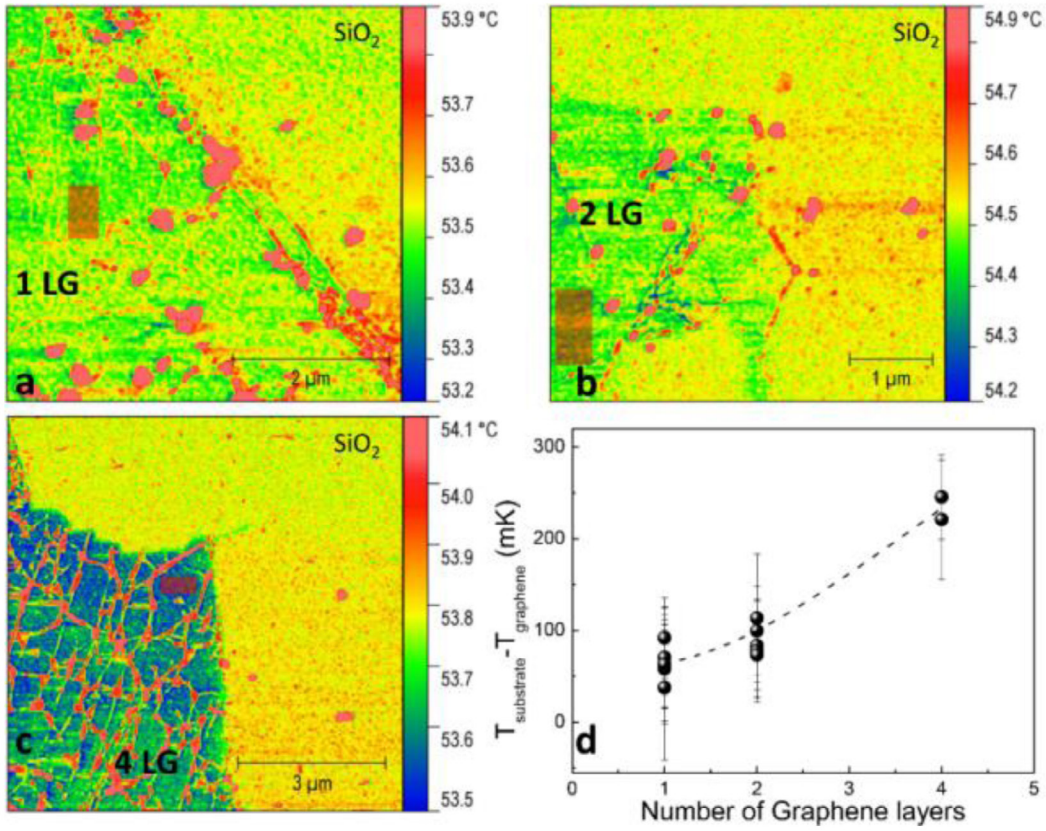


Figure IX.34. SThM maps of (a) 1LG, (b) 2LG, and (c) 4LG, on Si/SiO_2. (d) Sensor T difference as a function of N. The dashed line is a guide for the eye.

conducting and also show that the use of a less conducting substrate enhances the sensitivity of the measurement. This is due to the decrease of spreading resistance [1508] of the substrate occuring when enlarging the heat flow area, being larger when the thermal conductivity of the substrate is smaller [334]. Thus, the T difference substrate-flake is also expected to be higher.

Figure IX.33 reports a summary of the SThM results obtained in terms of T differences between substrate and flakes for several samples on substrates. Although these are small and the error bars rather large, the result is reproducible on both substrates, showing that the annealing process improves the thermal conduction of flakes. No particular dependence on flake thickness of the flakes is observed, likely due to the fact that the in-plane component of the thermal conductivity is at least two orders of magnitude higher than the out-of-plane one, and a considerable amount of heat could be spread along the planes.

SThM was also applied on CVD 4LG, BLG, SLG supported by SiO_2/Si (figure IX.34). Figure IX.34(a) shows a thermal map os SLG on SiO_2/Si. The high-T spots are due to impurities and the corresponding T value is due to a topography artefact [1507]. When averaging over the flat areas (with no topography artefacts) the measured tip T is lower than on the substrate. By averaging the red masked area on one 1LG and on a similar area on the substrate (not shown), the T difference between substrate and sample was found to be $\Delta T = (71 \pm 42) \times 10^{-3}$ K [1790]. Figure IX.34(b) reports a similar image for 2LG. Apart from topological features giving rise to high-T spots, the flat areas of the surface feature on average a lower T than the substrate, with a T difference (averaged on the red masked area) increased to $\Delta T = (100 \pm 48) \times 10^{-3}$ K, suggesting that 2LG has a higher thermal conductance than 1LG. Figure IX.34(c) shows the 4LG case, in which both impurities and grain boundaries are visible due to the topography-related T readings. The representative T on the sample flat areas is much lower than on the substrate. The T difference between substrate and 4LG is now higher than for the two previous samples. $\Delta T = (245 \pm 46) \times 10^{-3}$ K, indicating that the thermal conductance of 4LG is further increased with respect to 1LG and 2LG. Figure IX.34(d) summarizes the results obtained by performing several SThM measurements as a function of N. Even though the error bars for 1 and 2LG overlap, the thermal conductance increases with N.

A similar trend was reported for mechanically exfoliated flakes using either the resistive Si [1509] or Pd probes [1506]. The topography of CVD graphene, with grain boundaries and crystallites, is considerably different from mechanically exfoliated flakes, that are much flatter and more regular. This affects also the heat dissipation properties and the thermal response of the SThM probe.

IX.2. Spectroscopies

IX.2.1. Raman

Raman spectroscopy is an integral part of graphene research. It may be used to determine the number and orientation of layers, the quality and types of edge, and the effects of perturbations, such as electric and magnetic fields, strain, doping, disorder an functional groups [96].

This, in turn, provides insight into all sp^2-bonded carbon allotropes, because graphene is their fundamental building block. Ref. [96] reviewed the state of the art, future directions and open questions in Raman spectroscopy of graphene. It described the key physical processes, such as the various types of resonances at play, and the role of quantum interference. It outlined the basic concepts and notations, and a terminology able to describe any result in literature for GRMs. Here we briefly describe some of the key concepts, referring the reader to Ref. [96] for a more complete overview.

An ideal characterization tool should be fast and non-destructive, offer high resolution, give structural and electronic information, and be applicable at both laboratory and mass-production scales. Raman spectroscopy fulfils all these requirements. The Raman spectrum of graphite was first recorded 50 years ago [1510] and, by the time the Raman spectrum of graphene was first measured [105], Raman spectroscopy had become one of the most popular techniques for the characterization of disordered and amorphous carbons, fullerenes, nanotubes, diamonds, carbon chains and polyconjugated molecules [1511]. Raman techniques are particularly useful for graphene, because the absence of a bandgap makes all wavelengths of incident radiation resonant, thus the Raman spectrum contains information about both atomic structure and electronic properties. Resonance could also be reached by ultraviolet excitation [1722] either with the M-point Van Hove singularity or in the case of bandgap opening, such as in fluorinated graphene.

Raman spectra are typically measured in the high frequency range >100 cm^{-1} because of the cut-off limit of Raman filters (edge or notch filters). In the low frequency (<100 cm^{-1}) range interlayer interaction can be estimated by the shear (C) and layer breathing modes (LBMs), which can also be used to determine N [1514, 1515]. Traditionally, a triple stage spectrometer is used to measure low frequency Raman spectra, but its low throughput and complexity for operation restrictsed its utilization. A new method was developed to get low frequency spectra easily, using volume Bragg grating filters to reject a strong laser line down to 5 cm^{-1} [1516, 1514]. When measuring GRMs, the damage threshold for the laser power should be considered. Typically, the power should be kept <1 mW for SLG, and few hundreds μW for TMDs, depending on the material. Some materials should be isolated from air with a protection layer or vacuum to avoid photo induced oxidation [189].

IX.2.1.1. Graphene

A typical Raman spectrum of defect-free SLG consists of two main peaks, the G peak located at ~1580 cm^{-1} and the 2D peak at ~2700 cm^{-1} [96], figure IX.35. In defective graphene, additional peaks such as the D, D' and their combination $D+D'$ appear [96, 1511, 1524, 1722], figure IX.35 bottom spectrum. $2D$ and $2D'$ are second order peaks involving two phonons and are thus always present even in the absence of defects. The fitting parameters, such as peak position Pos, FWHM, height (I) and area (A) are important to interpret Raman data. E.g.: $I(G)$ for G peak height, $A(G)$ for G peak area, Pos(G) for G peak position and FWHM(G) for G peak full-width at half-maximum.

The lineshape of the $2D$ peak can be used to distinguish between different N. For SLG it can be fitted with a single Lorentzian, while in BLG it splits into four components as result of the evolution of the band structure [105]. For $N>10$ the $2D$ peak shape is similar to that of graphite. For graphene on the carbon $(000-1)$face of SiC, each layer has the electronic structure of a single layer, due to the rotational stacking, and the Raman $2D$ peak is a single Lorentzian in most cases [1517], see figure IV.7(b). The C and LBMs can be observed for GRMs. Their positions change with N. They can also be used to calculate coupling constants related to in-plane and out-of-plane Young's moduli [1514]. Figure IX.36(b)) shows the low frequency Raman spectra of different graphene layers. While Pos(G) is nearly constant, Pos(C) changes and can be used to determine N.

Raman spectroscopy can also be used to determine the doping level [1321, 1518, 1519]. There are two major effects: (i) a change of the equilibrium lattice parameter with a consequent stiffening/softening of the phonons, and (ii) the onset of effects beyond the adiabatic Born–Oppenheimer approximation that modify the phonon dispersion close to the Kohn anomalies (KA) [1518, 1520].

In doped samples Pos(G) increases, while FWHM(G) decreases for both electron or hole doping [1518, 1521–1523]. The increase in Pos(G) is due to the non-adiabatic KA removal, while the decrease in FWHM(G) is due to Pauli blocking of the phonon decay channel into electron hole pairs due to the increase in E_F [1522, 1518]. The $2D$ peak instead shifts up for hole doping and down for electron doping, due to the change of the equilibrium lattice parameter. Therefore, Pos($2D$) can be used to determine the type of doping. Doping also has an effect on $I(2D)/I(G)$ and $A(2D)/A(G)$. Both are maximum for zero doping and decrease for increasing doping [1522, 1518]. Figure IX.37 summarizes the doping dependence of all the fitting parameters. Using Pos($2D$) one can distinguish between electron and hole doping, and then use all the remaining fitting parameters and Pos($2D$) to estimate the amount of doping. The charge carrier concentration is related to the Fermi level by [1518]: $E_F(n)=\hbar|v_F|\sqrt{(\pi n)}$, where $\hbar=h/2\pi$ is the reduced

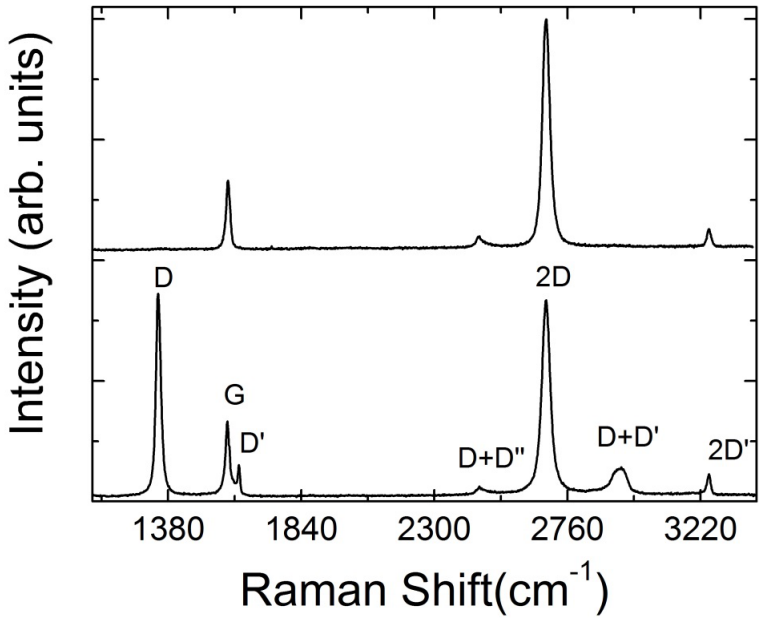


Figure IX.35. Typical Raman spectra of defect free (top) and defective (bottom) graphene. Figure taken from [96], with permission of Springer.

Planck constant, $v_F = 1.1 * 10^6$ m s^{-1} is the SLG Fermi velocity

Ref. [1524] introduced a three-stage classification of disorder, leading from graphite to amorphous carbons, that allows to simply assess all the Raman spectra of carbons:

- Stage 1: graphene to nanocrystalline graphene.
- Stage 2: nanocrystalline graphene to low-sp^3 amorphous carbon.
- Stage 3: low-sp^3 amorphous carbon to high-sp^3 amorphous carbon.

Here we focus on stage 1, the most relevant when considering the vast majority of publications dealing with graphene production, processing and applications. As shown in figure IX.38, in stage 1 the Raman spectrum evolves as follows: (a) the D peak appears, $I(D)/I(G)$ increases; (b) the D' peak appears; (c) all peaks broaden; (d) the $D + D'$ peak appears; (e) at the end of stage 1, the G and D' peaks are so wide that it is sometimes more convenient to consider them as a single, up-shifted, wide G band at ~1600 cm^{-1} [1524].

For a sample with rare defects $I(D)$ is proportional to the total number of point defects probed by the laser spot, giving rise to $I(D)/I(G) \sim 1/L_D^2$, where L_D is the average inter-defect distance. Taking into account the excitation energy dependence of the peak areas and intensities the inter-defect distance can be expressed by [1322, 1524]:

$$L_D^2\left[\text{nm}^2\right] = \frac{4.3 \times 10^3}{E_L^4\,(\text{eV})}\left[\frac{I(D)}{I(G)}\right]^{-1}. \quad \text{(IX.7)}$$

E_L is the laser excitation energy in eV. This relation is valid for $L_D \geqslant 10$ nm (stage 1). By considering point-like defects, separated from each other by L_D, equation (IX.7) can be restated in terms of defect density, n_D, given by $n_D\,(\text{cm}^{-2}) = 10^{14}/\pi L_D^2$, as [1322]:

$$n_D\left[\text{cm}^{-2}\right] = 7.3 \times 10^9 E_L^4\,(\text{eV})\,\frac{I(D)}{I(G)}. \quad \text{(IX.8)}$$

Equations (IX.7) and (IX.8) are limited to Raman-active defects. Perfect zig-zag edges [1526], charged impurities [1518, 1527], intercalants [1528], uniaxial and biaxial strain [1275, 1529–1534] do not generate a D peak.

Equations (IX.7) and (IX.8) are derived assuming negligible E_F shift. However, most samples in literature show doping levels ~200–500 meV. I(D) depends on the doping level [1321]: I(D) decreases for increasing doping. This needs to be taken into account when estimating the defect density. Equations (IX.7) and (IX.8) can be modified for samples with non-negligible doping [1321]:

$$L_D^2\left[\text{nm}^2\right] = \frac{(1.2 \pm 0.3) \times 10^3}{E_L^4\,[\text{eV}]}\left[\frac{I(D)}{I(G)}\right]^{-1}\{E_F\,[\text{eV}]\}^{-(0.54\pm0.04)} \quad \text{(IX.9)}$$

$$n_D\left[\text{cm}^{-2}\right] = (2.7 \pm 0.8) \times 10^{10} E_L^4\,[\text{eV}]\,\frac{I(D)}{I(G)}\{E_F\,[\text{eV}]\}^{(0.54\pm0.04)}. \quad \text{(IX.10)}$$

Equations (IX.9) and (IX.10) are valid for samples with a defect concentration corresponding to stage 1, and for $E_F < E_L/2$, which is by far the most relevant for graphene production and applications.

In order to extract the defect density correctly the flowchart presented in figure IX.39 should be followed.

After recording a Raman spectrum, one first has to check whether a D peak is present. In case no D peak is present, the standard procedure of estimating

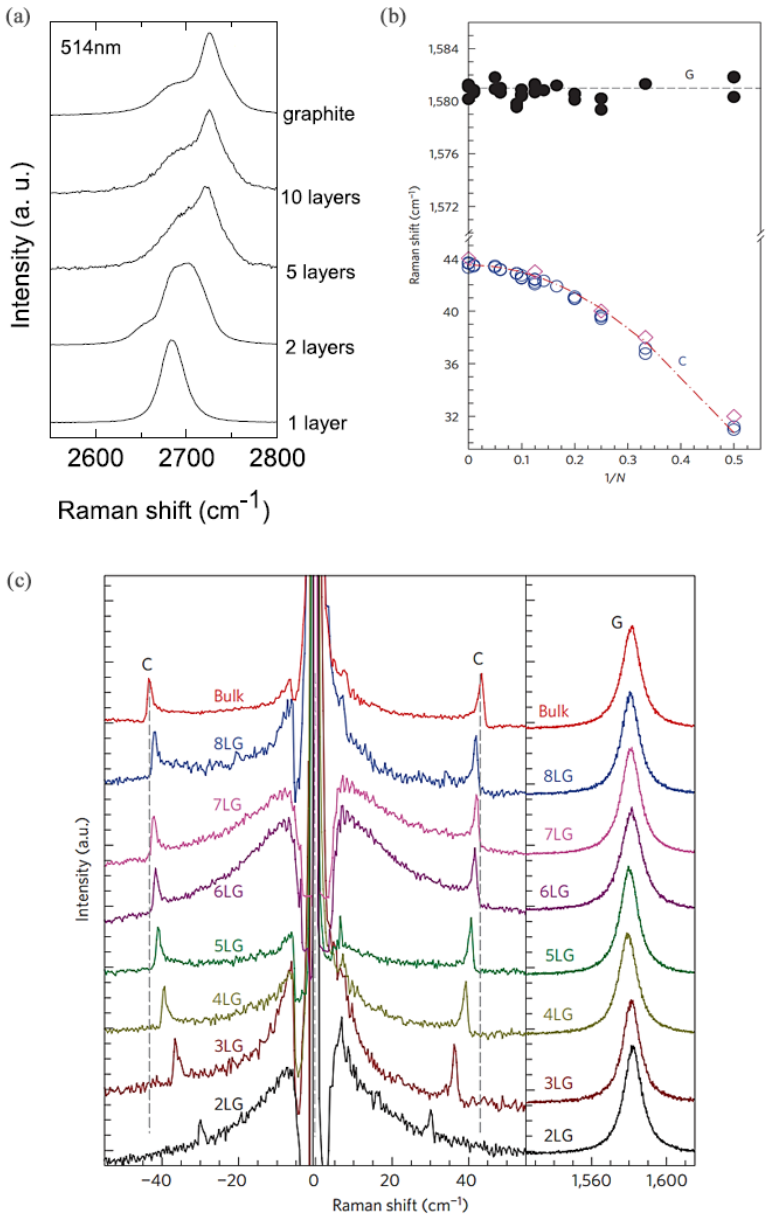


Figure IX.36. (a) Raman spectrum of 2*D* peak as function of N [78]. (b) and G peaks as function of *N*. (c) Pos(C) and Pos(*G*) as a function of 1/N [1514].

doping from the Raman fitting parameters, such as Pos(G), FWHM(G), Pos($2D$), $I(2D)/I(G)$ and $A(2D)/A(G)$, can be used. The presence of a D peak, leads to the next step, where one needs to check if the sample is doped or not, e.g. by looking at the relevant Raman peak fitting parameters. If the sample has doping $\leqslant$100 meV, equation (IX.8), can be used to estimate the defect density. If however the sample has non-negligible dopingequation (IX.10) has to be used. E.g. Figure IX.40 shows spectra of a defective SLG at low, $E_F = 100$ meV, and high, $E_F \sim 500$ meV, doping. By analysing the spectra of doped and defected SLG (black line in figure IX.40) Pos(G) = 1599 cm^{-1}, FWHM(G) = 12 cm^{-1} and $I(2D)/I(G) = 0.94$ are obtained. This allows us to estimate ~500 meV for the doping level of the sample using the graphs from Ref. [1518]. The $2D$ peak is upshifted with Pos($2D$) = 2651 cm^{-1} suggesting hole doping. A decrease of $I(D)$ with doping is seen. The red spectrum for the undoped case gives $I(D)/I(G) = 2.8$. Using equations (IX.7) and (IX.8) gives $n_D \sim 3.1 \times 10^{11}$ cm^{-2} $L_D = 10$ nm. The black line gives $I(D)/I(G) \sim 1.24$. Taking the doping level ~500 meV into account $n_D = 3.4 \times 10^{11}$ cm^{-1} and $L_D = 10$ nm, are obtained using equations (IX.9) and (IX.10).

Strain can be present in a material compressed or stretched out of equilibrium. Strain can be either compressive or tensile. While compressive strain causes an upshift or stiffening of the Raman peaks, tensile strain causes a downshift or softening. Strain can be either isotropic, i.e. biaxial strain, or along a certain axis, i.e. uniaxial. Biaxial strain does not cause any change in peak shape, while uniaxial strain causes splitting of the G peak into two components G^+ and G^- for $\varepsilon \geqslant 0.5\%$ [1529], figure IX.41. The G peak is due to a doubly degenerate E_{2g} mode [105]. By apply-

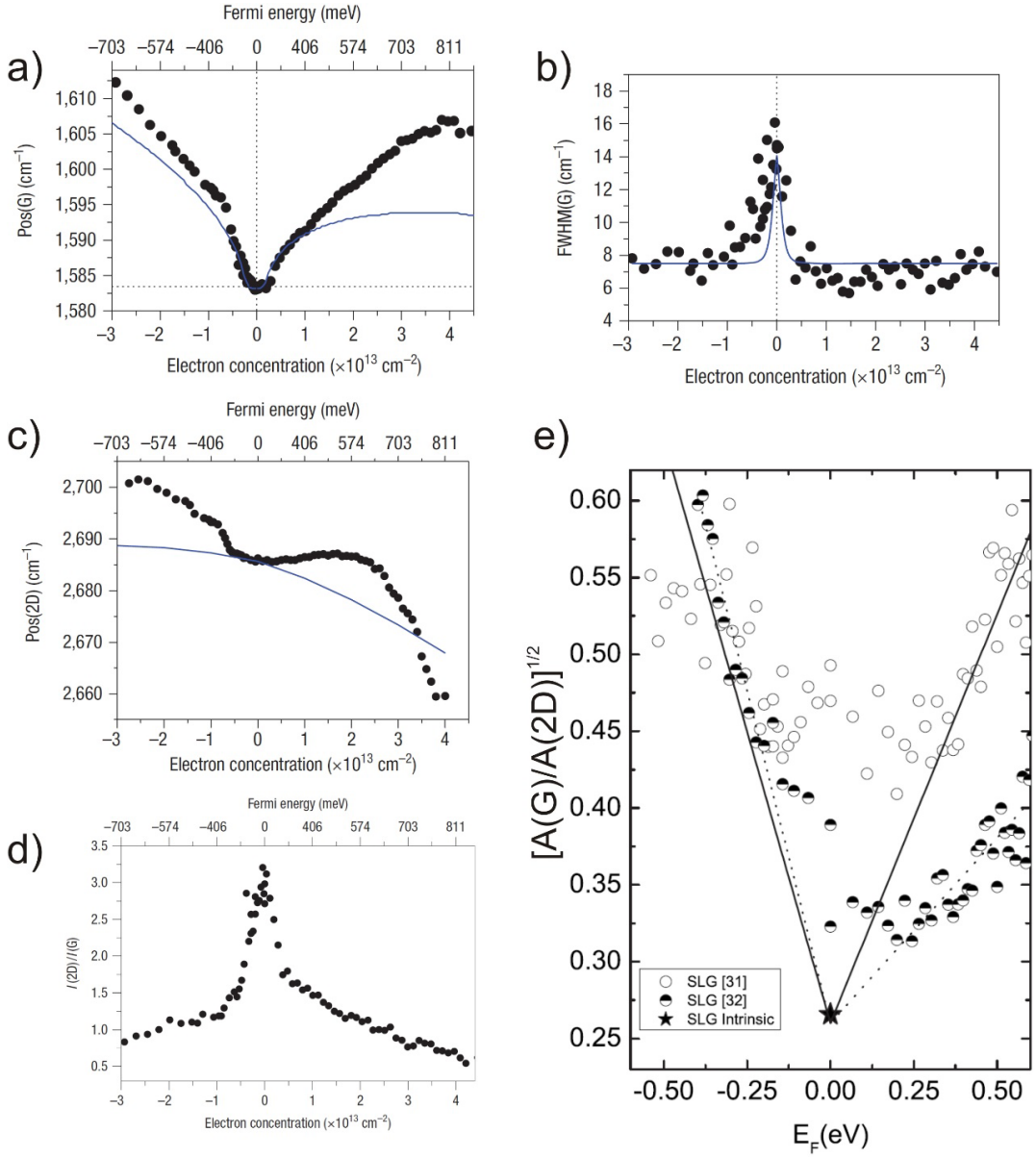


Figure IX.37. Doping dependence of Raman fitting parameters (a) Pos(G), (b) FWHM(G), (c) Pos($2D$), (d) $I(2D)/I(G)$ versus electron concentration ($\times 10^{13}$ cm^{-2}) and (e) $[A(2D)/A(G)]^{0.5}$ as a function of E_F. Adapted from Ref. [1518], with permission of Springer and from Ref. [1519], copyright by the American Physical Society.

ing uniaxial strain this splits into two components, one along the strain direction and one perpendicular to it. While Pos($2D$) changes as $\delta\text{Pos}(2D)/\delta\varepsilon \sim -64\,\text{cm}^{-1}/\%$, the G peak changes as $\delta\text{Pos}(G^+)/\delta\varepsilon \sim -10.8\,\text{cm}^{-1}/\%$ and $\delta\text{Pos}(\text{G}-)/\delta\varepsilon \sim -31.7\,\text{cm}^{-1}/\%$ [1529] in uniaxial, tensile strain experiments. Ref. [1529] reported $\delta\text{Pos}(2D)/\delta\varepsilon \sim -144\,\text{cm}^{-1}/\%$ and $\delta\text{Pos}(G)/\delta\varepsilon \sim -58\,\text{cm}^{-1}/\%$ for biaxial strain. To estimate the strain, the difference between fitted peak positions and unstrained reference peak positions needs to be derived. Then, by knowing how much the peaks shift with strain, i.e. $\delta\text{Pos}(2D)/\delta\varepsilon \sim -64\,\text{cm}^{-1}/\%$ in case of the 2D peak for uniaxial strain, one can calculate the strain. To distinguish and decouple the combined effects of doping and strain a thorough analysis of all the fitting parameters is necessary [1527].

IX.2.1.2. HBN

Two Raman peaks in hBN are observed with the excitation of visible laser light, the C peak near 50 cm^{-1} and a high frequency E_{2g} mode near 1366 cm^{-1} [1537]. The C peak strongly depends on N so that it can be used to estimate N [1048, 1538, 96]. The high frequency E_{2g} Raman peak weakly depends on N. The peak positions for the mono layer and bulk are ~1368 cm^{-1} and ~1366 cm^{-1} [1048, 1539–1541]

IX.2.1.3. Transition metal dichalcogenides

Many TMDs are composed of three atomic layers X–M–X, represented by MX_2, as well as ordering, 2H (Hexagonal symmetry), 3R (rhombohedral symmetry) and 1T (tetragonal symmetry).The most common polytype is 2H, e.g., MoS_2, $MoSe_2$, WS_2,

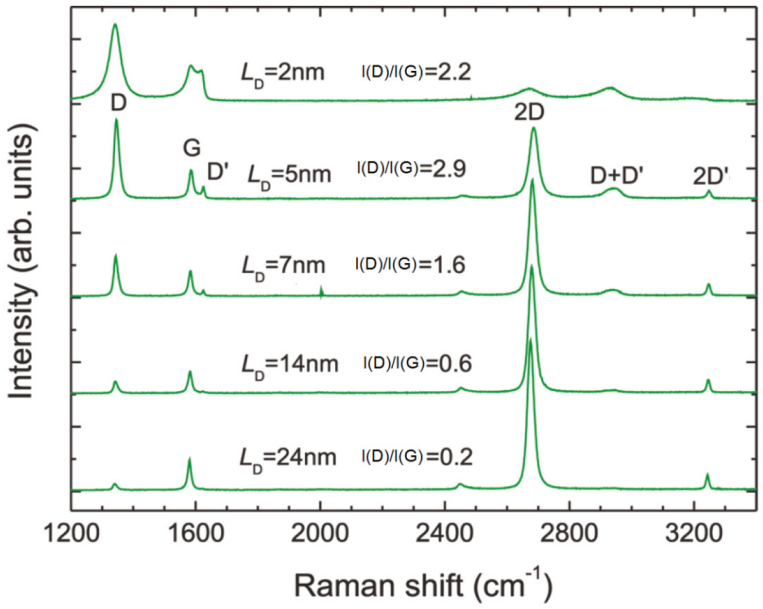


Figure IX.38. Representative Raman spectra of ion bombarded SLG measured at $E_L = 2.41$ eV [1322].

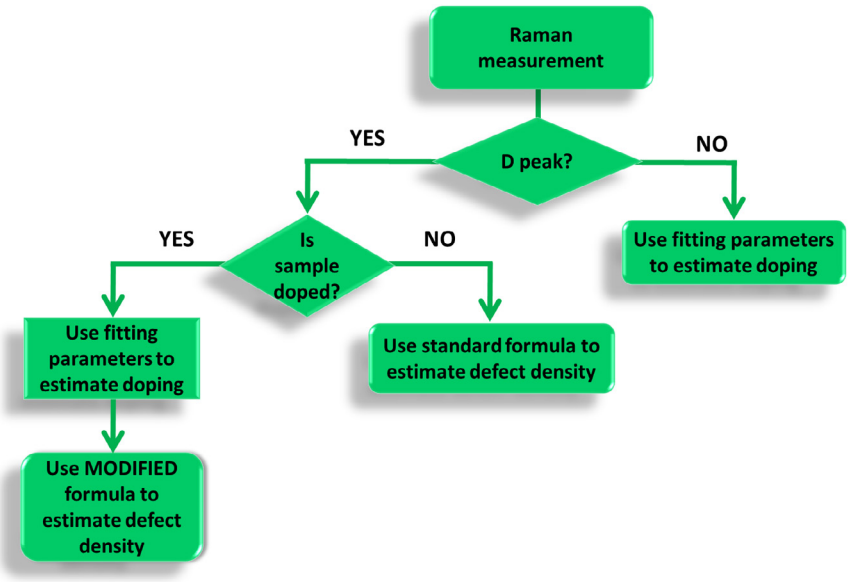


Figure IX.39. Flowchart to estimate defect density in doped and undoped samples.

and WSe_2. For 2H-MX_2, two prominent Raman peaks appear in the high frequency range, A_1' and E' modes. A_1' is an out-of-plane vibrational mode and E' is an in-plane one [1543, 1544]. The peak positions depend on N so that the difference of their positions may be used to estimate N. However, one needs to be careful since the dielectric environment can also change this difference, for a fixed N. Typically, A_1' decreases with decreasing N, and E' has the opposite trend. In the low frequency range, C and LBMs are observed and can be used to estimate the coupling strength between layers and N [96]. Defects in MoS_2 broaden the E' and A_1' peaks and E' becomes asymmetric towards lower frequencies [1545]. A peak ~ 200 cm^{-1} appears due to the defect induced longitudinal acoustic (LA) phonon at the M point [1545]. As uniaxial strain increases on 1L-MoS_2, the A_1' peak shows no measurable shift while the E' peak splits into two, E'^{+} and E'^{-} [1546]. The E'^{-} peak shifts ~ 4.5 cm^{-1}/% strain and E'^{+} ~1.0 cm^{-1}/% strain. A_1' is not sensitive to strain, while it is sensitive to doping. By increasing doping of 1L-MoS_2, A' redshifts and broadens due to electron–phonon interactions [1542].

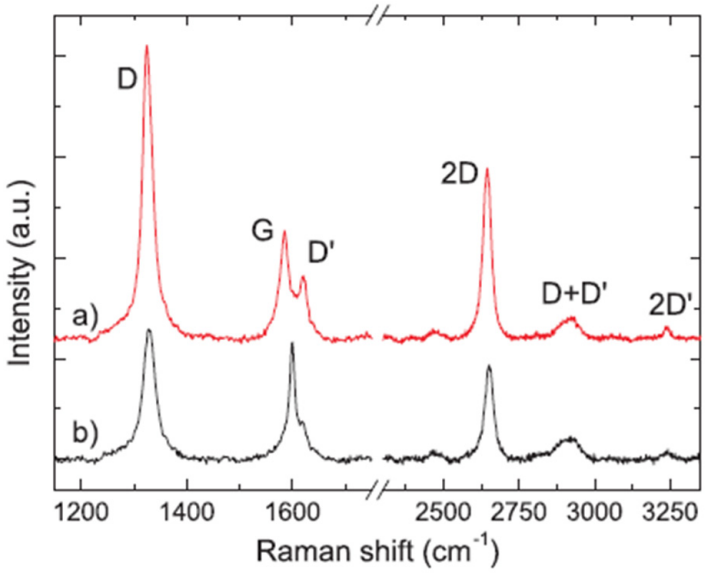


Figure IX.40. Raman spectra of a defective graphene sample (a) $E_F \leqslant 100$ meV and (b) $E_F \sim 500$ meV. Excitation wavelength: 633 nm. Adapted from [1321], copyright American Chemical Society.

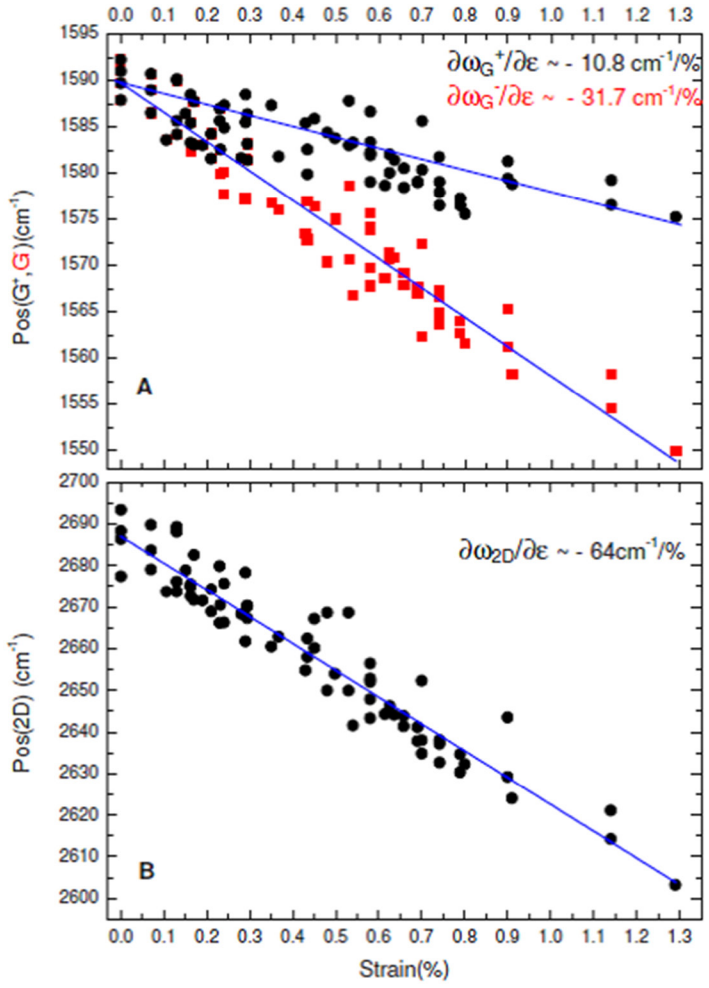


Figure IX.41. Change in Pos(G) and Pos($2D$) with increasing tensile, uniaxial strain. Adapted from [1529], copyright American Chemical Society.

IX.2.2. Absorbance and fluorescence

IX.2.2.1. Transition metal dichalcogenides

UV/Vis transmission spectroscopy can provide information GRM flakes, as inorganic LMs have well documented excitonic transitions [1547] characteristic for the material and even polytype or phase [378, 379, 1407]. Information on concentration can be extracted [185, 186, 236, 1407, 1548]. However, for this to be performed reliably, one needs to be aware that when transmittance mode is used, extinction and not absorbance spectra are obtained. Extinction is related to transmittance, T_r, via $T_r = 10^{-\mathrm{Ext}}$, where $\mathrm{Ext} = \varepsilon_c C_o l$, with ε_c the extinction coefficient, C_o the flakes concentration and l as the path length. This means that the quantity that is measured contains information related to both absorbance and scattering of light [185, 188, 190, 236, 240, 1549]. Although the scattering component of the extinction is size dependent [185, 188, 190, 236, 240, 1549], it is also the case that the absorbance coefficient is dependent on size, due to edge effects [185, 186, 188, 190]. Hence, the overall extinction coefficient is size-dependent and it is necessary to determine it gravimetrically for dispersions with a range of lateral sizes and thicknesses to achieve an accurate C_o determination.

The change in extinction and absorbance spectra with lateral size can be used to establish metrics for lateral size once the sizes are calibrated by statistical microscopy. Such relationships were established for MoS_2 [185], WS_2 [186], GaS [188] and black phosphors [190].

Changes in LM band structure as a result of confinement are reflected in changes in peak position of excitonic transitions. This means that information on N is encoded in optical extinction spectra [185, 186, 188].

An example of the spectral changes with size and thickness for LPE MoS_2 and WS_2 is in figure IX.42 [245]. Figures IX.42(A) and (C) plot optical extinction spectra of MoS_2 (A) and WS_2 (C) with different mean flake sizes and thicknesses. Due to the power law non-resonant scattering background (>680 nm for MoS_2, >650 nm for WS_2), peak positions are best found from the second derivative. Second derivative spectra of a subset of the samples in the region of the A-exciton are shown in figures IX.42(B) and (D). Peak intensity ratios can be used to express the changes associated with edge effects. Figures IX.42(E) and (F) plot peak intensity ratios as function of mean flake length for MoS_2 and WS_2, showing that both materials behave similarly. This means that the flake size for both materials can be quantitatively linked to the length via identical equations [245]. Due to the changes in spectral shape, extinction coefficients are also dependent on size. This is more or less severe depending on spectral position. E.g. as plotted in figure IX.42(G), the extinction coefficient of the A-exciton for both materials is strongly length dependent. However, this is not the case at 345 nm for MoS_2 and 235 nm for WS_2 so that the extinction coefficient at these spectral positions can be used as a robust measure for C_o over a broad range of sizes. In addition, extinction spectra do not only provide insight in lateral size and dispersed concentration, but also in thickness. N can be quantitatively related to the peak position/energy of the A-exciton (obtained from an analysis of the second derivative), as plotted in figure IX.42(H).

PL is also a very powerful tool to study GRMs, as it provides information on the band gap and its direct/indirect nature [1550, 1551]. In PL measurements, GRMs are excited with a laser with higher energy than the bandgap to create electron–hole pairs. The emission yield upon radiative recombination is studied with a spectrometer. The excitation laser is notch filtered at the entry of the spectrometer to remove the Rayleigh contribution, which is much larger than the PL yield and might saturate the detector. Figure IX.43(a) compares PL spectra in MoS_2 flakes with different N. The peaks correspond to the recombination of excitons. A and B are related to direct bandgap transitions at the K point of the Brillouin zone and I corresponds to an indirect bandgap transition along ΓK, that becomes favourable for MLs. Therefore, PL allows one to observe quantum confinement in MoS_2, resulting in a N dependent bandgap. PL also makes evident the direct-to-indirect transition that occurs due to the interlayer interaction in MoS_2. While 1L-MoS_2 has direct bandgap with a bright PL emission, ML flakes are indirect bandgap with a much lower PL yield.

IX.2.2.2. HBN

Spectroscopy can be used to investigate and to benchmark the optical and structural properties of both bulk and exfoliated hBN. The hyperspectral capabilities of cathodoluminescence at 10 K are particularly suited [1552, 1553], figure IX.44. This figure shows a typical cathodoluminescence spectrum at 10 K on a sample prepared from a reference single crystal [1554] together with monochromatic images recorded at energies related to the different emission bands. It displays emission lines in a broad energy range from almost 6 to 3 eV.

Luminescence properties of hBN are governed by strong excitonic effects resulting in recombinations at energies below the bandgap [1791]. It is according to *ab initio* calculations [1791], hBN is a large band gap material with an indirect band gap around 6 eV and a direct band gap ~6.5 eV [1791]. Excitonic recombinations are near band edge (NBE) in the deepest UV region in figure IX.44. Among them, a series of peaks at the shortest wavelength (210–215 nm) is referred to as the *S* series [1048, 1555]. The excitonic nature of these recombinations is supported by theoretical studies [1556, 1557], but their fine structure splitting and their correlation with absorption data are still debated [1555, 1558–1561].

Other features can be observed in the 210– 250 nm region, and tentatively assigned to NBE [1048].

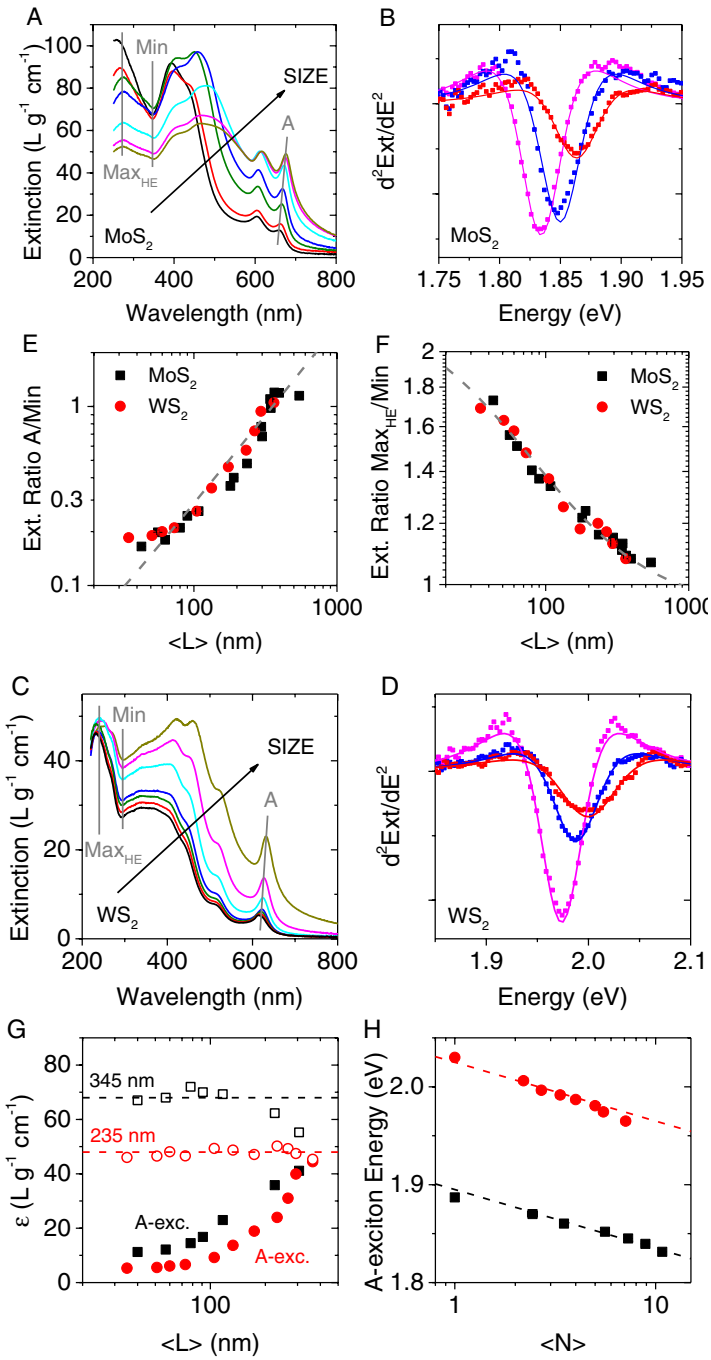


Figure IX.42. (A) and (C) Optical extinction spectra of LCC separated MoS_2 (A) and WS_2 (C). Peaks relevant for the analysis are indicated. (B) and (D) Second derivatives of the A-exciton versus energy for MoS_2 (B) and WS_2 (D) after smoothing the second derivative with Adjacent Averaging. The solid lines are fits to the second derivative of a Lorentzian to assess peak positions/energies. (E) and (F) peak intensity ratios as a function of $\langle L \rangle$. Data for MoS_2 and WS_2 fall on the same curve. Hence, the same equation can be used to quantify the flakes' length. (E) peak intensity ratio at the A-exciton/local minimum. (F) peak intensity ratio at the high energy maximum/local minimum. (G) Extinction coefficient at different spectral positions as function of flakes' length. At some spectra positions (such as the A-exciton), extinction coefficients are size dependent, while at others (345 nm for MoS_2 and 235 nm for WS_2) this is not the case. (H) A-exciton peak energies (from second derivatives) as function of $\langle N \rangle$. Adapted with permission from [245].

At larger wavelengths than the *S* series, the most documented luminescence feature is the so-called *D* series (220–227 nm) (see figure IX.44) related to the presence of extended structural defects. These emissions arise from recombinations of excitons trapped at structural defects [1048], such as stacking defects, dislocations, or grain boundaries [1553, 1562, 1563]. Finally, a weak and broader emission is often observed at 233 nm, figure IX.44, attributed to donor-acceptor pairs (DAP) recombination processes [1564].

The series of CL monochromatic images recorded from the same zone, figure IX.44, illustrates the distinct origins of the *S* and *D* features. The image, related to the intrinsic emissions (*S* series) and recorded by collecting photons at 215 ± 3 nm, is almost homogeneous, except along parallel black lines, due to thick-

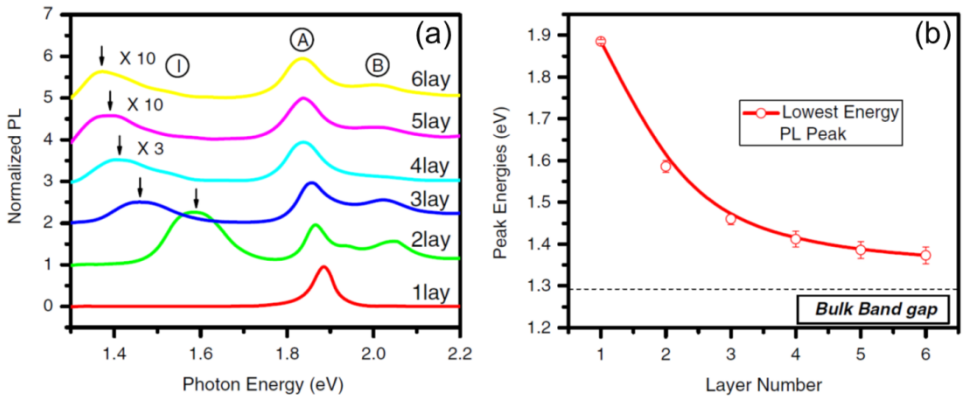


Figure IX.43. (a) PL spectra on MoS_2 flakes with $N = 1$–6. The spectra show peaks corresponding to excitonic features, labelled A, B and I. (b) N dependence of the lowest energy PL peak peak. Adapted from [1550], copyright American Physical Society.

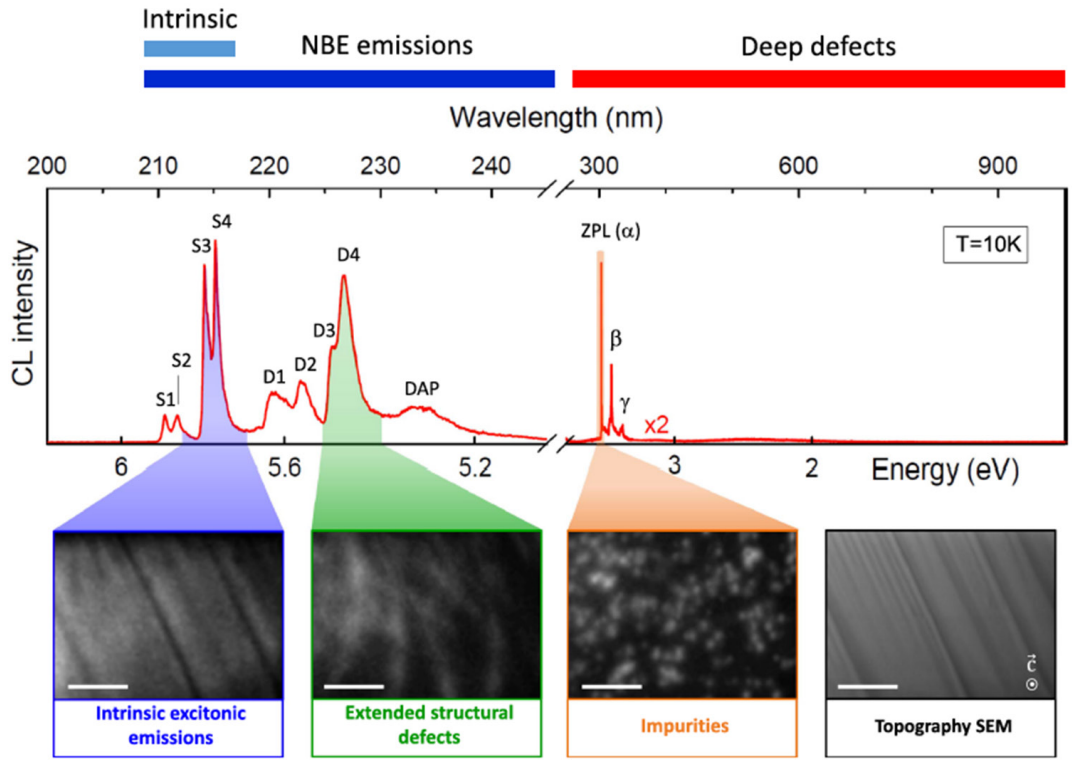


Figure IX.44. Upper: typical cathodoluminescence spectrum of hBN in the 200–1000 nm range acquired at 10 K on a sample prepared from a reference single crystal [1554].Lower: SEM image (black) with the corresponding monochromatic CL images recorded in the same area at ±3 nm around 215 nm(blue), 227 nm(green) and 303 nm(orange). Scale bar: 1 μm. Reproduced from [1048], © IOP Publishing Ltd.

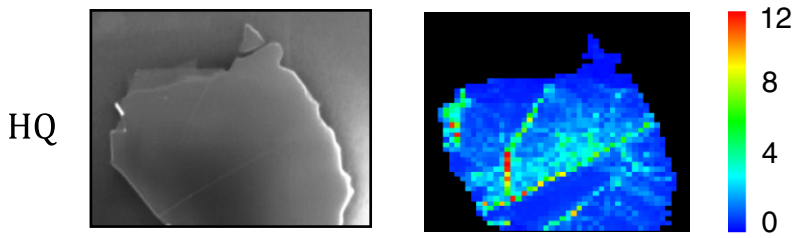


Figure IX.45. Left: SEM image of a hBN crystal flake. Right: Catholuminescence mapping of the *D*/*S* ratio of the integrated intensity of the *D* band relatively to that of the *S* band. Adapted from [1048], © IOP Publishing Ltd.

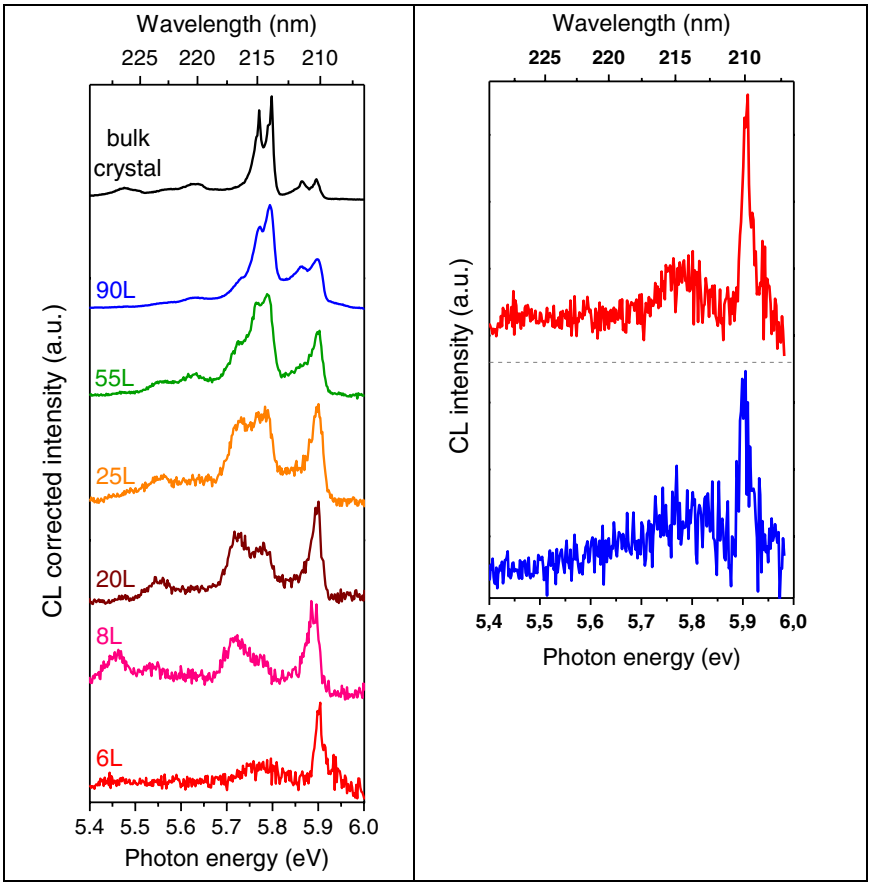


Figure IX.46. Left: series of CL spectra recorded at 10 K on MC flakes with different thicknesses from bulk to 6L and transferred on to Si/SiO_2. N is determined from both optical and AFM measurements. Right: CL spectra on 6L exfoliated flakes and from a grown single crystal [1554] (bottom spectrum). Adapted from [1555] with permission of The Royal Society of Chemistry.

ness variations along the sample (see the SEM image of the same area). The CL image taken from the *D* series (227 ± 3 nm) displays several continuous lines crossing the sample in random directions at places where structural defects are present. It was proposed to use the ratio of the integrated intensity of the *D* band relative to that of the *S* band, as an indicator of structural defects [1563]. Typically in defect-free areas, *D*/*S* can be as low as 0.3, while it can increase up to two order scales of magnitude at the location of structural defects. Therefore, as illustrated in figure IX.45, hyperspectral mapping of *D*/*S* is a valuable tool to get, in a non destructive way, the spatial distribution of structural defects in hBN and assess its crystalline quality [1048].

At larger wavelengths (>250 nm), the luminescence spectrum of figure IX.44 reveals deep defect emissions. A luminescence signal with a maximum at 302.8 nm is regularly detected in various hBN sources [1048]. This sharp: its linewidth <0.075 nm, the spectral resolution of the experiment. It has been identified as the zero-phonon emission line (ZPL), labelled here α, of impurities introduced in the lattice during synthesis, probably C (or possibly O) as revealed by a detailed SIMS analysis [1554]. The β and γ peaks are assigned to phonon replicas, with an energy ~195 meV, involving a local vibrational mode (LVM) [1565] or hBN phonos [1566]. In figure IX.44, the CL image recorded from the ZPL emission at 302.8 ± 3 nm reveals a spatial distribution which is typical of chemical impurities. The luminescence from the deep defects is distributed as bright spots, which confirms their distinct origin from *D* and *S* series. The observed luminescence spots unveil a discrete and random distribution of impurity centers throughout the sample. Similar spots were reported and identified as single photon emitters, indicating that they correspond to isolated atomic centers randomly diluted in the crystal lattice [1567]. Sharp emissions from deep defects have been identified as single emitters in the visible and the NIR after introducing defects in hBN [1568].

The dependence on N of NBE emission has been investigated on MC flakes [1555]. The samples were free of defects with no detectable *D* band. Typical thickness evolution of the CL spectra is shown in figure IX.46. The *S* series, characteristic of bulk hBN, progressively vanishes in the thinnest layers in favor of a single peak ~ 5.909 eV in 6L samples. Such an effect was observed in different kinds of samples, including reference single crystals and commercial sources, which points to an intrinsic behaviour and can be considered as a signature of low dimensionality effects on the intrinsic luminescence of hBN. With the support of combined *ab initio* and tight binding calculations,

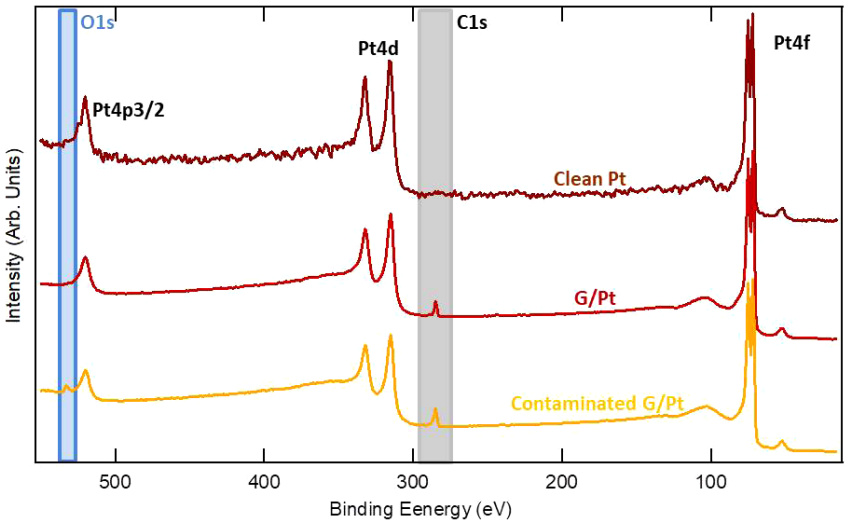


Figure IX.47. XPS spectra of three samples: (top) Pt(1 1 1), (middle) SLG/Pt(1 1 1), (bottom) contaminated SLG/Pt(1 1 1). Grey (blue) area represents the zone where C1s (O1s) related peaks appear.

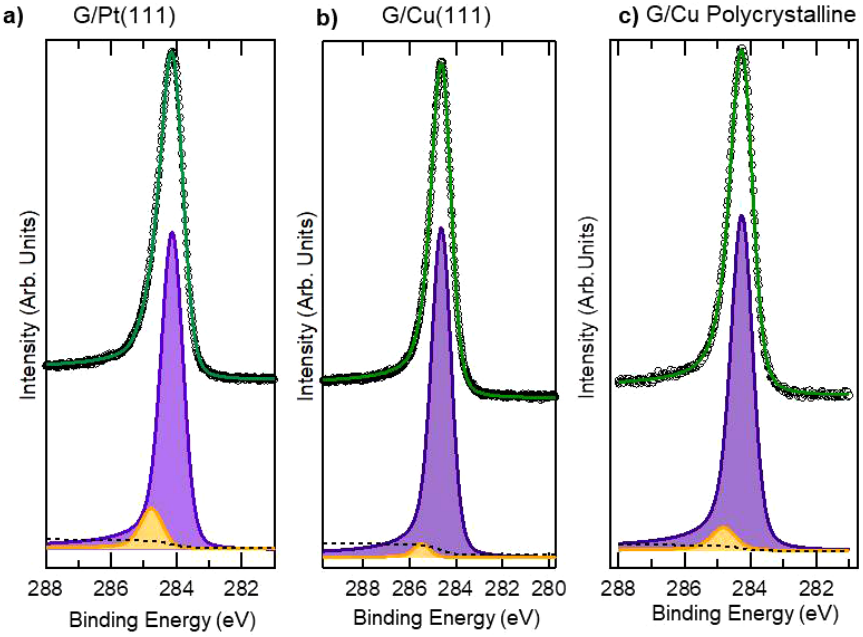


Figure IX.48. C1s XPS spectra of (a) SLG/ Pt(1 1 1) (b) SLG/Cu(1 1 1) and (c) SLG/Cu polycrystalline.

the remaining line observed in the thinnest layers was assigned to direct bright excitons, as theoretically expected for 1L [1556].

IX.2.3. XPS

XPS measures the kinetic energy of photoelectrons emitted from a sample irradiated with x-rays, which transfer their energy to a core-level electron. This electron is emitted out of the sample surface from its initial state with a kinetic energy dependent on the incident x-ray photon energy and the binding energy of the atomic orbital from which it is originated, $E_{\text{kinetic}} = E_{\text{photon}} - E_{\text{_binding-efective_wf}}$, where E_{kinetic} is the Kinetic Energy of the emitted electron, E_{photon} is the energy of the incident photon and $E_{\text{_binding-efective_wf}}$ is the effective binding energy of the corresponding atom. The energy and intensity of the emitted photoelectrons can be analysed to identify the elemental and chemical composition in the parts per thousand [1569, 1570]. Photoelectrons originate from depths below 10 nm, therefore the information obtained is surface-sensitive [1569]. The XPS equipment has to detect electrons, thus the sample has to be introduced in a UHV environment. The area illuminated is typically ~0.5–1 mm when a x-ray monochromator is used [1569], meaning that the information corresponds to an average on the irradiated area. The best energy resolution that one may have is ~ 0.4 eV in standard machines. However, this may increase to ~0.2 eV in synchrotron radiation XPS facilities.

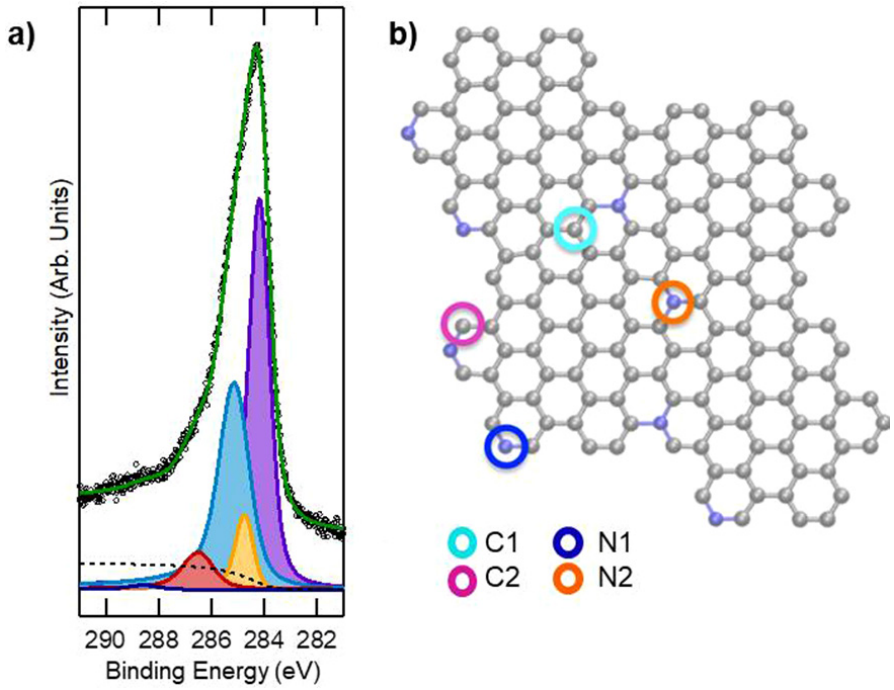


Figure IX.49. (a) C1s XPS spectrum of SLG/ Pt(1 1 1) after exposure to air and water. New components related with epoxy and hydroxyl groups appear as a tail of the main C-sp^2 one. (b) Schematic representation of N and C configuration of heteroatoms on a graphene flake related with the XPS peaks assignments. C1 (light blue): sp^2 C atoms; C2 (purple): C–N pyridine ring; N1 (dark blue): N atoms in the pyridine ring interacting with the metal substrate (Cu in this example); N_2 (orange): substitutional N atoms in the graphene network. Adapted from [1577] with permission of the PCCP Owner Societies.

When analysing graphene based samples there are three main figures that can be extracted from the XPS spectra: presence of contaminants (or heteroatoms), coverage, and chemical state of the C atoms.

The presence of contaminants (heteroatoms reacting with graphene or other elements) can be derived from a survey spectrum of the sample, i.e. measuring in a wide range all the relevant peaks. This usually covers from the $E_F$to ~50 eV less than the x-ray photon energy, and shows core-level peaks from all elements on the sample surface. The amount of impurities can be determined by integrating the area of the different levels and comparing the ratio of the different peaks. The analytic expressions for deriving the coverage of impurities or graphene patches with respect to a substrate can be found in Refs. [1569, 1570].

The upper spectrum in figure IX.47 was recorded from a clean Pt(1 1 1) surface. Only Pt peaks are visible. The middle one belongs to the same sample after SLG growth. In addition to the Pt peaks, a new peak related to carbon (C1s) appears. If the sample is exposed to air, it can get contaminated, mainly with O that binds to SLG as epoxy or hydroxyl groups [935, 1035, 806]. The lower XPS survey spectrum shows in addition to the Pt and C peaks the oxygen peak (O1s). This technique is surface-sensitive. Whenever the sample gets something on top, i.e. graphene, O, etc, the intensity of its main peaks decreases. In figure IX.47 the Pt4f peaks intensity decrease from the upper spectrum to the lower one, as SLG is grown, and then exposed to air.

The chemical state of the C atoms of graphene can be also derived from XPS. The characteristic binding energy of C 1s when C is in a sp^2 configuration (either graphene or HOPG) is ~284.5 eV [1571] (the precise value depends on the analyser) [1572]. When SLG is grown on substrates, such as metals or semiconductors, the C 1s binding energy might slightly change due to the interaction between graphene and substrate [1569]. C-sp^2 is ubiquitous as many contaminants include carbonaceous species that are difficult to discern from graphene.

Bonding of C with other atoms leads to different binding energies, therefore a precise determination of the C1s binding energy may give the type of bonding. This is known as core level shift, and most of the values are tabulated [1570]. C-sp^3 appears ~285.0 eV [1573–1576]. To derive the different components of an XPS peak, a curve fitting is necessary.

Figure IX.48 shows three C1S XPS spectra of SLG grown on different substrates by thermal decomposition of fullerenes in a UHV environment on Pt(1 1 1) [1035] Cu(1 1 1) and polycrystalline Cu. The peaks are fitted with two components. The purple and narrow one is related with C-sp^2. This component is fitted using a Doniach-Sunjic curve, which is the mathematical function that better fits an XPS core level peak [1569]. In this curve, the asymmetry parameter is 0.068 eV [1569]. The Lorentzian FWHM is ~0.13 eV. The binding energies for the C-sp^2 are 284.1, 284.6, 284.3 eV for SLG on Pt(1 1 1), Cu(1 1 1) and polycrystalline Cu respectively. Another small component is

Table IX.2. Binding energies of graphene C atoms in different chemical states. C1, C2, N1 and N2 are related with the scheme of figure IX.49(b) and represent C-sp^2 (C1), C-N pyridine (C2), N atoms in the pyridine ring interacting with the metal (N1) and substitutional N atoms in the graphene network (N2). In addition, binding energies of C-metal, sp^3 configuration, radical-N, epoxy and hydroxyl groups are also given. The values may slightly change depending on substrate.

	C1	C2	N1	N2	R–N–C	C-metal	sp^3	C–OH	C–O	C=O	O–C= C/C–C=O
Binding energy (eV)	284.4	285.9	398.0	400.6	399.5	283.2	284.7	285.4	286.7	288.5	290.5
Ref	[1577]	[1577]	[1577]	[1577]	[1340]	[1577]	[1035]	[926]	[926]	[926]	[926]

needed to complete the fitting, with a binding energy that depends on the substrate. This can be assigned to C-sp^3 [1573–1575].This component appears in defective SLG due to different domains and grain boundaries [902]. In figure IX.48 the fitted values are: 284.7, 285.4, 284.8 eV for SLG on Pt(1 1 1), Cu(1 1 1) and polycrystalline Cu. The width of these peaks (0.13 eV) may increase when the graphene surface is damaged, contaminated or oxidized.

Figure IX.49(a) shows an example C1s peak of SLG exposed to air and water. This is a broad with many components. The purple one at 284.1 corresponds to C-sp^2 and the yellow one at 284.7 to C-sp^3 (as in the clean sample in figure IX.48(a)). Three new components related to surface contaminants are also present: the light blue at 285.1 assigned to C–OH, the red one at 286.5 assigned to C–O and the dark blue at 288.5 assigned to C=O [806, 1573]. They can be fitted using Gaussian-Lorentzians. These epoxy groups (CO bonding or oxidized species) and hydroxyl groups appear as a tail of the main peak at higher binding energies and they are a fingerprint of the 'cleanliness' of a graphene sample. A soft annealing in vacuum will remove these type of contaminants. Table IX.2 shows typical binding energies of some of the most important oxygenated species (epoxy and hydroxyl) bonded to C The binding energy may slightly change (within ±0.5 eV) depending on system or substrate used.

It is important not to mistake the contamination of graphene with GO. RGO can be derived from GO by reducing it with chemical reducing agents. This process can be followed by XPS by evaluating the ratio of the component ~286.5 eV (mainly C–O bonds) with the C-sp^2 [1578].

Heteroatoms. In some cases one may be interested in the binding energy not of the C atoms, but of other elements covalently linked to graphene. The most important case corresponds to N heteroatoms. Its binding energy strongly depends on the adsorption configuration inside the graphene network. A scheme C and N atoms configuration in relation with the XPS components is shown in figure IX.49(b). Four possible configurations are shown: C-sp^2 (C1, light blue circle), C in a pyridine ring (C2, purple circle), N in the pyridine ring interacting with the metal substrate (Cu for this case) (N1, dark blue circle) and a substitutional N in the graphene network (N_2, orange circle). The XPS binding energies in these particular configurations are in table IX.2.

IX.2.3.1. Graphene grown on SiC

XPS characterization of C-rich SiC(0 0 0 1) surfaces can be used to extract the degree of graphitization. SiC surfaces prepared in UHV conditions present a series of surface reconstructions depending on the C/Si stoichiometry [1579]. For $T > 1350$ K, Si depletion from the surface eventually leads a reconstruction presenting a $(6\sqrt{3} \times 6\sqrt{3})$R30° LEED pattern [592, 645, 659, 1580, 1581]. The atomic structure is normally described as a graphene-like honeycomb carbon layer highly buckled and partially covalently bonded to the uppermost Si layer [1582] (see section IV).

This covalent interaction alters the electronic properties of the graphene-like layer and it becomes a semiconductor [594]. XPS is presented in figure IX.50. The lower spectrum is an overview on a $(6\sqrt{3} \times 6\sqrt{3})$ R30° surface. The C1s peak (284.8 eV) has higher intensity than the two Si-related peaks: Si2p (101.4 eV) and Si2s (152.0 eV) [926, 1570]. The C1s/Si2p ratio is ~1.15 for 1486.6 eV, indicating that the surface is C-rich [659].

A SLG/SiC(0 0 0 1) spectrum is presented in figure IX.50 for comparison. The upper black spectrum corresponds to a synchrotron radiation-based overview of a sample annealed at 1400 K recorded with a photon energy of 600 eV [1583] The C1s peak dominates, with C1s/Si2p ~ 2.53, which indicates a higher C concentration on the surface than in the $(6\sqrt{3} \times 6\sqrt{3})$R30. The good resolution of the XPS in figure IX.51 allowed to decompose the peaks into their curve-components, which results from a convolution of a purely Lorentzian one (FWHM, 0.12–0.2 eV) with a Gaussian distribution (FWHM, 0.4–0.7 eV) [1584].

C chemistry is very rich and the interpretation of the C1s spectra is complicated. One could decompose the C1s peak of SLG/SiC(0 0 0 1) in five components. That at 284.83 eV can be assigned to C-sp^2, and is the biggest contribution to the C1s core level peak, with 58.2% of the total area. This is used for calibration of the the Lorentzian and Gaussian widths. The components at lower binding energies (283.98 eV) can be attributed to carbides [1585], due to the C in the SiC bulk [588, 589]. There are three other components at higher binding energies, which can in principle be assigned to different configurations of C in the rearrangement that takes place on surface reconstruction [589]. These can be assigned to surface-related peaks: C-Si 1 at 285.26 eV (orange component in figure IX.51(a)), C–Si 2 at 285.73 eV (pink component in figure IX.51(a)) and S. C-Si 3 at 286.4 eV (bordeaux component in figure IX.51(b)).

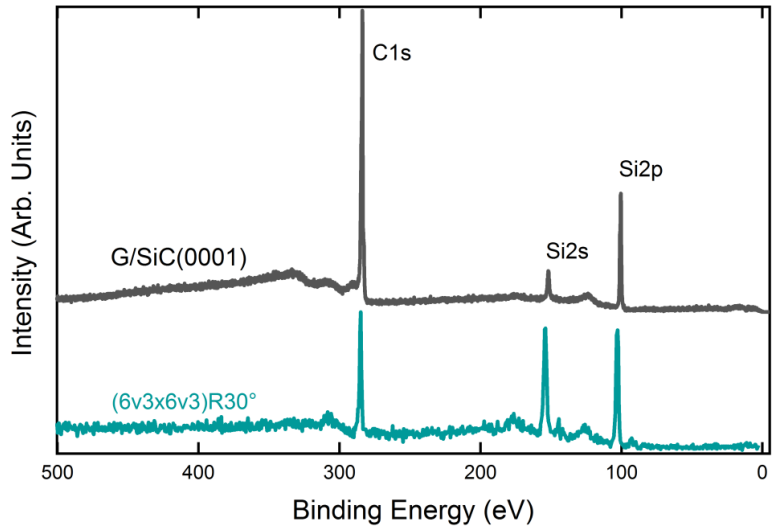


Figure IX.50. Lower spectrum: $(6\sqrt{3} \times 6\sqrt{3})$R30° surface using an Al Kα anode (1486.6 eV) as x-ray source. Upper spectrum: synchrotron radiation XPS overview of SLG/SiC(0 0 0 1) annealed at 1400 K for 600 eV photons.

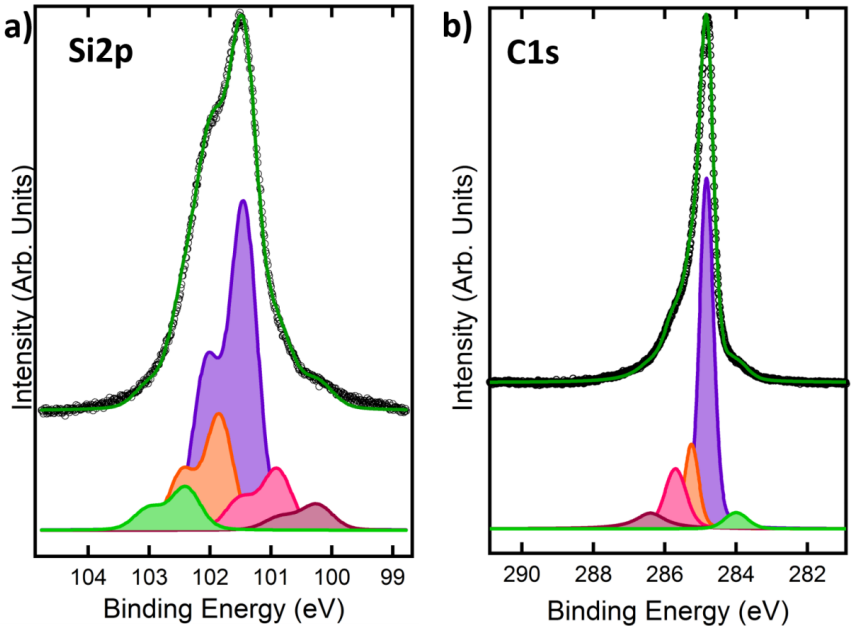


Figure IX.51. (a) XPS Spectrum of Si2p peak of SLG/SiC annealed at 1400 K recorded with a photon energy of 150 eV. (b) XPS spectrum of C1s peak of SLG/SiC annealed at 1400 K recorded at 400 eV.

The Si2p curve can be decomposed in five Si doublets. Based on H adsorption it is possible to distinguish surface-related from bulk-related components. Three components present intensity decrease upon H exposition. The intensity of the components at 100.4, 101.45 and 101.85 eV decrease ~15% after H exposure, while the other two at 100.9 and 102.4 eV present a small (3%–4%) increase [1585]. This suggests that the components which decrease and those that increase are related to surface and bulk Si atoms respectively.

IX.2.4. ARPES

ARPES is a technique that extracts the information retained by the electrons, emitted from a solid surface upon excitation with a photon. Due to the confinement of the electronic wavefunctions in the (x,y) plane, the band structure of GRMs can be fully determined through angle-resolved photoemission spectroscopy (ARPES) [1586–1588]. This technique takes advantage of the photoelectric effect [1589], hence UV or soft x-ray radiation is used to extract electrons from the investigated sample.

The photons can be generated by laboratory sources, such as He or Hg lamps, or by synchrotron radiation. During photoemission, the crystal momentum of the electron inside the material is conserved in the plane parallel to the samples's surface. As a consequence, one can relate the electron's crystal momentum with the photoemission angle and determine the band structure. A typical experimental set-up for

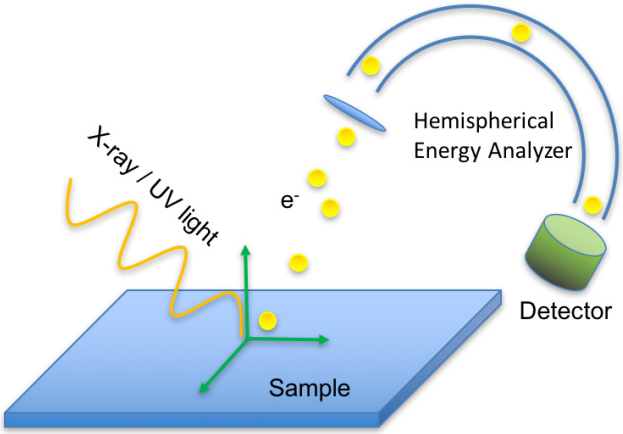


Figure IX.52. ARPES set up scheme. Electromagnetic radiation provides enough energy for electrons to the sample to leave and travel towards the analyzer.

ARPES is sketched in figure IX.52. The radiation is shone over the sample so that the photon beam and the analyzer lay in the same plane. The photoemitted electrons are collected, within a certain angular acceptance, through a series of focusing electrostatic lenses into a hemispherical analyzer. Here, only the electrons with a certain kinetic energy E_0 travel in the middle of the hemispherical capacitor. The width of the energy window about E_0 is called pass energy, and it is a relevant parameter in determining the energy resolution of the instrument. The other important parameter is the radius of the hemispherical capacitor. Finally, the electrons impinge onto the detector, which in most cases is a fluorescent screen. A charge-coupled device (CCD) camera records the light intensity emitted by the detector.

In the UV, soft x-ray regime, the momentum carried by the photon $p_{\mathrm{ph}} = h\upsilon/c$ is negligible compared to the crystal momentum of the electron $\hbar k \gg p_{\mathrm{ph}}$, and this ensures the identity between the final and initial electron momentuma, i.e. $\mathbf{k}_f = \mathbf{k}_i$. Hence, the von Laue equation $\mathbf{k}_f = \mathbf{k}_i + \mathbf{G}$ is fulfilled, where $\mathbf{G}$ is a base vector of the crystal's reciprocal space. Experiments are usually performed using photon energy <100 eV corresponding to a momentum $\frac{p}{\hbar} \sim 0.05\ \mathrm{\AA}^{-1}$. In the so-called *sudden approximation*, the electron is extracted instantaneously —from the material with no time to interact with the remaining $N-1$ electrons [1586]. This allows one to consider the obtained dispersion as the non-interacting state of the system, or the one particle dispersion. As a consequence, for GRMs, the emitted photocurrent takes the form [1792]:

$$I(\mathbf{k},\ E, h\upsilon) \propto \left|M_{i,f}\right|^2 A(\boldsymbol{k}, E)\, f(E,T) + B \qquad \text{(IX.11)}$$

where $\left|M_{i,f}\right|$ is the matrix element of the transition from the initial (i) to the final (f) state, $A(\boldsymbol{k}, E)$ is the spectral function, $f(E,T)$ is the Fermi–Dirac distribution and B is a background term coming from inelastically scattered electrons. The spectral function takes into account the angular dependence of the photoemitted electrons.

When the electrons leave the material, they end in a free particle state. Considering the scheme in figure IX.53 and assuming the conservation of the electron momentum parallel to the surface, the following expression holds [1586]:

$$k_{||\,\mathrm{int}} = k_{||\mathrm{ext}} = \sqrt{\frac{2mE_{\mathrm{kin}}}{\hbar^2}}\sin(\theta) \qquad \text{(IX.12)}$$

where θ is the emission angle and E_{kin} is the kinetic energy. When considering the perpendicular component, the description is not this simple, since it is not conserved when crossing the crystal surface [1586]. An expression to determine it is [1586]:

$$k_{\perp\,\mathrm{int}} = \sqrt{\frac{2m}{\hbar^2}}\sqrt{E_{\mathrm{kin}}\cos^2(\theta) + V_0} \qquad \text{(IX.13)}$$

where V_0 is the *inner potential*, defined as the energy difference between the vacuum level and the top of the valence band.

The resolution on the measurement of $k_{||}$ is:

$$\Delta k_{||} = k_{||}\sqrt{\left(\frac{\Delta E}{2E_{\mathrm{kin}}}\right)^2 + \left(\frac{\Delta\theta}{\tan(\theta)}\right)^2} \qquad \text{(IX.14)}$$

where $\Delta\theta$ is the angular acceptance of the analyzer.

If the electron signal is spin-filtered, e.g. by letting it passing through a Mott detector, it is possible to reveal the contribution of a single spin component projected onto the detector's plane [1590] on a particular band. This technique is called spin-resolved ARPES (SARPES) and it is fundamental for determining the spin-polarization of electronic bands.

A recent development in ultra-fast lasers gave the opportunity to realize facilities for pump-probe experiments that can access the time scales of the quasiparticle dynamics in solid-state materials [1794]. Time-resolved ARPES (Tr-ARPES) is being used more and more to investigate the carrier dynamics in GRMs as well as charge transfer in LMhs.

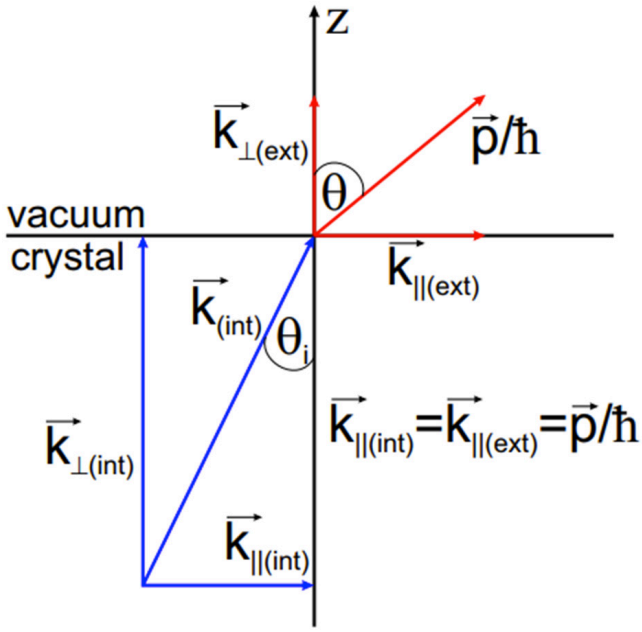


Figure IX.53. Momentum component conservation at the crystal vacuum interface. Only $k_{||}$ is conserved.

IX.2.4.1. ARPES on graphene and vertical LMHs

A large amount of photoemission measurements have been carried out on graphene since the early 1970s [586, 663, 664], and ARPES measurements have since mapped the dispersion of the π-bands over the entire BZ.

The energy loss due to quasiparticle excitation, the electron phonon interaction in π and σ bands [671, 1591–1593] were investigated. Graphene on metals [1594], exfoliated, suspended and GNRs [592, 618, 620] have been measured. Perhaps the most investigated graphene with ARPES is that grown on SiC, because it has cm^2 area coverage, and because of its flatness (figure VII.10) [592, 671, 673, 679, 1591].

The electronic properties of buffer, 1LG, 2LG, 3LG have been characterized by means of ARPES [598]. Quasi-free standing graphene on SiC has been investigated [645, 647, 678]. This method can be applied also to other LMs, such as TMDs [1595], and their combination in vertical LMHs [1217, 1596]. The possibility of studying the electronic properties of such a structure allows for understanding how the layers interact with each other.

The band structure of WS_2/SLG can be retrieved by means of μ-ARPES on a single WS_2 crystal. μ-ARPES (or micro-spot ARPES) is a technique capable of measuring the electronic properties of a material with a spatial resolution ~1 μm. The price for the higher spatial resolution is paid in terms of energy resolution, which is slightly worse. Figure IX.54(a) show a LEEM image of a single triangular WS_2 crystal on graphene on SiC [1217].

Overlapping ARPES measurements with DFT minimizes the error in interpreting the measured signal. Figure IX.55(a) reports the graphene π- and π^*-bands measured via μ-ARPES on the crystal shown in figure IX.54. The bands are well visible and

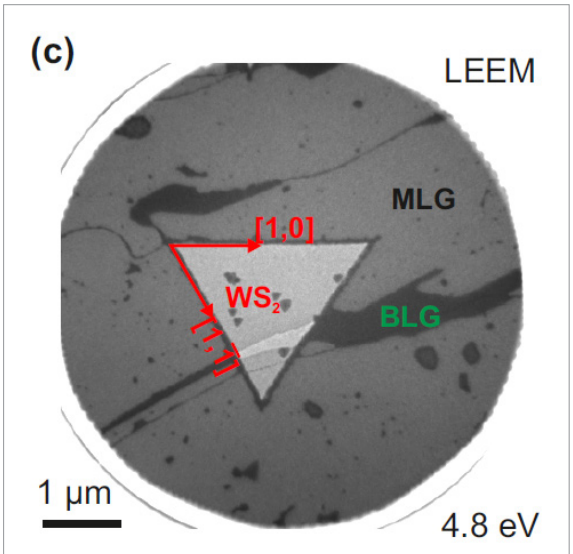


Figure IX.54. Micrograph of a single WS_2 crystal. Areas with different contrast are labeled MLG, BLG and WS_2, respectively. Red arrows indicate the crystallographic orientation of WS_2 crystal. Adapted from [1217] with permission of The Royal Society of Chemistry.

highlighted by orange dots, corresponding to DFT bands on the graphene single cell. Calculated graphene σ-bands are not superimposed, since they are not detectable due to their low intensity. The bands visible in Γ belong to WS_2, as also indicated by DFT. At the points where the bands of graphene and WS_2 cross (indicated by green arrows in the panel), no apparent splitting or gap is observed. In order to confirm this, DFT calculations were carried out, the result of which is summarized in figure IX.55(b), where the bands 'unfolded' onto graphene's BZ are displayed for better readability.

When crystals with different lattice parameter are superimposed, they can give rise to a superlattice.

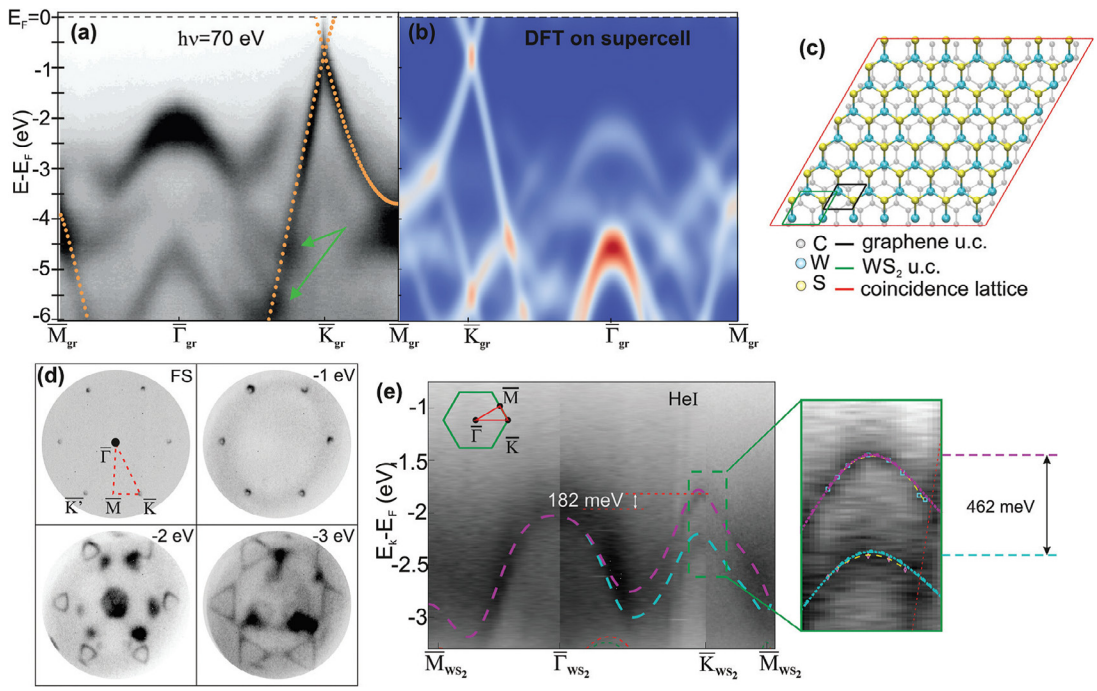


Figure IX.55. Band structure of WS_2/MLG. (a) μARPES measured on a single WS_2 triangle with photons~70 eV. (b) DFT band structure evaluated on the WS_2/graphene supercell depicted in panel (c) and unfolded into graphene's BZ. (c) Coincidence supercell (7×7) over (9×9) of WS_2/graphene. (d) Experimental ARPES CESs recorded with p-polarized photons ~ 27.5 eV (e) Experimental ARPES band structure of WS_2/EG measured with He I light along the path indicated in the inset by the red line. DFT bands including spin–orbit effects are overlapped to the raw data. On the right: zoom-in of the region around $\overline{K}_{WS_2}$ (green-dashed line in panel (e)). Both DFT and experimental bands fit are superimposed to the raw data. The red-dashed line is on the graphene's π-bands. Adapted from [1217] with permission of The Royal Society of Chemistry.

When multiples of the different unit cells match in size, they form a supercell which behaves as a new unit cell of a hybrid crystal. This new periodicity alters the overall band structure, opening minigaps in high symmetry points. The smallest coincidence lattice for the WS_2/graphene system was found to be the (7×7) WS_2 unit cells (u.c.) on (9×9) of graphene, figure IX.55(c). DFT calculations were carried out on this supercell and as a result, no mini-gap opening was predicted, unlike what observed for MoS_2 on graphene [1596]. To better visualize the relation between the graphene π-bands and the WS_2 bands, constant energy surfaces (CESs) are shown in figure IX.55(d), extracted from the Fermi surface (FS) at binding energies indicated in the figure. The CESs in this case are small volumes in k-space integrated over #250 meV, corresponding to the resolution of the instrument. The data were acquired with photon energy 27.5 eV in order to maximize the intensity of the WS_2 bands with respect to graphene.

ARPES measurements with He I radiation of 21.2 eV are presented in figure IX.55(e), together with the DFT-calculated bands including spin–orbit coupling. The image was obtained by scanning the BZ along the red line traced within the green hexagon in the inset. In this image the high symmetry points are for the WS_2 BZ, whereas for panels (a) and (b) they refer to graphene's BZ. Single spectra were measured perpendicular to the red line. The experimental data are fitted in the proximity ($\pm$~0.1 Å^{-1}) of $\overline{K}$ with a parabolic function in order to extract the effective mass values of the holes. The result along the $\overline{\Gamma KM}$ direction is displayed on the right side of figure IX.55(e), representing the zoom-in of the region framed with a green-dashed line in the panel. This gives $m_{h1} \sim 0.39 m_e$ for the low energy band and $m_{h2} \sim 0.53 m_e$ for the high energy band, confirming the asymmetry reported in Ref. [1597]. The spin–orbit splitting of the WS_2 bands in K was retrieved from integrated energy distribution curves to be 462 ± 5 meV. This is ~10% larger than what was measured for 1L-WS_2 on Au(1 1 1) and Ag(1 1 1) [1598, 1599] and ~7% larger than the highest value reported so far [1599]. This is comparable with measurements on bulk WS_2 [1594].

IX.3. Electrical characterization

IX.3.1. Four probe configuration

The basic electronic properties of a homogeneous metallic diffusive material are captured in the primary parameters: resistivity ρ ($\Omega \cdot$ cm), n (cm^{-3}) and μ (cm^2 V^{-1} s^{-1}). For a LM, the resistivity is replaced by R_S (Ω), i.e the resistance that would have a (homogeneous) sheet of material with equal length and width. For a sheet of thickness t, $R_S = \rho/t$. Similarly the surface charge density n_s (cm^{-2}) is $n_s = n\ t$ where σ is the conductivity. $\sigma/(n_e) = 1/(n_s e R_S)$. It is usual to define $\mu = \sigma/(n_s e) = 1/(n_s e R_S)$. It is common in the GRM literature for R_S to be written as ρ_{xx}.

Resistances are measured in a four-probe configuration, where a current I is applied on 2 probes (source and drain) and the voltage drop V measured

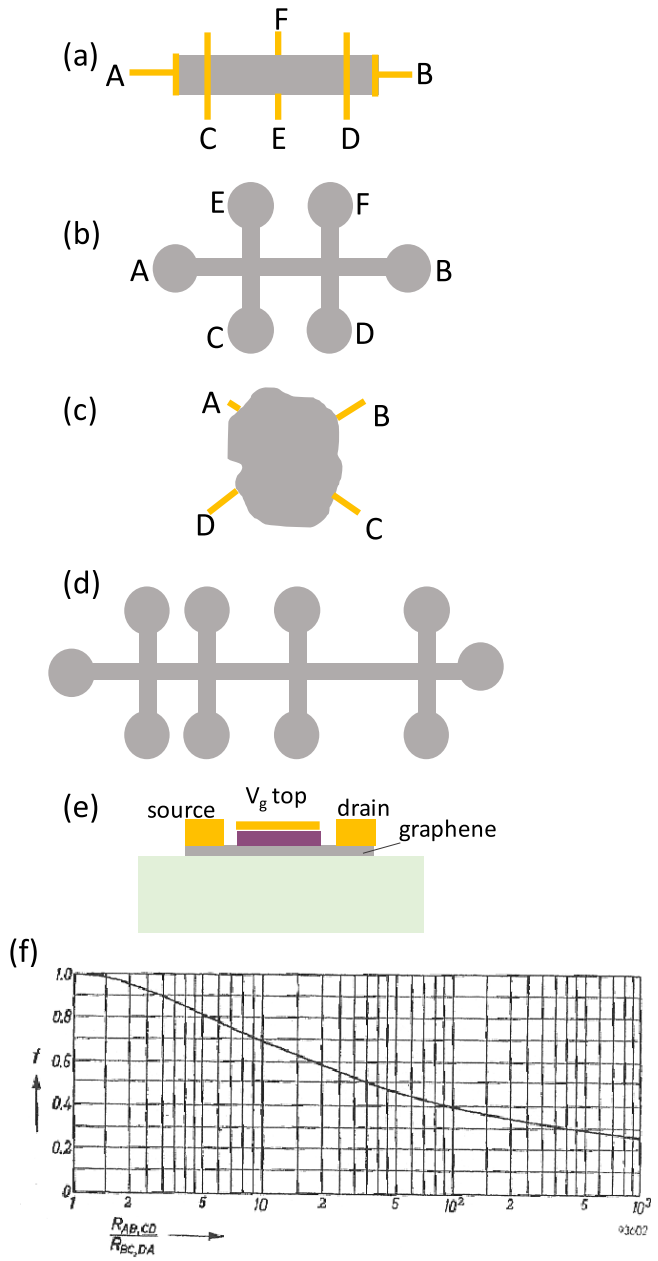


Figure IX.56. (a) 4-probe configuration. (b) Hall bar. (c) Van der Pauw. (d) TLM configuration; (e) FET, showing a SLG with a top gate deposited on a dielectric, and source and drain contacts. (f) *f* coefficient of the Van der Pauw method.

on two others following the schemes in figure IX.56. This removes the contribution from contacts, i.e. that of the leads (wires), to the measurement apparatus, so that the measured resistance V/I is intrinsic to the sample. In a linear configuration (figure IX.56(a) and Hall bar figure IX.56(b), $R_S = (V_{CD}/I_{AB})\cdot(W/L)$, where W and L are the width of the sheet and distance between the voltage probes C and D, respectively. In a Van der Paw configuration [1600] (figure IX.56(c)), contacts are attached to the edges of a sheet and $R_S = \pi(R_{AB,CD} + R_{BC,DA})/[2Ln(2)]$. $f(R_{AB,CD}/R_{BC,DA})$, where $R_{AB,CD}$ is the resistance measured injecting the current between A and B and the voltage probes are C and D. $R_{BC,DA}$ is measured by permutation. The f is a function of $R_{AB,CD}/R_{BC,DA}$ only, and satisfies the condition [1600]:

$$(R_{AB,CD} + R_{BC,DA}) / (R_{AB,CD} + R_{BC,DA}) = f \arccos h\left[\exp\left((Ln2/f)/2\right)\right]. \quad \text{(IX.15)}$$

f is plotted in figure IX.56(f). The Van der Pauw configuration allows measuring a sheet of arbitrary shape, like a cross e.g.

Standard techniques [1601] are used to measure the SLG resistance.This is usually in the range a few tens Ω to a few 100 kΩ. In the low current range, low-frequency (typically a few Hz to a few kHz) AC measurements with a lock-in amplifier, either in current or voltage source mode, provide the best SNR. I-V characteristics are measured in DC mode, or by recording the current change (Iac) induced by modulating the voltage around a DC bias ($V = V_{dc} + V_{ac}$). In all cases, the current must be kept low enough not to heat the

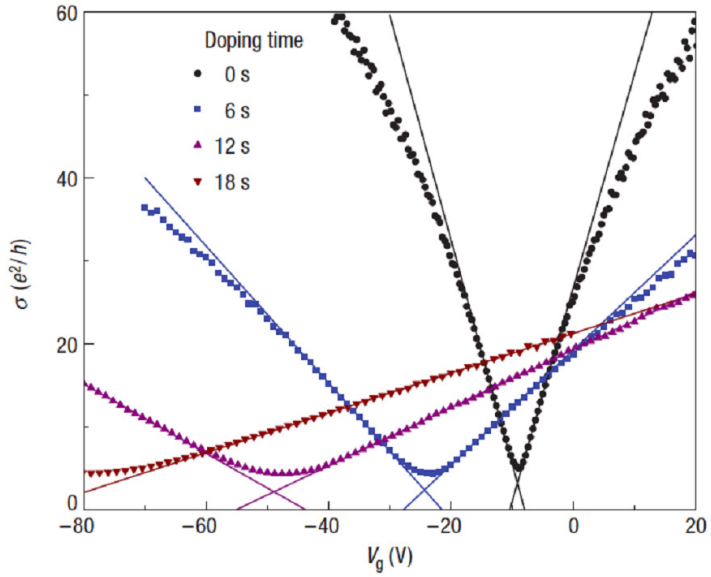


Figure IX.57. σ versus gate voltage at 20 K in UHV, for SLG and three different K doping concentrations. Lines are fits to equation (IX.16) and give μ, and the crossing of the lines defines the points of the residual conductivity and the gate voltage at minimum conductivity (σ_{res}, $V_{g,min}$) for each data set [1599].

sample, or to induce changes. At cryogenic T, typical currents range between nA to hundreds μA. High currents (~mA per μm width) can be used to anneal SLG to clean up impurities [1602, 1603] or to produce narrow constrictions tens of nm wide in suspended SLG [1604].

Ultra-high frequency measurements (>100 GHz [1605–1607]) or high precision resistance measurements for quantum Hall effect [612, 635] require specialized equipment.

The charge density is determined either from the Hall effect, or from electrostatic field effect. The Hall voltage, $V_{H,}$ is measured perpendicular to both current and magnetic field. Typically Hall bars such as in figure IX.56(b) are used. With the magnetic field B perpendicular to SLG and current from A to B, $V_H = V_{CE} = V_{DF}$. For SLG, $n_S = B/(e\rho_{xy})$, where $\rho_{xy} = (V_H/I)$. In the van de Pauw geometry, current leads and voltage probed are placed in cross configuration, such that $\rho_{xy} = V_{AC,BD} = V_{BD,AC}$ following figure IX.56(c).

In the simplest approximation, μ is deduced from resistance and charge density measurements: $\mu = \rho_{xy}/(R_{sq}\ B)$. In the simplest picture of short range scatters, the Boltzmann conductivity σ is independent of energy, i.e. independent of n [1608]. In this picture, the usual definition $\sigma = n_s e\mu$, would give μ with unphysically large values at charge neutrality. In reality, σ varies with n_s, being minimum at and around charge neutrality. This calls for other scattering mechanisms, like charge impurity scattering or resonant scattering [1608]. A better description of the relation between σ and n was given in Refs. [1608, 1599]:

$$\sigma = \sigma_{res} + Ke\left|n_s/n_{imp}\right| \qquad \text{(IX.16)}$$

as shown in figure IX.57. Here n_{imp} is the charge impurity concentration, K/n_{imp} has the unit of mobility and σ_{res} reflects the fact that SLG conducts even at zero carrier density [1610].

In the previous examples n_s is modulated with an electrostatic gate. In principle this is a parallel plate capacitor, with one plate being the gate and the other SLG. Either SLG is deposited on the dielectric or vice-versa. In the former case, the gate below SLG (bottom gate) often consists of conducting Si (the gate) covered with a dielectric (SiO_2) onto which SLG is deposited. All devices fabricated on the substrate are subjected to the same field when a voltage V_G is applied to the Si gate. Top gates are realized by depositing a dielectric (Al_2O_3, HfO, SiN, h-BN, etc) on SLG, e.g. by ALD or thermal evaporation. Sputtering is not recommended since it damages SLG [1611]. This is followed by coating with a metal (Au, Al). Top gates are usually patterned and can be addressed individually to switch one device at a time. The gate can also be brought close to SLG from the side in the same plane as SLG (side-gate). If the gate itself is also made of SLG, this allows patterning the SLG device and the gate all at once [730, 1612].

In the top/bottom gate configuration, the simplest assumption gives a charge variation Δn_s induced on SLG as:

$$\Delta n_s = (\varepsilon_0\varepsilon/t_d)\ V_g \qquad \text{(IX.17)}$$

where ε and t_d are the dielectric constant and thickness of the dielectric. In most FET configurations the SLG channel is provided with only 2-contacts (plus the gate, see figure IX.56(e)), therefore the contact resistance is included in the measurements, which results in underestimating μ. More precise methods have been developed [1613, 1614]. For sufficiently large bias

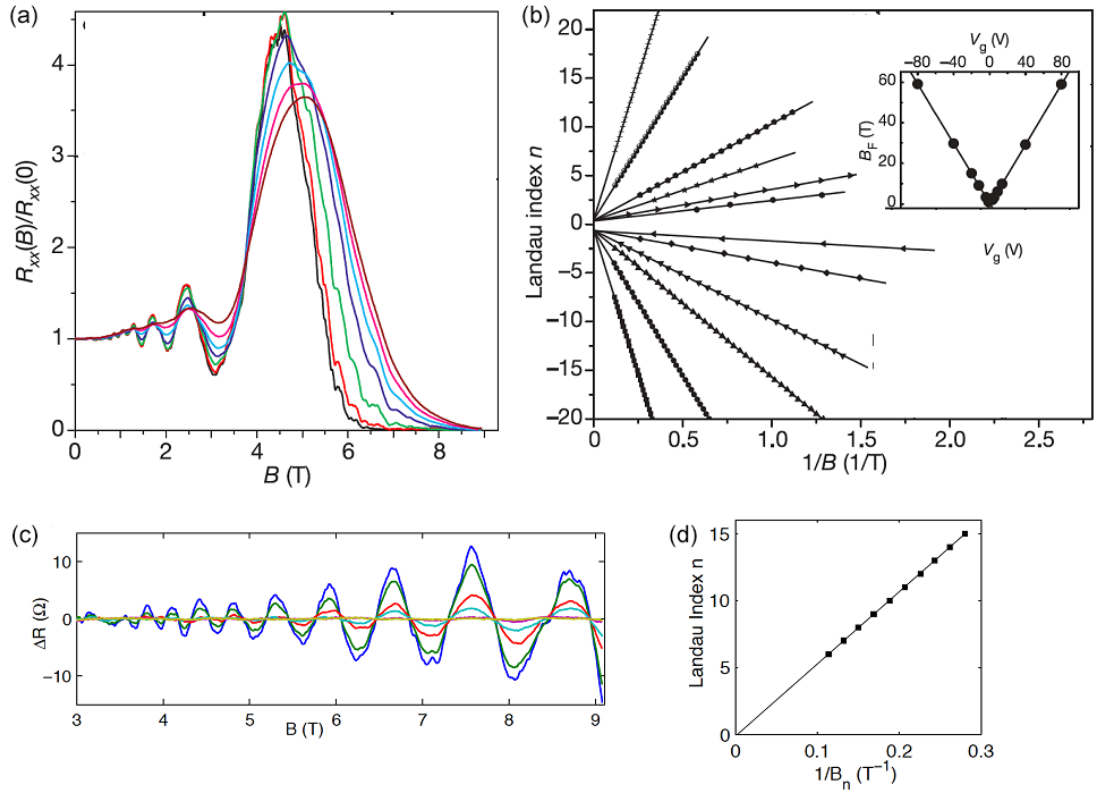


Figure IX.58. Shubnikov–de Haas oscillations of the magnetoresistance in (a) and (b) SLG on SiO_2 [1617] and (c), (d) MLG on 4H-SiC(0 0 0 −1) (C-face)[1620] for different T from 4 to 70 K. (b) The minima in ρ_{xx} are plotted as a function of $1/B$ (so called fan plots) to determine the charge density at a particular gate voltage. (d) Same analysis for the data in (c), but plotting the maxima in ρ_{xx}.

voltage, the n may vary along the SLG channel, an even change sign, due to the SLG ambipolar nature, leading to a complex interplay between $V_{SD}$and V_G (top, bottom or both) [1615]. Equation (IX.12) does not take into account the variation of chemical potential with n, which introduces an extra capacitance term $e^2D(E_F)$ [1616], the so-called quantum capacitance per unit area, with $D(E_F)$ the density of states, which cannot be neglected close to the Dirac point [1616].

n_s can also be determined from magnetoresistance measurements in high (generally several Tesla) magnetic fields, and at low (cryogenic) T by analyzing the periodic oscillations of the magnetoresistance (Shubnikov–de Haas oscillations) as a function of $1/B$ [107, 622, 1617]. Examples are given in Figure IX.58 for SLG on SiO_2 and MLG on 4H-SiC(0 0 0 − 1). The $1/B$ oscillation period is $B_F = (h/4\pi e)k_F^2$ with $k_F^2 = ns\pi$. With increasing field, the oscillations develop into the quantum Hall effect, and the quantification of Hall resistivity also give access to n [107, 1617]. These measurement techniques can be useful in case of mixed (electron and hole) doping in the vicinity of the Dirac point [1618, 1619].

In semiconductors a current saturation regime is reached by applying a sufficiently large V_{SD}, and μ can be deduced from the current saturation value [1621]. However, this regime is difficult to reach in SLG because of the requirement of extremely high V_{SD}, which will cause inhomogeneity in n along the channel [1615, 1622].

Standard electrical measurements require contacts on SLG. Besides the fundamental interest of how to inject from a 3d to a 2d material, from planar (2d) or edge (1d) contacts, while matching energy and momentum (at charge neutrality the SLG Fermi surface is reduced to points in k-space), it is technically difficult to realize contacts to SLG of low (in the 10 s Ω) resistance. Because there are no dangling bonds to adhere to, metals like Au tend to bead up on SLG [1623], which requires an adhesion layer, like Pd, Ti or Cr. Low resistance contacts (50–100 Ω μm) are a combination of mechanical adhesion and charge transfer to SLG, due to a large metal-SLG work function difference (to increase the SLG conductivity under the contact by heavily doping it) [1624–1626]. Metal induced doping can create p-n junctions from the SLG under the contact to the channel, which have to be taken into account in the resistance analysis [1625, 1626].

Contacts are usually defined by lift-off after development of the lithographic resist. Resists commonly used are positive e-beam resist (e.g. 200 nm PMMA spun onto 200 nm MMA), or photoresist (e.g. S1813 ~ 1.8 μm thick). Good contacts are obtained with 5–10 nm Cr, Pd, Ni or Ti (or combination of these metals, Ti/Pd 2 nm/10 nm) evaporated on SLG, followed by 30–50 nm Au, by e-beam or thermal evaporation. The contact resistance, R_c, can be measured by the transfer length method (TLM), see figure IX.56(d). A SLG strip is provided with a series of contacts. The

2-point resistance $R_{TLM} = R_c(W) + 2R_s\,L/W$ is measured and plotted as a function of distance L between the contacts, with W the channel width. The advantage is that this apporach fast and involves only resistance measurements. However this assumes that contacts the same, and R_s constant along the graphene channel (i.e, homogeneous scattering, homogeneous gate or bias induced charge density). This may be questionable very close to the contacts, due to metal-induced doping. Alternatively, R_c can be derived from Kelvin probe microscopy, by measuring locally with an AFM tip the voltage drop from contacts to channel [1627]. The lowest intrinsic R_c measured are in the range $\rho_c = R_c \cdot W = 50$–$100\,\Omega\,\mu$m [1607]. Ref. [1628] developed edge contacts, where lateral contacts inject current through the SLG edges. R_C are of the same order of magnitude [1628].

Deposition of gate dielectrics is a challenge for the same reason that metals do not adhere on SLG. ALD or evaporation of high K dielectrics (Al_2O_3, HfO_2, SiO_2) [1629] or Si_3N_4 [1630] have best RF performances (in terms of cut-off frequency) [585], [1631], and hBN encapsulation provides protection [1184, 1632].

SLG was the first measured LM that was exposed, i.e. not buried at the interface between two semiconductors. While this presents great opportunities (spectroscopy in particular), exposure to the ambient degrades the SLG pristine properties, by doping and scattering by impurities. The transport properties drift with a time constant ~1 h or so, and are recovered after annealing (e.g. ~1 h at 420 K in He) [1633]. SLG protection is therefore required (top layer, or measurement in neutral or vacuum environment), unless the exposure provides useful counter doping (like for the measurement of the quantum Hall effect [625]).

SLG is a flexible membrane, therefore the roughness of the substrate matters. Sharp ripples or bubbles introduce field gauge effects [450, 632], equivalent to high magnetic field of up to several hundred Tesla [632], with consequences on transport [450].

It is relevant for graphene nano/microstructures of size $L \times W$ to keep in mind that the energy scale is set by $E = \hbar k v_F = \hbar v_F \sqrt{\frac{n\Pi}{L} + \frac{m\Pi}{W}}$, so that the energy separation between modes in charge neutral SLG is ~20 K for $L = 1\,\mu$m. Therefore, submicrometer structures of SLG at low T are effectively quantum dots [620].

1d ballistic transport was measured in GRNs at RT [620]. In this case the nature of the contacts (invasive or not) determines the voltage. For invasive contacts the electron flow is interrupted by the voltage probe which then acts like a current injector, and a resistance close to the quantum of conductance $R_q = (e^2/h)^{-1} = 25.812\,k\Omega$ is measured independent of distance between voltage probes, even in a 4-probe configuration [620, 1634].

IX.3.2. THz-TDS mapping of electrical properties

R_s, μ and n can also be measured quickly, accurately and non-destructively using terahertz time-domain spectroscopy (THz-TDS) [1635–1639, 1641–1643]. This method has been thoroughly benchmarked against van der Pauw electrical measurements with fixed electrodes [1638, 1643] as well as scanning micro four-point probes [1636, 1637, 1795].

THz-TDS is based on the fact that the absorption in the THz range is highly dependent on the complex-valued and frequency-dependent electrical conductivity [1644]. This is because the absorption of light in the THz frequency range is dominated by low-energy intra-band transitions, as opposed to the inter-band transitions that give rise to graphene's constant absorption of light in the visible spectrum [1645].

The electrical field attenuation caused by the charge carriers in the thin film can be established by dividing the electrical field, $\tilde{E}_{graphene}$, through the sample area, with a reference, $\tilde{E}_{ref}$, from an area without the conducting film, which is then related to the conductivity through [1641]:

$$\frac{\tilde{E}_{graphene}(\omega)}{\tilde{E}_{ref}(\omega)} = \frac{1 + n_{sub}}{1 + n_{sub} + Z_0\tilde{\sigma}(\omega)} \quad \text{(IX.18)}$$

where n_{sub} is the refractive index of the substrate, Z_0 is the free-space impedance, and $\tilde{\sigma}(\omega)$ is the frequency-dependent (complex-valued) Drude conductivity,

$$\tilde{\sigma}(\omega) = \frac{\sigma_{dc}}{1 - i\omega\tau}. \quad \text{(IX.19)}$$

The THz radiation is focused into a 300 μm spot, limited by the long wavelength in the THz frequency range, which enables the average sheet conductivity (or resistivity) of a graphene film to be determined. In contrast, electrical measurements probe the device conductance (or resistance), which can differ significantly from the average conductivity for the same device area, in case of spatially non-uniform conductivity [1637, 1642].

Figure IX.59(a) is a conceptual schematic of a THz absorption setup, with a femtosecond laser pulse hitting a photoconductive antenna (PCA). The resulting THz pulse is focused by a lens, and transmitted through a thin conductive film. Finally, after refocusing by another lens, the attenuated THz pulse is picked up by a PCA operating as a detector. Figure IX.59(b) is a photo of a Si wafer covered with graphene, which is raster scanned across the focal plane of the beam line, while acquiring THz-spectra at a rate ~1 Hz. In figure IX.59(c) the time-resolved electrical field is shown. The initial peak is followed by smaller echo peaks, spaced by the round trip time of flight for internal reflections inside the substrate. Using equation (IX.18) the real (green triangles) and imaginary (green circles) parts of the conductivity can be plotted against frequency (figure IX.59(d)), and fitting the Drude conductivity (equation (IX.19)) yields the low frequency (DC) limit of the conductivity, σ_{DC}, and the momentum relaxation time (elastic scattering time), τ [1641]. Under the assumption of diffusive transport, the semiclassical Boltzmann transport equation,

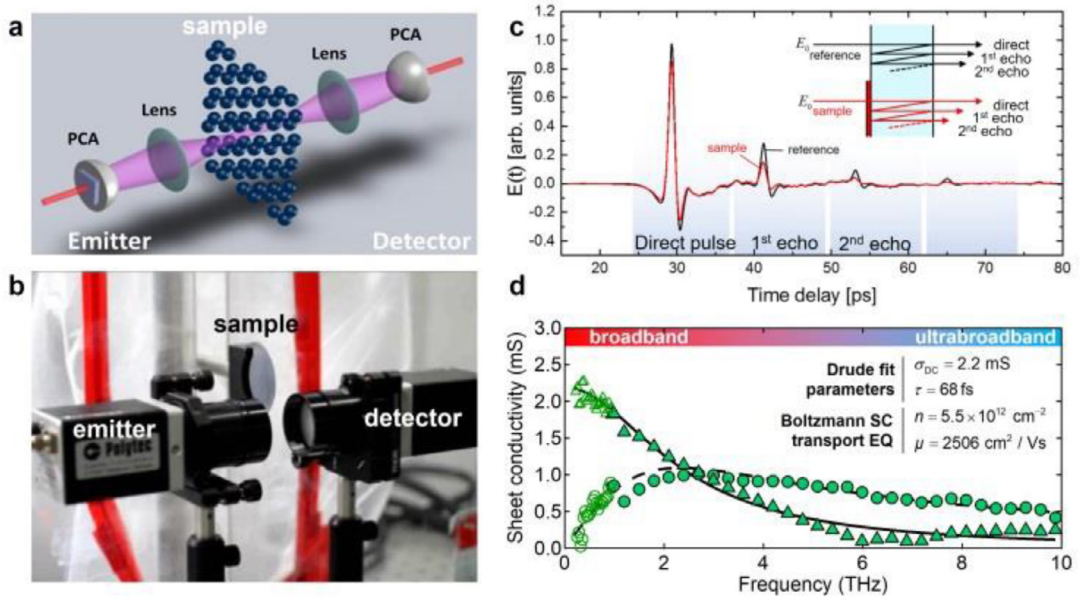


Figure IX.59. (a) Schematic of THz-TDS setup. (b) Photo of equivalent THz beam line, with a graphene-coated Si wafer held by a motorized raster scanner. (c) THz direct pulse and weaker echoes from multiple internal reflections. The black curve is from an uncoated reference area, while the red curve is attenuated by the conducting sample. (d) Conductivity spectrum of graphene grown on single crystal, which closely follows the Drude model (equation (IX.18)). The fitting parameters (σ_{DC}, τ) can be used to calculate n and μ. For large-area conductivity mapping, commercial spectrometers that cover up to 2–3 THz are used, while a more sophisticated air-THz setup allows spectra up to 15–20 THz to be recorded [1637].

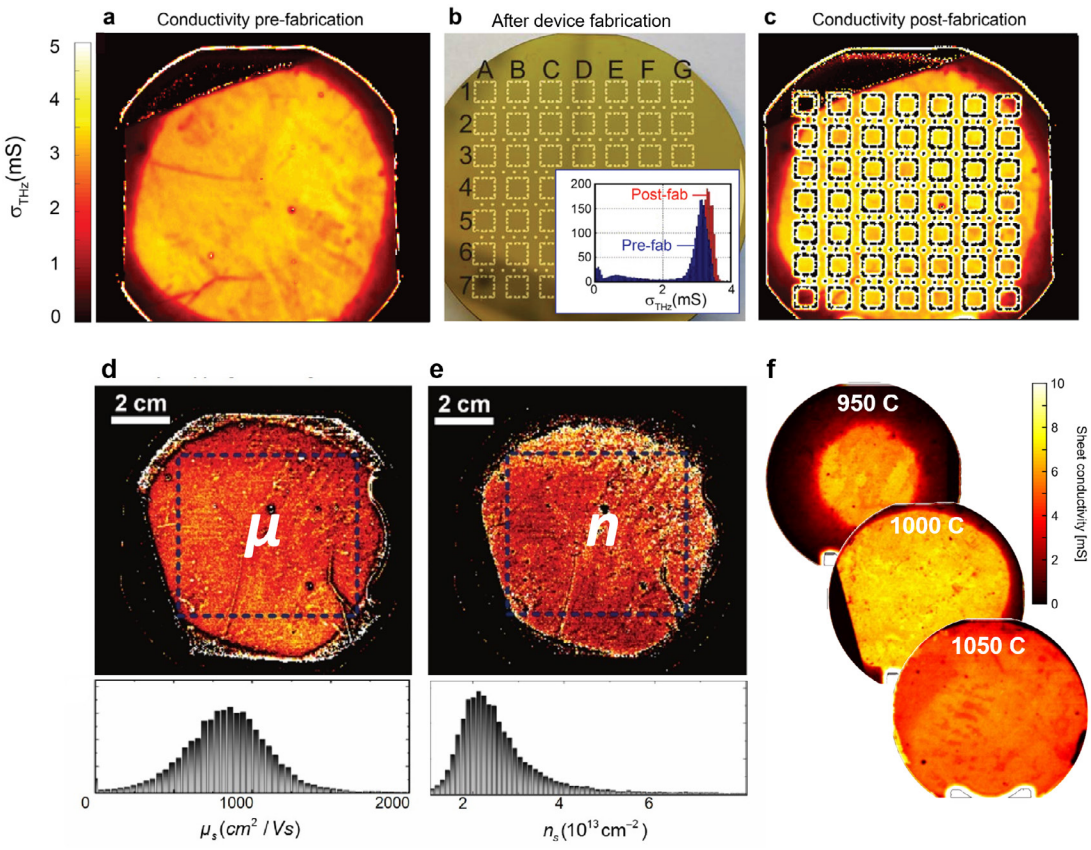


Figure IX.60. Examples of THz-TDS electrical characterization of graphene. Conductivity of graphene coated Si wafer mapped before (a) and after (c) fabrication of 49 electrical devices to test how individual process steps affect the conductivity [1641]. (b) wafer after laser-etching and physical mask deposition of metal contacts [1796]. Histogram (inset) of the sheet conductivity across the wafer before and after fabrication. (d) and (e) μ and n for a Si wafer determined by equations (IX.20), with histograms below showing scale and distribution of n and μ [1638]. (f) Investigation of how CVD growth T affect large-scale uniformity of sheet conductivity of graphene transferred to 4″ Si wafers [1641].

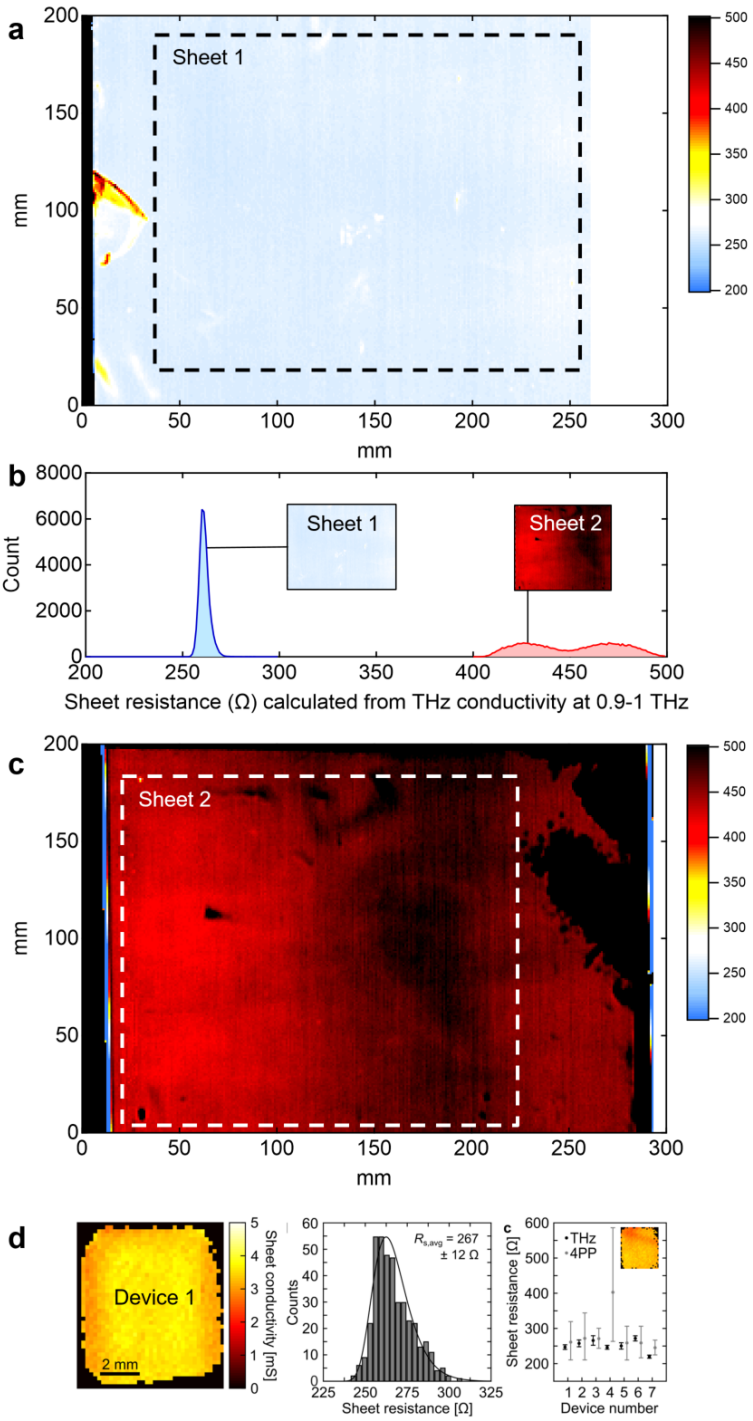


Figure IX.61. (a) Terahertz resistivity maps (0.9–1.0 THz) of two A4 sized sheets of doped graphene on PET with (a) high and (c) lower uniformity (color scale is from 200 Ω to 500 Ω. The histograms corresponding to the white dashed rectangles are shown in (b), where sheet 1 shows a very narrow peak, while sheet 2 exhibits a bimodal distribution. (d) THz conductivity map of a $10 \times 10\,\mathrm{mm}^2$ device, by THz and van der Pauw measurements. After Drude-fitting, the DC R_s is ~267 ± 12Ω for the shown device, as for the histogram. The measurements for 7 such devices agree well, except device 4, which had a visible scratch. With permission from [1643], The Optical Society.

$\sigma = (2e^2/h)k_F v_F \tau$ in combination with the fundamental relation $\sigma = ne\mu$ yields expressions for n and μ that can be calculated from the fitting parameters (σ_{DC}, τ):

$$\mu = \frac{e^3 v_F^2}{\pi\hbar^2}\frac{\tau^2}{\sigma_{DC}}, \quad n = \frac{\pi\hbar^2}{e^4 v_F^2}\frac{\sigma_{DC}^2}{\tau^2}, \qquad \text{(IX.20)}$$

where e is the electron charge, v_F is the Fermi velocity, and $\hbar$ is the reduced Planck constant. Therefore, the average μ and n can be spatially mapped with a resolution approximately equal to the THz spotsize $d_{THz} = 300\,\mu$m, by recording a full spectrum in every pixel, and computing equation (IX.20) with the Drude fitting parameters.

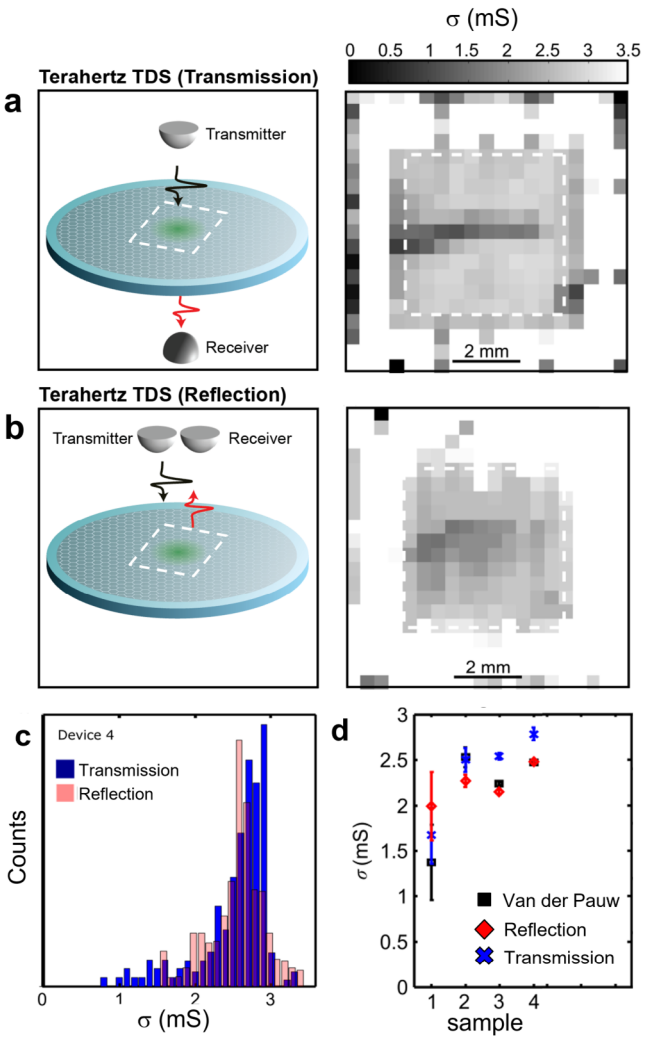


Figure IX.62. Comparison of (a) transmission and (b) reflection mode measurements on the same four samples, with comparable spatial conductivity pattern and (c) overlapping statistical distributions of measured conductivity (d) Direct comparison of van der Pauw four terminal measurements with reflection (diamonds) and transmission (crosses) measurements, showing good agreement except sample 1, which was less homogeneous compared to samples 2–4 [1642].

Figures IX.60(a)–(c) shows the conductivity map of the same CVD grown graphene film before and after definition of 49 test devices, verifying that the laser ablation/shadow mask device fabrication method has little impact on the device characteristics, due to the complete absence of solvents and resists [1640, 1642]. Figures IX.60(d) and (e) show the μ and n maps obtained by the methodology described above, with the histograms below showing both the scale and distributions of values within a rectangular zone indicated with dark dashed lines. Figure IX.60(f) shows how the method can be used to map the large-scale changes in uniformity of electrical key parameters with growth T in a CVD process, indicating that higher T tends to give more uniform growth and larger usable areas of graphene [1641].

The THz mapping technique can be used for graphene on flexible substrates [1641, 1643]. Graphene grown on Cu, transferred to PET and doped by $AuCl_3$ showed very high uniformity across 15 inch ($25 \times 30\,cm^2$) PET sheets. The THz-resistivity in the frequency range (0.9–1.0 THz) is in figures IX.61(a) and (c), typically within 5%–10% of the DC R_s, as can also be seen by noting the small drop in $\sigma(\omega)$ from 0 to 1.0 THz in figure IX.59(d).

The histogram in figure IX.61(b) shows a very narrow distribution for sheet 1, and a broader, bimodal peak for sheet 2, consistent with the difference in the visual appearance of the THz resistivity maps (a and c). The histogram of DC R_s after fitting the Drude equation, equation (IX.19), to every pixel, shows a narrow distribution across the ~750 cm^2 graphene area (dashed rectangle). Figure IX.61(d) is a THz map of a cm-sized device with the corresponding histogram of DC R_s. R_s by van der Pauw and THz mapping show excellent agreement, however, with larger statistical spread for the THz because of the avoidance of physical contact, and the greater number of measurement points. One of the devices (device 4) had a scratch, which typically offsets electrical measurements in unpredictable ways, while having little impact on the THz-measurements [1641].

THz-TDS electrical characterization can be done in transmission mode, the most used in literature

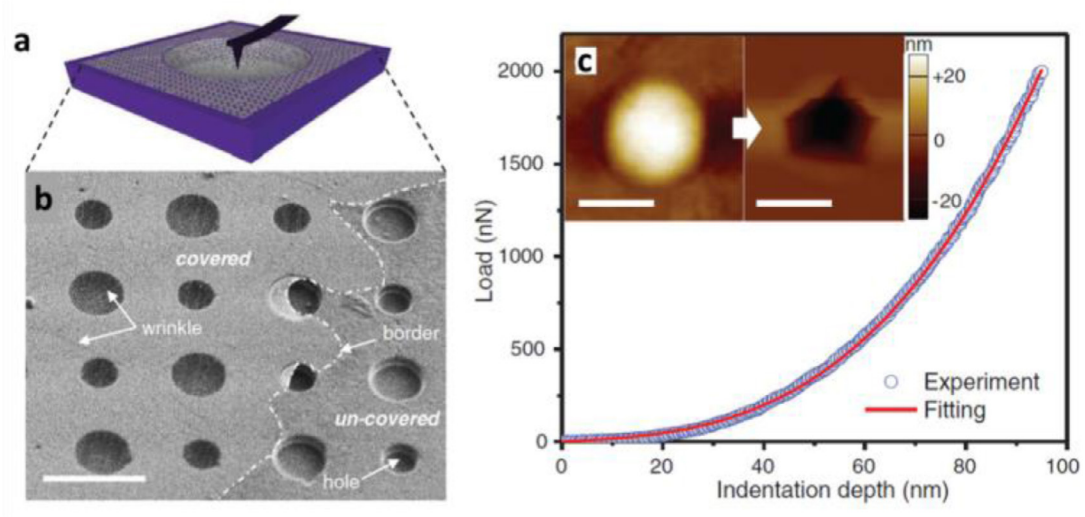


Figure IX.63. (a) Schematic of suspended SLG over hole for AFM nanoindentation. (b) SEM images of suspended SLG over holes. The border of the SLG-covered area is indicated by a dashed line. Wrinkles often present in the transferred SLG can be seen. (c) Force-displacement curve of SLG in AFM nanoindentation. The red line is a fit to equation (IX.22). Inset:AFM topography images of suspended SLG before and after fracture. Scale bars in (b) 2 μm and (c) 1 μm Adapted from [1653], with permission from AAAS.

[1641], or in reflection mode [1798]. Comparison of THz conductivity maps recorded in transmission (see figure IX.62(a)) and with a commercial reflection mode THz-system (DasNano, see figure IX.62(b)) showed negligible difference [1642], and good agreement with electrical measurements, for the same samples. Despite the large CVD graphene samples not being encapsulated, the measurements agreed well within the statistical errors, as clear from the conductivity histograms in figure IX.62(c) and the direct comparison between electrical four point probe sheet conductance with THz sheet conductivity measurements for both transmission and reflection mode systems in figure IX.62(d).

For transmission mode THz-TDS it is important that the substrate has high resistivity, to reduce THz absorption. The highly doped Si commonly used as a backgate, can be replaced by a custom-made substrate with a THz-transparent gate [1639] to enable THz-TDS and electrostatic gating on the same samples. The advantage of reflection mode is that there is no need for using high resistive substrates, while transmission mode can measure buried conductive layers at any depth.

THz-TDS is a fast, clean, and accurate way of measuring the transport characteristics of graphene on many substrates. Apart from Si and PET substrates, the method was used for graphene on SiC [1643, 1797] and graphene on Ge (on Si). As clear from figure IX.59(b) there is no limit for the size of samples, as a THz-TDS measurement head could easily be integrated in a roll-to-roll production line, giving instant feedback on the quality of graphene. The technique can also measure buried and encapsulated conducting layers, which provides essential information on the impact of intermediate process steps on the electrical characteristics before device fabrication.

IX.4. Mechanical characterization

GRMs compared to existing materials, combine high stiffness, strength, strain-to-failure and high flexibility [1646]. SLG compared to existing membranes has high ductility, as can be stretched up to 30%, however. Beyond that point it fractures in a brittle manner like glass [1647]. However, up to date, experimental evidence under uniaxial tension that confirms the above is missing, as these properties have been predicted via theoretical or modelling [1647, 1648]. The main reason for the lack of experimental data is associated with the sample quality (and size) and the damage inflicted by handling and subsequent transfer onto the loading devices. E.g. MC of graphite produces flakes of at best 100 $\times$ 100 μm^2 depending on substrate interaction [1007]. Suspended SLG samples over relatively large areas (~ 1 mm^2) as required for classical tensile experiments are difficult to produce [1007]. Wet methods for transferring CVD graphene from a metal substrate to arbitrary target substrates lead to samples with defects such as wrinkles, folds and tears, as well as residues, voids and polymer contaminants that can induce uncertainties in the measurements. Normally, optimization work has to be done in order to minimize the influence of defects and select the gauge area of the membrane to be tested. Due to limitations posed by the accuracy in force sensing in the nN range and sample gripping techniques, there is a lack of specialized instrumentation for in plane tensile testing of GRMs. This has triggered intense research for applying either AFM based, or thin film metrology techniques [1646, 1649]. A comparison of the measured mechanical properties with bulk materials is still an open question.

Measuring techniques can be categorized as direct and indirect. In *direct methods* the force or strain is applied directly to the GRM membrane. In *indirect methods*, Raman spectroscopy can be used for assess-

ing the mechanical response of GRMs supported or embedded into polymers, where the strain is applied by shear forces from the deformed substrate. Other methodologies for applying strain are budge test and electrostatic actuation.

IX.4.1. AFM nanoindentation

The elastic properties of suspended SLG can be measured by nanoindentation using an AFM. The samples are made either by MC of graphite or by transferring CVD grown SLG onto pre-patterned substrates with holes or trenches. Usually an AFM tip applies a point load at the center of GRM sheets suspended over a hole on a pre-patterned substrate. Because of the high strength of SLG, higher than steel and Kevlar [1650], cantilevers with diamond tips are preferable for these experiments. For a doubly clamped SLG ribbon, a wedge indentation tip was used to introduce a uniform tensile strain [1651]. During nanoindentation the force, F, versus deformation, δ, of the suspended layer (at the point where the load is applied, figure IX.63(a) and (b)) is continuously recorded up to fracture. By employing third order elasticity theory and a number of assumptions based on classical membrane mechanics, the conversion of nanoindentation force-deflection measurements into an axial stress–strain curve for a free standing SLG membrane was performed (figure IX.63(c)) [1652]. By this procedure, the 2d Young's modulus, E_{2D}, breaking stress, σ_{2d}^{max}, and strain at break, ε_{max} were estimated [1652]. In order to obtain the corresponding bulk parameters, these quantities were divided by the interlayer spacing in graphite $h = 0.335$ nm (assumed as SLG thickness) yielding values of Young's modulus ~1 TPa and of tensile strength of ~140 GPa [1652].

To convert the experimental nanoindentation data to uniaxial stress–strain curves, GRMs are normally modelled as a membrane (thin plate) of negligible bending stiffness and nonlinear elastic properties [1652]. For doubly clamped beam shaped membranes (GNRs) [1649, 1651] the force-displacement behaviour can be expressed as [1649]:

$$F = \left[30.78w\left(\frac{t}{l}\right)^3 E_{2D} + \frac{12.32}{l}\sigma_0\right]\delta + tE_{2D}\frac{8w}{3}\left(\frac{\delta}{l}\right)^3. \quad \text{(IX.21)}$$

For circular shaped membranes the corresponding relation is as follows [1652, 1653]:

$$F = \left[\frac{4\pi a}{3(1-\nu^2)}\left(\frac{t}{\alpha}\right)^3 E_{2D} + \pi\sigma_0\right]\delta + tE_{2D}q\left(\frac{\delta}{\alpha}\right)^3. \quad \text{(IX.22)}$$

In equations (IX.21) and (IX.22), σ_0 is the pretension in the membrane due to the preparation procedure, t is the thickness and ν is the Poisson's ratio (for SLG this is taken as 0.165, the Poisson's ratio for graphite in the basal plane [1652, 1654]). In equation (IX.21), w, l are the width and length of the GNR, while in equation (IX.22) a is the hole radius and $q = a/(1.05 - 0.15\nu - 0.16\nu^2)^3$ is a dimensionless constant [1649, 1654]. The microindentation experiment is in essence biaxial. The conversion of biaxial deflection data to uniaxial stress–strain curves by assuming zero bending stiffness is problematic, and not fully representative of true uniaxial tensile loading [1652].

Table IX.3. Indicative values of Young's modulus and breaking strength for 1L-GRMs measured by AFM nanoidentation.

1L-GRM	E_{2D} (N m^{-1})	σ_{2D}^{max} (N m^{-1})	Strain-at-break (%)
Graphene (MC) [1652]	340 (50)	42 (4)	25
Graphene (CVD)	328 (15)	39.5	—
MoS_2 (MC)	130	16.5	—
MoS_2 (CVD) [1657]	123	—	—
WS_2 (CVD) [1657]	137	—	—
BN [1087]	220–510	8.8	—

AFM indentation experiments were conducted on graphene on SiC [1014] and CVD grown SLG of different grain size [1653]. Ref. [1653] showed that the elastic stiffness of CVD-SLG is similar to that of MC SLG, provided that the sample is free of pleats and ripples.

The mechanical properties of 1L-MoS_2 [1655, 1656] and h-BN [1087] were measured by AFM nanoindentation. Similar modelling approaches were pursued for the interpretation of the force-displacement traces. In table IX.3 the elastic properties of various GRMs measured by AFM nanoindentation are summarized.

IX.4.2. Bulge testing

The elastic properties of GRMs can be assessed by bulge [1658] or pressurized blister test [1659], commonly applied for thin film testing. The advantage of the bulge test is the ability to measure not only E but also ν, whereas, in the case of AFM nanoidentation, ν should be known in advance (see equation (IX.22)) [1659]. Another advantage is that the stress concentration caused by the AFM tip is avoided by the application of a uniform pressure. In Ref. [1660] suspended MC SLG over microcavities (diameter ~ 5 μm) etched in a SiO_2 substrate (figure IX.64(a)). The SLG membrane remains flat due to the balance of internal (atmospheric) and external pressures (figure IX.64(b)). It is adhered to the substrate by van der Waals forces and can confine gas molecules (e.g. N_2). The SLG membrane inflates forming a blister, when a pressure difference across its surface is applied (figure IX.64(c)). AFM was used to define the SLG membrane shape and measure its maximum deflection δ at the center of the blister and its radius α (figure IX.64(d)). The deflection can be correlated with the pressure difference, Δp, across the SLG membrane (figure IX.64(e)) using Hencky's solution [1661, 1662], which gives the deformation of the membrane for the geometrically nonlinear response of a clamped circular elastic membrane subjected to a pressure difference, Δp, provided that the bending stiffness

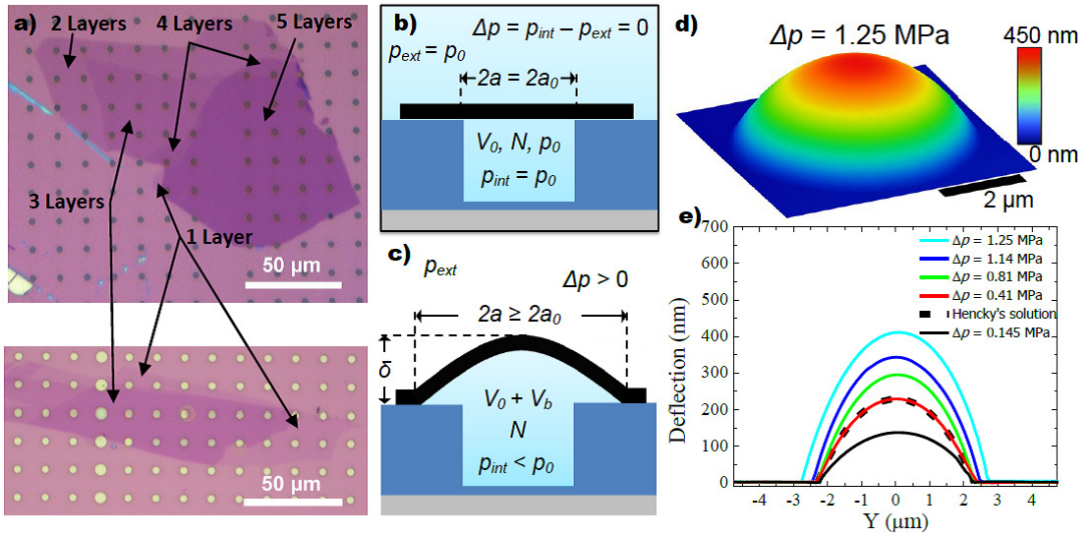


Figure IX.64. (a) Optical images showing flakes with regions of 2–5 L (top) and 1 and 3 L (bottom). Schematic illustration of a SLG-sealed microcavity (b) at rest where $\Delta p = 0$, the pressure inside the microcavity is equal to the external pressure p^{ext}, and (c) at higher Δp, (d) an AFM image showing the deformed shape of a SLG membrane with $\Delta p = 1.25$ MPa and (e) deflection versus position for various levels Δp (cyan). The dashed black line is the shape obtained from Hencky's solution for $\Delta p = 0.41$ MPa. The deflection is measured by an AFM along a line that passes through the centre of the membrane. Adapted from [1660], © Springer Nature.

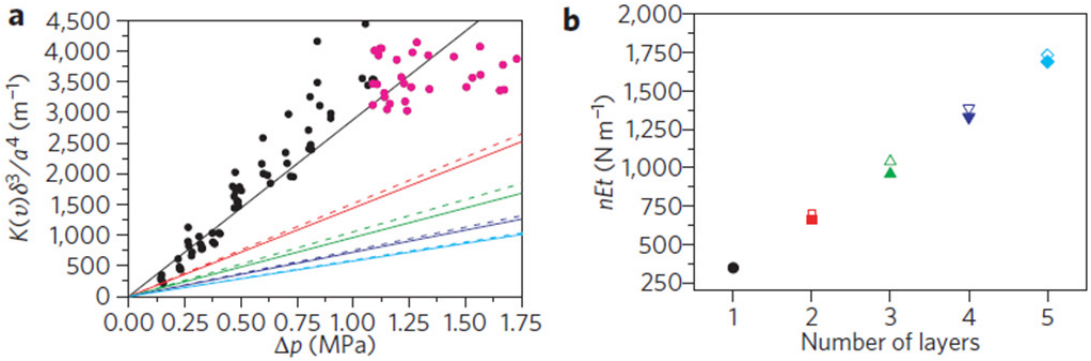


Figure IX.65. (a) $K(\nu)\delta^3/\alpha^4$ versus Δp for SLG membranes before delamination (black symbols) and after delamination (magenta), (b) nE_t versus number of layers n. Closed shapes are for the fitted lines; open shapes are for nE_t, with $E_t = E_{2D} = 347\,\mathrm{N\,m^{-1}}$.

of the membrane is negligible. Therefore, Δp can be written as [1660]:

$$\Delta p = K(\nu) E \delta^3/\alpha^4 \qquad \text{(IX.23)}$$

where $K(\nu)$ is a constant that depends on ν.

By plotting $K(\nu)\,\delta^3/\alpha^4$ versus Δp, E can be estimated as the slope of the linear dependence. In figure IX.65(a) the experimental data for $K(\nu)\,\delta^3/\alpha^4$ versus Δp are shown for SLG. A linear fit to equation (IX.23) gives $E_{2D} = 347\,\mathrm{N\ m^{-1}}$, in good agreement with the AFM nanoindentatation measurements [1008, 1653]. Ref. [1660] measured E of up to 5LG. The results are summarized in figure IX.65(b) and show that E_{2D} is quantized to the SLG E_{2D} ($347\,\mathrm{N\,m^{-1}}$). These findings are based on a continuum model in which SLG is considered as a membrane with negligible bending stiffness and the crystal is of high structural quality i.e. free of ripples, folds and defects.

Bulge testing has also been used for 1L and ML-MoS_2 as a way to apply biaxial strains up to 7% for band gap engineering [1663]. The strong adhesion, comparable to solid–liquid adhesion [1660], between 1L-GRMs and an atomically flat substrate (e.g. SLG/SLG, SLG/hBN, MoS_2/MoS_2) results in atomically clean interfaces since any contaminants (water and hydrocarbons) are repelled by the van der Waals forces between the layers forming microbubbles [1664]. These bubbles have constant volume, and their shape is determined by the competition between van der Waals adhesion of the crystal to the substrate and the elastic energy needed to deform it [1665]. In figure IX.66(a), typical force-displacement curves (solid lines) recorded from bubbles of different sizes are presented. The symbols correspond to numerical fits by taking into account the changes in area of contact and the increase in bubble's radius [1665]. The data in figure IX.66(b) correspond to SLG bubbles for which the fitting curve to the experimental data is drawn by assuming a SLG axial stiffness ~420 ± 20 N m^{-1} [1665]. Similarly, the stiffness of 1L-MoS_2 was

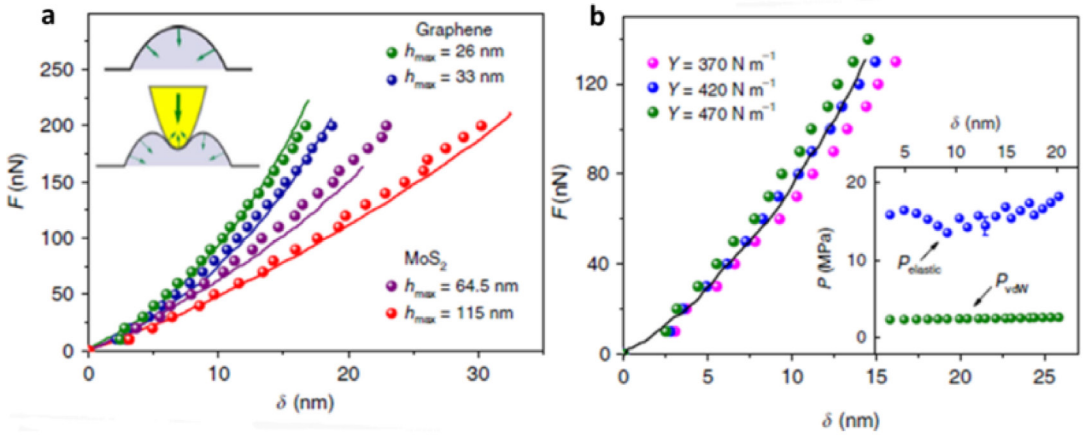


Figure IX.66. (a) Experimental force-deflection curves (solid lines) and numerical fits (symbols) for two SLG and 1L-MoS_2 bubbles of different sizes. (b) A force-deflection curve (solid curve) and corresponding numerical fits for three values of $Y = E_{2D}$.

Table IX.4. Fracture toughness of 1LG, 2LG, MLG ML-hBN.

Sample	Fracture toughness MPa $\sqrt{m}$	Mechanical testing/device
CVD SLG [1667]	4.00	Tensile/MEMS device (SEM)
BLG [1671]	21.25	Tensile/MEMS device (SEM)
MLG [1428]	12.00	Tensile/MEMS device (TEM)
ML-hBN [1428]	5.50	Tensile/MEMS device (TEM)

estimated as $210 \pm 20\,\mathrm{N\,m^{-1}}$. Both values are somewhat higher than those given in table IX.3.

IX.4.3. Fracture toughness and bending stiffness

Large-scale applications of GRMs, beyond microscale, require the knowledge of fracture toughness, rather than the intrinsic strength, which corresponds to a uniform breaking of atomic bonds in a perfect GRM crystal. Fracture toughness is a property that describes the ability of a material containing a crack or a defect to resist fracture [1666]. The absence of reliable tensile testing devices with force sensing at the pN or nN range and the cumbersome fabrication/transferring procedure has hindered progress. Thus, the direct determination of fracture toughness has been challenging for GRMs. Fracture data for CVD SLG were measured using *in situ* MEMS-based uniaxial tension devices in a Scanning [1667], Transmission [1428] electron microscope and AFM nanoindentation [1668, 1669]. Ref. [1667] conducted *in situ* tensile testing of centre-cracked CVD SLG in a SEM and obtained fracture toughness based on the classical Griffith's fracture theory [1670]. Ref. [1667] conducted *in situ* fracture toughness testing in a HRTEM on MLG having V/U-shaped single-edge notches. For comparative purposes fracture toughness testing on ML-h BN samples was also conducted. Ref. [1671] performed fracture mechanics experiments under uniaxial tension on MC BLG and measured its fracture toughness. In table IX.4 the measured fracture toughness for various SLG and MLG and ML-hBN are summarized.

GRMs are modelled as membrane-like materials i.e. with approximately zero bending stiffness [1672]. Therefore, the effect of bending modulus is usually ignored [1652, 1653]. Refs. [1649, 1655] explored the effect of bending modulus as being proportional to the third power of the crystal thickness (see first term in equation (IX.21)) in AFM nanoindentation of MoS_2 crystals with various thicknesses. The force-displacement curves for the FL crystals were strongly nonlinear, while for number of layers $N > 10$ were linear. This is important when considering membrane-to-plate like transition for $N > 10$. The determination of bending stiffness of either 1L or FL-GRMs has been mainly based on various types of theoretical calculation [1673]. *Ab initio* or first-principles quantum mechanical calculations and empirical potential calculations were used to determine the bending modulus of SLG [1646, 1673], with higher values (mean value ~ 1.51 eV) in comparison with those derived by empirical potentials (mean value ~ 1.12 eV). These models treat SLG as an isotropic body. To introduce anisotropy and to incorporate bending effects, a finite elasticity model was proposed [1674]. This provides the means to introduce (and handle) additional degrees of freedom through dependence on the shift vector which separates the two Bravais sublattices of SLG [1674]. Continuum mechanics was applied to describe the SLG flexural deformation, leading to a nonlinear von-Karman plate theory with two elastic bending moduli [1646, 1674, 1675]. However, from the experimental point of view, Ref. [1676] criticized the use of the continuum mechanics shell model. By exploring the nm scale rippling of SLG, Ref. [1676] claimed that phenomenology fails to predict correctly E_{2D}, as well as the SLG thickness of 0.335 nm, since classical continuum plate theory assumes that bending always induces in-plane stretching.

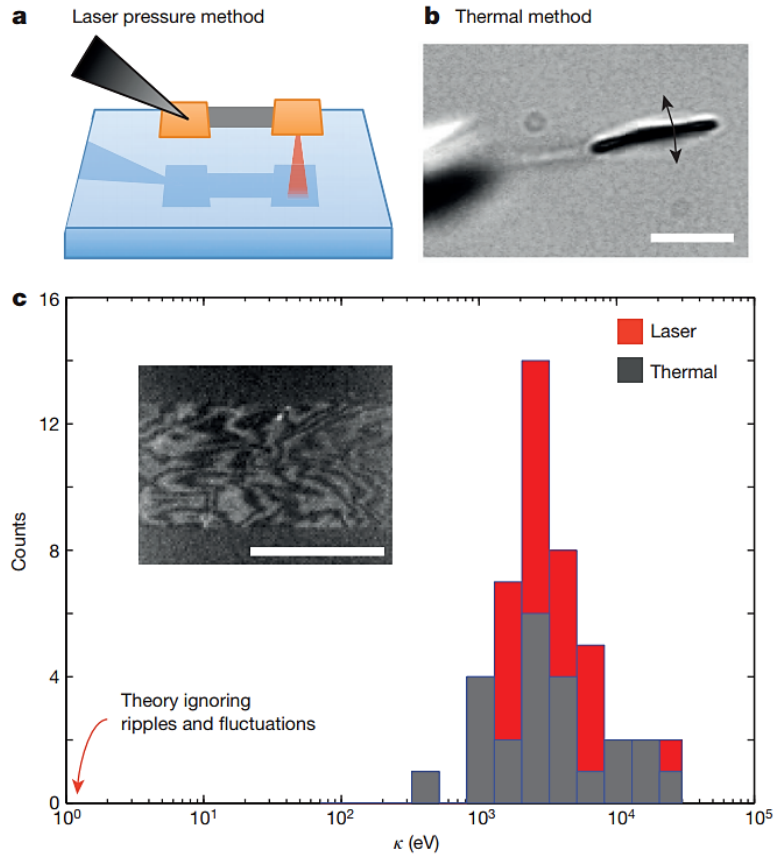


Figure IX.67. Bending stiffness of SLG by (a) applying controlled forces using an IR laser and (b) tracking the motion of a rotated device under thermal fluctuations. (c) Stacked histogram of bending stiffness measured by the methods in (a) and (b). The red arrow points to the bending stiffness ~1.2 eV calculated theoretically. Scale bars are 10 mm. Adapted from [1680], © Springer Nature.

A few attempts have been made to measure experimentally the bending stiffness of FLG and MoS_2 and confirmed the dependence on the third power of thickness in accordance with the membrane theory of shells with pure bending [1673]. Ref. [1677] performed AFM nanoindentation in FLG membranes onto a circular hole, while Ref. [1678], fabricated and measured the bending stiffness of convex-buckled suspended BLG ribbons. By exploiting the abrupt switching from convex to concave geometry of the ribbons, under electrostatic actuation, they measured a bending rigidity ~35.5 eV. Ref. [1679] proposed a different experimental approach to measure the bending stiffness of 1L-GRMs. The method is based on atomic mapping of the crystal lattice within a fold by using HRTEM for SLG and scanning TEM imaging for MoS_2 and WSe_2. They confirmed the applicability of the linear elastic shell model and derived the bending rigidity. They found that bending rigidity for TMDs is in the range ~10–16 eV, five to six times that of SLG, in agreement with theory [1679].

Ref. [1680] measured the bending modulus of CVD SLG. They produced cantilever structures (length, 10–100 μm and width, 10 μm) and measured their spring constants by assuming them to be related to the bending rigidity. By using the photon pressure from an infrared laser, the spring constant of the cantilever and the bending rigidity was measured (figure IX.67(a)). Using the thermal fluctuations of the SLG cantilevers and based on the equipartition theorem of classical statistical mechanics, the cantilever spring constant was also measured independently (figure IX.66(b)). As shown in figure IX.67(c) both methods yield a high bending stiffness for SLG, ~10^3 to 10^4 eV. These values are orders of magnitude higher than 1.2 eV, predicted from simulations [1673] and measurements of the phonon modes in graphite [1681]. This high value is attributed to both thermal and static rippling stiffening ultrathin crystalline membranes in a manner similar to how a flat sheet of paper becomes more rigid when crumpled [1680].

IX.4.4. Raman spectroscopy

Information on GRM mechanical properties may be obtained by Raman spectroscopy combined with various types of external loadings (uniaxial, biaxial, hydrostatic, etc) [1529, 1682–1685]. Due to the anharmonicity of the interatomic potentials phonon frequencies soften upon tension and harden under compression [1529]. As a result, Raman peak positions red (blue) shifted under tensile (compressive) loading. The magnitude of shift depends on the interatomic force constants and the mode eigenvectors relative to the directions of the strain axis [1529]. However, in

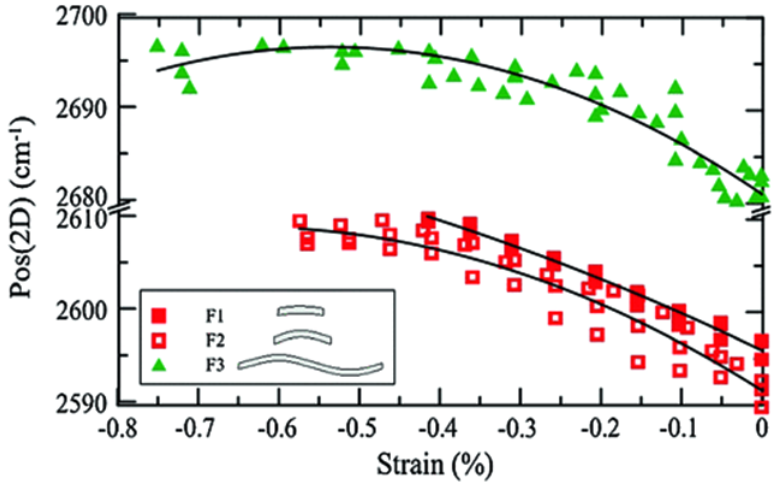


Figure IX.68. Pos(2*D*) as a function of uniaxial compressive strain for SLG flakes of various aspect ratios. Adapted from [1703] © Springer Nature.

GRM many other effects can shift peaks, e.g. doping [1518], hence caution needs to be taken when using Raman spectroscopy to derive these information.

Several groups investigated the effect of uniaxial strain in tension or compression by bending flexible substrates (e.g. PDMS) or plastic beams (e.g. PMMA) on which GRMs are deposited without slippage [1529, 1536, 1546, 1686–1693, 1723]. The samples can be supported or embedded within a thin polymer film. In these experiments the application of uniaxial stress/strain leads to the development of interfacial shear between the GRM membrane and the underlying or surrounding polymer, transmitted into a normal stress [1694]. Care should be taken for the examined area of the flake to be free of residual stresses [1694]. Pos(*G*) is an indicator that the applied strain is transferred to the interatomic bonds, provided one can ensure that other effects, also leading to peak shifts, are not present. Under uniaxial strain the doubly degenerate E_{2g} optical mode splits in two components, one polarized along the strain and the other perpendicular to it. This leads to the splitting of the G peak into two bands, which are usually called G^+ and G^- [1529]. Both peaks red shift with increasing tensile strain, and their splitting increases, in agreement with first-principles calculations. Their relative intensities are found to depend on light polarization, which provides a useful tool to probe the graphene crystallographic orientation with respect to the strain. A detailed explanation of these effects is also given in section IX.2/Raman and figure IX.41.

In tension, the shift of the main Raman modes is linear up to 1.5% [1695]. The 2D peak position downshifts with uniaxial strain at a much higher rate of $\sim -60\,\mathrm{cm}^{-1}/\%$ [1529, 1688]. An analogous but not as pronounced splitting to two distinct components $2D^-$ and $2D^+$ was observed [1534, 1536] depending on laser wavelength. The strain-induced splitting and the red shift depend on the strain axis direction relative to the crystallographic axis. The underlying mechanism of the strain variation of the 2*D* peak depends on the shifting of the Dirac cones and the anisotropic phonon softening which, in turn, cause alteration in the scatterings paths participating in the double resonance mechanism for the 2*D* band [1534, 1696–1697].

Under compression, by monitoring the Pos(2*D*) shift of rectangular SLG embedded into polymer flakes of various sizes the critical strain-to-failure was determined [1692]. These were found to be independent of flake size at a mean value $\sim -0.60\%$ corresponding to a yield stress up to ~ -6 GPa [1691]. CVD SLG can be considerably wrinkled [1698]. Upon uniaxial deformation the Raman response for the 2*D* peak was <25% of that of flat exfoliated flakes [1698]. In all cases in which SLG is either supported on or embedded in a polymer matrix, parameters such as interfacial shear strength, onset of interfacial sliding and critical compressive strain-to-failure may be extracted via *in situ* Raman spectroscopy under tensile or compressive loading [1699, 1700].

Raman spectroscopy was also used to investigate SLG bubbles as a function of strain [1531, 1658, 1701]. These are formed by the pressure difference on both sides of SLG during the deposition of flakes over apertures of various size and shape. SLG membranes can support pressures up to 14 bar, corresponding to reversible strains up to 2% [1701]. The advantage of intentionally pressurized membranes is to avoid the influence of the substrate, excluding complications from SLG-substrate interactions. Biaxial strain enables the determination of the Grüneisen parameters. Ref. [1702] determined the SLG *E2D* by comparing the strain induced on pressurized balloons and the response of the G peak, with numerical simulations. The estimated E_{2D} as 2.4 and 2.0 TPa, is much larger than previous values [1652, 1660]. This discrepancy was attributed to the small attainable strain (~0.2%), since E may depend on the strain range being larger in small strain ranges.

In Ref. [1689] an effective bending stiffness of SLG embedded into a polymer cantilever was estimated.

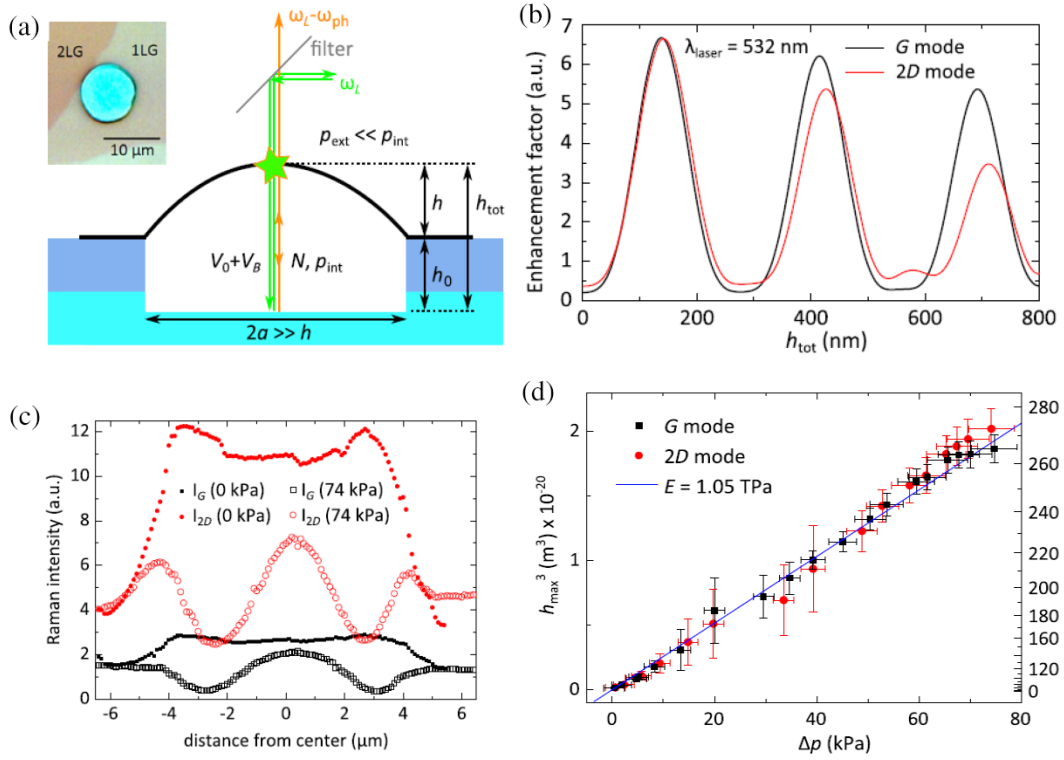


Figure IX.69. (a) Schematic of blister geometry. The optical path of the Raman signal and excitation is also depicted. SLG suspended over the hole (Inset), (b) enhancement factor for *G* and 2*D*. (c) $I(G)$ and $I(2D)$ versus distance from the centre of the hole with SLG at rest (0 kPa) and at a higher pressure difference. (d) Third power of SLG blister at its center versus pressure difference. From the slope of the linear fit, E is determined.

Flakes of various aspect ratios (length to width) were embedded on the surface of a PMMA bar covered by a 200 nm PMMA layer. SLG was modelled as a thin plate and subjected to uniaxial compression [1689]. SLG was buckled at a critical strain determined by the response of the 2*D* peak (figure IX.68). Pos(2*D*) relaxed after an abrupt uptake, while the strain at the onset of the Pos(2*D*) relaxation defines the critical strain for each flake, see figure IX.68. For flakes with lengths smaller than the critical length (twice the distance it needs for strain to increase to the externally applied value) the externally applied strain is not fully transmitted to the flake [1687, 1694, 1698]. For flake lengths higher than the critical length, the critical strain for buckling is $\sim -0.6\%$ [1692]. By considering the critical buckling strain for an embedded flake in the classical Euler regime [1672, 1689], the effective bending rigidity of SLG fully embedded in a polymer matrix was estimated ~70 MeV. This means that SLG encapsulation into a matrix affects the resistance to bending and paves the way for the development of novel composite materials with higher values of compression strength compared to conventional ones. This value, however, is six orders of magnitude higher than in air and one order of magnitude higher than CVD SLG in water [1680]. This could imply that encapsulation into a matrix or in water, affects the resistance of SLG to bending.

The bulging test combined with Raman spectroscopy was used [1704] on a multireflection model for a SLG-air-Si stack (figure IX.69(a)) that takes into account the variation of $I(2D)$ and $I(G)$ (figure IX.69(b)). Both oscillate between a minimum and a maximum which depend on the height of the blister at various pressure differences (figure IX.69(c)) [1704]. The enhancement factor of $I(D)$ and $I(G)$ was correlated by a multireflection model [1705] with h_{tot}, the total distance between SLG and the underlying Si (figure IX.69(a) and (c)), and was used for the metrology of the blister height. Following Hencky's model (equation (IX.23)), the third power of the height at the centre point of the blister is linearly dependent on the pressure difference across SLG (figure IX.69(d)) resulting in a slope from which the suspended SLG E_{2D} was estimated ~352 Nm^{-1}, in agreement with values derived from direct methods (see table IX.3).

Instead of using the pressure difference, the bulging test can be also implemented with electrostatic actuation of SLG suspended onto holes with large diameters (7.5–30 μm) over a gating chip forming a parallel plate capacitor with an inter-plate distance, d, (figure IX.70(a)) [1706]. By applying a gate voltage, SLG deflects subjecting to a pressure which defines the radial in plane stress and corresponds to a radial strain. Therefore E_{2D} can be estimated (figure IX.70(d)). The radial strain depends on the height of the membrane dome at the centre deflection point, measured by employing interferometric profilometry (figure IX.70(b). A number of different devices were tested and the estimated E are presented in the histogram of

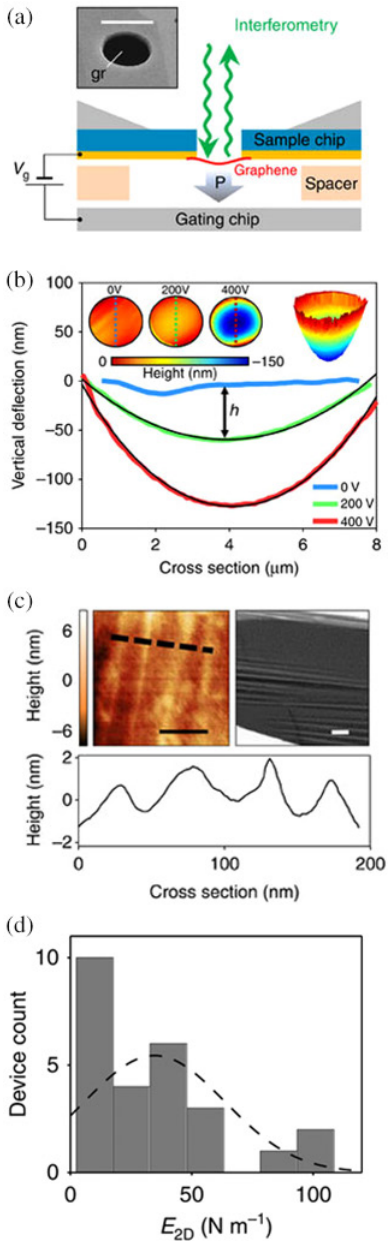


Figure IX.70. (a) Device schematic. Inset: SEM image of a representative free-standing SLG membrane (scale bar, 8 μm). (b) Cross-sections of SLG membrane at various applied voltages. Height data obtained from interferometric profilometry corresponding to these cross-sections are in the inset. Also shown is a 3d view of the data at $V_g = 400$ V. (c) AFM measurements of SLG membrane with nm-scale static wrinkles (left, scale bar, 100 nm). A cross section of the AFM data is shown in the bottom panel. Wrinkling is also evident on the high-angle tilted SEM image (right, scale bar, 1 μm). (d) Histogram for all measured CVD SLG devices.

figure IX.70(d) and are significantly lower than those from other techniques (table IX.3).

Ref. [1707] employed Raman spectroscopy using the aforementioned SLG-sealed micro-chambers under variable external pressure to determine the pressure induced sliding friction between SiO_2 and 1L-, 2L- and 3LG. Tensile radial strain ~ 0.6% and compressive tangential strain ~ −0.3% were achieved. A violation of the Amonton's law [1708, 1709] for 1L and 2LG was found. In 3LG, however, the sliding friction is directly proportional to the applied load in accordance with the Amonton's law. This behaviour was attributed the lower bending rigidity of 3LG, enabling higher surface conformation and stronger adhesion.

Several diamond anvil cell experiments were conducted on MC 1L and FLG on Si/SiO_2 or Cu, employing different pressure transmitting media [1529, 1710]. The choice of transmitting medium, e.g. polar (4:1 methanol-ethanol) or non-polar (e.g Fluorinert), is important due to pressure mediated doping that occurs from the substrate. Assuming that SLG follows the pressure-induced substrate contraction, its compression is determined by the bulk modulus of the substrate (140 GPa for Cu [1710]). In Ref. [1710] suggested that the expected value of the pressure dependent wavenumber shift is ~15 cm^{-1}/GPa (for SiO_2/Si, which is more compressible, this is ~21.4 cm^{-1}/GPa). The significant deviation was ascribed to the non-ideal adherence of SLG on Cu.

From the applications point of view, it is important to understand how atomically thin membranes respond to mechanical deformations at the nanoscale. Sample preparation and handling hinders systematic studies, since a defect-free gauge area of the sample is difficult to be placed and gripped onto the loading device. The development of specific instruments with low force sensing and capable of applying in-plane stress in GRM membranes is necessary to capture their full response under axial deformation up to failure and to measure directly the elastic (e.g. stiffness) and inelastic properties (e.g. fracture strength and strain-to-failure). Fundamental questions have been raised on the effects of defects, out-of-plane deformations and wrinkling in either elastic or inelastic properties of GRMs [1669, 1711].Therefore, further research is needed in order for novel applications to take full advantage of these superior properties.

Conclusions

We presented the main techniques for production, transfer and functionalization of graphene, related layered materials, and heterostructures. We also summarized the key characterization techniques. We provided key practical details and procedures, to help the reader reproduce the results. We hope this work will stimulate both fundamental and practical interest in GRMs, and facilitate their use in a variety of novel applications.

Acknowledgment

We acknowledge funding from the European Commission Graphene Flagship Core1 (grant agreement 696656) and Core2 (grant agreement 785219). We thank Dr Elena López-Elvira for editing this manuscript.

ORCID iDs

Mar Garcia-Hernandez https://orcid.org/0000-0002- 5987-0647

References

[1] Chen L, Hernandez Y, Feng X and Müllen K 2012 From nanographene and graphene nanoribbons to graphene sheets: chemical synthesis *Angew. Chem, Int. Ed. Engl.* **51** 7640–54

[2] Bai J and Huang Y 2010 Fabrication and electrical properties of graphene nanoribbons *Mater. Sci. Eng.* R **70** 341–53

[3] Ma L, Wang J and Ding F 2013 Recent progress and challenges in graphene nanoribbon synthesis *ChemPhysChem* **14** 47–54

[4] Terrones M *et al* 2010 Graphene and graphite nanoribbons: morphology, properties, synthesis, defects and applications *Nano Today* **5** 351–72

[5] Barone V, Hod O and Scuseria G E 2006 Electronic structure and stability of semiconducting graphene nanoribbons *Nano Lett.* **6** 2748–54

[6] Wakabayashi K, Sasaki K-I, Nakanishi T and Enoki T 2010 Electronic states of graphene nanoribbons and analytical solutions *Sci. Technol. Adv. Mater.* **11** 054504

[7] Nakada K, Fujita M, Dresselhaus G and Dresselhaus M S 1996 Edge state in graphene ribbons: nanometer size effect and edge shape dependence *Phys. Rev.* B **54** 17954–61

[8] Obradovic B, Kotlyar R, Heinz F, Matagne P, Rakshit T, Giles M D, Stettler M A and Nikonov D E 2006 Analysis of graphene nanoribbons as a channel material for field-effect transistors *Appl. Phys. Lett.* **88** 142102

[9] Wang J, Zhao R, Yang M, Liu Z and Liu Z 2013 Inverse relationship between carrier mobility and bandgap in graphene *J. Chem. Phys.* **138** 084701

[10] Son Y-W, Cohen M L and Louie S G 2006 Energy gaps in graphene nanoribbons *Phys. Rev. Lett.* **97** 216803

[11] Yang L, Park C-H, Son Y-W, Cohen M L and Louie S G 2007 Quasiparticle energies and band gaps in graphene nanoribbons *Phys. Rev. Lett.* **99** 186801

[12] Fujita M, Wakabayashi K, Nakada K and Kusakabe K 1996 Peculiar localized state at zigzag graphite edge *J. Phys. Soc. Japan* **65** 1920–3

[13] Wang X and Dai H 2010 Etching and narrowing of graphene from the edges *Nat. Chem.* **2** 661

[14] Bai J, Duan X and Huang Y 2009 Rational fabrication of graphene nanoribbons using a nanowire etch mask *Nano Lett.* **9** 2083–7

[15] Han M Y, Özyilmaz B, Zhang Y and Kim P 2007 Energy band-gap engineering of graphene nanoribbons *Phys. Rev. Lett.* **98** 206805

[16] Palma C-A and Samorì P 2011 Blueprinting macromolecular electronics *Nat. Chem.* **3** 431

[17] Kosynkin D V, Higginbotham A L, Sinitskii A, Lomeda J R, Dimiev A, Price B K and Tour J M 2009 Longitudinal unzipping of carbon nanotubes to form graphene nanoribbons *Nature* **458** 872

[18] Jiao L, Zhang L, Wang X, Diankov G and Dai H 2009 Narrow graphene nanoribbons from carbon nanotubes *Nature* **458** 877

[19] Jiao L, Wang X, Diankov G, Wang H and Dai H 2010 Facile synthesis of high-quality graphene nanoribbons *Nat. Nanotechnol.* **5** 321

[20] Elías A L, Botello-Méndez A R, Meneses-Rodríguez D, Jehová González V, Ramírez-González D, Ci L, Muñoz-Sandoval E, Ajayan P M, Terrones H and Terrones M 2010 Longitudinal cutting of pure and doped carbon nanotubes to form graphitic nanoribbons using metal clusters as nanoscalpels *Nano Lett.* **10** 366–72

[21] Cai J *et al* 2010 Atomically precise bottom-up fabrication of graphene nanoribbons *Nature* **466** 470–3

[22] Narita A, Wang X-Y, Feng X and Müllen K 2015 New advances in nanographene chemistry *Chem. Soc. Rev.* **44** 6616–43

[23] Wang X-Y, Narita A and Müllen K 2017 Precision synthesis versus bulk-scale fabrication of graphenes *Nat. Rev. Chem.* **2** 0100

[24] Dössel L, Gherghel L, Feng X and Müllen K 2011 Graphene nanoribbons by chemists: nanometer-sized, soluble, and defect-free *Angew. Chem, Int. Ed. Engl.* **50** 2540–3

[25] Schwab M G *et al* 2015 Bottom-up synthesis of necklace-like graphene nanoribbons *Chemistry* **10** 2134–8

[26] Yang X, Dou X, Rouhanipour A, Zhi L, Räder H J and Müllen K 2008 Two-dimensional graphene nanoribbons *J. Am. Chem. Soc.* **130** 4216–7

[27] Schwab M G, Narita A, Hernandez Y, Balandina T, Mali K S, De Feyter S, Feng X and Müllen K 2012 Structurally defined graphene nanoribbons with high lateral extension *J. Am. Chem. Soc.* **134** 18169–72

[28] Watson M D, Fechtenkötter A and Müllen K 2001 Big is beautiful-'aromaticity' revisited from the viewpoint of macromolecular and supramolecular benzene chemistry *Chem. Rev.* **101** 1267–300

[29] Wu J, Pisula W and Müllen K 2007 Graphenes as potential material for electronics *Chem. Rev.* **107** 718–47

[30] Stille J K 1981 Step-growth polymerization *J. Chem. Educ.* **58** 862

[31] Zhang W *et al* 2017 Monitoring the on-surface synthesis of graphene nanoribbons by mass spectrometry *Anal. Chem.* **89** 7485–92

[32] Narita A *et al* 2013 Synthesis of structurally well-defined and liquid-phase-processable graphene nanoribbons *Nat. Chem.* **6** 126–32

[33] Carothers W H 1936 Polymers and polyfunctionality *Trans. Faraday Soc.* **32** 39

[34] Odian G 2004 *Principles of Polymerization* (New York: Wiley)

[35] Lee J, Cho H-J, Jung B-J, Cho N S and Shim H-K 2004 Stabilized blue luminescent polyfluorenes: introducing polyhedral oligomeric silsesquioxane *Macromolecules* **37** 8523–9

[36] Setayesh S, Grimsdale A C, Weil T, Enkelmann V, Müllen K, Meghdadi F, List E J W and Leising G 2001 Polyfluorenes with polyphenylene dendron side chains: toward non-aggregating, light-emitting polymers *J. Am. Chem. Soc.* **123** 946–53

[37] Talirz L, Ruffieux P and Fasel R 2016 On-surface synthesis of atomically precise graphene nanoribbons *Adv. Mater.* **28** 6222–31

[38] Grill L, Rieder K H, Moresco F, Rapenne G, Stojkovic S, Bouju X and Joachim C 2007 Rolling a single molecular wheel at the atomic scale *Nat. Nanotechnol.* **2** 95–8

[39] Huang H, Wei D, Sun J, Wong S L, Feng Y P, Neto A H C and Wee A T S 2012 Spatially resolved electronic structures of atomically precise armchair graphene nanoribbons *Sci. Rep.* **2** 983

[40] Fairbrother A, Sanchez-Valencia J-R, Lauber B, Shorubalko I, Ruffieux P, Hintermann T and Fasel R 2017 High vacuum synthesis and ambient stability of bottom-up graphene nanoribbons *Nanoscale* **9** 2785–92

[41] Chen Z *et al* 2016 Synthesis of graphene nanoribbons by ambient-pressure chemical vapor deposition and device integration *J. Am. Chem. Soc.* **138** 15488–96

[42] Chen Z *et al* 2017 Chemical vapor deposition synthesis and terahertz photoconductivity of low-band-gap $N = 9$ armchair graphene nanoribbons *J. Am. Chem. Soc.* **139** 3635–8

[43] Greenwood A E A N 1997 Chemistry of elements ISBN: 9780750633659 https://www.elsevier.com/books/chemistry-of-the-elements/greenwood/978-0-7506-3365-9

[44] Kimouche A, Ervasti M M, Drost R, Halonen S, Harju A, Joensuu P M, Sainio J and Liljeroth P 2015 Ultra-narrow metallic armchair graphene nanoribbons *Nat. Commun.* **6** 10177

[45] Chen Z *et al* 2017 Lateral fusion of chemical vapor deposited $N = 5$ armchair graphene nanoribbons *J. Am. Chem. Soc.* **139** 9483–6

[46] Sakaguchi H, Kawagoe Y, Hirano Y, Iruka T, Yano M and Nakae T 2014 Width-controlled sub-nanometer graphene nanoribbon films synthesized by radical-polymerized chemical vapor deposition *Adv. Mater.* **26** 4134–8

[47] Zhang H *et al* 2015 On-surface synthesis of rylene-type graphene nanoribbons *J. Am. Chem. Soc.* **137** 4022–5

[48] Talirz L *et al* 2017 On-surface synthesis and characterization of 9-atom wide armchair graphene nanoribbons *ACS Nano* **11** 1380–8

[49] Chen Y-C, de Oteyza D G, Pedramrazi Z, Chen C, Fischer F R and Crommie M F 2013 Tuning the band gap of graphene nanoribbons synthesized from molecular precursors *ACS Nano* **7** 6123–8
[50] Nguyen G D *et al* 2016 Bottom-up synthesis of $N = 13$ sulfur-doped graphene nanoribbons *J. Phys. Chem.* C **120** 2684–7
[51] Kawai S, Saito S, Osumi S, Yamaguchi S, Foster A S, Spijker P and Meyer E 2015 Atomically controlled substitutional boron-doping of graphene nanoribbons *Nat. Commun.* **6** 8098
[52] Cloke R R, Marangoni T, Nguyen G D, Joshi T, Rizzo D J, Bronner C, Cao T, Louie S G, Crommie M F and Fischer F R 2015 Site-specific substitutional boron doping of semiconducting armchair graphene nanoribbons *J. Am. Chem. Soc.* **137** 8872–5
[53] Zhang Y, Zhang Y, Li G, Lu J, Lin X, Du S, Berger R, Feng X, Müllen K and Gao H-J 2014 Direct visualization of atomically precise nitrogen-doped graphene nanoribbons *Appl. Phys. Lett.* **105** 023101
[54] Bronner C, Stremlau S, Gille M, Brauße F, Haase A, Hecht S and Tegeder P 2013 Aligning the band gap of graphene nanoribbons by monomer doping *Angew. Chem, Int. Ed. Engl.* **52** 4422–5
[55] Cai J *et al* 2014 Graphene nanoribbon heterojunctions *Nat. Nanotechnol.* **9** 896–900
[56] Marangoni T, Haberer D, Rizzo D J, Cloke R R and Fischer F R 2016 Heterostructures through divergent edge reconstruction in nitrogen-doped segmented graphene nanoribbons *Chemistry* A **22** 13037–40
[57] Ruffieux P *et al* 2016 On-surface synthesis of graphene nanoribbons with zigzag edge topology *Nature* **531** 489–92
[58] de Oteyza D G *et al* 2016 Substrate-independent growth of atomically precise chiral graphene nanoribbons *ACS Nano* **10** 9000–8
[59] Bronner C *et al* 2018 Hierarchical on-surface synthesis of graphene nanoribbon heterojunctions *ACS Nano* **12** 2193–200
[60] Chen Y-C, Cao T, Chen C, Pedramrazi Z, Haberer D, de Oteyza D G, Fischer F R, Louie S G and Crommie M F 2015 Molecular bandgap engineering of bottom-up synthesized graphene nanoribbon heterojunctions *Nat. Nanotechnol.* **10** 156–60
[61] Jacobse P H, Kimouche A, Gebraad T, Ervasti M M, Thijssen J M, Liljeroth P and Swart I 2017 Electronic components embedded in a single graphene nanoribbon *Nat. Commun.* **8** 119
[62] Nguyen G D *et al* 2017 Atomically precise graphene nanoribbon heterojunctions from a single molecular precursor *Nat. Nanotechnol.* **12** 1077–82
[63] Gröning O *et al* 2018 Engineering of robust topological quantum phases in graphene nanoribbons *Nature* **560** 209–13
[64] Rizzo D J, Veber G, Cao T, Bronner C, Chen T, Zhao F, Rodriguez H, Louie S G, Crommie M F and Fischer F R 2018 Topological band engineering of graphene nanoribbons *Nature* **560** 204–8
[65] Vandescuren M, Hermet P, Meunier V, Henrard L and Lambin P 2008 Theoretical study of the vibrational edge modes in graphene nanoribbons *Phys. Rev.* B **78** 195401
[66] Gross L, Mohn F, Moll N, Liljeroth P and Meyer G 2009 The chemical structure of a molecule resolved by atomic force microscopy *Science* **325** 1110–4
[67] Giessibl F J 2000 Atomic resolution on Si(1 1 1)-(7 × 7) by noncontact atomic force microscopy with a force sensor based on a quartz tuning fork *Appl. Phys. Lett.* **76** 1470–2
[68] Bartels L, Meyer G, Rieder K H, Velic D, Knoesel E, Hotzel A, Wolf M and Ertl G 1998 Dynamics of electron-induced manipulation of individual CO molecules on Cu(1 1 1) *Phys. Rev. Lett.* **80** 2004–7
[69] Denk R *et al* 2014 Exciton-dominated optical response of ultra-narrow graphene nanoribbons *Nat. Commun.* **5** 4253
[70] Li G, Yoon K-Y, Zhong X, Zhu X and Dong G 2016 Efficient bottom-up preparation of graphene nanoribbons by mild Suzuki-Miyaura polymerization of simple triaryl monomers *Chemistry* A **22** 9116–20
[71] Llinas J P *et al* 2017 Short-channel field-effect transistors with 9-atom and 13-atom wide graphene nanoribbons *Nat. Commun.* **8** 633
[72] Bennett P B, Pedramrazi Z, Madani A, Chen Y-C, de Oteyza D G, Chen C, Fischer F R, Crommie M F and Bokor J 2013 Bottom-up graphene nanoribbon field-effect transistors *Appl. Phys. Lett.* **103** 253114
[73] Angelova P *et al* 2013 A universal scheme to convert aromatic molecular monolayers into functional carbon nanomembranes *ACS Nano* **7** 6489–97
[74] Matei D G *et al* 2013 Functional single-layer graphene sheets from aromatic monolayers *Adv. Mater.* **25** 4146–51
[75] Nottbohm C T, Turchanin A, Beyer A and Gölzhäuser A 2009 Direct e-beam writing of 1 nm thin carbon nanoribbons *J. Vac. Sci. Technol.* B **27** 3059
[76] Nottbohm C T, Turchanin A, Beyer A, Stosch R and Gölzhäuser A 2011 Mechanically stacked 1 nm-thick carbon nanosheets: ultrathin layered materials with tunable optical, chemical, and electrical properties *Small* **7** 874–83
[77] Rhinow D, Weber N-E and Turchanin A 2012 Atmospheric pressure, temperature-induced conversion of organic monolayers into nanocrystalline graphene *J. Phys. Chem.* C **116** 12295–303
[78] Turchanin A, Beyer A, Nottbohm C T, Zhang X, Stosch R, Sologubenko A, Mayer J, Hinze P, Weimann T and Gölzhäuser A 2009 One nanometer thin carbon nanosheets with tunable conductivity and stiffness *Adv. Mater.* **21** 1233–7
[79] Turchanin A, Weber D, Büenfeld M, Kisielowski C, Fistul M V, Efetov K B, Weimann T, Stosch R, Mayer J and Gölzhäuser A 2011 Conversion of self-assembled monolayers into nanocrystalline graphene: structure and electric transport *ACS Nano* **5** 3896–904
[80] Weber N-E, Wundrack S, Stosch R and Turchanin A 2016 Direct growth of patterned graphene *Small* **12** 1440–5
[81] Turchanin A and Gölzhäuser A 2016 Carbon nanomembranes *Adv. Mater.* **28** 6075–103
[82] Turchanin A, Käfer D, El-Desawy M, Wöll C, Witte G and Gölzhäuser A 2009 Molecular mechanisms of electron-induced cross-linking in aromatic SAMs *Langmuir* **25** 7342–52
[83] Turchanin A, Schnietz M, El-Desawy M, Solak H H, David C and Gölzhäuser A 2007 Fabrication of molecular nanotemplates in self-assembled monolayers by extreme-ultraviolet-induced chemical lithography *Small* **3** 2114–9
[84] Kankate L, Turchanin A and Gölzhäuser A 2009 On the release of hydrogen from the S–H groups in the formation of self-assembled monolayers of thiols *Langmuir* **25** 10435–8
[85] Matei D G, Muzik H, Gölzhäuser A and Turchanin A 2012 Structural investigation of 1,1′-biphenyl-4-thiol self-assembled monolayers on Au(1 1 1) by scanning tunneling microscopy and low-energy electron diffraction *Langmuir* **28** 13905–11
[86] Love J C, Estroff L A, Kriebel J K, Nuzzo R G and Whitesides G M 2005 Self-assembled monolayers of thiolates on metals as a form of nanotechnology *Chem. Rev.* **105** 1103–70
[87] Geyer W, Stadler V, Eck W, Zharnikov M, Gölzhäuser A and Grunze M 1999 Electron-induced crosslinking of aromatic self-assembled monolayers: negative resists for nanolithography *Appl. Phys. Lett.* **75** 2401–3
[88] Turchanin A and Gölzhäuser A 2012 Carbon nanomembranes from self-assembled monolayers: functional surfaces without bulk *Prog. Surf. Sci.* **87** 108–62
[89] Chesneau F, Hamoudi H, Schüpbach B R, Terfort A and Zharnikov M 2011 Modification of self-assembled monolayers of perfluoroterphenyl-substituted alkanethiols by low-energy electrons *J. Phys. Chem.* C **115** 4773–82
[90] Amiaud L, Houplin J, Bourdier M, Humblot V, Azria R, Pradier C M and Lafosse A 2014 Low-energy electron induced resonant loss of aromaticity: consequences on cross-linking in terphenylthiol SAMs *Phys. Chem. Chem. Phys.* **16** 1050–9
[91] Mrugalla A and Schnack J 2014 Classical molecular dynamics investigations of biphenyl-based carbon nanomembranes *Beilstein J. Nanotechnol.* **5** 865–71

[92] Zharnikov M, Geyer W, Gölzhäuser A, Frey S and Grunze M 1999 Modification of alkanethiolate monolayers on Au-substrate by low energy electron irradiation: alkyl chains and the S/Au interface *Phys. Chem. Chem. Phys.* **1** 3163–71
[93] Zharnikov M and Grunze M 2002 Modification of thiol-derived self-assembling monolayers by electron and x-ray irradiation: scientific and lithographic aspects *J. Vac. Sci. Technol.* B **20** 1793
[94] Zhang X, Vieker H, Beyer A and Gölzhäuser A 2014 Fabrication of carbon nanomembranes by helium ion beam lithography *Beilstein J. Nanotechnol.* **5** 188–94
[95] Beyer A, Turchanin A, Nottbohm C T, Mellech N, Schnietz M and Gölzhäuser A 2010 Fabrication of metal patterns on freestanding graphenoid nanomembranes *J. Vac. Sci. Technol.* B **28** C6D5–10
[96] Ferrari A C and Basko D M 2013 Raman spectroscopy as a versatile tool for studying the properties of graphene *Nat. Nanotechnol.* **8** 235–46
[97] Kim K, Lee Z, Regan W, Kisielowski C, Crommie M F and Zettl A 2011 Grain boundary mapping in polycrystalline graphene *ACS Nano* **5** 2142–6
[98] Warner J H, Rümmeli M H, Gemming T, Büchner B and Briggs G A D 2009 Direct imaging of rotational stacking faults in few layer graphene *Nano Lett.* **9** 102–6
[99] Kotakoski J, Krasheninnikov A V, Kaiser U and Meyer J C 2011 From point defects in graphene to two-dimensional amorphous carbon *Phys. Rev. Lett.* **106** 105505
[100] Jung I, Dikin D A, Piner R D and Ruoff R S 2008 Tunable electrical conductivity of individual graphene oxide sheets reduced at 'low' temperatures *Nano Lett.* **8** 4283–7
[101] Eda G, Mattevi C, Yamaguchi H, Kim H and Chhowalla M 2009 Insulator to semimetal transition in graphene oxide *J. Phys. Chem.* C **113** 15768–71
[102] Loh K P, Bao Q, Eda G and Chhowalla M 2010 Graphene oxide as a chemically tunable platform for optical applications *Nat. Chem.* **2** 1015–24
[103] Parvez K, Yang S, Hernandez Y, Winter A, Turchanin A, Feng X and Müllen K 2012 Nitrogen-doped graphene and its iron-based composite as efficient electrocatalysts for oxygen reduction reaction *ACS Nano* **6** 9541–50
[104] Wu Z-S, Winter A, Chen L, Sun Y, Turchanin A, Feng X and Müllen K 2012 Three-dimensional nitrogen and boron Co-doped graphene for high-performance all-solid-state supercapacitors *Adv. Mater.* **24** 5130–5
[105] Ferrari A C *et al* 2006 Raman spectrum of graphene and graphene layers *Phys. Rev. Lett.* **97** 187401
[106] Meyer J C, Geim A K, Katsnelson M I, Novoselov K S, Obergfell D, Roth S, Girit C and Zettl A 2007 On the roughness of single- and bi-layer graphene membranes *Solid State Commun.* **143** 101–9
[107] Novoselov K S, Geim A K, Morozov S V, Jiang D, Katsnelson M I, Grigorieva I V, Dubonos S V and Firsov A A 2005 Two-dimensional gas of massless Dirac fermions in graphene *Nature* **438** 197–200
[108] Gao L *et al* 2012 Repeated growth and bubbling transfer of graphene with millimetre-size single-crystal grains using platinum *Nat. Commun.* **3** 699
[109] Wang D-Y *et al* 2013 Clean-lifting transfer of large-area residual-free graphene films *Adv. Mater.* **25** 4521–6
[110] Lercel M J, Redinbo G F, Pardo F D, Rooks M, Tiberio R C, Simpson P, Craighead H G, Sheen C W, Parikh A N and Allara D L 1994 Electron beam lithography with monolayers of alkylthiols and alkylsiloxanes *J. Vac. Sci. Technol.* B **12** 3663–7
[111] Ferrari A C *et al* 2015 Science and technology roadmap for graphene, related two-dimensional crystals, and hybrid systems *Nanoscale* **7** 4598–810
[112] Geim A K and Grigorieva I V 2013 Van der Waals heterostructures *Nature* **499** 419–25
[113] Zheng Z, Zhang X, Neumann C, Emmrich D, Winter A, Vieker H, Liu W, Lensen M, Gölzhäuser A and Turchanin A 2015 Hybrid van der Waals heterostructures of zero-dimensional and two-dimensional materials *Nanoscale* **7** 13393–7
[114] Zheng Z, Nottbohm C T, Turchanin A, Muzik H, Beyer A, Heilemann M, Sauer M and Gölzhäuser A 2010 Janus nanomembranes: a generic platform for chemistry in two dimensions *Angew. Chem, Int. Ed. Engl.* **49** 8493–7
[115] Bonaccorso F, Lombardo A, Hasan T, Sun Z, Colombo L and Ferrari A C 2012 Production and processing of graphene and 2d crystals *Mater. Today* **15** 564–89
[116] Cano-Márquez A G, Rodríguez-Macías F J, Campos-Delgado J, Espinosa-González C G, Tristán-López F, Ramírez-González D, Cullen D A, Smith D J, Terrones M and Vega-Cantú Y I 2009 Ex-MWNTs: graphene sheets and ribbons produced by lithium intercalation and exfoliation of carbon nanotubes *Nano Lett.* **9** 1527–33
[117] Varela-Rizo H, Rodriguez-Pastor I, Merino C, Terrones M and Martin-Gullon I 2011 Graphene oxide nanoplatelets of different crystallinity synthesized from helical-ribbon carbon nanofibers and multiwall carbon nanotubes *J. Mater. Res.* **26** 2632–41
[118] Yeon Y, Lee M Y, Kim S Y, Lee J, Kim B, Park B and In I 2015 Production of quasi-2D graphene nanosheets through the solvent exfoliation of pitch-based carbon fiber *Nanotechnology* **26** 375602
[119] Lee M, Lee J, Park S Y, Min B, Kim B and In I 2015 Production of graphene oxide from pitch-based carbon fiber *Sci. Rep.* **5** 11707
[120] Botas C, Álvarez P, Blanco C, Santamaría R, Granda M, Ares P, Rodríguez-Reinoso F and Menéndez R 2012 The effect of the parent graphite on the structure of graphene oxide *Carbon* **50** 275–82
[121] Bernal J D 1924 The structure of graphite *Proc. R. Soc.* A **106** 749–73
[122] Lipson H and Stokes A R 1942 The structure of graphite *Proc. R. Soc.* A **181** 101–5
[123] Franklin R E 1951 Crystallite growth in graphitizing and non-graphitizing carbons *Proc. R. Soc.* A **209** 196–218
[124] Marsh J A G H 1979 *14th Biennial Conf. on Carbon* ed ACS (Penn State University) p 117 www.tib.eu/en/search/id/TIBKAT%3A041557468/Contributions-for-the-14th-Biennial-Conference/
[125] Meyer M I R A 1999 *Stress Graphitization in Chemistry and Physics of Carbon* (New York: Dekker)
[126] Loh G C and Baillargeat D 2013 Graphitization of amorphous carbon and its transformation pathways *J. Appl. Phys.* **114** 033534
[127] Rodriguez-Reinoso F 1989 Comite internacional para la caracterizacion y la terminologia del carbon *Carbon* **27** 305–12
[128] Li X, Magnuson C W, Venugopal A, Tromp R M, Hannon J B, Vogel E M, Colombo L and Ruoff R S 2011 Large-area graphene single crystals grown by low-pressure chemical vapor deposition of methane on copper *J. Am. Chem. Soc.* **133** 2816–9
[129] Wassei J K, Mecklenburg M, Torres J A, Fowler J D, Regan B C, Kaner R B and Weiller B H 2012 Graphene: chemical vapor deposition of graphene on copper from methane, ethane and propane: evidence for bilayer selectivity (*Small* 9/2012) *Small* **8** 1289
[130] Novoselov K S, Jiang D, Schedin F, Booth T J, Khotkevich V V, Morozov S V and Geim A K 2005 Two-dimensional atomic crystals *Proc. Natl Acad. Sci.* **102** 10451–3
[131] Hernandez Y V *et al* 2008 High-yield production of graphene by liquid-phase exfoliation of graphite *Nat. Nanotechnol.* **3** 563–8
[132] Botas C, Pérez-Mas A M, Álvarez P, Santamaría R, Granda M, Blanco C and Menéndez R 2013 Optimization of the size and yield of graphene oxide sheets in the exfoliation step *Carbon* **63** 576–8
[133] Cai M, Thorpe D, Adamson D H and Schniepp H C 2012 Methods of graphite exfoliation *J. Mater. Chem.* **22** 24992
[134] Bourlinos A B, Georgakilas V, Zboril R, Steriotis T A and Stubos A K 2009 Liquid-phase exfoliation of graphite towards solubilized graphenes *Small* **5** 1841–5
[135] González Z, Botas C, Blanco C, Santamaría R, Granda M, Álvarez P and Menéndez R 2013 Graphite oxide-based

graphene materials as positive electrodes in vanadium redox flow batteries *J. Power Sources* **241** 349–54
[136] Liscio A, Kouroupis-Agalou K, Betriu X D, Kovtun A, Treossi E, Pugno N M, De Luca G, Giorgini L and Palermo V 2017 Evolution of the size and shape of 2D nanosheets during ultrasonic fragmentation *2D Mater.* **4** 025017
[137] Xia Z Y, Pezzini S, Treossi E, Giambastiani G, Corticelli F, Morandi V, Zanelli A, Bellani V and Palermo V 2013 The exfoliation of graphene in liquids by electrochemical, chemical, and sonication-assisted techniques: a nanoscale study *Adv. Funct. Mater.* **23** 4684–93
[138] Ghosh P K B A S 1997 *Elements of Prospecting for Non-Fuel Mineral Deposits* (Allied Publisher Ltd)
[139] Peng W, Li H, Hu Y, Liu Y and Song S 2016 Characterisation of reduced graphene oxides prepared from natural flaky, lump and amorphous graphites *Mater. Res. Bull.* **78** 119–27
[140] Peng W, Li H, Hu Y, Liu Y and Song S 2016 Does silicate mineral impurities in natural graphite affect the characteristics of synthesized graphene? *Mater. Res. Bull.* **74** 333–9
[141] Colonna S, Monticelli O, Gomez J, Novara C, Saracco G and Fina A 2016 Effect of morphology and defectiveness of graphene-related materials on the electrical and thermal conductivity of their polymer nanocomposites *Polymer* **102** 292–300
[142] Colonna S, Monticelli O, Gomez J, Saracco G and Fina A 2017 Morphology and properties evolution upon ring-opening polymerization during extrusion of cyclic butylene terephthalate and graphene-related-materials into thermally conductive nanocomposites *Eur. Polym. J.* **89** 57–66
[143] Galindo B, Alcolea S G, Gómez J, Navas A, Murguialday A O, Fernandez M P and Puelles R C 2014 Effect of the number of layers of graphene on the electrical properties of TPU polymers *IOP Conf. Ser.: Mater. Sci. Eng.* **64** 012008
[144] Gomez J 2017 Preparation and processing of large lateral size graphene materialsin epoxy matrix composites *Graphene Week (Athens, Greece)*
[145] Casaluci S, Gemmi M, Pellegrini V, Di Carlo A and Bonaccorso F 2016 Graphene-based large area dye-sensitized solar cell modules *Nanoscale* **8** 5368–78
[146] Villaro E 2013 Preparación y caracterización de nanocompuestos de grafeno en una suspensión de partículas de PVC (plastisol) MsD Thesis Facultad de Ciencias UNED
[147] Sun L and Fugetsu B 2013 Mass production of graphene oxide from expanded graphite *Mater. Lett.* **109** 207–10
[148] Sierra U, Álvarez P, Blanco C, Granda M, Santamaría R and Menéndez R 2015 New alternatives to graphite for producing graphene materials *Carbon* **93** 812–8
[149] Sierra U, Álvarez P, Blanco C, Granda M, Santamaría R and Menéndez R 2016 Cokes of different origin as precursors of graphene oxide *Fuel* **166** 400–3
[150] Alvarez P, Díez N, Santamaría R, Blanco C, Menéndez R and Granda M 2012 Novel coal-based precursors for cokes with highly oriented microstructures *Fuel* **95** 400–6
[151] Oberlin A 1984 Carbonization and graphitization *Carbon* **22** 521–41
[152] Fitzer E, Kochling K H, Boehm H P and Marsh H 1995 Recommended terminology for the description of carbon as a solid (IUPAC Recommendations 1995) *Pure Appl. Chem.* **67** 473–506
[153] Del Rio-Castillo A E, Merino C, Díez-Barra E and Vázquez E 2014 Selective suspension of single layer graphene mechanochemically exfoliated from carbon nanofibres *Nano Res.* **7** 963–72
[154] Lobato B, Merino C, Barranco V and Centeno T A 2016 Large-scale conversion of helical-ribbon carbon nanofibers to a variety of graphene-related materials *RSC Adv.* **6** 57514–20
[155] Vera-Agullo J, Varela-Rizo H, Conesa J A, Almansa C, Merino C and Martin-Gullon I 2007 Evidence for growth mechanism and helix-spiral cone structure of stacked-cup carbon nanofibers *Carbon* **45** 2751–8
[156] Hummers W S and Offeman R E 1958 Preparation of graphitic oxide *J. Am. Chem. Soc.* **80** 1339
[157] Moon I K, Lee J, Ruoff R S and Lee H 2010 Reduced graphene oxide by chemical graphitization *Nat. Commun.* **1** 1–6
[158] Park S and Ruoff R S 2009 Chemical methods for the production of graphenes *Nat. Nanotechnol.* **4** 217–24
[159] Benavente E, Santa Ana M A, Mendizábal F and González G 2002 Intercalation chemistry of molybdenum disulfide *Coord. Chem. Rev.* **224** 87–109
[160] Eigler S and Hirsch A 2014 Chemistry with graphene and graphene oxide—challenges for synthetic chemists *Angew. Chem, Int. Ed. Engl.* **53** 7720–38
[161] Grayfer E D, Kozlova M N and Fedorov V E 2017 Colloidal 2D nanosheets of MoS2 and other transition metal dichalcogenides through liquid-phase exfoliation *Adv. Colloid Interface Sci.* **245** 40–61
[162] Nicolosi V, Chhowalla M, Kanatzidis M G, Strano M S and Coleman J N 2013 Liquid exfoliation of layered materials *Science* **340** 1420
[163] Yi M and Shen Z 2015 A review on mechanical exfoliation for the scalable production of graphene *J. Mater. Chem.* C **3** 11700–15
[164] Tao H, Zhang Y, Gao Y, Sun Z, Yan C and Texter J 2017 Scalable exfoliation and dispersion of two-dimensional materials—an update *Phys. Chem. Chem. Phys.* **19** 921–60
[165] Ciesielski A and Samorì P 2016 Supramolecular approaches to graphene: from self-assembly to molecule-assisted liquid-phase exfoliation *Adv. Mater.* **28** 6030–51
[166] Bonaccorso F, Bartolotta A, Coleman J N and Backes C 2016 2D-crystal-based functional inks *Adv. Mater.* **28** 6136–66
[167] Gutiérrez M and Henglein A 1989 Preparation of colloidal semiconductor solutions of MoS2 and WSe2 via sonication *Ultrasonics* **27** 259–61
[168] Kang J, Sangwan V K, Wood J D and Hersam M C 2017 Solution-based processing of monodisperse two-dimensional nanomaterials *Acc. Chem. Res.* **50** 943–51
[169] Abellán G, Martí-Gastaldo C, Ribera A and Coronado E 2015 Hybrid materials based on magnetic layered double hydroxides: a molecular perspective *Acc. Chem. Res.* **48** 1601–11
[170] Naguib M, Mochalin V N, Barsoum M W and Gogotsi Y 2014 25th anniversary article: MXenes: a new family of two-dimensional materials *Adv. Mater.* **26** 992–1005
[171] Kim H, Saiz E, Chhowalla M and Mattevi C 2013 Modeling of the self-limited growth in catalytic chemical vapor deposition of graphene *New J. Phys.* **15** 053012
[172] Ciesielski A and Samori P 2014 Graphene via sonication assisted liquid-phase exfoliation *Chem. Soc. Rev.* **43** 381–98
[173] Parvez K, Yang S, Feng X and Müllen K 2015 Exfoliation of graphene via wet chemical routes *Synth. Met.* **210** 123–32
[174] Coleman J N *et al* 2011 Two-dimensional nanosheets produced by liquid exfoliation of layered materials *Science* **331** 568–71
[175] Zhong Y L, Tian Z, Simon G P and Li D 2015 Scalable production of graphene via wet chemistry: progress and challenges *Mater. Today* **18** 73–8
[176] Paton K R 2014 Scalable production of large quantities of defect-free few-layer graphene by shear exfoliation in liquids *Nat. Mater.* **13** 624–30
[177] Varrla E, Paton K R, Backes C, Harvey A, Smith R J, McCauley J and Coleman J N 2014 Turbulence-assisted shear exfoliation of graphene using household detergent and a kitchen blender *Nanoscale* **6** 11810–9
[178] Karagiannidis P G *et al* 2017 Microfluidization of graphite and formulation of graphene-based conductive inks *ACS Nano* **11** 2742–55
[179] León V, Quintana M, Herrero M A, Fierro J L G, Hoz A D L, Prato M and Vázquez E 2011 Few-layer graphenes from ball-milling of graphite with melamine *Chem. Commun.* **47** 10936
[180] Qian W, Hao R, Hou Y, Tian Y, Shen C, Gao H and Liang X 2009 Solvothermal-assisted exfoliation process to produce graphene with high yield and high quality *Nano Res.* **2** 706–12

[181] Tang Z, Zhuang J and Wang X 2010 Exfoliation of graphene from graphite and their self-assembly at the oil–water interface *Langmuir* **26** 9045–9
[182] Guardia L, Fernandez-Merino M J, Paredes J I, Solis-Fernandez P, Villar-Rodil S, Martinez-Alonso A and Tascon J M D 2011 High-throughput production of pristine graphene in an aqueous dispersion assisted by non-ionic surfactants *Carbon* **49** 1653–62
[183] Green A A and Hersam M C 2009 Solution phase production of graphene with controlled thickness via density differentiation *Nano Lett.* **9** 4031–6
[184] Lotya M *et al* 2009 Liquid phase production of graphene by exfoliation of graphite in surfactant/water solutions *J. Am. Chem. Soc.* **131** 3611–20
[185] Backes C *et al* 2014 Edge and confinement effects allow *in situ* measurement of size and thickness of liquid-exfoliated nanosheets *Nat. Commun.* **5** 4576
[186] Backes C *et al* 2016 Production of highly monolayer enriched dispersions of liquid-exfoliated nanosheets by liquid cascade centrifugation *ACS Nano* **10** 1589–601
[187] Lee K P, Chromey N C, Culik R, Barnes J R and Schneider P W 1987 Toxicity of N-methyl-2-pyrrolidone (NMP): teratogenic, subchronic, and two-year inhalation studies *Fundam. Appl. Toxicol.* **9** 222–35
[188] Harvey A *et al* 2015 Preparation of gallium sulfide nanosheets by liquid exfoliation and their application as hydrogen evolution catalysts *Chem. Mater.* **27** 3483–93
[189] Favron A, Gaufres E, Fossard F, Phaneuf-Lheureux A-L, Tang N Y W, Levesque P L, Loiseau A, Leonelli R, Francoeur S and Martel R 2015 Photooxidation and quantum confinement effects in exfoliated black phosphorus *Nat. Mater.* **14** 826–32
[190] Hanlon D C *et al* 2015 Liquid exfoliation of solvent-stabilised few-layer black phosphorus for applications beyond electronics *Nat. Commun.* **6** 8563
[191] Guo Y, Zhou S, Bai Y and Zhao J 2017 Defects and oxidation of group-III monochalcogenide monolayers *J. Chem. Phys.* **147** 104709
[192] Wang S, Yi M and Shen Z 2016 The effect of surfactants and their concentration on the liquid exfoliation of graphene *RSC Adv.* **6** 56705–10
[193] Liscio A *et al* 2017 Exfoliation of few-layer graphene in volatile solvents using aromatic perylene diimide derivatives as surfactants *ChemPlusChem* **82** 358–67
[194] Schlierf A *et al* 2013 Nanoscale insight into the exfoliation mechanism of graphene with organic dyes: effect of charge, dipole and molecular structure *Nanoscale* **5** 4205–16
[195] Svedberg T, Pederson K O and Bauer J H 1940 *The Ultracentrifuge* (London: Oxford University Press)
[196] Hansen C 1967 *The Three Dimensional Solubility Parameter and Solvent Diffusion Coefficient and Their Importance in Surface Coating Formulation* (Copenhagen: Danish Technical Press)
[197] Hughes J M, Aherne D and Coleman J N 2013 Generalizing solubility parameter theory to apply to one- and two-dimensional solutes and to incorporate dipolar interactions *J. Appl. Polym. Sci.* **127** 4483–91
[198] Shen J *et al* 2015 Liquid phase exfoliation of two-dimensional materials by directly probing and matching surface tension components *Nano Lett.* **15** 5449–54
[199] Kim J *et al* 2015 Direct exfoliation and dispersion of two-dimensional materials in pure water via temperature control *Nat. Commun.* **6** 8294
[200] Zhi C Y, Bando Y, Tang C C, Kuwahara H and Golberg D 2009 Large-scale fabrication of boron nitride nanosheets and their utilization in polymeric composites with improved thermal and mechanical properties *Adv. Mater.* **21** 2889
[201] Finn D J, Lotya M, Cunningham G, Smith R J, McCloskey D, Donegan J F and Coleman J N 2014 Inkjet deposition of liquid-exfoliated graphene and MoS_2 nanosheets for printed device applications *J. Mater. Chem.* C **2** 925–32
[202] Niyogi S, Hamon M A, Perea D E, Kang C B, Zhao B, Pal S K, Wyant A E, Itkis M E and Haddon R C 2003 Ultrasonic dispersions of single-walled carbon nanotubes *J. Phys. Chem.* B **107** 8799–804
[203] Yau H C, Bayazit M K, Steinke J H G and Shaffer M S P 2015 Sonochemical degradation of N-methylpyrrolidone and its influence on single walled carbon nanotube dispersion *Chem. Commun.* **51** 16621–4
[204] Ciesielski A *et al* 2016 Modifying the size of ultrasound-induced liquid-phase exfoliated graphene: from nanosheets to nanodots *ACS Nano* **10** 10768–77
[205] Solomon H M, Burgess B A, Kennedy G L and Staples R E 1995 1-methyl-2-pyrrolidone (nmp): reproductive and developmental toxicity study by inhalation in the rat *Drug Chem. Toxicol.* **18** 271–93
[206] Capasso A, Del Rio Castillo A E, Sun H, Ansaldo A, Pellegrini V and Bonaccorso F 2015 Ink-jet printing of graphene for flexible electronics: an environmentally-friendly approach *Solid State Commun.* **224** 53–63
[207] Zhou K-G, Mao N-N, Wang H-X, Peng Y and Zhang H-L 2011 A mixed-solvent strategy for efficient exfoliation of inorganic graphene analogues *Angew. Chem, Int. Ed. Engl.* **50** 10839–42
[208] May P, Khan U, Hughes J M and Coleman J N 2012 Role of solubility parameters in understanding the steric stabilization of exfoliated two-dimensional nanosheets by adsorbed polymers *J. Phys. Chem.* C **116** 11393–400
[209] Liang Y T and Hersam M C 2010 Highly concentrated graphene solutions via polymer enhanced solvent exfoliation and iterative solvent exchange *J. Am. Chem. Soc.* **132** 17661–3
[210] Bourlinos A B, Georgakilas V, Zboril R, Steriotis T A, Stubos A K and Trapalis C 2009 Aqueous-phase exfoliation of graphite in the presence of polyvinylpyrrolidone for the production of water-soluble graphenes *Solid State Commun.* **149** 2172–6
[211] Liu W S, Zhou R, Zhou D, Ding G G, Soah J M, Yue C Y and Lu X H 2015 Lignin-assisted direct exfoliation of graphite to graphene in aqueous media and its application in polymer composites *Carbon* **83** 188–97
[212] Ahadian S *et al* 2015 Facile and green production of aqueous graphene dispersions for biomedical applications *Nanoscale* **7** 6436–43
[213] Irin F, Hansen M J, Bari R, Parviz D, Metzler S D, Bhattacharia S K and Green M J 2015 Adsorption and removal of graphene dispersants *J. Colloid Interface Sci.* **446** 282–9
[214] Schlierf A, Samorì P and Palermo V 2014 Graphene–organic composites for electronics: optical and electronic interactions in vacuum, liquids and thin solid films *J. Mater. Chem.* C **2** 3129
[215] Englert J M, Röhrl J, Schmidt C D, Graupner R, Hundhausen M, Hauke F and Hirsch A 2009 Soluble graphene: generation of aqueous graphene solutions aided by a perylenebisimide-based bolaamphiphile *Adv. Mater.* **21** 4265–9
[216] Melucci M *et al* 2012 Graphene-organic hybrids as processable, tunable platforms for pH-dependent photoemission, obtained by a new modular approach *J. Mater. Chem.* **22** 18237–43
[217] Melucci M, Treossi E, Ortolani L, Giambastiani G, Morandi V, Klar P, Casiraghi C, Samorì P and Palermo V 2010 Facile covalent functionalization of graphene oxide using microwaves: bottom-up development of functional graphitic materials *J. Mater. Chem.* **20** 9052
[218] Schlierf A, Cha K, Schwab M G, Samori P and Palermo V 2014 Exfoliation of graphene with an industrial dye: teaching an old dog new tricks *2D Mater.* **1** 035006
[219] Yang H, Withers F, Gebremedhn E, Lewis E, Britnell L, Felten A, Palermo V, Haigh S, Beljonne D and Casiraghi C 2014 Dielectric nanosheets made by liquid-phase exfoliation in water and their use in graphene-based electronics *2D Mater.* **1** 011012
[220] Bianco A 2013 Graphene: safe or toxic? the two faces of the medal *Angew. Chem, Int. Ed. Eng.* **52** 4986–97
[221] Feng X L, Marcon V, Pisula W, Hansen M R, Kirkpatrick J, Grozema F, Andrienko D, Kremer K and Müllen K 2009 Towards high charge-carrier mobilities by rational design of the shape and periphery of discotics *Nat. Mater.* **8** 421–6

[222] Li C, Liu M Y, Pschirer N G, Baumgarten M and Müllen K 2010 Polyphenylene-based materials for organic photovoltaics *Chem. Rev.* **110** 6817–55
[223] Fujigaya T and Nakashima N 2008 Methodology for homogeneous dispersion of single-walled carbon nanotubes by physical modification *Polym. J.* **40** 577–89
[224] Dong X, Shi Y, Zhao Y, Chen D, Ye J, Yao Y, Gao F, Ni Z, Yu T and Shen Z 2009 Symmetry breaking of graphene monolayers by molecular decoration *Phys. Rev. Lett.* **102** 135501
[225] Jang J-H, Rangappa D, Kwon Y-U and Honma I 2010 Direct preparation of 1-PSA modified graphene nanosheets by supercritical fluidic exfoliation and its electrochemical properties *J. Mater. Chem.* **21** 3462–6
[226] Parviz D, Das S, Ahmed H S T, Irin F, Bhattacharia S and Green M J 2012 Dispersions of non-covalently functionalized graphene with minimal stabilizer *ACS Nano* **6** 8857–67
[227] Zhang L, Zhang Z J, He C Z, Dai L M, Liu J and Wang L X 2014 Rationally designed surfactants for few-layered graphene exfoliation: ionic groups attached to electron-deficient pi-conjugated unit through alkyl spacers *ACS Nano* **8** 6663–70
[228] Sampath S, Basuray A N, Hartlieb K J, Aytun T, Stupp S I and Stoddart J F 2013 Direct exfoliation of graphite to graphene in aqueous media with diazaperopyrenium dications *Adv. Mater.* **25** 2740–5
[229] Chua L L, Zaumseil J, Chang J F, Ou E C W, Ho P K H, Sirringhaus H and Friend R H 2005 General observation of n-type field-effect behaviour in organic semiconductors *Nature* **434** 194–9
[230] Ciesielski A *et al* 2014 Liquid-phase exfoliation of graphene using intercalating compounds: a supramolecular approach *Angew. Chem, Int. Ed. Eng.* **53** 10355–61
[231] Haar S *et al* 2015 A supramolecular strategy to leverage the liquid-phase exfoliation of graphene in the presence of surfactants: unraveling the role of the length of fatty acids *Small* **11** 1691–702
[232] Haar S, El Gemayel M, Shin Y Y, Melinte G, Squillaci M A, Ersen O, Casiraghi C, Ciesielski A and Samori P 2015 Enhancing the liquid-phase exfoliation of graphene in organic solvents upon addition of n-octylbenzene *Sci. Rep.* **5** 16684
[233] Conti S *et al* 2016 Perchlorination of coronene enhances its propensity for self-assembly on graphene *ChemPhysChem* **17** 352–7
[234] Döbbelin M *et al* 2016 Light-enhanced liquid-phase exfoliation and current photoswitching in graphene-azobenzene composites *Nat. Commun.* **7** 11090
[235] Haar S *et al* 2016 Liquid-phase exfoliation of graphite into single- and few-layer graphene with alpha-functionalized alkanes *J. Phys. Chem. Lett.* **7** 2714–21
[236] Backes C, Paton K R, Hanlon D, Yuan S, Katsnelson M I, Houston J, Smith R J, McCloskey D, Donegan J F and Coleman J N 2016 Spectroscopic metrics allow *in situ* measurement of mean size and thickness of liquid-exfoliated few-layer graphene nanosheets *Nanoscale* **8** 4311–23
[237] Duncan B and Perry C 1977 Uncancelled hypnotic suggestions: initial studies *Am. J. Clin. Hypn.* **19** 166–76
[238] Varrla E, Backes C, Paton K R, Harvey A, Gholamvand Z, McCauley J and Coleman J N 2015 Large-scale production of size-controlled MoS_2 nanosheets by shear exfoliation *Chem. Mater.* **27** 1129–39
[239] Hanlon D *et al* 2014 Production of molybdenum trioxide nanosheets by liquid exfoliation and their application in high-performance supercapacitors *Chem. Mater.* **26** 1751–63
[240] Harvey A *et al* 2016 Production of $Ni(OH)_2$ nanosheets by liquid phase exfoliation: from optical properties to electrochemical applications *J. Mater. Chem.* C **4** 11046–59
[241] Khan U, O'Neill A, Lotya M, De S and Coleman J N 2010 High-concentration solvent exfoliation of graphene *Small* **6** 864–71
[242] Lotya M, King P J, Khan U, De S and Coleman J N 2010 High-concentration, surfactant-stabilized graphene dispersions *ACS Nano* **4** 3155–62
[243] Ashokkumar M 2016 *Handbook of Ultrasonics and Sonochemistry* (Singapore: Springer)
[244] O'Neill A, Khan U and Coleman J N 2012 Preparation of high concentration dispersions of exfoliated MoS_2 with increased flake size *Chem. Mater.* **24** 2414–21
[245] Backes C, Hanlon D, Szydlowska B M, Harvey A, Smith R J, Higgins T M and Coleman J N 2016 Preparation of liquid-exfoliated transition metal dichalcogenide nanosheets with controlled size and thickness: a state of the art protocol *J. Vis. Exp.* **118** e54806 (https://doi.org/10.3791/54806)
[246] Ueberricke L, Coleman J N and Backes C 2017 Robustness of size selection and spectroscopic size, thickness and monolayer metrics of liquid-exfoliated WS_2 *Phys. Status Solidi* b **254** 1700443
[247] Panagiotou T, Mesite S, Bernard J, Chomistek K and Fisher R 2008 Production of polymer nanosuspensions using microfluidizerTM processor based processes *NSTI Nanotechnol.* **1** 688–91 (www.nsti.org/)
[248] Goldberg S 2008 Mechanical/physical methods of cell disruption and tissue homogenization *2D PAGE: Sample Preparation and Fractionation* pp 3–22
[249] M.I. Corporation (www.microfluidicscorp.com)
[250] Lajunen T, Hisazumi K, Kanazawa T, Okada H, Seta Y, Yliperttula M, Urtti A and Takashima Y 2014 Topical drug delivery to retinal pigment epithelium with microfluidizer produced small liposomes *Eur. J. Pharm. Sci.* **62** 23–32
[251] Tang S Y, Shridharan P and Sivakumar M 2013 Impact of process parameters in the generation of novel aspirin nanoemulsions—comparative studies between ultrasound cavitation and microfluidizer *Ultrason. Sonochem.* **20** 485–97
[252] Jafari S M, He Y and Bhandari B 2007 Production of sub-micron emulsions by ultrasound and microfluidization techniques *J. Food Eng.* **82** 478–88
[253] Panagiotou T, Bernard J M and Mesite S V 2008 Deagglomeration and dispersion of carbon nanotubes using microfluidizer high shear fluid processors *Conf. and Expo Proc. Nano Science and Technology Institute* pp 1–5
[254] dos Reis Benatto G A, Roth B, Madsen M V, Hösel M, Søndergaard R R, Jørgensen M and Krebs F C 2014 Carbon: the ultimate electrode choice for widely distributed polymer solar cells *Adv. Energy Mater.* **4** 1400732
[255] Lucera L, Kubis P, Fecher F W, Bronnbauer C, Turbiez M, Forberich K, Ameri T, Egelhaaf H-J and Brabec C J 2015 Guidelines for closing the efficiency gap between hero solar cells and roll-to-roll printed modules *Energy Technol.* **3** 373–84
[256] Nisato G, Lupo D and Ganz S 2016 *Organic and Printed Electronics: Fundamentals and Applications* (Pan Stanford)
[257] Huang X, Leng T, Zhang X, Chen J C, Chang K H, Geim A K, Novoselov K S and Hu Z 2015 Binder-free highly conductive graphene laminate for low cost printed radio frequency applications *Appl. Phys. Lett.* **106** 203105
[258] Welham N J, Berbenni V and Chapman P G 2003 Effect of extended ball milling on graphite *J. Alloys Compd.* **349** 255–63
[259] Servant A, Leon V, Jasim D, Methven L, Limousin P, Fernandez-Pacheco E V, Prato M and Kostarelos K 2014 Graphene-based electroresponsive scaffolds as polymeric implants for on-demand drug delivery *Adv. Healthcare Mater.* **3** 1334–43
[260] Gossner C M-E, Schlundt J, Ben Embarek P, Hird S, Lo-Fo-Wong D, Beltran J J O, Teoh K N and Tritscher A 2009 The melamine incident: implications for international food and feed safety *Environ. Health Perspect.* **117** 1803–8
[261] Rodríguez A M, Muñoz-García A B, Crescenzi O, Vázquez E and Pavone M 2016 Stability of melamine-exfoliated graphene in aqueous media: quantum-mechanical insights at the nanoscale *Phys. Chem. Chem. Phys.* **18** 22203–9
[262] Mottier A *et al* 2016 Surface area of carbon nanoparticles: a dose metric for a more realistic ecotoxicological assessment *Nano Lett.* **16** 3514–8
[263] Bramini M, Sacchetti S, Armirotti A, Rocchi A, Vázquez E, León Castellanos V, Bandiera T, Cesca F and Benfenati F 2016 Graphene oxide nanosheets disrupt lipid composition, Ca^{2+} homeostasis, and synaptic transmission in primary cortical neurons *ACS Nano* **10** 7154–71

[264] Rauti R et al 2016 Graphene oxide nanosheets reshape synaptic function in cultured brain networks *ACS Nano* **10** 4459–71
[265] Frišcic T 2010 New opportunities for materials synthesis using mechanochemistry *J. Mater. Chem.* **20** 7599
[266] Abdelkader A M and Kinloch I A 2016 Mechanochemical exfoliation of 2D crystals in deep eutectic solvents *ACS Sustain. Chem. Eng.* **4** 4465–72
[267] Abbott A P, Boothby D, Capper G, Davies D L and Rasheed R K 2004 Deep eutectic solvents formed between choline chloride and carboxylic acids: versatile alternatives to ionic liquids *J. Am. Chem. Soc.* **126** 9142–7
[268] Zhang Q, De Oliveira Vigier K, Royer S and Jérôme F 2016 Deep eutectic solvents: syntheses, properties and applications *Chem. Soc. Rev.* **41** 7108
[269] Shahbaz K, Mjalli F S, Vakili-Nezhaad G, Alnashef I M, Asadov A and Farid M M 2016 Thermogravimetric measurement of deep eutectic solvents vapor pressure *J. Mol. Liq.* **222** 61–6
[270] Ruß C and König B 2012 Low melting mixtures in organic synthesis – an alternative to ionic liquids? *Green Chem.* **14** 2969
[271] 2010 Contents *Chem. Soc. Rev.* **39** 3339
[272] Treossi E, Melucci M, Liscio A, Gazzano M, Samorì P and Palermo V 2009 High-contrast visualization of graphene oxide on dye-sensitized glass, quartz, and silicon by fluorescence quenching *J. Am. Chem. Soc.* **131** 15576–7
[273] Boehm H P, Clauss A, Fischer G O and Hofmann U 1962 Dünnste kohlenstoff-folien *Z. Nat.forsch.* **17B** 150–3
[274] Boehm H P, Clauss A, Fischer G and Hofmann U 1962 Surface properties of extremely thin graphite lamellae *Proc. of the Fifth Conf. on Carbon* (Elsevier) pp 73–80
[275] Boehm H-P and Stumpp E 2007 Citation errors concerning the first report on exfoliated graphite *Carbon* **45** 1381–3
[276] Dreyer D R, Park S, Bielawski C W and Ruoff R S 2010 The chemistry of graphene oxide *Chem. Soc. Rev.* **39** 228–40
[277] Liscio A, Veronese G P, Treossi E, Suriano F, Rossella F, Bellani V, Rizzoli R, Samorì P and Palermo V 2011 Charge transport in graphene–polythiophene blends as studied by kelvin probe force microscopy and transistor characterization *J. Mater. Chem.* **21** 2924
[278] Chen D, Feng H and Li J 2012 Graphene oxide: preparation, functionalization, and electrochemical applications *Chem. Rev.* **112** 6027–53
[279] Wang Y, Li Z, Wang J, Li J and Lin Y 2001 Graphene and graphene oxide: biofunctionalization and applications in biotechnology *Trends Biotechnol.* **29** 205–12
[280] Zlotea C, Oumellal Y, Hwang S-J, Ghimbeu C M, de Jongh P E and Latroche M 2015 Ultrasmall MgH_2 nanoparticles embedded in an ordered microporous carbon exhibiting rapid hydrogen sorption kinetics *J. Phys. Chem.* C **119** 18091–8
[281] Chung C, Kim Y-K, Shin D, Ryoo S-R, Hong B H and Min D-H 2013 Biomedical applications of graphene and graphene oxide *Acc. Chem. Res.* **46** 2211–24
[282] Georgakilas V, Tiwari J N, Kemp K C, Perman J A, Bourlinos A B, Kim K S and Zboril R 2016 Noncovalent functionalization of graphene and graphene oxide for energy materials, biosensing, catalytic, and biomedical applications *Chem. Rev.* **116** 5464–519
[283] Nanda S S, Papaefthymiou G C and Yi D K 2015 Functionalization of graphene oxide and its biomedical applications *Crit. Rev. Solid State Mater. Sci.* **40** 291–315
[284] Lee J, Kim J, Kim S and Min D-H 2016 Biosensors based on graphene oxide and its biomedical application *Adv. Drug Delivery Rev.* **105** 275–87
[285] Liu Y, Dong X and Chen P 2012 Biological and chemical sensors based on graphene materials *Chem. Soc. Rev.* **41** 2283–307
[286] Kucki M et al 2016 Interaction of graphene-related materials with human intestinal cells: an *in vitro* approach *Nanoscale* **8** 8749–60
[287] Kurapati R, Russier J, Squillaci M A, Treossi E, Ménard-Moyon C, Del Rio-Castillo A E, Vazquez E, Samorì P, Palermo V and Bianco A 2015 Dispersibility-dependent biodegradation of graphene oxide by myeloperoxidase *Small* **11** 3985–94
[288] Russier J, Treossi E, Scarsi A, Perrozzi F, Dumortier H, Ottaviano L, Meneghetti M, Palermo V and Bianco A 2013 Evidencing the mask effect of graphene oxide: a comparative study on primary human and murine phagocytic cells *Nanoscale* **5** 11234–47
[289] An S S, Wu S-Y and Hulme J 2015 Current applications of graphene oxide in nanomedicine *Int. J. Nanomed.* **10** 9–24
[290] Eftekhari A, Shulga Y M, Baskakov S A and Gutsev G L 2018 Graphene oxide membranes for electrochemical energy storage and conversion *Int. J. Hydrog. Energy* **43** 2307–26
[291] Li F, Jiang X, Zhao J and Zhang S 2015 Graphene oxide: a promising nanomaterial for energy and environmental applications *Nano Energy* **16** 488–515
[292] Wei Y, Zhang Y, Gao X, Ma Z, Wang X and Gao C 2018 Multilayered graphene oxide membranes for water treatment: a review *Carbon* **139** 964–81
[293] Joshi R K, Alwarappan S, Yoshimura M, Sahajwalla V and Nishina Y 2015 Graphene oxide: the new membrane material *Appl. Mater. Today* **1** 1–12
[294] Shao J-J, Lv W and Yang Q-H 2014 Self-assembly of graphene oxide at interfaces *Adv. Mater.* **26** 5586–612
[295] Padmajan Sasikala S, Lim J, Kim I H, Jung H J, Yun T, Han T H and Kim S O 2018 Graphene oxide liquid crystals: a frontier 2D soft material for graphene-based functional materials *Chem. Soc. Rev.* **47** 6013–45
[296] Brodie B C 1859 On the atomic weight of graphite *Phil. Trans. R. Soc.* **149** 249
[297] Staudenmaier L 2016 Verfahren zur darstellung der graphitsaure *Ber. Deut. Chem. Ges.* **31** 1481
[298] Marcano D C, Kosynkin D V, Berlin J M, Sinitskii A, Sun Z Z, Slesarev A, Alemany L B, Lu W and Tour J M 2010 Improved synthesis of graphene oxide *ACS Nano* **4** 4806–14
[299] Kim S, Zhou S, Hu Y, Acik M, Chabal Y J, Berger C, de Heer W, Bongiorno A and Riedo E 2012 Room-temperature metastability of multilayer graphene oxide films *Nat. Mater.* **11** 544–9
[300] Wei Z et al 2010 Nanoscale tunable reduction of graphene oxide for graphene electronics *Science* **328** 1373–6
[301] Wu X, Sprinkle M, Li X, Ming F, Berger C and de Heer W A 2008 Epitaxial-graphene/graphene-oxide junction: an essential step towards epitaxial graphene electronics *Phys. Rev. Lett.* **101** 026801
[302] Sanchez V C, Jachak A, Hurt R H and Kane A B 2012 Biological interactions of graphene-family nanomaterials: an interdisciplinary review *Chem. Res. Toxicol.* **25** 15–34
[303] De Marzi L, Ottaviano L, Perrozzi F, Nardone M, Santucci S, De Lapuente J, Borras M, Treossi E, Palermo V and Poma A 2014 Flake size-dependent cyto and genotoxic evaluation of graphene oxide on *in vitro* A549, Caco2 and vero cell lines *J. Biol. Regul. Homeost. Agents* **28** 281–9
[304] Ardini M et al 2016 Supramolecular self-assembly of graphene oxide and metal nanoparticles into stacked multilayers by means of a multitasking protein ring *Nanoscale* **8** 6739–53
[305] Panzavolta S et al 2014 Structural reinforcement and failure analysis in composite nanofibers of graphene oxide and gelatin *Carbon* **78** 566–77
[306] Pei S, Wei Q, Huang K, Cheng H-M and Ren W 2018 Green synthesis of graphene oxide by seconds timescale water electrolytic oxidation *Nat. Commun.* **9** 145
[307] Morimoto N, Kubo T and Nishina Y 2016 Tailoring the oxygen content of graphite and reduced graphene oxide for specific applications *Sci. Rep.* **6** 21715
[308] Tang L-C, Wan Y-J, Yan D, Pei Y-B, Zhao L, Li Y-B, Wu L-B, Jiang J-X and Lai G-Q 2013 The effect of graphene dispersion on the mechanical properties of graphene/epoxy composites *Carbon* **60** 16–27
[309] Wu G and Gao W 2015 *GO/rGO as Advanced Materials for Energy Storage and Conversion, Graphene Oxide* (Berlin: Springer) pp 97–127

[310] Chee S Y, Poh H L, Chua C K, Šaněk F, Sofer Z and Pumera M 2012 Influence of parent graphite particle size on the electrochemistry of thermally reduced graphene oxide *Phys. Chem. Chem. Phys.* **14** 12794
[311] Gómez J, Villaro E, Navas A and Recio I 2017 Testing the influence of the temperature, RH and filler type and content on the universal power law for new reduced graphene oxide TPU composites *Mater. Res. Express* **4** 105020
[312] Singh G, Divakar Botcha V, Sutar D S, Talwar S S, Srinivasa R S and Major S S 2015 Graphite mediated reduction of graphene oxide monolayer sheets *Carbon* **95** 843–51
[313] Zhang H, Liu Y, Huo S, Briscoe J, Tu W, Picot O T, Rezai A, Bilotti E and Peijs T 2017 Filtration effects of graphene nanoplatelets in resin infusion processes: problems and possible solutions *Compos. Sci. Technol.* **139** 138–45
[314] Ambrosetti G, Grimaldi C, Balberg I, Maeder T, Danani A and Ryser P 2010 Solution of the tunneling-percolation problem in the nanocomposite regime *Phys. Rev.* B **81** 155434
[315] Aleksandrzak M, Adamski P, Kukułka W, Zielinska B and Mijowska E 2015 Effect of graphene thickness on photocatalytic activity of TiO_2-graphene nanocomposites *Appl. Surf. Sci.* **331** 193–9
[316] Su C and Loh K P 2013 Carbocatalysts: graphene oxide and its derivatives *Acc. Chem. Res.* **46** 2275–85
[317] Casco M E *et al* 2014 CO_2 adsorption on crystalline graphitic nanostructures *J. CO_2 Util.* **5** 60–5
[318] Huang X, Qi X, Boey F and Zhang H 2012 Graphene-based composites *Chem. Soc. Rev.* **41** 666–86
[319] Jeon I-Y *et al* 2013 Facile, scalable synthesis of edge-halogenated graphene nanoplatelets as efficient metal-free eletrocatalysts for oxygen reduction reaction *Sci. Rep.* **3** 1810
[320] Jabari Seresht R, Jahanshahi M, Rashidi A and Ghoreyshi A A 2013 Synthesize and characterization of graphene nanosheets with high surface area and nano-porous structure *Appl. Surf. Sci.* **276** 672–81
[321] Blanco-Villalba I R J F, Gómez J and Hübner C 2017 Improving the processability of graphene nanoplatelets in polyamide 6 during melt compounding extrusion *PPS2017 (Dresden, Germany)*
[322] Park S, An J, Potts J R, Velamakanni A, Murali S and Ruoff R S 2011 Hydrazine-reduction of graphite- and graphene oxide *Carbon* **49** 3019–23
[323] Bo Z, Shuai X, Mao S, Yang H, Qian J, Chen J, Yan J and Cen K 2014 Green preparation of reduced graphene oxide for sensing and energy storage applications *Sci. Rep.* **4** 4684
[324] Dreyer D R, Murali S, Zhu Y, Ruoff R S and Bielawski C W 2011 Reduction of graphite oxide using alcohols *J. Mater. Chem.* **21** 3443–7
[325] Agharkar M, Kochrekar S, Hidouri S and Azeez M A 2014 Trends in green reduction of graphene oxides, issues and challenges: a review *Mater. Res. Bull.* **59** 323–8
[326] Sarkar S and Basak D 2013 The reduction of graphene oxide by zinc powder to produce a zinc oxide-reduced graphene oxide hybrid and its superior photocatalytic activity *Chem. Phys. Lett.* **561–2** 125–30
[327] Chua C K and Pumera M 2014 Chemical reduction of graphene oxide: a synthetic chemistry viewpoint *Chem. Soc. Rev.* **43** 291–312
[328] Pei S, Zhao J, Du J, Ren W and Cheng H-M 2010 Direct reduction of graphene oxide films into highly conductive and flexible graphene films by hydrohalic acids *Carbon* **48** 4466–74
[329] Zhao J, Pei S, Ren W, Gao L and Cheng H-M 2010 Efficient preparation of large-area graphene oxide sheets for transparent conductive films *ACS Nano* **4** 5245–52
[330] Storm M M, Johnsen R E and Norby P 2016 *In situ* x-ray powder diffraction studies of the synthesis of graphene oxide and formation of reduced graphene oxide *J. Solid State Chem.* **240** 49–54
[331] Hu K, Xie X, Szkopek T and Cerruti M 2016 Understanding hydrothermally reduced graphene oxide hydrogels: from reaction products to hydrogel properties *Chem. Mater.* **28** 1756–68
[332] Zhou Y, Bao Q, Tang L A L, Zhong Y and Loh K P 2009 Hydrothermal dehydration for the 'green' reduction of exfoliated graphene oxide to graphene and demonstration of tunable optical limiting properties *Chem. Mater.* **21** 2950–6
[333] Bagri A, Mattevi C, Acik M, Chabal Y J, Chhowalla M and Shenoy V B 2010 Structural evolution during the reduction of chemically derived graphene oxide *Nat. Chem.* **2** 581–7
[334] Tortello M *et al* 2016 Effect of thermal annealing on the heat transfer properties of reduced graphite oxide flakes: a nanoscale characterization via scanning thermal microscopy *Carbon* **109** 390–401
[335] Cheng M, Yang R, Zhang L, Shi Z, Yang W, Wang D, Xie G, Shi D and Zhang G 2012 Restoration of graphene from graphene oxide by defect repair *Carbon* **50** 2581–7
[336] López V, Sundaram R S, Gómez-Navarro C, Olea D, Burghard M, Gómez-Herrero J, Zamora F and Kern K 2009 Graphene monolayers: chemical vapor deposition repair of graphene oxide: a route to highly-conductive graphene monolayers (*Adv. Mater.* 46/2009) *Adv. Mater.* **21** 4683–6
[337] Acik M, Lee G, Mattevi C, Pirkle A, Wallace R M, Chhowalla M, Cho K and Chabal Y 2011 The role of oxygen during thermal reduction of graphene oxide studied by infrared absorption spectroscopy *J. Phys. Chem.* C **115** 19761–81
[338] Su C-Y, Xu Y, Zhang W, Zhao J, Liu A, Tang X, Tsai C-H, Huang Y and Li L-J 2010 Highly efficient restoration of graphitic structure in graphene oxide using alcohol vapors *ACS Nano* **4** 5285–92
[339] Wang Z-L, Xu D, Huang Y, Wu Z, Wang L-M and Zhang X-B 2012 Facile, mild and fast thermal-decomposition reduction of graphene oxide in air and its application in high-performance lithium batteries *Chem. Commun.* **48** 976–8
[340] Chabot V, Higgins D, Yu A, Xiao X, Chen Z and Zhang J 2014 A review of graphene and graphene oxide sponge: material synthesis and applications to energy and the environment *Energy Environ. Sci.* **7** 1564
[341] Wang M, Duan X, Xu Y and Duan X 2016 Functional three-dimensional graphene/polymer composites *ACS Nano* **10** 7231–47
[342] Sun H, Xu Z and Gao C 2013 Multifunctional, ultra-flyweight, synergistically assembled carbon aerogels *Adv. Mater.* **25** 2554–60
[343] Xu Y, Sheng K, Li C and Shi G 2010 Self-assembled graphene hydrogel via a one-step hydrothermal process *ACS Nano* **4** 4324–30
[344] Zhao J, Ren W and Cheng H-M 2012 Graphene sponge for efficient and repeatable adsorption and desorption of water contaminations *J. Mater. Chem.* **22** 20197
[345] Cong H-P, Ren X-C, Wang P and Yu S-H 2012 Macroscopic multifunctional graphene-based hydrogels and aerogels by a metal ion induced self-assembly process *ACS Nano* **6** 2693–703
[346] Qiu L, Liu J Z, Chang S L Y, Wu Y and Li D 2012 Biomimetic superelastic graphene-based cellular monoliths *Nat. Commun.* **3** 1241
[347] Xia Z, Wei D, Anitowska E, Bellani V, Ortolani L, Morandi V, Gazzano M, Zanelli A, Borini S and Palermo V 2015 Electrochemically exfoliated graphene oxide/iron oxide composite foams for lithium storage, produced by simultaneous graphene reduction and $Fe(OH)_3$ condensation *Carbon* **84** 254–62
[348] Xia Z Y *et al* 2014 Synergic exfoliation of graphene with organic molecules and inorganic ions for the electrochemical production of flexible electrodes *ChemPlusChem* **79** 439–46
[349] Vickery J L, Patil A J and Mann S 2009 Fabrication of graphene-polymer nanocomposites with higher-order three-dimensional architectures *Adv. Mater.* **21** 2180–4
[350] Nardecchia S, Carriazo D, Ferrer M L, Gutiérrez M C and del Monte F 2013 Three dimensional macroporous architectures and aerogels built of carbon nanotubes and/or graphene: synthesis and applications *Chem. Soc. Rev.* **42** 794–830
[351] Mao J, Iocozzia J, Huang J, Meng K, Lai Y and Lin Z 2018 Graphene aerogels for efficient energy storage and conversion *Energy Environ. Sci.* **11** 772–99

[352] Botas C, Carriazo D, Singh G and Rojo T 2015 Sn–and SnO_2–graphene flexible foams suitable as binder-free anodes for lithium ion batteries *J. Mater. Chem.* A **3** 13402–10
[353] Quesnel E *et al* 2015 Graphene-based technologies for energy applications, challenges and perspectives *2D Mater.* **2** 030204
[354] Gutiérrez M C, Ferrer M L and del Monte F 2008 Ice-templated materials: sophisticated structures exhibiting enhanced functionalities obtained after unidirectional freezing and ice-segregation-induced self-assembly *Chem. Mater.* **20** 634–8
[355] Botas C, Carriazo D, Zhang W, Rojo T and Singh G 2016 Silicon-reduced graphene oxide self-standing composites suitable as binder-free anodes for lithium-ion batteries *ACS Appl. Mater. Interfaces* **8** 28800–8
[356] Lee J K, Smith K B, Hayner C M and Kung H H 2010 Silicon nanoparticles-graphene paper composites for Li ion battery anodes *Chem. Commun.* **46** 2025
[357] Zhou X, Yin Y-X, Wan L-J and Guo Y-G 2012 Facile synthesis of silicon nanoparticles inserted into graphene sheets as improved anode materials for lithium-ion batteries *Chem. Commun.* **48** 2198
[358] Botas C, Álvarez P, Blanco C, Santamaría R, Granda M, Gutiérrez M D, Rodríguez-Reinoso F and Menéndez R 2013 Critical temperatures in the synthesis of graphene-like materials by thermal exfoliation–reduction of graphite oxide *Carbon* **52** 476–85
[359] Li G, Sun J, Hou W, Jiang S, Huang Y and Geng J 2016 Three-dimensional porous carbon composites containing high sulfur nanoparticle content for high-performance lithium–sulfur batteries *Nat. Commun.* **7** 10601
[360] Ajuria J, Arnaiz M, Botas C, Carriazo D, Mysyk R, Rojo T, Talyzin A V and Goikolea E 2017 Graphene-based lithium ion capacitor with high gravimetric energy and power densities *J. Power Sources* **363** 422–7
[361] Nair R R, Wu H A, Jayaram P N, Grigorieva I V and Geim A K 2012 Unimpeded permeation of water through helium-leak-tight graphene-based membranes *Science* **335** 442–4
[362] Boretti A, Al-Zubaidy S, Vaclavikova M, Al-Abri M, Castelletto S and Mikhalovsky S 2018 Outlook for graphene-based desalination membranes *npj Clean Water* **1** 5
[363] Liu G, Jin W and Xu N 2015 Graphene-based membranes *Chem. Soc. Rev.* **44** 5016–30
[364] Sun P, Wang K and Zhu H 2016 Recent developments in graphene-based membranes: structure, mass-transport mechanism and potential applications *Adv. Mater.* **28** 2287–310
[365] An D, Yang L, Wang T-J and Liu B 2016 Separation performance of graphene oxide membrane in aqueous solution *Ind. Eng. Chem. Res.* **55** 4803–10
[366] Morelos-Gomez A *et al* 2017 Effective NaCl and dye rejection of hybrid graphene oxide/graphene layered membranes *Nat. Nanotechnol.* **12** 1083
[367] Kim H W *et al* 2013 Selective gas transport through few-layered graphene and graphene oxide membranes *Science* **342** 91–5
[368] Englert J M, Knirsch K C, Dotzer C, Butz B, Hauke F, Spiecker E and Hirsch A 2012 Functionalization of graphene by electrophilic alkylation of reduced graphite *Chem. Commun.* **48** 5025
[369] Schäfer R A, Englert J M, Wehrfritz P, Bauer W, Hauke F, Seyller T and Hirsch A 2013 On the way to graphane—pronounced fluorescence of polyhydrogenated graphene *Angew. Chem, Int. Ed. Engl.* **52** 754–7
[370] Vecera P, Edelthalhammer K, Hauke F and Hirsch A 2014 Reductive arylation of graphene: Insights into a reversible carbon allotrope functionalization reaction *Phys. Status Solidi* b **251** 2536–40
[371] Abellán G, Schirowski M, Edelthalhammer K, Fickert M, Hauke F and Hirsch A 2017 Unifying aspects of the reductive covalnet graphene functionalization *J. Am. Chem. Soc.* **139** 5175 – 82
[372] Catheline A, Ortolani L, Morandi V, Melle-Franco M, Drummond C, Zakri C and Penicaud A 2012 Solutions of fully exfoliated individual graphene flakes in low boiling point solvents *Soft Matter* **8** 7882–7
[373] Pénicaud A and Drummond C 2012 Deconstructing graphite: graphenide solutions *Acc. Chem. Res.* **46** 129–37
[374] Kelly K F and Billups W E 2013 Synthesis of soluble graphite and graphene *Acc. Chem. Res.* **46** 4–13
[375] Vecera P, Holzwarth J, Edelthalhammer K F, Mundloch U, Peterlik H, Hauke F and Hirsch A 2016 Solvent-driven electron trapping and mass transport in reduced graphites to access perfect graphene *Nat. Commun.* **7** 12411
[376] Hodge S A, Tay H H, Anthony D B, Menzel R, Buckley D J, Cullen P L, Skipper N T, Howard C A and Shaffer M S P 2014 Probing the charging mechanisms of carbon nanomaterial polyelectrolytes *Faraday Discuss.* **172** 311–25
[377] Bepete G, Anglaret E, Ortolani L, Morandi V, Huang K, Pénicaud A and Drummond C 2016 Surfactant-free single-layer graphene in water *Nat. Chem.* **9** 347
[378] Eda G, Yamaguchi H, Voiry D, Fujita T, Chen M and Chhowalla M 2011 Photoluminescence from chemically exfoliated MoS_2 *Nano Lett.* **11** 5111–6
[379] Knirsch K C *et al* 2015 Basal-plane functionalization of chemically exfoliated molybdenum disulfide by diazonium salts *ACS Nano* **9** 6018–30
[380] Voiry D, Goswami A, Kappera R, SilvaCecilia de Carvalho Castro E, Kaplan D, Fujita T, Chen M, Asefa T andChhowalla M 2015 Covalent functionalization of monolayered transition metal dichalcogenides by phase engineering *Nat. Chem.* **7** 45–9
[381] Pagona G, Bittencourt C, Arenal R and Tagmatarchis N 2015 Exfoliated semiconducting pure 2H-MoS_2 and 2H-WS_2 assisted by chlorosulfonic acid *Chem. Commun.* **51** 12950–3
[382] Yang S, Lohe M R, Müllen K and Feng X 2016 New-generation graphene from electrochemical approaches: production and applications *Adv. Mater.* **28** 6213–21
[383] Maccaferri G, Zanardi C, Xia Z, Kovtun A, Liscio A, Terzi F, Palermo V and Seeber R 2017 Systematic study of the correlation between surface chemistry, conductivity and electrocatalytic properties of graphene oxide nanosheets *Carbon* **120** 165–75
[384] Su C-Y, Lu A-Y, Xu Y, Chen F-R, Khlobystov A N and Li L-J 2011 High-quality thin graphene films from fast electrochemical exfoliation *ACS Nano* **5** 2332–9
[385] Parvez K, Li R, Punirredd S R, Hernandez Y, Hinkel F, Wang S, Feng X and Müllen K 2013 Electrochemically exfoliated graphene as solution-processable, highly conductive electrodes for organic electronics *ACS Nano* **7** 3598–606
[386] Rao K S, Sentilnathan J, Cho H-W, Wu J-J and Yoshimura M 2014 Soft processing of graphene nanosheets by glycine-bisulfate ionic-complex-assisted electrochemical exfoliation of graphite for reduction catalysis *Adv. Funct. Mater.* **25** 298–305
[387] Parvez K, Wu Z-S, Li R, Liu X, Graf R, Feng X and Müllen K 2014 Exfoliation of graphite into graphene in aqueous solutions of inorganic salts *J. Am. Chem. Soc.* **136** 6083–91
[388] Yang S, Brüller S, Wu Z-S, Liu Z, Parvez K, Dong R, Richard F, Samorì P, Feng X and Müllen K 2015 Organic radical-assisted electrochemical exfoliation for the scalable production of high-quality graphene *J. Am. Chem. Soc.* **137** 13927–32
[389] Wang J, Manga K K, Bao Q and Loh K P 2011 High-yield synthesis of few-layer graphene flakes through electrochemical expansion of graphite in propylene carbonate electrolyte *J. Am. Chem. Soc.* **133** 8888–91
[390] Cabana J, Monconduit L, Larcher D and Palacín M R 2010 Beyond intercalation-based li-ion batteries: the state of the art and challenges of electrode materials reacting through conversion reactions *Adv. Mater.* **22** E170–92
[391] Ohzuku T 1993 Formation of lithium-graphite intercalation compounds in nonaqueous electrolytes and their application as a negative electrode for a lithium ion (shuttlecock) cell *J. Electrochem. Soc.* **140** 2490
[392] Tarascon J M and Armand M 2001 Issues and challenges facing rechargeable lithium batteries *Nature* **414** 359–67

[393] Weller T E, Ellerby M, Saxena S S, Smith R P and Skipper N T 2005 Superconductivity in the intercalated graphite compounds C_6Yb and C_6Ca *Nat. Phys.* **1** 39–41
[394] Zhong Y L and Swager T M 2012 Enhanced electrochemical expansion of graphite for *in situ* electrochemical functionalization *J. Am. Chem. Soc.* **134** 17896–9
[395] Abdelkader A M, Kinloch I A and Dryfe R A W 2014 Continuous electrochemical exfoliation of micrometer-sized graphene using synergistic ion intercalations and organic solvents *ACS Appl. Mater. Interfaces* **6** 1632–9
[396] Yu P 1999 Determination of the lithium ion diffusion coefficient in graphit *J. Electrochem. Soc.* **146** 8
[397] Abdelkader A M, Cooper A J, Dryfe R A W and Kinloch I A 2015 How to get between the sheets: a review of recent works on the electrochemical exfoliation of graphene materials from bulk graphite *Nanoscale* **7** 6944–56
[398] Abdelkader A M, Patten H V, Li Z, Chen Y and Kinloch I A 2015 Electrochemical exfoliation of graphite in quaternary ammonium-based deep eutectic solvents: a route for the mass production of graphane *Nanoscale* **7** 11386–92
[399] Kamali A R, Feighan J and Fray D J 2016 Towards large scale preparation of graphene in molten salts and its use in the fabrication of highly toughened alumina ceramics *Faraday Discuss.* **190** 451–70
[400] Kamali A R and Fray D J 2015 Large-scale preparation of graphene by high temperature insertion of hydrogen into graphite *Nanoscale* **7** 11310–20
[401] Kim H-K, Kamali A R, Roh K C, Kim K-B and Fray D J 2016 Dual coexisting interconnected graphene nanostructures for high performance supercapacitor applications *Energy Environ. Sci.* **9** 2249–56
[402] Kamali A R 2016 Eco-friendly production of high quality low cost graphene and its application in lithium ion batteries *Green Chem.* **18** 1952–64
[403] Zhuang H L and Hennig R G 2014 Computational discovery, characterization, and design of single-layer materials *J. Miner. Met. Mater. Soc.* **66** 366–74
[404] Gould T, Lebègue S, Björkman T and Dobson J F 2016 *2D Structures Beyond Graphene, Semiconductors and Semimetals* (New York: Elsevier) pp 1–33
[405] Lebègue S, Björkman T, Klintenberg M, Nieminen R M and Eriksson O 2013 Two-dimensional materials from data filtering and *ab initio* calculations *Phys. Rev.* X **3** 031002
[406] Ashton M, Paul J, Sinnott S B and Hennig R G 2017 Topology-scaling identification of layered solids and stable exfoliated 2D materials *Phys. Rev. Lett.* **118** 106101
[407] Mounet N *et al* 2018 Two-dimensional materials from high-throughput computational exfoliation of experimentally known compounds *Nat. Nanotechnol.* **13** 246–52
[408] Zhuang H L, Kent P R C and Hennig R G 2016 Strong anisotropy and magnetostriction in the two-dimensional Stoner ferromagnet Fe_3GeTe_2 *Phys. Rev.* B **93** 054429
[409] Zhang S, Yan Z, Li Y, Chen Z and Zeng H 2015 Atomically thin arsenene and antimonene: semimetal-semiconductor and indirect-direct band-gap transitions *Angew. Chem, Int. Ed. Engl.* **127** 3155–8
[410] Schusteritsch G, Uhrin M and Pickard C J 2016 Single-layered hittorf's phosphorus: a wide-bandgap high mobility 2D material *Nano Lett.* **16** 2975–80
[411] Cahangirov S, Topsakal M, Aktürk E, Şahin H and Ciraci S 2009 Two- and one-dimensional honeycomb structures of silicon and germanium *Phys. Rev. Lett.* **102** 236804
[412] Rasmussen F A and Thygesen K S 2015 Computational 2D materials database: electronic structure of transition-metal dichalcogenides and oxides *J. Phys. Chem.* C **119** 13169–83
[413] Ataca C, Şahin H and Ciraci S 2012 Stable, single-layer MX2 transition-metal oxides and dichalcogenides in a honeycomb-like structure *J. Phys. Chem.* C **116** 8983–99
[414] Miró P, Audiffred M and Heine T 2014 An atlas of two-dimensional materials *Chem. Soc. Rev.* **43** 6537–54
[415] Bahmann S and Kortus J 2013 EVO—evolutionary algorithm for crystal structure prediction *Comput. Phys. Commun.* **184** 1618–25
[416] Zhou X-F, Dong X, Oganov A R, Zhu Q, Tian Y and Wang H-T 2014 Semimetallic two-dimensional boron allotrope with massless dirac fermions *Phys. Rev. Lett.* **112** 085502
[417] Revard B C, Tipton W W, Yesypenko A and Hennig R G 2016 Grand-canonical evolutionary algorithm for the prediction of two-dimensional materials *Phys. Rev.* B **93** 054117
[418] Luo W, Ma Y, Gong X and Xiang H 2014 Prediction of silicon-based layered structures for optoelectronic applications *J. Am. Chem. Soc.* **136** 15992–7
[419] Luo X, Yang J, Liu H, Wu X, Wang Y, Ma Y, Wei S-H, Gong X and Xiang H 2011 Predicting two-dimensional boron–carbon compounds by the global optimization method *J. Am. Chem. Soc.* **133** 16285–90
[420] Yang J-H, Zhang Y, Yin W-J, Gong X G, Yakobson B I and Wei S-H 2016 Two-dimensional SiS layers with promising electronic and optoelectronic properties: theoretical prediction *Nano Lett.* **16** 1110–7
[421] Wu X, Dai J, Zhao Y, Zhuo Z, Yang J and Zeng X C 2012 Two-dimensional boron monolayer sheets *ACS Nano* **6** 7443–53
[422] Zhang Z, Mannix A J, Hu Z, Kiraly B, Guisinger N P, Hersam M C and Yakobson B I 2016 Substrate-induced nanoscale undulations of borophene on silver *Nano Lett.* **16** 6622–7
[423] Zhang Z, Penev E S and Yakobson B I 2016 Two-dimensional materials: polyphony in B flat *Nat. Chem.* **8** 525–7
[424] Hassoun J *et al* 2014 An advanced lithium-ion battery based on a graphene anode and a lithium iron phosphate cathode *Nano Lett.* **14** 4901–6
[425] Kang J, Wells S A, Wood J D, Lee J-H, Liu X, Ryder C R, Zhu J, Guest J R, Husko C A and Hersam M C 2016 Stable aqueous dispersions of optically and electronically active phosphorene *Proc. Natl Acad. Sci.* **113** 11688–93
[426] Bunch J S, Yaish Y, Brink M, Bolotin K and McEuen P L 2005 Coulomb oscillations and hall effect in quasi-2D graphite quantum dots *Nano Lett.* **5** 287–90
[427] Hasan T, Torrisi F, Sun Z, Popa D, Nicolosi V, Privitera G, Bonaccorso F and Ferrari A C 2010 Solution-phase exfoliation of graphite for ultrafast photonics *Phys. Status Solidi* b **247** 2953–7
[428] Liu L, Shen Z, Yi M, Zhang X and Ma S 2014 A green, rapid and size-controlled production of high-quality graphene sheets by hydrodynamic forces *RSC Adv.* **4** 36464
[429] Pattammattel A and Kumar C V 2015 Kitchen chemistry 101: multigram production of high quality biographene in a blender with edible proteins *Adv. Funct. Mater.* **25** 7088–98
[430] Yi M and Shen Z 2014 Kitchen blender for producing high-quality few-layer graphene *Carbon* **78** 622–6
[431] Damm C, Nacken T J and Peukert W 2015 Quantitative evaluation of delamination of graphite by wet media milling *Carbon* **81** 284–94
[432] Fabbro A *et al* 2016 Graphene-based interfaces do not alter target nerve cells *ACS Nano* **10** 615–23
[433] Ibrahem M A, Lan T-W, Huang J K, Chen Y-Y, Wei K-H, Li L-J and Chu C W 2013 High quantity and quality few-layers transition metal disulfide nanosheets from wet-milling exfoliation *RSC Adv.* **3** 13193
[434] Knieke C, Berger A, Voigt M, Taylor R N K, Röhrl J and Peukert W 2010 Scalable production of graphene sheets by mechanical delamination *Carbon* **48** 3196–204
[435] Yao Y, Lin Z, Li Z, Song X, Moon K-S and Wong C-P 2012 Large-scale production of two-dimensional nanosheets *J. Mater. Chem.* **22** 13494
[436] Zhao W, Fang M, Wu F, Wu H, Wang L and Chen G 2010 Preparation of graphene by exfoliation of graphite using wet ball milling *J. Mater. Chem.* **20** 5817
[437] Shen Z, Li J, Yi M, Zhang X and Ma S 2011 Preparation of graphene by jet cavitation *Nanotechnology* **22** 365306
[438] Yi M, Li J, Shen Z, Zhang X and Ma S 2011 Morphology and structure of mono- and few-layer graphene produced by jet cavitation *Appl. Phys. Lett.* **99** 123112
[439] Yi M, Shen Z, Zhang W, Zhu J, Liu L, Liang S, Zhang X and Ma S 2013 Hydrodynamics-assisted scalable production of boron nitride nanosheets and their application in improving

oxygen-atom erosion resistance of polymeric composites *Nanoscale* **5** 10660
[440] Del Rio Castillo A E *et al* 2018 High-yield production of 2D crystals by wet-jet milling *Mater. Horiz.* **5** 890–904
[441] Bonaccorso F, Zerbetto M, Ferrari A C and Amendola V 2013 Sorting nanoparticles by centrifugal fields in clean media *J. Phys. Chem.* C **117** 13217–29
[442] O'Connell M J *et al* 2002 Band gap fluorescence from individual single-walled carbon nanotubes *Science* **297** 593–6
[443] Hasan T, Tan P H, Bonaccorso F, Rozhin A G, Scardaci V, Milne W I and Ferrari A C 2008 Polymer-assisted isolation of single wall carbon nanotubes in organic solvents for optical-quality nanotube-polymer composites *J. Phys. Chem.* C **112** 20227–32
[444] Maragò O M *et al* 2008 Optical trapping of carbon nanotubes *Physica* E **40** 2347–51
[445] Tan P H, Hasan T, Bonaccorso F, Scardaci V, Rozhin A G, Milne W I and Ferrari A C 2008 Optical properties of nanotube bundles by photoluminescence excitation and absorption spectroscopy *Physica* E **40** 2352–9
[446] Maragó O M *et al* 2010 Brownian motion of graphene *ACS Nano* **4** 7515–23
[447] Torrisi F *et al* 2012 Inkjet-printed graphene electronics *ACS Nano* **6** 2992–3006
[448] Capasso A, Matteocci F, Najafi L, Prato M, Buha J, Cinà L, Pellegrini V, Carlo A D and Bonaccorso F 2016 Few-layer MoS_2 flakes as active buffer layer for stable perovskite solar cells *Adv. Energy Mater.* **6** 1600920
[449] Li D, Del Rio Castillo A E, Jussila H, Ye G, Ren Z, Bai J, Chen X, Lipsanen H, Sun Z and Bonaccorso F 2016 Black phosphorus polycarbonate polymer composite for pulsed fibre lasers *Appl. Mater. Today* **4** 17–23
[450] Morozov S V, Novoselov K S, Katsnelson M I, Schedin F, Ponomarenko L A, Jiang D and Geim A K 2006 Strong suppression of weak localization in graphene *Phys. Rev. Lett.* **97** 016801
[451] Khattab I S, Bandarkar F, Fakhree M A A and Jouyban A 2012 Density, viscosity, and surface tension of water + ethanol mixtures from 293 to 323 K *Korean J. Chem. Eng.* **29** 812–7
[452] Gholamvand Z, McAteer D, Harvey A, Backes C and Coleman J N 2016 Electrochemical applications of two-dimensional nanosheets: the effect of nanosheet length and thickness *Chem. Mater.* **28** 2641–51
[453] Vega-Mayoral V, Backes C, Hanlon D, Khan U, Gholamvand Z, O'Brien M, Duesberg G S, Gadermaier C and Coleman J N 2016 Photoluminescence from liquid-exfoliated WS_2 monomers in poly(vinyl alcohol) polymer composites *Adv. Funct. Mater.* **26** 1028–39
[454] Sun H *et al* 2017 How much does size really matter? Exploring the limits of graphene as Li ion battery anode material *Solid State Commun.* **251** 88–93
[455] Woomer A H, Farnsworth T W, Hu J, Wells R A, Donley C L and Warren S C 2015 Phosphorene: synthesis, scale-up, and quantitative optical spectroscopy *ACS Nano* **9** 8869–84
[456] Majekodunmi S O 2015 A review on centrifugation in the pharmaceutical industry *Am. J. Biomed. Eng.* **5** 67–78
[457] Williams J W, Van Holde K E, Baldwin R L and Fujita H 1958 The theory of sedimentation analysis *Chem. Rev.* **58** 715–44
[458] Bildirici L and Rickwood D 2000 Fractionation of differentiating cells using density perturbation *J. Immunol. Methods* **240** 93–9
[459] Patel D and Rickwood D 1995 Optimization of conditions for specific binding of antibody-coated beads to cells *J. Immunol. Methods* **184** 71–80
[460] Cacace M G, Landau E M and Ramsden J J 1997 The Hofmeister series: salt and solvent effects on interfacial phenomena *Q. Rev. Biophys.* **30** 241–77
[461] Collins K D and Washabaugh M W 1985 The Hofmeister effect and the behaviour of water at interfaces *Q. Rev. Biophys.* **18** 323
[462] Kaminsky M 1957 Ion-solvent interaction and the viscosity of strong-electrolyte solutions *Discuss. Faraday Soc.* **24** 171
[463] Coombs D H and Watts N R M 1985 Generating sucrose gradients in three minutes by tilted tube rotation *Anal. Biochem.* **148** 254–9
[464] Brakke M K and Daly J M 1965 Density-gradient centrifugation: non-ideal sedimentation and the interaction of major and minor components *Science* **148** 387–9
[465] Cohen R and Claverie J-M 1975 Sedimentation of generalized systems of interacting particles. II. Active enzyme centrifugation? theory and extensions of its validity range *Biopolymers* **14** 1701–16
[466] Smale G and Sasse J 1992 RNA isolation from cartilage using density gradient centrifugation in cesium trifluoroacetate: an RNA preparation technique effective in the presence of high proteoglycan content *Anal. Biochem.* **203** 352–6
[467] Arnold M S, Green A A, Hulvat J F, Stupp S I and Hersam M C 2006 Sorting carbon nanotubes by electronic structure using density differentiation *Nat. Nanotechnol.* **1** 60–5
[468] Arnold M S, Stupp S I and Hersam M C 2005 Enrichment of single-walled carbon nanotubes by diameter in density gradients *Nano Lett.* **5** 713–8
[469] Bonaccorso F, Hasan T, Tan P H, Sciascia C, Privitera G, Di Marco G, Gucciardi P G and Ferrari A C 2010 Density gradient ultracentrifugation of nanotubes: interplay of bundling and surfactants encapsulation *J. Phys. Chem.* C **114** 17267–85
[470] Vieira O V, Laranjinha J A N, Madeira V M C and Almeida L M 2014 Rapid isolation of low density lipoproteins in a concentrated fraction free from water-soluble plasma antioxidants *J. Lipid Res.* **37** 2715–21
[471] Li S, Zhu F, Meng F, Li H, Wang L, Zhao J, Yue Q, Liu J and Jia J 2013 Separation of graphene oxide by density gradient centrifugation and study on their morphology-dependent electrochemical properties *J. Electroanal. Chem.* **703** 135–45
[472] Kang J, Seo J-W T, Alducin D, Ponce A, Yacaman M J and Hersam M C 2014 Thickness sorting of two-dimensional transition metal dichalcogenides via copolymer-assisted density gradient ultracentrifugation *Nat. Commun.* **5** 5478
[473] Zhu J, Kang J, Kang J, Jariwala D, Wood J D, Seo J-W T, Chen K-S, Marks T J and Hersam M C 2015 Solution-processed dielectrics based on thickness-sorted two-dimensional hexagonal boron nitride nanosheets *Nano Lett.* **15** 7029–36
[474] Kang J, Sangwan V K, Wood J D, Liu X, Balla I, Lam D and Hersam M C 2016 Layer-by-layer sorting of rhenium disulfide via high-density isopycnic density gradient ultracentrifugation *Nano Lett.* **16** 7216–23
[475] Brakke M K 1953 Zonal separations by density-gradient centrifugation *Arch. Biochem. Biophys.* **45** 275–90
[476] Sun X, Luo D, Liu J and Evans D G 2010 Monodisperse chemically modified graphene obtained by density gradient ultracentrifugal rate separation *ACS Nano* **4** 3381–9
[477] Huebler A, Hahn U, Beier W, Lasch N and Fischer T 2002 High volume printing technologies for the production of polymer electronic structures *2nd Int. IEEE Conf. on Polymers and Adhesives in Microelectronics and Photonics. POLYTRONIC 2002. Conf. Proc. (Cat. No.02EX599)* (IEEE)
[478] Kawahara T 2003 *J. Sol-Gel Sci. Technol.* **27** 301–7
[479] Bergsmann F K M, Bauer G, Domnick R and Walter H 2003 *The 46th Annual Technical Conf.—Society of the Vacuum Coaters (San Francisco, USA, 4–8 May 2003)* p 566
[480] Maaninen A, Tuomikoski M, Kivimäki L, Kololuoma T, Välimäki M, Leinonen M and Känsäkoski M 2005 Roll to roll fabrication technologies for optoelectronic and electronic devices and sensors *Proc. SPIE*
[481] Sirringhaus H 2006 Device physics and reliability of solution processed organic TFTs *Flexidis Training Workshop (Stuttgart, Germany, 2006)*
[482] Schrödner M, Schultheis K, Stohn R, Schache H, Blankenburg L and Roth H 2006 *Technologies for Polymer Electronics (Frankfurt, Germany, 2006)*
[483] Blayo A and Pineaux B 2005 Printing processes and their potential for RFID printing *Proc. of the 2005 Joint Conf. on Smart Objects and Ambient Intelligence Innovative Context-*

Aware Services: Usages and Technologies—sOc-EUSAI '05 (ACM Press)
[484] Jabbour G E, Radspinner R and Peyghambarian N 2001 Screen printing for the fabrication of organic light-emitting devices *IEEE J. Sel. Top. Quantum Electron.* **7** 769–73
[485] Park J and Moon J 2006 Control of colloidal particle deposit patterns within picoliter droplets ejected by ink-jet printing *Langmuir* **22** 3506–13
[486] Pekarovicova A and Husovska V 2016 *Printing Ink Formulations, Printing on Polymers* (New York: Elsevier) pp 41–55
[487] The colloidal domain: where physics, chemistry, biology, and technology meet *Choice Rev.* **37** 0334
[488] Viswanath D S, Ghosh T K, Prasad D H L, Dutt N V K and Rani K Y *Correlations And Estimation of Pure Liquid Viscosity* (*Viscosity of Liquids*) (Berlin: Springer) pp 135–405
[489] Willenbacher N and Georgieva K 2013 *Rheology of Disperse Systems, Product Design and Engineering* (New York: Wiley) pp 7–49
[490] Hiemenz P C and Rajagopalan R 1997 *Principles of Colloid and Surface Chemistry* (Boca Raton, FL: CRC Press)
[491] Garg J *et al* 2008 Enhanced thermal conductivity and viscosity of copper nanoparticles in ethylene glycol nanofluid *J. Appl. Phys.* **103** 074301
[492] Mahbubul I M, Saidur R and Amalina M A 2012 Latest developments on the viscosity of nanofluids *Int. J. Heat Mass Transfer* **55** 874–85
[493] Mishra P C, Mukherjee S, Nayak S K and Panda A 2014 A brief review on viscosity of nanofluids *Int. Nano Lett.* **4** 109–20
[494] Bose S, Keller S S, Alstrøm T S, Boisen A and Almdal K 2013 Process optimization of ultrasonic spray coating of polymer films *Langmuir* **29** 6911–9
[495] Xing L-L, Glass J E and Fernando R H 1997 Spray application of waterborne coatings *ACS Symp. Series* (American Chemical Society) pp 265–95
[496] Owen J W, Azarova N A, Loth M A, Paradinas M, Coll M, Ocal C, Anthony J E and Jurchescu O D 2011 Effect of processing parameters on performance of spray-deposited organic thin-film transistors *J. Nanotechnol.* **2011** 1–6
[497] Perfetti G, Alphazan T, van Hee P, Wildeboer W J and Meesters G M H 2011 Relation between surface roughness of free films and process parameters in spray coating *Eur. J. Pharm. Sci.* **42** 262–72
[498] Singh M, Haverinen H M, Dhagat P and Jabbour G E 2010 Inkjet printing-process and its applications *Adv. Mater.* **22** 673–85
[499] Bergeron V, Bonn D, Martin J Y and Vovelle L 2000 *Nature* **405** 772–5
[500] Squire L C 1967 *An Introduction to Fluid Dynamics* ed G K Batchelor (Cambridge: Cambridge University Press) 616p (Figures. 15s *J. R. Aeronaut. Soc.* **71** 801–2)
[501] de Gans B-J, Kazancioglu E, Meyer W and Schubert U S 2004 Ink-jet printing polymers and polymer libraries using micropipettes *Macromol. Rapid Commun.* **25** 292–6
[502] Dong H, Carr W W and Morris J F 2006 An experimental study of drop-on-demand drop formation *Phys. Fluids* **18** 072102
[503] Fromm J E 1984 Numerical calculation of the fluid dynamics of drop-on-demand jets *IBM J. Res. Dev.* **28** 322–33
[504] Hsiao W-K, Hoath S D, Martin G D and Hutchings I M 2009 Ink jet printing for direct mask deposition in printed circuit board fabrication *J. Imaging Sci. Technol.* **53** 050304
[505] Jang D, Kim D and Moon J 2009 Influence of fluid physical properties on ink-jet printability *Langmuir* **25** 2629–35
[506] Jung S and Hutchings I M 2012 The impact and spreading of a small liquid drop on a non-porous substrate over an extended time scale *Soft Matter* **8** 2686
[507] Shin P, Sung J and Lee M H 2011 Control of droplet formation for low viscosity fluid by double waveforms applied to a piezoelectric inkjet nozzle *Microelectron. Reliab.* **51** 797–804
[508] van Osch T H J, Perelaer J, de Laat A W M and Schubert U S 2008 Inkjet printing of narrow conductive tracks on untreated polymeric substrates *Adv. Mater.* **20** 343–5
[509] Perelaer J, de Gans B J and Schubert U S 2006 Ink-jet printing and microwave sintering of conductive silver tracks *Adv. Mater.* **18** 2101–4
[510] de Gennes P G 1985 Wetting: statics and dynamics *Rev. Mod. Phys.* **57** 827–63
[511] Saunders R E and Derby B 2014 Inkjet printing biomaterials for tissue engineering: bioprinting *Int. Mater. Rev.* **59** 430–48
[512] Baker J, Deganello D, Gethin D T and Watson T M 2014 Flexographic printing of graphene nanoplatelet ink to replace platinum as counter electrode catalyst in flexible dye sensitised solar cell *Mater. Res. Innov.* **18** 86–90
[513] Secor E B, Lim S, Zhang H, Frisbie C D, Francis L F and Hersam M C 2014 Gravure printing of graphene for large-area flexible electronics *Adv. Mater.* **26** 4533–8
[514] Yamazaki K 1993 Report on 1993 TAPPI coating conference *Japan Tappi J.* **47** 1213–22
[515] Kim Y-J, Yoo H, Lee C-H, Park J B, Baek H, Kim M and Yi G-C 2012 Position- and morphology-controlled ZnO nanostructures grown on graphene layers *Adv. Mater.* **24** 5565–9
[516] Hyun W J, Secor E B, Rojas G A, Hersam M C, Francis L F and Frisbie C D 2015 All-printed, foldable organic thin-film transistors on glassine paper *Adv. Mater.* **27** 7058–64
[517] Liu B and Wang S 2012 Preparation of patterned biological film for nanolithography *J. Biosens. Bioelectron.* **01**
[518] Qian M, Feng T, Ding H, Lin L, Li H, Chen Y and Sun Z 2009 Electron field emission from screen-printed graphene films *Nanotechnology* **20** 425702
[519] Zhang D W, Li X D, Li H B, Chen S, Sun Z, Yin X J and Huang S M 2011 Graphene-based counter electrode for dye-sensitized solar cells *Carbon* **49** 5382–8
[520] Wróblewski G and Janczak D 2012 Screen printed, transparent, and flexible electrodes based on graphene nanoplatelet pastes *Proc. SPIE*
[521] Xu Y, Schwab M G, Strudwick A J, Hennig I, Feng X, Wu Z and Müllen K 2013 Screen-printable thin film supercapacitor device utilizing graphene/polyaniline inks *Adv. Energy Mater.* **3** 1035–40
[522] Arapov K, Rubingh E, Abbel R, Laven J, de With G and Friedrich H 2015 Conductive screen printing inks by gelation of graphene dispersions *Adv. Funct. Mater.* **26** 586–93
[523] Whistler R and BeMiller J 1993 *Industrial Gums : Polysaccharides and Their Derivatives* (New York: Academic) pp 558–9
[524] Mezger T G 2006 *The Rheology Handbook: For Users of Rotational and Oscillatory Rheometers* (Vincentz Network)
[525] Benchabane A and Bekkour K 2008 Rheological properties of carboxymethyl cellulose (CMC) solutions *Colloid Polym. Sci.* **286** 1173–80
[526] Nijenhuis K, McKinley G, Spiegelberg S, Barnes H, Aksel N, Heymann L and Odell J 2007 *Non-Newtonian Flows, Springer Handbook of Experimental Fluid Mechanics* (Berlin: Springer) pp 619–743
[527] Irgens F 2014 *Rheology and Non-Newtonian Fluids* (Berlin: Springer)
[528] deButts E H, Hudy J A and Elliott J H 1957 Rheology of sodium carboxymethylcellulose solutions *Ind. Eng. Chem.* **49** 94–8
[529] Elliot J H and Ganz A J 1974 Some rheological properties of sodium carboxymethylcellulose solutions and gels *Rheol. Acta* **13** 670–4
[530] Robaeys P *et al* 2014 Enhanced performance of polymer:fullerene bulk heterojunction solar cells upon graphene addition *Appl. Phys. Lett.* **105** 083306
[531] Hu L, Kim H S, Lee J-Y, Peumans P and Cui Y 2010 Scalable coating and properties of transparent, flexible, silver nanowire electrodes *ACS Nano* **4** 2955–63
[532] Dan B, Irvin G C and Pasquali M 2009 Continuous and scalable fabrication of transparent conducting carbon nanotube films *ACS Nano* **3** 835–43
[533] Liu Z, Parvez K, Li R, Dong R, Feng X and Müllen K 2014 Transparent conductive electrodes from graphene/PEDOT:PSS hybrid inks for ultrathin organic photodetectors *Adv. Mater.* **27** 669–75

[534] Liu Z, Wu Z-S, Yang S, Dong R, Feng X and Müllen K 2016 Ultraflexible in-plane micro-supercapacitors by direct printing of solution-processable electrochemically exfoliated graphene *Adv. Mater.* **28** 2217–22
[535] Zaugg C A *et al* 2013 Ultrafast and widely tuneable vertical-external-cavity surface-emitting laser, mode-locked by a graphene-integrated distributed Bragg reflector *Opt. Express* **21** 31548–59
[536] Bianchi V *et al* 2017 Terahertz saturable absorbers from liquid phase exfoliation of graphite *Nat. Commun.* **8** 15763
[537] Higgins T M *et al* 2014 Effect of percolation on the capacitance of supercapacitor electrodes prepared from composites of manganese dioxide nanoplatelets and carbon nanotubes *ACS Nano* **8** 9567–79
[538] McAteer D, Gholamvand Z, McEvoy N, Harvey A, O'Malley E, Duesberg G S and Coleman J N 2016 Thickness dependence and percolation scaling of hydrogen production rate in MoS_2 nanosheet and nanosheet-carbon nanotube composite catalytic electrodes *ACS Nano* **10** 672–83
[539] Purdie D, Popa D, Wittwer V J, Jiang Z, Torrisi F and Ferrari A C 2014 Sub-50 fs compressed pulses from a graphene-mode locked fiber laser *CLEO: 2014 OSA*
[540] Jiang Z, Bonacchini G E, Popa D, Torrisi F, Ott A K, Wittwer V J, Purdie D and Ferrari A C 2014 Graphene saturable absorber power scaling laser *CLEO: 2014 OSA*
[541] Yingying R, Brown G, Mary R, Demetriou G, Popa D, Torrisi F, Ferrari A C, Feng C and Kar A K 2015 7.8 GHz graphene-based 2 μm monolithic waveguide laser *IEEE J. Sel. Top. Quantum Electron.* **21** 395–400
[542] Dikin D A, Stankovich S, Zimney E J, Piner R D, Dommett G H B, Evmenenko G, Nguyen S T and Ruoff R S 2007 Preparation and characterization of graphene oxide paper *Nature* **448** 457–60
[543] Kim B, Jang S, Geier M L, Prabhumirashi P L, Hersam M C and Dodabalapur A 2014 High-Speed, inkjet-printed carbon nanotube/zinc tin oxide hybrid complementary ring oscillators *Nano Lett.* **14** 3683–7
[544] Secor E B, Prabhumirashi P L, Puntambekar K, Geier M L and Hersam M C 2013 Inkjet printing of high conductivity, flexible graphene patterns *J. Phys. Chem. Lett.* **4** 1347–51
[545] Novacentrix (www.novacentrix.com)
[546] Rinaldi A, Proietti A, Tamburrano A, De Bellis G, Mulattieri M and Sarto M S 2014 Multilayer Graphene-based films for strain sensing *14th IEEE Int. Conf. on Nanotechnology* (IEEE)
[547] Bessonov A, Kirikova M, Haque S, Gartseev I and Bailey M J A 2014 Highly reproducible printable graphite strain gauges for flexible devices *Sensors Actuators* A **206** 75–80
[548] Bao M-H 2000 Capacitive pressure transducers and accelerometers *Micro Mechanical Transducers—Pressure Sensors, Accelerometers and Gyroscopes* (Amsterdam: Elsevier) pp 319–52
[549] Zlebic C, Zivanov L, Menicanin A, Blaz N and Damnjanovic M 2016 Inkjet printed resistive strain gages on flexible substrates *Facta Universitatis—Series: Electronics and Energetics* vol 29 pp 89–100
[550] McManus D *et al* 2017 Water-based and biocompatible 2D crystal inks for all-inkjet-printed heterostructures *Nat. Nanotechnol.* **12** 343
[551] Sommer-Larsen P, Jørgensen M, Søndergaard R R, Hösel M and Krebs F C 2013 It is all in the pattern-high-efficiency power extraction from polymer solar cells through high-voltage serial connection *Energy Technol.* **1** 15–9
[552] Krebs F C, Espinosa N, Hösel M, Søndergaard R R and Jørgensen M 2013 25th anniversary article: rise to power—OPV-based solar parks *Adv. Mater.* **26** 29–39
[553] Lee D H, Choi J S, Chae H, Chung C H and Cho S M 2009 Screen-printed white OLED based on polystyrene as a host polymer *Curr. Appl. Phys.* **9** 161–4
[554] Jung S, Hoath S D, Martin G D and Hutchings I M 2015 *Inkjet Printing Process for Large Area Electronics, Large Area and Flexible Electronics* (New York: Wiley) pp 315–44
[555] Khan S, Lorenzelli L and Dahiya R S 2015 Technologies for printing sensors and electronics over large flexible substrates: a review *IEEE Sens. J.* **15** 3164–85
[556] Tobjörk D and Österbacka R 2011 Paper electronics *Adv. Mater.* **23** 1935–61
[557] Merilampi S, Laine-Ma T and Ruuskanen P 2009 The characterization of electrically conductive silver ink patterns on flexible substrates *Microelectron. Reliabil.* **49** 782–90
[558] Birkenshaw J W Printing processes *The Printing Ink Manual* (Netherlands: Springer) pp 14–85
[559] Hyun W J, Lim S, Ahn B Y, Lewis J A, Frisbie C D and Francis L F 2015 Screen printing of highly loaded silver inks on plastic substrates using silicon stencils *ACS Appl. Mater. Interfaces* **7** 12619–24
[560] Abbott S, Church T, Parker D and Harris A 2008 *How to be a Great Screen Printer* ed S Abbott (MacDermid Autotype Ltd)
[561] Novalia (www.audioposter.com/)
[562] Hu G, Kang J, Ng L W T, Zhu X, Howe R C T, Jones C G, Hersam M C and Hasan T 2018 Functional inks and printing of two-dimensional materials *Chem. Soc. Rev.* **47** 3265–300
[563] Bonaccorso F, Colombo L, Yu G H, Stoller M, Tozzini V, Ferrari A C, Ruoff R S and Pellegrini V 2015 Graphene, related two-dimensional crystals, and hybrid systems for energy conversion and storage *Science* **347** 1246501
[564] Mohan V B, Lau K-T, Hui D and Bhattacharyya D 2018 Graphene-based materials and their composites: a review on production, applications and product limitations *Composites* B **142** 200–20
[565] Miranzo P, Belmonte M and Osendi M I 2017 From bulk to cellular structures: a review on ceramic/graphene filler composites *J. Eur. Ceram. Soc.* **37** 3649–72
[566] Wang F, Wang H and Mao J 2019 Aligned-graphene composites: a review *J. Mater. Sci.* **54** 36–61
[567] Boland C S *et al* 2016 Sensitive electromechanical sensors using viscoelastic graphene-polymer nanocomposites *Science* **354** 1257–60
[568] Boland C S *et al* 2014 Sensitive, high-strain, high-rate bodily motion sensors based on graphene-rubber composites *ACS Nano* **8** 8819–30
[569] Layani M, Kamyshny A and Magdassi S 2014 Transparent conductors composed of nanomaterials *Nanoscale* **6** 5581–91
[570] Secor E B, Gao T Z, Islam A E, Rao R, Wallace S G, Zhu J, Putz K W, Maruyama B and Hersam M C 2017 Enhanced conductivity, adhesion, and environmental stability of printed graphene inks with nitrocellulose *Chem. Mater.* **29** 2332–40
[571] Carey T, Cacovich S, Divitini G, Ren J, Mansouri A, Kim J M, Wang C, Ducati C, Sordan R and Torrisi F 2017 Fully inkjet-printed two-dimensional material field-effect heterojunctions for wearable and textile electronics *Nat. Commun.* **8** 1202
[572] Kelly A G *et al* 2017 All-printed thin-film transistors from networks of liquid-exfoliated nanosheets *Science* **356** 69–73
[573] Lin Z *et al* 2018 Solution-processable 2D semiconductors for high-performance large-area electronics *Nature* **562** 254–8
[574] Hu G *et al* 2017 Black phosphorus ink formulation for inkjet printing of optoelectronics and photonics *Nat. Commun.* **8** 278
[575] Anichini C, Czepa W, Pakulski D, Aliprandi A, Ciesielski A and Samorì P 2018 Chemical sensing with 2D materials *Chem. Soc. Rev.* **47** 4860–908
[576] Santra S, Hu G, Howe R C T, De Luca A, Ali S Z, Udrea F, Gardner J W, Ray S K, Guha P K and Hasan T 2015 CMOS integration of inkjet-printed graphene for humidity sensing *Sci. Rep.* **5** 17374
[577] Huang L, Wang Z, Zhang J, Pu J, Lin Y, Xu S, Shen L, Chen Q and Shi W 2014 Fully printed, rapid-response sensors based on chemically modified graphene for detecting NO_2 at room temperature *ACS Appl. Mater. Interfaces* **6** 7426–33
[578] Cho S-Y, Lee Y, Koh H-J, Jung H, Kim J-S, Yoo H-W, Kim J and Jung H-T 2016 Superior chemical sensing performance of black phosphorus: comparison with MoS_2 and graphene *Adv. Mater.* **28** 7020–8
[579] Sun S, Liao C, Hafez A M, Zhu H and Wu S 2018 Two-dimensional MXenes for energy storage *Chem. Eng. J.* **338** 27–45

[580] Foster C W, Down M P, Zhang Y, Ji X, Rowley-Neale S J, Smith G C, Kelly P J and Banks C E 2017 3D printed graphene based energy storage devices *Sci. Rep.* **7** 42233
[581] Hyun W J, Secor E B, Kim C-H, Hersam M C, Francis L F and Frisbie C D 2017 Scalable, self-aligned printing of flexible graphene micro-supercapacitors *Adv. Energy Mater.* **7** 1700285
[582] Shi L and Zhao T 2017 Recent advances in inorganic 2D materials and their applications in lithium and sodium batteries *J. Mater. Chem.* C **5** 3735–58
[583] Nguyen V L *et al* 2015 Seamless stitching of graphene domains on polished copper (1 1 1) foil *Adv. Mater.* **27** 1376–82
[584] Berger C *et al* 2004 Ultrathin epitaxial graphite: 2D electron gas properties and a route toward graphene-based nanoelectronics *J. Phys. Chem.* B **108** 19912–6
[585] Berger C, Conrad E H and de Heer W A 2018 *Epigraphene in Physics of Solid Surfaces* (*Landolt-Borstein Encyclopedia*) ed P Chiaradia and G Chiarotti pp 727–807
[586] Van Bommel A J, Crobeen J E and Van Tooren A 1975 LEED and Auger electron observations of the SiC(0 0 0 1) surface *Surf. Sci.* **48** 463–72
[587] de Heer W A, Berger C and First P N 2006 Patterned thin films graphite devices and methods for making the same *US Patent* 7015142 (provisional Application No. 60/477997 filed June 12 2003, Issued March 21 2006)
[588] Virojanadara C, Syvajarvi M, Yakimova R, Johansson L I, Zakharov A A and Balasubramanian T 2008 Homogeneous large-area graphene layer growth on 6H–SiC (0 0 0 1) *Phys. Rev.* B **78** 245403
[589] Emtsev K V *et al* 2009 Towards wafer-size graphene layers by atmospheric pressure graphitization of silicon carbide *Nat. Mater.* **8** 203–7
[590] Varchon F *et al* 2007 Electronic structure of epitaxial graphene layers on SiC: effect of the substrate *Phys. Rev. Lett.* **99** 126805
[591] Emery J D, Detlefs B, Karmel H J, Nyakiti L O, Gaskill D K, Hersam M C, Zegenhagen J and Bedzyk M J 2013 Chemically resolved interface structure of epitaxial graphene on SiC(0 0 0 1) *Phys. Rev. Lett.* **111** 215501
[592] Emtsev K V, Speck F, Seyller T, Ley L and Riley J D 2008 Interaction, growth, and ordering of epitaxial graphene on SiC{0 0 0 1} surfaces: A comparative photoelectron spectroscopy study *Phys. Rev.* B **77** 155303
[593] Conrad M *et al* 2016 Wide band gap semiconductor from a hidden 2D incommensurate graphene phase *Nano Lett.* **17** 341–7
[594] Nevius M S, Conrad M, Wang F, Celis A, Nair M N, Taleb-Ibrahimi A, Tejeda A and Conrad E H 2015 Semiconducting graphene from highly ordered substrate interactions *Phys. Rev. Lett.* **115** 136802
[595] Rutter G M, Guisinger N P, Crain J N, Jarvis E A A, Stiles M D, Li T, First P N and Stroscio J A 2007 Imaging the interface of epitaxial graphene with silicon carbide via scanning tunneling microscopy *Phys. Rev.* B **76** 235416
[596] Hass J, de Heer W A and Conrad E H 2008 The growth and morphology of epitaxial multilayer graphene *J. Phys.: Condens. Matter* **20** 323202
[597] de Heer W A, Berger C, Ruan M, Sprinkle M, Li X, Hu Y, Zhang B, Hankinson J and Conrad E H 2011 Large area and structured epitaxial graphene produced by confinement controlled sublimation of silicon carbide *Proc. Natl Acad. Sci.* **108** 16900–5
[598] Coletti C *et al* 2013 Revealing the electronic band structure of trilayer graphene on SiC: an angle-resolved photoemission study *Phys. Rev.* B **88** 155439
[599] Hass J, Varchon F, Millan-Otoya J E, Sprinkle M, Sharma N, De Heer W A, Berger C, First P N, Magaud L and Conrad E H 2008 Why multilayer graphene on 4H-SiC(0 0 0(1)over-bar) behaves like a single sheet of graphene *Phys. Rev. Lett.* **100** 125504
[600] Miller D L, Kubista K D, Rutter G M, Ruan M, de Heer W A, First P N and Stroscio J A 2010 Structural analysis of multilayer graphene via atomic moireacute interferometry *Phys. Rev.* B **81** 223108
[601] Hupalo M, Conrad E H and Tringides M C 2009 Growth mechanism for epitaxial graphene on vicinal 6H–SiC (0 0 0 1) surfaces: a scanning tunneling microscopy study *Phys. Rev.* B **80** 041401
[602] Borovikov V and Zangwill A 2009 Step-edge instability during epitaxial growth of graphene from SiC (0 0 0 1) *Phys. Rev.* B **80** 121406
[603] Ohta T, Bartelt N C, Nie S, Thurmer K and Kellogg G L 2010 Role of carbon surface diffusion on the growth of epitaxial graphene on SiC *Phys. Rev.* B **81** 121411
[604] Hu Y, Ruan M, Guo Z L, Dong R, Palmer J, Hankinson J, Berger C and de Heer W A 2012 Structured epitaxial graphene: growth and properties *J. Phys. D: Appl. Phys.* **45** 154010
[605] Hite J K, Twigg M E, Tedesco J L, Friedman A L, Myers-Ward R L, Eddy C R and Gaskill D K 2011 Epitaxial graphene nucleation on C-face silicon carbide *Nano Lett.* **11** 1190–4
[606] Zhang R, Dong Y L, Kong W J, Han W P, Tan P H, Liao Z M, Wu X S and Yu D P 2012 Growth of large domain epitaxial graphene on the C-face of SiC *J. Appl. Phys.* **112** 104307
[607] Yazdi G R, Iakimov T and Yakimova R 2016 Epitaxial graphene on SiC: a review of growth and characterization *Crystals* **6** 53
[608] Råback P, Yakimova R, Syväjärvi M, Nieminen R and Janzén E 1999 A practical model for estimating the growth rate in sublimation growth of SiC *Mater. Sci. Eng.* B **61–62** 89–92
[609] Tromp R M and Hannon J B 2009 Thermodynamics and kinetics of graphene growth on SiC(0 0 0 1) *Phys. Rev. Lett.* **102** 106104
[610] Riedl C, Starke U, Bernhardt J, Franke M and Heinz K 2007 Structural properties of the graphene-SiC(0 0 0 1) interface as a key for the preparation of homogeneous large-terrace graphene surfaces *Phys. Rev.* B **76** 245406
[611] Strupinski W *et al* 2011 Graphene epitaxy by chemical vapor deposition on SiC *Nano Lett.* **11** 1786–91
[612] Lafont F *et al* 2015 Quantum Hall resistance standards from graphene grown by chemical vapour deposition on silicon carbide *Nat. Commun.* **6** 6806
[613] Ostler M, Speck F, Gick M and Seyller T 2010 Automated preparation of high-quality epitaxial graphene on 6H–SiC(0 0 0 1) *Phys. Status Solidi* b **247** 2924–6
[614] Yakimova R, Virojanadara C, Gogova D, Syvajarvi M, Siche D, Larsson K and Johansson L I 2010 Analysis of the formation conditions for large area epitaxial graphene on SiC substrates *Silicon Carbide Relat. Mater.* **645–8** 565–8
[615] Berger C *et al* Epitaxial graphene on SiC: 2D sheets, selective growth and nanoribbons *Growing Graphene on Semiconductors* ed C C N Motta and F Iacopi (PanStanford) (arXiv:1611.089372016)
[616] Palmer J 2014 Pre-growth structures for nanoelectronics of EG on SiC School of Physics—Georgia Institute of Technology
[617] Camara N, Huntzinger J R, Rius G, Tiberj A, Mestres N, Perez-Murano F, Godignon P and Camassel J 2009 Anisotropic growth of long isolated graphene ribbons on the C face of graphite-capped 6H–SiC *Phys. Rev.* B **80** 125410
[618] Sprinkle M, Ruan M, Hu Y, Hankinson J, Rubio-Roy M, Zhang B, Wu X, Berger C and de Heer W A 2010 Scalable templated growth of graphene nanoribbons on SiC *Nat. Nanotechnol.* **5** 727–31
[619] Ruan M 2012 Structured epitaxial graphene for electronics, *PhD* School of Physics, Georgia Institute of Technology, Atlanta
[620] Baringhaus J *et al* 2014 Exceptional ballistic transport in epitaxial graphene nanoribbons *Nature* **506** 349–54
[621] Cambaz Z G, Yushin G, Osswald S, Mochalin V and Goyotsi Y 2008 Noncatalytic synthesis of carbon nanotubes, graphene and graphite on SiC *Carbon* **46** 841–9
[622] Berger C *et al* 2006 Electronic confinement and coherence in patterned epitaxial graphene *Science* **312** 1191–6
[623] Maysonnave J *et al* 2014 Terahertz generation by dynamical photon drag effect in graphene excited by femtosecond optical pulses *Nano Lett.* **14** 5797–802

[624] Sadowski M L, Martinez G, Potemski M, Berger C and de Heer W A 2007 Magnetospectroscopy of epitaxial few-layer graphene *Solid State Commun.* **143** 123–5
[625] Wu X S, Hu Y K, Ruan M, Madiomanana N K, Hankinson J, Sprinkle M, Berger C and de Heer W A 2009 Half integer quantum Hall effect in high mobility single layer epitaxial graphene *Appl. Phys. Lett.* **95** 223108
[626] Hass J 2008 Structural characterization of epitaxial graphene on silicon carbide *PhD* School of Physics, Georgia Institute of Technology
[627] Miller D L, Kubista K D, Rutter G M, Ruan M, de Heer W A, First P N and Stroscio J A 2009 Observing the quantization of zero mass carriers in graphene *Science* **324** 924–7
[628] Orlita M, Faugeras C, Grill R, Wysmolek A, Strupinski W, Berger C, de Heer W A, Martinez G and Potemski M 2011 Carrier scattering from dynamical magnetoconductivity in quasineutral epitaxial graphene *Phys. Rev. Lett.* **107** 216603
[629] Sprinkle M *et al* 2009 First direct observation of a nearly ideal graphene band structure *Phys. Rev. Lett.* **103** 226803
[630] de Heer W A *et al* 2010 Epitaxial graphene electronic structure and transport *J. Phys. D: Appl. Phys.* **43** 374007
[631] Kunc J, Hu Y, Palmer J, Berger C and de Heer W A 2013 A method to extract pure Raman spectrum of epitaxial graphene on SiC *Appl. Phys. Lett.* **103** 201911
[632] Levy N, Burke S A, Meaker K L, Panlasigui M, Zettl A, Guinea F, Neto A H C and Crommie M F 2010 Strain-induced pseudo-magnetic fields greater than 300 tesla in graphene nanobubbles *Science* **329** 544–7
[633] Orlita M *et al* 2008 Approaching the dirac point in high-mobility multilayer epitaxial graphene *Phys. Rev. Lett.* **101** 267601
[634] Sadowski M L, Martinez G, Potemski M, Berger C and de Heer W A 2006 Landau level spectroscopy of ultrathin graphite layers *Phys. Rev. Lett.* **97** 266405
[635] Tzalenchuk A, Lara-Avila S, Kalaboukhov A, Paolillo S, Syvajarvi M, Yakimova R, Kazakova O, Janssen T J B M, Fal'ko V and Kubatkin S 2010 Towards a quantum resistance standard based on epitaxial graphene *Nat. Nanotechnol.* **5** 186–9
[636] Borovikov V and Zangwill A 2009 Step bunching of vicinal 6H–SiC{0 0 0 1} surfaces *Phys. Rev.* B **79** 121406
[637] Chua C *et al* 2014 Quantum Hall effect and quantum point contact in bilayer-patched epitaxial graphene *Nano Lett.* **14** 3369–73
[638] Michon A, Vezian S, Roudon E, Lefebvre D, Zielinski M, Chassagne T and Portail M 2013 Effects of pressure, temperature, and hydrogen during graphene growth on SiC(0 0 0 1) using propane-hydrogen chemical vapor deposition *J. Appl. Phys.* **113** 203501
[639] Mattias K *et al* 2016 Comeback of epitaxial graphene for electronics: large-area growth of bilayer-free graphene on SiC *2D Mater.* **3** 041002
[640] Yazdi G R, Vasiliauskas R, Iakimov T, Zakharov A, Syvajarvi M and Yakimova R 2013 Growth of large area monolayer graphene on 3C–SiC and a comparison with other SiC polytypes *Carbon* **57** 477–84
[641] Yakimova R and Yazdi G R 2015 private commnication
[642] Palmer J, Kunc J, Hu Y K, Hankinson J, Guo Z L, Berger C and De Heer W A 2014 Controlled epitaxial graphene growth within removable amorphous carbon corrals *Appl. Phys. Lett.* **105** 023106
[643] Yakimova R 2017 unpublished
[644] Norimatsu W and Kusunoki M 2014 Growth of graphene from SiC{0 0 0 1} surfaces and its mechanisms *Semicond. Sci. Technol.* **29** 064009
[645] Riedl C, Coletti C, Iwasaki T, Zakharov A A and Starke U 2009 Quasi-free-standing epitaxial graphene on SiC obtained by hydrogen intercalation *Phys. Rev. Lett.* **103** 246804
[646] Riedl C, Coletti C, Iwasaki T and Starke U 2010 Hydrogen intercalation below epitaxial graphene on SiC(0 0 0 1) *Mater. Sci. Forum* **645–8** 623–8
[647] Coletti C, Emtsev K V, Zakharov A A, Ouisse T, Chaussende D and Starke U 2011 Large area quasi-free standing monolayer graphene on 3C–SiC(1 1 1) *Appl. Phys. Lett.* **99** 081904
[648] Kruskopf M *et al* 2012 Epitaxial graphene on SiC: modification of structural and electron transport properties by substrate pretreatment *J. Phys.: Condens. Matter* **27** 185303
[649] Ivanov I G, Hassan J U, Iakimov T, Zakharov A A, Yakimova R and Janzen E 2014 Layer-number determination in graphene on SiC by reflectance mapping *Carbon* **77** 492–500
[650] Camara N, Jouault B, Caboni A, Jabakhanji B, Desrat W, Pausas E, Consejo C, Mestres N, Godignon P and Camassel J 2010 Growth of monolayer graphene on 8 degrees off-axis 4H-SiC (0 0 0 − 1) substrates with application to quantum transport devices *Appl. Phys. Lett.* **97** 093107
[651] Eddy C R and Gaskill D K 2009 Silicon carbide as a platform for power electronics *Science* **324** 1398–400
[652] Giannazzo F, Deretzis I, Nicotra G, Fisichella G, Ramasse Q M, Spinella C, Roccaforte F and La Magna A 2014 High resolution study of structural and electronic properties of epitaxial graphene grown on off-axis 4H-SiC (0 0 0 1) *J. Cryst. Growth* **393** 150–5
[653] Sonde S, Giannazzo F, Huntzinger J R, Tiberj A, Syvajarvi M, Yakimova R, Raineri V and Camassel J 2010 Uniformity of epitaxial graphene on on-axis and off-axis SiC probed by raman spectroscopy and nanoscale current mapping *Silicon Carbide Relat. Mater.* **645–8** 607–10
[654] Vecchio C, Sonde S, Bongiorno C, Rambach M, Yakimova R, Raineri V and Giannazzo F 2011 Nanoscale structural characterization of epitaxial graphene grown on off-axis 4H-SiC (0 0 0 1) *Nanoscale Res. Lett.* **6** 269
[655] Penuelas J, Ouerghi A, Lucot D, David C, Gierak J, Estrade-Szwarckopf H and Andreazza-Vignolle C 2009 Surface morphology and characterization of thin graphene films on SiC vicinal substrate *Phys. Rev.* B **79** 033408
[656] Maassen T, van den Berg J J, Huisman E H, Dijkstra H, Fromm F, Seyller T and van Wees B J 2013 Localized states influence spin transport in epitaxial graphene *Phys. Rev. Lett.* **110** 067209
[657] Shtepliuk I, Khranovskyy V and Yakimova R 2016 Combining graphene with silicon carbide: synthesis and properties—a review *Semicond. Sci. Technol.* **31** 113004
[658] Speck F, Jobst J, Fromm F, Ostler M, Waldmann D, Hundhausen M, Weber H B and Seyller T 2011 The quasi-free-standing nature of graphene on H-saturated SiC(0 0 0 1) *Appl. Phys. Lett.* **99** 122106
[659] Riedl C, Coletti C and Starke U 2010 Structural and electronic properties of epitaxial graphene on SiC(0 0 0 1): a review of growth, characterization, transfer doping and hydrogen intercalation *J. Phys. D: Appl. Phys.* **43** 374009
[660] Ostler M, Deretzis I, Mammadov S, Giannazzo F, Nicotra G, Spinella C, Seyller T and La Magna A 2013 Direct growth of quasi-free-standing epitaxial graphene on nonpolar SiC surfaces *Phys. Rev.* B **88** 085408
[661] Hens P, Zakharov A A, Iakimov T, Syvajarvi M and Yakimova R 2014 Large area buffer-free graphene on non-polar (0 0 1) cubic silicon carbide *Carbon* **80** 823–9
[662] Jabakhanji B, Camara N, Caboni A, Consejo C, Jouault B, Godignon P and Camassel J 2012 Almost free standing graphene on SiC(0 0 0 − 1) and SiC(1 1 − 2 0) *Heterosic Wasmpe* **711** 235–41
[663] Forbeaux I, Themlin J M and Debever J M 1998 Heteroepitaxial graphite on 6H–SiC(0 0 0 1): interface formation through conduction-band electronic structure *Phys. Rev.* B **58** 16396–406
[664] Forbeaux I, Themlin J M, Charrier A, Thibaudau F and Debever J M 2001 Solid-state graphitization mechanisms of silicon carbide 6H–SiC polar faces *Appl. Surf. Sci.* **162–3** 406–12
[665] Starke U 2003 *Atomic Structure of SiC Surfaces* (*Recent Major Advances in Silicon Carbide*) ed W J Choyke *et al* (Berlin: Springer)
[666] Deretzis I and La Magna A 2016 Simulating structural transitions with kinetic Monte Carlo: the case of epitaxial graphene on SiC *Phys. Rev.* E **93** 033304
[667] Daas B K, Omar S U, Shetu S, Daniels K M, Ma S, Sudarshan T S and Chandrashekhar M V S 2012 Comparison of epitaxial graphene growth on polar and nonpolar 6H–SiC

faces: on the growth of multilayer films *Cryst. Growth Des.* **12** 3379–87
[668] Goler S *et al* 2013 Revealing the atomic structure of the buffer layer between SiC(0 0 0 1) and epitaxial graphene *Carbon* **51** 249–54
[669] Mattausch A and Pankratov O 2007 *Ab initio* study of graphene on SiC *Phys. Rev. Lett.* **99** 076802
[670] Seyller T 2012 Epitaxial graphene on SiC(0 0 0 1) *Graphene Nanoelectronics: Metrology, Synthesis, Properties and Applications* ed H Raza (Berlin: Springer) pp 135–59
[671] Bostwick A, Ohta T, Seyller T, Horn K and Rotenberg E 2007 Quasiparticle dynamics in graphene *Nat. Phys.* **3** 36–40
[672] Rollings E, Gweon G H, Zhou S Y, Mun B S, McChesney J L, Hussain B S, Fedorov A, First P N, de Heer W A and Lanzara A 2006 Synthesis and characterization of atomically thin graphite films on a silicon carbide substrate *J. Phys. Chem. Solids* **67** 2172–7
[673] Ohta T, Bostwick A, Seyller T, Horn K and Rotenberg E 2006 Controlling the electronic structure of bilayer graphene *Science* **313** 951–54
[674] Ohta T, Bostwick A, McChesney J L, Seyller T, Horn K and Rotenberg E 2007 Interlayer interaction and electronic screening in multilayer graphene investigated with angle-resolved photoemission spectroscopy *Phys. Rev. Lett.* **98** 206802
[675] Jobst J, Waldmann D, Speck F, Hirner R, Maude D K, Seyller T and Weber H B 2010 Quantum oscillations and quantum Hall effect in epitaxial graphene *Phys. Rev.* B **81** 195434
[676] Jobst J, Waldmann D, Speck F, Hirner R, Maude D K, Seyller T and Weber H B 2011 Transport properties of high-quality epitaxial graphene on 6H–SiC(0 0 0 1) *Solid State Commun.* **151** 1061–4
[677] Farías D, Rieder K H, Shikin A M, Adamchuk V K, Tanaka T and Oshima C 2000 Modification of the surface phonon dispersion of a graphite monolayer adsorbed on Ni(1 1 1) caused by intercalation of Yb, Cu and Ag *Surf. Sci.* **454–6** 437–41
[678] Forti S, Emtsev K V, Coletti C, Zakharov A A, Riedl C and Starke U 2011 Large-area homogeneous quasifree standing epitaxial graphene on SiC(0 0 0 1): electronic and structural characterization *Phys. Rev.* B **84** 125449
[679] Bostwick A, Speck F, Seyller T, Horn K, Polini M, Asgari R, MacDonald A H and Rotenberg E 2010 Observation of plasmarons in quasi-freestanding doped graphene *Science* **328** 999–1002
[680] Virojanadara C, Zakharov A A, Yakimova R and Johansson L I 2010 Buffer layer free large area bi-layer graphene on SiC(0 0 0 1) *Surf. Sci.* **604** L4–7
[681] Watcharinyanon S, Virojanadara C, Osiecki J R, Zakharov A A, Yakimova R, Uhrberg R I G and Johansson L I 2011 Hydrogen intercalation of graphene grown on 6H–SiC(0 0 0 1) *Surf. Sci.* **605** 1662–8
[682] Oida S, McFeely F R, Hannon J B, Tromp R M, Copel M, Chen Z, Sun Y, Farmer D B and Yurkas J 2010 Decoupling graphene from SiC(0 0 0 1) via oxidation *Phys. Rev.* B **82** 041411
[683] Oliveira M H Jr, Schumann T, Fromm F, Koch R, Ostler M, Ramsteiner M, Seyller T, Lopes J M J and Riechert H 2013 Formation of high-quality quasi-free-standing bilayer graphene on SiC(0 0 0 1) by oxygen intercalation upon annealing in air *Carbon* **52** 83–9
[684] Ostler M, Fromm F, Koch R J, Wehrfritz P, Speck F, Vita H, Böttcher S, Horn K and Seyller T 2014 Buffer layer free graphene on SiC(0 0 0 1) via interface oxidation in water vapor *Carbon* **70** 258–65
[685] Ostler M, Koch R J, Speck F, Fromm F, Vita H, Hundhausen M, Horn K and Seyller T 2012 Decoupling the graphene buffer layer from SiC(0 0 0 1) via interface oxidation *Mater. Sci. Forum* **717–20** 649–52
[686] Walter A L *et al* 2011 Highly p-doped epitaxial graphene obtained by fluorine intercalation *Appl. Phys. Lett.* **98** 184102
[687] Wong S L, Huang H, Wang Y, Cao L, Qi D, Santoso I, Chen W and Wee A T S 2011 Quasi-free-standing epitaxial graphene on SiC (0 0 0 1) by fluorine intercalation from a molecular source *ACS Nano* **5** 7662–8
[688] Masuda Y, Norimatsu W and Kusunoki M 2015 Formation of a nitride interface in epitaxial graphene on SiC (0 0 0 1) *Phys. Rev.* B **91** 104508
[689] Xia C, Watcharinyanon S, Zakharov A A, Yakimova R, Hultman L, Johansson L I and Virojanadara C 2012 Si intercalation/deintercalation of graphene on 6H–SiC(0 0 0 1) *Phys. Rev.* B **85** 045418
[690] Wang F *et al* 2012 Silicon intercalation into the graphene-SiC interface *Phys. Rev.* B **85** 165449
[691] Emtsev K V, Zakharov A A, Coletti C, Forti S and Starke U 2011 Ambipolar doping in quasifree epitaxial graphene on SiC(0 0 0 1) controlled by Ge intercalation *Phys. Rev.* B **84** 125423
[692] Baringhaus J, Stöhr A, Forti S, Starke U and Tegenkamp C 2015 Ballistic bipolar junctions in chemically gated graphene ribbons *Sci. Rep.* **5** 9955
[693] Gierz I *et al* 2010 Electronic decoupling of an epitaxial graphene monolayer by gold intercalation *Phys. Rev.* B **81** 235408
[694] Premlal B, Cranney M, Vonau F, Aubel D, Casterman D, De Souza M M and Simon L 2009 Surface intercalation of gold underneath a graphene monolayer on SiC(0 0 0 1) studied by scanning tunneling microscopy and spectroscopy *Appl. Phys. Lett.* **94** 263115
[695] Pillai P B, Desouza M, Narula R, Reich S, Wong L Y, Batten T and Pokorny J 2015 Decoupling of epitaxial graphene via gold intercalation probed by dispersive Raman spectroscopy *J. Appl. Phys.* **117** 183103
[696] Marchenko D, Varykhalov A, Sánchez-Barriga J, Seyller T and Rader O 2016 Rashba splitting of 100 meV in Au-intercalated graphene on SiC *Appl. Phys. Lett.* **108** 172405
[697] Yagyu K, Tajiri T, Kohno A, Takahashi K, Tochihara H, Tomokage H and Suzuki T 2014 Fabrication of a single layer graphene by copper intercalation on a SiC(0 0 0 1) surface *Appl. Phys. Lett.* **104** 053115
[698] Virojanadara C, Watcharinyanon S, Zakharov A A and Johansson L I 2010 Epitaxial graphene on 6H–SiC and Li intercalation *Phys. Rev.* B **82** 205402
[699] Virojanadara C, Watcharinyanon S, Zakharov A A, Yakimova R and Johansson L I 2012 Studies of Li intercalation into epitaxial graphene on SiC(0 0 0 1) *Mater. Sci. Forum* **717–20** 653–6
[700] Xia C, Watcharinyanon S, Zakharov A A, Johansson L I, Yakimova R and Virojanadara C 2013 Detailed studies of Na intercalation on furnace-grown graphene on 6H–SiC(0 0 0 1) *Surf. Sci.* **613** 88–94
[701] Seyller T 2005 Hydrogen-saturated SiC-surfaces: model systems for studies of passivation, reconstruction, and interface formation *5th European Conf. on Silicon Carbide and Related Materials, ECRSCRM2004* vol 483–5 pp 535–40
[702] Seyller T *et al* 2006 Structural and electronic properties of graphite layers grown on SiC(0 0 0 1) *Surf. Sci.* **600** 3906–11
[703] Sieber N, Mantel B F, Seyller T, Ristein J, Ley L, Heller T, Batchelor D R and Schmeisser D 2001 Electronic and chemical passivation of hexagonal 6H–SiC surfaces by hydrogen termination *Appl. Phys. Lett.* **78** 1216–8
[704] Speck F, Ostler M, Röhrl J, Jobst J, Waldmann D, Hundhausen M, Ley L, Weber H B and Seyller T 2010 Quasi-freestanding graphene on SiC(0 0 0 1) *Mater. Sci. Forum* **645–8** 629–32
[705] Daniels K M, Jadidi M M, Sushkov A B, Boyd A K, Nath A, Drew H D, Murphy T E, Myers-Ward R L and Gaskill D K 2016 Narrow terahertz plasmon resonance of quasi-freestanding bilayer epitaxial graphene *2016 74th Annual Device Research Conf.* pp 1–2
[706] Tanabe S, Sekine Y, Kageshima H and Hibino H 2012 Electrical characterization of bilayer graphene formed by hydrogen intercalation of monolayer graphene on SiC(0 0 0 1) *Japan. J. Appl. Phys.* **51** 02BN02
[707] Mammadov S, Ristein J, Krone J, Raidel C, Wanke M, Wiesmann V, Speck F and Seyller T 2017 Work function of graphene multilayers on SiC(0 0 0 1) *2D Mater.* **4** 015043

[708] Mammadov S, Ristein J, Koch R J, Ostler M, Raidel C, Wanke M, Vasiliauskas R, Yakimova R and Seyller T 2014 Polarization doping of graphene on silicon carbide *2D Mater.* **1** 035003
[709] Ristein J, Mammadov S and Seyller T 2012 Origin of doping in quasi-free-standing graphene on silicon carbide *Phys. Rev. Lett.* **108** 246104
[710] Sławińska J, Aramberri H, Muñoz M C and Cerdá J I 2015 *Ab initio* study of the relationship between spontaneous polarization and p-type doping in quasi-freestanding graphene on H-passivated SiC surfaces *Carbon* **93** 88–104
[711] Ferralis N and Carraro C 2014 Evolution of interfacial intercalation chemistry on epitaxial graphene/SiC by surface enhanced Raman spectroscopy *Appl. Surf. Sci.* **320** 441–7
[712] Melios C, Spencer S, Shard A, Strupiński W, Silva S R P and Kazakova O 2016 Surface and interface structure of quasi-free standing graphene on SiC *2D Mater.* **3** 025023
[713] Robinson J A, Hollander M, LaBella M, Trumbull K A, Cavalero R and Snyder D W 2011 Epitaxial graphene transistors: enhancing performance via hydrogen intercalation *Nano Lett.* **11** 3875–80
[714] Ciuk T and Strupinski W 2015 Statistics of epitaxial graphene for Hall effect sensors *Carbon* **93** 1042–9
[715] Murata Y, Mashoff T, Takamura M, Tanabe S, Hibino H, Beltram F and Heun S 2014 Correlation between morphology and transport properties of quasi-free-standing monolayer graphene *Appl. Phys. Lett.* **105** 221604
[716] Pallecchi E, Lafont F, Cavaliere V, Schopfer F, Mailly D, Poirier W and Ouerghi A 2014 High electron mobility in epitaxial graphene on 4H–SiC(0 0 0 1) via post-growth annealing under hydrogen *Sci. Rep.* **4** 4558
[717] Tanabe S, Takamura M, Harada Y, Kageshima H and Hibino H 2012 Quantum Hall effect and carrier scattering in quasi-free-standing monolayer graphene *Appl. Phys. Express* **5** 125101
[718] Tanabe S, Takamura M, Harada Y, Kageshima H and Hibino H 2014 Effects of hydrogen intercalation on transport properties of quasi-free-standing monolayer graphene *Japan. J. Appl. Phys.* **53** 115101
[719] Sieber N 2002 *Wasserstoff- und Sauerstofftabilisierte 6H–SiC{0 0 0 1}-Oberflächen—Eine Studie Chemischer, Struktureller und Elektronischer Eigenschaften* (Friedrich-Alexander-Universität Erlangen-Nürnberg)
[720] Sieber N, Seyller T, Ley L, James D, Riley J D, Leckey R C G and Polcik M 2003 Synchrotron x-ray photoelectron spectroscopy study of hydrogen-terminated 6H–SiC{0 0 0 1} surfaces *Phys. Rev.* B **67** 205304
[721] Emery J D, Wheeler V H, Johns J E, McBriarty M E, Detlefs B, Hersam M C, Gaskill D K and Bedzyk M J 2014 Structural consequences of hydrogen intercalation of epitaxial graphene on SiC(0 0 0 1) *Appl. Phys. Lett.* **105** 161602
[722] Deretzis I and Magna A L 2013 Process simulation of hydrogen intercalation in epitaxial graphene on SiC(0 0 0 1) *Phys. Status Solidi* b **250** 1478–82
[723] Deretzis I and La Magna A 2011 Role of covalent and metallic intercalation on the electronic properties of epitaxial graphene on SiC(0 0 0 1) *Phys. Rev.* B **84** 235426
[724] Fromm F, Oliveira J M H, Molina-Sánchez A, Hundhausen M, Lopes J M J, Riechert H, Wirtz L and Seyller T 2013 Contribution of the buffer layer to the Raman spectrum of epitaxial graphene on SiC(0 0 0 1) *New J. Phys.* **15** 043031
[725] Giannazzo F, Hertel S, Albert A, La Magna A, Roccaforte F, Krieger M and Weber H B 2014 Electrical nanocharacterization of epitaxial graphene/silicon carbide Schottky contacts *Silicon Carbide and Related Materials 2013, Parts 1 and* 2 ed H Okumura *et al* (Stafa-Zurich: Trans Tech Publications Ltd) pp 1142–5
[726] Caffrey N M, Armiento R, Yakimova R and Abrikosov I A 2015 Charge neutrality in epitaxial graphene on 6H–SiC(0 0 0 1) via nitrogen intercalation *Phys. Rev.* B **92** 081490
[727] Rubio-Roy M, Zaman F, Hu Y K, Berger C, Moseley M W, Meindl J D and de Heer W A 2010 Structured epitaxial graphene growth on SiC by selective graphitization using a patterned AlN cap *Appl. Phys. Lett.* **96** 082112
[728] Puybaret R, Hankinson J, Palmer J, Bouvier C, Ougazzaden A, Voss P L, Berger C and de Heer W A 2015 Scalable control of graphene growth on 4H–SiC C-face using decomposing silicon nitride masks *J. Phys. D: Appl. Phys.* **48** 152001
[729] Han M Y, Brant J C and Kim P 2010 Electron transport in disordered graphene nanoribbons *Phys. Rev. Lett.* **104** 056801
[730] Stampfer C *et al* 2011 Transport in graphene nanostructures *Frontiers Phys.* **6** 271–93
[731] Hicks J *et al* 2013 A wide-bandgap metal-semiconductor-metal nanostructure made entirely from graphene *Nat. Phys.* **9** 49–54
[732] Yakimova R, Iakimov T, Yazdi G R, Bouhafs C, Eriksson J, Zakharov A, Boosalis A, Schubert M and Darakchieva V 2014 Morphological and electronic properties of epitaxial graphene on SiC *Physica* B **439** 54–9
[733] Ruan M, Hu Y, Guo Z, Dong R, Palmer J, Hankinson J, Berger C and de Heer W A 2012 Epitaxial graphene on silicon carbide: introduction to structured graphene *MRS Bull.* **37** 1138–47
[734] Palacio I *et al* 2014 Atomic structure of epitaxial graphene sidewall nanoribbons: flat graphene, miniribbons, and the confinement gap *Nano Lett.* **15** 182–9
[735] Norimatsu W and Kusunoki M 2010 Formation process of graphene on SiC (0 0 0 1) *Physica* E **42** 691–4
[736] Baringhaus J, Aprojanz J, Wiegand J, Laube D, Halbauer M, Hubner J, Oestreich M and Tegenkamp C 2015 Growth and characterization of sidewall graphene nanoribbons *Appl. Phys. Lett.* **106** 043109
[737] Dong R, Guo Z L, Palmer J, Hu Y K, Ruan M, Hankinson J, Kunc J, Bhattacharya S K, Berger C and de Heer W A 2014 Wafer bonding solution to epitaxial graphene-silicon integration *J. Phys. D: Appl. Phys.* **47** 904001
[738] Suemitsu M, Jiao S, Fukidome H, Tateno Y, Makabe I and Nakabayashi T 2014 Epitaxial graphene formation on 3C–SiC/Si thin films *J. Phys. D: Appl. Phys.* **47** 094016
[739] Aristov V Y *et al* 2010 Graphene synthesis on cubic SiC/Si wafers. Perspectives for mass production of graphene-based electronic devices *Nano Lett.* **10** 992–5
[740] Ouerghi A *et al* 2011 Sharp interface in epitaxial graphene layers on 3C–SiC(1 0 0)/Si(1 0 0) wafers *Phys. Rev.* B **83** 205429
[741] Zarotti F, Gupta B, Iacopi F, Sgarlata A, Tomellini M and Motta N 2016 Time evolution of graphene growth on SiC as a function of annealing temperature *Carbon* **98** 307–12
[742] Iacopi F, Mishra N, Cunning B V, Goding D, Dimitrijev S, Brock R, Dauskardt R H, Wood B and Boeckl J 2015 A catalytic alloy approach for graphene on epitaxial SiC on silicon wafers *J. Mater. Res.* **30** 609–16
[743] Strupinski W, Grodecki K, Caban P, Ciepielewski P, Jozwik-Biala I and Baranowski J M 2015 Formation mechanism of graphene buffer layer on SiC(0 0 0 1) *Carbon* **81** 63–72
[744] Strupinski W 2010 Method of graphene manufacturing PAT-213291 *US* 9,067,796 B2; JP 5662249; ZL 201180027996.X; Korea 10-1465452; EP 11168749.7
[745] Weber M E 1974 *Momentum, Heat and Mass Transfer* 2nd edn ed C O Bennett and J E Myers (New York: McGraw-Hill) p 810 Weber M E 1974 *AIChE J.* **20** 1037
[746] Ciuk T, Petruk O, Kowalik A, Jozwik I, Rychter A, Szmidt J and Strupinski W 2016 Low-noise epitaxial graphene on SiC Hall effect element for commercial applications *Appl. Phys. Lett.* **108** 223504
[747] Tokarczyk M, Kowalski G, Możdżonek M, Borysiuk J, Stępniewski R, Strupiński W, Ciepielewski P and Baranowski J M 2013 Structural investigations of hydrogenated epitaxial graphene grown on 4H–SiC (0 0 0 1) *Appl. Phys. Lett.* **103** 241915
[748] Ciuk T, Cakmakyapan S, Ozbay E, Caban P, Grodecki K, Krajewska A, Pasternak I, Szmidt J and Strupinski W 2014 Step-edge-induced resistance anisotropy in quasi-free-standing bilayer chemical vapor deposition graphene on SiC *J. Appl. Phys.* **116** 123708
[749] Melios C, Panchal V, Giusca C E, Strupiński W, Silva S R P and Kazakova O 2015 Carrier type inversion in quasi-free standing graphene: studies of local electronic and structural properties *Sci. Rep.* **5** 10505

[750] Habibpour O, He Z S, Strupinski W, Rorsman N and Zirath H 2017 Wafer scale millimeter-wave integrated circuits based on epitaxial graphene in high data rate communication *Sci. Rep.* **7** 41828
[751] Strupinski W 2017 unpublished
[752] Karu A E and Beer M 1966 Pyrolytic formation of highly crystalline graphite films *J. Appl. Phys.* **37** 2179–81
[753] Shelton J C, Patil H R and Blakely J M 1974 Equilibrium segretation of carbon to a nickel(1 1 1) surface: a surface phase transition *Surf. Sci.* **43** 493–520
[754] Eizenberg M and Blakely J M 1979 Carbon interaction with nickel surfaces: monolayer formation and structural stability *J. Chem. Phys.* **71** 3467–77
[755] Li X, Magnuson C W, Venugopal A, An J, Suk J W, Han B, Borysiak M, Cai W, Velamakanni A and Zhu Y 2010 Graphene films with large domain size by a two-step chemical vapor deposition process *Nano Lett.* **10** 4328–34
[756] Reina A, Jia X, Ho J, Nezich D, Son H, Bulovic V, Dresselhaus M S and Kong J 2009 Large area, few-layer graphene films on arbitrary substrates by chemical vapor deposition *Nano Lett.* **9** 30–5
[757] Chae S J *et al* 2009 Synthesis of large-area graphene layers on poly-nickel substrate by chemical vapor deposition: wrinkle formation *Adv. Mater.* **21** 2328–33
[758] Cabrero-Vilatela A, Weatherup R S, Braeuninger-Weimer P, Caneva S and Hofmann S 2016 Towards a general growth model for graphene CVD on transition metal catalysts *Nanoscale* **8** 2149–58
[759] Kim K S, Zhao Y, Jang H, Lee S Y, Kim J M, Kim K S, Ahn J H, Kim P, Choi J Y and Hong B H 2009 Large-scale pattern growth of graphene films for stretchable transparent electrodes *Nature* **457** 706–10
[760] De Arco L G, Zhang Y, Schlenker C W, Ryu K, Thompson M E and Zhou C W 2010 Continuous, highly flexible, and transparent graphene films by chemical vapor deposition for organic photovoltaics *ACS Nano* **4** 2865–73
[761] Ramón M E *et al* 2011 CMOS-compatible synthesis of large-area, high-mobility graphene by chemical vapor deposition of acetylene on cobalt thin films *ACS Nano* **5** 7198–204
[762] Gong Y P *et al* 2012 Layer-controlled and wafer-scale synthesis of uniform and high-quality graphene films on a polycrystalline nickel catalyst *Adv. Funct. Mater.* **22** 3153–9
[763] Lin W-H, Chen T-H, Chang J-K, Taur J-I, Lo Y-Y, Lee W-L, Chang C-S, Su W-B and Wu C-I 2014 A direct and polymer-free method for transferring graphene grown by chemical vapor deposition to any substrate *ACS Nano* **8** 1784–91
[764] Liang X L *et al* 2011 Toward clean and crackless transfer of graphene *ACS Nano* **5** 9144–53
[765] Li X *et al* 2009 Large-area synthesis of high-quality and uniform graphene films on copper foils *Science* **324** 1312–4
[766] Miseikis V *et al* 2015 Rapid CVD growth of millimetre-sized single crystal graphene using a cold-wall reactor *2D Mater.* **2** 014006
[767] Huang L, Chang Q H, Guo G L, Liu Y, Xie Y Q, Wang T, Ling B and Yang H F 2012 Synthesis of high-quality graphene films on nickel foils by rapid thermal chemical vapor deposition *Carbon* **50** 551–6
[768] Kim Y, Song W, Lee S Y, Jeon C, Jung W, Kim M and Park C Y 2011 Low-temperature synthesis of graphene on nickel foil by microwave plasma chemical vapor deposition *Appl. Phys. Lett.* **98** 263106
[769] Vlassiouk I, Fulvio P, Meyer H, Lavrik N, Dai S, Datskos P and Smirnov S 2013 Large scale atmospheric pressure chemical vapor deposition of graphene *Carbon* **54** 58–67
[770] Luo Z T, Lu Y, Singer D W, Berck M E, Somers L A, Goldsmith B R and Johnson A T C 2011 Effect of substrate roughness and feedstock concentration on growth of wafer-scale graphene at atmospheric pressure *Chem. Mater.* **23** 1441–7
[771] Liu L *et al* 2012 A systematic study of atmospheric pressure chemical vapor deposition growth of large-area monolayer graphene *J. Mater. Chem.* **22** 1498–503
[772] Tan Y Y, Jayawardena K, Adikaari A, Tan L W, Anguita J V, Henley S J, Stolojan V, Carey J D and Silva S R P 2012 Photo-thermal chemical vapor deposition growth of graphene *Carbon* **50** 668–73
[773] Ryu J *et al* 2014 Fast synthesis of high-performance graphene films by hydrogen-free rapid thermal chemical vapor deposition *ACS Nano* **8** 950–6
[774] Muñoz R, Munuera C, Martínez J I, Azpeitia J, Gómez-Aleixandre C and García-Hernández M 2016 Low temperature metal free growth of graphene on insulating substrates by plasma assisted chemical vapor deposition *2D Mater.* **4** 015009
[775] Riikonen J, Kim W, Li C, Svensk O, Arpiainen S, Kainlauri M and Lipsanen H 2013 Photo-thermal chemical vapor deposition of graphene on copper *Carbon* **62** 43–50
[776] Mathieu G, Guiot S and Cabane J 1973 Solubility of carbon in silver, copper and gold *Scr. Metall.* **7** 421–5
[777] McLellan R B 1969 Solubility of carbon in solid gold copper and silver *Scr. Metall.* **3** 389–91
[778] Eizenberg M and Blakely J M 1979 Carbon monolayer phase condensation on Ni(1 1 1) *Surf. Sci.* **82** 228–36
[779] Wang Y, Zheng Y, Xu X F, Dubuisson E, Bao Q L, Lu J and Loh K P 2011 Electrochemical delamination of CVD-grown graphene film: toward the recyclable use of copper catalyst *ACS Nano* **5** 9927–33
[780] Ciuk T, Pasternak I, Krajewska A, Sobieski J, Caban P, Szmidt J and Strupinski W 2013 Properties of chemical vapor deposition graphene transferred by high-speed electrochemical delamination *J. Phys. Chem.* C **117** 20833–7
[781] Li X, Cai W, Colombo L and Ruoff R S 2009 Evolution of graphene growth on Ni and Cu by carbon isotope labeling *Nano Lett.* **9** 4268–72
[782] Ma T, Ren W, Zhang X, Liu Z, Gao Y, Yin L C, Ma X L, Ding F and Cheng H M 2013 Edge-controlled growth and kinetics of single-crystal graphene domains by chemical vapor deposition *Proc. Natl Acad. Sci. USA* **110** 20386–91
[783] Hao Y F *et al* 2016 Oxygen-activated growth and bandgap tunability of large single-crystal bilayer graphene *Nat. Nanotechnol.* **11** 426–31
[784] Nie S, Wu W, Xing S R, Yu Q K, Bao J M, Pei S S and McCarty K F 2012 Growth from below: bilayer graphene on copper by chemical vapor deposition *New J. Phys.* **14** 093028
[785] Braeuninger-Weimer P, Brennan B, Pollard A J and Hofmann S 2016 Understanding and controlling Cu-catalyzed graphene nucleation: the role of impurities, roughness, and oxygen scavenging *Chem. Mater.* **28** 8905–15
[786] Vlassiouk I *et al* 2013 Graphene nucleation density on copper: fundamental role of background pressure *J. Phys. Chem.* C **117** 18919–26
[787] Li X 2009 personal communication Austin, TX
[788] Li X *et al* 2010 Graphene films with large domain size by a two-step chemical vapor deposition process *Nano Lett.* **10** 4328–34
[789] Gao L *et al* 2010 Efficient growth of high-quality graphene films on Cu foils by ambient pressure chemical vapor deposition *Appl. Phys. Lett.* **97** 183109
[790] López G A and Mittemeijer E J 2004 The solubility of C in solid Cu *Scr. Mater.* **51** 1–5
[791] Hao Y *et al* 2013 The role of surface oxygen in the growth of large single-crystal graphene on copper *Science* **342** 720–3
[792] Artyukhov V I, Liu Y and Yakobson B I 2012 Equilibrium at the edge and atomistic mechanisms of graphene growth *Proc. Natl Acad. Sci. USA* **109** 15136–40
[793] Kim H, Mattevi C, Calvo M R, Oberg J C, Artiglia L, Agnoli S, Hirjibehedin C F, Chhowalla M and Saiz E 2012 Activation energy paths for graphene nucleation and growth on Cu *ACS Nano* **6** 3614–23
[794] Xu X *et al* 2017 Ultrafast epitaxial growth of metre-sized single-crystal graphene on industrial Cu foil *Sci. Bull.* **62** 1074–80
[795] Nie S, Wofford J M, Bartelt N C, Dubon O D and McCarty K F 2011 Origin of the mosaicity in graphene grown on Cu(1 1 1) *Phys. Rev.* B **84** 155425
[796] Jacobberger R M and Arnold M S 2013 Graphene growth dynamics on epitaxial copper thin films *Chem. Mater.* **25** 871–7

[797] Yan Z, Lin J, Peng Z W, Sun Z Z, Zhu Y, Li L, Xiang C S, Samuel E L, Kittrell C and Tour J M 2012 Toward the synthesis of wafer-scale single-crystal graphene on copper foils *ACS Nano* **6** 9110–7
[798] Wang H, Wang G Z, Bao P F, Yang S L, Zhu W, Xie X and Zhang W J 2012 Controllable synthesis of submillimeter single-crystal monolayer graphene domains on copper foils by suppressing nucleation *J. Am. Chem. Soc.* **134** 3627–30
[799] Wu Y A, Fan Y, Speller S, Creeth G L, Sadowski J T, He K, Robertson A W, Allen C S and Warner J H 2012 Large single crystals of graphene on melted copper using chemical vapor deposition *ACS Nano* **6** 5010–7
[800] Wu B, Geng D C, Xu Z P, Guo Y L, Huang L P, Xue Y Z, Chen J Y, Yu G and Liu Y Q 2013 Self-organized graphene crystal patterns *Npg Asia Mater.* **5** e36
[801] Robinson Z R, Ong E W, Mowll T R, Tyagi P, Gaskill D K, Geisler H and Ventrice C A 2013 Influence of chemisorbed oxygen on the growth of graphene on Cu(1 0 0) by chemical vapor deposition *J. Phys. Chem.* C **117** 23919–27
[802] Su C-Y *et al* 2011 Direct formation of wafer scale graphene thin layers on insulating substrates by chemical vapor deposition *Nano Lett.* **11** 3612–6
[803] Bointon T H, Barnes M D, Russo S and Craciun M F 2015 High quality monolayer graphene synthesized by resistive heating cold wall chemical vapor deposition *Adv. Mater.* **27** 4200–6
[804] Geng D, Wu B, Guo Y, Huang L, Xue Y, Chen J, Yu G, Jiang L, Hu W and Liu Y 2012 Uniform hexagonal graphene flakes and films grown on liquid copper surface *Proc. Natl Acad. Sci.* **109** 7992–6
[805] Piner R *et al* 2013 Graphene synthesis via magnetic inductive heating of copper substrates *ACS Nano* **7** 7495–9
[806] Hawaldar R, Merino P, Correia M R, Bdikin I, Gracio J, Mendez J, Martin-Gago J A and Singh M K 2012 Large-area high-throughput synthesis of monolayer graphene sheet by hot filament thermal chemical vapor deposition *Sci. Rep.* **2** 682
[807] Chen S, Ji H, Chou H, Li Q, Li H, Suk J W, Piner R, Liao L, Cai W and Ruoff R S 2013 Millimeter-size single-crystal graphene by suppressing evaporative loss of Cu during low pressure chemical vapor deposition *Adv. Mater.* **25** 2062–5
[808] Cummings A W, Duong D L, Nguyen V L, Tuan D V, Kotakoski J, Vargas J E B, Lee Y H and Roche S 2014 Charge transport in polycrystalline graphene: challenges and opportunities *Adv. Mater.* **26** 5079–94
[809] Isacsson A, Cummings A W, Colombo L, Colombo L, Kinaret J M and Roche S 2017 Scaling properties of polycrystalline graphene: a review *2D Mater.* **4** 012002
[810] Yazyev O V and Louie S G 2010 Electronic transport in polycrystalline graphene *Nat. Mater.* **9** 806–9
[811] Grantab R, Shenoy V B and Ruoff R S 2010 Anomalous strength characteristics of tilt grain boundaries in graphene *Science* **330** 946–8
[812] Wlasny I, Dabrowski P, Rogala M, Kowalczyk P J, Pasternak I, Strupinski W, Baranowski J M and Klusek Z 2013 Publisher's note: 'role of graphene defects in corrosion of graphene-coated Cu(1 1 1) surface' [*Appl. Phys. Lett.* **102** 111601] *Appl. Phys. Lett.* **102** 149901
[813] Kim W, Li C, Chekurov N, Arpiainen S, Akinwande D, Lipsanen H and Riikonen J 2015 All-graphene three-terminal-junction field-effect devices as rectifiers and inverters *ACS Nano* **9** 5666–74
[814] Kwak J *et al* 2012 Near room-temperature synthesis of transfer-free graphene films *Nat. Commun.* **3** 645
[815] Addou R, Dahal A, Sutter P and Batzill M 2012 Monolayer graphene growth on Ni(1 1 1) by low temperature chemical vapor deposition *Appl. Phys. Lett.* **100** 021601
[816] Muñoz R and Gómez-Aleixandre C 2013 Fast and non-catalytic growth of transparent and conductive graphene-like carbon films on glass at low temperature *J. Phys. D: Appl. Phys.* **47** 045305
[817] Weatherup R S, Baehtz C, Dlubak B, Bayer B C, Kidambi P R, Blume R, Schloegl R and Hofmann S 2013 Introducing carbon diffusion barriers for uniform, high-quality graphene growth from solid sources *Nano Lett.* **13** 4624–31
[818] Li X *et al* 2010 Graphene films with large domain size by a two-step chemical vapor deposition process *Nano Lett.* **10** 4328 – 34
[819] Gan L and Luo Z 2013 Turning off hydrogen to realize seeded growth of subcentimeter single-crystal graphene grains on copper *ACS Nano* **7** 9480–8
[820] Fang W, Hsu A L, Song Y, Birdwell A G, Amani M, Dubey M, Dresselhaus M S, Palacios T and Kong J 2014 Asymmetric growth of bilayer graphene on copper enclosures using low-pressure chemical vapor deposition *ACS Nano* **8** 6491–9
[821] Petrone N, Dean C R, Meric I, van der Zande A M, Huang P Y, Wang L, Muller D, Shepard K L and Hone J 2012 Chemical vapor deposition-derived graphene with electrical performance of exfoliated graphene *Nano Lett.* **12** 2751–6
[822] Banszerus L, Janssen H, Otto M, Epping A, Taniguchi T, Watanabe K, Beschoten B, Neumaier D and Stampfer C 2017 Identifying suitable substrates for high-quality graphene-based heterostructures *2D Mater.* **4** 025030
[823] Banszerus L, Schmitz M, Engels S, Goldsche M, Watanabe K, Taniguchi T, Beschoten B and Stampfer C 2016 Ballistic transport exceeding 28 μm in CVD grown graphene *Nano Lett.* **16** 1387–91
[824] Schmitz M, Engels S, Banszerus L, Watanabe K, Taniguchi T, Stampfer C and Beschoten B 2017 High mobility dry-transferred CVD bilayer graphene *Appl. Phys. Lett.* **110** 263110
[825] Xu X *et al* 2016 Ultrafast growth of single-crystal graphene assisted by a continuous oxygen supply *Nat. Nanotechnol.* **11** 930–5
[826] Magnuson C W, Kong X H, Ji H X, Tan C, Li H F, Piner R, Ventrice C A and Ruoff R S 2014 Copper oxide as a 'self-cleaning' substrate for graphene growth *J. Mater. Res.* **29** 403–9
[827] Lin L, Li J Y, Ren H Y, Koh A L, Kang N, Peng H L, Xu H Q and Liu Z F 2016 Surface engineering of copper foils for growing centimeter-sized single-crystalline graphene *ACS Nano* **10** 2922–9
[828] Reckinger N, Tang X, Joucken F, Lajaunie L, Arenal R, Dubois E, Hackens B, Henrard L and Colomer J-F 2016 Oxidation-assisted graphene heteroepitaxy on copper foil *Nanoscale* **8** 18751–9
[829] Kim S M, Hsu A, Lee Y-H, Dresselhaus M, Palacios T, Kim K K and Kong J 2013 The effect of copper pre-cleaning on graphene synthesis *Nanotechnology* **24** 365602
[830] Kim Y, Moyen E, Yi H M, Avila J, Chen C Y, Asensio M C, Lee Y H and Pribat D 2018 Synthesis of high quality graphene on capped (1 1 1) Cu thin films obtained by high temperature secondary grain growth on *c*-plane sapphire substrates *2D Mater.* **5** 035008
[831] Jin S *et al* 2018 Colossal grain growth yields single-crystal metal foils by contact-free annealing *Science* **362** 1021–5
[832] Banszerus L, Schmitz M, Engels S, Dauber J, Oellers M, Haupt F, Watanabe K, Taniguchi T, Beschoten B and Stampfer C 2015 Ultrahigh-mobility graphene devices from chemical vapor deposition on reusable copper *Sci. Adv.* **1** e1500222
[833] Brown L *et al* 2014 Polycrystalline graphene with single crystalline electronic structure *Nano Lett.* **14** 5706–11
[834] Xue X, Xu Q, Wang H, Liu S, Jiang Q, Yu Z, Zhou X, Ma T, Wang L and Yu G 2019 Gas-flow-driven aligned growth of graphene on liquid copper *Chem. Mater.* **31** 1231 – 6
[835] Yu H K, Balasubramanian K, Kim K, Lee J L, Maiti M, Ropers C, Krieg J, Kern K and Wodtke A M 2014 Chemical vapor deposition of graphene on a 'peeled-off' epitaxial Cu(1 1 1) foil: a simple approach to improved properties *ACS Nano* **8** 8636–43
[836] Mishra N, Miseikis V, Convertino D, Gemmi M, Piazza V and Coletti C 2016 Rapid and catalyst-free van der Waals epitaxy of graphene on hexagonal boron nitride *Carbon* **96** 497–502
[837] Wu T *et al* 2016 Fast growth of inch-sized single-crystalline graphene from a controlled single nucleus on Cu–Ni alloys *Nat. Mater.* **15** 43–7

[838] Vlassiouk I V et al 2018 Evolutionary selection growth of two-dimensional materials on polycrystalline substrates Nat. Mater. 17 318–22
[839] Yu Q et al 2011 Control and characterization of individual grains and grain boundaries in graphene grown by chemical vapour deposition Nat. Mater. 10 443–9
[840] Wu W, Jauregui L A, Su Z, Liu Z, Bao J, Chen Y P and Yu Q 2011 Graphene: growth of single crystal graphene arrays by locally controlling nucleation on polycrystalline Cu using chemical vapor deposition (Adv. Mater. 42/2011) Adv. Mater. 23 4897–7
[841] Miseikis V, Bianco F, David J, Gemmi M, Pellegrini V, Romagnoli M and Coletti C 2017 Deterministic patterned growth of high-mobility large-crystal graphene: a path towards wafer scale integration 2D Mater. 4 021004
[842] Luo Z, Kim S, Kawamoto N, Rappe A M and Johnson A T C 2011 Growth mechanism of hexagonal-shape graphene flakes with zigzag edges ACS Nano 5 9154–60
[843] Alcock C B, Itkin V P and Horrigan M K 1984 Vapour pressure equations for the metallic elements: 298–2500 K Can. Metall. Q. 23 309–13
[844] Guermoune A, Chari T, Popescu F, Sabri S S, Guillemette J, Skulason H S, Szkopek T and Siaj M 2011 Chemical vapor deposition synthesis of graphene on copper with methanol, ethanol, and propanol precursors Carbon 49 4204–10
[845] Srivastava A, Galande C, Ci L, Song L, Rai C, Jariwala D, Kelly K F and Ajayan P M 2010 Novel liquid precursor-based facile synthesis of large-area continuous, single, and few-layer graphene films Chem. Mater. 22 3457–61
[846] Yao Y G, Li Z, Lin Z Y, Moon K S, Agar J and Wong C P 2011 Controlled growth of multilayer, few-layer, and single-layer graphene on metal substrates J. Phys. Chem. C 115 5232–8
[847] Li Z, Wu P, Wang C, Fan X, Zhang W, Zhai X, Zeng C, Li Z, Yang J and Hou J 2011 Low-temperature growth of graphene by chemical vapor deposition using solid and liquid carbon sources ACS Nano 5 3385–90
[848] Zhang B, Lee W H, Piner R, Kholmanov I, Wu Y P, Li H F, Ji H X and Ruoff R S 2012 Low-temperature chemical vapor deposition growth of graphene from toluene on electropolished copper foils ACS Nano 6 2471–6
[849] Jang J, Son M, Chung S, Kim K, Cho C, Lee B H and Ham M-H 2015 Low-temperature-grown continuous graphene films from benzene by chemical vapor deposition at ambient pressure Sci. Rep. 5 12402
[850] Wirtz C, Lee K, Hallam T and Duesberg G S 2014 Growth optimisation of high quality graphene from ethene at low temperatures Chem. Phys. Lett. 595 192–6
[851] Chan J, Venugopal A, Pirkle A, McDonnell S, Hinojos D, Magnuson C W, Ruoff R S, Colombo L, Wallace R M and Vogel E M 2012 Reducing extrinsic performance-limiting factors in graphene grown by chemical vapor deposition ACS Nano 6 3224–9
[852] Boyd D A et al 2015 Single-step deposition of high-mobility graphene at reduced temperatures Nat. Commun. 6 6620
[853] Tontegode A Y 1991 Carbon on transition metal surfaces Prog. Surf. Sci. 38 201–429
[854] Cai M, Outlaw R A, Quinlan R A, Premathilake D, Butler S M and Miller J R 2014 Fast response, vertically oriented graphene nanosheet electric double layer capacitors synthesized from C_2H_2 ACS Nano 8 5873–82
[855] Miller J R, Outlaw R A and Holloway B C 2010 Graphene double-layer capacitor with ac line-filtering performance Science 329 1637–9
[856] Miller J R, Outlaw R A and Holloway B C 2011 Graphene electric double layer capacitor with ultra-high-power performance Electrochim. Acta 56 10443–9
[857] Nicholson M E 1962 Solubility of carbon in nickel-copper alloys at 1000 degrees C Trans. Metall. Soc. Aime 224 533
[858] Hasebe M, Ohtani H and Nishizawa T 1985 Effect of magnetic transition on solubility of carbon in bcc Fe and fee Co–Ni alloys Metall. Trans. A 16 913–21
[859] Amato G, Beccaria F and Celegato F 2017 Growth of strained, but stable, graphene on Co Thin Solid Films 638 324–31
[860] Zeng M, Wang W-L and Bai X-D 2013 Preparing three-dimensional graphene architectures: Review of recent developments Chin. Phys. B 22 098105
[861] Chen Z, Ren W, Gao L, Liu B, Pei S and Cheng H-M 2011 Three-dimensional flexible and conductive interconnected graphene networks grown by chemical vapour deposition Nat. Mater. 10 424–8
[862] Li N, Chen Z, Ren W, Li F and Cheng H M 2012 Flexible graphene-based lithium ion batteries with ultrafast charge and discharge rates Proc. Natl Acad. Sci. 109 17360–5
[863] Chen Z, Xu C, Ma C, Ren W and Cheng H-M 2013 Lightweight and flexible graphene foam composites for high-performance electromagnetic interference shielding Adv. Mater. 25 1296–300
[864] Cao X, Shi Y, Shi W, Lu G, Huang X, Yan Q, Zhang Q and Zhang H 2011 Preparation of novel 3D graphene networks for supercapacitor applications Small 7 3163–8
[865] Zhang W et al 2017 Nitrogen-superdoped 3D graphene networks for high-performance supercapacitors Adv. Mater. 29 1701677
[866] Hu G, Xu C, Sun Z, Wang S, Cheng H-M, Li F and Ren W 2015 3D graphene-foam-reduced-graphene-oxide hybrid nested hierarchical networks for high-performance Li-S batteries Adv. Mater. 28 1603–9
[867] Zhu L, Peng H-J, Liang J, Huang J-Q, Chen C-M, Guo X, Zhu W, Li P and Zhang Q 2015 Interconnected carbon nanotube/graphene nanosphere scaffolds as free-standing paper electrode for high-rate and ultra-stable lithium–sulfur batteries Nano Energy 11 746–55
[868] Yavari F, Chen Z, Thomas A V, Ren W, Cheng H-M and Koratkar N 2011 High sensitivity gas detection using a macroscopic three-dimensional graphene foam network Sci. Rep. 1 166
[869] Chen W, Fan Z, Zeng G and Lai Z 2013 Layer-dependent supercapacitance of graphene films grown by chemical vapor deposition on nickel foam J. Power Sources 225 251–6
[870] Li N, Zhang Q, Gao S, Song Q, Huang R, Wang L, Liu L, Dai J, Tang M and Cheng G 2013 Three-dimensional graphene foam as a biocompatible and conductive scaffold for neural stem cells Sci. Rep. 3 1604
[871] Singh E, Chen Z, Houshmand F, Ren W, Peles Y, Cheng H-M and Koratkar N 2012 Superhydrophobic graphene foams Small 9 75–80
[872] Jeong Y R, Park H, Jin S W, Hong S Y, Lee S-S and Ha J S 2015 Highly stretchable and sensitive strain sensors using fragmentized graphene foam Adv. Funct. Mater. 25 4228–36
[873] Christian L O M, Liscio F, Rizzoli R, Palermo V and Morandi V 2017 Synthesis of high-density graphene foams using nanoparticle templates GraphITA ed V Morandi and L Ottaviano (Bologna: Springer) pp 185–96
[874] Wang L, Li X, Guo T, Yan X and Tay B K 2014 Three-dimensional $Ni(OH)_2$ nanoflakes/graphene/nickel foam electrode with high rate capability for supercapacitor applications Int. J. Hydrogen Energy 39 7876–84
[875] Drieschner S, Weber M, Wohlketzetter J, Vieten J, Makrygiannis E, Blaschke B M, Morandi V, Colombo L, Bonaccorso F and Garrido J A 2016 High surface area graphene foams by chemical vapor deposition 2D Mater. 3 045013
[876] Dai B, Fu L, Zou Z, Wang M, Xu H, Wang S and Liu Z 2011 Rational design of a binary metal alloy for chemical vapour deposition growth of uniform single-layer graphene Nat. Commun. 2 522
[877] Kim E S, Shin H-J, Yoon S-M, Han G H, Chae S J, Bae J J, Gunes F, Choi J-Y and Lee Y H 2011 Low-temperature graphene growth using epochal catalyst of PdCo alloy Appl. Phys. Lett. 99 223102
[878] Weatherup R S, Bayer B C, Blume R, Ducati C, Baehtz C, Schlögl R and Hofmann S 2011 In situ characterization of alloy catalysts for low-temperature graphene growth Nano Lett. 11 4154–60
[879] Zou Z Y, Fu L, Song X J, Zhang Y F and Liu Z F 2014 Carbide-forming groups IVB-VIB metals: a new territory in the

periodic table for CVD Growth of graphene *Nano Lett.* **14** 3832–9
[880] Zou Z Y, Song X J, Chen K, Ji Q Q, Zhang Y F and Liu Z F 2015 Uniform single-layer graphene growth on recyclable tungsten foils *Nano Res.* **8** 592–9
[881] Bhaviripudi S, Jia X, Dresselhaus M S and Kong J 2010 Role of kinetic factors in chemical vapor deposition synthesis of uniform large area graphene using copper catalyst *Nano Lett.* **10** 4128–33
[882] Losurdo M, Giangregorio M M, Capezzuto P and Bruno G 2011 Graphene CVD growth on copper and nickel: role of hydrogen in kinetics and structure *Phys. Chem. Chem. Phys.* **13** 20836
[883] Zhang W, Wu P, Li Z and Yang J 2011 First-principles thermodynamics of graphene growth on Cu surfaces *J. Phys. Chem.* C **115** 17782–7
[884] Niu T, Zhou M, Zhang J, Feng Y and Chen W 2013 Growth intermediates for CVD graphene on Cu(1 1 1): carbon clusters and defective graphene *J. Am. Chem. Soc.* **135** 8409–14
[885] Fogarassy Z, Rümmeli M H, Gorantla S, Bachmatiuk A, Dobrik G, Kamarás K, Biró L P, Havancsák K and Lábár J L 2014 Dominantly epitaxial growth of graphene on Ni (1 1 1) substrate *Appl. Surf. Sci.* **314** 490–9
[886] Al-Shurman H N K M 2014 Chemical vapor deposition (CVD) growth of graphene films *Proc. of the 2014 COMSOL Conf. in Boston* (Elsevier) pp 27–49
[887] Lahiri J, Miller T, Adamska L, Oleynik I I and Batzill M 2011 Graphene growth on Ni(1 1 1) by transformation of a surface carbide *Nano Lett.* **11** 518–22
[888] Reina A and Kong J 2012 Graphene growth by CVD methods *Graphene Nanoelectronics* (Berlin: Springer) pp 167–203
[889] Baraton L, He Z B, Lee C S, Cojocaru C S, Châtelet M, Maurice J L, Lee Y H and Pribat D 2011 On the mechanisms of precipitation of graphene on nickel thin films *Europhys. Lett.* **96** 46003
[890] Cushing G W, Johánek V, Navin J K and Harrison I 2015 Graphene growth on Pt(1 1 1) by ethylene chemical vapor deposition at surface temperatures near 1000 K *J. Phys. Chem.* C **119** 4759–68
[891] Ma T, Ren W, Liu Z, Huang L, Ma L-P, Ma X, Zhang Z, Peng L-M and Cheng H-M 2014 Repeated growth–etching–regrowth for large-area defect-free single-crystal graphene by chemical vapor deposition *ACS Nano* **8** 12806–13
[892] Ma T *et al* 2017 Tailoring the thermal and electrical transport properties of graphene films by grain size engineering *Nat. Commun.* **8** 14486
[893] Vlassiouk I, Regmi M, Fulvio P, Dai S, Datskos P, Eres G and Smirnov S 2011 Role of hydrogen in chemical vapor deposition growth of large single-crystal graphene *ACS Nano* **5** 6069–76
[894] Choi J-K *et al* 2014 Growth of wrinkle-free graphene on texture-controlled platinum films and thermal-assisted transfer of large-scale patterned graphene *ACS Nano* **9** 679–86
[895] Rogge P C, Nie S, McCarty K F, Bartelt N C and Dubon O D 2014 Orientation-Dependent Growth Mechanisms of Graphene Islands on Ir(1 1 1) *Nano Lett.* **15** 170–5
[896] Jin L, Fu Q, Zhang H, Mu R, Zhang Y, Tan D and Bao X 2012 Tailoring the growth of graphene on Ru(0 0 0 1) via engineering of the substrate surface *J. Phys. Chem.* C **116** 2988–93
[897] Dong G and Frenken J W M 2013 Kinetics of graphene formation on Rh(1 1 1) investigated by *in situ* scanning tunneling microscopy *ACS Nano* **7** 7028–33
[898] Liu M, Zhang Y, Chen Y, Gao Y, Gao T, Ma D, Ji Q, Zhang Y, Li C and Liu Z 2012 Thinning segregated graphene layers on high carbon solubility substrates of rhodium foils by tuning the quenching process *ACS Nano* **6** 10581–9
[899] Coraux J, N'Diaye A T, Busse C and Michely T 2008 Structural coherency of graphene on Ir(1 1 1) *Nano Lett.* **8** 565–70
[900] Günther S, Dänhardt S, Ehrensperger M, Zeller P, Schmitt S and Wintterlin J 2012 High-temperature scanning tunneling microscopy study of the ordering transition of an amorphous carbon layer into graphene on Ruthenium(0 0 0 1) *ACS Nano* **7** 154–64
[901] Martínez J I, Merino P, Pinardi A L, Gonzalo O-I, López M F, Méndez J and Martín-Gago J A 2016 Role of the pinning points in epitaxial graphene moiré superstructures on the Pt(1 1 1) surface *Sci. Rep.* **6** 20354
[902] Merino P, S?vec M, Pinardi A L, Otero G and Martín-Gago J A 2011 Strain-driven moiré superstructures of epitaxial graphene on transition metal surfaces *ACS Nano* **5** 5627–34
[903] Gsell S, Fischer M, Schreck M and Stritzker B 2009 Epitaxial films of metals from the platinum group (Ir, Rh, Pt and Ru) on YSZ-buffered Si(1 1 1) *J. Cryst. Growth* **311** 3731–6
[904] Zeller P, Dänhardt S, Gsell S, Schreck M and Wintterlin J 2012 Scalable synthesis of graphene on single crystal Ir(1 1 1) films *Surf. Sci.* **606** 1475–80
[905] Hemmi A, Cun H, Roth S, Osterwalder J and Greber T 2014 Low cost photoelectron yield setup for surface process monitoring *J. Vac. Sci. Technol.* A **32** 023202
[906] Marti´nez-Galera A J, Brihuega I N and Go´mez-Rodri´guez J M 2011 Ethylene irradiation: a new route to grow graphene on low reactivity metals *Nano Lett.* **11** 3576–80
[907] Nie S, Bartelt N C, Wofford J M, Dubon O D, McCarty K F and Thürmer K 2012 Scanning tunneling microscopy study of graphene on Au(1 1 1): Growth mechanisms and substrate interactions *Phys. Rev.* B **85** 205406
[908] Lippert G, Dabrowski J, Lemme M, Marcus C, Seifarth O and Lupina G 2011 Direct graphene growth on insulator *Phys. Status Solidi* b **248** 2619–22
[909] Garcia J M *et al* 2012 Graphene growth on h-BN by molecular beam epitaxy *Solid State Commun.* **152** 975–8
[910] Hernández-Rodríguez I, García J M, Martín-Gago J A, de Andrés P L and Méndez J 2015 Graphene growth on Pt(1 1 1) and Au(1 1 1) using a MBE carbon solid-source *Diamond Relat. Mater.* **57** 58–62
[911] Martinez L N P J M G 2008 Devices with graphene layers
[912] Otero G *et al* 2010 Ordered vacancy network induced by the growth of epitaxial graphene on Pt(1 1 1) *Phys. Rev. Lett.* **105** 216102
[913] Pfeiffer L N 2008 Deposition of carbon-containing layers using vitreous carbon source
[914] Harris P J F 1997 Structure of non-graphitising carbons *Int. Mater. Rev.* **42** 206–18
[915] Garcia P W J M 2012 System and methods using a glassy carbon heater
[916] Giannozzi P *et al* 2009 Quantum espresso: a modular and open-source software project for quantum simulations of materials *J. Phys.: Condens. Matter* **21** 395502
[917] Henkelman G and Jónsson H 2000 Improved tangent estimate in the nudged elastic band method for finding minimum energy paths and saddle points *J. Chem. Phys.* **113** 9978–85
[918] Wu Z W P, Li Z, Yang J and Hou J G 2010 Communication: coalescence of carbon atoms on Cu (1 1 1) surface: emergence of a stable bridging-metal structure motif *J. Chem. Phys.* **133** 071101
[919] Bogicevic A, Strömquist J and Lundqvist B I 1998 First-principles diffusion-barrier calculation for atomic oxygen on Pt(1 1 1) *Phys. Rev.* B **57** R4289–92
[920] Taioli S, Garberoglio G, Simonucci S, Beccara S A, Aversa L, Nardi M, Verucchi R, Iannotta S, Dapor M and Alfè D 2013 Non-adiabatic *ab initio* molecular dynamics of supersonic beam epitaxy of silicon carbide at room temperature *J. Chem. Phys.* **138** 044701
[921] Verucchi R, Aversa L, Nardi M V, Taioli S, Beccara S A, Alfè D, Nasi L, Rossi F, Salviati G and Iannotta S 2012 Epitaxy of nanocrystalline silicon carbide on Si(1 1 1) at room temperature *J. Am. Chem. Soc.* **134** 17400–3
[922] Taioli S 2014 Computational study of graphene growth on copper by first-principles and kinetic Monte Carlo calculations *J. Mol. Modeling* **20** 2260
[923] Tatti R, Aversa L, Verucchi R, Cavaliere E, Garberoglio G, Pugno N M, Speranza G and Taioli S 2016 Synthesis of single layer graphene on Cu(1 1 1) by C_{60} supersonic molecular beam epitaxy *RSC Adv.* **6** 37982–93
[924] Kroto H W, Heath J R, O'Brien S C, Curl R F and Smalley R E 1985 C_{60}: buckminsterfullerene *Nature* **318** 162–3

[925] Pinardi A L *et al* 2014 Vacancy formation on C_{60}/Pt (1 1 1): unraveling the complex atomistic mechanism *Nanotechnology* **25** 385602
[926] Azpeitia J *et al* 2017 High-quality PVD graphene growth by fullerene decomposition on Cu foils *Carbon* **119** 535–43
[927] Muñoz R and Gómez-Aleixandre C 2013 Review of CVD synthesis of graphene *Chem. Vap. Depos.* **19** 297–322
[928] Yan Z, Peng Z and Tour J M 2014 Chemical vapor deposition of graphene single crystals *Acc. Chem. Res.* **47** 1327–37
[929] Castro Neto A H, Guinea F, Peres N M R, Novoselov K S and Geim A K 2009 The electronic properties of graphene *Rev. Mod. Phys.* **81** 109–62
[930] Olesinski R W and Abbaschian G J 1984 The C–Ge (carbon–germanium) system *Bull. Alloy Phase Diagr.* **5** 484–6
[931] Lee J-H *et al* 2014 Wafer-scale growth of single-crystal monolayer graphene on reusable hydrogen-terminated germanium *Science* **344** 286–9
[932] Kiraly B, Jacobberger R M, Mannix A J, Campbell G P, Bedzyk M J, Arnold M S, Hersam M C and Guisinger N P 2015 Electronic and mechanical properties of graphene-germanium interfaces grown by chemical vapor deposition *Nano Lett.* **15** 7414–20
[933] Lippert G *et al* 2014 Graphene grown on Ge(0 0 1) from atomic source *Carbon* **75** 104–12
[934] Pasternak I, Dabrowski P, Ciepielewski P, Kolkovsky V, Klusek Z, Baranowski J M and Strupinski W 2016 Large-area high-quality graphene on Ge(0 0 1)/Si(0 0 1) substrates *Nanoscale* **8** 11241–7
[935] Pasternak I, Wesolowski M, Jozwik I, Lukosius M, Lupina G, Dabrowski P, Baranowski J M and Strupinski W 2016 Graphene growth on Ge(1 0 0)/Si(1 0 0) substrates by CVD method *Sci. Rep.* **6** 21773
[936] Baba H 1956 Studies on the reduction processes of germanium dioxide by hydrogen *Bull. Chem. Soc. Japan* **29** 789–93
[937] Hasegawa R, Yagihash T and Kurosawa T 1972 Hydrogen reduction of germanium dioxide *Trans. Japan Inst. Met.* **13** 39
[938] Sun J, Lindvall N and Cole M 2011 Large-area uniform graphene-like thin films grown by chemical vapor deposition directly on silicon nitride *Appl. Phys. Lett.* **98** 252107
[939] Chen J, Guo Y and Wen Y 2013 Two-stage metal-catalyst-free growth of high-quality polycrystalline graphene films on silicon nitride substrates *Adv. Mater.* **25** 992
[940] Hwang J *et al* 2013 van der Waals epitaxial growth of graphene on sapphire by chemical vapor deposition without a metal catalyst *ACS Nano* **7** 385–95
[941] Song H J, Son M and Park C 2012 Large scale metal-free synthesis of graphene on sapphire and transfer-free device fabrication *Nanoscale* **4** 3050
[942] Jerng S K, Yu D S and Kim Y S 2011 Nanocrystalline graphite growth on sapphire by carbon molecular beam epitaxy *J. Phys. Chem.* C **115** 4491
[943] Fanton M A *et al* 2011 Characterization of graphene films and transistors grown on sapphire by metal-free chemical vapor deposition *ACS Nano* **5** 8062–9
[944] Sun J, Lindvall N and Cole M T 2012 Controllable chemical vapor deposition of large area uniform nanocrystalline graphene directly on silicon dioxide *J. Appl. Phys.* **111** 044103
[945] Chen J *et al* 2011 Oxygen-aided synthesis of polycrystalline graphene on silicon dioxide substrates *J. Am. Chem. Soc.* **133** 17548–51
[946] Chen J *et al* 2014 Near-equilibrium chemical vapor deposition of high-quality single-crystal graphene directly on various dielectric substrates *Adv. Mater.* **26** 1348
[947] Ding X, Ding G, Xie X, Huang F and Jiang M 2011 Direct growth of few layer graphene on hexagonal boron nitride by chemical vapor deposition *Carbon* **49** 2522–5
[948] Rümmeli M H, Bachmatiuk A and Scott A 2010 Direct low-temperature nanographene CVD synthesis over a dielectric insulator *ACS Nano* **4** 4206
[949] Sun J *et al* 2014 Direct growth of high-quality graphene on high-κ dielectric $SrTiO_3$ substrates *J. Am. Chem. Soc.* **136** 6574–7
[950] Sun J, Chen Y, Priydarshi M K, Gao T, Song X, Zhang Y and Liu Z 2016 Graphene glass from direct CVD routes: production and applications *Adv. Mater.* **28** 10333–9
[951] Chen Z *et al* 2016 Fast and uniform growth of graphene glass using confined-flow chemical vapor deposition and its unique applications *Nano Res.* **9** 3048–55
[952] Sun J *et al* 2015 Direct chemical vapor deposition-derived graphene glasses targeting wide ranged applications *Nano Lett.* **15** 5846–54
[953] Liu Q, Gong Y, Wang T, Chan W-L and Wu J 2016 Metal-catalyst-free and controllable growth of high-quality monolayer and AB-stacked bilayer graphene on silicon dioxide *Carbon* **96** 203–11
[954] Xu S C, Man B Y, Jiang S Z, Chen C S, Yang C, Liu M, Gao X G, Sun Z C and Zhang C 2013 Direct synthesis of graphene on SiO_2 substrates by chemical vapor deposition *CrystEngComm* **15** 1840–4
[955] Zhao J, Wang G, Yang R, Lu X, Cheng M, He C, Xie G, Meng J, Shi D and Zhang G 2015 Tunable piezoresistivity of nanographene films for strain sensing *ACS Nano* **9** 1622–9
[956] Pang J *et al* 2017 Self-terminating confinement approach for large-area uniform monolayer graphene directly over Si/SiO_x by chemical vapor deposition *ACS Nano* **11** 1946–56
[957] Bi H, Sun S, Huang F, Xie X and Jiang M 2012 Direct growth of few-layer graphene films on SiO_2 substrates and their photovoltaic applications *J. Mater. Chem.* **22** 411–6
[958] Weber N-E, Binder A, Kettner M, Hirth S, Weitz R T and Tomovic Ž 2017 Metal-free synthesis of nanocrystalline graphene on insulating substrates by carbon dioxide-assisted chemical vapor deposition *Carbon* **112** 201–7
[959] Iwai H 2009 Roadmap for 22 nm and beyond (invited paper) *Microelectron. Eng.* **86** 1520–8
[960] Zhang L, Shi Z and Wang Y 2011 Catalyst-free growth of nanographene films on various substrates *Nano Res.* **4** 315
[961] Medina H, Lin Y-C and Jin C 2012 Metal-free growth of nanographene on silicon oxides for transparent conducting applications *Adv. Funct. Mater.* **22** 2123
[962] Nguyen V L and Lee Y H 2015 Towards wafer-scale monocrystalline graphene growth and characterization *Small* **11** 3512
[963] Yang W *et al* 2013 Epitaxial growth of single-domain graphene on hexagonal boron nitride *Nat. Mater.* **12** 792–7
[964] Tang S, Wang H and Zhang Y 2013 Precisely aligned graphene grown on hexagonal boron nitride by catalyst free chemical vapor deposition *Sci. Rep.* **3** 2666
[965] Zhang L, Shi Z and Liu D 2012 Vapour-phase graphene epitaxy at low temperatures *Nano Res.* **5** 258
[966] Bo Z, Yang Y and Chen J 2013 Plasma-enhanced chemical vapor deposition synthesis of vertically oriented graphene nanosheets *Nanoscale* **5** 5180
[967] Buijnsters J G, Camero M and Gago R 2008 Direct spectroscopic evidence of self-formed C_{60} inclusions in fullerenelike hydrogenated carbon films *Appl. Phys. Lett.* **92** 141920
[968] Tamor M A, Vassell W C and Carduner K R 1990 Atomic constraint in hydrogenated 'diamond-like' carbon *Appl. Phys. Lett.* **58** 592
[969] Buijnsters J G, Camero M and Vázquez L 2007 DC substrate bias effects on the physical properties of hydrogenated amorphous carbon films grown by plasma-assisted chemical vapour deposition *Vacuum* **81** 1412
[970] Zhang L, Ni M and Liu D 2012 Competitive growth and etching of epitaxial graphene *J. Phys. Chem.* C **116** 26929
[971] Yang R, Zhang L and Wang Y 2010 An anisotropic etching effect in the graphene basal plane *Adv. Mater.* **22** 4014
[972] Diankov G, Neumann M and Goldhaber-Gordon D 2013 Extreme monolayer-selectivity of hydrogen-plasma reactions with graphene *ACS Nano* **7** 1324–32
[973] Nishijima M, Yoshinobu J and Tsuda H 1987 The adsorption and thermal decomposition of acetylene on Si(1 0 0) and vicinal Si(1 0 0) 9° *Surf. Sci.* **192** 383
[974] Riikonen S, Krasheninnikov A V and Halonen L 2012 The role of stable and mobile carbon adspecies in copper-promoted graphene growth *J. Phys. Chem.* C **116** 5802

[975] Zhang J, Wang Z and Niu T 2014 Elementary process for CVD graphene on Cu(1 1 0): size-selective carbon clusters *Sci. Rep.* **4** 4431
[976] Koretsky C M, Sverjensky D A and Sahai N 1998 A model of surface site types on oxide and silicate minerals based on crystal chemistry; implications for site types and densities, multi-site adsorption, surface infrared spectroscopy, and dissolution kinetics *Am. J. Sci.* **298** 349–438
[977] Liu D, Yang W, Zhang L, Zhang J, Meng J, Yang R, Zhang G and Shi D 2014 Two-step growth of graphene with separate controlling nucleation and edge growth directly on SiO_2 substrates *Carbon* **72** 387–92
[978] Kim Y S, Joo K, Jerng S-K, Lee J H, Yoon E and Chun S-H 2014 Direct growth of patterned graphene on SiO_2 substrates without the use of catalysts or lithography *Nanoscale* **6** 10100–5
[979] Sun J, Schmidt M E, Muruganathan M, Chong H M H and Mizuta H 2016 Large-scale nanoelectromechanical switches based on directly deposited nanocrystalline graphene on insulating substrates *Nanoscale* **8** 6659–65
[980] Chugh S, Mehta R, Lu N, Dios F D, Kim M J and Chen Z 2015 Comparison of graphene growth on arbitrary non-catalytic substrates using low-temperature PECVD *Carbon* **93** 393–9
[981] Muñoz R, Martínez L, López-Elvira E, Munuera C, Huttel Y and García-Hernández M 2018 Direct synthesis of graphene on silicon oxide by low temperature plasma enhanced chemical vapor deposition *Nanoscale* **10** 12779–87
[982] Elias D C *et al* 2009 Control of graphene's properties by reversible hydrogenation: evidence for graphane *Science* **323** 610–3
[983] Wang Y, Xu X, Lu J, Lin M, Bao Q, Özyilmaz B and Loh K P 2010 Toward high throughput interconvertible graphane-to-graphene growth and patterning *ACS Nano* **4** 6146–52
[984] Kaplas T, Sharma D and Svirko Y 2012 Few-layer graphene synthesis on a dielectric substrate *Carbon* **50** 1503–9
[985] Kaplas T, Zolotukhin A and Svirko Y 2011 Thickness determination of graphene on metal substrate by reflection spectroscopy *Opt. Express* **19** 17226
[986] Chavez K L and Hess D W 2001 A novel method of etching copper oxide using acetic acid *J. Electrochem. Soc.* **148** G640
[987] Kaplas T and Svirko Y 2014 Self-assembled graphene on dielectric micro- and nanostructures *Carbon* **70** 273–8
[988] Kosterlitz J M and Thouless D J 1972 Long range order and metastability in two dimensional solids and superfluids (application of dislocation theory) *J. Phys. C: Solid State Phys.* **5** L124–6
[989] Vlassiouk I, Smirnov S, Ivanov I, Fulvio P F, Dai S, Meyer H, Chi M, Hensley D, Datskos P and Lavrik N V 2011 Electrical and thermal conductivity of low temperature CVD graphene: the effect of disorder *Nanotechnology* **22** 275716
[990] Kumar R, Mehta B R, Bhatnagar M, Ravi S, Mahapatra S, Salkalachen S and Jhawar P 2014 Graphene as a transparent conducting and surface field layer in planar Si solar cells *Nanoscale Res. Lett.* **9** 349
[991] Jawhari T, Roid A and Casado J 1995 Raman spectroscopic characterization of some commercially available carbon black materials *Carbon* **33** 1561–5
[992] Kaplas T, Karvonen L, Ahmadi S, Amirsolaimani B, Mehravar S, Peyghambarian N, Kieu K, Honkanen S, Lipsanen H and Svirko Y 2016 Optical characterization of directly deposited graphene on a dielectric substrate *Opt. Express* **24** 2965
[993] Cassie A B D and Baxter S 1944 Wettability of porous surfaces *Trans. Faraday Soc.* **40** 546
[994] Peng Z, Yan Z, Sun Z and Tour J M 2011 Direct growth of bilayer graphene on SiO_2 substrates by carbon diffusion through nickel *ACS Nano* **5** 8241–7
[995] Marchena M, Janner D, Chen T L, Finazzi V and Pruneri V 2016 Low temperature direct growth of graphene patterns on flexible glass substrates catalysed by a sacrificial ultrathin Ni film *Opt. Mater. Express* **6** 2487
[996] Shin H-J *et al* 2011 Transfer-free growth of few-layer graphene by self-assembled monolayers *Adv. Mater.* **23** 4392–7
[997] Sun Z, Yan Z, Yao J, Beitler E, Zhu Y and Tour J M 2010 Growth of graphene from solid carbon sources *Nature* **468** 549–52
[998] Mattevi C, Kim H and Chhowalla M 2011 A review of chemical vapour deposition of graphene on copper *J. Mater. Chem.* **21** 3324–34
[999] ASM International 2002 *A.P. ASM Handbook* vol **3**
[1000] Yu Q, Lian J, Siriponglert S, Li H, Chen Y P and Pei S-S 2008 Graphene segregated on Ni surfaces and transferred to insulators *Appl. Phys. Lett.* **93** 113103
[1001] Kaplas T, Matikainen A, Nuutinen T, Suvanto S, Vahimaa P and Svirko Y 2017 Scalable fabrication of the graphitic substrates for graphene-enhanced Raman spectroscopy *Sci. Rep.* **7** 8561
[1002] Xiong W, Zhou Y S, Jiang L J, Sarkar A, Mahjouri-Samani M, Xie Z Q, Gao Y, Ianno N J, Jiang L and Lu Y F 2012 Single-step formation of graphene on dielectric surfaces *Adv. Mater.* **25** 630–4
[1003] Reina A, Son H, Jiao L, Fan B, Dresselhaus M S, Liu Z and Kong J 2008 Transferring and identification of single- and few-layer graphene on arbitrary substrates *J. Phys. Chem.* C **112** 17741–4
[1004] Hallam T, Berner N C, Yim C and Duesberg G S 2014 Strain, bubbles, dirt, and folds: a study of graphene polymer-assisted transfer *Adv. Mater. Interfaces* **1** 1400115
[1005] Li X, Zhu Y, Cai W, Borysiak M, Han B, Chen D, Piner R D, Colombo L and Ruoff R S 2009 Transfer of large-area graphene films for high-performance transparent conductive electrodes *Nano Lett.* **9** 4359–63
[1006] Zhang X, Beyer A and Gölzhäuser A 2011 Mechanical characterization of carbon nanomembranes from self-assembled monolayers *Beilstein J. Nanotechnol.* **2** 826–33
[1007] Beyer A, Vieker H, Klett R, Meyer zu Theenhausen H, Angelova P and Gölzhäuser A 2015 Imaging of carbon nanomembranes with helium ion microscopy *Beilstein J. Nanotechnol.* **6** 1712–20
[1008] Lee C-K *et al* 2014 Monatomic chemical–vapor–deposited graphene membranes bridge a half-millimeter-scale gap *ACS Nano* **8** 2336–44
[1009] Gong C *et al* 2013 Rapid selective etching of PMMA residues from transferred graphene by carbon dioxide *J. Phys. Chem.* C **117** 23000–8
[1010] Lin Y-C, Lu C-C, Yeh C-H, Jin C, Suenaga K and Chiu P-W 2011 Graphene annealing: how clean can it be? *Nano Lett.* **12** 414–9
[1011] Islam A E, Zakharov D N, Carpena-Nunez J, Hsiao M-S, Drummy L F, Stach E A and Maruyama B 2017 Atomic level cleaning of poly-methyl-methacrylate residues from the graphene surface using radiolized water at high temperatures *Appl. Phys. Lett.* **111** 103101
[1012] Zhang Z, Du J, Zhang D, Sun H, Yin L, Ma L, Chen J, Ma D, Cheng H-M and Ren W 2017 Rosin-enabled ultraclean and damage-free transfer of graphene for large-area flexible organic light-emitting diodes *Nat. Commun.* **8** 14560
[1013] Fisichella G, Di Franco S, Roccaforte F, Ravesi S and Giannazzo F 2014 Microscopic mechanisms of graphene electrolytic delamination from metal substrates *Appl. Phys. Lett.* **104** 233105
[1014] Gao Y *et al* 2015 Elastic coupling between layers in two-dimensional materials *Nat. Mater.* **14** 714
[1015] Liu L *et al* 2016 Graphene transfer: a mechanism for highly efficient electrochemical bubbling delamination of CVD-grown graphene from metal substrates *Adv. Mater. Interfaces* **3** 1500492
[1016] Chen Z, Ge X, Zhang H, Zhang Y, Sui Y, Yu G, Jin Z and Liu X 2016 High pressure-assisted transfer of ultraclean chemical vapor deposited graphene *Appl. Phys. Lett.* **108** 132106
[1017] Lee J, Kim Y, Shin H-J, Lee C, Lee D, Moon C-Y, Lim J and Chan Jun S 2013 Clean transfer of graphene and its effect on contact resistance *Appl. Phys. Lett.* **103** 103104
[1018] Jeong H J, Kim H Y, Jeong S Y, Han J T, Baeg K-J, Hwang J Y and Lee G-W 2014 Improved transfer of chemical-vapor-deposited graphene through modification of intermolecular interactions and solubility of poly(methylmethacrylate) layers *Carbon* **66** 612–8

[1019] Koefoed L et al 2015 Facile electrochemical transfer of large-area single crystal epitaxial graphene from Ir(1 1 1) J. Phys. D: Appl. Phys. 48 115306
[1020] Miniussi E et al 2017 Fermi surface map of large-scale single-orientation graphene on SiO_2 J. Phys.: Condens. Matter 29 475001
[1021] Krajewska A, Pasternak I, Sobon G, Sotor J, Przewloka A, Ciuk T, Sobieski J, Grzonka J, Abramski K M and Strupinski W 2017 Fabrication and applications of multi-layer graphene stack on transparent polymer Appl. Phys. Lett. 110 041901
[1022] Pirkle A, Chan J, Venugopal A, Hinojos D, Magnuson C W, McDonnell S, Colombo L, Vogel E M, Ruoff R S and Wallace R M 2011 The effect of chemical residues on the physical and electrical properties of chemical vapor deposited graphene transferred to SiO_2 Appl. Phys. Lett. 99 122108
[1023] Taubner T, Keilmann F and Hillenbrand R 2005 Nanoscale-resolved subsurface imaging by scattering-type near-field optical microscopy Opt. Express 13 8893
[1024] Hillenbrand F K A R 2008 Nano-Optics and Near-Field Optical Microscopy (Boston, MA: Artech House Publishers)
[1025] Hillenbrand R and Keilmann F 2002 Material-specific mapping of metal/semiconductor/dielectric nanosystems at 10 nm resolution by backscattering near-field optical microscopy Appl. Phys. Lett. 80 25–7
[1026] Hillenbrand R and Keilmann F 2000 Complex optical constants on a subwavelength scale Phys. Rev. Lett. 85 3029–32
[1027] Taubner T, Hillenbrand R and Keilmann F 2004 Nanoscale polymer recognition by spectral signature in scattering infrared near-field microscopy Appl. Phys. Lett. 85 5064–6
[1028] Gunde M K 2000 Vibrational modes in amorphous silicon dioxide Physica B 292 286–95
[1029] Huth F, Govyadinov A, Amarie S, Nuansing W, Keilmann F and Hillenbrand R 2012 Nano-FTIR absorption spectroscopy of molecular fingerprints at 20 nm spatial resolution Nano Lett. 12 3973–8
[1030] Venugopal A 2012 Effect of Contacts, Graphene Type and Underlying Substrate on The Transport Properties Of Graphene (The University of Texas at Dallas)
[1031] Batzill M 2012 The surface science of graphene: Metal interfaces, CVD synthesis, nanoribbons, chemical modifications, and defects Surf. Sci. Rep. 67 83–115
[1032] Simonet J and Lund H 1977 Electrochemical behaviour of graphite cathodes in the presence of tetraalkylammonium cations J. Electroanal. Chem. Interfacial Electrochem. 75 719–30
[1033] Verguts K et al 2017 Controlling water intercalation is key to a direct graphene transfer ACS Appl. Mater. Interfaces 9 37484–92
[1034] Gómez-Marín A M, Clavilier J and Feliu J M 2013 Sequential Pt(1 1 1) oxide formation in perchloric acid: an electrochemical study of surface species inter-conversion J. Electroanal. Chem. 688 360–70
[1035] Palacio I et al 2018 Chemistry below graphene: Decoupling epitaxial graphene from metals by potential-controlled electrochemical oxidation Carbon 129 837–46
[1036] Feng X, Maier S and Salmeron M 2012 Water splits epitaxial graphene and intercalates J. Am. Chem. Soc. 134 5662–8
[1037] Alonso C, Alonso C G-Aand Escudero M L 2008 Spanish Patent ES-200801041
[1038] Bae S et al 2010 2010 Roll-to-roll production of 30-inch graphene films for transparent electrodes Nat. Nanotechnol. 5 574–8
[1039] Kang M H, Milne W I and Cole M T 2016 Temporal stability of metal-chloride-doped chemical–vapour–deposited graphene ChemPhysChem 17 2545–50
[1040] Kang M H, Prieto López L O, Chen B, Teo K, Williams J A, Milne W I and Cole M T 2016 Mechanical robustness of graphene on flexible transparent substrates ACS Appl. Mater. Interfaces 8 22506–15
[1041] Kim K K, Reina A, Shi Y, Park H, Li L-J, Lee Y H and Kong J 2010 Enhancing the conductivity of transparent graphene films via doping Nanotechnology 21 285205
[1042] Kwon S-J et al 2018 Extremely stable graphene electrodes doped with macromolecular acid Nat. Commun. 9 2037
[1043] Kim H H, Chung Y, Lee E, Lee S K and Cho K 2014 Graphene: water-free transfer method for CVD-grown graphene and its application to flexible air-stable graphene transistors Adv. Mater. 26 3166–6
[1044] Batrakov K, Kuzhir P, Maksimenko S, Paddubskaya A, Voronovich S, Lambin P, Kaplas T and Svirko Y 2014 Flexible transparent graphene/polymer multilayers for efficient electromagnetic field absorption Sci. Rep. 4 7191
[1045] Kotsilkova R, Todorov P, Ivanov E, Kaplas T, Svirko Y, Paddubskaya A and Kuzhir P 2016 Mechanical properties investigation of bilayer graphene/poly(methyl methacrylate) thin films at macro, micro and nanoscale Carbon 100 355–66
[1046] Kaplas T, Bera A, Matikainen A, Pääkkönen P and Lipsanen H 2018 Transfer and patterning of chemical vapor deposited graphene by a multifunctional polymer film Appl. Phys. Lett. 112 073107
[1047] Niu T and Li A 2015 From two-dimensional materials to heterostructures Prog. Surf. Sci. 90 21–45
[1048] Schué L, Stenger I, Fossard F, Loiseau A and Barjon J 2016 Characterization methods dedicated to nanometer-thick hBN layers 2D Mater. 4 015028
[1049] Kim K K et al 2011 Synthesis of monolayer hexagonal boron nitride on cu foil using chemical vapor deposition Nano Lett. 12 161–6
[1050] Chatterjee S, Kim M J, Zakharov D N, Kim S M, Stach E A, Maruyama B and Sneddon L G 2012 Syntheses of boron nitride nanotubes from borazine and decaborane molecular precursors by catalytic chemical vapor deposition with a floating nickel catalyst Chem. Mater. 24 2872–9
[1051] Jang S K, Youn J, Song Y J and Lee S 2016 Synthesis and characterization of hexagonal boron nitride as a gate dielectric Sci. Rep. 6 30449
[1052] Gibb A, Alem N and Zettl A 2013 Low pressure chemical vapor deposition synthesis of hexagonal boron nitride on polycrystalline metal foils Phys. Status Solidi b 250 2727–31
[1053] Suzuki S and Hibino H 2012 Chemical vapor deposition of hexagonal boron nitride e-J. Surf. Sci. Nanotechnol. 10 133–8
[1054] Ismach A et al 2012 Toward the controlled synthesis of hexagonal boron nitride films ACS Nano 6 6378–85
[1055] Ismach A, Chou H, Mende P, Dolocan A, Addou R, Aloni S, Wallace R, Feenstra R, Ruoff R S and Colombo L 2017 Carbon-assisted chemical vapor deposition of hexagonal boron nitride 2D Mater. 4 025117
[1056] Sonde S, Dolocan A, Lu N, Corbet C, Kim M J, Tutuc E, Banerjee S K and Colombo L 2017 Ultrathin, wafer-scale hexagonal boron nitride on dielectric surfaces by diffusion and segregation mechanism 2D Mater. 4 025052
[1057] Cho H, Park S, Won D-I, Kang S O, Pyo S-S, Kim D-I, Kim S M, Kim H C and Kim M J 2015 Growth kinetics of white graphene (h-BN) on a planarised Ni foil surface Sci. Rep. 5 11985
[1058] Lee Y-H et al 2012 Growth selectivity of hexagonal-boron nitride layers on Ni with various crystal orientations RSC Adv. 2 111–5
[1059] Andrieux-Ledier N D A, Fossard F, Mérot J S, Prevost H, Schué L, Plaud A, Héripré E, Barjon J and Loiseau A 2017 Under review
[1060] Shi Y et al 2010 Synthesis of few-layer hexagonal boron nitride thin film by chemical vapor deposition Nano Lett. 10 4134–9
[1061] Gao Y, Ren W, Ma T, Liu Z, Zhang Y, Liu W-B, Ma L-P, Ma X and Cheng H-M 2013 Repeated and controlled growth of monolayer, bilayer and few-layer hexagonal boron nitride on Pt foils ACS Nano 7 5199–206
[1062] Corso M 2004 Boron nitride nanomesh Science 303 217–20
[1063] Hemmi A et al 2014 High quality single atomic layer deposition of hexagonal boron nitride on single crystalline Rh(1 1 1) four-inch wafers Rev. Sci. Instrum. 85 035101
[1064] Mertens S F L, Hemmi A, Muff S, Gröning O, De Feyter S, Osterwalder J and Greber T 2016 Switching stiction and adhesion of a liquid on a solid Nature 534 676–9

[1065] Widmer R, Berner S, Gröning O, Brugger T, Osterwalder J and Greber T 2007 Electrolytic *in situ* STM investigation of h-BN-Nanomesh *Electrochem. Commun.* **9** 2484–8
[1066] Cun H *et al* 2018 Centimeter-sized single-orientation monolayer hexagonal boron nitride with or without nanovoids *Nano Lett.* **18** 1205–12
[1067] Berner S *et al* 2007 Boron nitride nanomesh: functionality from a corrugated monolayer *Angew. Chem., Int. Ed.* **46** 5115–9
[1068] Brugger T, Ma H, Iannuzzi M, Berner S, Winkler A, Hutter J, Osterwalder J and Greber T 2010 Nanotexture switching of single-layer hexagonal boron nitride on rhodium by intercalation of hydrogen atoms *Angew. Chem., Int. Ed.* **49** 6120–4
[1069] Gubó R, Vári G, Kiss J, Farkas A P, Palotás K, Óvári L, Berkó A and Kónya Z 2018 Tailoring the hexagonal boron nitride nanomesh on Rh(1 1 1) with gold *Phys. Chem. Chem. Phys.* **20** 15473–85
[1070] Stania R *et al* 2016 Self-assembly of nanoscale lateral segregation profiles, *Phys. Rev.* B **93** 161402(R)
[1071] Cho Y-J *et al* 2016 Hexagonal boron nitride tunnel barriers grown on graphite by high temperature molecular beam epitaxy *Sci. Rep.* **6** 34474
[1072] Nakhaie S, Wofford J M, Schumann T, Jahn U, Ramsteiner M, Hanke M, Lopes J M J and Riechert H 2015 Synthesis of atomically thin hexagonal boron nitride films on nickel foils by molecular beam epitaxy *Appl. Phys. Lett.* **106** 213108
[1073] Wofford J M, Nakhaie S, Krause T, Liu X, Ramsteiner M, Hanke M, Riechert H and Lopes J M J 2017 A hybrid MBE-based growth method for large-area synthesis of stacked hexagonal boron nitride/graphene heterostructures *Sci. Rep.* **7** 43644
[1074] Jang A R *et al* 2016 Wafer-scale and wrinkle-free epitaxial growth of single-orientated multilayer hexagonal boron nitride on sapphire *Nano Lett.* **16** 3360–6
[1075] Kobayashi Y and Akasaka T 2008 Hexagonal BN epitaxial growth on (0 0 0 1) sapphire substrate by MOVPE *J. Cryst. Growth* **310** 5044–7
[1076] Caretti I, Jiménez I and Albella J M 2003 BCN films with controlled composition obtained by the interaction between molecular beams of B and C with nitrogen ion beams *Diamond Relat. Mater.* **12** 1079–83
[1077] Caretti I and Jiménez I 2011 Composition and bonding structure of boron nitride $B_{1-x}N_x$ thin films grown by ion-beam assisted evaporation *Chem. Phys. Lett.* **511** 235–40
[1078] Jiménez I, Torres R, Caretti I, Gago R and Albella J M 2012 A review of monolithic and multilayer coatings within the boron–carbon–nitrogen system by ion-beam-assisted deposition *J. Mater. Res.* **27** 743–64
[1079] Caretti I and Jiménez I 2011 Point defects in hexagonal BN, BC_3 and BCxN compounds studied by x-ray absorption near-edge structure *J. Appl. Phys.* **110** 023511
[1080] Torres R, Caretti I, Serin V, Brun N, Radnóczic G and Jiménez I 2014 Reversed texture in nanometric carbon/boron nitride multilayers *Carbon* **74** 374–8
[1081] Cascales Fernandez J 2016 Estudio de capas nanométricas de h-BN y grafeno para su apilamiento en multicapas (study of nanometric layers of h-BN and graphene for piling up as multilayers) *PhD Thesis* Universidad Autonoma de Madrid
[1082] Gago R, Abendroth B, Cerdá J I, Jiménez I and Möller W 2007 Detection of intrinsic stress in cubic boron nitride films by x-ray absorption near-edge structure: Stress relaxation mechanisms by simultaneous ion implantation during growth *Phys. Rev.* B **76** 174111
[1083] Gago R, Jiménez I, Albella J M and Terminello L J 2001 Identification of ternary boron–carbon–nitrogen hexagonal phases by x-ray absorption spectroscopy *Appl. Phys. Lett.* **78** 3430–2
[1084] Jiménez I, Jankowski A F, Terminello L J, Sutherland D G J, Carlisle J A, Doll G L, Tong W M, Shuh D K and Himpsel F J 1997 Core-level photoabsorption study of defects and metastable bonding configurations in boron nitride *Phys. Rev.* B **55** 12025–37
[1085] Caretti I, Torres R, Gago R, Landa-Cánovas A R and Jiménez I 2010 Effect of carbon incorporation on the microstructure of BC_xN ($x = 0.25$ 1, and 4) ternary solid solutions studied by transmission electron microscopy *Chem. Mater.* **22** 1949–51
[1086] Shim J *et al* 2018 Controlled crack propagation for atomic precision handling of wafer-scale two-dimensional materials *Science* **362** 665–70
[1087] Song L *et al* 2010 Large scale growth and characterization of atomic hexagonal boron nitride layers *Nano Lett.* **10** 3209–15
[1088] Wen Y, Shang X, Dong J, Xu K, He J and Jiang C 2015 Ultraclean and large-area monolayer hexagonal boron nitride on Cu foil using chemical vapor deposition *Nanotechnology* **26** 275601
[1089] Park J-H *et al* 2014 Large-area monolayer hexagonal boron nitride on Pt foil *ACS Nano* **8** 8520–8
[1090] Kim G, Jang A R, Jeong H Y, Lee Z, Kang D J and Shin H S 2013 Growth of high-crystalline, single-layer hexagonal boron nitride on recyclable platinum foil *Nano Lett.* **13** 1834–9
[1091] Caneva S *et al* 2016 Controlling catalyst bulk reservoir effects for monolayer hexagonal boron nitride CVD *Nano Lett.* **16** 1250–61
[1092] Wang R *et al* 2016 Catalyst interface engineering for improved 2D film lift-off and transfer *ACS Appl. Mater. Interfaces* **8** 33072–82
[1093] Gatensby R, McEvoy N, Lee K, Hallam T, Berner N C, Rezvani E, Winters S, O'Brien M and Duesberg G S 2014 Controlled synthesis of transition metal dichalcogenide thin films for electronic applications *Appl. Surf. Sci.* **297** 139–46
[1094] Gatensby R, Hallam T, Lee K, McEvoy N and Duesberg G S 2016 Investigations of vapour-phase deposited transition metal dichalcogenide films for future electronic applications *Solid-State Electron.* **125** 39–51
[1095] Jung Y, Shen J, Liu Y, Woods J M, Sun Y and Cha J J 2014 Metal seed layer thickness-induced transition from vertical to horizontal growth of MoS_2 and WS_2, *Nano Lett.* **14** 6842–9
[1096] Lee K, Gatensby R, McEvoy N, Hallam T and Duesberg G S 2013 High-performance sensors based on molybdenum disulfide thin films *Adv. Mater.* **25** 6699–702
[1097] O'Brien M, Lee K, Morrish R, Berner N C, McEvoy N, Wolden C A and Duesberg G S 2014 Plasma assisted synthesis of WS_2 for gas sensing applications *Chem. Phys. Lett.* **615** 6–10
[1098] O'Brien M, McEvoy N, Hallam T, Kim H-Y, Berner N C, Hanlon D, Lee K, Coleman J N and Duesberg G S 2014 Transition metal dichalcogenide growth via close proximity precursor supply *Sci. Rep.* **4** 7374
[1099] Yim C *et al* 2016 High-performance hybrid electronic devices from layered $PtSe_2$ films grown at low temperature *ACS Nano* **10** 9550–8
[1100] Zhang S *et al* 2015 Direct observation of degenerate two-photon absorption and its saturation in WS_2 and MoS_2 monolayer and few-layer films *ACS Nano* **9** 7142–50
[1101] Yim C, McEvoy N and Duesberg G S 2013 Characterization of graphene-silicon Schottky barrier diodes using impedance spectroscopy *Appl. Phys. Lett.* **103** 193106
[1102] Yim C *et al* 2014 Heterojunction hybrid devices from vapor phase grown MoS_2, *Sci. Rep.* **4** 5458
[1103] Yim C, O'Brien M, McEvoy N, Winters S, Mirza I, Lunney J G and Duesberg G S 2014 Investigation of the optical properties of MoS_2 thin films using spectroscopic ellipsometry *Appl. Phys. Lett.* **104** 103114
[1104] Bandurin D A *et al* 2017 High electron mobility, quantum Hall effect and anomalous optical response in atomically thin InSe *Nat. Nanotechnol.* **12** 223–7
[1105] Huang W, Gan L, Li H, Ma Y and Zhai T 2016 2D layered group IIIA metal chalcogenides: synthesis, properties and applications in electronics and optoelectronics *CrystEngComm* **18** 3968–84
[1106] Lei S *et al* 2016 Surface functionalization of two-dimensional metal chalcogenides by Lewis acid-base chemistry *Nat. Nanotechnol.* **11** 465–71

[1107] Lei S *et al* 2015 An atomically layered InSe avalanche photodetector *Nano Lett.* **15** 3048–55
[1108] Mudd G W *et al* 2015 High broad-band photoresponsivity of mechanically formed InSe-graphene van der Waals heterostructures *Adv. Mater.* **27** 3760–6
[1109] Debbichi L, Eriksson O and Lebegue S 2015 Two-dimensional indium selenides compounds: an *ab initio* study *J. Phys. Chem. Lett.* **6** 3098–103
[1110] Rybkovskiy D V, Osadchy A V and Obraztsova E D 2014 Transition from parabolic to ring-shaped valence band maximum in few-layer GaS, GaSe, and InSe *Phys. Rev.* B **90** 235302
[1111] Sánchez-Royo J F *et al* 2014 Electronic structure, optical properties, and lattice dynamics in atomically thin indium selenide flakes *Nano Res.* **7** 1556–68
[1112] Wickramaratne D, Zahid F and Lake R K 2015 Electronic and thermoelectric properties of van der Waals materials with ring-shaped valence bands *J. Appl. Phys.* **118** 075101
[1113] Zólyomi V, Drummond N D and Fal'ko V I 2014 Electrons and phonons in single layers of hexagonal indium chalcogenides from *ab initio* calculations *Phys. Rev.* B **89** 205416
[1114] Han G, Chen Z G, Drennan J and Zou J 2014 Indium selenides: structural characteristics, synthesis and their thermoelectric performances *Small* **10** 2747–65
[1115] Lin M *et al* 2013 Controlled growth of atomically thin In_2Se_3 flakes by van der Waals epitaxy *J. Am. Chem. Soc.* **135** 13274–7
[1116] Zhou J, Zeng Q, Lv D, Sun L, Niu L, Fu W, Liu F, Shen Z, Jin C and Liu Z 2015 Controlled synthesis of high-quality monolayered alpha-In_2Se_3 via physical vapor deposition *Nano Lett.* **15** 6400–5
[1117] Balakrishnan N *et al* 2016 Quantum confinement and photoresponsivity of β-In_2Se_3 nanosheets grown by physical vapour transport *2D Mater.* **3** 025030
[1118] Zhou S, Tao X and Gu Y 2016 Thickness-dependent thermal conductivity of suspended two-dimensional single-crystal In_2Se_3 layers grown by chemical vapor deposition *J. Phys. Chem.* C **120** 4753–8
[1119] Lauth J *et al* 2016 Solution-processed two-dimensional ultrathin InSe nanosheets *Chem. Mater.* **28** 1728–36
[1120] Balakrishnan N, Steer E D, Smith E F, Kudrynskyi Z R, Kovalyuk Z D, Eaves L, Patanè A and Beton P H 2018 Epitaxial growth of γ-InSe and α, β, and γ-In_2Se_3 on ε-GaSe *2D Mater.* **5** 035026
[1121] Tao X and Gu Y 2013 Crystalline-crystalline phase transformation in two-dimensional In_2Se_3 thin layers *Nano Lett.* **13** 3501–5
[1122] Huang Y-T, Huang C-W, Chen J-Y, Ting Y-H, Lu K-C, Chueh Y-L and Wu W-W 2014 Dynamic observation of phase transformation behaviors in indium(III) selenide nanowire based phase change memory *ACS Nano* **8** 9457–62
[1123] Jacobs-Gedrim R B, Shanmugam M, Jain N, Durcan C A, Murphy M T, Murray T M, Matyi R J, Moore R L and Yu B 2014 Extraordinary photoresponse in two-dimensional In_2Se_3 nanosheets *ACS Nano* **8** 514–21
[1124] Mudd G W *et al* 2013 Tuning the bandgap of exfoliated InSe nanosheets by quantum confinement *Adv. Mater.* **25** 5714–8
[1125] Kovalyuk Z D, Sydor O M, Sydor O A, Tkachenko V G, Maksymchuk I M, Dubinko V I and Ostapchuk P M 2012 X-ray diffractometry and raman spectroscopy investigation of irradiated layered III-VI crystals *J. Mater. Sci. Eng.* A **2** 537–43
[1126] Bakhtinov A P, Boledzyuk V B, Kovalyuk Z D, Kudrynskyi Z R, Lytvyn O S and Shevchenko A D 2013 Magnetic properties and surface morphology of layered In_2Se_3 crystals intercalated with cobalt *Phys. Solid State* **55** 1148–55
[1127] Ke F *et al* 2014 Interlayer-glide-driven isosymmetric phase transition in compressed In_2Se_3 *Appl. Phys. Lett.* **104** 212102
[1128] Nakayama T and Hishikawa M 1997 Bonding and optical anisotropy of vacancy ordered Ga_2Se_3 *J. Phys. Soc. Japan* **66** 3887–92
[1129] Zhao J, Nam H, Ly T H, Yun S J, Kim S, Cho S, Yang H and Lee Y H 2016 Chain vacancies in 2D crystals *Small* **13** 1601930
[1130] Dumcenco D *et al* 2015 Large-area epitaxial monolayer MoS_2 *ACS Nano* **9** 4611–20
[1131] Najmaei S, Liu Z, Zhou W, Zou X, Shi G, Lei S, Yakobson B I, Idrobo J-C, Ajayan P M and Lou J 2013 Vapour phase growth and grain boundary structure of molybdenum disulphide atomic layers *Nat. Mater.* **12** 754–9
[1132] van der Zande A M, Huang P Y, Chenet D A, Berkelbach T C, You Y, Lee G-H, Heinz T F, Reichman D R, Muller D A and Hone J C 2013 Grains and grain boundaries in highly crystalline monolayer molybdenum disulphide *Nat. Mater.* **12** 554–61
[1133] Kim H, Dumcenco D, Frégnaux M, Benayad A, Chen M-W, Kung Y-C, Kis A and Renault O 2016 Free-standing electronic character of monolayerMoS_2 in van der Waals epitaxy *Phys. Rev.* B **94** 081401(R)
[1134] Boxhoorn G, Jesse A, Ernsting J and Oskam A 1978 Vapour pressure measurements on M (CO) 5PX3 (M = Cr, Mo, W; X = F, Cl, Br) *Thermochim. Acta* **27** 261–7
[1135] Liu Z, Li X, Close M R, Kugler E L, Petersen J L and Dadyburjor D B 1997 Screening of alkali-promoted vapor-phase-synthesized molybdenum sulfide catalysts for the production of alcohols from synthesis gas *Ind. Eng. Chem. Res.* **36** 3085–93
[1136] Close M R, Petersen J L and Kugler E L 1999 Synthesis and characterization of nanoscale molybdenum sulfide catalysts by controlled gas phase decomposition of $Mo(CO)_6$ and H_2S *Inorg. Chem.* **38** 1535–42
[1137] Shi Y *et al* 2012 van der Waals epitaxy of MoS_2 layers using graphene as growth templates *Nano Lett.* **12** 2784–91
[1138] Hara K, Kojima T and Kukimoto H 1987 Epitaxial growth of cugas$_2$ by metalorganic chemical vapor deposition *Japan. J. Appl. Phys.* **26** L1107–9
[1139] Zhang X, Choudhury T H, Chubarov M, Xiang Y, Jariwala B, Zhang F, Alem N, Wang G-C, Robinson J A and Redwing J M 2018 Diffusion-controlled epitaxy of large area coalesced WSe_2 monolayers on sapphire *Nano Lett.* **18** 1049–56
[1140] Kang K, Xie S, Huang L, Han Y, Huang P Y, Mak K F, Kim C-J, Muller D and Park J 2015 High-mobility three-atom-thick semiconducting films with wafer-scale homogeneity *Nature* **520** 656–60
[1141] Kranthi Kumar V, Dhar S, Choudhury T H, Shivashankar S A and Raghavan S 2015 A predictive approach to CVD of crystalline layers of TMDs: the case of MoS_2 *Nanoscale* **7** 7802–10
[1142] Kim H, Ovchinnikov D, Deiana D, Unuchek D and Kis A 2017 Suppressing nucleation in metal–organic chemical vapor deposition of MoS_2 monolayers by Alkali metal halides *Nano Lett.* **17** 5056–63
[1143] Wei W-C J and Lo M-H 1998 Processing and properties of (Mo,Cr) oxycarbides from MOCVD *Appl. Organomet. Chem.* **12** 201–20
[1144] Kaplan L H and d'Heurle F M 1970 The deposition of molybdenum and tungsten films from vapor decomposition of carbonyls *J. Electrochem. Soc.* **117** 693
[1145] Stubbles J R and Richardson F D 1960 Equilibria in the system molybdenum + sulphur + hydrogen *Trans. Faraday Soc.* **56** 1460
[1146] Kaloidas V E and Papayannakos N G 1987 Hydrogen production from the decomposition of hydrogen sulphide. Equilibrium studies on the system $H_2S/H_2/Si$, (i = 1,…,8) in the gas phase *Int. J. Hydrogen Energy* **12** 403–9
[1147] Dhar S, Kranthi Kumar V, Choudhury T H, Shivashankar S A and Raghavan S 2016 Chemical vapor deposition of MoS_2 layers from Mo-S-C-O-H system: thermodynamic modeling and validation *Phys. Chem. Chem. Phys.* **18** 14918–26
[1148] Fannin L W, Webb D W and Pearce R H 1992 Cause and resolution of problem of erratic and decreasing trimethylindium bubbler delivery rates *J. Cryst. Growth* **124** 307–10
[1149] Koma A 1999 Van der Waals epitaxy for highly lattice-mismatched systems *J. Cryst. Growth* **201–2** 236–41

[1150] Koma A 1992 Van der Waals epitaxy—a new epitaxial growth method for a highly lattice-mismatched system *Thin Solid Films* **216** 72–6
[1151] Dobkin D M and Zuraw M K 2013 *Principles of Chemical Vapor Deposition* (Netherlands: Springer)
[1152] Li H, Wu H, Yuan S and Qian H 2016 Synthesis and characterization of vertically standing MoS_2 nanosheets *Sci. Rep.* **6** 21171
[1153] Yu Y, Li C, Liu Y, Su L, Zhang Y and Cao L 2013 Controlled scalable synthesis of uniform, high-quality monolayer and few-layer MoS_2 films *Sci. Rep.* **3** 1866
[1154] Zhu D, Shu H, Jiang F, Lv D, Asokan V, Omar O, Yuan J, Zhang Z and Jin C 2017 Capture the growth kinetics of CVD growth of two-dimensional MoS_2 *NPJ 2D Mater. Appl.* **1** 8
[1155] Xuan W, Yong Ping Z and Zhi Qian C 2016 Effect of MoO_3 constituents on the growth of MoS_2 nanosheets by chemical vapor deposition *Mater. Res. Express* **3** 065014
[1156] Robinson V N E and Robins J L 1974 Nucleation kinetics of gold deposited onto UHV cleaved surfaces of NaCl and KBr *Thin Solid Films* **20** 155–75
[1157] Pyeon J J, Kim S H, Jeong D S, Baek S-H, Kang C-Y, Kim J-S and Kim S K 2016 Wafer-scale growth of MoS_2 thin films by atomic layer deposition *Nanoscale* **8** 10792–8
[1158] Marx M *et al* 2017 Large-area MoS_2 deposition via MOVPE *J. Cryst. Growth* **464** 100–4
[1159] Jeong-Gyu S *et al* 2017 Catalytic chemical vapor deposition of large-area uniform two-dimensional molybdenum disulfide using sodium chloride *Nanotechnology* **28** 465103
[1160] Zhan W *et al* 2017 NaCl-assisted one-step growth of MoS_2–WS_2 in-plane heterostructures *Nanotechnology* **28** 325602
[1161] Reale F *et al* 2017 High-mobility and high-optical quality atomically thin WS_2 *Sci. Rep.* **7** 14911
[1162] Li S *et al* 2018 Vapor–liquid–solid growth of monolayer MoS_2 nanoribbons *Nat. Mater.* **17** 535 − 42
[1163] Chen J *et al* 2017 Chemical vapor deposition of large-size monolayer MoSe2 crystals on molten glass *J. Am. Chem. Soc.* **139** 1073–6
[1164] Zhang L *et al* 2017 Damage-free and rapid transfer of CVD-grown two-dimensional transition metal dichalcogenides by dissolving sacrificial water-soluble layers *Nanoscale* **9** 19124–30
[1165] Boandoh S *et al* 2017 A novel and facile route to synthesize atomic-layered MoS_2 film for large-area electronics *Small* **13** 1701306
[1166] Yang P *et al* 2018 Batch production of 6-inch uniform monolayer molybdenum disulfide catalyzed by sodium in glass *Nat. Commun.* **9** 4905
[1167] Chen J *et al* 2017 Homoepitaxial growth of large-scale highly organized transition metal dichalcogenide patterns *Adv. Mater.* **30** 1704674
[1168] Eichfeld S M *et al* 2015 Highly scalable, atomically thin WSe_2 grown via metal–organic chemical vapor deposition *ACS Nano* **9** 2080–7
[1169] Xu W, Ye Z, Zhou T, Zhao B, Zhu L and Huang J 2004 Low-pressure MOCVD growth of p-type ZnO thin films by using NO as the dopant source *J. Cryst. Growth* **265** 133–6
[1170] Suzuki M, Nishio J, Onomura M and Hongo C 1998 Doping characteristics and electrical properties of Mg-doped AlGaN grown by atmospheric-pressure MOCVD *J. Cryst. Growth* **189–90** 511–5
[1171] Tan L K, Liu B, Teng J H, Guo S, Low H Y and Loh K P 2014 Atomic layer deposition of a MoS_2 film *Nanoscale* **6** 10584–8
[1172] Jin Z, Shin S, Kwon D H, Han S-J and Min Y-S 2014 Novel chemical route for atomic layer deposition of MoS_2 thin film on SiO_2/Si substrate *Nanoscale* **6** 14453–8
[1173] Cadot S *et al* 2017 A novel 2-step ALD route to ultra-thin MoS_2 films on SiO2 through a surface organometallic intermediate *Nanoscale* **9** 538–46
[1174] Lewis D J *et al* 2015 Thin films of molybdenum disulfide doped with chromium by aerosol-assisted chemical vapor deposition (AACVD) *Chem. Mater.* **27** 1367–74
[1175] Cheon J, Gozum J E and Girolami G S 1997 Chemical vapor deposition of MoS_2 and TiS_2 films from the metal–organic precursors $Mo(S\text{-}t\text{-}Bu)_4$ and $Ti(S\text{-}t\text{-}Bu)_4$ *Chem. Mater.* **9** 1847–53
[1176] Huang C, Wu S, Sanchez A M, Peters J J P, Beanland R, Ross J S, Rivera P, Yao W, Cobden D H and Xu X 2014 Lateral heterojunctions within monolayer $MoSe_2$–WSe_2 semiconductors *Nat. Mater.* **13** 1096–101
[1177] Iannaccone G, Bonaccorso F, Colombo L and Fiori G 2018 Quantum engineering of transistors based on 2D materials heterostructures *Nat. Nanotechnol.* **13** 183–91
[1178] Banerjee S K, Register L F, Tutuc E, Reddy D and MacDonald A H 2009 Bilayer pseudospin field-effect transistor (BiSFET): a proposed new logic device *IEEE Electron Device Lett.* **30** 158–60
[1179] Burg G W *et al* 2017 Coherent interlayer tunneling and negative differential resistance with high current density in double bilayer graphene-WSe_2 heterostructures *Nano Lett.* **17** 3919–25
[1180] Burg G W, Prasad N, Kim K, Taniguchi T, Watanabe K, MacDonald A H, Register L F and Tutuc E 2018 Strongly enhanced tunneling at total charge neutrality in double-bilayer graphene-WSe_2 heterostructures *Phys. Rev. Lett.* **120** 1777702
[1181] Kim K, Prasad N, Movva H C P, Burg G W, Wang Y M, Larentis S, Taniguchi T, Watanabe K, Register L F and Tutuc E 2018 Spin-conserving resonant tunneling in twist-controlled WSe_2-hBN-WSe_2 heterostructures *Nano Lett.* **18** 5967–73
[1182] Movva H C P, Kang S W, Rai A, Kim K, Fallahazad B, Taniguchi T, Watanabe K, Tutuc E and Banerjee S K 2016 Room temperature gate-tunable negative differential resistance in MoS_2/hBN/WSe_2 heterostructures *Proc. 74th Annual Device Research Conf. (DRC)* (http://doi.org/10.1109/DRC.2016.7548486)
[1183] Britnell L *et al* 2012 Field-effect tunneling transistor based on vertical graphene heterostructures *Science* **335** 947–50
[1184] Dean C R *et al* 2010 Boron nitride substrates for high-quality graphene electronics *Nat. Nanotechnol.* **5** 722–6
[1185] Georgiou T *et al* 2013 Vertical field-effect transistor based on graphene-WS_2 heterostructures for flexible and transparent electronics *Nat. Nanotechnol.* **8** 100–3
[1186] Endler I, Leonhardt A, König U, van den Berg H, Pitschke W and Sottke V 1999 Chemical vapour deposition of MoS_2 coatings using the precursors $MoCl_5$ and H_2S *Surf. Coat. Technol.* **120–1** 482–8
[1187] Lee W Y, Besmann T M and Stott M W 1994 Preparation of MoS_2 thin films by chemical vapor deposition *J. Mater. Res.* **9** 1474–83
[1188] Liu K-K *et al* 2012 Growth of large-area and highly crystalline MoS_2 thin layers on insulating substrates *Nano Lett.* **12** 1538–44
[1189] Zhan Y, Liu Z, Najmaei S, Ajayan P M and Lou J 2012 Large-area vapor-phase growth and characterization of MoS_2 atomic layers on a SiO_2 substrate *Small* **8** 966–71
[1190] Suzuki S, Molto Pallares R, Orofeo C M and Hibino H 2013 Boron nitride growth on metal foil using solid sources *J. Vac. Sci. Technol.* B **31** 041804
[1191] Suzuki S, Pallares R M and Hibino H 2012 Growth of atomically thin hexagonal boron nitride films by diffusion through a metal film and precipitation *J. Phys. D: Appl. Phys.* **45** 385304
[1192] Rong Y, Fan Y, Leen Koh A, Robertson A W, He K, Wang S, Tan H, Sinclair R and Warner J H 2014 Controlling sulphur precursor addition for large single crystal domains of WS_2 *Nanoscale* **6** 12096–103
[1193] Fu Q, Wang W, Yang L, Huang J, Zhang J and Xiang B 2015 Controllable synthesis of high quality monolayer WS_2 on a SiO_2/Si substrate by chemical vapor deposition *RSC Adv.* **5** 15795–9
[1194] Giusca C E *et al* 2016 Excitonic effects in tungsten disulfide monolayers on two-layer graphene *ACS Nano* **10** 7840–6
[1195] Bianco G V, Losurdo M, Giangregorio M M, Sacchetti A, Prete P, Lovergine N, Capezzuto P and Bruno G 2015 Direct epitaxial CVD synthesis of tungsten disulfide on epitaxial and CVD graphene *RSC Adv.* **5** 98700–8

[1196] Okada M, Sawazaki T, Watanabe K, Taniguch T, Hibino H, Shinohara H and Kitaura R 2014 Direct chemical vapor deposition growth of WS_2 atomic layers on hexagonal boron nitride *ACS Nano* **8** 8273–7
[1197] Chen K, Wan X, Wen J X, Xie W G, Kang Z W, Zeng X L, Chen H J and Xu J B 2015 Electronic properties of MoS_2–WS_2 heterostructures synthesized with two-step lateral epitaxial strategy *ACS Nano* **9** 9868–76
[1198] Gong Y *et al* 2014 Vertical and in-plane heterostructures from WS_2/MoS_2 monolayers *Nat. Mater.* **13** 1135–42
[1199] Tongay S *et al* 2014 Tuning interlayer coupling in large-area heterostructures with CVD-grown MoS_2 and WS_2 monolayers *Nano Lett.* **14** 3185–90
[1200] Zhang X Q, Lin C H, Tseng Y W, Huang K H and Lee Y H 2015 Synthesis of lateral heterostructures of semiconducting atomic layers *Nano Lett.* **15** 410–5
[1201] Nie Y F, Liang C P, Cha P R, Colombo L G, Wallace R M and Cho K 2017 A kinetic Monte Carlo simulation method of van der Waals epitaxy for atomistic nucleation-growth processes of transition metal dichalcogenides *Sci. Rep.* **7** 2977
[1202] Yue R Y *et al* 2017 Nucleation and growth of WSe2: enabling large grain transition metal dichalcogenides *2D Mater.* **4** 045019
[1203] Tang S *et al* 2015 Silane-catalysed fast growth of large single-crystalline graphene on hexagonal boron nitride *Nat. Commun.* **6** 6499
[1204] Song X *et al* 2016 Seed-assisted growth of single-crystalline patterned graphene domains on hexagonal boron nitride by chemical vapor deposition *Nano Lett.* **16** 6109–16
[1205] Tang S, Ding G, Xie X, Chen J, Wang C, Ding X, Huang F, Lu W and Jiang M 2012 Nucleation and growth of single crystal graphene on hexagonal boron nitride *Carbon* **50** 329–31
[1206] Saddow A A 2004 *Advances in Silicon Carbide Processing and Applications* (Boston, MA: Artech House Publisher)
[1207] Gao Y *et al* 2015 Large-area synthesis of high-quality and uniform monolayer WS_2 on reusable Au foils *Nat. Commun.* **6** 8569
[1208] Iqbal M W, Iqbal M Z, Khan M F, Shehzad M A, Seo Y, Park J H, Hwang C and Eom J 2015 High-mobility and air-stable single-layer WS_2 field-effect transistors sandwiched between chemical vapor deposition-grown hexagonal BN films *Sci. Rep.* **5** 10699
[1209] Rossi A, Büch H, Di Rienzo C, Miseikis V, Convertino D, Al-Temimy A, Voliani V, Gemmi M, Piazza V and Coletti C 2016 Scalable synthesis of WS_2 on graphene and h-BN: an all-2D platform for light-matter transduction *2D Mater.* **3** 031013
[1210] Tan H J, Fan Y, Zhou Y Q, Chen Q, Xu W S and Warner J H 2016 Ultrathin 2D photodetectors utilizing chemical vapor deposition grown WS_2 with graphene electrodes *ACS Nano* **10** 7866–73
[1211] Huang J, Yang L, Liu D, Chen J J, Fu Q, Xiong Y J, Lin F and Xiang B 2015 Large-area synthesis of monolayer WSe_2 on a SiO_2/Si substrate and its device applications *Nanoscale* **7** 4193–8
[1212] Liu B L, Fathi M, Chen L, Abbas A, Ma Y Q and Zhou C W 2015 Chemical vapor deposition growth of monolayer WSe_2 with tunable device characteristics and growth mechanism study *ACS Nano* **9** 6119–27
[1213] Nie Y F, Liang C P, Zhang K H, Zhao R, Eichfeld S M, Cha P R, Colombo L, Robinson J A, Wallace R M and Cho K 2016 First principles kinetic Monte Carlo study on the growth patterns of WSe_2 monolayer *2D Mater.* **3** 025029
[1214] Nie Y F *et al* 2018 Dislocation driven spiral and non-spiral growth in layered chalcogenides *Nanoscale* **10** 15023–34
[1215] Lin Y C, Zhang W J, Huang J K, Liu K K, Lee Y H, Liang C T, Chu C W and Li L J 2012 Wafer-scale MoS_2 thin layers prepared by MoO3 sulfurization *Nanoscale* **4** 6637–41
[1216] Wang S S, Wang X C and Warner J H 2015 All chemical vapor deposition growth of MoS_2:h-BN vertical van der Waals heterostructures *ACS Nano* **9** 5246–54
[1217] Forti S *et al* 2017 Electronic properties of single-layer tungsten disulfide on epitaxial graphene on silicon carbide *Nanoscale* **9** 16412–9
[1218] Duan X *et al* 2014 Lateral epitaxial growth of two-dimensional layered semiconductor heterojunctions *Nat. Nanotechnol.* **9** 1024–30
[1219] Li M Y *et al* 2015 Epitaxial growth of a monolayer WSe_2–MoS_2 lateral p-n junction with an atomically sharp interface *Science* **349** 524–8
[1220] Zhang Z, Chen P, Duan X, Zang K, Luo J and Duan X 2017 Robust epitaxial growth of two-dimensional heterostructures, multiheterostructures, and superlattices *Science* **357** 788–92
[1221] Xie S *et al* 2018 Coherent, atomically thin transition-metal dichalcogenide superlattices with engineered strain *Science* **359** 1131–6
[1222] Yu H, Kutana A and Yakobson B I 2016 Carrier delocalization in two-dimensional coplanar p–n junctions of graphene and metal dichalcogenides *Nano Lett.* **16** 5032–6
[1223] Pulkin A and Yazyev O V 2016 Spin- and valley-polarized transport across line defects in monolayerMoS_2 *Phys. Rev.* B **93** 041409(R)
[1224] Dumcenco D O, Chen K Y, Wang Y P, Huang Y S and Tiong K K 2010 Raman study of 2H-$Mo_{1-x}W_xS_2$ layered mixed crystals *J. Alloys Compd.* **506** 940–3
[1225] Woods J M, Jung Y, Xie Y, Liu W, Liu Y, Wang H and Cha J J 2016 One-step synthesis of MoS_2/WS_2 layered heterostructures and catalytic activity of defective transition metal dichalcogenide films *ACS Nano* **10** 2004–9
[1226] Xue Y *et al* 2015 Scalable production of a few-layer MoS_2/WS_2 vertical heterojunction array and its application for photodetectors *ACS Nano* **10** 573–80
[1227] Georgakilas V, Otyepka M, Bourlinos A B, Chandra V, Kim N, Kemp K C, Hobza P, Zboril R and Kim K S 2012 Functionalization of graphene: covalent and non-covalent approaches, derivatives and applications *Chem. Rev.* **112** 6156–214
[1228] Yang G-H, Bao D-D, Liu H, Zhang D-Q, Wang N and Li H-T 2017 Functionalization of graphene and applications of the derivatives *J. Inorg. Organomet. Polym. Mater.* **27** 1129–41
[1229] Bertolazzi S, Gobbi M, Zhao Y, Backes C and Samorì P 2018 Molecular chemistry approaches for tuning the properties of two-dimensional transition metal dichalcogenides *Chem. Soc. Rev.* **47** 6845–88
[1230] Hirsch A, Englert J M and Hauke F 2013 Wet chemical functionalization of graphene *Acc. Chem. Res.* **46** 87–96
[1231] Huang P, Jing L, Zhu H and Gao X 2013 Diazonium functionalized graphene: microstructure, electric, and magnetic properties *Acc. Chem. Res.* **46** 43–52
[1232] Bekyarova E, Sarkar S, Wang F, Itkis M E, Kalinina I, Tian X and Haddon R C 2013 Effect of covalent chemistry on the electronic structure and properties of carbon nanotubes and graphene *Acc. Chem. Res.* **46** 65–76
[1233] Milner E M, Skipper N T, Howard C A, Shaffer M S P, Buckley D J, Rahnejat K A, Cullen P L, Heenan R K, Lindner P and Schweins R 2012 Structure and morphology of charged graphene platelets in solution by small-angle neutron scattering *J. Am. Chem. Soc.* **134** 8302–5
[1234] Hodge S A, Buckley D J, Yau H C, Skipper N T, Howard C A and Shaffer M S P 2017 Chemical routes to discharging graphenides *Nanoscale* **9** 3150–8
[1235] Schäfer R A, Dasler D, Mundloch U, Hauke F and Hirsch A 2016 Basic insights into tunable graphene hydrogenation *J. Am. Chem. Soc.* **138** 1647–52
[1236] Strauss V, Schäfer R A, Hauke F, Hirsch A and Guldi D M 2015 Polyhydrogenated graphene: excited state dynamics in photo- and electroactive two-dimensional domains *J. Am. Chem. Soc.* **137** 13079–86
[1237] Schäfer R A, Weber K, Kolesnik-Gray M, Hauke F, Krstic V, Meyer B and Hirsch A 2016 Substrate-modulated reductive graphene functionalization *Angew. Chem., Int. Ed.* **55** 14858–62
[1238] Knirsch K C, Englert J M, Dotzer C, Hauke F and Hirsch A 2013 Screening of the chemical reactivity of three different graphite sources using the formation of reductively alkylated graphene as a model reaction *Chem. Commun.* **49** 10811–3

[1239] Morishita T, Clancy A J and Shaffer M S P 2014 Optimised exfoliation conditions enhance isolation and solubility of grafted graphenes from graphite intercalation compounds *J. Mater. Chem.* C **2** 15022–8
[1240] Hof F, Schäfer R A, Weiss C, Hauke F and Hirsch A 2014 Novel λ_3-iodane-based functionalization of synthetic carbon allotropes (SCAs)—common concepts and quantification of the degree of addition *Chem. Eur. J.* **20** 16644–51
[1241] Englert J M, Vecera P, Knirsch K C, Schäfer R A, Hauke F and Hirsch A 2013 Scanning-Raman-microscopy for the statistical analysis of covalently functionalized graphene *ACS Nano* **7** 5472–82
[1242] Hof F, Bosch S, Eigler S, Hauke F and Hirsch A 2013 New basic insight into reductive functionalization sequences of single walled carbon nanotubes (SWCNTs) *J. Am. Chem. Soc.* **135** 18385–95
[1243] Vecera P, Chacón-Torres J C, Pichler T, Reich S, Soni H R, Görling A, Edelthalhammer K, Peterlik H, Hauke F and Hirsch A 2017 Precise determination of graphene functionalisation by *in situ* Raman spectroscopy *Nat. Commun.* **8** 15192
[1244] Knirsch K C, Schäfer R A, Hauke F and Hirsch A 2016 Mono- and ditopic bisfunctionalization of graphene *Angew. Chem., Int. Ed.* **55** 5861–4
[1245] Quintana M, Vazquez E and Prato M 2013 Organic functionalization of graphene in dispersions *Acc. Chem. Res.* **46** 138–48
[1246] Paulus G L C, Wang Q H and Strano M S 2013 Covalent electron transfer chemistry of graphene with diazonium salts *Acc. Chem. Res.* **46** 160–70
[1247] Park J and Yan M 2013 Covalent functionalization of graphene with reactive intermediates *Acc. Chem. Res.* **46** 181–9
[1248] Kozhemyakina N V, Eigler S, Dinnebier R E, Inayat A, Schwieger W and Hirsch A 2013 Effect of the structure and morphology of natural, synthetic and post-processed graphites on their dispersibility and electronic properties, fullerenes, nanotubes and carbon *Nanostructures* **21** 804–23
[1249] Birch A J 1944 117. Reduction by dissolving metals. Part I *J. Chem. Soc.* **1944** 430 – 6
[1250] Birch A J 1955 212. Reduction by dissolving metals. Part II *J. Chem. Soc.* **1945** 809 – 13
[1251] Birch A J 1946 119. Reduction by dissolving metals. Part III *J. Chem. Soc.* **1946** 593–7
[1252] Birch A J 1947 25. Reduction by dissolving metals. Part IV *J. Chem. Soc.* **1947** 102–5
[1253] Englert J M, Dotzer C, Yang G, Schmid M, Papp C, Gottfried J M, Steinrück H-P, Spiecker E, Hauke F and Hirsch A 2011 Covalent bulk functionalization of graphene *Nat. Chem.* **3** 279–86
[1254] Dresselhaus M S and Dresselhaus G 1981 Intercalation compounds of graphite *Adv. Phys.* **30** 139–326
[1255] Knirsch K C, Hof F, Lloret V, Mundloch U, Hauke F and Hirsch A 2016 Topology-driven reductive silylation of synthetic carbon allotropes *J. Am. Chem. Soc.* **138** 15642–7
[1256] Clancy A J, Melbourne J and Shaffer M S P 2015 A one-step route to solubilised, purified or functionalised single-walled carbon nanotubes *J. Mater. Chem.* C **3** 16708–15
[1257] Dasler D, Schäfer R A, Minameyer M B, Hitzenberger J F, Hauke F, Drewello T and Hirsch A 2017 Direct covalent coupling of porphyrins to graphene *J. Am. Chem. Soc.* **139** 11760–5
[1258] Chan C K, Beechem T E, Ohta T, Brumbach M T, Wheeler D R and Stevenson K J 2013 Electrochemically driven covalent functionalization of graphene from fluorinated aryl iodonium salts *J. Phys. Chem.* C **117** 12038–44
[1259] Hof F, Hauke F and Hirsch A 2014 Brominated single walled carbon nanotubes as versatile precursors for covalent sidewall functionalization *Chem. Commun.* **50** 6582–4
[1260] Dyke C A and Tour J M 2013 Unbundled and highly functionalized carbon nanotubes from aqueous reactions *Nano Lett.* **3** 1215–8
[1261] Chattopadhyay J, Chakraborty S, Mukherjee A, Wang R, Engel P S and Billups W E 2007 SET mechanism in the functionalization of single-walled carbon nanotubes *J. Phys. Chem.* C **111** 17928–32
[1262] Hioe J and Zipse H 2010 Radical stability and its role in synthesis and catalysis *Org. Biomol. Chem.* **8** 3609–17
[1263] Xia Z *et al* 2016 Electrochemical functionalization of graphene at the nanoscale with self-assembling diazonium salts *ACS Nano* **10** 7125–34
[1264] Shih C-J, Wang Q H, Jin Z, Paulus G L C, Blankschtein D, Jarillo-Herrero P and Strano M S 2013 Disorder imposed limits of mono- and bilayer graphene electronic modification using covalent chemistry *Nano Lett.* **13** 809–17
[1265] Allongue P, Delamar M, Desbat B, Fagebaume O, Hitmi R, Pinson J and Savéant J-M 1997 Covalent modification of carbon surfaces by aryl radicals generated from the electrochemical reduction of diazonium salts *J. Am. Chem. Soc.* **119** 201–7
[1266] Gu S-Y, Hsieh C-T, Yuan J-Y, Hsueh J-H and Gandomi Y A 2018 Amino-functionalization of graphene nanosheets by electrochemical exfoliation technique *Diamond Relat. Mater.* **87** 99–106
[1267] Jokar E, Shahrokhian S and Zad A I 2014 Electrochemical functionalization of graphene nanosheets with catechol derivatives as an effective method for preparation of highly performance supercapacitors *Electrochim. Acta* **147** 136–42
[1268] Yadav A, Rodrigo Iost M, Neubert T J, Baylan S, Schmid T and Balasubramanian K 2019 Selective electrochemical functionalization of the graphene edge *Chem. Sci.* **10** 936
[1269] Sarkar S, Bekyarova E and Haddon R C 2012 Reversible grafting of α-naphthylmethyl radicals to epitaxial graphene *Angew. Chem.* **124** 4985–8
[1270] Dreyer D R, Todd A D and Bielawski C W 2014 Harnessing the chemistry of graphene oxide *Chem. Soc. Rev.* **43** 5288
[1271] Wu H, Shi H, Wang Y, Jia X, Tang C, Zhang J and Yang S 2014 Hyaluronic acid conjugated graphene oxide for targeted drug delivery *Carbon* **69** 379–89
[1272] Eigler S, Hu Y, Ishii Y and Hirsch A 2013 Controlled functionalization of graphene oxide with sodium azide *Nanoscale* **5** 12136
[1273] Lee J U, Lee W, Yi J W, Yoon S S, Lee S B, Jung B M, Kim B S and Byun J H 2013 Preparation of highly stacked graphene papers via site-selective functionalization of graphene oxide *J. Mater. Chem.* C **1** 12893
[1274] Mei Q, Zhang K, Guan G, Liu B, Wang S and Zhang Z 2010 Highly efficient photoluminescent graphene oxide with tunable surface properties *Chem. Commun.* **46** 7319
[1275] Neumann C *et al* 2015 Raman spectroscopy as probe of nanometre-scale strain variations in graphene *Nat. Commun.* **6** 8429
[1276] Thomas H R, Marsden A J, Walker M, Wilson N R and Rourke J P 2014 Sulfur-functionalized graphene oxide by epoxide ring-opening *Angew. Chem., Int. Ed.* **53** 7613–8
[1277] Wang S *et al* 2008 Band-like transport in surface-functionalized highly solution-processable graphene nanosheets *Adv. Mater.* **20** 3440–6
[1278] Yang H, Shan C, Li F, Han D, Zhang Q andNiu L 2009 Covalent functionalization of polydisperse chemically-converted graphene sheets with amine-terminated ionic liquid *Chem. Commun.* **2009** 3880
[1279] Vacchi I A, Spinato C, Raya J, Bianco A and Ménard-Moyon C 2016 Chemical reactivity of graphene oxide towards amines elucidated by solid-state NMR *Nanoscale* **8** 13714–21
[1280] Stankovich S, Dikin D A, Piner R D, Kohlhaas K A, Kleinhammes A, Jia Y, Wu Y, Nguyen S T and Ruoff R S 2007 Synthesis of graphene-based nanosheets via chemical reduction of exfoliated graphite oxide *Carbon* **45** 1558–65
[1281] Jiang J-X *et al* 2008 Conjugated microporous poly(aryleneethynylene) networks *Angew. Chem. Int., Ed.* **47** 1167–7
[1282] Peigney A, Laurent C, Flahaut E, Bacsa R R and Rousset A 2001 Specific surface area of carbon nanotubes and bundles of carbon nanotubes *Carbon* **39** 507–14

[1283] Stoller M D, Park S J, Zhu Y W, An J H and Ruoff R S 2008 Graphene-based ultracapacitors *Nano Lett.* **8** 3498–502
[1284] Zhu Y W, Murali S, Cai W W, Li X S, Suk J W, Potts J R and Ruoff R S 2010 Graphene and graphene oxide: synthesis, properties, and applications *Adv. Mater.* **22** 3906–24
[1285] Cao X H, Yin Z Y and Zhang H 2014 Three-dimensional graphene materials: preparation, structures and application in supercapacitors *Energy Environ. Sci.* **7** 1850–65
[1286] Dai L M, Chang D W, Baek J B and Lu W 2012 Carbon nanomaterials for advanced energy conversion and storage *Small* **8** 1130–66
[1287] Sudeep P M *et al* 2013 Covalently interconnected three-dimensional graphene oxide solids *ACS Nano* **7** 7034–40
[1288] Burress J W, Gadipelli S, Ford J, Simmons J M, Zhou W and Yildirim T 2010 Graphene oxide framework materials: theoretical predictions and experimental results *Angew. Chem., Int. Ed.* **49** 8902–4
[1289] Tsoufis T, Tuci G, Caporali S, Gournis D and Giambastiani G 2013 p-Xylylenediamine intercalation of graphene oxide for the production of stitched nanostructures with a tailored interlayer spacing *Carbon* **59** 100–8
[1290] Zhang X Y, Ciesielski A, Richard F, Chen P K, Prasetyanto E A, De Cola L and Samorì P 2016 Modular graphene-based 3D covalent networks: functional architectures for energy applications *Small* **12** 1044–52
[1291] Zhuang X, Gehrig D, Forler N, Liang H, Wagner M, Hansen M R, Laquai F, Zhang F and Feng X 2015 Conjugated microporous polymers with dimensionality-controlled heterostructures for green energy devices *Adv. Mater.* **27** 3789–96
[1292] Zhuang X, Zhang F, Wu D, Forler N, Liang H, Wagner M, Gehrig D, Hansen M R, Laquai F and Feng X 2013 Two-dimensional sandwich-type, graphene-based conjugated microporous polymers *Angew. Chem., Int. Ed.* **52** 9668–72
[1293] Jasim D A, Ménard-Moyon C, Bégin D, Bianco A and Kostarelos K 2015 Tissue distribution and urinary excretion of intravenously administered chemically functionalized graphene oxide sheets *Chem. Sci.* **6** 3952–64
[1294] Wan Y-J, Tang L-C, Yan D, Zhao L, Li Y-B, Wu L-B, Jiang J-X and Lai G-Q 2013 Improved dispersion and interface in the graphene/epoxy composites via a facile surfactant-assisted process *Compos. Sci. Technol.* **82** 60–8
[1295] Bai H, Xu Y, Zhao L, Li C and Shi G 2009 Non-covalent functionalization of graphene sheets by sulfonated polyaniline *Chem. Commun.* 1667 (https://doi.org/10.1039/b821805f)
[1296] Atif R and Inam F 2016 Reasons and remedies for the agglomeration of multilayered graphene and carbon nanotubes in polymers *Beilstein J. Nanotechnol.* **7** 1174–96
[1297] Bhattacharya M 2016 Polymer nanocomposites—a comparison between carbon nanotubes, graphene, and clay as nanofillers *Materials* **9** 262
[1298] Wei J, Vo T and Inam F 2015 Epoxy/graphene nanocomposites—processing and properties: a review *RSC Adv.* **5** 73510–24
[1299] Salavagione H J, Martí´nez G and Ellis G 2011 Graphene-based polymer nanocomposites *Physics and Applications of Graphene—Experiments* (Rijeka: Intech) ch 9 DOI: 10.5772/14665
[1300] Ramanathan T *et al* 2008 Functionalized graphene sheets for polymer nanocomposites *Nat. Nanotechnol.* **3** 327
[1301] Yang H, Li F, Shan C, Han D, Zhang Q, Niu L and Ivaska A 2009 Covalent functionalization of chemically converted graphene sheets via silane and its reinforcement *J. Mater. Chem.* **19** 4632–8
[1302] Alam A, Wan C and McNally T 2017 Surface amination of carbon nanoparticles for modification of epoxy resins: plasma-treatment versus wet-chemistry approach *Eur. Polym. J.* **87** 422–48
[1303] Ji X, Xu Y, Zhang W, Cui L and Liu J 2016 Review of functionalization, structure and properties of graphene/polymer composite fibers *Composites* A **87** 29–45
[1304] Vaisman L, Wagner H D and Marom G 2006 The role of surfactants in dispersion of carbon nanotubes *Adv. Colloid Interface Sci.* **128–30** 37–46
[1305] Verdejo R, Bernal M M, Romasanta L J and Lopez-Manchado M A 2011 Graphene filled polymer nanocomposites *J. Mater. Chem.* **21** 3301–10
[1306] Li Z, Wang R, Young R J, Deng L, Yang F, Hao L, Jiao W and Liu W 2013 Control of the functionality of graphene oxide for its application in epoxy nanocomposites *Polymer* **54** 6437–46
[1307] Wajid A S, Das S, Irin F, Ahmed H S T, Shelburne J L, Parviz D, Fullerton R J, Jankowski A F, Hedden R C and Green M J 2012 Polymer-stabilized graphene dispersions at high concentrations in organic solvents for composite production *Carbon* **50** 526–34
[1308] Wan Y-J, Gong L-X, Tang L-C, Wu L-B and Jiang J-X 2014 Mechanical properties of epoxy composites filled with silane-functionalized graphene oxide *Composites* A **64** 79–89
[1309] Hou S, Su S, Kasner M L, Shah P, Patel K and Madarang C J 2010 Formation of highly stable dispersions of silane-functionalized reduced graphene oxide *Chem. Phys. Lett.* **501** 68–74
[1310] Dhakal K P, Duong D L, Lee J, Nam H, Kim M, Kan M, Lee Y H and Kim J, Confocal absorption spectral imaging of MoS_2: optical transitions depending on the atomic thickness of intrinsic and chemically doped MoS_2 *Nanoscale* **6** 13028–35
[1311] Yuan B, Sheng H, Mu X, Song L, Tai Q, Shi Y, Liew K M and Hu Y 2015 Enhanced flame retardancy of polypropylene by melamine-modified graphene oxide *J. Mater. Sci.* **50** 5389–401
[1312] Xie M, Lei H, Zhang Y, Xu Y, Shen S, Ge Y, Li H and Xie J 2016 Non-covalent modification of graphene oxide nanocomposites with chitosan/dextran and its application in drug delivery *RSC Adv.* **6** 9328–37
[1313] Mao Y, Wen S, Chen Y, Zhang F, Panine P, Chan T W, Zhang L, Liang Y and Liu L 2013 High performance graphene oxide based rubber composites *Sci. Rep.* **3** 2508
[1314] Vladár A E *Strategies For Scanning Electron Microscopy Sample Preparation and Characterization of Multiwall Carbon Nanotube Polymer Composites* (National Institute of Standards and Technology) (https://doi.org/10.6028/NIST.SP.1200-17)
[1315] Rabe J P and Buchholz S 1991 Commensurability and mobility in 2-dimensional molecular-patterns on graphite *Science* **253** 424–7
[1316] Grande M, Bianco G V, Vincenti M A, de Ceglia D, Capezzuto P, Scalora M, D'Orazio A and Bruno G 2015 Optically transparent microwave polarizer based on quasi-metallic graphene *Sci. Rep.* **5** 17083
[1317] Sachs B, Wehling T O, Lichtenstein A I and Katsnelson M I 2011 Theory of doping: monovalent adsorbates *Physics and Applications of Graphene—Theory* (Rijeka: InTech)
[1318] Karlický F, Kumara Ramanatha Datta K, Otyepka M and Zboril R 2013 Halogenated graphenes: rapidly growing family of graphene derivatives *ACS Nano* **7** 6434–64
[1319] Poh H L, Šimek P, Sofer Z and Pumera M 2013 Halogenation of graphene with chlorine, bromine, or iodine by exfoliation in a halogen atmosphere *Chem. Eur. J.* **19** 2655–62
[1320] Mansour A E, Dey S, Amassian A and Tanielian M H 2015 Bromination of graphene: a new route to making high performance transparent conducting electrodes with low optical losses *ACS Appl. Mater. Interfaces* **7** 17692–9
[1321] Bruna M, Ott A K, Ijäs M, Yoon D, Sassi U and Ferrari A C 2014 Doping dependence of the raman spectrum of defected graphene *ACS Nano* **8** 7432–41
[1322] Cançado L G *et al* 2011 Quantifying defects in graphene via raman spectroscopy at different excitation energies *Nano Lett.* **11** 3190–6
[1323] Berner N C, Winters S, Backes C, Yim C, Dumbgen K C, Kaminska I, Mackowski S, Cafolla A A, Hirsch A and Duesberg G S 2015 Understanding and optimising the packing density of perylene bisimide layers on CVD-grown graphene *Nanoscale* **7** 16337–42

[1324] Tian X Q, Xu J B and Wang X M 2010 Self-assembly of PTCDA ultrathin films on graphene: structural phase transition and charge transfer saturation *J. Phys. Chem.* C **114** 20917–24
[1325] Huang H, Chen S, Gao X, Chen W and Wee A T S 2009 Structural and electronic properties of PTCDA thin films on epitaxial graphene *ACS Nano* **3** 3431–6
[1326] Wang Q H and Hersam M C 2009 Room-temperature molecular-resolution characterization of self-assembled organic monolayers on epitaxial graphene *Nat. Chem.* **1** 206
[1327] Winters S, Berner N C, Mishra R, Dumbgen K C, Backes C, Hegner M, Hirsch A and Duesberg G S 2015 On-surface derivatisation of aromatic molecules on graphene: the importance of packing density *Chem. Commun.* **51** 16778–81
[1328] Woszczyna M, Winter A, Grothe M, Willunat A, Wundrack S, Stosch R, Weimann T, Ahlers F and Turchanin A 2014 All-carbon vertical van der Waals heterostructures: non-destructive functionalization of graphene for electronic applications *Adv. Mater.* **26** 4831–7
[1329] Chua C K and Pumera M 2013 Covalent chemistry on graphene *Chem. Soc. Rev.* **42** 3222–33
[1330] Sun Z, Kohama S-I, Zhang Z, Lomeda J R and Tour J M 2010 Soluble graphene through edge-selective functionalization *Nano Res.* **3** 117–25
[1331] Bellunato A, Arjmandi Tash H, Cesa Y and Schneider G F 2016 Chemistry at the edge of graphene *ChemPhysChem* **17** 785–801
[1332] Koehler F M, Jacobsen A, Ensslin K, Stampfer C and Stark W J 2010 Selective chemical modification of graphene surfaces: distinction between single- and bilayer graphene *Small* **6** 1125–30
[1333] Lomeda J R, Doyle C D, Kosynkin D V, Hwang W-F and Tour J M 2008 Diazonium functionalization of surfactant-wrapped chemically converted graphene sheets *J. Am. Chem. Soc.* **130** 16201–6
[1334] Quintana M, Montellano A, del Rio Castillo A E, Tendeloo G V, Bittencourt C and Prato M 2011 Selective organic functionalization of graphene bulk or graphene edges *Chem. Commun.* **47** 9330–2
[1335] Wang A *et al* 2016 Covalent functionalization of reduced graphene oxide with porphyrin by means of diazonium chemistry for nonlinear optical performance *Sci. Rep.* **6** 23325
[1336] Niyogi S, Bekyarova E, Hong J, Khizroev S, Berger C, de Heer W and Haddon R C 2011 Covalent chemistry for graphene electronics *J. Phys. Chem. Lett.* **2** 2487–98
[1337] Bernal M M, Di Pierro A, Novara C, Giorgis F, Mortazavi B, Saracco G and Fina A 2018 Edge-grafted molecular junctions between graphene nanoplatelets: applied chemistry to enhance heat transfer in nanomaterials *Adv. Funct. Mater.* **28** 1706954
[1338] Farmer D B, Golizadeh-Mojarad R, Perebeinos V, Lin Y-M, Tulevski G S, Tsang J C and Avouris P 2009 Chemical doping and electron–hole conduction asymmetry in graphene devices *Nano Lett.* **9** 388–92
[1339] Bouša D, Jankovský O, Sedmidubský D, Luxa J, Šturala J, Pumera M and Sofer Z 2015 Mesomeric effects of graphene modified with diazonium salts: substituent type and position influence its properties *Chem. Eur. J.* **21** 17728–38
[1340] Bueno R A *et al* 2017 Highly selective covalent organic functionalization of epitaxial graphene *Nat. Commun.* **8** 15306
[1341] Castelaín M, Martínez G, Marco C, Ellis G and Salavagione H J 2013 Effect of click-chemistry approaches for graphene modification on the electrical, thermal, and mechanical properties of polyethylene/graphene nanocomposites *Macromolecules* **46** 8980–7
[1342] Criado A, Melchionna M, Marchesan S and Prato M 2015 The covalent functionalization of graphene on substrates *Angew. Chem., Int. Ed.* **54** 10734–50
[1343] Hossain M Z, Walsh M A and Hersam M C 2010 Scanning tunneling microscopy, spectroscopy, and nanolithography of epitaxial graphene chemically modified with aryl moieties *J. Am. Chem. Soc.* **132** 15399–403
[1344] Niyogi S *et al* 2010 Spectroscopy of covalently functionalized graphene *Nano Lett.* **10** 4061–6
[1345] Gass M H, Bangert U, Bleloch A L, Wang P, Nair R R and Geim A K 2008 Free-standing graphene at atomic resolution *Nat. Nanotechnol.* **3** 676–81
[1346] Meyer J C, Kisielowski C, Erni R, Rossell M D, Crommie M F and Zettl A 2008 Direct imaging of lattice atoms and topological defects in graphene membranes *Nano Lett.* **8** 3582–6
[1347] Rodrigo L, Pou P and Pérez R 2016 Graphene monovacancies: electronic and mechanical properties from large scale *ab initio* simulations *Carbon* **103** 200–8
[1348] Ugeda M M, Fernández-Torre D, Brihuega I, Pou P, Martínez-Galera A J, Pérez R and Gómez-Rodríguez J M 2011 Point defects on graphene on metals *Phys. Rev. Lett.* **107** 116803
[1349] Kelly K F, Sarkar D, Hale G D, Oldenburg S J and Halas N J 1996 Threefold electron scattering on graphite observed with C60-adsorbed STM tips *Science* **273** 1371–3
[1350] Lehtinen O, Kotakoski J, Krasheninnikov A V, Tolvanen A and Nordlund K, Keinonen J 2010 Effects of ion bombardment on a two-dimensional target: atomistic simulations of graphene irradiation *Phys. Rev.* B **81** 153401
[1351] Li Q, Mahmood N, Zhu J, Hou Y and Sun S 2014 Graphene and its composites with nanoparticles for electrochemical energy applications *Nano Today* **9** 668–83
[1352] Choi H C, Shim M, Bangsaruntip S and Dai H 2002 Spontaneous reduction of metal ions on the sidewalls of carbon nanotubes *J. Am. Chem. Soc.* **124** 9058–9
[1353] Fogden S, Howard C A, Heenan R K, Skipper N T and Shaffer M S P 2012 Scalable method for the reductive dissolution, purification, and separation of single-walled carbon nanotubes *ACS Nano* **6** 54–62
[1354] Howard C A, Thompson H, Wasse J C and Skipper N T 2004 Formation of giant solvation shells around fulleride anions in liquid ammonia *J. Am. Chem. Soc.* **126** 13228–9
[1355] Catheline A, Vallés C, Drummond C, Ortolani L, Morandi V, Marcaccio M, Iurlo M, Paolucci F and Pénicaud A 2011 Graphene solutions *Chem. Commun.* **47** 5470
[1356] Pénicaud A, Poulin P, Derré A, Anglaret E and Petit P 2005 Spontaneous dissolution of a single-wall carbon nanotube salt *J. Am. Chem. Soc.* **127** 8–9
[1357] Hodge S A, Fogden S, Howard C A, Skipper N T and Shaffer M S P 2013 Electrochemical processing of discrete single-walled carbon nanotube anions *ACS Nano* **7** 1769–78
[1358] Bayazit M K, Suri A and Coleman K S 2010 Formylation of single-walled carbon nanotubes *Carbon* **48** 3412–9
[1359] Chen K, Ge C and Li J 1998 Phase formation and thermodynamic analysis of self-propagating high-temperature synthesis Al–Zr–N system composites *J. Mater. Res.* **13** 2610–3
[1360] Graupner R, Abraham J, Wunderlich D, Vencelová A, Lauffer P, Röhrl J, Hundhausen M, Ley L and Hirsch A 2006 Nucleophilic–alkylation–reoxidation: a functionalization sequence for single-wall carbon nanotubes *J. Am. Chem. Soc.* **128** 6683–9
[1361] Mukherjee A, Combs R, Chattopadhyay J, Abmayr D W, Engel P S and Billups W E 2008 Attachment of nitrogen and oxygen centered radicals to single-walled carbon nanotube salts *Chem. Mater.* **20** 7339–43
[1362] Wunderlich D, Hauke F and Hirsch A 2008 Preferred functionalization of metallic and small-diameter single-walled carbon nanotubes by nucleophilic addition of organolithium and-magnesium compounds followed by reoxidation *Chem. Eur. J.* **14** 1607–14
[1363] Howard C A, Dean M P M and Withers F 2011 Phonons in potassium-doped graphene: the effects of electron-phonon interactions, dimensionality, and adatom ordering *Phys. Rev.* B **84** 241404(R)
[1364] Bard A J and Faulkner L R 2001 *Electrochemical Methods* 2nd edn (New York: Wiley)

[1365] Wei W, Wang G, Yang S, Feng X and Müllen K 2015 Efficient coupling of nanoparticles to electrochemically exfoliated graphene *J. Am. Chem. Soc.* **137** 5576–81
[1366] Huttel Y 2017 *Gas-Phase Synthesis of Nanoparticles* (New York: Wiley)
[1367] Frank F, Schulze W, Tesche B, Urban J and Winter B 1985 Formation of metal clusters and molecules by means of the gas aggregation technique and characterisation of size distribution *Surf. Sci.* **156** 90–9
[1368] Llamosa D, Ruano M, Martínez L, Mayoral A, Roman E, García-Hernández M and Huttel Y 2014 The ultimate step towards a tailored engineering of core@shell and core@shell@shell nanoparticles *Nanoscale* **6** 13483–6
[1369] Martínez L, Díaz M, Román E, Ruano M, Llamosa P D and Huttel Y 2012 Generation of nanoparticles with adjustable size and controlled stoichiometry: recent advances *Langmuir* **28** 11241–9
[1370] Martínez L, Mayoral A, Espiñeira M, Roman E, Palomares F J and Huttel Y 2017 Core@shell, Au@TiO_x nanoparticles by gas phase synthesis *Nanoscale* **9** 6463–70
[1371] Ferrando R, Jellinek J and Johnston R L 2008 Nanoalloys: from theory to applications of alloy clusters and nanoparticles *Chem. Rev.* **108** 845–910
[1372] Ghosh Chaudhuri R and Paria S 2012 Core/shell nanoparticles: classes, properties, synthesis mechanisms, characterization, and applications *Chem. Rev.* **112** 2373–433
[1373] Pohl D, Surrey A, Schultz L and Rellinghaus B 2012 The impact of oxygen on the morphology of gas-phase prepared Au nanoparticles *Appl. Phys. Lett.* **101** 263105
[1374] Garcia M A, Fernandez Pinel E, de la Venta J, Quesada A, Bouzas V, Fernández J F, Romero J J, Martín González M S and Costa-Krämer J L 2009 Sources of experimental errors in the observation of nanoscale magnetism *J. Appl. Phys.* **105** 013925
[1375] Ruano M, Díaz M, Martínez L, Navarro E, Román E, García-Hernandez M, Espinosa A, Ballesteros C, Fermento R and Huttel Y 2013 Matrix and interaction effects on the magnetic properties of Co nanoparticles embedded in gold and vanadium *Phys. Chem. Chem. Phys.* **15** 316–29
[1376] Plant S R, Cao L and Palmer R E 2014 Atomic structure control of size-selected gold nanoclusters during formation *J. Am. Chem. Soc.* **136** 7559–62
[1377] Krajewska A, Oberda K, Azpeitia J, Gutierrez A, Pasternak I, López M F, Mierczyk Z, Munuera C and Strupinski W 2016 Influence of Au doping on electrical properties of CVD graphene *Carbon* **100** 625–31
[1378] Azpeitia J, Garcia-Hernandez M, Martinez L, Huttel Y, Lopez Fagundez M F and Munuera C 2019 submitted
[1379] Jordá-Beneyto M, Suárez-García F, Lozano-Castelló D, Cazorla-Amorós D and Linares-Solano A 2007 Hydrogen storage on chemically activated carbons and carbon nanomaterials at high pressures *Carbon* **45** 293–303
[1380] Züttel A, Nützenadel C, Sudan P, Mauron P, Emmenegger C, Rentsch S, Schlapbach L, Weidenkaff A and Kiyobayashi T 2002 Hydrogen sorption by carbon nanotubes and other carbon nanostructures *J. Alloys Compd.* **330–32** 676–82
[1381] Shen C and Aguey-Zinsou K-F 2017 Nanosized magnesium electrochemically deposited on a carbon nanotubes suspension: synthesis and hydrogen storage *Frontiers Energy Res.* **5** 27
[1382] Hwang S-J and Chuang Y-S 2016 Enhanced hydrogen storage properties of MgH_2 co-catalyzed with zirconium oxide and single-walled carbon nanotubes *J. Alloys Compd.* **664** 284–90
[1383] Liu Y, Zou J, Zeng X, Wu X, Tian H, Ding W, Wang J and Walter A 2013 Study on hydrogen storage properties of Mg nanoparticles confined in carbon aerogels *Int. J. Hydrog. Energy* **38** 5302–8
[1384] Popilevsky L, Skripnyuk V M, Beregovsky M, Sezen M, Amouyal Y and Rabkin E 2016 Hydrogen storage and thermal transport properties of pelletized porous Mg-2 wt.% multiwall carbon nanotubes and Mg-2 wt.% graphite composites *Int. J. Hydrog. Energy* **41** 14461–74
[1385] Yürüm Y, Taralp A and Veziroglu T N 2009 Storage of hydrogen in nanostructured carbon materials *Int. J. Hydrog. Energy* **34** 3784–98
[1386] Zhang S, Gross A F, Van Atta S L, Lopez M, Liu P, Ahn C C, Vajo J J and Jensen C M 2009 The synthesis and hydrogen storage properties of a MgH_2 incorporated carbon aerogel scaffold *Nanotechnology* **20** 204027
[1387] Liu W, Setijadi E, Crema L, Bartali R, Laidani N, Aguey-Zinsou K F and Speranza G 2018 Carbon nanostructures/Mg hybrid materials for hydrogen storage *Diamond Relat. Mater.* **82** 19–24
[1388] Aguey-Zinsou K-F and Ares-Fernández J-R 2008 Synthesis of colloidal magnesium: a near room temperature store for hydrogen *Chem. Mater.* **20** 376–8
[1389] Lu Z, Schechter A, Moshkovich M and Aurbach D 1999 On the electrochemical behavior of magnesium electrodes in polar aprotic electrolyte solutions *J. Electroanal. Chem.* **466** 203–17
[1390] Setijadi E J, Boyer C and Aguey-Zinsou K-F 2012 Remarkable hydrogen storage properties for nanocrystalline MgH_2 synthesised by the hydrogenolysis of Grignard reagents *Phys. Chem. Chem. Phys.* **14** 11386
[1391] Setijadi E J, Boyer C and Aguey-Zinsou K-F 2014 Switching the thermodynamics of MgH2nanoparticles through polystyrene stabilisation and oxidation *RSC Adv.* **4** 39934
[1392] Liu W and Aguey-Zinsou K-F 2014 Size effects and hydrogen storage properties of Mg nanoparticles synthesised by an electroless reduction method *J. Mater. Chem.* C **2** 9718
[1393] Cho E S, Ruminski A M, Aloni S, Liu Y-S, Guo J and Urban J J 2016 Graphene oxide/metal nanocrystal multilaminates as the atomic limit for safe and selective hydrogen storage *Nat. Commun.* **7** 10804
[1394] Liu G, Wang Y, Jiao L and Yuan H 2014 Understanding the role of few-layer graphene nanosheets in enhancing the hydrogen sorption kinetics of magnesium hydride *ACS Appl. Mater. Interfaces* **6** 11038–46
[1395] Tachikawa H, Iyama T and Kawabata H 2009 MD simulation of the interaction of magnesium with graphene *Thin Solid Films* **518** 877–9
[1396] Liu R, Zhao Y and Chu T 2015 Theoretical exploration of MgH_2 and graphene nano-flakes in cyclohexane: proposing a new perspective toward functional hydrogen storage material *Chem. Commun.* **51** 2429–32
[1397] Tozzini V and Pellegrini V 2013 Prospects for hydrogen storage in graphene *Phys. Chem. Chem. Phys.* **15** 80–9
[1398] Barkhordarian G, Klassen T and Bormann R 2006 Kinetic investigation of the effect of milling time on the hydrogen sorption reaction of magnesium catalyzed with different Nb_2O_5 contents *J. Alloys Compd.* **407** 249–55
[1399] Bogdanovic B, Bohmhammel K, Christ B, Reiser A, Schlichte K, Vehlen R and Wolf U 1999 Thermodynamic investigation of the magnesium–hydrogen system *J. Alloys Compd.* **282** 84–92
[1400] Aguey-Zinsou K-F and Ares-Fernández J-R 2010 Hydrogen in magnesium: new perspectives toward functional stores *Energy Environ. Sci.* **3** 526
[1401] Graetz J 2009 New approaches to hydrogen storage *Chem. Soc. Rev.* **38** 73–82
[1402] Kim K C, Dai B, Karl Johnson J and Sholl D S 2009 Assessing nanoparticle size effects on metal hydride thermodynamics using the Wulff construction *Nanotechnology* **20** 204001
[1403] Makarova M, Okawa Y and Aono M 2012 Selective adsorption of thiol molecules at sulfur vacancies on MoS_2(0 0 0 1), followed by vacancy repair via S–C dissociation *J. Phys. Chem.* C **116** 22411–6
[1404] Chou S S, De M, Kim J, Byun S, Dykstra C, Yu J, Huang J and Dravid V P 2013 Ligand conjugation of chemically exfoliated MoS_2 *J. Am. Chem. Soc.* **135** 4584–7
[1405] Zhou L, He B, Yang Y and He Y 2014 Facile approach to surface functionalized MoS_2 nanosheets *RSC Adv.* **4** 32570–8
[1406] Chhowalla M, Shin H S, Eda G, Li L-J, Loh K P and Zhang H 2013 The chemistry of two-dimensional layered transition metal dichalcogenide nanosheets *Nat. Chem.* **5** 263

[1407] Fan X, Xu P, Li Y C, Zhou D, Sun Y, Nguyen M A T, Terrones M and Mallouk T E 2016 Controlled exfoliation of MoS_2 crystals into trilayer nanosheets *J. Am. Chem. Soc.* **138** 5143–9
[1408] Yuan K, Zhuang X, Fu H, Brunklaus G, Forster M, Chen Y, Feng X and Scherf U 2016 Two-dimensional core-shelled porous hybrids as highly efficient catalysts for the oxygen reduction reaction *Angew. Chem., Int. Ed.* **55** 6858–63
[1409] Backes C, Berner N C, Chen X, Lafargue P, LaPlace P, Freeley M, Duesberg G S, Coleman J N and McDonald A R 2015 Functionalization of liquid-exfoliated two-dimensional 2H-MoS_2 *Angew. Chem., Int. Ed.* **54** 2638–42
[1410] Chen X and McDonald A R 2016 Functionalization of two-dimensional transition-metal dichalcogenides *Adv. Mater.* **28** 5738–46
[1411] Hirsch A and Hauke F Post graphene 2D chemistry: the emerging field of molybdenum disulfide and black phosphorus functionalization *Angew. Chem., Int. Ed.* **57** 4338 – 54 (https://doi.org/10.1002/anie.201708211)
[1412] Canton-Vitoria R, Sayed-Ahmad-Baraza Y, Pelaez-Fernandez M, Arenal R, Bittencourt C, Ewels C P and Tagmatarchis N 2017 Functionalization of MoS_2 with 1,2-dithiolanes: toward donor-acceptor nanohybrids for energy conversion *NPJ 2D Mater. Appl.* **1** 13
[1413] Vallan L, Canton-Vitoria R, Gobeze H B, Jang Y, Arenal R, Benito A M, Maser W K, D'Souza F and Tagmatarchis N 2018 Interfacing transition metal dichalcogenides with carbon nanodots for managing photoinduced energy and charge-transfer processes *J. Am. Chem. Soc.* **140** 13488–96
[1414] Wirtz C, Hallam T, Cullen C P, Berner N C, O'Brien M, Marcia M, Hirsch A and Duesberg G S 2015 Atomic layer deposition on 2D transition metal chalcogenides: layer dependent reactivity and seeding with organic ad-layers *Chem. Commun.* **51** 16553–6
[1415] Wang Y Y, Gao R X, Ni Z H, He H, Guo S P, Yang H P, Cong C X and Yu T 2012 Thickness identification of two-dimensional materials by optical imaging *Nanotechnology* **23** 495713
[1416] Castellanos-Gomez A, Navarro-Moratalla E, Mokry G, Quereda J, Pinilla-Cienfuegos E, Agraït N, van der Zant H S, Coronado E, Steele G A and Rubio-Bollinger G 2013 Fast and reliable identification of atomically thin layers of $TaSe_2$ crystals *Nano Res.* **6** 191–9
[1417] Zhang H, Ran F, Shi X, Fang X, Wu S, Liu Y, Zheng X, Yang P, Liu Y and Wang L 2017 Optical thickness identification of transition metal dichalcogenide nanosheets on transparent substrates *Nanotechnology* **28** 164001
[1418] Blake P, Hill E, Castro Neto A, Novoselov K, Jiang D, Yang R, Booth T and Geim A 2007 Making graphene visible *Appl. Phys. Lett.* **91** 063124
[1419] Casiraghi C, Hartschuh A, Lidorikis E, Qian H, Harutyunyan H, Gokus T, Novoselov K S and Ferrari A C 2007 Rayleigh imaging of graphene and graphene layers *Nano Lett.* **7** 2711–7
[1420] Roddaro S, Pingue P, Piazza V, Pellegrini V and Beltram F 2007 The optical visibility of graphene: interference colors of ultrathin graphite on SiO_2 *Nano Lett.* **7** 2707–10
[1421] Castellanos-Gomez A, Agraït N and Rubio-Bollinger G 2010 Optical identification of atomically thin dichalcogenide crystals *Appl. Phys. Lett.* **96** 213116
[1422] Benameur M, Radisavljevic B, Heron J, Sahoo S, Berger H and Kis A 2011 Visibility of dichalcogenide nanolayers *Nanotechnology* **22** 125706
[1423] Castellanos-Gomez A, Wojtaszek M, Tombros N, Agraït N, van Wees B J and Rubio-Bollinger G 2011 Atomically thin mica flakes and their application as ultrathin insulating substrates for graphene *Small* **7** 2491–7
[1424] Ares P, Zamora F and Gomez-Herrero J 2017 Optical identification of few-layer antimonene crystals *ACS Photonics* **4** 600–5
[1425] Brotons-Gisbert M, Andres-Penares D, Martínez-Pastor J, Cros A and Sánchez-Royo J 2017 Optical contrast of 2D InSe on SiO_2/Si and transparent substrates using bandpass filters *Nanotechnology* **28** 115706
[1426] Abergel D, Russell A and Fal'ko V I 2007 Visibility of graphene flakes on a dielectric substrate *Appl. Phys. Lett.* **91** 063125
[1427] Castellanos Gómez A 2011 Propiedades electrónicas, mecánicas y ópticas de cristales bidimensionales de espesor atómico *PhD Thesis* Universidad Autónoma de Madrid
[1428] Zhang H, Ma Y, Wan Y, Rong X, Xie Z, Wang W and Dai L 2015 Measuring the refractive index of highly crystalline monolayer MoS_2 with high confidence *Sci. Rep.* **5** 18357
[1429] Ghasemi F, Frisenda R, Dumcenco D, Kis A, Perez de Lara D and Castellanos-Gomez A 2017 High throughput characterization of epitaxially grown single-layer MoS_2 *Electronics* **6** 28
[1430] Gant P, Ghasemi F, Maeso D, Munuera C, López-Elvira E, Frisenda R, De Lara D P, Rubio-Bollinger G, Garcia-Hernandez M and Castellanos-Gomez A 2017 Optical contrast and refractive index of natural van der Waals heterostructure nanosheets of franckeite *Beilstein J. Nanotechnol.* **8** 2357
[1431] Castellanos-Gomez A, Quereda J, van der Meulen H P, Agraït N and Rubio-Bollinger G 2016 Spatially resolved optical absorption spectroscopy of single-and few-layer MoS_2 by hyperspectral imaging *Nanotechnology* **27** 115705
[1432] Rubio-Bollinger G, Guerrero R, de Lara D P, Quereda J, Vaquero-Garzon L, Agraït N, Bratschitsch R and Castellanos-Gomez A 2015 Enhanced visibility of MoS_2, $MoSe_2$, WSe_2 and black-phosphorus: making optical identification of 2D semiconductors easier *Electronics* **4** 847–56
[1433] Zhao W, Ghorannevis Z, Chu L, Toh M, Kloc C, Tan P-H and Eda G 2012 Evolution of electronic structure in atomically thin sheets of WS_2 and WSe2 *ACS Nano* **7** 791–7
[1434] Frisenda R, Niu Y, Gant P, Molina-Mendoza A J, Schmidt R, Bratschitsch R, Liu J, Fu L, Dumcenco D and Kis A 2017 Micro-reflectance and transmittance spectroscopy: a versatile and powerful tool to characterize 2D materials *J. Phys. D: Appl. Phys.* **50** 074002
[1435] Quereda J, San-Jose P, Parente V, Vaquero-Garzon L, Molina-Mendoza A J, Agraït N, Rubio-Bollinger G, Guinea F, Roldán R and Castellanos-Gomez A 2016 Strong modulation of optical properties in black phosphorus through strain-engineered rippling *Nano Lett.* **16** 2931–7
[1436] Niu Y *et al* 2018 Thickness-dependent optical properties of MoS_2, $MoSe_2$, WS_2 and WSe_2 *Nanomaterials* **8** 725
[1437] Kouroupis-Agalou K, Liscio A, Treossi E, Ortolani L, Morandi V, Pugno N M and Palermo V 2014 Fragmentation and exfoliation of 2-dimensional materials: a statistical approach *Nanoscale* **6** 5926–33
[1438] Ridings C, Warr G G and Andersson G G 2012 Composition of the outermost layer and concentration depth profiles of ammonium nitrate ionic liquid surfaces *Phys. Chem. Chem. Phys.* **14** 16088–95
[1439] Nemes-Incze P, Osváth Z, Kamarás K and Biró L P 2008 Anomalies in thickness measurements of graphene and few layer graphite crystals by tapping mode atomic force microscopy *Carbon* **46** 1435–42
[1440] Rubinstein M and Colby R H 2003 *Polymer Physics* (Oxford: Oxford University Press)
[1441] Mativetsky J M, Treossi E, Orgiu E, Melucci M, Veronese G P, Samorì` P and Palermo V 2010 Local current mapping and patterning of reduced graphene oxide *J. Am. Chem. Soc.* **132** 14130–6
[1442] Song X *et al* 2017 Enhanced piezoelectric effect at the edges of stepped molybdenum disulfide nanosheets *Nanoscale* **9** 6237–45
[1443] Sadewasser S and Lux-Steiner M C 2003 Correct height measurement in noncontact atomic force microscopy *Phys. Rev. Lett.* **91** 266101
[1444] Yang K M, Chung J Y, Hsieh M F, Ferng S S, Lin D S and Chiang T C 2016 Systematic variations in apparent topographic height as measured by noncontact atomic force microscopy *Phys. Rev.* B **74** 193313
[1445] Novoselov K S 2004 Electric field effect in atomically thin carbon films *Science* **306** 666–9

[1446] Tamayo J and García R 1997 Effects of elastic and inelastic interactions on phase contrast images in tapping-mode scanning force microscopy *Appl. Phys. Lett.* **71** 2394–6
[1447] Paradinas M, Munuera C, Silien C, Buck M and Ocal C 2013 Heterogeneous nanotribological response of polymorphic self-assembled monolayers arising from domain and phase dependent friction *Phys. Chem. Chem. Phys.* **15** 1302–9
[1448] García R 2002 Dynamic atomic force microscopy methods *Surf. Sci. Rep.* **47** 197–301
[1449] Wiesendanger R 1994 *Scanning Probe Microscopy and Spectroscopy* (Cambridge: Cambridge University Press)
[1450] Tamayo J and García R 1996 Deformation, contact time, and phase contrast in tapping mode scanning force microscopy *Langmuir* **12** 4430–5
[1451] García R, Magerle R and Perez R 2007 Nanoscale compositional mapping with gentle forces *Nat. Mater.* **6** 405–11
[1452] Obraztsov A N, Obraztsova E A, Tyurnina A V and Zolotukhin A A 2007 Chemical vapor deposition of thin graphite films of nanometer thickness *Carbon* **45** 2017–21
[1453] Deng S and Berry V 2016 Wrinkled, rippled and crumpled graphene: an overview of formation mechanism, electronic properties, and applications *Mater. Today* **19** 197–212
[1454] Filleter T, McChesney J L, Bostwick A, Rotenberg E, Emtsev K V, Seyller T, Horn K and Bennewitz R 2009 Friction and dissipation in epitaxial graphene films *Phys. Rev. Lett.* **102** 086102
[1455] Vasic B, Matkovic A, Gajic R and Stankovic I 2016 Wear properties of graphene edges probed by atomic force microscopy based lateral manipulation *Carbon* **107** 723–32
[1456] Martínez N F and García R 2006 Measuring phase shifts and energy dissipation with amplitude modulation atomic force microscopy *Nanotechnology* **17** S167–72
[1457] Palacios-Lidón E, Munuera C, Ocal C and Colchero J 2010 Contrast inversion in non-contact dynamic scanning force microscopy: what is high and what is low? *Ultramicroscopy* **110** 789–800
[1458] Carpick R W and Salmeron M 1997 Scratching the surface: fundamental investigations of tribology with atomic force microscopy *Chem. Rev.* **97** 1163–94
[1459] Berman D, Erdemir A and Sumant A V 3014 Graphene: a new emerging lubricant *Mater. Today* **17** 31–42
[1460] Butt H-J, Cappella B and Kappl M 2005 Force measurements with the atomic force microscope: technique, interpretation and applications *Surf. Sci. Rep.* **59** 1–152
[1461] Cappella B and Dietler G 1999 Force-distance curves by atomic force microscopy *Surf. Sci. Rep.* **34** 1–104
[1462] Kazakova O, Panchal V and Burnett T 2013 Epitaxial graphene and graphene–based devices studied by electrical scanning probe microscopy *Crystals* **3** 191–233
[1463] Hormeño S, Penedo M, Manzano C V and Luna M 2013 Gold nanoparticle coated silicon tips for Kelvin probe force microscopy in air *Nanotechnology* **24** 395701
[1464] Filleter T, Emtsev K V, Seyller T and Bennewitz R 2008 Local work function measurements of epitaxial graphene *Appl. Phys. Lett.* **93** 133117
[1465] Ziegler D, Gava P, Güttinger J, Molitor F, Wirtz L, Lazzeri M, Saitta A M, Stemmer A, Mauri F and Stampfer C 2011 Variations in the work function of doped single- and few-layer graphene assessed by Kelvin probe force microscopy and density functional theory *Phys. Rev.* B **83** 235434
[1466] Eriksson J, Pearce R, Iakimov T, Virojanadara C, Gogova D, Andersson M, Syväjärvi M, Lloyd Spetz A and Yakimova R 2012 The influence of substrate morphology on thickness uniformity and unintentional doping of epitaxial graphene on SiC *Appl. Phys. Lett.* **100** 241607
[1467] Nonnenmacher M, O'Boyle M P and Wickramasinghe H K 1991 Kelvin probe force microscopy *Appl. Phys. Lett.* **58** 2921–3
[1468] Mohn F, Gross L, Moll N and Meyer G 2012 Imaging the charge distribution within a single molecule *Nat. Nanotechnol.* **7** 227–31
[1469] Collins L, Belianinov A, Somnath S, Balke N, Kalinin S V and Jesse S 2016 Full data acquisition in Kelvin probe force microscopy: mapping dynamic electric phenomena in real space *Sci. Rep.* **6** 30557
[1470] O'Neill A, Khan U, Nirmalraj P N, Boland J and Coleman J N 2011 Graphene dispersion and exfoliation in low boiling point solvents *J. Phys. Chem.* C **115** 5422–8
[1471] Scherzer O D 1970 Die Strahlenschädigung der Objekte als Grenze für die hochauflösende Elektronenmikroskopie *Berichte der Bunsengesellschaft für physikalische Chemie* **74** 1154–67
[1472] Egerton R F, Li P and Malac M 2004 Radiation damage in the TEM and SEM *Micron* **35** 399–409
[1473] Kaiser U *et al* 2011 Transmission electron microscopy at 20kV for imaging and spectroscopy *Ultramicroscopy* **111** 1239–46
[1474] Eder F R, Kotakoski J, Kaiser U and Meyer J C 2014 A journey from order to disorder—atom by atom transformation from graphene to a 2D carbon glass *Sci. Rep.* **4** 4060
[1475] Banhart F 1999 Irradiation effects in carbon nanostructures *Rep. Progr. Phys.* **62** 1181–221
[1476] Cherns D, Minter F J and Nelson R S 1976 Sputtering in the high voltage electron microscope *Nucl. Instrum. Methods* **132** 369–76
[1477] Egerton R F, McLeod R, Wang F and Malac M 2010 Basic questions related to electron-induced sputtering in the TEM *Ultramicroscopy* **110** 991–7
[1478] Suenaga K, Iizumi Y and Okazaki T 2011 Single atom spectroscopy with reduced delocalization effect using a 30 kV-STEM *Eur. Phys. J. Appl. Phys.* **54** 33508
[1479] Ricolleau C, Nelayah J, Oikawa T, Kohno Y, Braidy N, Wang G, Hue F, Florea L, Pierron Bohnes V and Alloyeau D 2012 Performances of an 80–200 kV microscope employing a cold-FEG and an aberration-corrected objective lens *Microscopy* **62** 283–93
[1480] Krivanek O L, Ursin J P, Bacon N J, Corbin G J, Dellby N, Hrncirik P, Murfitt M F, Own C S and Szilagyi Z S 2009 High-energy-resolution monochromator for aberration-corrected scanning transmission electron microscopy/electron energy-loss spectroscopy *Phil. Trans. R. Soc.* A **367** 3683–97
[1481] Morishita S, Mukai M, Suenaga K and Sawada H 2016 Resolution enhancement in transmission electron microscopy with 60 kV monochromated electron source *Appl. Phys. Lett.* **108** 013107
[1482] Linck M *et al* 2016 Chromatic aberration correction for atomic resolution TEM imaging from 20 to 80 kV *Phys. Rev. Lett.* **117** 076101
[1483] Lee Z, Meyer J C, Rose H and Kaiser U 2012 Optimum HRTEM image contrast at 20 kV and 80 kV—exemplified by graphene *Ultramicroscopy* **112** 39–46
[1484] Egerton R F 2014 Choice of operating voltage for a transmission electron microscope *Ultramicroscopy* **145** 85–93
[1485] Algara-Siller G, Lehtinen O, Turchanin A and Kaiser U 2014 Dry-cleaning of graphene *Appl. Phys. Lett.* **104** 153115
[1486] Algara-Siller G, Kurasch S, Sedighi M, Lehtinen O and Kaiser U 2013 The pristine atomic structure of MoS_2 monolayer protected from electron radiation damage by *Appl. Phys. Lett.* **103** 203107
[1487] Chamberlain T W, Biskupek J, Skowron S T, Bayliss P A, Bichoutskaia E, Kaiser U and Khlobystov A N 2015 Transmission electron microscopy: isotope substitution extends the lifetime of organic molecules in transmission electron microscopy (Small 5/2015) *Small* **11** 510
[1488] Wiesendanger R *Related scanning probe methods Scanning Probe Microscopy and Spectroscopy* (Cambridge: Cambridge University Press) pp 265–88
[1489] Wiesendanger R *Applications of scanning probe microscopy and spectroscopy Scanning Probe Microscopy and Spectroscopy* (Cambridge: Cambridge University Press) pp 289–90
[1490] Merino P, Rodrigo L, Pinardi A L, Méndez J, López M F, Pou P, Pérez R and Martín Gago J A 2014 Sublattice localized electronic states in atomically resolved graphene-Pt(1 1 1) edge-boundaries *ACS Nano* **8** 3590–6
[1491] Merino P, Santos H, Pinardi A L, Chico L and Martin-Gago J A 2017 Atomically-resolved edge states on surface-

nanotemplated graphene explored at room temperature *Nanoscale* **9** 3905–11
[1492] Telychko M *et al* 2015 Electronic and chemical properties of donor, acceptor centers in graphene *ACS Nano* **9** 9180–7
[1493] Lauffer P, Emtsev K V, Graupner R, Seyller T, Ley L, Reshanov S A and Weber H B 2008 Atomic and electronic structure of few-layer graphene on SiC(0 0 0 1) studied with scanning tunneling microscopy and spectroscopy *Phys. Rev.* B **77** 155426
[1494] Varchon F, Mallet P, Magaud L and Veuillen J-Y 2008 Rotational disorder in few-layer graphene films on 6H–SiC(0 0 0 − 1): a scanning tunneling microscopy study *Phys. Rev.* B **77** 165415
[1495] Nika D L and Balandin A A 2016 Thermal transport in graphene, few-layer graphene and graphene nanoribbons *Thermal Transport in Low Dimensions* (Berlin: Springer) pp 339–63
[1496] Xu X *et al* 2014 Length-dependent thermal conductivity in suspended single-layer graphene *Nat. Commun.* **5** 3689
[1497] Sadeghi M M, Pettes M T and Shi L 2012 Thermal transport in graphene *Solid State Commun.* **152** 1321–30
[1498] Balandin A A 2011 Thermal properties of graphene and nanostructured carbon materials *Nat. Mater.* **10** 569–81
[1499] Ho C Y, Powell R W and Liley P E 1972 Thermal conductivity of the elements *J. Phys. Chem. Ref. Data* **1** 279–21
[1500] Nika D L and Balandin A A 2017 Phonons and thermal transport in graphene and graphene-based materials *Rep. Prog. Phys.* **80** 036502
[1501] Seol J H *et al* 2010 Two-dimensional phonon transport in supported graphene *Science* **328** 213–6
[1502] Balandin A A, Ghosh S, Bao W, Calizo I, Teweldebrhan D, Miao F and Lau C N 2008 Superior thermal conductivity of single-layer graphene *Nano Lett.* **8** 902–7
[1503] Majumdar A 1999 Scanning thermal microscopy *Annu. Rev. Mater. Sci.* **29** 505–85
[1504] Gomès S, Assy A and Chapuis P-O 2015 Scanning thermal microscopy: a review *Phys. Status Solidi* a **212** 477–94
[1505] Yoon K, Hwang G, Chung J, Kim H G, Kwon O, Kihm K D and Lee J S 2014 Measuring the thermal conductivity of residue-free suspended graphene bridge using null point scanning thermal microscopy *Carbon* **76** 77–83
[1506] Pumarol M E, Rosamond M C, Tovee P, Petty M C, Zeze D A, Falko V and Kolosov O V 2012 Direct nanoscale imaging of ballistic and diffusive thermal transport in graphene nanostructures *Nano Lett.* **12** 2906–11
[1507] Martinek J, Klapetek P and Campbell A C 2015 Methods for topography artifacts compensation in scanning thermal microscopy *Ultramicroscopy* **155** 55–61
[1508] Yovanovich M M, Culham J R and Teertstra P 1998 Analytical modeling of spreading resistance in flux tubes, half spaces, and compound disks *IEEE Trans. Compon. Packag. Manuf. Technol.* A **21** 168–76
[1509] Menges F, Riel H, Stemmer A, Dimitrakopoulos C and Gotsmann B 2013 Thermal transport into graphene through nanoscopic contacts *Phys. Rev. Lett.* **111** 205901
[1510] Tuinstra F and Koenig J L 1970 Raman spectrum of graphite *J. Chem. Phys.* **53** 1126–30
[1511] Ferrari A C and Robertson J 2004 Raman spectroscopy of amorphous, nanostructured, diamond-like carbon, and nanodiamond *Phil. Trans. R. Soc.* A **362** 2477–512
[1512] Saito R, Nugraha A R T, Hasdeo E H, Siregar S, Guo H and Yang T 2015 Ultraviolet Raman spectroscopy of graphene and transition-metal dichalcogenides *Phys. Status Solidi* b **252** 2363–74
[1513] Tyborski C, Herziger F, Gillen R and Maultzsch J 2015 Beyond double-resonant Raman scattering: Ultraviolet Raman spectroscopy on graphene, graphite, and carbon nanotubes *Phys. Rev.* B **92** 041401
[1514] Tan P H *et al* 2012 The shear mode of multilayer graphene *Nat. Mater.* **11** 294–300
[1515] Zhang X, Han W P, Wu J B, Milana S, Lu Y, Li Q Q, Ferrari A C and Tan P H, 2012 Raman spectroscopy of shear and layer breathing modes in multilayer MoS_2 *Phys. Rev.* B **87** 115413
[1516] Glebov A L, Mokhun O, Rapaport A, Vergnole S, Smirnov V and Glebov L B 2012 Volume Bragg gratings as ultra-narrow and multiband optical filters *Proc. SPIE* **8428** 84280C
[1517] Faugeras C, Nerrière A, Potemski M, Mahmood A, Dujardin E, Berger C and de Heer W A 2008 Few-layer graphene on SiC, pyrolitic graphite, and graphene: a Raman scattering study *Appl. Phys. Lett.* **92** 011914
[1518] Das A *et al* 2008 Monitoring dopants by Raman scattering in an electrochemically top-gated graphene transistor *Nat. Nanotechnol.* **3** 210–5
[1519] Basko D M, Piscanec S and Ferrari A C 2009 Electron-electron interactions and doping dependence of the two-phonon Raman intensity in graphene *Phys. Rev.* B **80** 165413
[1520] Piscanec S, Lazzeri M, Mauri F, Ferrari A C and Robertson J 2004 Kohn anomalies and electron–phonon interactions in graphite *Phys. Rev. Lett.* **93** 185503
[1521] Das A, Chakraborty B, Piscanec S, Pisana S, Sood A K and Ferrari A C 2009 Phonon renormalization in doped bilayer graphene *Phys. Rev.* B **79** 155417
[1522] Pisana S, Lazzeri M, Casiraghi C, Novoselov K S, Geim A K, Ferrari A C and Mauri F 2007 Breakdown of the adiabatic Born–Oppenheimer approximation in graphene *Nat. Mater.* **6** 198–201
[1523] Yan J, Zhang Y, Kim P and Pinczuk A 2007 Electric field effect tuning of electron–phonon coupling in graphene *Phys. Rev. Lett.* **98** 166802
[1524] Ferrari A C and Robertson J 2000 Interpretation of Raman spectra of disordered and amorphous carbon *Phys. Rev.* B **61** 14095–107
[1525] Casiraghi C 2007 Probing disorder and charged impurities in graphene by Raman spectroscopy *Phys. Status Solidi* **3** 175–77
[1526] Cançado L G, Pimenta M A, Neves B R A, Dantas M S S and Jorio A 2004 Influence of the atomic structure on the Raman spectra of graphite edges *Phys. Rev. Lett.* **93** 247401
[1527] Casiraghi C, Pisana S, Novoselov K S, Geim A K and Ferrari A C 2007 Raman fingerprint of charged impurities in graphene *Appl. Phys. Lett.* **91** 233108
[1528] Zhao W, Tan P H, Liu J and Ferrari A C 2011 Intercalation of few-layer graphite flakes with $FeCl_3$: Raman determination of fermi level, layer by layer decoupling, and stability *J. Am. Chem. Soc.* **133** 5941–6
[1529] Mohiuddin T M G *et al* 2009 Uniaxial strain in graphene by Raman spectroscopy:Gpeak splitting, Grüneisen parameters, and sample orientation, *Phys. Rev.* B **79** 205433
[1530] Proctor J E, Gregoryanz E, Novoselov K S, Lotya M, Coleman J N and Halsall M P 2009 High-pressure Raman spectroscopy of graphene *Phys. Rev.* B **80** 073408
[1531] Zabel J, Nair R R, Ott A, Georgiou T, Geim A K, Novoselov K S and Casiraghi C 2012 Raman spectroscopy of graphene and bilayer under biaxial strain: bubbles and balloons *Nano Lett.* **12** 617–21
[1532] Huang M, Yan H, Heinz T F and Hone J 2010 Probing strain-induced electronic structure change in graphene by Raman spectroscopy *Nano Lett.* **10** 4074–9
[1533] Mohr M, Maultzsch J and Thomsen C 2010 Splitting of the Raman 2D band of graphene subjected to strain *Phys. Rev.* B **82** 209905
[1534] Yoon D, Son Y-W and Cheong H 2011 Strain-dependent splitting of the double-resonance Raman scattering band in graphene *Phys. Rev. Lett.* **106** 155502
[1535] Ni Z H, Yu T, Lu Y H, Wang Y Y, Feng Y P and Shen Z X 2008 Uniaxial strain on graphene: Raman spectroscopy study and band-gap opening *ACS Nano* **2** 2301–5
[1536] Huang M, Yan H, Chen C, Song D, Heinz T F and Hone J 2009 Phonon softening and crystallographic orientation of strained graphene studied by Raman spectroscopy *Proc. Natl Acad. Sci.* **106** 7304–8
[1537] Kuzuba T, Era K, Ishii T and Sato T 1978 A low frequency Raman-active vibration of hexagonal boron nitride *Solid State Commun.* **25** 863–5
[1538] Stenger I, Schué L, Boukhicha M, Berini B, Plaçais B, Loiseau A and Barjon J 2017 Low frequency Raman

spectroscopy of few-atomic-layer thick hBN crystals *2D Mater.* **4** 031003
[1539] Arenal R, Ferrari A C, Reich S, Wirtz L, Mevellec J Y, Lefrant S, Rubio A and Loiseau A 2006 Raman spectroscopy of single-wall boron nitride nanotubes *Nano Lett.* **6** 1812–6
[1540] Nemanich R J, Solin S A and Martin R M 1981 Light scattering study of boron nitride microcrystals *Phys. Rev.* B **23** 6348–56
[1541] Reich S, Ferrari A C, Arenal R, Loiseau A, Bello I and Robertson J 2005 Resonant Raman scattering in cubic and hexagonal boron nitride *Phys. Rev.* B **71** 205201
[1542] Chakraborty B, Bera A, Muthu D V S, Bhowmick S, Waghmare U V and Sood A K 2012 Symmetry-dependent phonon renormalization in monolayer MoS_2 transistor *Phys. Rev.* B **85** 161403(R)
[1543] Ribeiro-Soares J, Almeida R M, Barros E B, Araujo P T, Dresselhaus M S, Cançado L G and Jorio A 2014 Group theory analysis of phonons in two-dimensional transition metal dichalcogenides *Phys. Rev.* B **90** 115438
[1544] Scheuschner N, Gillen R, Staiger M and Maultzsch J 2015 Interlayer resonant Raman modes in few-layer MoS_2 *Phys. Rev.* B **91** 235409
[1545] Mignuzzi S, Pollard A J, Bonini N, Brennan B, Gilmore I S, Pimenta M A, Richards D and Roy D 2015 Effect of disorder on Raman scattering of single-layerMoS_2 *Phys. Rev.* B **91** 195411
[1546] Conley H J, Wang B, Ziegler J I, Haglund R F, Pantelides S T and Bolotin K I 2013 Bandgap engineering of strained monolayer and bilayer MoS_2 *Nano Lett.* **13** 3626–30
[1547] Wilson J A and Yoffe A D 1969 Transition metal dichalcogenides. Discussion and interpretation of the observed optical, electrical, and structural properties *Adv. Phys.* **18** 193–335
[1548] Paton K R and Coleman J N 2016 Relating the optical absorption coefficient of nanosheet dispersions to the intrinsic monolayer absorption *Carbon* **107** 733–8
[1549] Yadgarov L, Choi C L, Sedova A, Cohen A, Rosentsveig R, Bar-Elli O, Oron D, Dai H and Tenne R 2014 Dependence of the absorption and optical surface plasmon scattering of MoS_2 nanoparticles on aspect ratio, size, and media *ACS Nano* **8** 3575–83
[1550] Mak K F, Lee C, Hone J, Shan J and Heinz T F 2010 Atomically thin MoS_2: a new direct-gap semiconductor *Phys. Rev. Lett.* **105** 136805
[1551] Splendiani A, Sun L, Zhang Y, Li T, Kim J, Chim C-Y, Galli G and Wang F 2010 Emerging photoluminescence in monolayer MoS_2 *Nano Lett.* **10** 1271–5
[1552] Watanabe K, Taniguchi T and Kanda H 2004 Direct-bandgap properties and evidence for ultraviolet lasing of hexagonal boron nitride single crystal *Nat. Mater.* **3** 404–9
[1553] Jaffrennou P, Barjon J, Lauret J S, Attal-Trétout B, Ducastelle F and Loiseau A 2007 Origin of the excitonic recombinations in hexagonal boron nitride by spatially resolved cathodoluminescence spectroscopy *J. Appl. Phys.* **102** 116102
[1554] Taniguchi T and Watanabe K 2007 Synthesis of high-purity boron nitride single crystals under high pressure by using Ba–BN solvent *J. Cryst. Growth* **303** 525–9
[1555] Schué L, Berini B, Betz A C, Plaçais B, Ducastelle F, Barjon J and Loiseau A 2016 Dimensionality effects on the luminescence properties of hBN *Nanoscale* **8** 6986–93
[1556] Galvani T, Paleari F, Miranda H P C, Molina-Sánchez A, Wirtz L, Latil S, Amara H and Ducastelle F 2016 Excitons in boron nitride single layer *Phys. Rev.* B **94** 125303
[1557] Arnaud B, Lebègue S, Rabiller P and Alouani M 2008 Arnaud, lebègue, rabiller, and alouani reply *Phys. Rev. Lett.* **100** 189702
[1558] Watanabe K and Taniguchi T 2009 Jahn–Teller effect on exciton states in hexagonal boron nitride single crystal *Phys. Rev.* B **79** 180405
[1559] Museur L *et al* 2011 Exciton optical transitions in a hexagonal boron nitride single crystal *Phys. Status Solidi* **5** 214–6
[1560] Cao X K, Clubine B, Edgar J H, Lin J Y and Jiang H X 2013 Two-dimensional excitons in three-dimensional hexagonal boron nitride *Appl. Phys. Lett.* **103** 191106
[1561] Cassabois G, Valvin P and Gil B 2016 Hexagonal boron nitride is an indirect bandgap semiconductor *Nat. Photon.* **10** 262–6
[1562] Watanabe K, Taniguchi T, Miya K, Sato Y, Nakamura K, Niiyama T and Taniguchi M 2011 Hexagonal boron nitride as a new ultraviolet luminescent material and its application—Fluorescence properties of hBN single-crystal powder *Diamond Relat. Mater.* **20** 849–52
[1563] Pierret A, Loayza J, Berini B, Betz A, Plaçais B, Ducastelle F, Barjon J and Loiseau A 2014 Excitonic recombinations inh − BN: from bulk to exfoliated layers *Phys. Rev.* B **89** 035414
[1564] Museur L and Kanaev A 2008 Near band-gap photoluminescence properties of hexagonal boron nitride *J. Appl. Phys.* **103** 103520
[1565] Silly M G, Jaffrennou P, Barjon J, Lauret J S, Ducastelle F, Loiseau A, Obraztsova E, Attal-Tretout B and Rosencher E 2007 Luminescence properties of hexagonal boron nitride: Cathodoluminescence and photoluminescence spectroscopy measurements *Phys. Rev.* B **75** 085205
[1566] Vuong T Q P, Cassabois G, Valvin P, Ouerghi A, Chassagneux Y, Voisin C and Gil B 2016 Phonon–photon mapping in a color center in hexagonal boron nitride *Phys. Rev. Lett.* **117** 097402
[1567] Bourrellier R, Meuret S, Tararan A, Stéphan O, Kociak M, Tizei L H G and Zobelli A 2016 Bright UV Single Photon Emission at Point Defects inh-BN, *Nano Lett.* **16** 4317–21
[1568] Tran T T, Elbadawi C, Totonjian D, Lobo C J, Grosso G, Moon H, Englund D R, Ford M J, Aharonovich I and Toth M 2016 Robust multicolor single photon emission from point defects in hexagonal boron nitride *ACS Nano* **10** 7331–8
[1569] Castle J E 1894 Practical surface analysis by Auger and x-ray photoelectron spectroscopy. D. Briggs and M. P. Seah (Editors). John Wiley and Sons Ltd, Chichester **198**3 **533** pp., £44.50 *Surf. Interface Anal.* **6** 302
[1570] Crist B V 2005 *Handbooks of Monochromatic XPS Spectra* (Mountain View, CA: XPS International LLC)
[1571] Preobrajenski A B, Ng M L, Vinogradov A S and Mårtensson N 2008 Controlling graphene corrugation on lattice-mismatched substrates *Phys. Rev.* B **78** 073401
[1572] IkeoY I N, Nimura N, Sigematsu M, Tazawa T, Matsumoto S, Kojima K and Nagasawa Y 1991 *Handbook of x-ray Photoelectron Spectroscopy* (JEOL)
[1573] Bianco G V, Losurdo M, Giangregorio M M, Capezzuto P and Bruno G 2014 Exploring and rationalising effective n-doping of large area CVD-graphene by NH_3 *Phys. Chem. Chem. Phys.* **16** 3632
[1574] Blume R *et al* 2014 The influence of intercalated oxygen on the properties of graphene on polycrystalline Cu under various environmental conditions *Phys. Chem. Chem. Phys.* **16** 25989–6003
[1575] Vinogradov N A, Schulte K, Ng M L, Mikkelsen A, Lundgren E, Mårtensson N and Preobrajenski A B 2011 Impact of atomic oxygen on the structure of graphene formed on Ir(1 1 1) and Pt(1 1 1) *J. Phys. Chem.* C **115** 9568–77
[1576] Barinov A, Malcioğu O B, Fabris S, Sun T, Gregoratti L, Dalmiglio M and Kiskinova M 2009 Initial stages of oxidation on graphitic surfaces: photoemission study and density functional theory calculations *J. Phys. Chem.* C **113** 9009–13
[1577] Palacio I *et al* 2017 Spectroscopic characterization of the on-surface induced (cyclo)dehydrogenation of a N-heteroaromatic compound on noble metal surfaces *Phys. Chem. Chem. Phys.* **19** 22454–61
[1578] Casero E *et al* 2012 Comparative response of biosensing platforms based on synthesized graphene oxide and electrochemically reduced graphene *Electroanalysis* **25** 154–65
[1579] Starke U 1997 Atomic structure of hexagonal SiC surfaces *Phys. Status Solidi* b **202** 475–99

[1580] Owman F and Mårtensson P 1996 The SiC(0 0 0 1)6 $\sqrt{3} \times 6\sqrt{3}$ reconstruction studied with STM and LEED *Surf. Sci.* **369** 126–36
[1581] Varchon F, Mallet P, Veuillen J Y and Magaud L 2008 Ripples in epitaxial graphene on the Si-terminated SiC(0 0 0 1) surface *Phys. Rev.* B **77** 235412
[1582] de Lima L H, de Siervo A, Landers R, Viana G A, Goncalves A M B, Lacerda R G and Häberle P 2013 Atomic surface structure of graphene and its buffer layer on SiC(0 0 0 1): a chemical-specific photoelectron diffraction approach *Phys. Rev.* B **87** 081403
[1583] Abrami A *et al* 1995 Super ESCA: first beamline operating at ELETTRA *Rev. Sci. Instrum.* **66** 1618–20
[1584] Zampieri G, Lizzit S, Petaccia L, Goldoni A, Baraldi A, Bremholm M, Gayone J E, Hoffmann S V and Hofmann P 2005 Photoelectron diffraction study of the6H–SiC(0 0 0 1)3 × 3R30 reconstruction *Phys. Rev.* B **72** 165327
[1585] Merino P, Švec M, Martinez J I, Jelinek P, Lacovig P, Dalmiglio M, Lizzit S, Soukiassian P, Cernicharo J and Martin-Gago J A 2014 Graphene etching on SiC grains as a path to interstellar polycyclic aromatic hydrocarbons formation *Nat. Commun.* **5** 3054
[1586] Damascelli A 2004 Probing the electronic structure of complex systems by ARPES *Phys. Scr.* **T109** 61
[1587] Reinert F and Hüfner S 2005 Photoemission spectroscopy—from early days to recent applications *New J. Phys.* **7** 97
[1588] Himpsel F J 1983 Angle-resolved measurements of the photoemission of electrons in the study of solids *Adv. Phys.* **32** 1–51
[1589] Einstein A 1905 Über einen die Erzeugung und Verwandlung des Lichtes betreffenden heuristischen Gesichtspunkt *Ann. Phys., Lpz.* **322** 132–48
[1590] Huang D J, Lee J Y, Suen J S, Mulhollan G A, Andrews A B and Erskine J L 1993 Adapting a compact Mott spin polarimeter to a large commercial electron energy analyzer for spin-polarized electron spectroscopy *Rev. Sci. Instrum.* **64** 3474–9
[1591] McChesney J L, Bostwick A, Ohta T, Seyller T, Horn K, González J and Rotenberg E 2010 Extended van Hove singularity and superconducting instability in doped graphene *Phys. Rev. Lett.* **104** 136803
[1592] Mazzola F, Frederiksen T, Balasubramanian T, Hofmann P, Hellsing B and Wells J W 2017 Strong electron-phonon coupling in the σ band of graphene *Phys. Rev.* B **95** 075430
[1593] Mazzola F *et al* 2013 Publisher's Note: Kinks in the σ band of graphene induced by electron–phonon coupling (2013 *Phys. Rev. Lett.* **111** 216806) *Phys. Rev. Lett.* **111** 216806
[1594] Pletikosic I, Kralj M, Pervan P, Brako R, Coraux J, N'Diaye A T, Busse C and Michely T 2009 Dirac cones and minigaps for graphene on Ir(1 1 1) *Phys. Rev. Lett.* **102** 056808
[1595] Yuan H *et al* 2016 Evolution of the valley position in bulk transition-metal chalcogenides and their monolayer limit *Nano Lett.* **16** 4738–45
[1596] Pierucci D *et al* 2016 Band alignment and minigaps in monolayer MoS_2-graphene van der Waals heterostructures *Nano Lett.* **16** 4054–61
[1597] Dendzik M, Michiardi M, Sanders C, Bianchi M, Miwa J A, Grønborg S S, Lauritsen J V, Bruix A, Hammer B and Hofmann P 2015 Growth and electronic structure of epitaxial single-layerWS_2 on Au(1 1 1) *Phys. Rev.* B **92** 245442
[1598] Ulstrup S *et al* 2017 Spin and valley control of free carriers in single-layer WS_2 *Phys. Rev.* B **95** 041405(R)
[1599] Katoch J *et al* 2018 Giant spin-splitting and gap renormalization driven by trions in single-layer WS_2/h-BN heterostructures *Nat. Phys.* **14** 355–9
[1600] van der Pauw L J 1958 A method for measuring resistivity and Hall effects of disks of arbitrary shape *Phil. Res. Rep.* **13** 1–9
[1601] Edwards D F A 1971 *Electronic Measurement Techniques* (Butterworth-Heinemann)
[1602] Moser J, Barreiro A and Bachtold A 2007 Current-induced cleaning of graphene *Appl. Phys. Lett.* **91** 163513
[1603] Hertel S, Kisslinger F, Jobst J, Waldmann D, Krieger M and Weber H B 2011 Current annealing and electrical breakdown of epitaxial graphene *Appl. Phys. Lett.* **98** 212109
[1604] Tombros N, Veligura A, Junesch J, Guimaraes M H D, Vera-Marun I J, Jonkman H T and van Wees B J 2011 Quantized conductance of a suspended graphene nanoconstriction *Nat. Phys.* **7** 697–700
[1605] Lin Y M, Dimitrakopoulos C, Jenkins K A, Farmer D B, Chiu H Y, Grill A and Avouris P 2010 GHz transistors from wafer-scale epitaxial graphene *Science* **327** 662–2
[1606] Moon J S *et al* 2010 Top-gated epitaxial graphene FETs on Si-face SiC wafers with a peak transconductance of 600 mS mm^{-1} *IEEE Electron Device Lett.* **31** 260–2
[1607] Guo Z L *et al* 2013 Record maximum oscillation frequency in C-face epitaxial graphene transistors *Nano Lett.* **13** 942–7
[1608] Das Sarma S, Adam S, Hwang E H and Rossi E 2011 Electronic transport in two-dimensional graphene *Rev. Mod. Phys.* **83** 407–66
[1609] Chen J H, Jang C, Adam S, Fuhrer M S, Williams E D and Ishigami M 2008 Charged-impurity scattering in graphene *Nat. Phys.* **4** 377–81
[1610] Shon N H and Ando T 1998 Quantum transport in two-dimensional graphite system *J. Phys. Soc. Japan* **67** 2421–9
[1611] Dlubak B, Seneor P, Anane A, Barraud C, Deranlot C, Deneuve D, Servet B, Mattana R, Petroff F and Fert A 2010 Are Al_2O_3 and MgO tunnel barriers suitable for spin injection in graphene? *Appl. Phys. Lett.* **97** 092502
[1612] Li X, Wu X, Sprinkle M, Ming F, Ruan M, Hu Y, Berger C and de Heer W A 2010 Top- and side-gated epitaxial graphene field effect transistors *Phys. Status Solidi* a **207** 286–90
[1613] Kim S, Nah J, Jo I, Shahrjerdi D, Colombo L, Yao Z, Tutuc E and Banerjee S K 2009 Realization of a high mobility dual-gated graphene field-effect transistor with Al_2O_3 dielectric *Appl. Phys. Lett.* **94** 062107
[1614] Zhong H, Zhang Z Y, Xu H T, Qiu C G and Peng L M 2015 Comparison of mobility extraction methods based on field-effect measurements for graphene *AIP Adv.* **5** 057136
[1615] Meric I, Han M Y, Young A F, Ozyilmaz B, Kim P and Shepard K L 2008 Current saturation in zero-bandgap, topgated graphene field-effect transistors *Nat. Nanotechnol.* **3** 654–9
[1616] Droscher S, Roulleau P, Molitor F, Studerus P, Stampfer C, Ensslin K and Ihn T 2010 Quantum capacitance and density of states of graphene *Appl. Phys. Lett.* **96** 152104
[1617] Zhang Y, Tan Y-W, Stormer H L and Kim P 2005 Experimental observation of the quantum Hall effect and Berry's phase in graphene *Nature* **438** 201
[1618] Poumirol J M, Escoffier W, Kumar A, Goiran M, Raquet B and Broto J M 2010 Electron–hole coexistence in disordered graphene probed by high-field magneto-transport *New J. Phys.* **12** 83006
[1619] Wiedmann S *et al* 2011 Coexistence of electron and hole transport in graphene *Phys. Rev.* B **84** 115314
[1620] de Heer W A *et al* 2007 Epitaxial graphene *Solid State Commun.* **143** 92–100
[1621] Schwierz F 2010 Graphene transistors *Nat. Nanotechnol.* **5** 487
[1622] Dorgan V E, Bae M H and Pop E 2010 Mobility and saturation velocity in graphene on SiO_2 *Appl. Phys. Lett.* **97** 082112
[1623] Robinson J A, LaBella M, Zhu M, Hollander M, Kasarda R, Hughes Z, Trumbull K, Cavalero R and Snyder D 2011 Contacting graphene *Appl. Phys. Lett.* **98** 053103
[1624] Ferney A C, David J, Abhay A S, Wonjae K, Juha R, Harri L and Daniel N 2015 A physics-based model of gate-tunable metal–graphene contact resistance benchmarked against experimental data *2D Mater.* **2** 025006
[1625] Nagashio K and Toriumi A 2011 Density-of-states limited contact resistance in graphene field-effect transistors *Japan. J. Appl. Phys.* **50** 070108
[1626] Xia F N, Perebeinos V, Lin Y M, Wu Y Q and Avouris P 2011 The origins and limits of metal-graphene junction resistance *Nat. Nanotechnol.* **6** 179–84

[1627] Shaygan M, Otto M, Sagade A A, Chavarin C A, Bacher G, Mertin W and Neumaier D 2017 Low resistive edge contacts to CVD-grown graphene using a CMOS compatible metal *Ann. Phys., Lpz.* **529** 1600410
[1628] Wang L *et al* 2013 One-dimensional electrical contact to a two-dimensional material *Science* **342** 614–7
[1629] Robinson J A, LaBella M, Trumbull K A, Weng X J, Cavelero R, Daniels T, Hughes Z, Hollander M, Fanton M and Snyder D 2010 Epitaxial graphene materials integration: effects of dielectric overlayers on structural and electronic properties *ACS Nano* **4** 2667–72
[1630] Wu Y Q, Farmer D B, Valdes-Garcia A, Zhu W J, Jenkins K A, Dimitrakopoulos C, Avouris P and Lin Y M 2011 Record high RF performance for epitaxial graphene transistors *2011 IEEE Int. Electron Devices Meeting (IEDM)*
[1631] Cheng R, Bai J, Liao L, Zhou H, Chen Y, Liu L, Lin Y C, Jiang S, Huang Y and Duan X 2012 High-frequency self-aligned graphene transistors with transferred gate stacks *Proc. Natl Acad. Sci.* **109** 11588–92
[1632] Mayorov A S *et al* 2011 Micrometer-scale ballistic transport in encapsulated graphene at room temperature *Nano Lett.* **11** 2396–9
[1633] Deniz J P D, Hu Y, Hu Y, Turmaud J-P, Prudkovskiy V S, Berger C and de Heer W A 2018 Unpublished
[1634] Datta S 1995 *Electronic Transport in Mesoscopic Systems* (Cambridge: Cambridge University Press)
[1635] Tomaino J L, Jameson A D, Kevek J W, Paul M J, van der Zande A M, Barton R A, McEuen P L, Minot E D and Lee Y S 2011 Terahertz imaging and spectroscopy of large-area single-layer graphene *Opt. Express* **19** 141–6
[1636] Buron J D *et al* 2012 Graphene conductance uniformity mapping *Nano Lett.* **12** 5074–81
[1637] Buron J D *et al* 2014 Electrically continuous graphene from single crystal copper verified by terahertz conductance spectroscopy and micro four-point probe *Nano Lett.* **14** 6348–55
[1638] Buron J D, Mackenzie D M A, Petersen D H, Pesquera A, Centeno A, Boggild P, Zurutuza A and Jepsen P U 2015 Terahertz wafer-scale mobility mapping of graphene on insulating substrates without a gate *Opt. Express* **23** 30721–9
[1639] Buron J D, Pizzocchero F, Jepsen P U, Petersen D H, Caridad J M, Jessen B S, Booth T J and Boggild P 2015 Graphene mobility mapping *Sci. Rep.* **5** 12305
[1640] Mackenzie D M A, Buron J D, Whelan P R, Jessen B S, Silajdzic A, Pesquera A, Centeno A, Zurutuza A, Boggild P and Petersen D H 2015 Fabrication of CVD graphene-based devices via laser ablation for wafer-scale characterization *2D Mater.* **2** 045003
[1641] Bøggild P, Mackenzie D M A, Whelan P R, Petersen D H, Buron J D, Zurutuza A, Gallop J, Hao L and Jepsen P U 2017 Mapping the electrical properties of large-area graphene *2D Mater.* **4** 042003
[1642] Mackenzie D M A, Whelan P R, Boggild P, Jepsen P U, Redo-Sanchez A, Etayo D, Fabricius N and Petersen D H 2018 Quality assessment of terahertz time-domain spectroscopy transmission and reflection modes for graphene conductivity mapping *Opt. Express* **26** 9220–9
[1643] Whelan P *et al* 2018 Conductivity mapping of graphene on polymeric films by terahertz time-domain spectroscopy *Opt. Express* **26** 17748
[1644] Horng J *et al* 2011 Drude conductivity of Dirac fermions in graphene *Phys. Rev.* B **83** 165113
[1645] Sensale-Rodriguez B, Yan R S, Liu L, Jena D and Xing H G 2013 Graphene for reconfigurable terahertz optoelectronics *Proc. IEEE* **101** 1705–16
[1646] Akinwande D *et al* 2017 A review on mechanics and mechanical properties of 2D materials—graphene and beyond *Extreme Mech. Lett.* **13** 42–77
[1647] Geim A K 2009 Graphene: status and prospects *Science* **324** 1530–4
[1648] Amorim B *et al* 2016 Novel effects of strains in graphene and other two dimensional materials *Phys. Rep.* **617** 1–54
[1649] Castellanos-Gomez A, Singh V, van der Zant H S J and Steele G A 2014 Mechanics of freely-suspended ultrathin layered materials *Ann. Phys., Lpz.* **527** 27–44
[1650] Novoselov K S 2011 Nobel lecture: graphene: materials in the flatland *Rev. Mod. Phys.* **83** 837–49
[1651] Huang M, Pascal T A, Kim H, Goddard W A and Greer J R 2011 Electronic–mechanical coupling in graphene from *in situ* nanoindentation experiments and multiscale atomistic simulations *Nano Lett.* **11** 1241–6
[1652] Lee C, Wei X, Kysar J W and Hone J 2008 Measurement of the elastic properties and intrinsic strength of monolayer graphene *Science* **321** 385–8
[1653] Lee G H *et al* 2013 High-strength chemical-vapor-deposited graphene and grain boundaries *Science* **340** 1073–6
[1654] Blakslee O L, Proctor D G, Seldin E J, Spence G B and Weng T 1970 Elastic constants of compression-annealed pyrolytic graphite *J. Appl. Phys.* **41** 3373–82
[1655] Castellanos-Gomez A, Poot M, Steele G A, van der Zant H S J, Agraït N and Rubio-Bollinger G 2012 Elastic properties of freely suspended MoS_2 nanosheets, *Adv. Mater.* **24** 772–5
[1656] Bertolazzi S, Brivio J and Kis A 2011 Stretching and breaking of ultrathin MoS_2, *ACS Nano* **5** 9703–9
[1657] Liu K *et al* 2014 Elastic properties of chemical–vapor–deposited monolayer MoS_2, WS_2, and their bilayer heterostructures *Nano Lett.* **14** 5097–03
[1658] Georgiou T, Britnell L, Blake P, Gorbachev R V, Gholinia A, Geim A K, Casiraghi C and Novoselov K S 2011 Graphene bubbles with controllable curvature *Appl. Phys. Lett.* **99** 093103
[1659] Vlassak J J and Nix W D 1992 A new bulge test technique for the determination of Young's modulus and Poisson's ratio of thin films *J. Mater. Res.* **7** 3242–9
[1660] Koenig S P, Boddeti N G, Dunn M L and Bunch J S 2011 Ultrastrong adhesion of graphene membranes *Nat. Nanotechnol.* **6** 543–6
[1661] Hencky H 1921 Die Berechnung dünner rechteckiger Platten mit verschwindender Biegungsteifigkeit *ZAMM—Z. Angew. Math. Mech.* **1** 81–9
[1662] Wan K-T and Mai Y-W 1995 Fracture mechanics of a new blister test with stable crack growth *Acta Metall. Mater.* **43** 4109–15
[1663] Yang R, Lee J, Ghosh S, Tang H, Sankaran R M, Zorman C A and Feng P X L 2017 Tuning optical signatures of single- and few-layer MoS_2 by blown-bubble bulge straining up to fracture *Nano Lett.* **17** 4568–75
[1664] Haigh S J, Gholinia A, Jalil R, Romani S, Britnell L, Elias D C, Novoselov K S, Ponomarenko L A, Geim A K and Gorbachev R 2012 Cross-sectional imaging of individual layers and buried interfaces of graphene-based heterostructures and superlattices *Nat. Mater.* **11** 764–7
[1665] Khestanova E, Guinea F, Fumagalli L, Geim A K and Grigorieva I V 2016 Universal shape and pressure inside bubbles appearing in van der Waals heterostructures *Nat. Commun.* **7** 12587
[1666] Courtney T H 2005 *Mechanical Behavior of Materials* (Long Grove, IL: Waveland Press) ch 9, pp 433–6
[1667] Zhang P *et al* 2014 Fracture toughness of graphene *Nat. Commun.* **5** 5059
[1668] Hwangbo Y *et al* 2014 Fracture characteristics of monolayer CVD-graphene *Sci. Rep.* **4** 4439
[1669] López-Polín G, Gómez-Herrero J and Gómez-Navarro C 2015 Confining crack propagation in defective graphene *Nano Lett.* **15** 2050–4
[1670] Griffith A A 1921 The phenomena of rupture and flow in solids *Phil. Trans. R. Soc.* A **221** 163–98
[1671] Jang B, Mag-isa A E, Kim J-H, Kim B, Lee H-J, Oh C-S, Sumigawa T and Kitamura T 2016 Uniaxial fracture test of freestanding pristine graphene using *in situ* tensile tester under scanning electron microscope *Extreme Mech. Lett.* **14** 10–5
[1672] Timoshenko S P, Gere J M and Prager W 1962 Theory of elastic stability, second edition *J. Appl. Mech.* **29** 220
[1673] Berinskii I E, Krivtsov A M and Kudarova A M 2014 Bending stiffness of a graphene sheet *Phys. Mesomech.* **17** 356–64

[1674] Sfyris D, Sfyris G I and Galiotis C 2014 Curvature dependent surface energy for a free standing monolayer graphene: some closed form solutions of the non-linear theory *Int. J. Non-Linear Mech.* **67** 186–97
[1675] Wei Y, Wang B, Wu J, Yang R and Dunn M L 2013 Bending rigidity and gaussian bending stiffness of single-layered graphene *Nano Lett.* **13** 26–30
[1676] Tapasztó L, Dumitrica T, Kim S J, Nemes-Incze P, Hwang C and Biró L P 2012 Breakdown of continuum mechanics for nanometre-wavelength rippling of graphene *Nat. Phys.* **8** 739–42
[1677] Poot M and van der Zant H S J 2008 Nanomechanical properties of few-layer graphene membranes *Appl. Phys. Lett.* **92** 063111
[1678] Lindahl N, Midtvedt D, Svensson J, Nerushev O A, Lindvall N, Isacsson A and Campbell E E B 2012 Determination of the bending rigidity of graphene via electrostatic actuation of buckled membranes *Nano Lett.* **12** 3526–31
[1679] Zhao J, Deng Q, Ly T H, Han G H, Sandeep G and Rümmeli M H 2015 Two-dimensional membrane as elastic shell with proof on the folds revealed by three-dimensional atomic mapping *Nat. Commun.* **6** 8935
[1680] Blees M K *et al* Graphene kirigami *Nature* **524** 204–7
[1681] Nicklow R, Wakabayashi N and Smith H G 1972 Lattice dynamics of pyrolytic graphite *Phys. Rev.* B **5** 4951–62
[1682] Ferralis N 2010 Probing mechanical properties of graphene with Raman spectroscopy *J. Mater. Sci.* **45** 5135–49
[1683] Bissett M A, Tsuji M and Ago H 2014 Strain engineering the properties of graphene and other two-dimensional crystals *Phys. Chem. Chem. Phys.* **16** 11124
[1684] Roldán R, Castellanos-Gomez A, Cappelluti E and Guinea F 2015 Strain engineering in semiconducting two-dimensional crystals *J. Phys.: Condens. Matter* **27** 313201
[1685] Si C, Sun Z and Liu F 2016 Strain engineering of graphene: a review *Nanoscale* **8** 3207–17
[1686] Gong L, Young R J, Kinloch I A, Riaz I, Jalil R and Novoselov K S 2012 Optimizing the reinforcement of polymer-based nanocomposites by graphene *ACS Nano* **6** 2086–95
[1687] Gong L, Kinloch I A, Young R J, Riaz I, Jalil R and Novoselov K S 2010 Interfacial stress transfer in a graphene monolayer nanocomposite *Adv. Mater.* **22** 2694–7
[1688] Tsoukleri G, Parthenios J, Papagelis K, Jalil R, Ferrari A C, Geim A K, Novoselov K S and Galiotis C 2009 Subjecting a graphene monolayer to tension and compression *Small* **5** 2397–402
[1689] Frank O, Tsoukleri G, Parthenios J, Papagelis K, Riaz I, Jalil R, Novoselov K S and Galiotis C 2010 Compression behavior of single-layer graphenes *ACS Nano* **4** 3131–8
[1690] Frank O, Bouša M, Riaz I, Jalil R, Novoselov K S, Tsoukleri G, Parthenios J, Kavan L, Papagelis K and Galiotis C 2012 Phonon and structural changes in deformed bernal stacked bilayer graphene *Nano Lett.* **12** 687–93
[1691] Androulidakis C, Koukaras E N, Frank O, Tsoukleri G, Sfyris D, Parthenios J, Pugno N, Papagelis K, Novoselov K S and Galiotis C 2014 Failure processes in embedded monolayer graphene under axial compression *Sci. Rep.* **4** 5271
[1692] Androulidakis C, Koukaras E N, Parthenios J, Kalosakas G, Papagelis K and Galiotis C 2015 Graphene flakes under controlled biaxial deformation *Sci. Rep.* **5** 18129
[1693] Rice C, Young R J, Zan R, Bangert U, Wolverson D, Georgiou T, Jalil R and Novoselov K S 2013 Raman-scattering measurements and first-principles calculations of strain-induced phonon shifts in monolayer MoS_2 *Phys. Rev.* B **87** 121304
[1694] Anagnostopoulos G, Androulidakis C, Koukaras E N, Tsoukleri G, Polyzos I, Parthenios J, Papagelis K and Galiotis C 2015 Stress transfer mechanisms at the submicron level for graphene/polymer systems *ACS Appl. Mater. Interfaces* **7** 4216–23
[1695] Papageorgiou D G, Kinloch I A and Young R J 2017 Mechanical properties of graphene and graphene-based nanocomposites *Prog. Mater. Sci.* **90** 75–127
[1696] Frank O *et al* 2011 Raman 2D-band splitting in graphene: theory and experiment *ACS Nano* **5** 2231–9
[1697] Mohr M, Papagelis K, Maultzsch J and Thomsen C 2009 Two-dimensional electronic and vibrational band structure of uniaxially strained graphene from *ab initio* calculations *Phys. Rev.* B **80** 205410–4
[1698] Li Z, Kinloch I A, Young R J, Novoselov K S, Anagnostopoulos G, Parthenios J, Galiotis C, Papagelis K, Lu C-Y and Britnell L 2015 Deformation of Wrinkled graphene *ACS Nano* **9** 3917–25
[1699] Xu C, Xue T, Guo J, Qin Q, Wu S, Song H and Xie H 2015 An experimental investigation on the mechanical properties of the interface between large-sized graphene and a flexible substrate *J. Appl. Phys.* **117** 164301
[1700] Jiang T, Huang R and Zhu Y 2013 Interfacial sliding and buckling of monolayer graphene on a stretchable substrate *Adv. Funct. Mater.* **24** 396–402
[1701] Shin Y, Lozada-Hidalgo M, Sambricio J L, Grigorieva I V, Geim A K and Casiraghi C 2016 Raman spectroscopy of highly pressurized graphene membranes *Appl. Phys. Lett.* **108** 221907
[1702] Lee J-U, Yoon D and Cheong H 2012 Estimation of Young's modulus of graphene by Raman spectroscopy *Nano Lett.* **12** 4444–8
[1703] Papagelis K T G, Parthenios J, Novoselov K and Galiotis C 2012 Axial deformation of monolayer graphene under tension and compression *GraphITA 2011* ed L Ottaviano and V Morandi (Berlin: Springer) pp 87–97
[1704] Metten D, Federspiel F, Romeo M and Berciaud S 2014 All-optical blister test of suspended graphene using micro-Raman spectroscopy *Phys. Rev. Appl.* **2** 054008
[1705] Yoon D, Moon H, Son Y-W, Choi J S, Park B H, Cha Y H, Kim Y D and Cheong H 2009 Interference effect on Raman spectrum of graphene onSiO_2/Si *Phys. Rev.* B **80** 125422
[1706] Nicholl R J T, Conley H J, Lavrik N V, Vlassiouk I, Puzyrev Y S, Sreenivas V P, Pantelides S T and Bolotin K I 2015 The effect of intrinsic crumpling on the mechanics of free-standing graphene *Nat. Commun.* **6** 8789
[1707] Kitt A L, Qi Z, Rémi S, Park H S, Swan A K and Goldberg B B 2013 How graphene slides: measurement and theory of strain-dependent frictional forces between graphene and SiO_2 *Nano Lett.* **13** 2605–10
[1708] Bhushan B, Israelachvili J N and Landman U 1995 Nanotribology: friction, wear and lubrication at the atomic scale *Nature* **374** 607–16
[1709] Gao J, Luedtke W D, Gourdon D, Ruths M, Israelachvili J N and Landman U 2004 Frictional forces and Amontons' law: from the molecular to the macroscopic scale *J. Phys. Chem.* B **108** 3410–25
[1710] Filintoglou K, Papadopoulos N, Arvanitidis J, Christofilos D, Frank O, Kalbac M, Parthenios J, Kalosakas G, Galiotis C and Papagelis K 2013 Raman spectroscopy of graphene at high pressure: effects of the substrate and the pressure transmitting media *Phys. Rev.* B **88** 045418
[1711] Zandiatashbar A, Lee G-H, An S J, Lee S, Mathew N, Terrones M, Hayashi T, Picu C R, HSone J and Koratkar N 2014 Effect of defects on the intrinsic strength and stiffness of graphene *Nat. Commun.* **5** 3186
[1712] Son Y W *et al* 2006 Energy gaps in graphene nanoribbons *Phys. Rev. Lett.* **97** 216803
[1713] Cervantes-Sodi F *et al* 2008 Two-dimensional bipolar junction transistors *Phys. Rev.* B **77** 165427
[1714] Overbeck J *et al* 2019 Optimized substrates and measurement approaches for Raman spectroscopy of graphene nanoribbons (arXiv:1907.01797)
[1715] Verzhbitskiy I *et al* 2016 Raman fingerprints of atomically precise graphene nanoribbons *Nano Lett.* **16** 3442
[1716] Guidetti G *et al* 2019 Photocatalytic activity of exfoliated graphite-TiO2 nanocomposites (arXiv:1903.05407)
[1717] Fabbro A *et al* 2016 Graphene-based interfaces do not alter target nerve cells *ACS Nano* **10** 615
[1718] Romagnoli M *et al* 2018 Graphene-based integrated photonics for next-generation datacom and telecom *Nat. Rev. Mater.* **3** 392

[1719] Purdie D G et al 2018 Cleaning interfaces in layered materials heterostructures Nat. Commun. 9 5387
[1720] De Fazio D et al 2019 High-mobility, wet-transferred graphene grown by chemical vapor deposition ACS Nano. 13 8926
[1721] Mertens J et al 2013 Controlling subnanometer gaps in plasmonic dimers using graphene Nano Lett. 13 5033
[1722] Ferrari A C and Robertson J 2001 Resonant Raman spectroscopy of disordered, amorphous, and diamondlike carbon Phys. Rev. B 64 075414
[1723] Frank O et al 2011 Development of a universal stress sensor for graphene and carbon fibres Nat. Commun. 2 255
[1724] Corso M et al 2018 Bottom-up fabrication of atomically precise graphene nanoribbons On-Surface Synthesis II (Cham: Springer) pp 113–52
[1725] Barin G et al 2019 Surface-synthesized graphene nanoribbons for room temperature switching devices: substrate transfer and ex situ characterization ACS App. Nanomater. 2 2184–92
[1726] Corso M, Carbonell-Sanromà E and de Oteyza D G 2018 Bottom-up fabrication of atomically precise graphene nanoribbons On-Surface Synthesis II. Advances in Atom and Single Molecule Machines ed D de Oteyza and C Rogero (Cham: Springer)
[1727] Durr R A et al 2018 J. Am. Chem. Soc. 140 807–13
[1728] León V, González-Domínguez J M, Fierro J L G, Prato M and Vázquez E 2016 Production and stability of mechanochemically exfoliated graphene in water and culture media Nanoscale 8 14548–55
[1729] González-Domínguez J M, León V, Lucío M I, Prato M and Vázquez E 2018 Nat. Protocols 13 495–506
[1730] Wang H et al 2019 Superhydrophobic and superoleophilic graphene aerogel for adsorption of oil pollutants from water RSC Adv. 9 8569
[1731] Lyu J et al 2018 Separation and purification using GO and r-GO membranes RSC Adv. 8 23130
[1732] Kagkoura A, Pelaez-Fernandez M, Arenal R and Tagmatarchis N 2019 Sulfur-doped graphene/transition metal dichalcogenide heterostructured hybrids with electrocatalytic activity toward the hydrogen evolution reaction Nanoscale Adv. 1 1489–96
[1733] Istif E, Kagkoura A, Hernández-Ferrer J, Stergiou A, Skaltsas T, Arenal R, Benito A M, Maser W K and Tagmatarchis N 2018 Self-assembled core–shell CdTe/poly(3-hexylthiophene) nanoensembles as novel donor–acceptor light harvesting systems ACS Appl. Mater. Interfaces 9 44695–703
[1734] Cooper A J, Wilson N R, Kinloch I A and Dryfe R A W 2014 Single stage electrochemical exfoliation method for the production of few-layer graphene via intercalation of tetraalkylammonium cations Carbon 66 340–50
[1735] Xia Z, Arbizzani C, Ortolani L, Morandi V, Bellani V, Giambastiani G, Gazzano M and Palermo V 2017 High yield production of graphene-Fe_2O_3 nano-composites via electrochemical intercalation of nitromethane and iron chloride, and their application in lithium storage Flatchem 3 8–15
[1736] Haastrup S et al 2018 2D Mater. 5 042002
[1737] Cheon G, Duerloo K-A N, Sendek A D, Porter C, Chen Y and Reed E J 2017 Data mining for new two- and one-dimensional weakly bonded solids and lattice-commensurate heterostructures Nano Lett. 17 1915–23
[1738] Choudhary K, Kalish I, Beams R and Tavazza F 2017 High-throughput identification and characterization of two-dimensional materials using density functional theory Sci. Rep. 7 5179
[1739] Zhou J et al 2019 2DMatPedia, an open computational database of two-dimensional materials from top-down and bottom-up approaches Sci. Data 6 86
[1740] Larsen P M, Pandey M, Strange M and Jacobsen K W 2019 Definition of a scoring parameter to identify low-dimensional materials components Phys. Rev. Mater. 3 034003
[1741] Aguiar-Ricardo A, Duarte C M M, Nunes da Ponte M, Marsh K N and Stølen S 2003 Properties of mixing Experimental Thermodynamics ed A R H Goodwin et al (New York: Elsevier) vol 6, pp 387–432
[1742] Meng Y, Xu X-B, Li H, Wang Y, Ding E-X, Zhang Z-C and Geng H-Z 2014 Optimisation of carbon nanotube ink for large-area transparent conducting films fabricated by controllable rod-coating method Carbon 70 103–10
[1743] Worsley K A, Kalinina I, Bekyarova E and Haddon R C 2009 Functionalization and dissolution of nitric acid treated single-walled carbon nanotubes J. Am. Chem. Soc. 131 18153–8
[1744] Thayer A 2000 What's that stuff? Silly putty Chem. Eng. News 78 27
[1745] Kimoto T, Itoh A and Matsunami H 1995 Step bunching in chemical vapor deposition of 6H- and 4H-SiC on vicinal SiC(0 0 0 1) faces Appl. Phys. Lett. 66 3645
[1746] Ciuk T et al 2018 Thermally activated double-carrier transport in epitaxial graphene on vanadium-compensated 6H-SiC as revealed by Hall effect measurements Carbon 139 776–81
[1747] Ciuk T, Stanczyk B, Przyborowska K, Czolak D, Dobrowolski A, Jagiello J, Kaszub W, Kozubal M, Kozlowski R and Kaminski P 2019 High-temperature Hall effect sensor based on epitaxial graphene on high-purity semiinsulating 4H-SiC IEEE Trans. Electron Devices 66 3134–8
[1748] Ishihara M, Koga Y, Kim J, Tsugawa K and Hasegawa M 2011 Direct evidence of advantage of Cu(1 1 1) for graphene synthesis by using Raman mapping and electron backscatter diffraction Mater. Lett. 65 2864–7
[1749] Murdock A T, Koos A, Ben Britton T, Houben L, Batten T, Zhang T, Wilkinson A J, Dunin-Borkowski R E, Lekka C E and Grobert N 2013 Controlling the orientation, edge geometry, and thickness of chemical vapor deposition graphene ACS Nano 7 1351–9
[1750] Mullins W W and Sekerka R F 1963 Morphological stability of a particle growing by diffusion or heat flow J. Appl. Phys. 34 323–9
[1751] Xia K L, Artyukhov V I, Sun L F, Zheng J Y, Jiao L Y, Yakobson B I and Zhang Y Y 2016 Growth of large-area aligned pentagonal graphene domains on high-index copper surfaces Nano Res. 9 2182–9
[1752] Bloom D S, Putman J W and Grant N J 1952 Melting point and transformation of pure chromium JOM 4 626
[1753] Fujita J I, Hiyama T, Hirukawa A, Kondo T, Nakamura J, Ito S I, Araki R, Ito Y, Takeguchi M and Pai W W 2017 Near room temperature chemical vapor deposition of graphene with diluted methane and molten gallium catalyst Sci. Rep. 7
[1754] Chaitoglou S, Giannakopoulou T, Tsoutsou D, Vavouliotis A, Trepans C and Dimoulas A 2019 Direct versus reverse vertical two-dimensional Mo_2C/graphene heterostructures for enhanced hydrogen evolution reaction electrocatalysis Nanotechnology 30
[1755] Huang M et al 2018 Highly oriented monolayer graphene grown on a Cu/Ni(1 1 1) alloy foil ACS Nano 12 6117–27
[1756] Ullah Z, Riaz S, Li Q, Atiq S, Saleem M, Azhar M, Naseem S and Liu L W 2018 A comparative study of graphene growth by APCVD, LPCVD and PECVD Mater. Res. Express 5 035606
[1757] Koren E, Sutter E, Bliznakov S, Ivars-Barcelo F and Sutter P 2013 Isolation of high quality graphene from Ru by solution phase intercalation Appl. Phys. Lett. 103 121602
[1758] Sutter P, Albrecht P, Tong X and Sutter E 2013 Mechanical decoupling of graphene from Ru(0 0 0 1) by interfacial reaction with oxygen J. Phys. Chem. C 117 6320–4
[1759] Chandrashekar B N, Deng B, Smitha A S, Chen Y, Tan C, Zhang H, Peng H and Liu Z 2015 Roll-to-roll green transfer of CVD graphene onto plastic for a transparent and flexible triboelectric nanogenerator Adv. Mater. 27 5210–6
[1760] Xu P, Kang J, Suhr J, Smith J P, Booksh K S , Wei B, Yu J, Li F, Byun J H, Oh Y and Chou T S 2015 Spatial strain variation of graphene films for stretchable electrodes Carbon 93 620–4

[1761] Martins L G P, Song Y, Zeng T, Dresselhaus M S, Kong J, and Araujo P T 2013 Direct transfer of graphene onto flexible substrates *Proc. Natl Acad. Sci.* **110** 17762–7
[1762] Hong J Y, Shin Y C, Zubair A, Mao Y, Palacios T, Dresselhaus M S, Kim S H and Kong J 2016 A rational strategy for graphene transfer on substrates with rough features *Adv. Mater.* **28** 2382–92
[1763] Celebi K, Cole M T, Choi J W, Wyczisk F, Legagneux P, Rupesinghe N, Robertson J, Teo K B K and Park H G 2013 Evolutionary kinetics of graphene formation on copper *Nano Lett.* **13** 967–74
[1764] Tschierske C and Ungar G 2016 Mirror symmetry breaking by chirality synchronisation in liquids and liquid crystals of achiral molecules *ChemPhysChem* **17** 1–7
[1765] Deng W, Zhang Y, Yang L, Tan Y, Ma M, and Xie Q 2015 Sulfur-doped porous carbon nanosheets as an advanced electrode material for supercapacitors *RSC Adv.* **5** 13046–51
[1766] Stolyarov M A, Liu G, Rumyantsev S L, Shur M and Balandin A A 2015 Suppression of 1/f noise in near-ballistic h-BN-graphene-h-BN heterostructure field-effect transistors *Appl. Phys. Lett.* **107** 023106
[1767] Sen D, Novoselov K S, Reis P M and Buehle M J 2010 Tearing graphene sheets from adhesive substrates produces tapered nanoribbons *Small* **6** 1108–16
[1768] Tian H, Shu Y, Cui Y L, Mi W T, Yang Y, Xie D and Ren T L 2014 Scalable fabrication of high-performance and flexible graphene strain sensors *Nanoscale* **6** 699–705
[1769] Bunch J S and Dunn M L 2012 Adhesion mechanics of graphene membranes *Solid State Commun.* **152** 1359–64
[1770] Batrakov K, Kuzhir P, Maksimenko S, Paddubskaya A, Voronovich S, Lambin Ph, Kaplas T and Svirko Yu 2014 Flexible transparent graphene/polymer multilayers for efficient electromagnetic field absorption *Sci. Rep.* **4** 7191
[1771] Georgakilas V, Otyepka M, Bourlinos A B, Chandra V, Kim N, Kemp K C, Hobza P, Zboril R and Kim K S 2012 *Chem. Rev.* **112** 6156–214
[1772] Yan L, Zheng Y B, Zhao F, Li S, Gao X, Xu B, Weiss P S and Zhao Y 2012 *Chem. Soc. Rev.* **41** 97–114
[1773] Sun Z, James D K and Tour J M 2011 *J. Phys. Chem. Lett.* **2** 2425–32
[1774] Sun Z, Kohama S, Zhang Z, Lomeda J R and Tour J M 2010 Soluble graphene through edge-selective functionalization *Nano Res.* **3** 117–25
[1775] Lim H, Lee J S, Shin H J, Shin H S and Choi H C 2010 Spatially resolved spontaneous reactivity of diazonium salt on edge and basal plane of graphene without surfactant and its doping effect *Langmuir* **26** 12278–84
[1776] Jiang D, Sumpter B G and Dai S 2006 *J. Phys. Chem.* B **110** 23628–32
[1777] Bottari G, Herranz M Á, Wibmer L, Volland M, Rodríguez-Pérez L, Guldi D M, Hirsch A, Martín N, D'Souza F and Torres T 2017 Chemical functionalization and characterization of graphene-based materials *Chem. Soc. Rev.* **46** 4464–500
[1778] Kaplan A, Yuan Z, Benck J D, Govind Rajan A, Chu X S, Wang Q H and Strano M S 2017 Current and future directions in electron transfer chemistry of graphene *Chem. Soc. Rev.* **46** 4530–71
[1779] Malig J, Englert J M, Hirsch A and Guldi D M 2011 *Electrochem. Soc. Interface* **20** 53–6
[1780] Zhang H, Bekyarova E, Huang J-W, Zhao Z, Bao W, Wang F, Haddon R C and Lau C N 2011 *Nano Lett.* **11** 4047–51
[1781] Xu X, Liu C, Sun Z, Cao T, Zhang Z, Wang E, Liu Z and Liu K 2018 Interfacial engineering in graphene bandgap *Chem. Soc. Rev.* **47** 3059–99
[1782] Sakintuna B and Yürüm Y 2005 Templated porous carbons: a review article *Ind. Eng. Chem. Res.* **44** 2893–902
[1783] Chatzi E G and Koenig J L 1987 Morphology and structure of kevlar fibers: a review *Polym.-Plast. Technol. Eng.* **26** 229–70
[1784] Stafström S 1987 Electronic properties of polyaniline *Electronic Properties of Conjugated Polymers* ed H Kuzmany *et al* (*Springer Series in Solid-State Sciences* vol 76) (Berlin: Springer)
[1785] Kinloch I A, Suhr J, Lou J, Young R J and Ajayan P M 2018 Composites with carbon nanotubes and graphene: an outlook *Science* **362** 547–53
[1786] Haider S, Khan Y, Almasry W A and Haider A 2012 *Thermoplastic Nanocomposites and their Processing Techniques, Thermoplastic—Composite Materials* (Adel Zaki El-Sonbati: IntechOpen)
[1787] Pionteck J and Wypych G 2007 *Handbook of Antistatics* (ChemTec Publishing)
[1788] Zeng Z *et al* 2012 An effective method for the fabrication of few-layer-thick inorganic nanosheets *Angew. Chem., Int. Ed. Engl.* **51** 9052–6
[1789] Keil S 2017 The Wheatstone bridge circuit *Technology and Practical Use of Strain Gages* (Wilhelm Ernst & Sohn Verlag für Architektur und technische Wissenschaften GmbH & Co. KG) ch 4, pp 147–62
[1790] Tortello M, Pasternak I, Zeranska-Chudek K, Strupinski W, Gonnelli R S and Fina A 2019 Chemical-vapor-deposited graphene as a thermally conducting coating *ACS Appl. Nano Mater.* **2** 2621–33
[1791] Schué L, Sponza L, Plaud A, Bensalah H, Watanabe K, Taniguchi T, Ducastelle F, Loiseau A and Barjon J 2019 Bright luminescence from indirect and strongly bound excitons in h-BN *Phys. Rev. Lett.* **122** 067401
[1792] Damascelli A 2004 *Phys. Scr.* T **109** 61
[1793] Hüfner S 2003 *Photoelectron Spectroscopy* 3rd edn (Berlin: Springer)
[1794] Haworth C A *et al* 2007 *Nat. Phys.* **3** 52
[1795] Whelan P *et al* 2018 Electrical homogeneity mapping of epitaxial graphene on silicon carbide *ACS Appl. Mater. Interfaces* **10** 31641–7
[1796] Mackenzie D M A *et al* 2016 Contactless graphene conductance measurements: the effect of device fabrication on terahertz time-domain spectroscopy *Int. J. Nanotechnol.* **13** 591–6
[1797] Whelan P *et al* 2019 Non-contact mobility measurements of graphene on silicon carbide *Microelectron. Eng.* **212** 9–12
[1798] Lin H *et al* 2017 Contactless graphene conductivity mapping on a wide range of substrates with terahertz time-domain reflection spectroscopy *Sci. Rep.* **7** 10625
[1799] Halbig C, Martin O, Hauke F, Hirsch A and Eigler S 2018 Oxo-Functionalized Graphene: A Versatile Precursor for Alkylated Graphene Sheets by Reductive Functionalization *Chem. Eur. J.* **24** 13348–54